

**Synthesis of Mononuclear and Binuclear
Silver(I) *N*-Heterocyclic Carbene
Complexes for the Treatment of Breast
Cancer**

A thesis submitted by

Oliver Spencer King

in partial fulfilment of the requirements for the degree
of Doctor of Philosophy

UNIVERSITY OF EAST ANGLIA SCHOOL OF
CHEMISTRY

March 2025

© This copy of the thesis has been supplied on condition that anyone who consults it is understood to recognise that its copyright rests with the author and that use of any information derived there-from must be in accordance with current UK Copyright Law. In addition, any quotation or extract must include full attribution.

Acknowledgements

I would firstly like to thank my supervisor Dr Rianne Lord for all the encouragement and support that you have given during my PhD studies, believing in me and allowing me to make this project my own, you have pushed me to become a better scientist. I would also like to extend my gratitude to my co-supervisors Dr Maria J. Marin and Dr John Fielden who have provided me helpful feedback and offering a different perspective on the project.

I would like to thank UEA for funding my studentship and providing the facilities which have allowed me to carry out this research. I am grateful to for the administrative and technical staff from the School of Chemistry who have been supportive and helpful throughout my time at UEA. In particular I would like a thank Dr James Mccoll and Dr Colin Macdonald who assisted me with microscopy and NMR experiments respectively.

I would like to thank all the members of the Lord group and the wider UEA chemistry community who have made the last four years a fun and memorable experience I could not have asked for a better group of people. A special thanks goes to Dr Benjamin Hofmann who taught me Schlenk line techniques and was always there to offer advice. Another special mention goes to Dr Tameryn Stringer who along with Dr Rianne Lord taught me how to carry out the biological experiments. Your support and calmness helped keep me grounded during the more challenging times.

Finally, I would like to thank my family, mum, nan, Rhys and George for their encouragement and support during my studies. I would like to dedicate my thesis my dad and grandfather who were here to see the start of my academic journey but not here to see the end, you are both sorely missed.

Abstract

This thesis is concerned with the synthesis of novel mono- and binuclear Ag(I) *N*-heterocyclic carbene complexes and their utility as agents against breast cancer. The complexes were tested using *in-vitro* experiments to assess cell viabilities and activities, with additional studies to probe their possible mechanisms of action.

Chapter 1 Contains the background on cancer, metal-based chemotherapy, NHCs, synthesis of Ag(I)-NHC complexes and the current literature for their use against breast cancer. The project aims and complex design are also discussed.

Chapter 2 Outlines the synthesis and characterisation of bridged imidazolium salts and their corresponding binuclear Ag(I)-NHC complexes. The dynamics of the complexes were studied by variable temperature NMR spectroscopy and for some of the complexes crystal structures were analysed.

Chapter 3 Presents the synthesis and characterisation of both mono and binuclear derivatives of the complexes outlined in **Chapter 2** and discusses challenges associated with the synthesis. The dynamics of the complexes were studied by variable temperature NMR and for some of the complexes crystal structures were analysed, for the Ag(I)-NHC complex $[\text{Ag}_2(\text{L13})_2](\text{PF}_6)_2$ two conformers were obtained.

Chapter 4 Explores the stability, lipophilicity and cytotoxicity of the complexes that were described in **Chapters 2** and **3**. The *p*-fluoro derivatives were found to be the most active and selective of the complexes tested. For a smaller selection of the complexes mechanistic studies were undertaken.

Chapter 5 Expands work previously done by the group on vanadium β -diketonate complexes by exploring their chemistry with NHC ligands. The synthesis, characterisation and stability are discussed.

Chapter 6 Summarises the findings from the work carried out in this thesis and proposes future work and outlook.

Chapter 7 Contains the experimental, synthesis and characterisation data of the ligands and complexes described within this thesis and the procedures for the biological experiments.

Access Condition and Agreement

Access Condition and Agreement Each deposit in UEA Digital Repository is protected by copyright and other intellectual property rights, and duplication or sale of all or part of any of the Data Collections is not permitted, except that material may be duplicated by you for your research use or for educational purposes in electronic or print form. You must obtain permission from the copyright holder, usually the author, for any other use. Exceptions only apply where a deposit may be explicitly provided under a stated licence, such as a Creative Commons licence or Open Government licence. Electronic or print copies may not be offered, whether for sale or otherwise to anyone, unless explicitly stated under a Creative Commons or Open Government license. Unauthorised reproduction, editing or reformatting for resale purposes is explicitly prohibited (except where approved by the copyright holder themselves) and UEA reserves the right to take immediate ‘take down’ action on behalf of the copyright and/or rights holder if this Access condition of the UEA Digital Repository is breached. Any material in this database has been supplied on the understanding that it is copyright material and that no quotation from the material may be published without proper acknowledgement.

The candidate confirms that the work submitted is their own, except where work which has formed part of jointly authored publications. The additional researcher contributions are explicitly indicated throughout the thesis and the candidate confirms that appropriate credit has been given where reference has been made to the work of others. The reference for the jointly authored paper is stated below:

Fluorinated *N*-Heterocyclic Carbene Silver(I) Complexes with High Cancer Cell Selectivity

O. S. King, B. J. Hofmann, A. E. Boakye-Smith, A. J. Managh, T. Stringer and R. M. Lord, *Organometallics*, 2024, **43**, 2662–2673.

Work from this paper forms parts of chapters 2, 3, 4 and 7.

Abbreviations

Ac	Acetate
Ad	Adamantane
ATR-FTIR	Attenuated total reflectance Fourier-transform infrared spectroscopy
BBS	Bismuth subsalicylate
BF ₄	Tetrafluoroborate
BOC	<i>tert</i> -Butyloxycarbonyl
Bu	Butyl
Ca.	Circa
CDDP	Cis-diamminedichloroplatinum(II)
ct-DNA	Calf thymus DNA
Cy	Cylohexyl
d	Day
d	Doublet
DA	Adenine
DACH	1,2-Diaminocyclohexane
DC	Cytosine
DCF	Dichlorofluorescein
DCM	Dichloromethane
dd	Doublet of doublets
DG	Guanine
Dipp	2,6-diisopropylphenyl
DNA	Deoxyribonucleic acid
Dox	Doxorubicin
DT	Thymine
DTNB	5,5'-dithio-bis-(2-nitrobenzoic acid)
EA	Elemental analysis
eq	Equivalent
ER	Oestrogen receptor
Et	Ethyl
EtBr	Ethidium bromide
Et ₂ O	Diethyl ether
FDA	Food and Drug Administration
Gly	Glycine
h	Hour
H ₂ DFDA	2',7'-Dichlorodihydrofluorescein diacetate
HER2	Human epidermal growth factor receptor 2
HOMO	Highest occupied molecular orbital
HPLC-DAD	High-performance liquid chromatography with diode-array detection
IC ₅₀	Half maximal inhibitory concentration
ICP-MS	Inductively coupled plasma mass spectrometry
IMes	1,3-Bis(2,4,6-trimethylphenyl)-1,3-dihydro-2H-imidazol-2-ylidene

<i>in silico</i>	Computationally calculated
<i>in vitro</i>	Within the glass
<i>in vivo</i>	Within the living
ⁱ Pr	Isopropyl
K	Kelvin
k	Rate constant
K_b	Binding constant
LUMO	Lowest unoccupied molecular orbital
<i>m</i>	Meta
Me	Methyl
MeCN	Acetonitrile
MeOH	Methanol
mes	1,3,5-Trimethylbenzene
min	Minute
mt-DNA	Mitochondrial DNA
MTT	3-(4,5-Dimethylthiazol-2-yl)-2,5-diphenyltetrazolium bromide
NAC	<i>N</i> -acetyl-cysteine
NADPH	Nicotinamide adenine dinucleotide phosphate
ND	Not determined
NHC	<i>N</i> -heterocyclic carbene
NMR	Nuclear magnetic resonance
NO ₃	Nitrate
NOE	Nuclear Overhauser effect
NSCLC	Non-small cell lung cancer
<i>o</i>	Ortho
OTf	Triflate
p	Pentet
<i>p</i>	Para
PBS	Phosphate buffered saline
PF ₆	Hexafluorophosphate
Ph	Phenyl
Phe	Phenylalanine
ppm	Parts per million
Pr	Propyl
PR	Progesterone receptor
PTC	Phase transfer catalyst
q	Quartet
Q	Quaternary carbon
r.t.	Room temperature
ROS	Reactive oxygen species
RSD	Relative standard deviation
s	Singlet
SAR	Structure activity relationship

sc-XRD	Single crystal X-ray diffraction
SD	Standard deviation
SEM	Standard error of the mean
SI	Selectivity index
s.u.s	Standard uncertainties
t	Triplet
^t Bu	tert-Butyl
T _c	Coalescence temperature
THF	Tetrahydrofuran
TNBC	Triple negative breast cancer
Trx	Thioredoxin
TrxR	Thioredoxin reductase
UV-Vis	Ultraviolet–visible spectroscopy
WCRFI	World Cancer Research Fund International
x/s	Excess
Xy	Xylyl
2D	Two-dimensional
3WJ	Three-way junction
4WJ	Four-way junction
°C	Degrees Celsius
ΔΨ _m	Mitochondrial membrane potential

Table of Contents

1	Introduction	1
1.1	Cancer.....	1
1.1.1	Breast Cancers.....	2
1.2	Use of Metallodrugs to Treat Cancer	4
1.2.1	History of Metals in Medicine	4
1.2.2	Platinum-based Chemotherapy	5
1.2.3	Further Developments in Metal-based Chemotherapy.....	7
1.3	Silver(I) <i>N</i> -Heterocyclic Carbenes and their Applications for the Treatment of Breast Cancer.....	11
1.3.1	Background to <i>N</i> -Heterocyclic Carbenes.....	11
1.3.2	Silver in Medicine	16
1.3.3	Synthesis of Silver(I) <i>N</i> -Heterocyclic Carbene Complexes.....	17
1.3.4	Anticancer Activity of Silver(I) <i>N</i> -Heterocyclic Carbene Complexes.....	24
1.3.5	Mechanisms of Action of Silver(I) <i>N</i> -Heterocyclic Carbene Complexes.....	36
1.4	Aims of Project and Design of Complexes	38
1.4.1	Overall Aims and Rationale of the Study.....	38
1.4.2	Specific Objectives.....	40
2	Binuclear Homoleptic Silver(I) <i>N</i> -Heterocyclic Carbene Complexes	42
2.1	Synthesis and Characterisation of Bridged Imidazolium Ligands	43
2.2	Synthesis and Characterisation of Binuclear Silver(I) <i>N</i> -Heterocyclic Carbene Complexes.....	47
2.2.1	¹ H NMR Spectroscopy	49
2.2.2	Dynamic NMR Spectroscopy.....	51
2.2.3	¹³ C{ ¹ H} NMR Spectroscopy.....	60

2.2.4	ATR-FTIR Spectroscopy	62
2.2.5	Single Crystal X-ray Diffraction	63
2.3	Conclusions	75
3	Silver(I) <i>N</i> -Heterocyclic Carbene Derivatives	77
3.1	Benzimidazolium-based Bridged Homoleptic Silver(I) <i>N</i> -Heterocyclic Carbene Complexes.....	78
3.1.1	Synthesis and Characterisation of Bridged Benzimidazolium Ligands	78
3.1.2	Synthesis and Characterisation of Benzimidazole Binuclear Homoleptic Silver(I) <i>N</i> -Heterocyclic Carbene Complexes.....	82
3.1.3	Variable Temperature NMR Spectroscopy	89
3.1.4	X-ray Characterisation of [Ag ₂ (L9) ₂](PF ₆) ₂	94
3.1.5	X-ray Characterisation of Two Conformers of [Ag ₂ (L13) ₂](PF ₆) ₂	96
3.2	Synthesis of Monodentate Homoleptic Silver(I) <i>N</i> -Heterocyclic Carbene Complexes	103
3.2.1	Synthesis and Characterisation of Monodentate Imidazolium and Benzimidazolium Ligands.....	103
3.2.2	Synthesis and Characterisation of <i>p</i> -Fluoro Monodentate Silver(I) <i>N</i> -Heterocyclic Carbene Complexes	106
3.3	Conclusions and Future work.....	113
4	Biological Evaluation of Silver(I) <i>N</i> -Heterocyclic Carbene Complexes	115
4.1	Stability in Aqueous Media.....	115
4.2	Lipophilicity	118
4.3	Cytotoxicity Studies	120
4.3.1	24-hour MTT Assay	120
4.3.2	Varying Nuclearity	129
4.4	Mechanistic Studies.....	132
4.4.1	4-hour MTT Assay	132

4.4.2	Morphological Changes Upon Incubation	133
4.4.3	Interactions with DNA	137
4.4.4	Molecular Docking.....	141
4.4.5	Reactive Oxygen Species Generation	142
4.4.6	Cellular Uptake	146
4.5	Conclusions	148
5	Vanadium β -Diketonate <i>N</i> -Heterocyclic Carbene Complexes.....	151
5.1	Biological Relevance of Vanadium Complexes.....	151
5.2	Vanadium <i>N</i> -Heterocyclic Carbene Complexes	154
5.3	Synthesis and Characterisation of Vanadium (IV and V) β -diketonate <i>N</i> -Heterocyclic Carbene Complexes	156
5.3.1	Synthesis and Characterisation of VO(acac) ₂ (IMes) (V1).....	156
5.3.2	Synthesis and Characterisation of VO(bz bz) ₂ (IMes) (V2).....	160
5.3.3	Synthesis and Characterisation of VO(acac)Cl ₂ (IMes) (V3)	162
5.3.4	Synthesis and Characterisation of VO(bz bz) ₂ (L17) (V4)	164
5.4	Stability of Vanadium (IV) β -diketonate <i>N</i> -Heterocyclic Carbene Complexes.....	169
5.5	Conclusions and Outlook	170
6	Conclusions and Future work.....	173
6.1	Future Work and Outlook	175
7	Experimental and Procedures.....	178
7.1	General Information	178
7.2	Experimental	178
7.2.1	Bridged ligands	179
7.2.2	Binuclear Silver(I) <i>N</i> -Heterocyclic Carbene Complexes	194
7.2.3	Monodentate ligands	207
7.2.4	Mononuclear Silver(I) <i>N</i> -Heterocyclic Carbene Complexes	208

7.2.5	Vanadium <i>N</i> -Heterocyclic Carbene Complexes	210
7.3	Single Crystal X-ray Diffraction	213
7.4	Variable Temperature NMRs	213
7.5	NMR Stability Studies	214
7.6	UV-vis stability studies	214
7.6.1	Stability of Silver(I) <i>N</i> -Heterocyclic Carbene Complexes.....	214
7.6.2	Stability of Vanadium(IV) <i>N</i> -Heterocyclic Carbene Complexes.	214
7.7	Cell Viability Assay	214
7.7.1	Cell Culturing.....	214
7.7.2	MTT Assay.....	215
7.8	Optical Imaging Cell Studies	215
7.9	EtBr Intercalation Assay	215
7.10	Molecular Docking of DNA with [Ag ₂ (L13) ₂](PF ₆) ₂	216
7.11	Reactive Oxygen Species Studies	216
7.12	Cell Uptake.....	217
8	Appendix	218
8.1	ATR-FTIR spectra.....	218
8.1.1	Ligands	218
8.1.2	Silver Complexes	227
8.1.3	Vanadium Complexes	235
8.2	Variable Temperature ¹ H NMR Spectra	236
8.3	Sc-XRD	243
8.4	NMR Stability	250
8.5	UV-Vis Stability.....	251
8.6	EtBr Data.....	255
8.7	ROS Images.....	260
8.8	⁵¹ V NMR Spectroscopy.....	263

9	References	264
---	------------------	-----

1 Introduction

1.1 Cancer

Cancer is an umbrella term for over 200 different diseases, all of which have uncontrolled abnormal cell growth as a defining characteristic.¹ Solid tumours can be malignant (cancerous), which is defined as abnormal cells dividing in an uncontrolled way, and these cells can travel to and infect other tissues of the body (metastasis).^{2,3} This is different from a benign tumour (non-cancerous) which remains in the primary tissue,² and where the cells resemble the surrounding tissue and the growth of the mass is usually slow.⁴

As of 2023, cancer is the second leading cause of death globally after heart disease, accounting for approximately one-sixth of all deaths.⁵ It has been predicted that between 2022 and 2050 the incidence of cancer globally will increase from 22 million (2022) to 35 million (2050), which is an increase of 77%, and this outpaces the predicted population growth in the same period (21%).⁵ This increase is due to a variety of factors including aging populations, increased tobacco use and poor diet.⁶

There is variance in the cancer incidence between men and women which is shown in **Figure 1.1**.⁷ The most prevalent cancers for men and women are lung and breast cancer, respectively, with breast cancer accounting for a quarter of all new cancer cases in women.⁷ For women, breast cancer is also the cause of the highest mortality followed by cervical and colorectal cancer.⁷ For men, lung, liver and colorectal cancer have the highest mortality rates.⁷

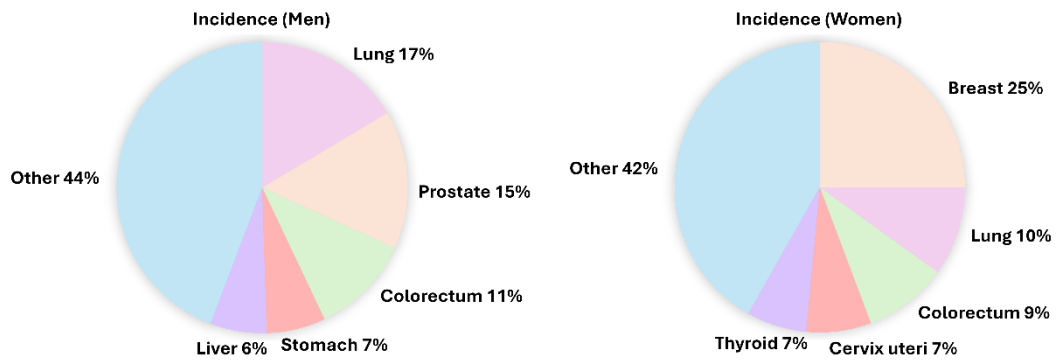


Figure 1.1: Charts showing the percentage incidence of cancer in men and women globally (in 2022). Data was taken from World Cancer Research Fund International (WCRFI) and the image reproduced.⁷

1.1.1 Breast Cancers

Breast cancer is divided into four subtypes: luminal A, luminal B, HER2 and triple negative.⁸ These are classified broadly on the receptors that are present on the cell surface; progesterone receptor (PR), oestrogen receptor (ER), and human epidermal growth factor receptor 2 (HER2).⁹ A summary of the classification is shown in Table 1.1.⁹

Table 1.1: Subtypes of breast cancer and the receptors that are present in each.⁹

Receptor	Subgroup			
	Luminal A	Luminal B	HER2	TNBC
ER	+	+	-	-
PR	-/+	-/+	-	-
HER2	-	-	+	-

The course of treatment is different for each subgroup. For luminal A and B, the term “luminal” refers to the observation that these cancers show protein expression similar to luminal epithelial cells.¹⁰ Luminal A is the most common type of breast cancer, it does not express HER2 receptors but does express oestrogen receptors. Luminal B breast cancer is a more aggressive subtype, and they have a higher level of the protein Ki-67 which makes them grow faster, for both types the progesterone receptor is only sometimes present.^{8,9} The two types of luminal breast cancers are often treated with a mixture of hormone and chemotherapeutic treatment such as tamoxifen and doxorubicin.¹¹ Cancers of the HER2 type are usually treated with

drugs that target the receptor (oestrogen) such as lapatinib.⁸ Out of the four subtypes triple-negative breast cancer (TNBC), which are negative for all the mentioned receptors, are the subtype with the worse prognosis.⁸ The treatment for these cancers is usually a combination of chemotherapy (e.g. doxorubicin or paclitaxel) and radiation to shrink the tumour, followed by surgery (such as mastectomy).¹²

Chemotherapy is used as part of most current treatment course for breast cancer. These agents have many different molecular targets. For example commonly used drugs such as doxorubicin and paclitaxel (**Figure 1.2**) are used, and these target the cell cycle.¹³ Doxorubicin is an anthracycline-based compound that can intercalate with deoxyribonucleic acid (DNA), and interferes with DNA replication mechanisms.¹³ Paclitaxel is a compound that stabilises the assembled form of microtubules during cell division, preventing the completion of mitosis.¹³ Both disruptions lead to apoptosis. As cell division is targeted, these compounds target all fast-growing cells, leading to side effects such as hair loss and anaemia.^{14,15} These side effects are detrimental to the patients, which means more efficient and less toxic alternatives are needed.

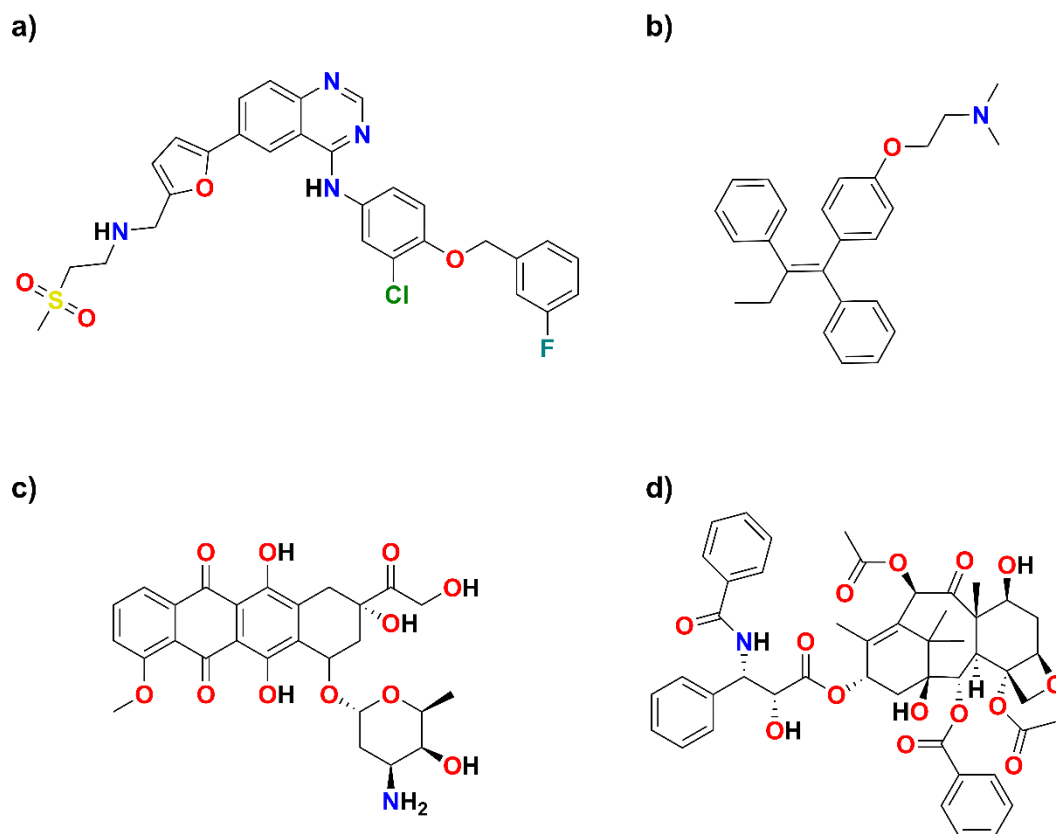


Figure 1.2: Chemotherapeutic drugs (a) lapatinib, (b) tamoxifen (c) doxorubicin and (c) paclitaxel.

1.2 Use of Metallodrugs to Treat Cancer

1.2.1 History of Metals in Medicine

Metals have diverse and varied properties which allow them to be useful for medicinal applications. Metals have been used to treat a variety of ailments since ancient times, such as the reported use of copper for water sterilisation, silver for the treatment of wounds from as early as 2600 BC and arsenic used by Hippocrates for treatment against ulcers.^{16,17} In the early 20th century there has been an expansion in drugs containing metals that have been brought to market, including Salvarsan (arsenic), bismuth subsalicylate (BBS) and gold salts, these were shown to be effective against syphilis, gastritis and tuberculosis respectively.^{18–20} The success of these drugs prompted research to explore the chemotherapeutic applications of metal-based compounds further.

1.2.2 Platinum-based Chemotherapy

The first metal-based anticancer drug to be used clinically is *cis*-diamminedichloroplatinum(II) (cisplatin) which is a square planar platinum(II) compound shown in **Figure 1.3(a)**. While the compound was known in the 1840's as Peyrone's salt, its promise as an anticancer drug was not discovered until the 1960's by Rosenberg et al.²¹ The group were working on the effects of magnetic fields on bacterial growth, where during their experiments they observed an arrest in cellular division.²¹ They discovered that it was not the magnetic field, but a platinum salt produced by the electrode and electrolyte solution was the cause of this inhibited growth.²¹ This finding prompted the group to explore the antitumour properties of platinum-based compounds. In 1969 they reported that a series of Pt(II) and Pt(IV) compounds which could inhibit the progression of sarcoma 180 and Leukaemia L120 in mice, with some showing full remission.²² In 1971 cisplatin entered clinical trials in the US with Food and Drug Administration (FDA) approval obtained in 1978.²³

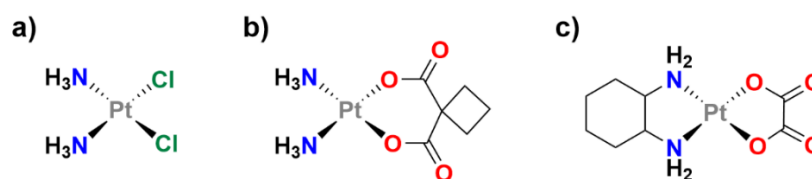
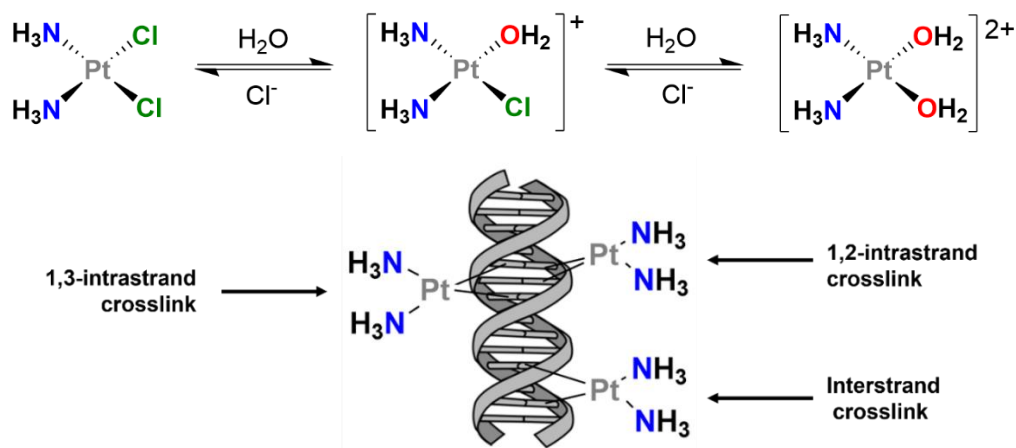


Figure 1.3: Commercial platinum(II) anticancer drugs a) cisplatin b) carboplatin and c) oxaliplatin.

Despite only approximately 1% of intracellular cisplatin being bound to the DNA, it remains a major cellular target of cisplatin.²⁴ Under physiological conditions, especially in the cytosol (with low chloride concentrations), the complex is hydrolysed, with two of the chloride ligands replaced with water (aquation), forming a reactive charged complex (**Scheme 1.1**).²⁵ The chloride gradient between the intra- and extracellular environments favour hydrolysis within the cell. This aqua species can then form intra- and interstrand crosslinks (**Scheme 1.1**) with DNA through nucleophilic attack of the N7 of purine bases of DNA (adenine and guanine).²⁶ The intramolecular 1,2-crosslinks are the most common type, accounting for 90% of the cisplatin-DNA adducts found.²⁶ These cisplatin-DNA adducts result in the inhibition of replication and transcription processes, leading to

apoptosis.²⁶ DNA is not the only target of cisplatin, it has also been shown to accumulate in the mitochondria, causing damage through the generation of mitochondrial reactive oxygen species (ROS), which leads to cell death.²⁷



Scheme 1.1: Hydrolysis of cisplatin under physiological conditions (top) and diagram depicting the three types of crosslinks possible between DNA and cisplatin. Image repurposed and used under creative commons licence (CC-BY) (bottom).²⁸

Cisplatin has found use in the treatment of a wide variety of cancers which include bladder, breast, lung and testicular.²⁹ However, despite its widespread use, cisplatin has two major drawbacks:

1) it has an unfavourable cytotoxicity profile due to the lack of selectivity, with all rapidly dividing cells being sensitive to the drug and causing unwanted patient side-effects such as anaemia and hair-loss.³⁰ Other more severe side effects include, nephrotoxicity (kidney), ototoxicity (hearing) and hepatotoxicity (liver), with the potential permanent damage caused by the treatment regimen.²⁴

2) the increase in cisplatin-resistance within cancer cells, which leads to a lack of effective treatment. There are two types of resistance, intrinsic and extrinsic.^{31,32} Intrinsic resistance is the case where the cancer cell has properties that make it less sensitive to treatment,³¹ whilst extrinsic is when the cancer becomes resistant during treatment.³²

The cancer cells have many mechanisms by which they can combat the toxicity of cisplatin, these include but are not limited to (i) efflux of the drug from the cell, (ii) detoxification of thiol containing proteins (metallothioneins), (iii) DNA repair

processes, and (iv) overexpression of antiapoptotic proteins such as BCL2 and reduced expression of proapoptotic proteins such as BAX and BAD (both implicated in poor response of ovarian cancers to cisplatin).^{31,33,34}

Second and third generations of platinum-based drugs were developed to try and overcome these drawbacks, such as carboplatin **Figure 1.3(b)** and oxaliplatin **Figure 1.3(c)**.³⁵ Compared to cisplatin, carboplatin contains a bidentate cyclobutane dicarboxylate group, instead of two monodentate chloride ligands, which lowers the toxicity due to the slower rate of hydrolysis.³⁵ This allows for higher doses to be administered.³⁵ However, carboplatin has similar mechanisms of action to cisplatin, such as DNA binding, therefore cancers that are resistant to cisplatin are also resistant to carboplatin.^{35,36} Whereas oxaliplatin contains two bidentate ligands 1,2-diaminocyclohexane (DACH) and oxalate.³⁵ This drug has been shown to be active against cancers that are resistant to cisplatin such as metastatic colorectal cancer.³⁵ The lipophilic character of DACH helps the drug enter the cell passively.³⁵ In the case of colorectal cancer, organic cation transporters (OCT1 and OCT2) have been identified to possibly help mediate the entry of oxaliplatin into the cell, in this cancer type these transporter proteins are overexpressed.^{35,37}

1.2.3 Further Developments in Metal-based Chemotherapy

Since the development and success of platinum-based chemotherapy and the need to overcome the limitations of resistance and toxicity, research into metal-based drugs has surged.

After platinum, the most successful metal used in chemotherapy is ruthenium. The first ruthenium-based drug to enter clinical trials was NAMI-A (**Figure 1.4(a)**), a Ru(III) compound which exhibited antimetastatic activities against lung metastases in murine models, however, it was less effective against primary tumours.^{38,39} Phase I trials started in 1999, which focused on the pharmacokinetics and dose tolerance, followed by phase II in 2008 where patients with non-small cell lung cancer (NSCLC) were treated with a combination of NAMI-A and gemcitabine, the results from this trial were deemed “insufficiently effective for further use” and no further trials were conducted.⁴⁰

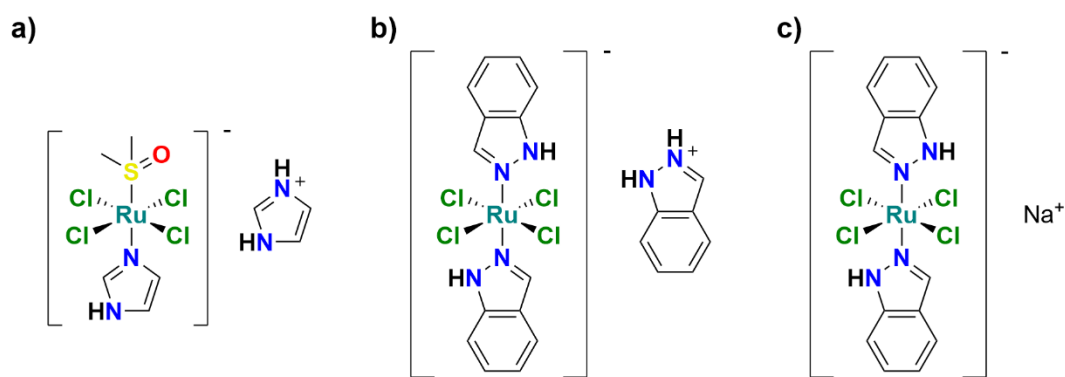


Figure 1.4: Ruthenium-based drugs that have made it to clinical trials a) NAMI-A, b) KP1019 and c) KP1339/BOLD-100.

KP1019, a Ru(III) compound similar to NAMI-A, where the axial ligands were replaced by indazoles and a protonated indazole as the counterion, was reported by Keppler et al. (**Figure 1.4(b)**).⁴¹ It was shown to be active against primary tumours,⁴¹ and effective at reducing the tumour volume of colorectal tumours transplanted into rats.⁴¹ During this study only mild side effects were reported, and this was thought to be in part due to the selective drug uptake by transferrins and/or selective tumour environment reduction of Ru(III) to Ru(II).⁴¹

Due to the promising *in vivo* work, KP1019 entered phase I clinical trials. Compared to NAMI-A, KP1019 had no major side effects, however, the maximum tolerated dose could not be determined due to solubility issues.⁴¹ Despite this limitation to the maximum dose, there was disease stabilisation in the patients treated of up to ten weeks.⁴¹ The solubility issues led to the development the analogous compound KP1339 (later renamed BOLD-100) (**Figure 1.4(c)**) in which the indazolium counterion was replaced by sodium to improve solubility.⁴² BOLD-100 has been through phase I trials, which aimed to demonstrate its effectiveness against solid tumours and to find the maximum tolerated dose.⁴³ The recommendation from this trial was that further studies should use this compound as part of combination therapies.⁴³ Phase I/II trials are ongoing with BOLD-100 and FOLFOX (folinic acid, fluorouracil and oxaliplatin) as a combination treatment, with the interim data suggesting improvements over other recommended treatments, with an increase in progression free survival.⁴⁴

The success of the Pt and Ru based drugs has led to interest in using metals to treat other cancer types such as breast cancer, and particularly the aggressive triple negative breast cancer. One strategy is to incorporate metals into known drug molecules with examples shown in **Figure 1.5**. Babak et al. reported a cyclometalated Au(III) complex (**Figure 1.5(a)**) containing metformin (an antidiabetic drug), and this complex was found to be extremely active against MDA-MB-231 (triple negative breast cancer) with a half maximal inhibitory concentration (IC_{50}) of $0.72 \pm 0.08 \mu\text{M}$ after 72 hours incubation.⁴⁵ Mechanistic studies highlighted that the complex triggers apoptosis through a mitochondrial caspase-3 dependent pathway through inhibition of extracellular signal-related kinase 1 (ERK1), protein kinase B β (PKB β) and insulin receptor kinases.⁴⁵ *In vivo* mouse models showed the complex could slow the progression of tumour growth.⁴⁵ Lu et al. reported a copper Schiff base complex with the non-steroidal anti-inflammatory drug naproxen coordinated to the copper centre (**Figure 1.5(b)**).⁴⁶ The complex was able to reduce both the size and the number of HMLER-shEcad (stem cancer cell enriched mammary epithelial cells) mammospheres when they were treated at IC_{20} (concentration to inhibit 20% of cell growth).⁴⁶ Further experiments indicated that the copper complex induced intracellular ROS and DNA damage, and activation of apoptosis through a caspase dependent pathway.⁴⁶

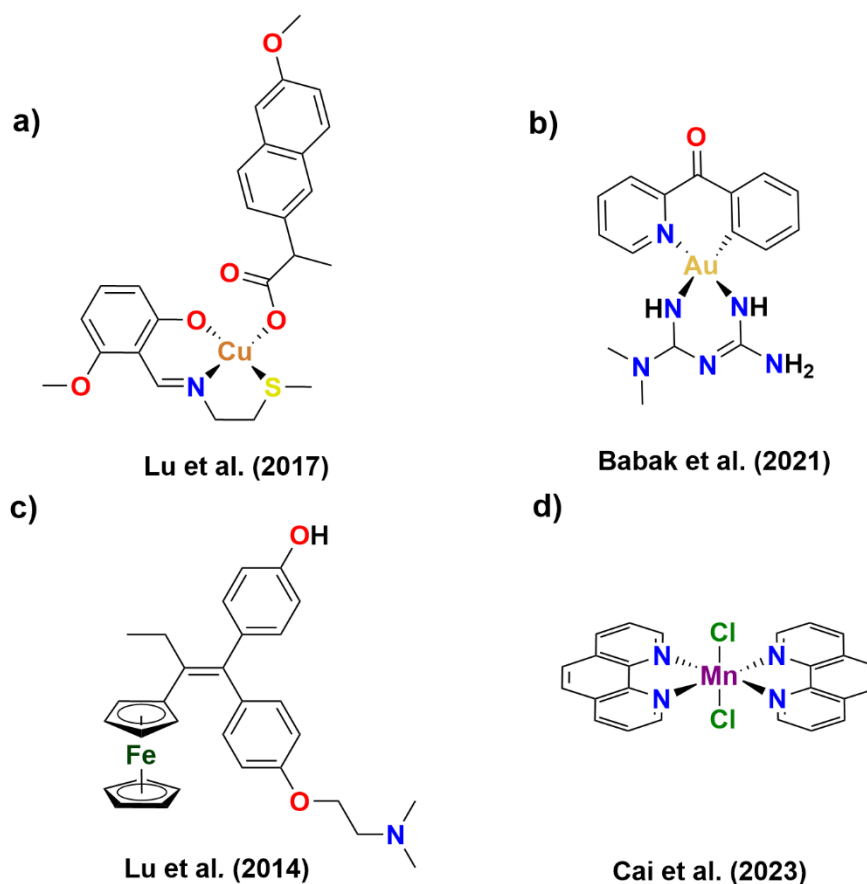


Figure 1.5: Metallodrugs that have shown promising activity against breast cancer.^{45–48}

Some of the metallodrugs discussed so far contain metals (ruthenium and platinum) that have innate toxicities that are associated with them. To help overcome this issue researchers have investigated using either metals that are already found in the body (e.g., vanadium, manganese and iron) or metals that are non-toxic to humans such as silver.^{49,50}

Ferrocifen (**Figure 1.5(c)**), an iron-containing complex, is one of the most promising examples.⁵¹ This molecule is a ferrocenyl modified version of tamoxifen and is active against TNBC (MDA-MB-321), this activity is not seen in the precursor.⁵² This is an example of how conjugating a metal to a known drug can increase its activity. They can generate ROS through Fenton-type reactions, which are catalysed by the iron centre, and this followed by subsequent apoptosis, is thought to be linked to their activity.⁴⁷ Another example of a biotic transition metal based breast cancer drug was reported by Cai et al. which is a manganese complex with phenanthroline and chloride ligands (**Figure 1.5(d)**).⁴⁸ The complex exhibits

activity against MDA-MB-231 and induces ROS generation. The complex caused cell cycle arrest at the G₂ phase, suggesting the complex interferes with DNA synthesis possibly due to ROS induced DNA damage.⁴⁸ It was shown to also inhibit the DNA repair proteins HDACs and PARP1, which leads to the activation of pro-apoptotic pathways.⁴⁸

1.3 Silver(I) *N*-Heterocyclic Carbenes and their Applications for the Treatment of Breast Cancer

1.3.1 Background to *N*-Heterocyclic Carbenes

1.3.1.1 Carbenes

Carbenes are compounds that have a neutral divalent carbon with six electrons in the valence shell.⁵³ The geometry of the carbon can either be bent or linear, and this is dependent on the hybridisation of the carbon, sp^2 or sp respectively. An energy level diagram for the bent and linear forms of the carbenes are shown in **Figure 1.6**.⁵⁴ For the linear mode the p_x and p_y orbitals are degenerate and each accommodate one unpaired electron.⁵⁴ If the molecule is bent the degeneracy of these orbitals is broken and sp^2 hybridisation is adopted. This lowers the energy of the σ -orbital compared to the p -orbital, and the energy gap between these orbitals dictates whether the carbene will be a triplet ($^1p\pi^1\sigma$) or singlet ($^0p\pi^2\sigma$), where a larger energy gap favours the singlet carbene.⁵³

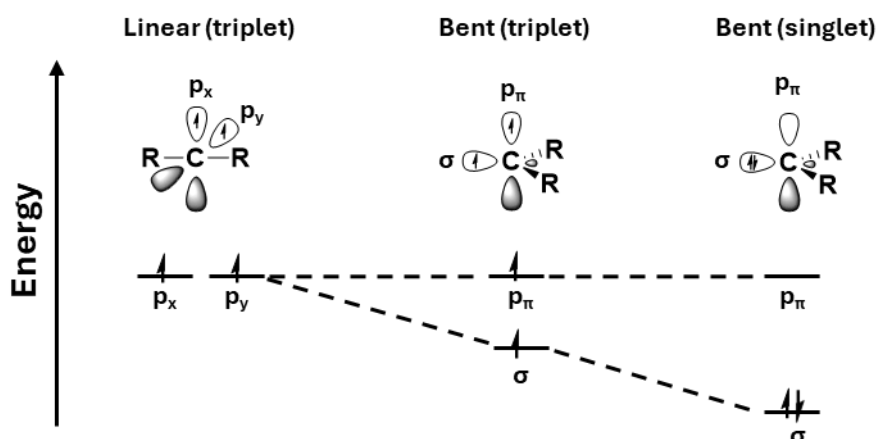


Figure 1.6: Frontier orbitals of the carbene carbon in both linear and bent geometries.⁵⁴

N-Heterocyclic carbenes (NHCs) are an example of a singlet carbene.⁵³ They are defined as heterocyclic compounds that contain at least one nitrogen atom and have at least one carbene carbon.⁵³ In classical NHCs, the carbene is stabilised by two adjacent nitrogens to the carbene carbon, and these nitrogens stabilise the carbene in two different ways, (i) inductively through the electron withdrawing effects of the nitrogens and (ii) mesomerically through the donation of the lone pairs in the p_π orbitals of the N atoms into the empty p_π orbital of the carbene carbon atoms (**Figure 1.7**).⁵³ The inductive stabilisation of the electron withdrawing nitrogen atoms lowers the energy of the σ -nonbonding orbital (highest occupied molecular orbital, HOMO) on the carbene carbon, and this favours the singlet state.⁵³ If the adjacent atoms were electropositive the triplet state would be favoured (due to the lowering of the σ - p_π gap). The mesomeric effect involves the interaction of the p_π orbital and the lone pairs of the nitrogen atoms, where the donation of electron density into the empty p_π orbital (lowest unoccupied molecular orbital, LUMO) on the carbene increases the energy.⁵³ The donation of the nitrogen lone pairs is so significant that the electrons are delocalised along the N-C-N bonds and the structure is drawn with this delocalisation represented.⁵³ The combination of both the inductive and mesomeric effects leads to the stabilisation of the singlet carbene. The ring also forces the carbene into a bent configuration which also favours the singlet state (see **Figure 1.6**).

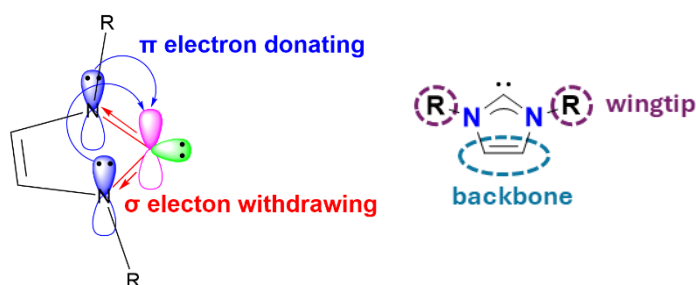
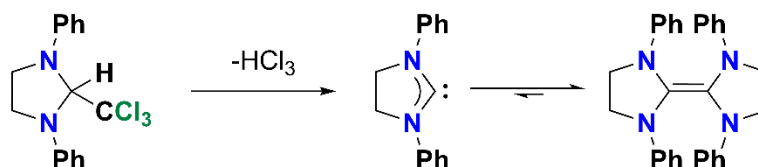


Figure 1.7: (left) Diagram depicting the carbene stabilising effects of the adjacent nitrogen atoms, (right) naming nomenclature for NHCs.⁵³

1.3.1.2 History of N-Heterocyclic Carbenes

NHCs were first discovered by Wanzlick in the 1960s.⁵⁵ The bis-[1,3-diphenyl-2-imidazolidinylidene] **Scheme 1.2(a)** was synthesised by the removal of chloroform from 1,3-diphenyl-2-trichloromethylimidazolidine and analysis of the white crystalline product indicated the species formed was an NHC dimer **Scheme 1.2(b)**.⁵⁵ The dimer exists in an equilibrium with the free carbene (Wanzlick equilibrium), and the free carbene is not stable enough to be isolated.⁵⁶



Scheme 1.2: Synthesis of first reported NHC compound and the Wanzlick equilibrium between free carbene and dimer.⁵⁵

In the late 1960s, the first transition metal NHC complexes were reported of mercury (Wanzlick and Schönherr) and cobalt (Öfele) respectively (**Figure 1.8**, top).^{57,58} The strong metal carbene bonds stabilised the NHC. However, the first free-carbene was not isolated until much later by Arduengo et al., where in 1991 they isolated an imidazolium-based carbene with adamantyl substituents (**Figure 1.8**, bottom).⁵⁹ The compound was found to be stable in an oxygen and moisture free environment and could melt without decomposition, which is why this compound is considered the first “bottleable carbene”.⁵⁹ Further work from Arduengo showed that large steric bulk was not required for stabilisation (electronic stabilisation was sufficient) of the free carbene, and they were able to isolate a

carbene that had methyl substituents, and where the carbene was found to be stable even up to a melting temperature of 110 °C.⁶⁰

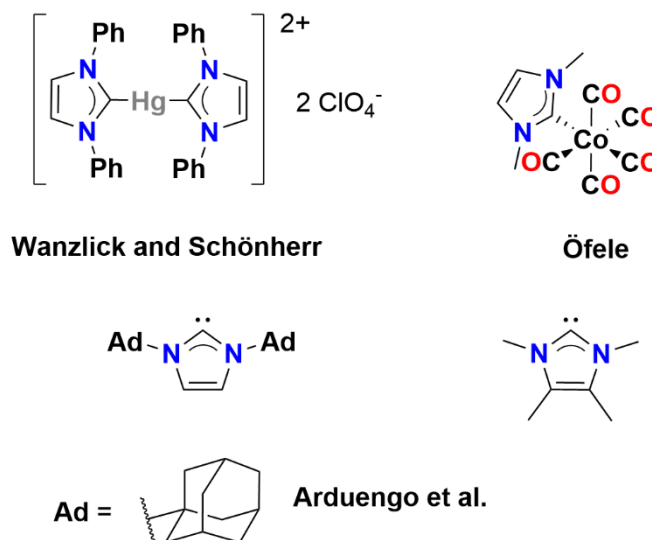


Figure 1.8: (top) The first metal-NHC complexes reported by Wanzlick and Öfele.^{57,58} (bottom) Free NHCs synthesised by Arduengo, Harlow and Kline including the first reported (adamantyl functionalised) free-NHC.^{59,60}

The strong σ donor character of NHCs make them good ligands for coordination to transition metals where they can interact with a σ accepting orbital on the metal.⁵³ There are examples of NHC complexes coordinated to every element in the d -block.⁶¹ These complexes have found utility in many areas such as hetero- and homogenous catalysis, C-H activation and as metallopharmaceuticals.^{53,62,63}

1.3.1.3 The Diversity of NHC Structures

The first reported NHCs were based on the imidazole scaffold and since then many different types of NHCs have been synthesised. Some important examples are shown in **Figure 1.9**. These show the diversity in azole structures, for example, variations have been made to the backbone (**Figure 1.9(a)**), heterocycle (**Figure 1.9(b)**), and heteroatom in the α -position (**Figure 1.9(c)**).⁵³ As well as the classical type, other abnormal NHCs (aNHCs), also referred to as mesoionic carbenes, have been reported (**Figure 1.9(d)**).⁵³ In this case, the carbene is on the C4 position (adjacent to one nitrogen) instead of the C2 position (between two nitrogens), which in the case of the example is substituted).⁵³

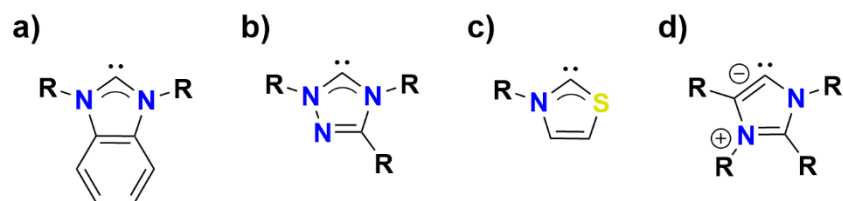


Figure 1.9: A selection of different possible azoles that can form NHCs, (a) benzimidazole, (b) 1,2,4-triazole, (c) thiazole and 2,4-disubstituted imidazole.⁵³

These carbenes have varied electronics which give rise to different σ donation capabilities, and the strengths have been quantified in different ways by various research groups. The first system uses Rh(I) or Ir(I) carbonyl complexes **Figure 1.10(a)**.⁶⁴ The more electron donating the NHC, the higher the electron density will be on the metal centre, causing a higher degree of back-bonding to the carbonyl and a weakening of the CO triple bond. This leads to a lower wavenumber for the CO stretches in the infrared spectra.⁶⁴ For this method the average value of the cis and trans carbonyl stretches (ν_{av}) of the square planar rhodium complex are taken.⁶⁴ Data taken from a recent review by Huynh shown in **Figure 1.10** exemplifies how this system can show that unsaturated **Figure 1.10(c)** and abnormal carbenes **Figure 1.10(d)** have stronger electron donation capability compared to the classical imidazole **Figure 1.10(b)** based Arduengo type. This can be seen in the lower ν_{av} values for abnormal and unsaturated carbenes.⁶⁴

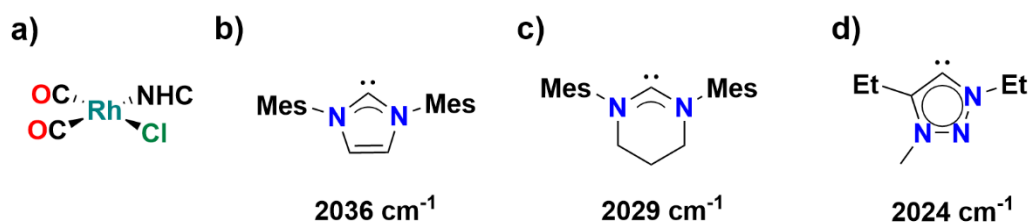


Figure 1.10: a) Reporter rhodium complex, NHC = b) saturated, c) unsaturated and d) abnormal NHCs with the carbonyl stretches measured when coordinated to the rhodium complex reporter complex.⁶⁴

An alternative method developed by Meng et al. uses ^1H NMR spectroscopy to access the hybridisation of the carbene carbon in the precursor salt. The s-character of the carbene carbon can be estimated by measuring the coupling of the C2 carbon and its proton ($^1J(^{13}\text{C}-^1\text{H})$), a larger coupling indicates more s character. The hybridisation (s-character) can be directly related to the σ donor ability, the larger

the s-character the weaker the donation. The results from their study confirmed experimentally that saturated NHCs are better donors than unsaturated NHCs.⁶⁵

1.3.2 Silver in Medicine

Silver is classed as a xenobiotic metal and serves no known biological function;^{50,66} it is generally considered to be non-toxic to humans, however prolonged exposure can lead to argyria.^{50,67} Silver is taken up in the body by many ways such as ingestion, inhalation and from use in medical wound dressings, however, only small amounts of silver are present in the body ($< 2.3 \mu\text{g/L}$).^{67,68} The biliary route is the main mode of excretion in humans.^{67,69} Despite not being toxic to humans silver has been shown to be toxic against bacterial and fungal cells.^{68,70}

For over 2000 years, silver has been used for medicinal applications, where it was first used in drinking vessels in antiquity to prevent mould growth.⁶⁸ In the 1800s silver nitrate (AgNO_3) was found to be beneficial in the treatment of severe burn wounds, helping prevent infection during the long healing process.⁷¹ The next milestone in silver burn treatment came in the form of silver sulfadiazine (**Figure 1.11(a)**), which is a combination of silver and the sulfonamide-based drug sulfadiazine. This is an example of combining two active drugs into one compound.⁷² Recent reviews have suggested that antibiotics are more effective against second degree burns, however silver sulfadiazine is still widely used for third degree burns.^{73,74}

Since the success of silver sulfadiazine, many groups have developed new silver complexes as antimicrobials. The polymeric complex shown in **Figure 1.11(b)** was the first Ag(I) -NHC complex to be tested for antibacterial properties, and it was found to be more active than AgNO_3 against multiple strains of bacteria including *Escherichia coli* (*E. coli*), *Pseudomonas aeruginosa* (*P. aeruginosa*) and *Staphylococcus aureus* (*S. aureus*).⁷⁵ Melaiye et al. then reported the antibacterial effects of the binuclear complex shown in **Figure 1.11(c)**, which was encapsulated on TecophilicTM nanofibers.⁷⁶ When encapsulated, the complex was more effective against a range of clinically relevant bacteria compared to AgNO_3 and silver sulfadiazine, however, the complex without encapsulation was not active.⁷⁶

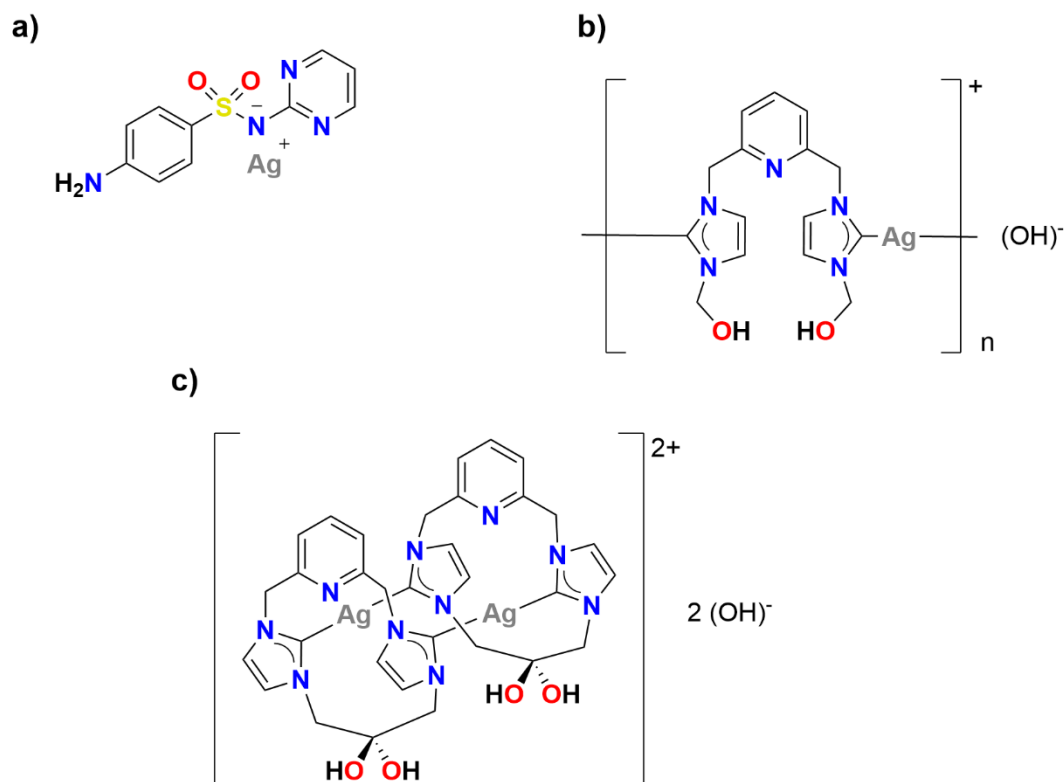
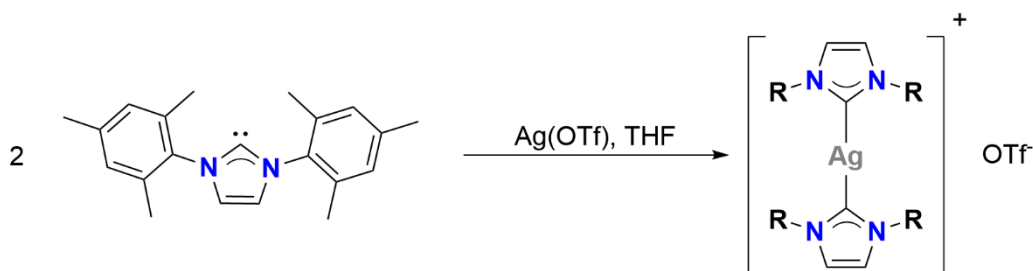


Figure 1.11: a) Silver sulfadiazine used in burn treatments⁷³, b) The first Ag(I)-NHC complex reported for use in medicinal applications⁷⁵ and c) A binuclear Ag(I)-NHC which was found to be more effective against clinically relevant bacteria.⁷⁶

1.3.3 Synthesis of Silver(I) N-Heterocyclic Carbene Complexes

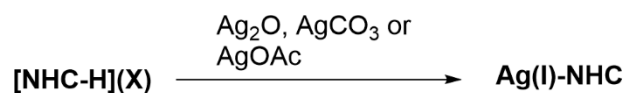
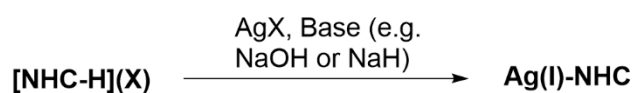
In 1993, Arduengo et al. reported the synthesis of the first Ag(I)-NHC complex, a homoleptic complex $[\text{Ag}(\text{IMes})_2](\text{OTf})$, where IMes is 1,3-bis-(2,4,6-trimethylphenyl)imidazol-2-ylidene and OTf is triflate.⁷⁷ The complex was synthesised by reacting the free IMes carbene with silver triflate (**Scheme 1.3**).⁷⁷ The complex was found to be stable to ligand exchange even in solvents such as pyridine (which is not the case for other silver complexes).⁷⁷



Scheme 1.3: Synthesis of first isolated Ag(I)-NHC complex ($[\text{Ag}(\text{IMes})_2](\text{OTf})$) reported by Arduengo et al.⁷⁷

Since their discovery by Arduengo, three main routes to access Ag(I)-NHC complexes have been established, these are summarised in **Scheme 1.4**. The first is the “free-carbene route” (route 1), which has the benefit that the carbene is preformed. However, this method requires air-sensitive conditions and the ability to isolate the free carbene of choice, which is not possible for some carbenes. The second approach is the use of a silver precursor with an internal base (route 2) which deprotonates the azolium salt and provides the silver ion for metalation. The first reported synthesis using this route was from Bertrand et al., where two equivalents of $\text{Ag}(\text{OAc})$ was reacted with a dicationic triazolium salt to form a bis-carbene complex $[\text{Ag}(\text{L})_2](\text{OTf})_3$ ($\text{L} = 2,4\text{-dihydro-}1,2,4\text{-trimethyl-}3\text{H-}1,2,4\text{-triazolium-}3\text{-ylidene}$).⁷⁸ Wang et al. then reported the use of silver(I) oxide as an efficient base for the formation of a bis-benzimidazole Ag(I)-NHC complex $[\text{Ag}(\text{L})_2](\text{AgBr}_2)$ ($\text{L} = 1,3\text{-diethylbenzimidazol-}2\text{-ylidene}$).⁷⁹ The third method is the external base route, where the azolium salt is deprotonated *in-situ* and the carbene then reacts with a silver source. This method was also reported by Wang et al. using sodium hydroxide as the base.⁷⁹

The silver(I) oxide method has become the most popular, as (i) there is an internal base and so an external based is not required, (ii) the metalation in most cases occurs at room temperature and does not require air sensitive conditions, and (iii) the base is tolerated by reactive H groups and mostly selectively deprotonates in the C2 position (between the nitrogens).^{80,81}

Free carbene route (route 1)**Internal base route (route 2)****External base route (route 3)**

Scheme 1.4: Three general synthetic routes for synthesising Ag(I)-NHCs ($X = \text{Cl}, \text{Br}, \text{I}, \text{NO}_3, \text{BF}_4, \text{PF}_6$).

1.3.3.1 Silver(I) N-Heterocyclic Complexes from Mono-azolium Salts

Silver(I) oxide and mono-azolium salts can be used to generate a wide variety of Ag(I)-NHC complexes, where the final structure is influenced by the counterions, and solvents used in the synthesis. There are seven common structures (described in the review of Lin et al.) that are reported from the silver(I) oxide route, examples of each are shown in **Figure 1.12**.^{79,82–85}

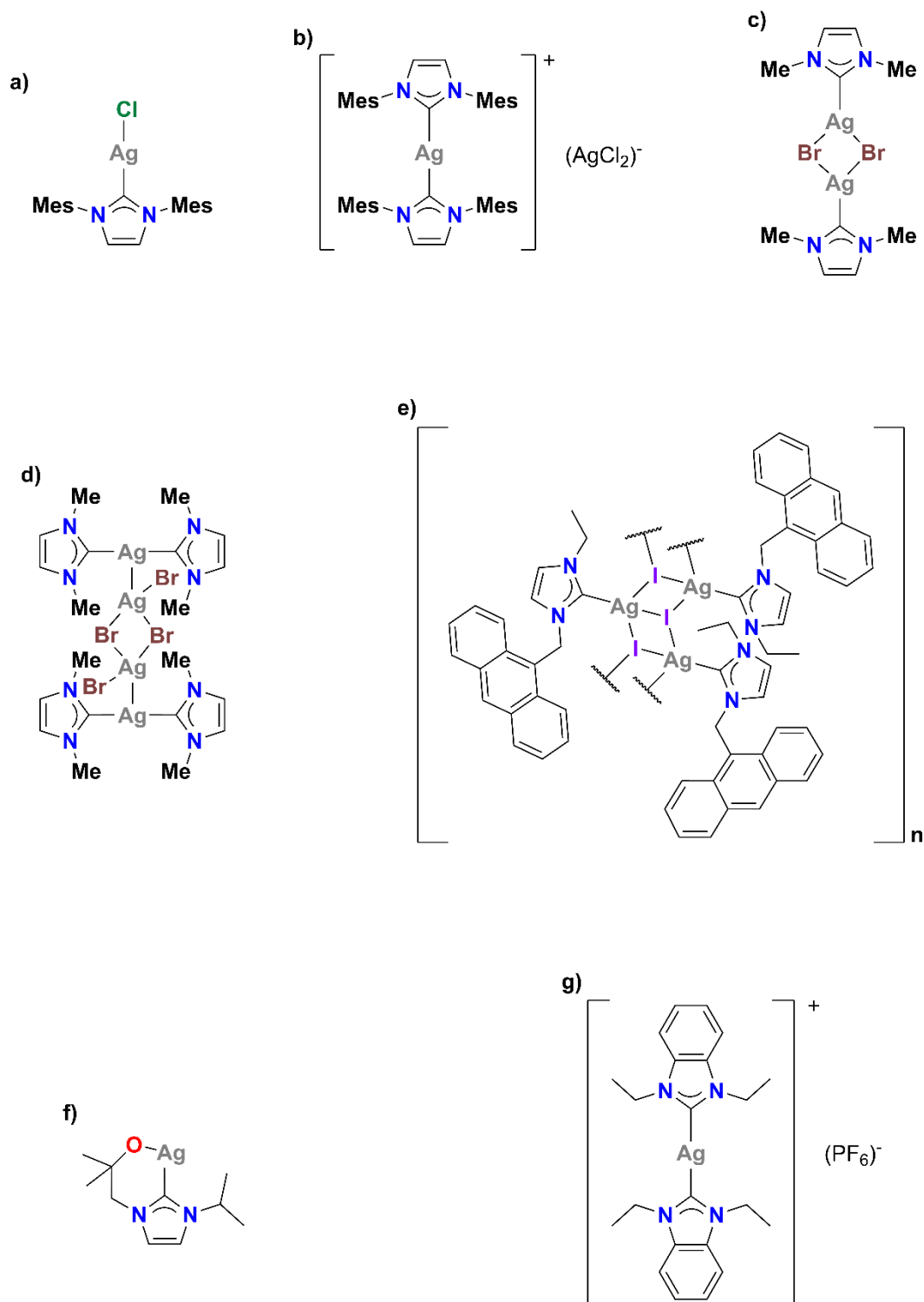
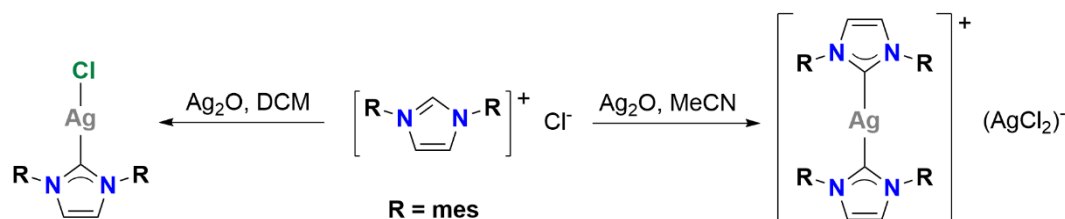


Figure 1.12: Examples of reported Ag(I)-NHCs showing the diversity in possible structures.^{79,82–85}

The azolium halide salts generate the most diverse array of structures, and this is due to the ability of the halide to coordinate to the silver centre. Frémont et al.

reported that solvent polarity can influence whether neutral or charged products are formed, and they reported a bis-carbene product $[\text{Ag}(\text{IMes})_2](\text{AgCl}_2)$ when MeCN was used as the reaction solvent (**Scheme 1.5**). However, Ramnial et al. had previously reported the neutral complex $\text{Ag}(\text{IMes})\text{Cl}$ (**Figure 1.12(a)**) when DCM was used.^{82,86} This result indicated that the more polar solvent MeCN ($\epsilon = 36.6$) stabilises the ionic bis-carbene product and the less polar solvent dichloromethane ($\epsilon = 9.1$) stabilises the neutral product.^{82,87}



Scheme 1.5: (Left) synthesis of neutral complex $\text{Ag}(\text{IMes})\text{Cl}$ reported by Ramnial et al. and (right) synthesis of charged bis complex $[\text{Ag}(\text{IMes})_2](\text{AgCl}_2)$ reported by Frémont et al.^{82,87}

:

The mononuclear species are not the only type that can form from the reaction of an azolium halide salt and silver(I) oxide in non-polar conditions. The halides can form bridges between silver centres forming multinuclear species, for example, Lee et al. reported two species which had the same stoichiometry but different structures.⁸³ The binuclear complex in **Figure 1.12(b)** was formed via the reaction of the imidazolium bromide salt with half an equivalent of silver(I) oxide and isolated by recrystallisation with acetone.⁸³ The product from the reaction was also recrystallised from DCM/hexane and gave the tetranuclear complex in **Figure 1.12(d)**.⁸³

The reactions of imidazolium salts with silver(I) oxide in non-polar solvents do not always generate discrete species. For example, Liu et al. reported a polymeric species **Figure 1.12(e)**, which was generated from the reaction of an imidazolium iodide salt with silver(I) oxide in DCM.⁸⁴ The polymer is one dimensional and forms a “staircase” structure.⁸⁴

Other binding modes are also possible when the wingtips have moieties that can also coordinate to the silver centre. These can include groups like alkoxides and pyridines, for example, the complex reported by Edworthy et al. (**Figure 1.12(f)**).⁸⁵ This complex is generated by the reaction of a tertiary alcohol functionalised imidazolium salt with silver(I) oxide, which in this case deprotonates both the C2 on the imidazolium and the alcohol.⁸⁵

When the pro-ligand has a weakly coordinating anion (X) such as hexafluorophosphate (PF₆) or tetrafluoroborate (BF₄), the complexes usually form [Ag(NHC)₂](X) structures. The weakly coordinating nature of the anion prevents the neutral complexes from forming. The first homoleptic Ag(I)-NHC complex of this type was reported by Wang et al. (**Figure 1.12(g)**), where a benzimidazolium hexafluorophosphate salt was reacted with silver(I) oxide in basic conditions with a phase transfer catalyst (PTC) in DCM.⁷⁹ It is notable that even though this reaction was carried out in DCM (a relatively non-polar solvent) the ionic bis-carbene complex was formed. This highlights the importance of the counter ion in dictating the structure of the product.

1.3.3.2 Silver(I) N-Heterocyclic Complexes from Multi-azolium Salts

If a multi-azolium ligand is used, complexes containing many silver centres can be accessed. The azoles are separated by a linker (called a “bridge” within literature), such as *o*-xylene shown in the **Figure 1.13(a)**, which was the first multi-carbene Ag(I)-NHC complex reported.⁸⁸ The first bis-carbene silver complex was reported by Tulloch et al. (**Figure 1.13(a)**), and this was synthesised from the bromide salt of the pro-ligand in DCM.⁸⁸

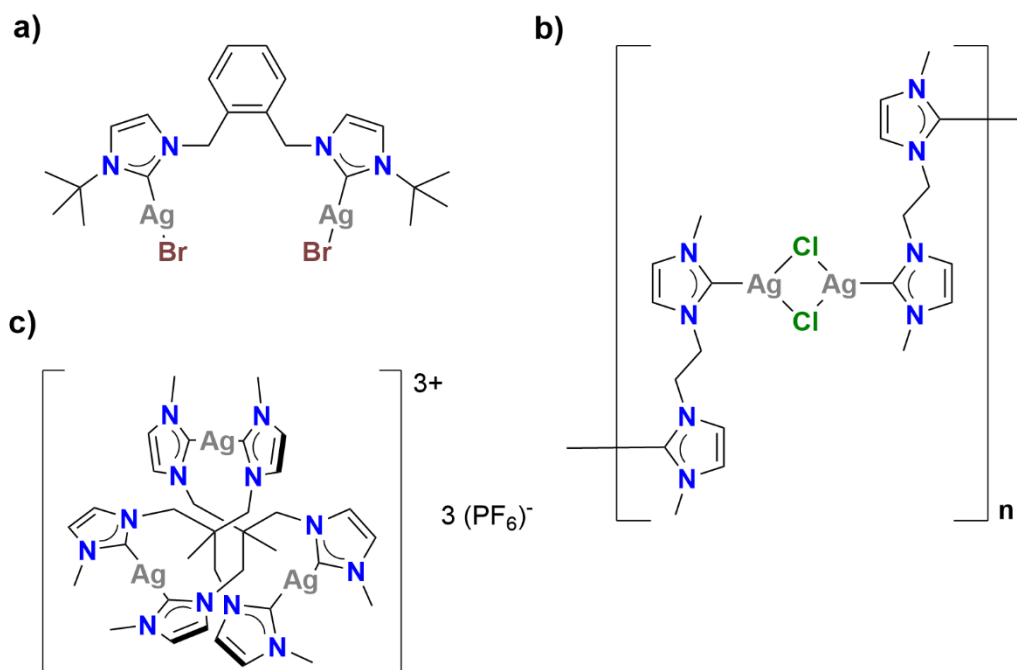


Figure 1.13: First reported multinuclear Ag(I)-NHC complexes.^{83,88,89}

Lee et al. reported a bis-carbene that was separated by an ethyl linker, and the chlorides from the pro-ligand form chloride bridges.⁹⁰ The other carbene on each ligand binds to a separate silver ion, thus forming a staggered one-dimensional chain (**Figure 1.13(b)**).⁹⁰ Hu et al. synthesised the first discrete homoleptic multi-carbene complex (**Figure 1.13(c)**), using a tripodal imidazolium hexafluorophosphate salt. This complex highlights the utility of using weakly coordinating anions to generate discrete ionic Ag(I)-NHC complexes.⁸⁹

Since these first reported complexes, there has been a major focus on the synthesis of multi-nuclear Ag(I)-NHC complexes, due to their diverse range of three-dimensional structures. One notable example was reported by Altmann et al. in which two carbene containing cyclophanes form an octameric Ag(I)-NHC complex (**Figure 1.14(a)**). This was coined as a “pillarplex” which contains a cavity that can participate in host-guest chemistry.⁹¹ More recently these complexes have been investigated for their ability to interact with DNA, and the complex was found to stabilise DNA three-way junctions (3WJ) and four-way junctions (4WJ).⁹²

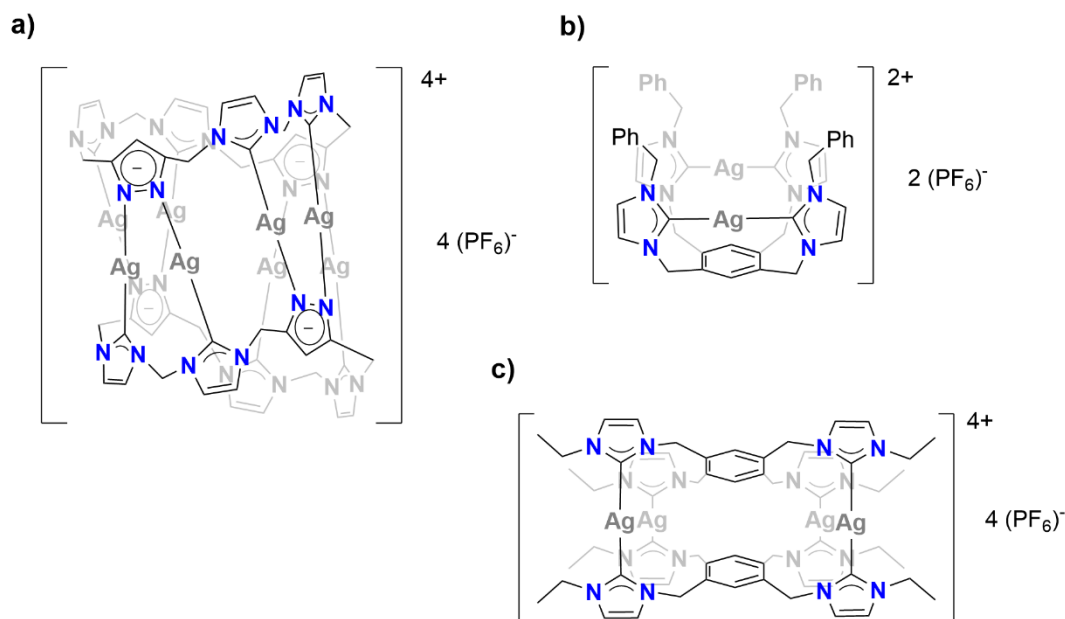


Figure 1.14: Multinuclear Ag(I)-NHC complex synthesised by (a) Altmann *et al.* and (b – c) Ahamed *et al.*.^{91,93}

The wingtip substituents can influence the conformation of the complex that is formed. This is highlighted by the work of Ahamed *et al.*, where a series of tetrapodal xylyl linked ligands in which the R group was varied from methyl, ethyl and benzyl were synthesised.⁹³ The two complexes shown in **Figure 1.14(b and c)** were synthesised using the same conditions (MeCN, r.t.) with the same equivalents of silver(I) oxide (4 eq).⁹³ The binuclear complex (**Figure 1.14(b)**) formed from the benzyl functionalised ligand is a basket-shape and includes one ligand with intra-ligand binding.⁹³ However, when the wingtip is changed from a benzyl to an ethyl, a complex with two ligand and four silvers forms (**Figure 1.14(c)**), highlighting how wingtip changes can significant influence the structure of the final complexes.⁹³

1.3.4 Anticancer Activity of Silver(I) *N*-Heterocyclic Carbene Complexes

The promising antimicrobial results of Ag(I)-NHC complexes (**Figure 1.11**) prompted Medvetz *et al.* to study the anticancer properties.⁹⁴ They tested complexes of the type Ag(OAc)NHC shown in **Figure 1.15** with the most active being R = butyl.⁹⁴ The complexes were tested against three cancer types, with this complex giving the highest activity (IC₅₀) against MB157 (breast, 8 μM) and moderate activity against OVCAR-3 (ovarian, 35 μM), however, it was inactive against HeLa

(cervical, $>200\ \mu\text{M}$).⁹⁴ Since this discovery, there has been a surge in research on the anticancer potential of Ag(I)-NHC complexes.

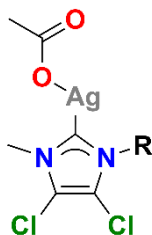


Figure 1.15: First anticancer Ag(I)-NHC reported by Medvetz et al., $R = \text{Me}$, butyl, 2-methylnaphthyl.⁹⁴

Since breast cancer remains one of the biggest contributors to cancer mortality rates, this thesis focuses on the use of Ag(I)-NHC complexes for breast cancer treatments. This section briefly outlines the activity of the NHC proligand and neutral Ag(I)-NHC complexes followed by a larger focus on homoleptic Ag(I)-NHC complexes and highlights any structure activity relationships (SARs) that can be established. It can be difficult to establish SARs by comparing the activities from different studies in the literature as often different incubation times, cell seeding, viability assays and conditions are used, so any comparisons made are not absolute.

In the literature there are three main breast cell lines that have been used for the testing of Ag(I)-NHC complexes, these include MDA-MB-231 (hormone independent TNBC), MCF-7 (hormone dependent) and MCF10A (non-cancerous). The differences between toxicity values will be considered statistically significant when $P \text{ value} < 0.05$, and a compound will be considered non-toxic when the IC_{50} values $>100\ \mu\text{M}$.

1.3.4.1 *N-Heterocyclic Carbene Proligands*

Both the imidazole and benzimidazole moiety are ubiquitous in medicinal chemistry and are found in many pharmaceuticals. It is for this reason that imidazolium and benzimidazolium salts (that are precursors to NHC complexes) have been explored as anticancer agents. The general structures and sites of possible modifications are shown in **Figure 1.16**. For the monodentate salts the (i) backbone, (ii) R_1 and (iii) R_2 wingtips and (iv) counterion can be modified, and the bridged versions are similar apart from R_2 is now the bridging group (in symmetric complexes $R_1 = R_2$).

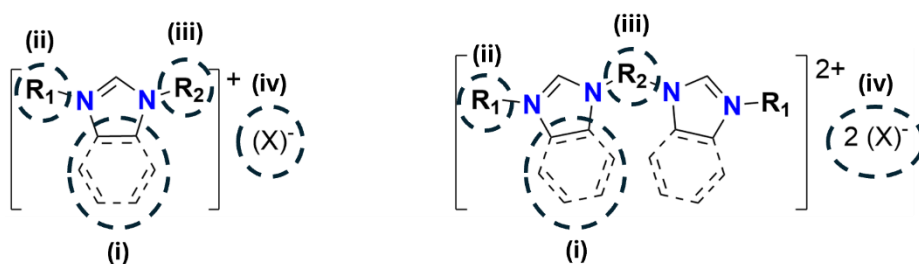


Figure 1.16: Sites of modification of monodentate (left) and bridged (right) azolium salts.

The effect of the backbone on anticancer activity was investigated by Lin et al.⁹⁵ They synthesised a series of symmetrical naphthyl functionalised azolium salts (**Figure 1.17**) with imidazole, benzimidazole and 1,2,4-triazole backbones, and determined their IC₅₀ values against the TNBC cell line MDA-MB-468 (72-hour incubation). The imidazole was the most active compound ($5.0 \pm 0.4 \mu\text{M}$) followed by benzimidazole ($9.7 \pm 0.4 \mu\text{M}$), and 1,2,4-triazole ($15.8 \pm 0.4 \mu\text{M}$).⁹⁵ An *N*-benzyl derivative of the 1,2,4-triazole salt was synthesised and the activity decreased to $86.4 \pm 0.2 \mu\text{M}$, highlighting the importance of the wingtip for activity. The results suggest a naphthyl pendant arms is a good motif for increasing activity.⁹⁵

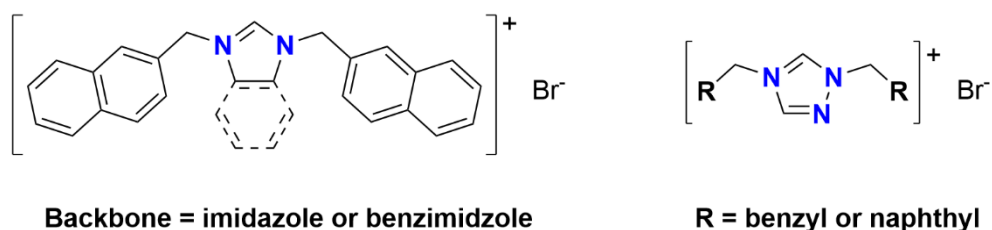
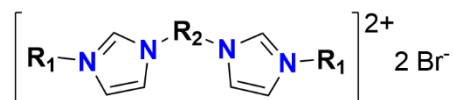


Figure 1.17: Salts investigated by Lin et al. for their activity against MDA-MB-468 with 72-hour incubation.⁹⁵

Habib et al. and Haque et al. both explored the activity of bridged imidazolium and benzimidazolium salts respectively against breast cancer (**Figure 1.18**). Haque et al. synthesised symmetric imidazolium salts with functionalised *o*- or *m*-cyanobenzyl wingtips.^{96,97} After 72-hour incubation against MCF-7, the *meta* derivative had low toxicity ($82.4 \pm 2.5 \mu\text{M}$), whereas the *ortho* derivative was non-toxic. Habib et al. kept the wingtips (methyl) the same but varied in the bridging substituent (butyl, pentyl, and *m*- or *p*-xylyl), all the derivatives apart from *p*-xylyl ($79.5 \pm 0.7 \mu\text{M}$) were non-toxic against MDA-MB-231 (72-hour incubation).⁹⁸ For

both of these series only one compound in each was active and for this reason no SAR could be established.



$\text{R}_1 = o$ or m -cyanobenzyl, $\text{R}_2 = \text{methyl}$, (Haque, 2014 and 2016)

$\text{R}_1 = \text{methyl}$, $\text{R}_2 = \text{butyl}$, pentyl , and m or p xylyl, (Habib, 2019)

Figure 1.18: Imidazolium complexes reported by Haque et al. and Habib et al. tested against MCF-7 and MDA-MB-231 respectively.^{96–98}

1.3.4.2 Neutral Silver(I) N-Heterocyclic Carbene Complexes

Following on from the work of Medvetz et al., several groups have focused on the development of active neutral-NHC complexes. These complexes can be modified in four positions **Figure 1.19**, (i) the backbone, (ii and iii) wingtip positions and (iv) ligand trans to the NHC. These complexes can be either symmetric or asymmetric depending on the wingtip substitution.

Backbone	R ₁	R ₂	X	Ref
benzimidazole	9-methylanthracenyl	methyl or <i>tert</i> -butyl	Cl	Karataş, 2024 ^(a) ⁹⁹
imidazole or 4,5-dichloroimidazole	2-hydroxy-2-phenylethyl	methyl	Gly-Boc Phe-Boc or OAc	Mariconda, 2022 ^(a, b, c) ¹⁰⁰ Iacopetta, 2023 ^(a, b, c) ¹⁰¹
imidazole or imidazoline	dipp or mes	dipp or Mes	Cl	Eloy, 2012 ^(c, d) ¹⁰²

Figure 1.19: Mononuclear neutral Ag(I)-NHC complexes that have been tested against breast cancer, references are shown in the table. *a* = MCF7, *b* = MDA-MB-23, *c* = MCF10A and *d* = MCF-R.

Karataş et al. investigated the lipophilicity (predicted *in silico*) of two asymmetric anthracene Ag(I)-NHC complexes (**Figure 1.19**), in which the *para* position was either methyl (LogP = 9.13) or *tert*-butyl (LogP = 10.5). The complexes are both active when tested against MCF-7 (24 hours), with IC₅₀ values of 2.8 ± 0.1 and 2.9 ± 0.1 µM respectively, but no SARs were determined between LogP and cytotoxicity.⁹⁹ The corresponding pro-ligands were also tested for their activity, and the *tert*-butyl (LogP = 5.60) substituted ligand was significantly more active (IC₅₀ = 0.3 ± 0.1 µM) than the methyl functionalised ligand (LogP = 4.27, IC₅₀ = 1.1 ± 0.2).⁹⁹

Iacopetta et al. investigated the impact of substituting the position opposite to the NHC ligand, which in most complexes, is either a halide or acetate.¹⁰¹ The exchange of the halide for a BOC (*tert*-butoxycarbonyl) protected α-amino acid was

investigated (**Figure 1.19**).¹⁰¹ The activity of these reported Ag(I)-NHC complexes is in the nanomolar range (23 – 97 nM) against MDA-MB-231 (72-hour incubation), which makes these complexes some of the most active of this type.¹⁰¹ However, the silver salts of the tested amino acids AgGly and AgPhe are just as active as the corresponding NHC complexes, which indicates that it is not the NHC that confers toxicity, but the silver amino acid adduct.¹⁰¹ This is confirmed by the lower toxicity of the acetate functionalised complexes synthesised by Mariconda et al., which are up to 4347 times less cytotoxic.^{100,101} All the complexes reported in these studies are more active against MDA-MB-231 compared to non-cancerous breast cells (MCF10A) by as much as 1739 times. For MCF-7 the amino acid derivatives are less active than the acetate analogues.^{100,101} This selectivity is important for the development of anticancer agents as it means that the compound have the potential to target the cancer cells while evading the healthy cells.

Eloy et al. explored the effects of saturation of the NHC (imidazole vs imidazoline) and substitution of the wingtip Mes (1,3,5-Trimethylbenzene) vs Dipp (2,6-diisopropylphenyl) (**Figure 1.19**) had on the complex's biological activity against MCF-7 and MCF-7R (doxorubicin resistant breast cancer) with a 72-hour incubation.¹⁰² All complexes were extremely active against both cell lines with IC₅₀ values between 0.055 – 2.48 μ M. The saturation of the backbone had no effect on the cytotoxicity the differences were not statistically significant (P -value > 0.05) for MCF-7 and MCF-7R. For MCF-7R the difference in substitution of the aromatic ring Dipp vs Mes in the imidazoline complexes leads to a statistically significant (P -value < 0.05) difference in activity, with IC₅₀ values of 0.125 ± 0.005 and 2.48 ± 0.52 μ M, respectively.¹⁰² For the resistant cell line, the substitution of the ring has more of an impact on toxicity than the saturation of the NHC.

Hackenberg et al. have carried out one of the largest systematic studies to ascertain structure activity relationships in Ag(I)-NHC complexes.^{103–106} They generated a large library of symmetric phenyl substituted Ag(I)-NHC complexes of the general form AgNHC(OAc), with the substitution patterns and activities shown in **Figure 1.20**.^{103–106} From this data SARs can be established, for example, complexes that are substituted with electron donating groups (OMe and Me) on the wingtip are more active than those with electron withdrawing groups (C(O)OMe and CN).^{103–}

¹⁰⁶ This trend is also generally true for the substituted backbone, where the electron-withdrawing Cl substituted complexes have significantly lower activity than the complexes containing electron donating groups OMe, ⁱPr and Me. The relationship between electronegativity is highlighted by the most active complex in the series bearing electron donating Me in both R₁ and R₂ with an IC₅₀ value of $1.4 \pm 0.7 \mu\text{M}$ and the least active having the electron withdrawing chloride on R₁ and nitrile on R₂ with an activity of $50 \pm 2 \mu\text{M}$.^{103–106}

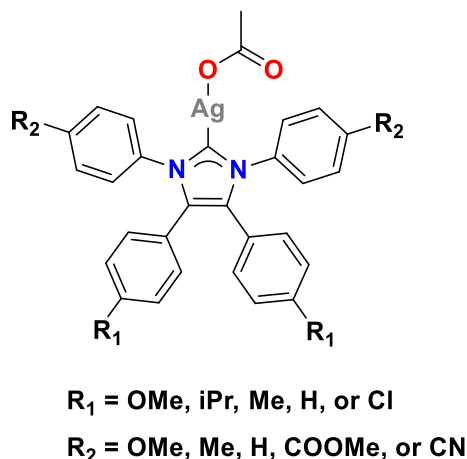


Figure 1.20: General structure of the complexes reported by Hackenberg, Streciwilk and Hopkinson *et al.*^{103–106}

1.3.4.3 Homoleptic Silver(I) N-heterocyclic Carbene Complexes

Homoleptic Ag(I)-NHC complexes are another class which have been widely studied for their activity against breast cancer. They comprise of a silver coordinated to two of the same NHC ligands (homoleptic) with a weakly coordinating anion, which is usually hexafluorophosphate. This section will cover both mononuclear and binuclear complexes.

Mononuclear homoleptic Ag(I)-NHC complexes can be altered in four positions (i) the backbone, (ii) and (iii) each wingtip and (iv) the counterion. A selection of complexes of this type that have been tested against breast cancers are shown in **Figure 1.21**.

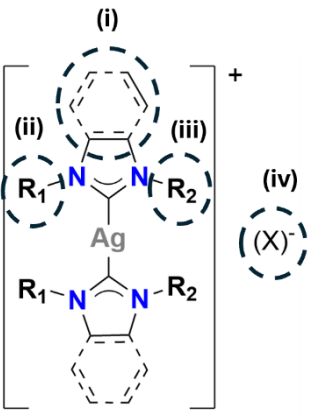
				
Backbone	R ₁	R ₂	X	Ref
imidazole or bezimidazole	octyl	octyl or ethylphenyl	PF ₆	Sarfraz, 2022 ^(a) 107
imidazole, 4-methylimidazole or benzimidazole	C ₃ H ₆ SO ₃ Na	C ₃ H ₆ SO ₃ Na or benzyl	Cl or Br	Marinelli, 2016 ^(a) 108 Gandin, 2013 ^(a) 109
benzimidazole	ethyl – hexyl or cyanopentyl	cyanobutyl or cyanopentyl	PF ₆	Hussaini, 2018 ^(a) 110 Hussaini, 2018 ^(a) 111 Hussaini, 2018 ^(a) 112
benzimidazole	octyl	benzyl, <i>o</i> or <i>p</i> -fluorobenzenzyl, <i>o</i> , <i>m</i> -difluorobenzenzyl and <i>p</i> -trifluoromethyl benzyl	PF ₆	Wong, 2024 ^(a,b) 113

Figure 1.21: Mononuclear homoleptic Ag(I)-NHC complexes that have been tested against breast cancer, references are shown in the table. *a* = MCF-7 and *b* = MDA-MB-231.

Sarfraz et al. synthesised a series of symmetric and asymmetric complexes with alkyl (octyl) functionalised wingtips where the backbone was either imidazole or benzimidazole (**Figure 1.21**).¹⁰⁷ The symmetric octyl functionalised complexes have high cytotoxicity against MCF-7 (IC₅₀ *ca.* 1 μM after 48-hour incubation), with no significant difference when the backbone is changed from imidazole to

benzimidazole, or when one wingtip was replaced by an aromatic ethylphenyl ligand.¹⁰⁷ Marinelli et al. and Gandin et al. investigated the influence of changing the backbone, and synthesised a series of hydrophilic symmetric sulfonate Ag(I)-NHC complexes which exhibited only moderate activity ($IC_{50} = 14.6 - 56.3 \mu M$, 72-hour incubation) towards MCF-7, but trends were the activity of each backbone were as follows, imidazole > benzimidazole > methyl-imidazole.^{108,109} A smaller series of asymmetric complexes were synthesised, where one of the arms was replaced with a benzyl, this lowered the activity in the imidazole derivative and left the activity unchanged in the benzimidazole derivative.^{108,109} The most important observation from these studies is that lipophilic Ag(I)-NHC complexes have higher activity compared to hydrophilic. Substitution of an alkyl chain with an aromatic group, in most cases, did not either improve nor hinder activity, this makes the aromatic group a good place for functionalisation.

Hussaini et al. investigated the effect of varying the alkyl chain length (ethyl to hexyl) of the wingtip in asymmetric complexes (**Figure 1.21**) where the other wingtip was cyanobutyl or cyanopentyl. These complexes were tested against MCF-7 (24-hour incubation), and the activity of the cyanobutyl series increases as the chain length is increased.^{110,111} However, there was no clear trends and the different chain lengths were not statistically different; $7.0 \pm 1.4 \mu M$ and $9.8 \pm 1.06 \mu M$ for the pentyl and propyl alkyl chains respectively.^{110,111} The complex with the longest (hexyl) and shortest (propyl) chains have the highest ($5.9 \pm 0.6 \mu M$) and lowest ($12.9 \pm 1.55 \mu M$) activity respectively. The group also reported a symmetric version with cyanopentyl wingtips and has the lowest activity ($3.7 \pm 0.4 \mu M$) of all the asymmetric series.¹¹⁰⁻¹¹²

Wong et al. synthesised a series of asymmetric homoleptic benzimidazole complexes (**Figure 1.21**) where one of the wingtips was octyl and the other was a functionalised fluoro benzyl.¹¹³ All the complexes are extremely active against both MDA-MB-231 and MCF-7, with IC_{50} values between $0.5 - 0.8 \mu M$ and $0.46 - 0.96 \mu M$ (24-hour incubation), respectively. However, there was no clear relationship between substitution and activity.¹¹³ Despite the shorter incubation time, these complexes are up to three times more active than the benzimidazole octyl

functionalised complexes reported by Sarfraz et al. (mentioned earlier), indicating that the addition of a benzyl group could be beneficial for activity.¹¹³

Ag(I)-NHC complexes containing two silver centres with homoleptic ligands have also been studied as potential anticancer agents. Due to the synthetic routes needed to prepare them (bridging of a functionalised azole to make the ligand precursor), these complexes are almost exclusively symmetrical and for most of the complexes the anion is PF₆. There are four positions that can be easily functionalised (i) backbone, (ii) the wingtip (R₁), (iii) the bridge (R₂) and (iv) the counterion. A summary of complexes of this type that have been tested against breast cancer are shown below in **Figure 1.22**.

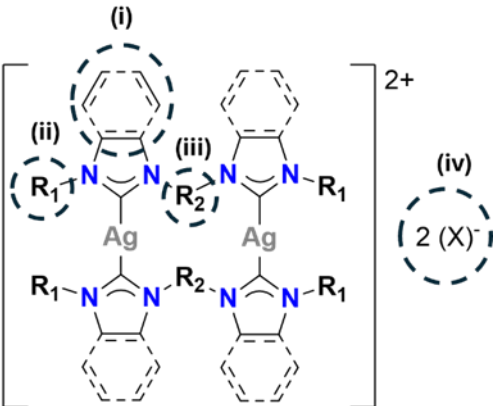
			
Backbone	R ₁	R ₂	Ref
benzimidazole	octyl or decyl	<i>m</i> -xylyl	Asif, 2016 ^(a) 114
imidazole	<i>o</i> or <i>m</i> -cyanobenzyl	methyl	Haque, 2014 ^(a) 96 Haque, 2016 ^(a) 97
benzimidazole	ethyl - pentyl	propyl	Hussaini, 2017 ^(a) 115
imidazole	methyl	butyl, pentyl, <i>m</i> -xylyl	Habib, 2019 ^(b) 98
5,6-dimethylbenzimidazole	butyl or pentyl	butyl, pentyl, <i>m</i> -xylyl	Habib, 2019 ^(b) 116
benzimidazole	methyl, hexyl, heptyl, octyl or <i>p</i> -methylbenzyl	propyl	Abdurrahman, 2024 ^(a) 117

Figure 1.22: Binuclear homoleptic Ag(I)-NHC complexes that have been tested against breast cancer in all cases $X = PF_6$, references are shown in the table. *a* = MCF-7 and *b* = MDA-MB-231

Asif et al. tested the activity of two symmetric binuclear benzimidazole complexes with a *meta*-xylyl bridges and either octyl or decyl wingtips (**Figure 1.22**).¹¹⁴ Two trends are observed, (i) for both cell lines the most lipophilic complex is the most active, and this agrees with what has been observed for other Ag(I)-NHC

complexes, and (ii) both complexes are more active against MCF-7 (48-hour incubation) when compared to MDA-MB-231.¹¹⁴

Hussaini et al. reported a series of complexes with a propyl bridge and varied alkyl wingtips from ethyl to pentyl (**Figure 1.22**). Their activities against MCF-7 (24-hour incubation) were moderate ($IC_{50} = 9 - 18 \mu M$), and no trends were observed, with the most and least active being the propyl ($7 \pm 1 \mu M$) and butyl ($18 \pm 3 \mu M$) respectively (other complexes falling within this range).¹¹⁵ Similar results were reported by Abdurrahman et al. in which the propyl bridge was retained and the wingtips had differing alkyl chain lengths.¹¹⁷ There was a noticeable change in activity between the methyl and hexyl derivatives, which is in line with the increase in lipophilicity. However, when the chain length is increased further to heptyl and octyl the activity decreases, suggesting there is a threshold for the lipophilicity, and that cytotoxicity decreases when lipophilicity is too high.¹¹⁷ Haque et al. explored the use of aromatic wingtips and synthesised a series of cyanobenzyl functionalised homoleptic binuclear complexes with the cyano either in the *ortho* or *meta* position (**Figure 1.22**). Both complexes showed nanomolar activity with IC_{50} values of 0.5 ± 0.15 and $0.9 \pm 0.4 \mu M$ respectively, when tested against MCF-7.^{96,118} The results indicate that functionalised aromatic wingtips in binuclear complexes could be a promising area to access highly active complexes against breast cancer.

Habib et al. explored how changing the bridge impacts the activity of a series of imidazole complexes with methyl as the wingtip (**Figure 1.22**).⁹⁸ Against MDA-MB-321, it was found that the *m*-xylyl bridge complex was more active than complexes with alkyl (butyl or pentyl) bridge, suggesting a more ridged core may lead to higher activity.⁹⁸ The same group investigated this series of bridges in 5,6-dimethylbenzimidazolium complexes with butyl or pentyl wingtips and in each case the same trend is of activity is observed, *m*-xylyl > pentyl > butyl.¹¹⁶

Monterio et al. synthesised a series of bi and mononuclear Ag(I)-NHC complexes (**Figure 1.23**), with varying nuclearity and denticity of the ligand.¹¹⁹ All complexes reported are active against MCF-7 (144-hour incubation), and this contrasts with the cytotoxicity of the silver salts AgBr and AgBF₄ which are inactive ($IC_{50} > 100 \mu M$) under these conditions, highlighting the NHC is vital for activity.¹¹⁹ Within the

binuclear series there is no significant improvement in activity as the lipophilicity increased.¹¹⁹ For the methyl derivative, the anion was changed from Br to BF₄ but the difference in activity was not statistically significant ($P > 0.05$), indicating that the anion in this case does not affect cytotoxicity.¹¹⁹ The least active complex is the mononuclear complex with an IC₅₀ of $17.8 \pm 3.8 \mu\text{M}$ and which is 3.5 – 4.1 times less active than the binuclear complexes, indicating nuclearity has an influence on activity.¹¹⁹

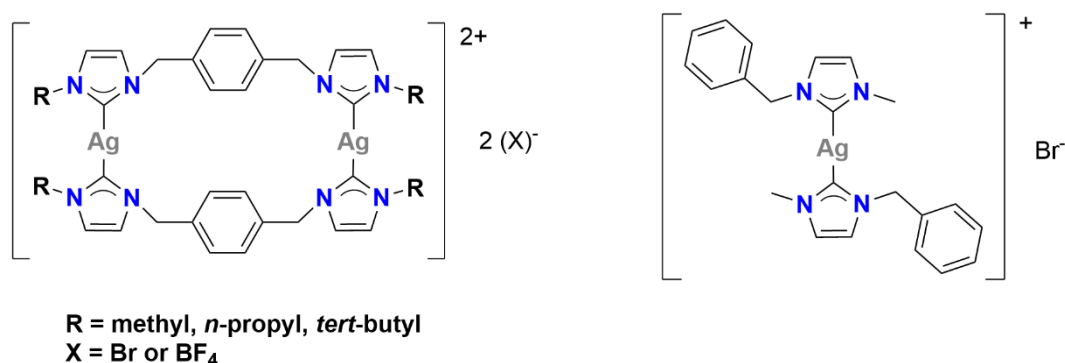


Figure 1.23: Complexes synthesised by Monterio *et al.*¹¹⁹

1.3.5 Mechanisms of Action of Silver(I) *N*-Heterocyclic Carbene Complexes

The mechanism of action of neutral Ag(I)-NHC complexes (**Figure 1.24**) was studied by Mariconda *et al.*, in which they observed notable changes in the shape of the cells (became round) with formation of cytoplasmic extensions.¹⁰⁰ They hypothesised that there was a disturbance within the cytoskeletal network.¹⁰⁰ They investigated how the complexes interact with actin and microtubules which are a major component of the cytoskeleton and are vital for cellular processes such as division and cell signalling. Both complexes inhibited actin polymerisation to similar levels as the positive control latrunculin (a known actin polymerisation inhibitor) in *in vitro* polymerisation experiments.¹⁰⁰ This was followed by *in vivo* studies using MDA-MB-231 and MCF-7 cells in which they were imaged after treatment with the complexes at their IC₅₀ concentration and dyes DAPI (stains nucleus) and Alexa Fluor 568 (stains β -actin).¹⁰⁰ Both of the cell types showed cytoskeletal disorganisation after treatment, comparable to the cells treated with latrunculin.¹⁰⁰ The group studied the ability of the complexes to induce apoptosis using a TUNEL assay which tests for DNA fragmentation using the dye CF488 (green fluorescent green in the presence of fragmented DNA), and both complexes

showed green fluorescence in the treated cells, which was not observed in the DMSO controls, indicating that they both cause apoptosis.

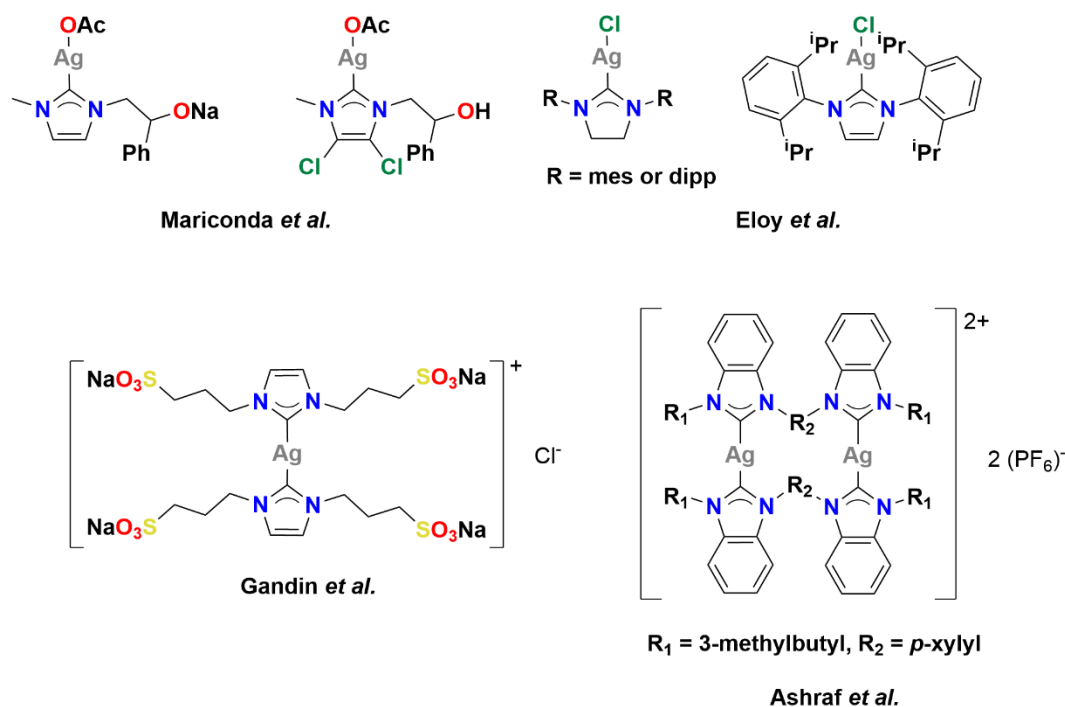


Figure 1.24: Structures of mono and binuclear Ag(I)-NHC complexes which have been probed for their mechanisms of action.^{100,102,109,120}

The mechanism of action of the symmetric aromatic functionalised Ag(I)-NHC complexes in leukaemia cells (HL60) was reported by Eloy *et al.* (**Figure 1.24**).¹⁰² They were found to lower the mitochondrial membrane potential ($\Delta\Psi_m$), making the membrane more permeable and thereby releasing proapoptotic proteins and promoting apoptosis.¹⁰² The depolarisation was monitored using the dye JC-10 which stains the polarised and depolarised membranes red and green respectively, and the degree of depolarisation was monitored by flow cytometry.¹⁰²

Gandin *et al.* investigated the mechanism of action of a symmetric cationic sulfonate functionalised Ag(I)-NHC complex (**Figure 1.24**), and it was found to be a potent inhibitor of thioredoxin reductase (TrxR, $IC_{50} = 12.5$ nM), an enzyme that is vital for redox homeostasis.¹⁰⁹ TrxR function is to reduce the protein thioredoxin (Trx) which is used in many functions within the cell such as H_2O_2 reduction (via reduction of peroxiredoxins), regulation of apoptosis and protein repair.¹²¹ TrxR has been shown to be overexpressed in breast cancer and has been linked to

metastasis.¹²¹ TrxR has an redox active cysteine-selenocysteine site which is a good target for metallodrugs especially metals such as silver and gold which have an affinity for sulfur.¹²² They observed generation (using the fluorescent probe (H₂DCFDA) in ovarian cancer cells (2008) treated with this complex, which would be expected if TrxR has been inhibited within the cell.¹⁰⁹

The group of Ashraf et al. investigated the anticancer activity of xylyl bridged binuclear Ag(I)-NHC complexes, with the most active depicted in **Figure 1.24**, which has an IC₅₀ of $7.83 \pm 0.59 \mu\text{M}$ against HTC-116 (human colon cancer). They probed the complexes interaction with calf thymus DNA (ct-DNA) using UV-Vis (Ultraviolet-visible spectroscopy) titrations to determine the binding constant (K_b). This was found to be $6.84 \times 10^4 \text{ M}^{-1}$ which is comparable to cisplatin ($5.51 \times 10^4 \text{ M}^{-1}$), and which is 10 times larger than the respective ligand ($4.12 \times 10^3 \text{ M}^{-1}$), indicating silver is important for improving the binding activity.

These results indicate that there are many different mechanisms of actions that Ag(I)-NHC complexes can be involved in that can lead to cell death with the major targets being redox homeostasis and DNA.

1.4 Aims of Project and Design of Complexes

1.4.1 Overall Aims and Rationale of the Study

As summarised in section 1.3.4 there has been a large volume of research in the use of Ag(I)-NHCs as anticancer agents for breast cancer. From these studies some SARs can be determined, with the main one being the relationship between lipophilicity and activity in the charged homoleptic complexes, which was highlighted by the low to moderate activity of the water-soluble complexes reported by Marinelli and Gandin et al. and the higher activity of complexes reported in section 1.3.4 with more lipophilic wingtips. There is also indication that there is a lipophilicity limit, and compounds which become too lipophilic can have a detrimental impact on activity. There is also some indication that higher nuclearity (mono vs binuclear) leads to higher activity, which was shown by Monterio et al. Finally, the work by Haque et al. reported nanomolar activity for binuclear Ag(I)-NHC with functionalised benzyl wingtips, indicating that complexes of this type are promising to explore further as active anticancer agents.

The complexes synthesised in this project will be of the charged homoleptic type, and aims to address the following literature gaps:

- (i) Most of the wingtips are simple alkyl chains, in which the length has been changed, however, there remains few examples which investigate aromatic groups and their effect on biological activity.
- (ii) There are few examples where the wingtips are kept consistent and the nuclearity changed, for example, mono versus binuclear.
- (iii) Likewise, there are fewer examples where the wingtips are kept consistent, and the azole has been changed.
- (iv) Finally, most of the studies involve the use of only one cell line (e.g., MCF-7 or MDA-MB-231), and they very rarely report multiple breast cell lines, and there is very limited data using a non-cancerous breast cell-lines (e.g. MCF10A)

The aim of this project is to gain a further understanding of parameters that affect the activity of Ag(I)-NHC complexes against breast cancers, which will help develop more active drug candidates. The proposed design of the new complexes is shown below **Figure 1.25**. The bridge (methyl) and anion (PF_6^-) have been chosen as parameters that will be kept the same, and the wingtips (aromatic) and backbones (imidazole and benzimidazole) will be changed. For the most active of the imidazole and benzimidazole series a mononuclear version will be synthesised. They will then be tested against two breast cancer cell lines MCF-7 and MDA-MB-231 and two non-cancerous cell lines MCF10A (breast) and ARPE-19 (retinal, used as a model for epithelial cells).

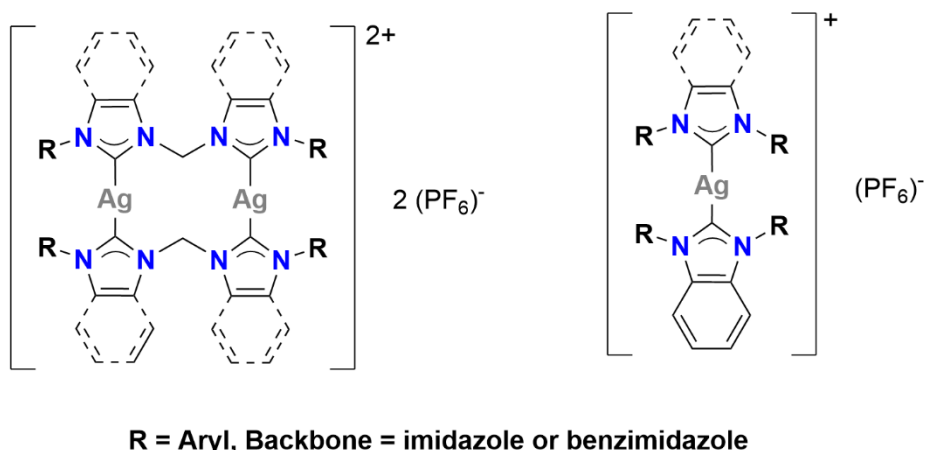


Figure 1.25: General structures of proposed new Ag(I)-NHC which will be by synthesised and tested in this work.

1.4.2 Specific Objectives

- (i) **Synthesis of NHC ligands** - First the pro-ligands will be synthesised using standard organic chemistry methods.
- (ii) **Synthesis of silver complexes** - The corresponding Ag(I)-NHC complexes (**Figure 1.25**) will then be synthesised using the standard silver(I) oxide route.
- (iii) **Characterisation of ligands and complexes** - The compounds will be characterised using nuclear magnetic resonance (NMR) spectroscopy (^1H and $^{13}\text{C}\{^1\text{H}\}$), attenuated total reflectance Fourier transform infrared spectroscopy (ATR-FTIR) and elemental analysis (EA). If a suitable crystal can be obtained, single crystal X-ray diffraction (sc-XRD) will also be performed.
- (iv) **Antiproliferative effects against breast cancer cell lines** – All compounds will be tested against a range of cell lines MDA-MB-231, MCF-7, MCF-10A and ARPE-19.
- (v) **Mode of action studies** – For the most active compounds, the following mechanisms of action will also be studied:
 - a. DNA interactions through molecular docking and fluorescence intercalator displacement studies (FID).
 - b. Cell morphology using optical microscope.
 - c. ROS generation using fluorescein staining.

- d. Cell uptake studies using Inductively coupled plasma mass spectrometry (ICP-MS).

2 Binuclear Homoleptic Silver(I) *N*-Heterocyclic Carbene Complexes

The modular nature of NHC ligands means that they can be easily functionalised to allow for large libraries of compounds to be synthesised and SARs to be established. This chapter outlines the synthesis and characterisation of a series of bridged imidazolium ligands and their corresponding homoleptic bridged Ag(I)-NHC complexes.

The general structure of the Ag(I)-NHCs reported in this chapter are shown in (Figure 2.1), and the wingtip substituents (shown as **R**) were selected to modulate the lipophilicity (with [Ag₂(L5)₂](PF₆)₂ being most lipophilic and [Ag₂(L6)₂](PF₆)₂ being the least) as literature has shown that increased lipophilicity will help increase the cytotoxicity.¹²³ Aromatic groups ([Ag₂(L1)₂](PF₆)₂, [Ag₂(L2)₂](PF₆)₂, [Ag₂(L3)₂](PF₆)₂, and [Ag₂(L4)₂](PF₆)₂) were chosen for potential interactions with DNA (or other biomolecules), as these groups are found in many active imidazolium salts reported.¹²⁴ Fluorine containing moieties ([Ag₂(L6)₂](PF₆)₂ and [Ag₂(L7)₂](PF₆)₂) are ubiquitous in medicinal chemistry and act as common bioisosteres.¹²⁵

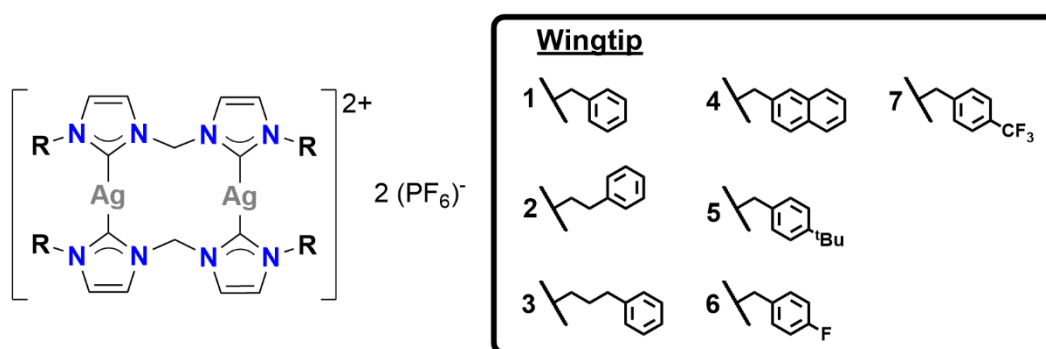


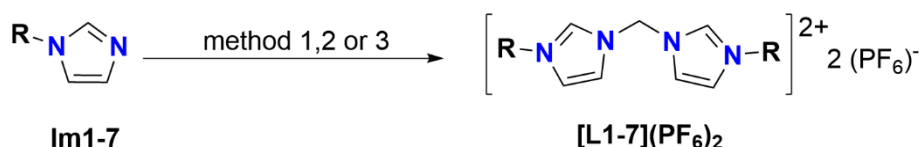
Figure 2.1: General structure of the imidazolium-based Ag(I)-NHC complexes [Ag₂(L1-7)₂](PF₆)₂ discussed in this chapter and their different R groups.

2.1 Synthesis and Characterisation of Bridged Imidazolium Ligands

The bidentate NHC precursor ligands shown in Error! Reference source not found. are prepared from the corresponding monofunctionalised imidazoles **Im1-7** (**Scheme 2.1**) which were prepared using standard literature methods via a nucleophilic substitution of imidazole with the respective benzyl halide in the presence of a base. The compounds are literature known and their successful syntheses were confirmed by ^1H NMR spectroscopy only.^{126–135}

The ligands were prepared as hexafluorophosphate salts for direct comparison to the corresponding Ag(I)-NHC complexes for biological testing. The bridged imidazolium hexafluorophosphate salts were synthesised using three different established bridging methods (**Scheme 2.1**).^{136,137} Two equivalents of the respective imidazole were heated to reflux either in neat dibromomethane (*method 1*) or reacted with diiodomethane in toluene (*method 2*). Ion exchange is then carried out using excess ammonium hexafluorophosphate in acetone. The consecutive ion exchange is confirmed by the compound's solubility in acetone and MeCN, as the initial halide salts are insoluble, whilst the hexafluorophosphate salt is soluble. Higher yields were achieved following *method 1* (50 – 92%) compared to the ligand synthesised via *method 2* was 33%. However, as these were not the same ligands the yields cannot be directly compared.

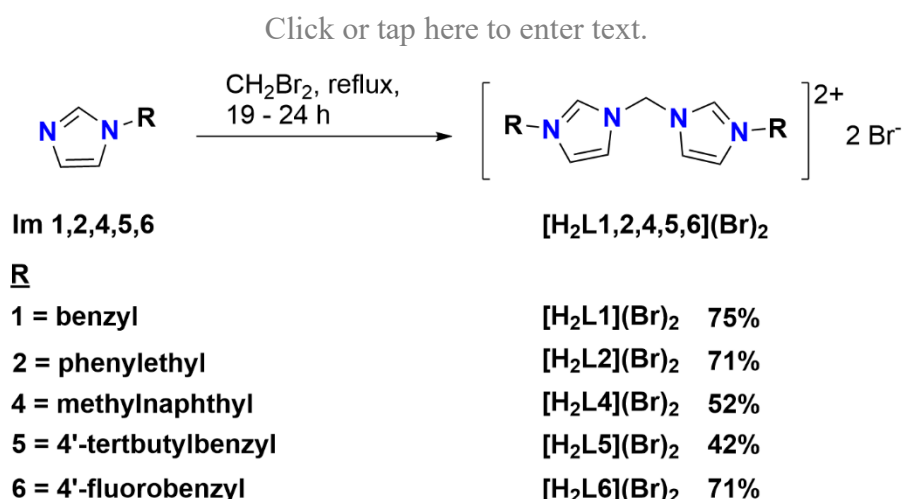
Microwave heating (*method 3*) was trialled, which gave a similar yield to *method 2* (30%). In most cases the ligands were prepared using *method 1* as the simple and efficient method is high yielding. All new ligands have been fully characterised by ^1H NMR, $^{13}\text{C}\{^1\text{H}\}$ NMR, ATR-FTIR spectroscopy and EA.



<u>R</u>	<u>Method</u>		
	<u>1</u>	<u>2</u>	<u>3</u>
1 = benzyl	[H ₂ L1](PF ₆) ₂ 50%	[H ₂ L3](PF ₆) ₂ 33%	[H ₂ L2](PF ₆) ₂ 30%
2 = phenylethyl	[H ₂ L4](PF ₆) ₂ 50%		
3 = phenylpropyl	[H ₂ L5](PF ₆) ₂ 71%		
4 = methylnaphthyl	[H ₂ L6](PF ₆) ₂ 69%		
5 = 4'-tertbutylbenzyl	[H ₂ L7](PF ₆) ₂ 92%		
6 = 4'-fluorobenzyl			
7 = 4'-trifluoromethylbenzyl			

Scheme 2.1: Synthetic routes and yields for the bridged imidazolium hexafluorophosphate salts. Method 1: i) CH₂Br₂, reflux, 1 day, ii) x/s NH₄PF₆, Method 2: i) CH₂I₂, toluene, reflux, 3 days, ii) x/s NH₄PF₆, Method 3: i) CH₂I₂, EtOAc, 170°C, 1h, ii) x/s NH₄PF₆.

For use in the synthesis of the target binuclear Ag(I)-NHC complexes (see **Section 2.2**), a series of bromide salts of the ligands were synthesised. Bridged imidazolium bromide ligands [H₂L1,2,4,5,6](Br)₂ were prepared using **method 1** (without the ion exchange). The yields obtained were moderate to high (42 – 75%) and of these ligands, only [H₂L2](Br)₂ was new, the others have been reported previously and the purity confirmed by ¹H NMR spectroscopy only.^{136,138}



Scheme 2.2: Synthesis of bridged imidazolium bromide salts.^{135,137}

Successful synthesis of all ligands was confirmed by ¹H NMR spectroscopy, monitoring the signal of the C2 proton, which shifts from 7.46 – 7.70 ppm to 9.23 – 9.67 ppm (due to the formation of the imidazolium ion). An example is shown in **Figure 2.2** for [H₂L6](PF₆)₂. Upon a counterion exchange, the ligands exhibit changes in the chemical shifts. An example is shown for [H₂L6](Br)₂ and [H₂L6](PF₆)₂ in **Figure 2.2** where C2 proton shifts from 9.65 to 9.41 ppm after the exchange from bromide to hexafluorophosphate. The chemical shift changes range between 0.13 to 0.34 ppm these are tabulated in **Table 2.1**. It has been suggested in literature that the ability of the counterion to have hydrogen bonding interactions influences the shift of the C2 proton.¹³⁹ The Br⁻ is more able to form hydrogen bonding interactions compared to PF₆⁻ which leads to the downfield shift.¹³⁹

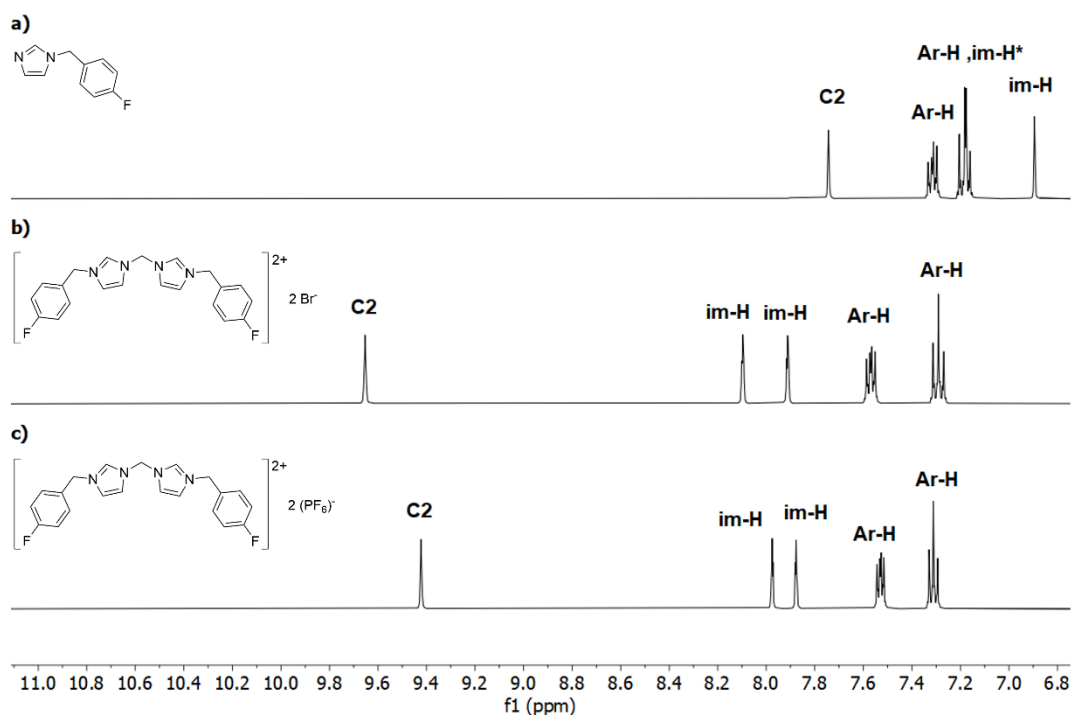


Figure 2.2: ^1H NMR spectra of the functionalised imidazole **Im6** (top), bridged imidazolium bromide salt $[\text{H}_2\text{L6}](\text{Br})_2$ (middle), and bridged imidazolium hexafluorophosphate salt $[\text{H}_2\text{L6}](\text{PF}_6)_2$ (bottom), highlighting the shift in resonances upon the formation of the bridge and ion exchange (d_6 -DMSO, 400 MHz) *denotes the overlap of two resonances.

Table 2.1: Tabulated chemical shifts of the C2 proton from the ^1H NMR spectra measured in d_6 -DMSO (either 400 MHz or 500 MHz). ND = not determined.

Compound	Chemical shift (δ)		
	X = Br	X = PF ₆	Difference
$[\text{H}_2\text{L1}](\text{X})_2$	9.61	9.45	0.16
$[\text{H}_2\text{L2}](\text{X})_2$	9.57	9.23	0.34
$[\text{H}_2\text{L3}](\text{X})_2$	ND	9.39	ND
$[\text{H}_2\text{L4}](\text{X})_2$	9.68	9.48	0.20
$[\text{H}_2\text{L5}](\text{X})_2$	9.57	9.44	0.13
$[\text{H}_2\text{L6}](\text{X})_2$	9.64	9.41	0.23
$[\text{H}_2\text{L7}](\text{X})_2$	ND	9.47	ND

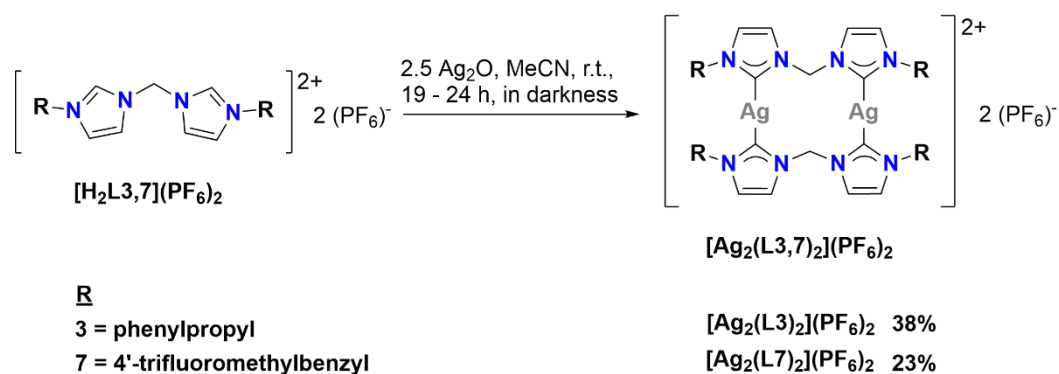
Further evidence for signs of successful bridging can be found in the $^{13}\text{C}\{^1\text{H}\}$ NMR spectra. There are two resonances in the aliphatic region (0 – 80 ppm), these are the wingtip and bridge methylene resonances at 49.0 – 52.6 ppm and 58.3 – 58.6 ppm respectively. Both are in the downfield part of the aliphatic region due to the carbon's proximity to electronegative nitrogens. The bridge is adjacent to two nitrogens hence the larger shift. The C2 carbon resonance is found further downfield between 137.3 – 138.1, and this is due to the carbon both being aromatic and adjacent to two nitrogens.

The successful ion exchange can also be observed in the ATR-IR spectra (**Appendix 8.1 - Appendix 8.6**), where the appearance of an intense and broad peak at approximately 830 cm^{-1} is observed and which is indicative of the stretching vibrations of the PF_6^- ion, and confirmation of the anion exchange.¹⁴⁰

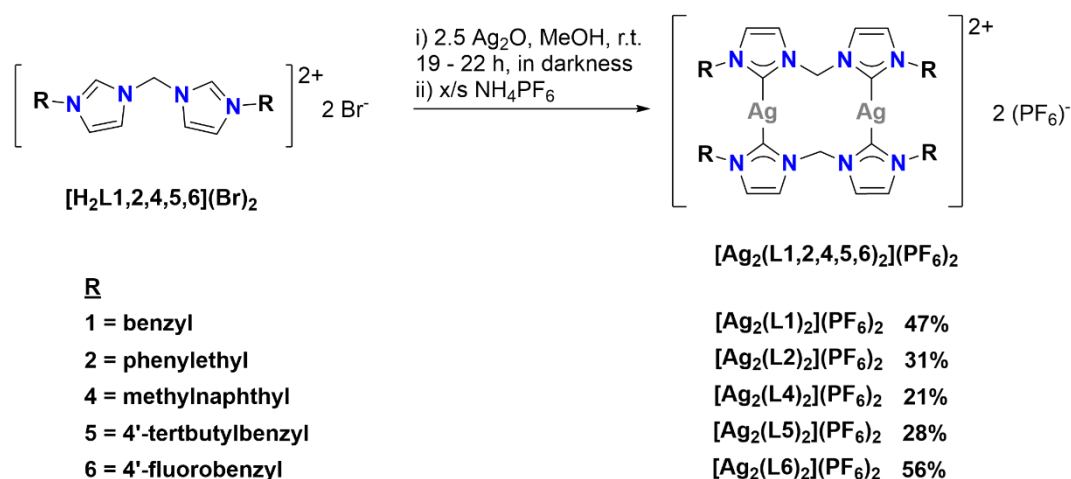
2.2 Synthesis and Characterisation of Binuclear Silver(I) *N*-Heterocyclic Carbene Complexes

Formation of the binuclear Ag(I)-NHC complexes $[\text{Ag}_2\text{L}(\mathbf{1-7})_2](\text{PF}_6)_2$ (**Scheme 2.3**) was achieved via two routes. **Method 1** is based on a synthetic route by Kühn et al., where $[\text{H}_2\text{L}](\text{PF}_6)_2$ is reacted with excess silver(I) oxide in MeCN for 19 hours and then filtered over Celite® to remove the remaining silver(I) oxide.¹⁴¹ **Method 2** is based on a modified procedure from Ashraf et al. where $[\text{H}_2\text{L}](\text{Br})_2$ is reacted with excess of silver(I) oxide in MeOH for *ca.* 19 hours, followed by filtering over Celite® and then an ion-exchange in a methanolic solution with aqueous ammonium hexafluorophosphate.¹⁴²

Method 1



Method 2



Scheme 2.3: Synthetic routes for the imidazole based binuclear Ag(I)-NHC complexes.

Method 1 leads to full conversion to the Ag(I)-NHC complex, however problems were encountered during their purification (only $[\text{Ag}_2(\text{L}3)_2](\text{PF}_6)_2$ and $[\text{Ag}_2(\text{L}7)_2](\text{PF}_6)_2$ were obtained pure). Established syntheses of Ag(I)-NHCs from literature often use a large excess of silver(I) oxide, however during the attempts made herein, silver(I) oxide or silver MeCN adducts $[\text{Ag}(\text{MeCN})_4](\text{PF}_6)$ were present after the reaction, and were difficult to remove.^{142,143} In several NMR spectra, a singlet was observed at 2.09 ppm which was assigned as the CH₃ of MeCN in the $[\text{Ag}(\text{MeCN})_4](\text{PF}_6)$ adduct (confirmed also by scXRD).

Varying equivalents of silver(I) oxide in the synthesis of $[\text{Ag}_2(\text{L5})_2](\text{PF}_6)_2$ (**Scheme 2.3** and **Table 2.2**) was trialled, in order to reduce the formation of the $[\text{Ag}(\text{MeCN})_4](\text{PF}_6)$ complex. However, after *ca.* 19 hours (timescale for the previous reaction), the reaction did not go to completion for equivalents below 2.5 of silver(I) oxide. It was for this reason that *method 2* was employed to reach the remaining target complexes. MeOH was selected, as like MeCN, this polar solvent favours the formation of charged Ag(I)-NHC complexes over neutral. Unlike, MeOH is less likely to form adducts with silver which avoids the issue encountered in *method 1*. The yields obtained using both routes were low to moderate (21 – 56%), and these are similar to those reported within the literature.^{144–147}

Table 2.2: Conversion of $[\text{H}_2\text{L5}](\text{PF}_6)_2$ to $[\text{Ag}_2(\text{L5})_2](\text{PF}_6)_2$ with varying equivalents of silver(I) oxide. Conversions are calculated from ^1H NMR spectra.

Ag ₂ O equivalents (x)	Reaction time (h)	% conversion
1	19	8
2	19	91
2.5	20	100

2.2.1 ^1H NMR Spectroscopy

There are three major changes observed in the ^1H NMR spectra that indicate that the complexation has been successful. One indicative change is the disappearance of the C2 proton indicating successful deprotonation. An example is shown in **Figure 2.3**, where the proton at 9.41 ppm for $[\text{H}_2\text{L6}](\text{Br})_2$ disappears upon complexation. The second change observed is the splitting pattern of the imidazole backbone proton, which changes from a doublet of doublets (or pseudo-triplet) to a doublet. This can be observed in **Figure 2.3** (insert) for $[\text{H}_2\text{L6}](\text{PF}_6)_2$ (top) and $[\text{Ag}_2(\text{L6})_2](\text{PF}_6)_2$ (bottom). This is due to the removal of the C2 proton which then leads to a simplification in coupling.

The third major change is the broadening and splitting of the methylene bridge resonances (6.22 - 7.02 ppm), which is the result of the restricted rotation within the 12-membered ring formed (shown in bold in **Figure 2.4**). The protons exchange at a rate slower than the timescale of the NMR experiment. At room temperature in

d_6 -DMSO this restricted movement places the molecule between a fast and a slow exchange regime. In the fast exchange regime, the two geminal protons H_a and H_b are equivalent which means that they will not couple. In the slow exchange regime, the two protons are observed as non-equivalent and will therefore couple to each other, this will give rise to a pair of doublets. The spectrum of $[Ag_2(L6)_2](PF_6)_2$ in **Figure 2.3** shows system between these two regimes, which leads to spectral broadening. As this exchange is a dynamic process it can be studied using variable temperature NMR spectroscopy (VT-NMR), using this technique the fluxionality (rigidity) of the molecule can be studied.

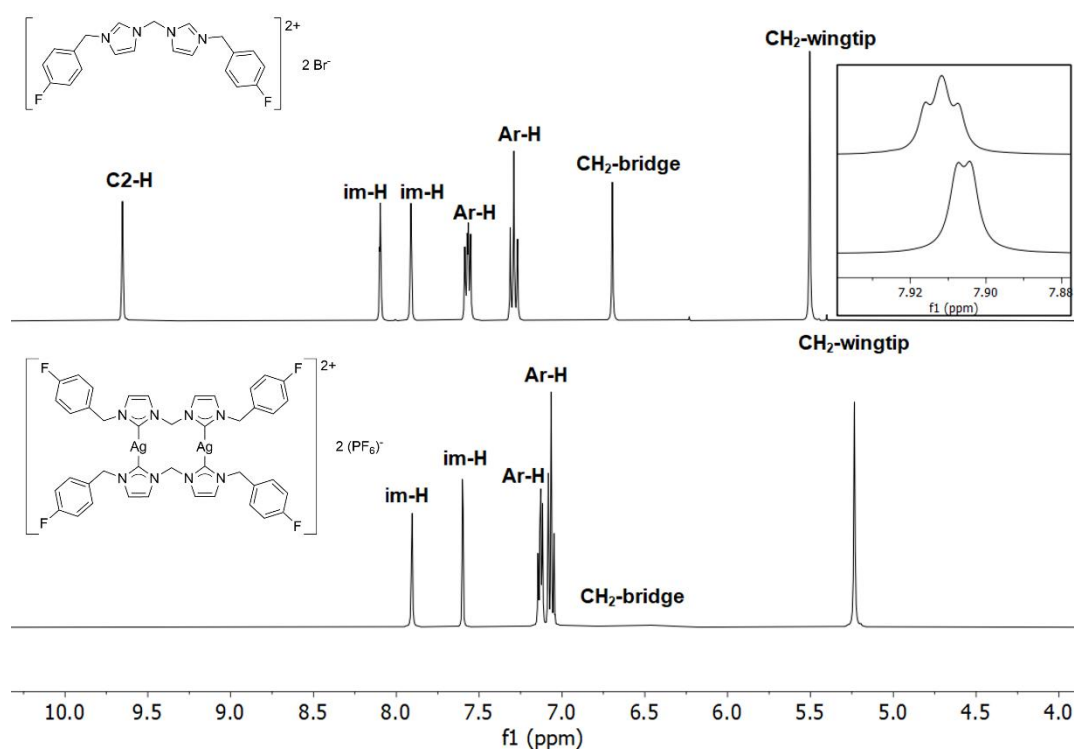


Figure 2.3: 1H NMR spectra of $[H_2L6](Br)_2$ (top) and $[Ag_2(L6)_2](PF_6)_2$ (bottom) with an expansion of the resonances of the backbone protons of the imidazole ring showing the difference in splitting (d_6 -DMSO, 500 MHz).

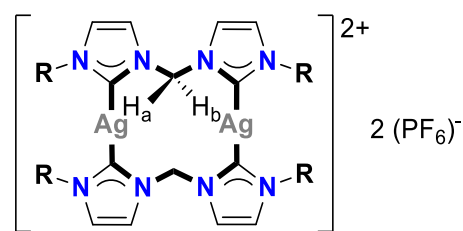


Figure 2.4: General structure of the imidazole based homoleptic bimetallic Ag(I)-NHCs. The intramolecular 12-membered ring is highlighted in bold and the geminal methylene bridge protons H_a and H_b are explicitly shown.

2.2.2 Dynamic NMR Spectroscopy

There are three exchange regimes which are shown in **Figure 2.5**. In these equations k is defined as the rate constant and $\Delta\nu$ is the separation of the exchanging resonances at the low temperature limit. The “low temperature limit” is defined as the temperature that is sufficiently lower than the coalescence temperature (T_c). The coalescence temperature is defined as the temperature in which the exchanging resonances combine into a single flat-topped peak, and at that temperature the NMR experiment can no longer distinguish the peaks.

$$\begin{array}{ll}
 k \ll \Delta\nu & \text{(Slow exchange)} \\
 k \approx \Delta\nu & \text{(intermediate exchange)} \\
 k \gg \Delta\nu & \text{(fast exchange)}
 \end{array}$$

Figure 2.5: The three different exchange regimes.

In the *slow-exchange* regime the exchange between the inequivalent protons is slow on the NMR timescale and therefore will be resolved as two distinct peaks. In the *fast-exchange* regime the resonances are averaged, resulting in one peak (**Figure 2.6**). This example is simple, as the two-protons described do not couple to each other. Between these two regimes is an intermediate regime the resonances ν_a and ν_b merge into a broad peak, the temperature at which this occurs is the coalescence temperature (T_c). From this information kinetic parameters can be calculated.

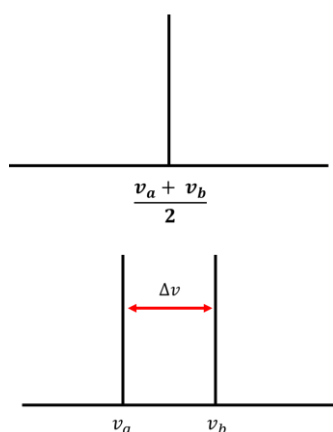


Figure 2.6: Diagram of fast (top) and slow (bottom) exchange regimes for non-coupled protons.

Usually line shape analysis is required to calculate the rate constant k (s^{-1}) from VT-NMR experiments, however, for a system with non-coupling protons, k at T_c can be approximately calculated using **Equation 1**, where $\Delta\nu$ is the chemical shift between resonances A and B in Hz at the low temperature limit.¹⁴⁸

$$k = \frac{\pi\Delta\nu}{\sqrt{2}} \quad \text{Equation 1}$$

For systems where the exchanging protons AB have scalar coupling, k can be approximated using **Equation 2**, where J_{AB} is the separation between the peaks in the doublets in Hz.¹⁴⁸ As the protons in the methylene protons couple this is the equation that will be utilised.

$$k = \frac{\pi}{\sqrt{2}} \sqrt{\Delta\nu_{AB}^2 + 6J_{AB}^2} \quad \text{Equation 2}$$

Variable temperature NMR experiments were performed for complexes $[\text{Ag}_2(\text{L1-7})_2](\text{PF}_6)_2$ to understand if the different R groups influenced the rigidity of the complex. Deuterated MeCN was selected as it readily solubilises the complexes and the temperature window is sufficiently large (-40 to 60 °C).

The structure shown in **Figure 2.7** explicitly shows the protons on the methylene bridge ($\text{H}_{4a/b}$) and wingtip ($\text{H}_{5a/b}$), these form an AB ($\Delta\nu/J < 10$) or AX ($\Delta\nu/J > 10$) type system, in which two isolated diastereotopic protons interact with each other.

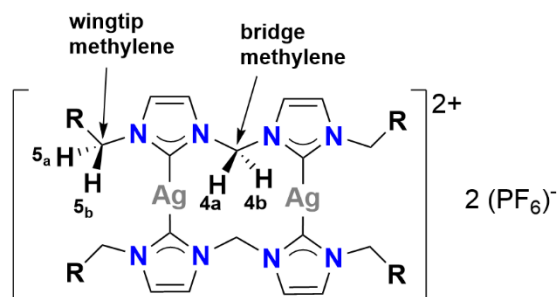


Figure 2.7: General structure of $[Ag_2(LX)](PF_6)_2$ with the geminal protons on the methylene groups (H_4 and H_5) explicitly highlighted.

Two 1H NMR spectra (**Figure 2.8**) of $[Ag_2(L1)_2](PF_6)_2$ in d_3 -MeCN were taken at $-40\text{ }^\circ\text{C}$ and $60\text{ }^\circ\text{C}$. There are two notable changes in these spectra, firstly, the methylene bridge $H_{4a/b}$ which is a singlet (6.33 ppm) at $60\text{ }^\circ\text{C}$ is now observed as two doublets at $-40\text{ }^\circ\text{C}$. The J -coupling of both doublets is 14.0 Hz which is in the range reported for in literature for $^2J(^1H-^1H)$.¹⁴⁹ Secondly, the methylene wingtip $H_{5a/b}$ which is a singlet (at 5.14 ppm) at $60\text{ }^\circ\text{C}$, was then observed as two doublets after cooling to $-40\text{ }^\circ\text{C}$. The $^2J(^1H-^1H)$ J -coupling of the doublets is 14.5 Hz, which is relatively close to the separation between the resonances ($\Delta\nu$, 31.5 Hz) this results in extreme roofing.

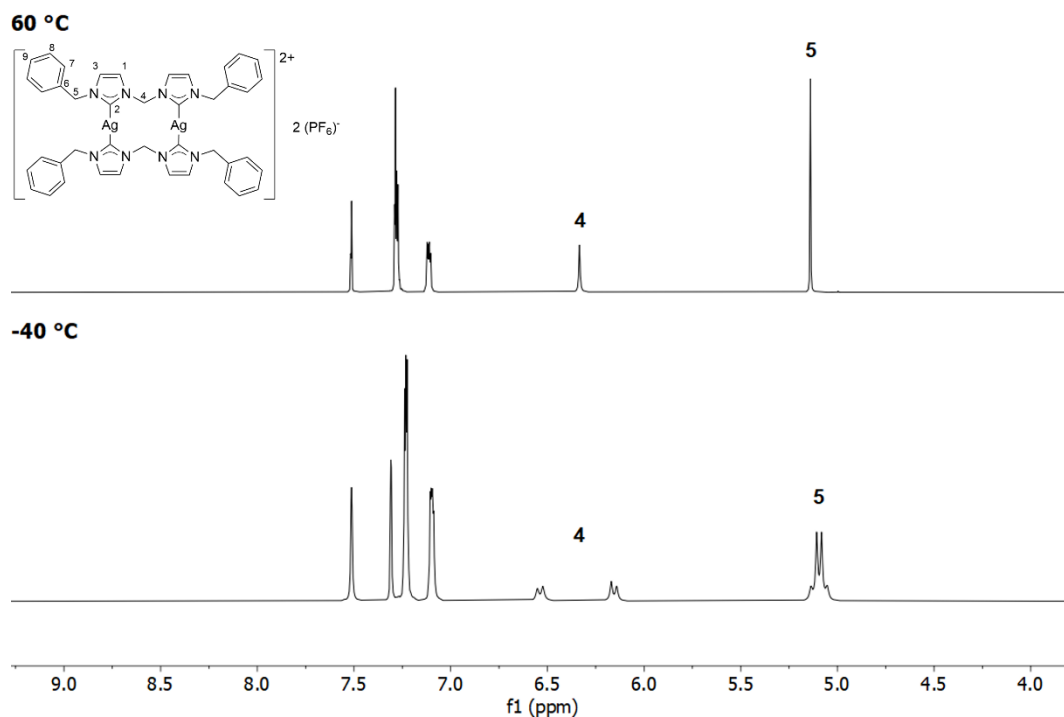


Figure 2.8: ^1H NMR spectra of $[\text{Ag}_2(\text{L1})_2](\text{PF}_6)_2$ measured at -40 (bottom) and 60 $^\circ\text{C}$ (top) ($d_3\text{-MeCN}$, 500 MHz).

The spectra were collected at a range of temperatures between -40 and $60\text{ }^\circ\text{C}$ to determine T_c . Example ^1H NMR spectra (**Figure 2.9**) are shown for $[\text{Ag}_2(\text{L1})_2](\text{PF}_6)_2$. As the temperature is increased from $-40\text{ }^\circ\text{C}$ the doublets at *ca.* 6.33 ppm become broader, after which they merge at $0\text{ }^\circ\text{C}$, and the $T_c = -10 - 0\text{ }^\circ\text{C}$ for the protons $\text{H}_{4\text{a/b}}$. The doublets at *ca.* 5.10 ppm which correspond to $\text{H}_{5\text{a/b}}$ broaden as the temperature increases, and T_c is between -10 and $-30\text{ }^\circ\text{C}$. The T_c for $\text{H}_{5\text{a/b}}$ is lower than $\text{H}_{4\text{a/b}}$, meaning the bridge methylene has more restricted rotation than the wingtip methylene.

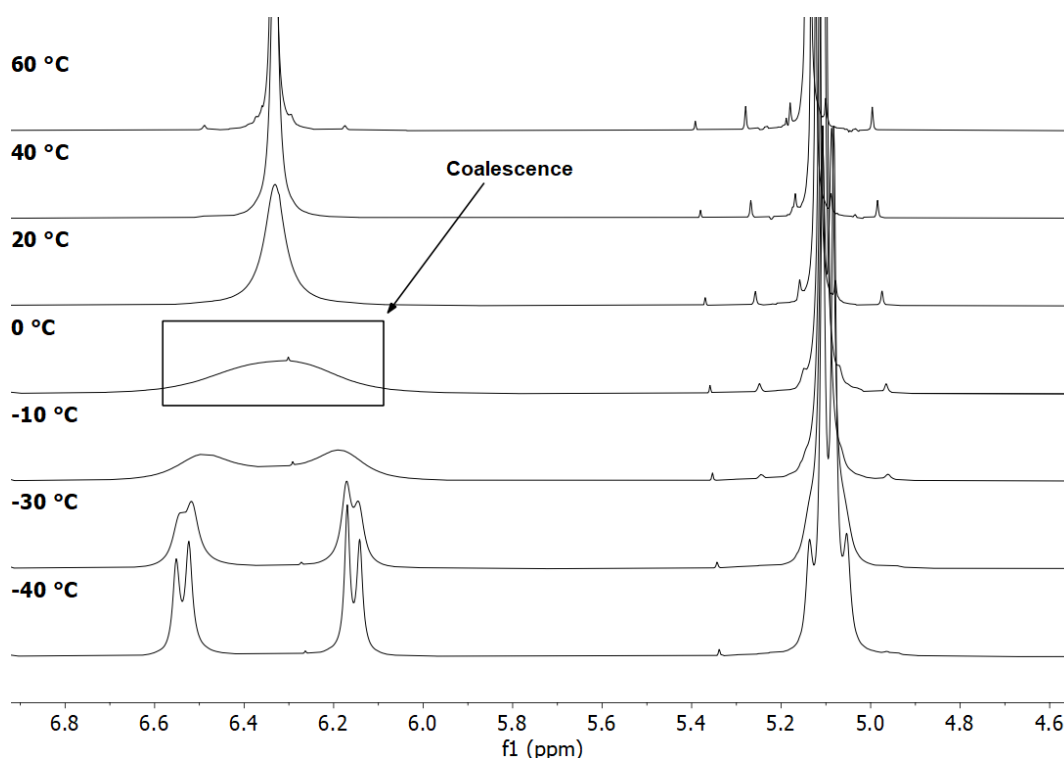


Figure 2.9: Variable temperature ^1H NMR spectra of $[\text{Ag}_2(\text{L1})_2](\text{PF}_6)_2$ between -40 and 60 $^\circ\text{C}$ showing the bridge (centered at 6.33 ppm) and wingtip methylene (5.10 ppm) resonances (d_3 -MeCN, 500 MHz).

There are three complexes in the series that have similar R groups with only the length of the arm changing between the phenyl and the imidazole core, these are $[\text{Ag}_2(\text{L1})_2](\text{PF}_6)_2$, $[\text{Ag}_2(\text{L2})_2](\text{PF}_6)_2$ and $[\text{Ag}_2(\text{L3})_2](\text{PF}_6)_2$, where R = benzyl, phenylethyl and phenylpropyl respectively.

Figure 2.10 shows the ^1H NMR spectra of complex $[\text{Ag}_2(\text{L2})_2](\text{PF}_6)_2$ (in which the wingtip alkyl chain has been extended by one carbon) in d_3 -MeCN at -40 and 60 $^\circ\text{C}$. At 60 $^\circ\text{C}$ the alkyl chains rotate freely, and the spectrum is well resolved with two triplets observed for H5 and H6, and the methylene bridge (H4, 6.17 ppm) is a sharp singlet. Whilst at -40 $^\circ\text{C}$ the methylene bridge resonance is more complex (inlet **Figure 2.10**). In contrast to $[\text{Ag}_2(\text{L1})_2](\text{PF}_6)_2$ the spectrum at -40 $^\circ\text{C}$ (bottom) shows four doublets corresponding to the methylene bridge protons. Two doublets are more intense than the other two, which represents a major (α) and a minor (β) conformer. The J -coupling of the doublets from both conformers is 14.0 Hz which is consistent with protons on a methylene bridge $^2J(^1\text{H}-^1\text{H})$ coupling. The distance

between the doublets in each conformer are different, the major and the minor have a $\Delta\nu$ of 52.0 and 131.6 Hz respectively. Further evidence for the existence of two conformers is shown by doubling of the other resonances expected for the complex (i.e. the backbone and aromatic resonances). The ratio between these forms is approximately 1:2. The T_c for the methylene bridge of $[\text{Ag}_2(\text{L2})_2](\text{PF}_6)_2$ is between -10 and 0°C (see **Appendix 8.35**). For $[\text{Ag}_2(\text{L2})_2](\text{PF}_6)_2$, the wingtip chain length is extended by one carbon (compared to $[\text{Ag}_2(\text{L1})_2](\text{PF}_6)_2$). At 60°C the alkyl chains rotate freely, and the spectrum is well resolved with two triplets observed for H5 and H6. At -40°C the signals turned into complex multiplets (centred at ca. 2.97 and 4.24 ppm for H5 and H6 respectively) as i) two conformers are present, which doubles the number of signals and ii) the arms have become so constrained that the protons H5a/b and H6a/b (**Figure 2.11**) on each carbon become diastereotopic, as all these protons couple a complex splitting pattern is formed.

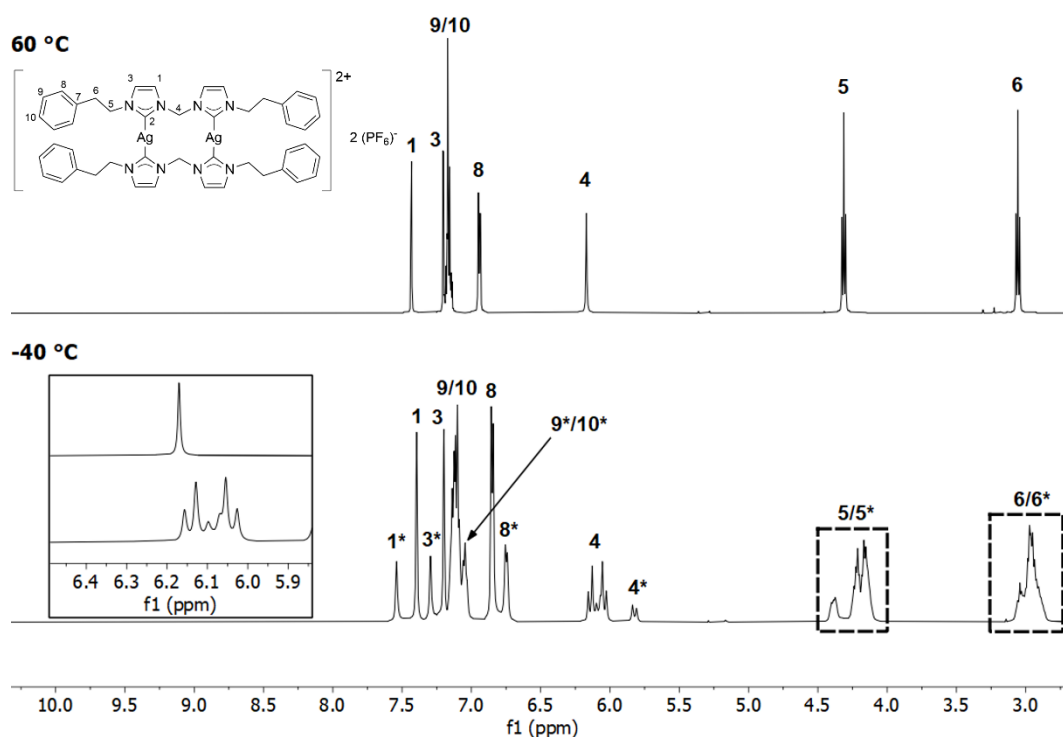


Figure 2.10: ^1H NMR spectra of $[\text{Ag}_2(\text{L2})_2](\text{PF}_6)_2$ measured at -40 and 60°C , with an expansion showing the methylene bridge region in more detail. The peaks from the minor conformer are labbed with an astrisk (d_3 -MeCN, 500 MHz).

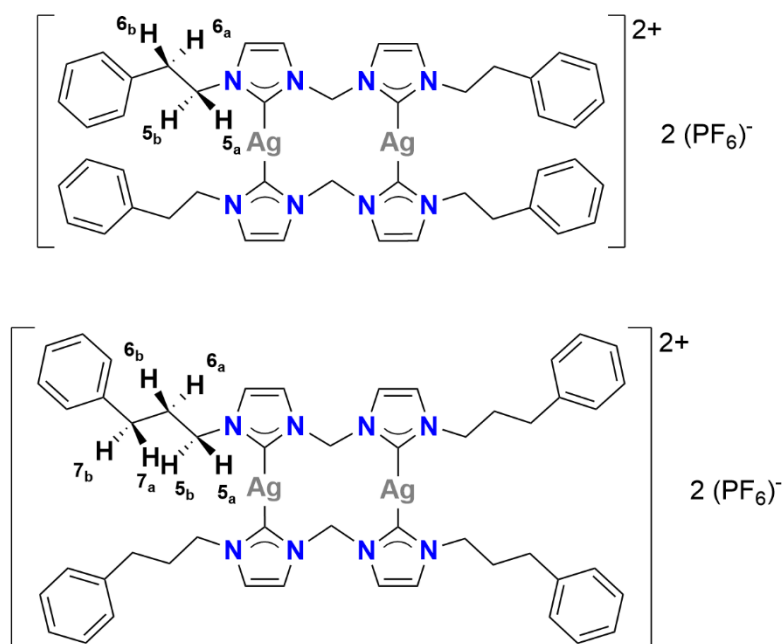


Figure 2.11: *Ag(I)-NHC complexes $[Ag_2(L2)_2](PF_6)_2$ (top) and $[Ag_2(L3)_2](PF_6)_2$ (bottom) with the hydrogens on the wingtips are shown explicitly.*

With the evidence that two conformers can be identified for an arm length of two it may be expected that when a third carbon is added, $[Ag_2(L3)_2](PF_6)_2$, we might also see multiple conformers. This is however not the case and can be seen in **Figure 2.12**. As with $[Ag_2(L1)_2](PF_6)_2$, at $-40\text{ }^{\circ}\text{C}$ only two doublets are present for the bridge methylene, indicating that only one conformer is present. The flexibility of the 12-membered ring and therefore the methylene bridge is different in $[Ag_2(L3)_2](PF_6)_2$ compared to the other two silver complexes as the T_c is much higher at $20\text{ }^{\circ}\text{C}$ (see **Appendix 8.36**). This means that the ring is more rigid and requires more energy for the bridge to rotate and for the protons to become equivalent.

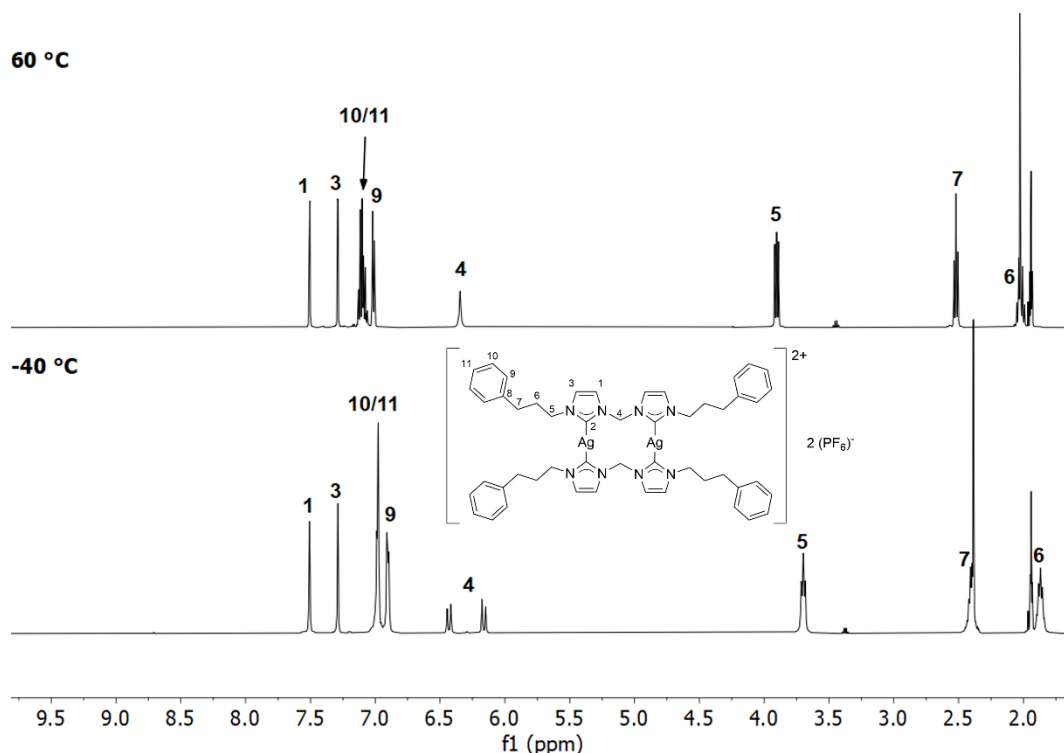


Figure 2.12: ^1H NMR spectra of $[\text{Ag}_2(\text{L3})_2](\text{PF}_6)_2$ measured at -40 and 60 °C (d_3 -MeCN, 500 MHz).

In $[\text{Ag}_2(\text{L4})_2](\text{PF}_6)_2$ the wingtip has been extended by a phenyl (compared to $[\text{Ag}_2(\text{L1})_2](\text{PF}_6)_2$). The T_c for the bridge methylene protons lays between -30 – -10 °C (See **Appendix 8.37**), indicating that the ring system in this compound is more flexible than the phenyl version $[\text{Ag}_2(\text{L1})_2](\text{PF}_6)_2$. The wingtip methylene of $[\text{Ag}_2(\text{L4})_2](\text{PF}_6)_2$ splits into a well resolved pair of doublets at -40 °C (See **Appendix 8.37**) with a large $\Delta\nu$ of 116.0 Hz. This large separation and relatively high (for the wingtip methylene) T_c between -30 – -10 °C is due to the poor rotation around the wingtip methylene carbon, and potentially due to π - π stacking interactions.

$[\text{Ag}_2(\text{L5})_2](\text{PF}_6)_2$ is substituted with a *tert*-butyl in the *para* position. This has a bridge methylene $T_c = 10$ °C (See **Appendix 8.38**) which does indicate that the bulky substituent raises the energy needed for the ring to interconvert. At -40 °C the wingtip methylene is still a singlet (see **Appendix 8.38**) which indicates that $T_c < -40$ °C and that the wingtips are flexible in this case. This could be due to the large *tert*-butyl preventing any kind of interaction (i.e. π - π stacking) between the rings of the four wingtips. A similar pattern is observed for the second bulkiest

complex $[\text{Ag}_2(\text{L7})_2](\text{PF}_6)_2$ in which the *tert*-butyl group has been replaced by a trifluoromethyl group. The T_c for the bridge and wingtip methylene protons are 20 and $-40 - -30$ °C respectively (See **Appendix 8.40**). This indicates that like $[\text{Ag}_2(\text{L5})_2](\text{PF}_6)_2$ the bridge is much more restricted to rotation than the wingtip methylene.

Complex $[\text{Ag}_2(\text{L6})_2](\text{PF}_6)_2$ is similar to complex $[\text{Ag}_2(\text{L1})_2](\text{PF}_6)_2$, differing by only a fluorine in the *para* position (*cf.* to a proton). **Figure 2.13** shows the ^1H NMR spectra of $[\text{Ag}_2(\text{L6})_2](\text{PF}_6)_2$ at both -40 and 60 °C. At -40 °C the methylene bridge splits into two doublets, and the $T_c = 0^\circ\text{C}$ (See **Appendix 8.23**), which is the same as $[\text{Ag}_2(\text{L1})_2](\text{PF}_6)_2$ and highlights the addition of a fluorine does not influence the flexibility of the molecule.

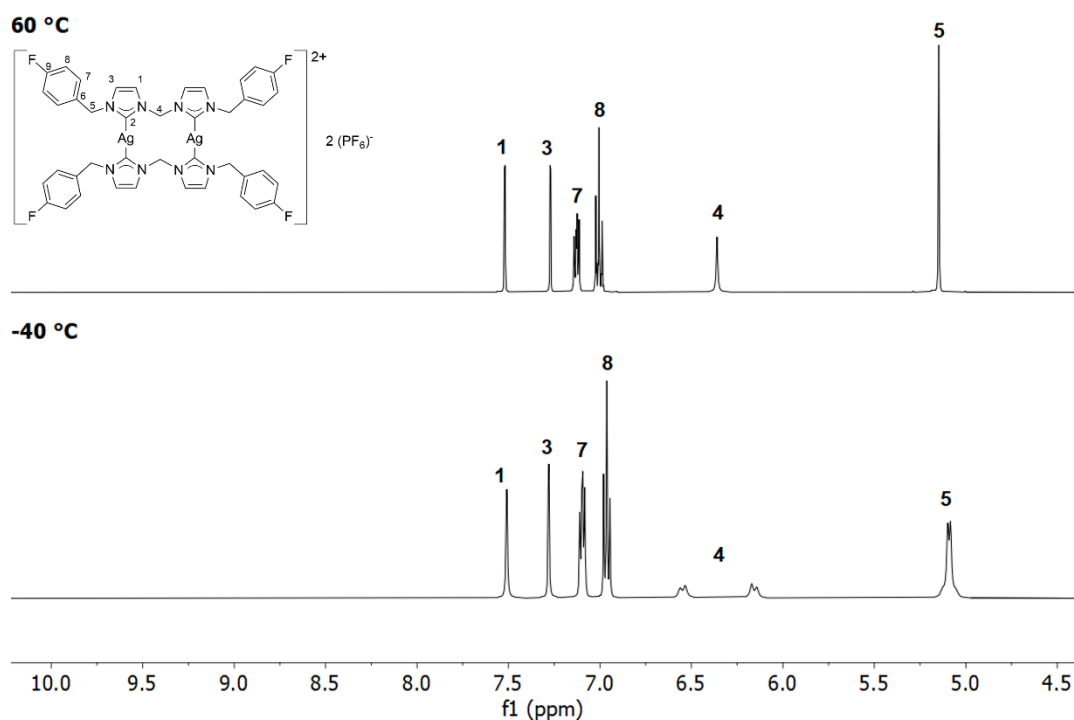


Figure 2.13: ^1H NMR spectra of $[\text{Ag}_2(\text{L6})_2](\text{PF}_6)_2$ measured at -40 and 60 °C (d_3 -MeCN, 500 MHz).

From the data extracted from the VT-NMR spectra, the approximate rate constants could be calculated using **Equation 2**. The results are summarised in **Table 2.3**, and all the rate constants are the same order of magnitude, between $140 - 480 \text{ s}^{-1}$. The complexes with the slowest interconversions are $[\text{Ag}_2(\text{L1})_2](\text{PF}_6)_2$, $[\text{Ag}_2(\text{L5})_2](\text{PF}_6)_2$, and $[\text{Ag}_2(\text{L7})_2](\text{PF}_6)_2$, with rate constants of 430, 450 and

480 s⁻¹ respectively, indicating that substitution of the ring has little effect on the exchange rate. The complexes that show the fastest interconversion between the methylene protons is the α -conformer of [Ag₂(L2)₂](PF₆)₂ and [Ag₂(L4)₂](PF₆)₂ with rate constants of 140 and 270 s⁻¹ respectively. The difference of the rate constants between the two conformers (α and β) of [Ag₂(L2)₂](PF₆)₂ (140 and 300 s⁻¹ respectively) indicates that the conformation of the 12-membered ring has an influence on the flexibility of the methylene bridge.

Table 2.3: Kinetic parameters for the methylene bridge protons in silver complexes [Ag₂(L1-7)₂](PF₆)₂. Where a range is given the T_c falls within that range.

Complex	T_c (°C)	J-coupling of doublets (Hz)	Chemical shift between doublets (Hz)	k (s ⁻¹)
[Ag ₂ (L1) ₂](PF ₆) ₂	-10 – 0	14	192	430
[Ag ₂ (L2) ₂](PF ₆) ₂ - α	0 – 20	14	52.0	140
[Ag ₂ (L2) ₂](PF ₆) ₂ - β	0 – 20	14	132	300
[Ag ₂ (L3) ₂](PF ₆) ₂	20	14	135	310
[Ag ₂ (L4) ₂](PF ₆) ₂	-30 – -10	13.5	116	270
[Ag ₂ (L5) ₂](PF ₆) ₂	10	14	200	450
[Ag ₂ (L6) ₂](PF ₆) ₂	0	13	197	440
[Ag ₂ (L7) ₂](PF ₆) ₂	0 - 20	14	212	480

2.2.3 ¹³C{¹H} NMR Spectroscopy

After complexation, the C2 carbon in the ¹³C{¹H} NMR spectra shift downfield from *ca.* 140 to 180 ppm. Both naturally occurring isotopes of silver ¹⁰⁷Ag and ¹⁰⁹Ag have a nuclear spin of a ½ which means both couple with the ¹³C and leads to two sets of doublets. For example, [Ag₂(L6)₂](PF₆)₂ (Figure 2.14) shows ¹J couplings of 183 and 210 Hz for ¹³C-¹⁰⁷Ag and ¹³C-¹⁰⁹Ag respectively, where the larger coupling of ¹⁰⁹Ag is due to its larger gyromagnetic ratio compared to ¹⁰⁷Ag. In the reported series of complexes, the C2 resonance is only observed for [Ag₂(L6)₂](PF₆)₂ under normal collection conditions. For the other complexes, the C2 peak is absent due to a weak quaternary signal and the slow relaxation because of the lack of Nuclear Overhauser Effect (NOE), the signal is also split into four peaks which further diminishes the intensity. The backbone carbons (C1 and C3)

exhibit no significant changes with complexation, and resonances appear between 122.0 – 124.1 ppm for the ligands and the complexes. Upon complexation, there is a consistent downfield shift of the C4 methylene carbon resonances by *ca.* 5 ppm. It is notable that for the fluorine containing complexes $[\text{Ag}_2(\text{L6})_2](\text{PF}_6)_2$ and $[\text{Ag}_2(\text{L7})_2](\text{PF}_6)_2$, the resonances on the benzyl group appear as doublets and quartets respectively due to ^{13}C - ^{19}F coupling. The same is true for the respective ligands. For $[\text{Ag}_2(\text{L6})_2](\text{PF}_6)_2$ the doublets are found at 116.0, 130.4, 131.2 and 162.4 ppm and have couplings of 20.2 (2J), 3.2 (4J), 8.5 (3J) and 246 (1J) Hz. The quartets found in the spectrum of $[\text{Ag}_2(\text{L7})_2](\text{PF}_6)_2$ are found at 124.1, 129.5 and 129.5 ppm and have couplings of 244.7 (1J), 3.8 (3J) and 31.9 (2J) Hz respectively.

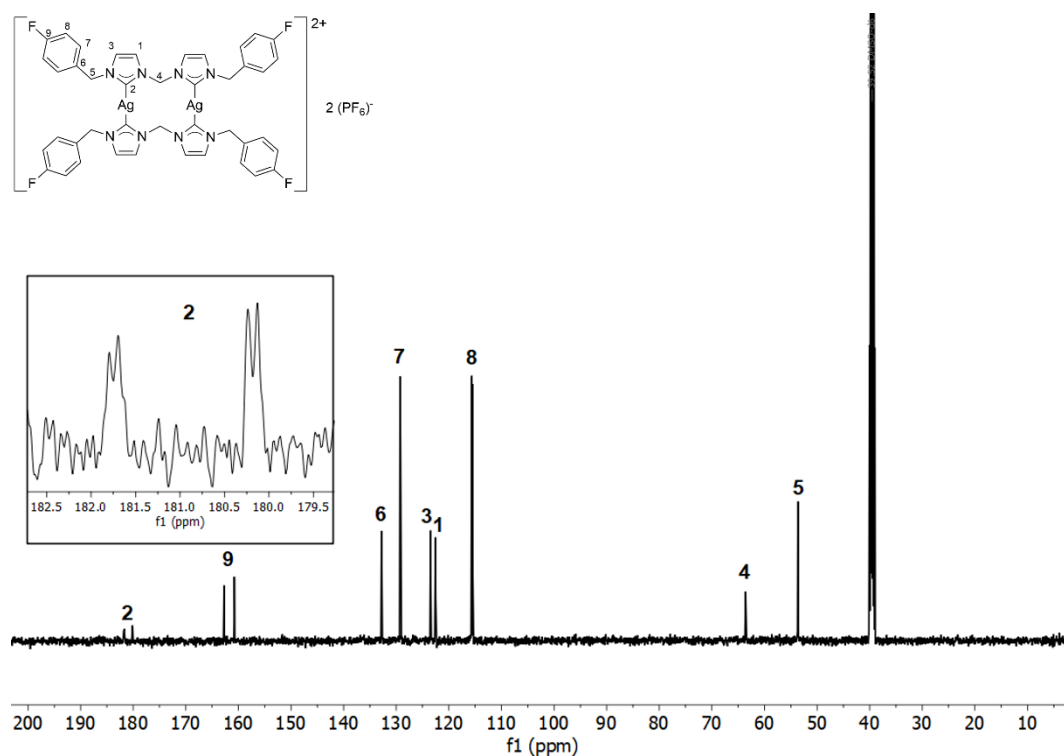


Figure 2.14: $^{13}\text{C}\{^1\text{H}\}$ NMR spectrum of $[\text{Ag}_2(\text{L6})_2](\text{PF}_6)_2$, with an expanded section showing the two doublets from the C2 carbon (d_6 -DMSO, 500 MHz).

To overcome the relaxation problem of quaternary carbons, a paramagnetic species, for example $\text{Cr}(\text{acac})_3$, can be added to reduce the relaxation time of the carbon nuclei.¹⁵⁰ **Figure 2.15** shows $[\text{Ag}_2(\text{L1})_2](\text{PF}_6)_2$ (10 mg) in d_6 -DMSO (0.5 mL) with varied experiment parameters (D_1 and number of scans). The shorter D_1 time allows for more scans in a shorter period, and collection of 1536 scans in under 30 minutes.

Under these parameters, the doublet of doublets for the C2 carbon becomes apparent.

D1 0.5, No scans 256

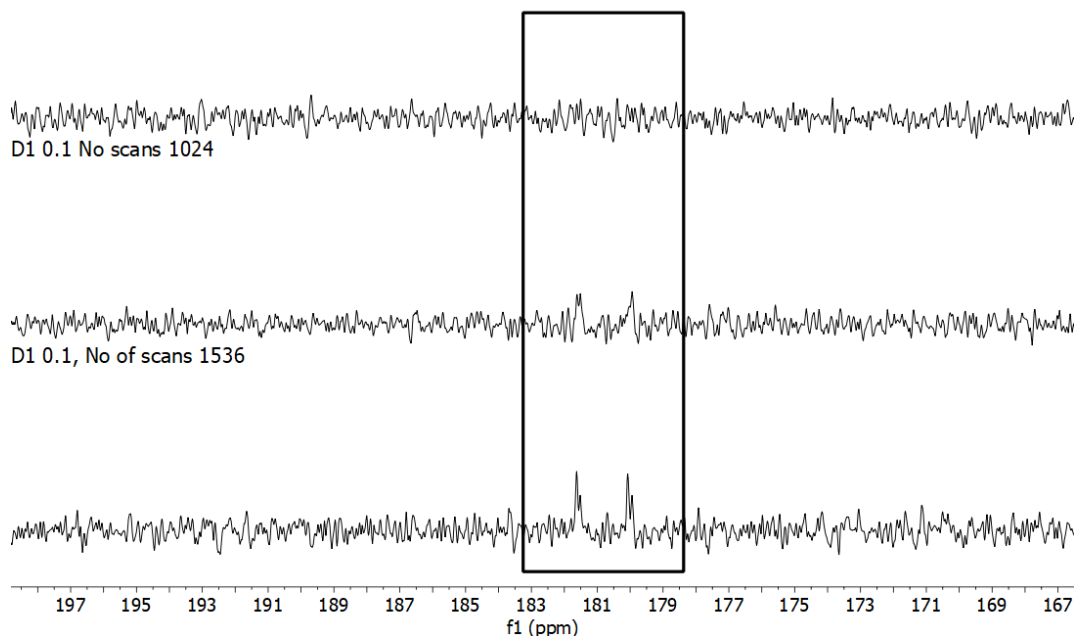


Figure 2.15: $^{13}\text{C}\{^1\text{H}\}$ NMR spectra of $[\text{Ag}_2(\text{L1})_2](\text{PF}_6)_2$ (10 mg) in d_6 -DMSO (0.5 mL) with $[\text{Cr}(\text{acac})_3]$ (5 mg), and collected with varied D_1 and number of scans. Region of C2 resonance is shown in the black box. (d_6 -DMSO, 500 MHz).

2.2.4 ATR-FTIR Spectroscopy

IR spectroscopy is a useful tool for confirming successful syntheses. **Figure 2.16** shows $[\text{H}_2\text{L6}](\text{PF}_6)_2$ and $[\text{Ag}_2(\text{L6})_2](\text{PF}_6)_2$ as an example. There are regions that are similar between ligand and complex, e.g., aromatic C-H stretches between 3130 – 3180 cm^{-1} and the retainment of the broad band at *ca.* 830 cm^{-1} , which is characteristic of the PF_6 anion. However, there are some noticeable differences, such as the disappearance of the C2-H bend peak found at 1550 cm^{-1} (for $[\text{H}_2\text{L6}](\text{PF}_6)_2$) and the decrease in the wavenumber of the C=N stretch from 1428 to 1418 cm^{-1} (for $[\text{Ag}_2(\text{L6})_2](\text{PF}_6)_2$), as the bond weakens upon complexation.

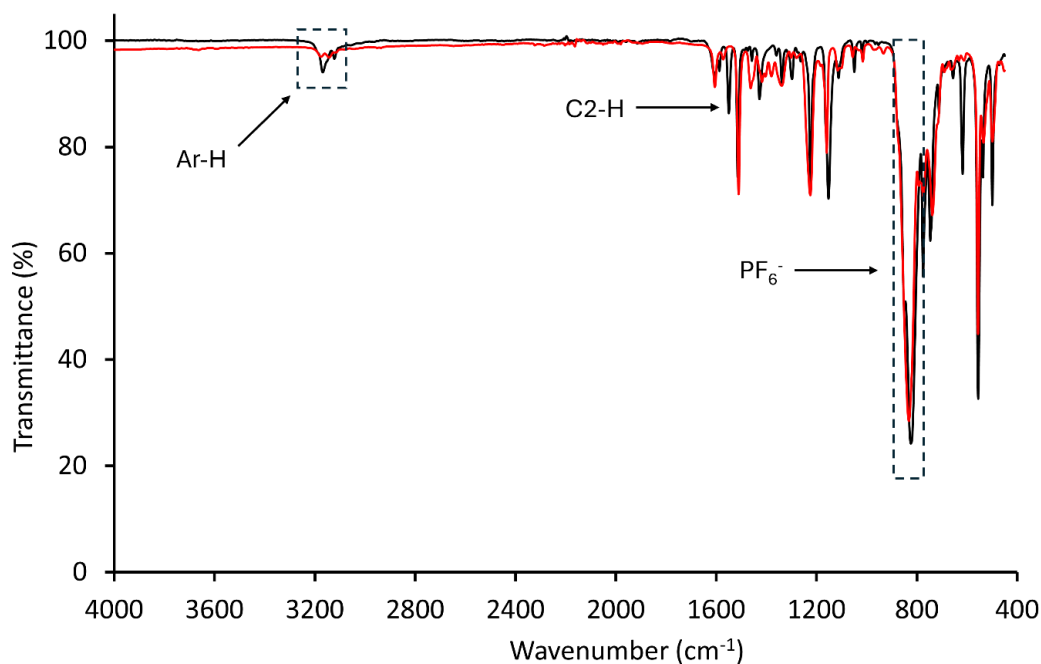


Figure 2.16: ATR-FTIR spectra of $[H_2L6](PF_6)_2$ (black) and $[Ag_2(L6)_2](PF_6)_2$ (red) collected between $450 - 4000\text{ cm}^{-1}$.

2.2.5 Single Crystal X-ray Diffraction

2.2.5.1 X-ray characterisation of $[Ag_2(L3)_2](PF_6)_2$

White needle like single crystals of $[Ag_2(L3)_2](PF_6)_2$ suitable for scXRD analysis were obtained via vapour diffusion of Et_2O into a concentrated MeCN solution. The data was collected and solved by Dr Rianne Lord. The crystal was solved in a monoclinic cell and the structural solution was performed in the space group $I2/m$, with half a molecule in the asymmetric unit. The molecular structure is shown in **Figure 2.17**, with the central 12-membered ring forming a boat shaped conformation, and both methylene bridges pointing in the same direction. The molecule also has a plane of symmetry along the Ag1-Ag2 axis. The geometry around the silver is slightly bent from the ideal linear mode at $170.5(3) - 171.6(3)^\circ$ (**Table 2.4**), and the carbene-silver bond lengths are between $2.076(5) - 2.087(6)\text{ \AA}$, which are in agreement with other reported Ag(I)-NHC complexes.¹⁴³ The distance between the two silvers is 3.50 \AA , this is too long to be considered an argentophilic interaction, which requires distances below the sum of the van der Waals radius of two silver atoms $< 3.44\text{ \AA}$.¹⁵¹

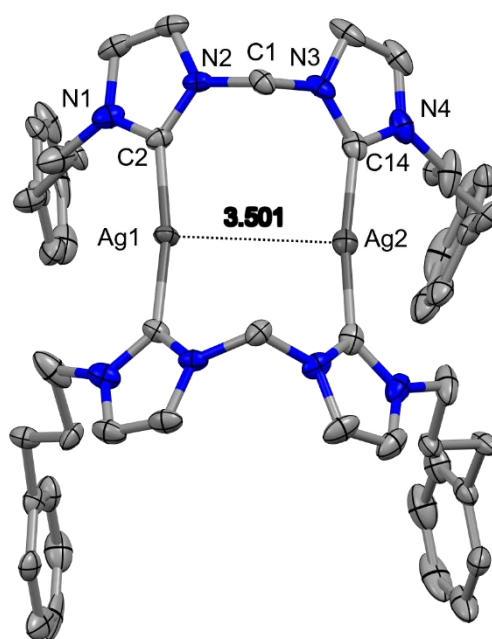


Figure 2.17: Molecular structure of $[Ag_2(L3)_2](PF_6)_2$ with solvent, counterions and hydrogen atoms omitted for clarity. Displacement ellipsoids are shown at the 50% probability level.

Table 2.4: Selected scXRD parameters for $[Ag_2(L3)_2](PF_6)_2$.

Atoms	Bond lengths (Å)
Ag1-C2	2.076(5)
Ag2-C14	2.087(6)
Ag---Ag	3.501
C-H---F	2.274 – 2.670
Atoms	Angle (°)
C2-Ag1-C2 ¹	170.5(3)
C14-Ag2-C14 ¹	171.6(3)

¹reflection parameters: 1+X,1-Y,+Z

The crystal packing of $[Ag_2(L3)_2](PF_6)_2$ is shown in **Figure 2.18** along the *b* axis. The molecules pack in an alternating fashion, but the distance between the aromatic rings is too long to be considered π - π interactions.

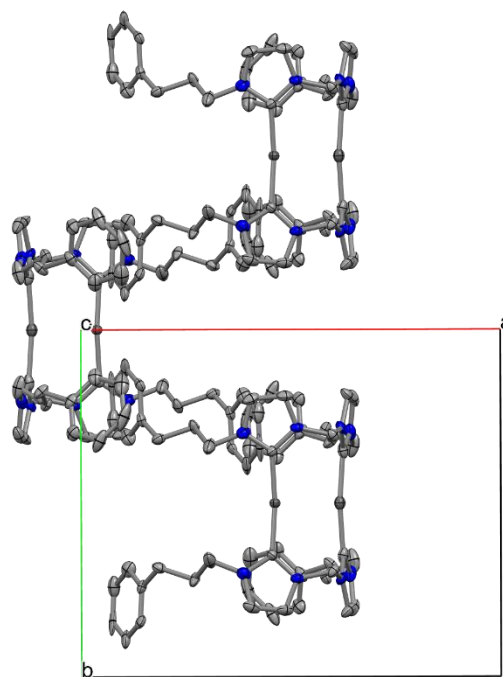


Figure 2.18: Crystal packing of $[Ag_2(L3)_2](PF_6)_2$ when viewed along the c -axis.

Within the lattice there are intermolecular hydrogen bonding interactions between the hydrogens on the methylene bridge and the imidazole backbone of the complex and between the fluorides of the PF_6 anion. The bond lengths range from 2.274 – 2.670 Å, which are considered weak hydrogen bonds (**Figure 2.19**).¹⁵²

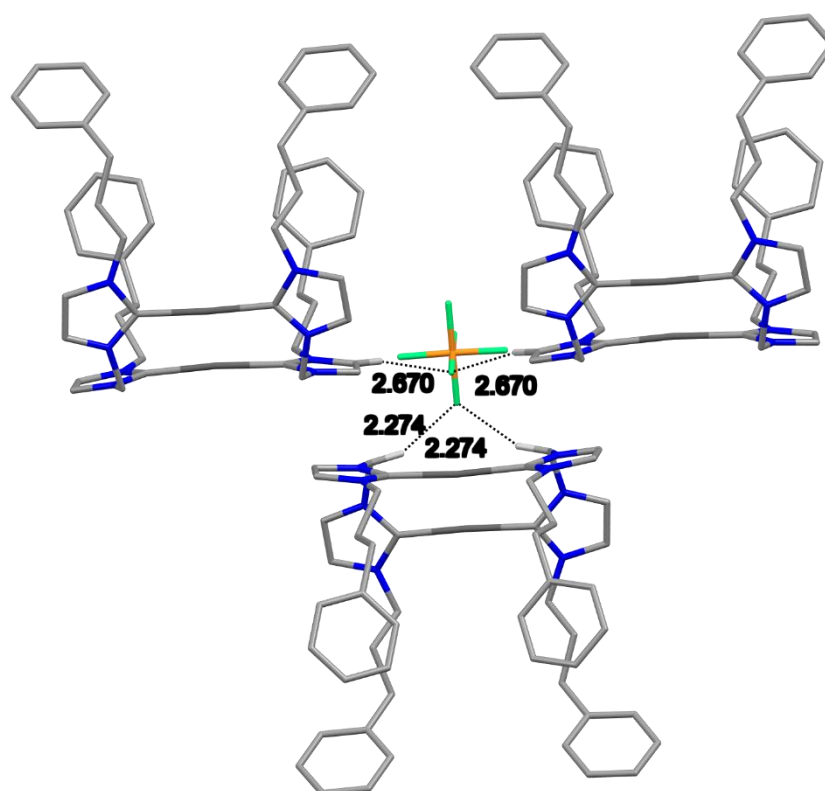


Figure 2.19: Crystal packing of $[\text{Ag}_2(\text{L3})_2](\text{PF}_6)_2$ showing the intermolecular hydrogen bonding interaction between three molecules of $[\text{Ag}_2(\text{L3})_2](\text{PF}_6)_2$ and the PF_6 anion. Only protons involved in interactions are shown.

2.2.5.2 X-ray characterisation of $[\text{Ag}_2(\text{L4})_2](\text{PF}_6)_2$

Clear block-like single crystals of $[\text{Ag}_2(\text{L4})_2](\text{PF}_6)_2$ suitable for scXRD analysis were obtained through vapour diffusion of Et_2O into a concentrated MeCN solution. The data was collected by Dr Rianne Lord. The crystal was solved in a monoclinic cell and the structural solution was performed in the $P2_1/c$ space group, with half a molecule in the asymmetric unit. The molecular structure is shown **Figure 2.20**, with the central 12-membered ring forming a chair-like conformation and the methylene bridges pointing in opposite directions. The naphthalene wingtips fall on both sides of the plane of the central ring. Like $[\text{Ag}_2(\text{L3})_2](\text{PF}_6)_2$ the carbene silver bond lengths are 2.091(2) – 2.093(2) Å (**Table 2.5**) and within the reported range for other reported Ag(I)-NHC complexes. The C-Ag-C bond angle deviates from the ideal linear geometry 168.87(8)°, and the complex shows an argentophilic

interaction between the two silver centres with a distance of 3.19 Å.¹⁵¹ The complex exhibits an intermolecular π - π stacking interaction (3.95 Å) between the imidazole and naphthyl group.

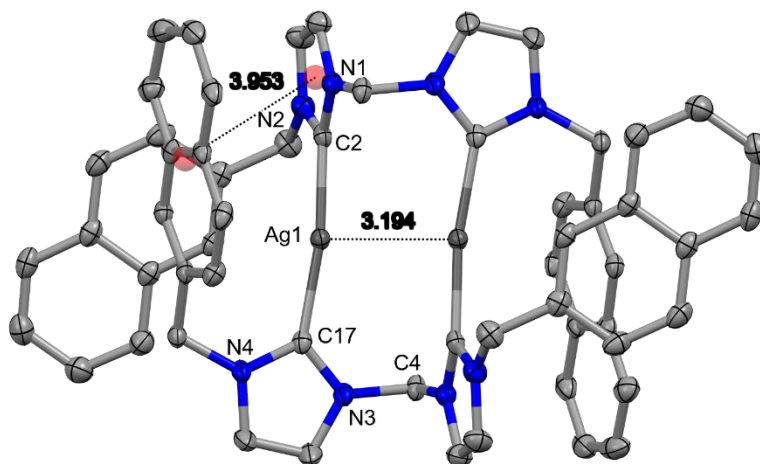


Figure 2.20: Molecular structure of $[Ag_2(L4)_2](PF_6)_2$, with solvent, counterions and hydrogen atoms are omitted for clarity. Displacement ellipsoids are shown at the 50% probability level. Intramolecular π - π stacking interaction between imidazole and naphthyl is shown.

Table 2.5: Selected scXRD parameters for $[Ag_2(L4)_2](PF_6)_2$.

Atoms	Bond lengths (Å)
Ag1-C2	2.091(3)
Ag1-C17 ¹	2.093(3)
Ag1---Ag1 ¹	3.1945(3)
C-H---F	2.461 – 2.665
Atoms	Angle (°)
C2-Ag1-C17 ¹	168.87(8)
C1-Ag1-Ag1 ¹ -C5	1.52

¹reflection parameters: -X,1-Y,1-Z

A packing diagram $[Ag_2(L4)_2](PF_6)_2$ when viewed along the *c*-axis is shown in **Figure 2.21**. There molecules form an alternating pattern, with parallel displaced π - π stacking (3.786 Å) interactions between the naphthyl groups of adjacent molecules.

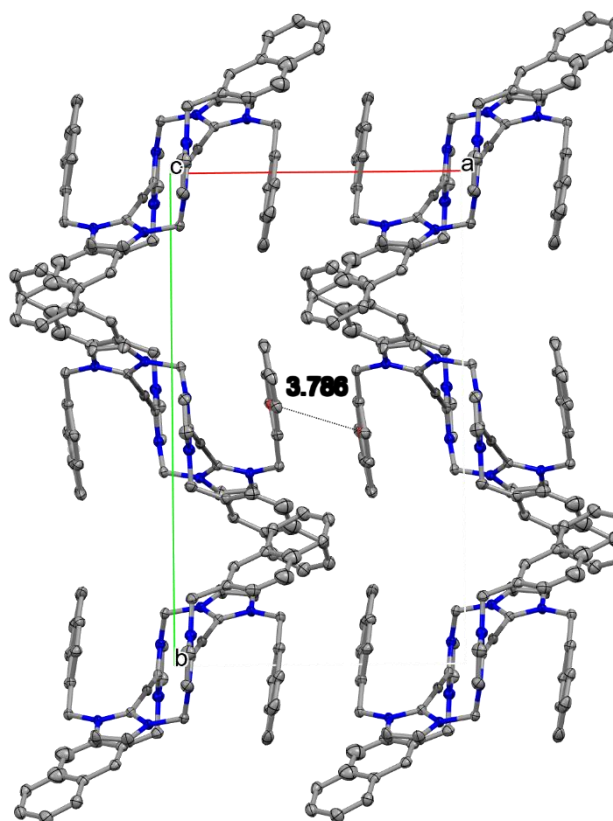


Figure 2.21: Crystal packing of $[\text{Ag}_2(\text{L4})_2](\text{PF}_6)_2$ when viewed along the c -axis. The intermolecular π - π stacking interaction between two naphthyls (3.786 \AA) is shown, solvent, PF_6 anions and hydrogens have been omitted for clarity.

Within the crystal lattice there are weak hydrogen bonding interactions (**Figure 2.22**)¹⁵² between the PF_6 anion and the protons on the Et_2O (solvent molecule in the crystal lattice), the naphthyl group, imidazole backbone and the methylene wingtip.¹⁵² These bond lengths are between $2.461 - 2.665 \text{ \AA}$.

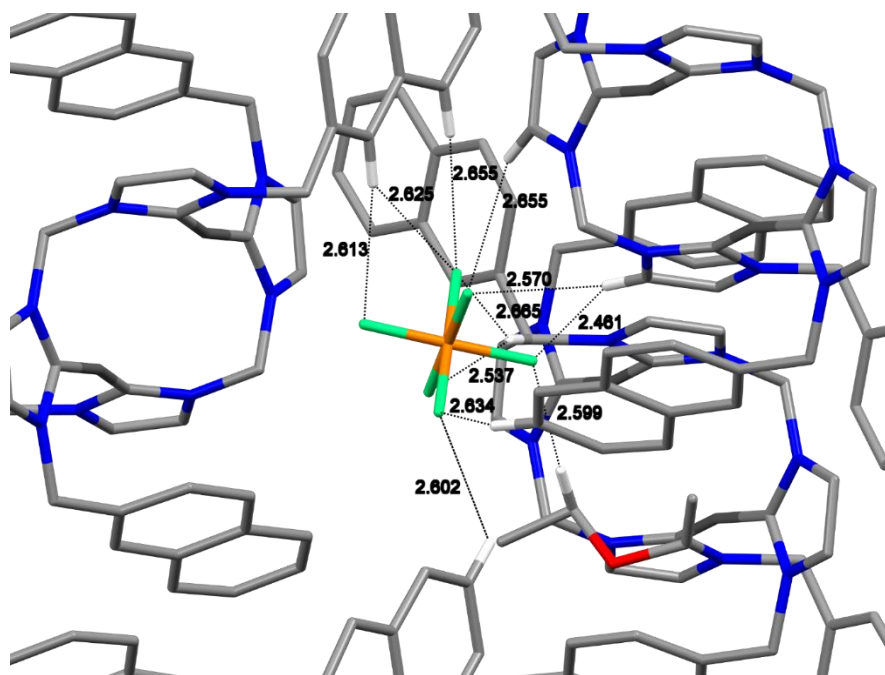


Figure 2.22: Crystal packing of $[\text{Ag}_2(\text{L4})_2](\text{PF}_6)_2$ showing the intermolecular hydrogen bonding interaction between three molecules of $[\text{Ag}_2(\text{L4})_2](\text{PF}_6)_2$ and one molecule of Et_2O with the PF_6 anion. Only protons involved in interactions are shown.

2.2.5.3 X-ray characterisation of $[\text{Ag}_2(\text{L6})_2](\text{PF}_6)_2$

Colourless plate-like single crystals of $[\text{Ag}_2(\text{L6})_2](\text{PF}_6)_2$ suitable for scXRD analysis were obtained through vapour diffusion of Et_2O into a concentrated MeCN solution. The data was collected by Dr Rianne Lord. The crystal was solved in a triclinic unit cell and the structural solution was performed in the $P-1$ space group, with one molecule in the asymmetric unit and a centre of inversion. The molecular structure is shown in **Figure 2.23**, with the central 12-membered ring forming a boat-like conformation, where both methylene bridge groups pointing in the same direction. The carbene silver bond lengths are between 2.084 – 2.096 Å (**Table 2.6**), and the complex shows an intermolecular argentophilic interaction with a Ag-Ag distance of 3.282 Å. The arrangement of the wingtip groups is similar to $[\text{Ag}_2(\text{L3})_2](\text{PF}_6)_2$ with them on the same side of the central ring.

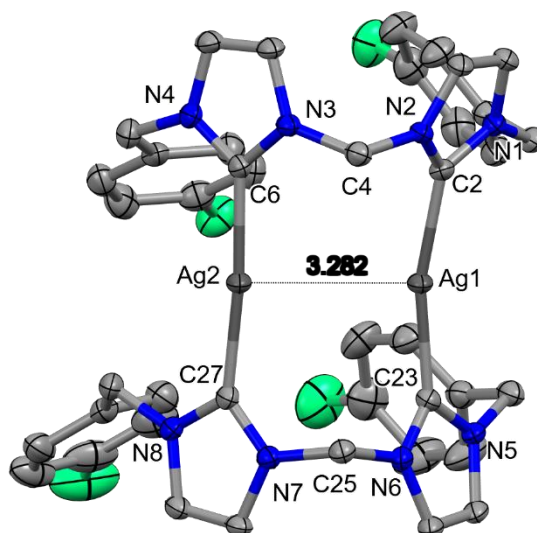


Figure 2.23: Molecular structure of $[Ag_2(L6)_2](PF_6)_2$ with solvent, counterions and hydrogen atoms are omitted for clarity. Displacement ellipsoids are shown at the 50% probability level.

Table 2.6: Selected scXRD parameters for $[Ag_2(L6)_2](PF_6)_2$.

Atoms	Bond lengths (Å)
Ag1-C2	2.096(3)
Ag1-C23	2.094(3)
Ag2-C6	2.090(3)
Ag2-C27	2.084(3)
Ag1---Ag2 (intramolecular)	3.2816(4)
Ag1---Ag1 (intermolecular)	3.698
C6(Im)--- C27(Im)	3.709
C-H---F	2.328 – 2.664
Atoms	Angle (°)
C2-Ag1-C23	164.80(12)
C6-Ag2-C27	174.55(13)
C2-Ag1-Ag2-C27	177.39
C23-Ag1-Ag2-C6	177.85
C2-Ag1-Ag2-C6	5.36
C23-Ag-Ag2-C27	-4.89
Plane	Angle (°)
C2(Im)-C23(Im)	33.84
C6(Im)- C27(Im)	2.62

The C-Ag-C angles are bent compared to the ideal linear geometry, with angles of 164.80(12) and 174.55(13)° for C2-Ag1-C23 and C6-Ag2-C27 respectively. This difference also leads to $[\text{Ag}_2(\text{L6})_2](\text{PF}_6)_2$ having no symmetry within the molecule (unlike the $[\text{Ag}_2(\text{L3})_2](\text{PF}_6)_2$ and $[\text{Ag}_2(\text{L4})_2](\text{PF}_6)_2$). The imidazoles that are *trans* to each other have different orientations. The planes of all the imidazoles are shown in **Figure 2.24**. The imidazoles C2(Im)-C23(Im) are bent out of plane with a dihedral angle of 33.84°, whereas C6(Im)-C27(Im) are in-plane with a dihedral angle 2.62°.

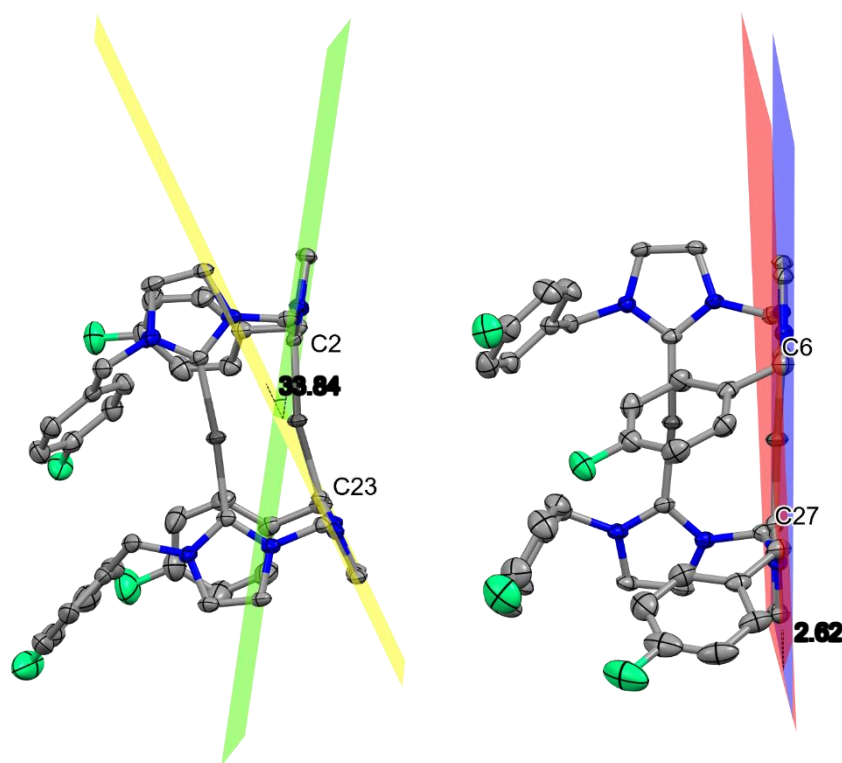


Figure 2.24: The planes of all for imidazoles C2(Im) (green), C6(Im) (blue), C23(Im) (yellow) and C27(Im) (red) for complex $[\text{Ag}_2(\text{L6})_2](\text{PF}_6)_2$. The dihedral angle between the planes of *trans* imidazoles is shown.

Figure 2.25 shows the intermolecular interactions between two molecules of $[\text{Ag}_2(\text{L6})_2](\text{PF}_6)_2$. There are π - π stacking interactions between the imidazole rings which interact in a parallel displaced manner, with a centroid distance of 3.709 Å. The intermolecular distance between the closest silver atoms between the two

molecules is 3.698 Å, which is too long to be considered an argentophilic interaction.

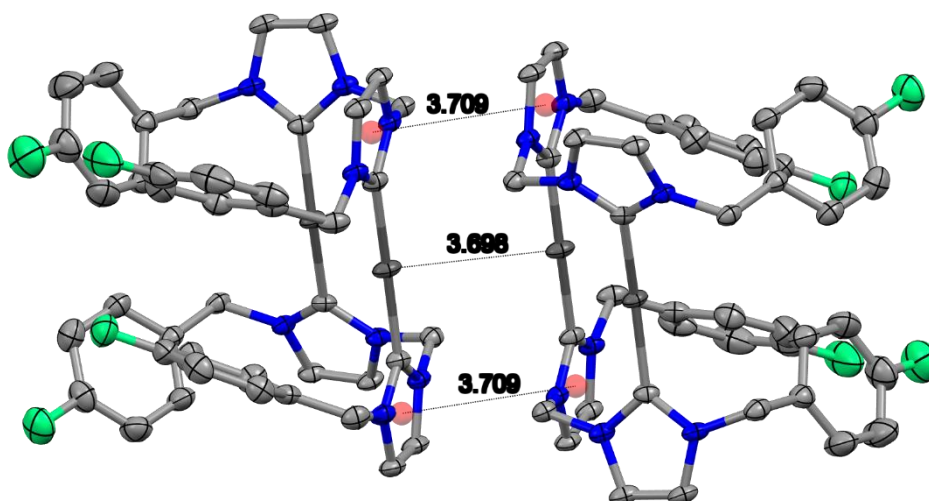


Figure 2.25: Crystal packing of $[Ag_2(L6)_2](PF_6)_2$ showing the π - π stacking interactions between two molecules and the intermolecular Ag-Ag interaction.

The PF₆ anion forms interactions with five molecules of $[Ag_2(L6)_2](PF_6)_2$, shown in **Figure 2.26**. Contacts are observed between the bridging and wingtip methylenes and the imidazole backbone hydrogen atoms, with hydrogen bond lengths between 2.328 – 2.664 Å indicating weak hydrogen bonding.

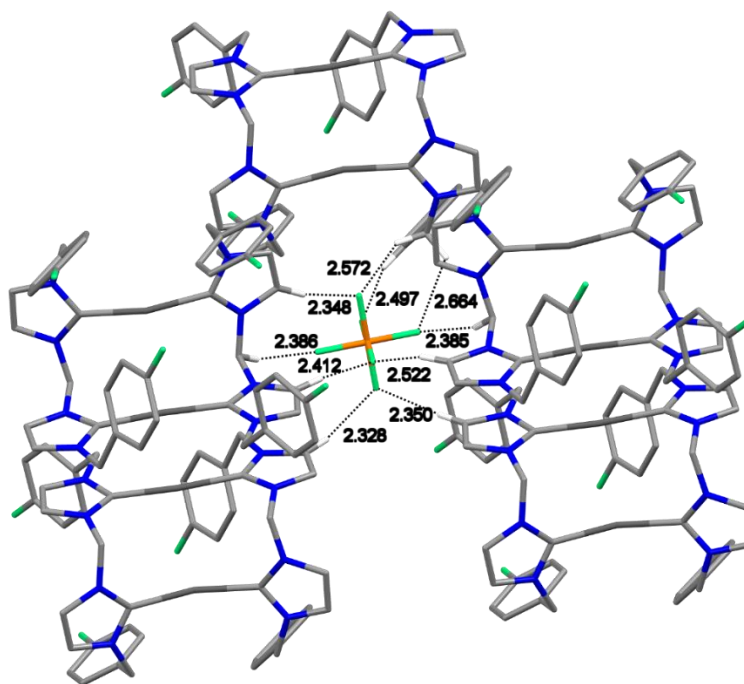


Figure 2.26: Crystal packing of $[Ag_2(L6)_2](PF_6)_2$ showing the hydrogen bonding interactions with the PF_6 anion within the crystal structure.

2.2.5.4 X-ray characterisation of $[Ag_2(L7)_2](PF_6)_2$

Colourless trapezoid single crystals of $[Ag_2(L7)_2](PF_6)_2$ suitable for scXRD analysis were obtained through vapour diffusion of Et_2O into a concentrated MeCN solution. The data was collected by Dr Benjamin Hofmann. The crystal was solved in a triclinic unit cell and the structural solution was performed in the $P-1$ space group, with half a molecule in the asymmetric unit and a centre of inversion. The molecular structure is shown in **Figure 2.27**, with the central 12-membered ring forming a chair-like conformation, where both methylene bridge groups pointing in opposite directions. The C-Ag bond lengths are between 2.084 – 2.096 Å (**Table 2.7**), and the complex shows an intramolecular argentophilic interaction with a Ag-Ag distance of 3.162 Å.

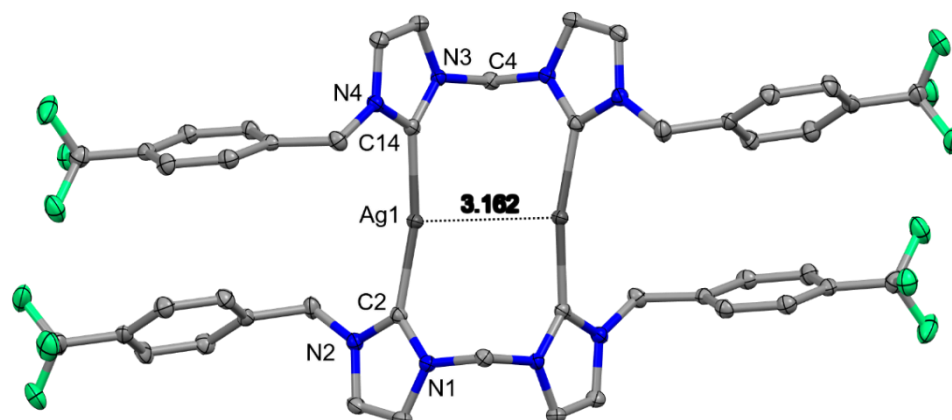


Figure 2.27: Molecular structure of $[Ag_2(L7)_2](PF_6)_2$ with counterions and hydrogen atoms omitted for clarity. Displacement ellipsoids are shown at the 50% probability level.

Table 2.7: Selected parameters for $[Ag_2(L7)_2](PF_6)_2$.

Atoms	Bond lengths (Å)
Ag1-C2	2.091(2)
Ag1-C14 ¹	2.095(2)
Ag1---Ag1 ¹	3.1616(3)
C-H---F	2.382 – 2.631
Atoms	Angle (°)
C2-Ag1-C14 ¹	167.13(8)

¹reflection parameters: 1-X,1-Y,1-Z

The PF_6 anion forms interactions with four molecules of $[Ag_2(L7)_2](PF_6)_2$, and this is shown in **Figure 2.28**. The contacts are observed between hydrogens of the bridging and wingtip methylene, the backbone imidazole rings and the benzyl, with the fluorides on the PF_6 anion, with hydrogen bond lengths between 2.328 – 2.631 Å, which are weak hydrogen bonds.

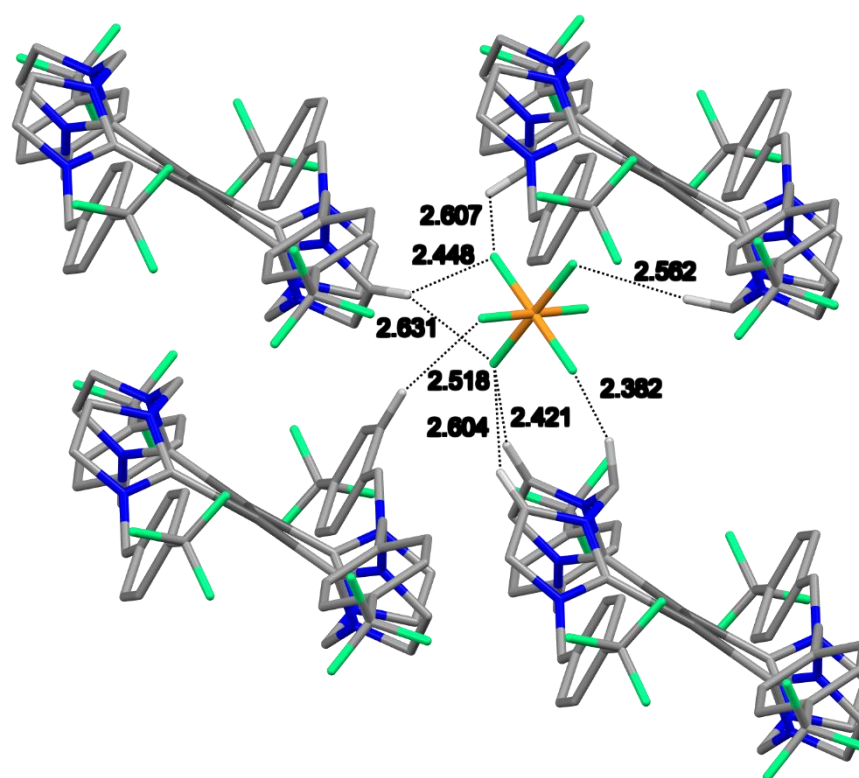


Figure 2.28: Crystal packing of $[Ag_2(L7)_2](PF_6)_2$ showing the hydrogen bonding interactions with the PF_6 anion within the crystal structure.

2.3 Conclusions

A range of methylene bridged imidazolium-based ligands were successfully synthesised from monofunctionalised imidazole precursors, with ligands $[H_2L2-7](PF_6)_2$ being reported for the first time. The ligands were fully characterised, and both 1H and $^{13}C\{^1H\}$ NMR spectroscopy show similar shifts downfield in the C2 proton resonance after the imidazolium salt formation. Ion exchange from a Br to PF_6 anion is confirmed by an upfield shift of the C2 proton and the appearance of a broad peak in the ATR-FTIR spectra at *ca.* 830 cm^{-1} . From the imidazolium salts, six new Ag(I)-NHC complexes, $[Ag_2(L2-7)_2](PF_6)_2$, were synthesised via two methods, either from the Br anion followed by an ion exchange with ammonium hexafluorophosphate, or directly from ligands containing the PF_6 anion. Low to modest yields were obtained for all reactions. Successful complexation was confirmed by 1H NMR spectroscopy, with the disappearance of the C2 proton resonance and the backbone resonances becoming doublets (from

doublet of doublets or triplets) after complexation. The methylene bridge resonance became notably broad upon complexation, indicating hindered rotation of the bridge. Conformational dynamics were further studied by VT-NMR spectroscopy, from which the approximate rate constants were calculated. The results showed that bulky substituents $[\text{Ag}_2(\text{L5})_2](\text{PF}_6)_2$ ($\text{R} = p\text{-tert-butylbenzyl}$) and $[\text{Ag}_2(\text{L7})_2](\text{PF}_6)_2$ ($\text{R} = p\text{-trifluoromethylbenzyl}$) exhibit slow rates of exchange, however the different exchange rates for two different conformers was observed for $[\text{Ag}_2(\text{L2})_2](\text{PF}_6)_2$ ($\text{R} = \text{phenylethyl}$), indicating that the ring conformation is also an important influence on the exchange rate and not just the wingtip. Upon analysis of the $^{13}\text{C}\{^1\text{H}\}$ NMR spectra, complexes $[\text{Ag}_2(\text{L1})_2](\text{PF}_6)_2$ and $[\text{Ag}_2(\text{L6})_2](\text{PF}_6)_2$ show carbene carbon resonances as two doublets which is characteristic of 1J coupling with the two naturally abundant isotopes of silver (Ag^{107} and Ag^{109}). Sc-XRD was conducted for four of the Ag(I)-NHC complexes and have C-Ag bond length in-line with those reported in the literature. The 12-membered ring have varied conformations in the complexes adopting a boat-like ($[\text{Ag}_2(\text{L3})_2](\text{PF}_6)_2$ and $[\text{Ag}_2(\text{L6})_2](\text{PF}_6)_2$) and chair-like ($[\text{Ag}_2(\text{L4})_2](\text{PF}_6)_2$ and $[\text{Ag}_2(\text{L7})_2](\text{PF}_6)_2$) structure. The constraint from the ring system led to a deviation from the ideal 180° C-Ag-C angle. Complexes $[\text{Ag}_2(\text{L4})_2](\text{PF}_6)_2$, $[\text{Ag}_2(\text{L6})_2](\text{PF}_6)_2$ and $[\text{Ag}_2(\text{L7})_2](\text{PF}_6)_2$ show intramolecular argentophilic interactions with Ag-Ag distance $< 3.44 \text{ \AA}$. Weak intermolecular hydrogen bonding interactions between the complex and the PF_6 anion were observed in all four crystal structures. Additionally, $[\text{Ag}_2(\text{L4})_2](\text{PF}_6)_2$ and $[\text{Ag}_2(\text{L6})_2](\text{PF}_6)_2$ exhibited intermolecular $\pi\text{-}\pi$ stacking interactions. The ligands $[\text{H}_2\text{L1-7}](\text{PF}_6)_2$ and Ag(I)-NHC complexes $[\text{Ag}_2(\text{L1-7})_2](\text{PF}_6)_2$ described in this chapter will be evaluated for their anticancer properties (see Chapter 4)

3 Silver(I) *N*-Heterocyclic Carbene Derivatives

The benzimidazole moiety is ubiquitous in medicinal chemistry and is found in many active drug compounds on the market today such as the antitumor drugs Bendamustine, Binimetinib and Galeterone.^{153,154} To further understand the structure activity relationship between the ligand scaffold and biological activity, benzimidazole derivatives of the complexes described in **Chapter 2** were synthesised. The general structure is shown below **Figure 3.1** (where ligands [H₂L10](Br)₂, [H₂L10](PF₆)₂, [H₂L13](Br)₂ and [H₂L13](PF₆)₂ were synthesised by BSc project student Aran Boakye-Smith).

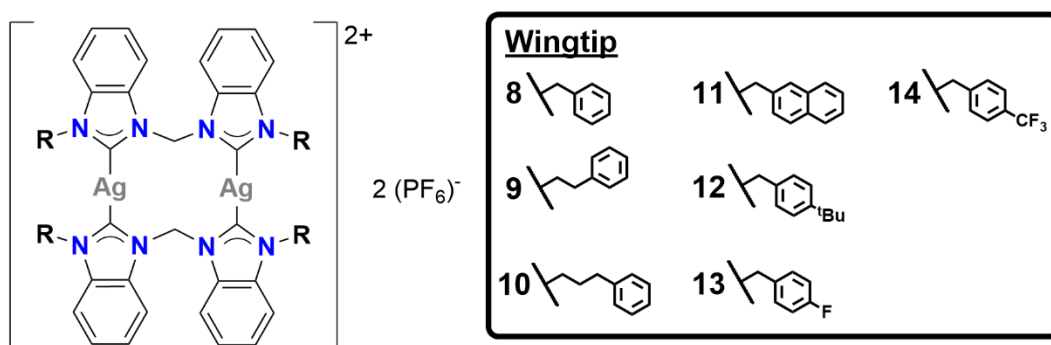


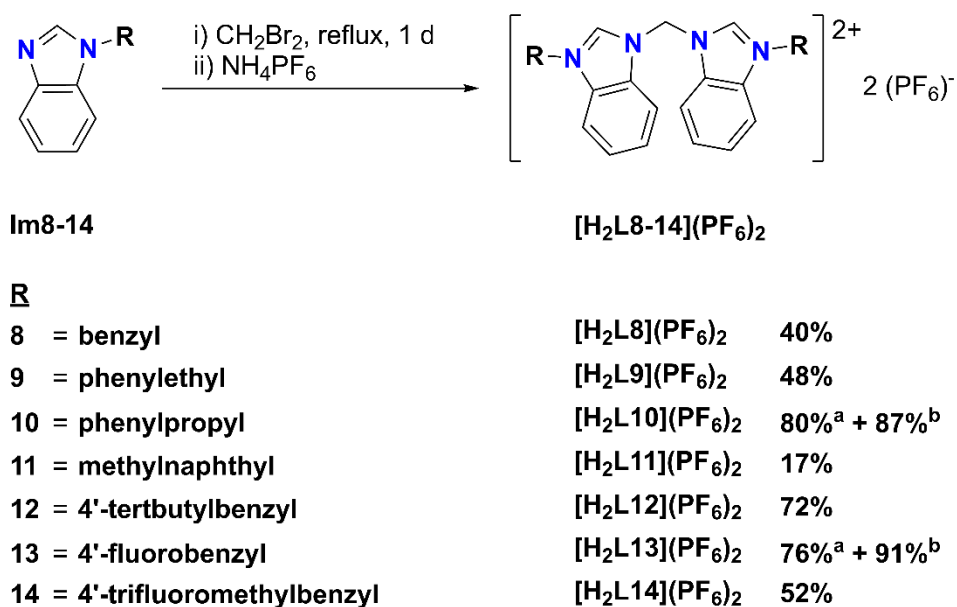
Figure 3.1: General structure of the bridged benzimidazolium-based Ag(I)-NHC complexes [Ag₂(L8-14)₂](PF₆)₂ discussed in this chapter (left), with the different R groups of the complexes.

Unlike the imidazole versions, methylene bridged benzimidazolium ligands are not widely explored, with few examples in literature. Most of the reported salts have aliphatic, amide, or phosphine-based wingtips, but few of them have been tested for their biological activity.^{155–162} There are limited examples with aromatic wingtips described in literature, the ones that have been reported have benzyl, Mes and pyridine wing.^{158,163,164} There are even fewer examples of benzimidazole based methylene bridged homoleptic Ag(I)-NHC complexes, those reported literature have wingtips including Me and pyridine, however, these have not been evaluated against cancer.^{165,166}

3.1 Benzimidazolium-based Bridged Homoleptic Silver(I) *N*-Heterocyclic Carbene Complexes

3.1.1 Synthesis and Characterisation of Bridged Benzimidazolium Ligands

The synthesis of the bridged benzimidazolium salts of the ligands was carried out using the same method as the one described previously in **Chapter 2** starting with monofunctionalised benzimidazoles. The monofunctionalised benzimidazole (**Im8** – **14**) were synthesised using a modified literature procedure.¹⁶⁷ These benzimidazoles were then bridged by heating to reflux in neat dibromomethane (both as the solvent and reactant). The ligands were isolated following an ion exchange with ammonium hexafluorophosphate (**Scheme 3.1**).



Scheme 3.1: Synthesis of bridged benzimidazolium hexafluorophosphate salts, ^astep (i), ^bstep(ii).

The yields for these reactions are moderate to high 48 – 72%. For **[H₂L10](PF₆)₂** and **[H₂L13](PF₆)₂** the bromide salt was isolated after step (i) with yields of 80% and 76% respectively. The yield for the ion exchange to obtain **[H₂L10](PF₆)₂** and **[H₂L13](PF₆)₂** was 87 and 91% respectively. The values for the other ligands mostly fall in the range expected for these types of reactions and those reported in literature (40 to 94%).^{164,168}

Successful bridging was confirmed by ^1H NMR spectroscopy, similar to the imidazole ligands in **Chapter 2**. The most indicative change is the shift of the C2 proton which shifts downfield upon bridging, due to the formation of the benzimidazolium cation. The C2 proton in each of the benzimidazolium ligands is further shifted when compared to the imidazolium equivalent. This is highlighted in **Figure 3.2**, where the C2 proton has shifted from 9.41 ppm for $[\text{H}_2\text{L6}](\text{PF}_6)_2$ to 10.31 ppm for $[\text{H}_2\text{L13}](\text{PF}_6)_2$. The difference is due to the electron withdrawing nature of the phenyl backbone of benzimidazoles compared to imidazoles. All of the other ligands $[\text{H}_2\text{L8-14}](\text{PF}_6)_2$ chemical shift changes between 0.89 – 0.94 ppm (see **Table 3.1**). The chemical shifts of the C2 carbon in the $^{13}\text{C}\{^1\text{H}\}$ NMR spectra of $[\text{H}_2\text{L8-14}](\text{PF}_6)_2$ are also shifted when compared to the imidazole analogues by 5.6 – 6.5 ppm (see **Table 3.1**).

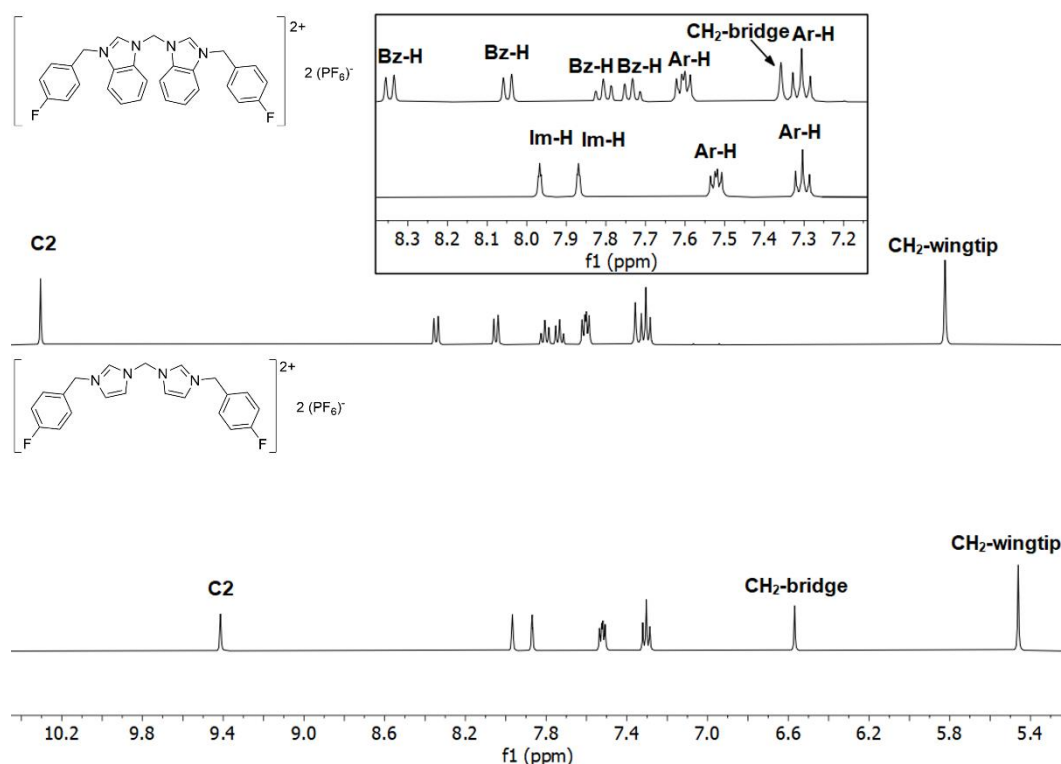


Figure 3.2: ^1H NMR spectra of $[\text{H}_2\text{L6}](\text{PF}_6)_2$ and $[\text{H}_2\text{L13}](\text{PF}_6)_2$ (d_6 -DMSO, 400 MHz), with an expansion of the aromatic region.

Table 3.1: Chemical shifts of the C2 proton obtained from the ^1H NMR and $^{13}\text{C}\{^1\text{H}\}$ NMR spectra and chemical shift difference between the benzimidazole and corresponding imidazole analogue, the latter is shown in brackets.

$[\text{H}_2\text{LX}](\text{PF}_6)_2$	^1H NMR chemical shift (δ)	Chemical shift difference (δ) between im and benz	C2 chemical shift (δ) by $^{13}\text{C}\{^1\text{H}\}$ NMR	Chemical shift difference (δ) between im and benz
8(1)	10.39	0.94	144.1	-
9(2)	10.13	0.90	143.6	6.3
10(3)	10.60	1.21	144	6.5
11(4)	10.38	0.90	143.4	5.6
12(5)	10.36	0.92	144	6.4
13(6)	10.31	0.90	144.1	6.4
14(7)	10.37	0.90	144.6	6.5

Both $[\text{H}_2\text{L13}](\text{Br})_2$ and $[\text{H}_2\text{L13}](\text{PF}_6)_2$ were isolated, and a $^{19}\text{F}\{^1\text{H}\}$ NMR spectrum obtained for both species (**Figure 3.3**). $[\text{H}_2\text{L13}](\text{Br})_2$ has one singlet at -112.8 ppm for the *p*-fluoro on the wingtip, however, after ion exchange a doublet appears at -70.1 ppm with a $^1J(^{19}\text{F}-^{31}\text{P})$ coupling from the PF_6 anion. The ratio of the integration of the doublet and singlet is *ca.* 6:1 which agrees with the number of fluorines in the complex and fluorides in the anion.

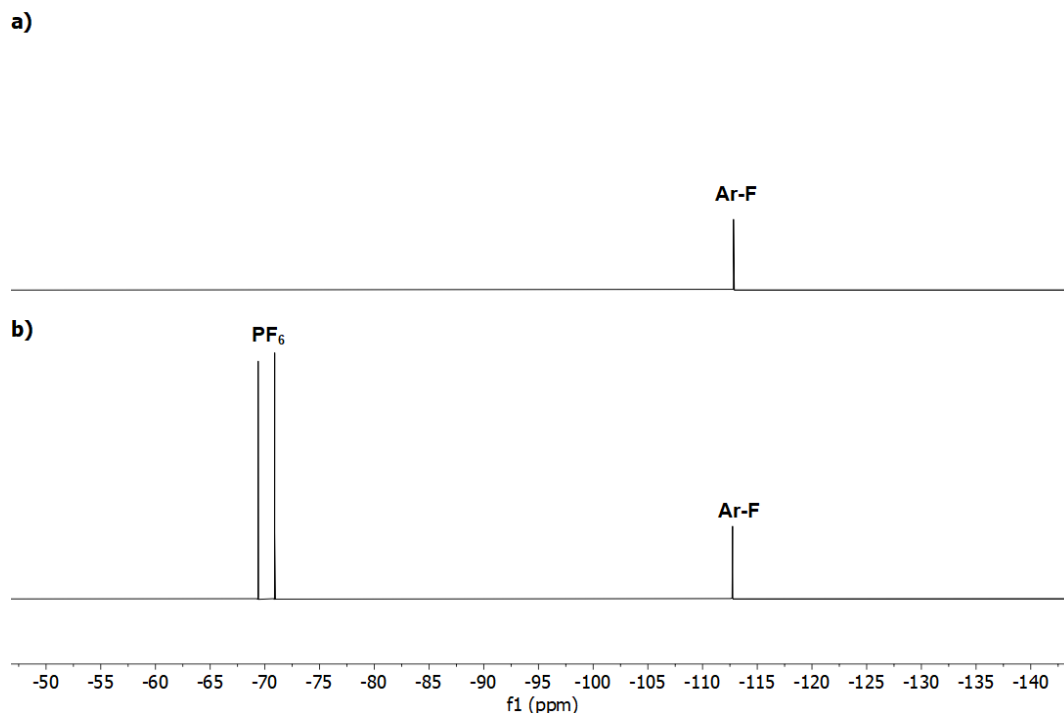


Figure 3.3: $^{19}\text{F}\{^1\text{H}\}$ NMR spectra of a) $[\text{H}_2\text{L13}](\text{Br})_2$ and $[\text{H}_2\text{L13}](\text{PF}_6)_2$ (d_6 -DMSO, 470.6 MHz).

For all the other ligands, successful ion exchange was confirmed by FT-IR spectroscopy and distinguishable due to the broad peak found at *ca.* 830 cm^{-1} (Appendix 8.7 – Appendix 8.15), which is indicative of the PF_6 anion. An example can be seen in Figure 3.4 (top), where the spectra of $[\text{H}_2\text{L13}](\text{Br})_2$ and $[\text{H}_2\text{L13}](\text{PF}_6)_2$ have been overlayed. An intense peak at *ca.* 830 cm^{-1} can be seen in the latter but not the former. There is evidence that $[\text{H}_2\text{L13}](\text{Br})_2$ is hygroscopic as the spectra contains a broad peak at *ca.* 3460 cm^{-1} which is indicative of water, however, this is not present in $[\text{H}_2\text{L13}](\text{PF}_6)_2$.

Figure 3.4 (bottom) shows the IR spectra of $[\text{H}_2\text{L6}](\text{PF}_6)_2$ and $[\text{H}_2\text{L13}](\text{PF}_6)_2$. There are peaks that are retained in both ligands such as 830 cm^{-1} (PF_6) and 1516 cm^{-1} C-C (aromatic) from the wingtip phenyl rings. The differences observed are due to the differences in imidazole and benzimidazole backbones. A peak is observed at 3109 cm^{-1} for the C-H (benz) stretch in $[\text{H}_2\text{L13}](\text{PF}_6)_2$, and this peak is not present in $[\text{H}_2\text{L6}](\text{PF}_6)_2$.

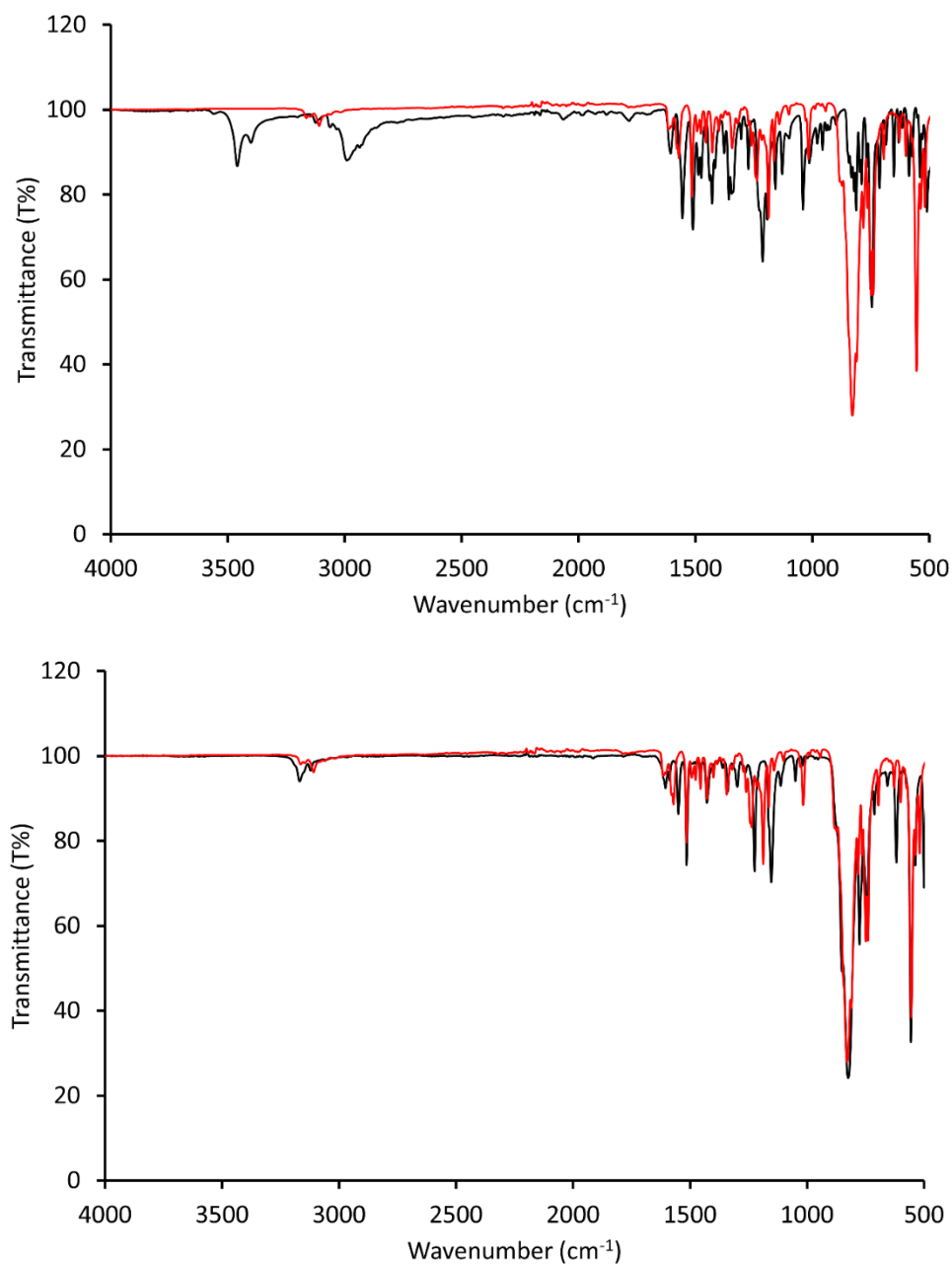
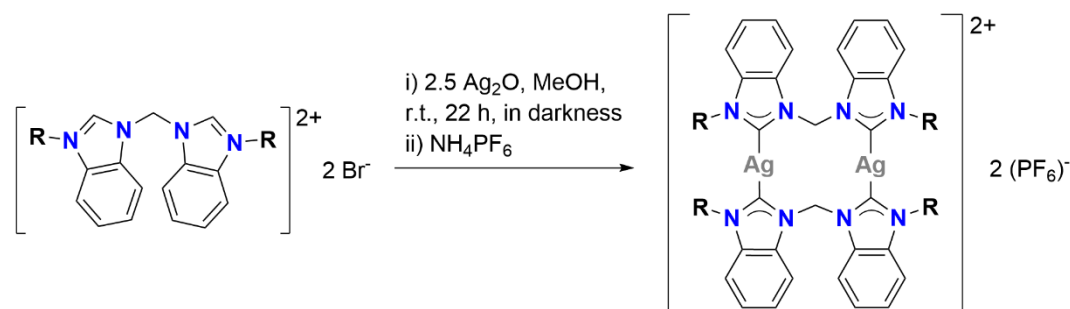


Figure 3.4: ATR-FTIR spectra of $[H_2L13](Br)_2$ (black) and $[H_2L13](PF_6)_2$ (red) (top) and $[H_2L6](PF_6)_2$ (black) and $[H_2L13](PF_6)_2$ (red).

3.1.2 Synthesis and Characterisation of Benzimidazole Binuclear Homoleptic Silver(I) *N*-Heterocyclic Carbene Complexes

The route that was taken to access the imidazole-based complexes described in **Chapter 2** was also trialled for the benzimidazolium derivatives (**Scheme 3.2**). This route starts with the bromide salt of the ligand and addition of silver(I) oxide in

MeOH, followed by passing the reaction mixture through Celite® and then via an ion exchange to the hexafluorophosphate salt.



Scheme 3.2: Attempted synthesis of $[\text{Ag}_2(\text{LX})_2](\text{PF}_6)_2$ using the MeOH route (*route 2*), where $R = \text{benzyl}$ or $p\text{-fluorobenzyl}$

The ^1H NMR spectra was collected of the product from the reaction (**Figure 3.5(a)**) and shows the presence of multiple species, however, due to the disappearance of the C2 proton (10.69 ppm) it was confirmed that no starting ligands $[\text{H}_2\text{L8}](\text{Br})_2$ (**Figure 3.5(b)**) or $[\text{H}_2\text{L8}](\text{PF}_6)_2$ (**Figure 3.5(c)**) remained in the reaction. It has been reported in other syntheses of Ag(I)-NHCs that the anion in the ligand can be incorporated into the Ag(I)-NHC complex upon complexation, this could have been the case in this synthesis.¹³⁶ For this reason *method 1* was employed, starting with a hexafluorophosphate salt to prevent the incorporation of the anion into the structure. The ^1H NMR spectrum from the product of this reaction agrees with the intended structure of $[\text{Ag}_2(\text{L8})_2](\text{PF}_6)_2$. Comparing **Figure 3.5(a)** and **Figure 3.5(d)** it can be seen that $[\text{Ag}_2(\text{L8})_2](\text{PF}_6)_2$ is a minor product from the MeOH route (*method 2*), but it contains other products that have yet to be identified.

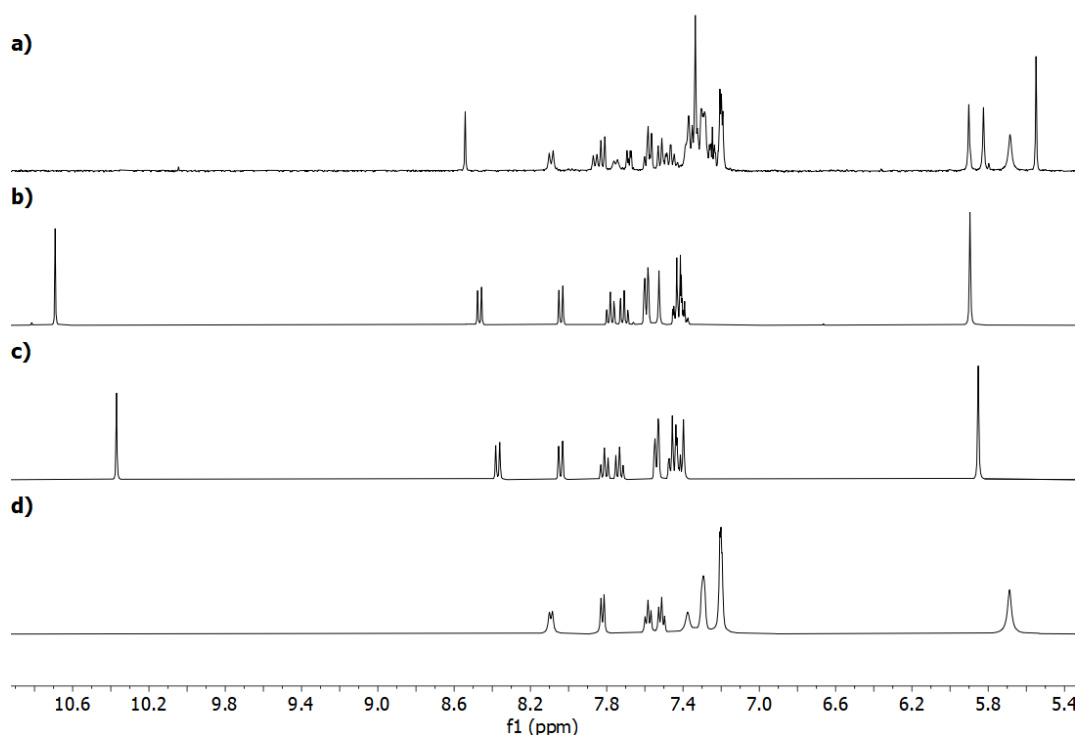


Figure 3.5: a) ^1H NMR spectra of the product from the synthesis of $[\text{Ag}_2(\text{L8})_2](\text{PF}_6)_2$ using the MeOH route. b) ^1H NMR spectra of $[\text{H}_2\text{L8}](\text{Br})_2$. c) ^1H NMR spectra of $[\text{H}_2\text{L8}](\text{PF}_6)_2$ d) ^1H NMR spectra of the product from the synthesis of $[\text{Ag}_2(\text{L8})_2](\text{PF}_6)_2$ using the MeCN route, (d_6 -DMSO, 400 MHz).

To further investigate the problems associated with the MeOH route, an attempt was made to synthesise the fluorinated derivative, $[\text{Ag}_2(\text{L13})_2](\text{PF}_6)_2$ (Scheme 3.2). The fluorine in this molecule is a useful NMR handle and can be used to help identify the number and type of species.

A $^{19}\text{F}\{^1\text{H}\}$ NMR spectrum was taken of the product from the attempted synthesis of $[\text{Ag}_2(\text{L13})_2](\text{PF}_6)_2$ (Figure 3.6(a)) and resonances were observed in the *p*-fluoro region (Ar-F are usually found between -100 and -200 ppm). There are three resonances present showing that this sample is impure (as only one should be found in this region). The resonances do not correspond to either $[\text{H}_2\text{L13}](\text{Br})_2$ (Figure 3.6(b)) or $[\text{H}_2\text{L13}](\text{PF}_6)_2$ (Figure 3.6(c)), which implies that there are three new fluorine containing species being formed.

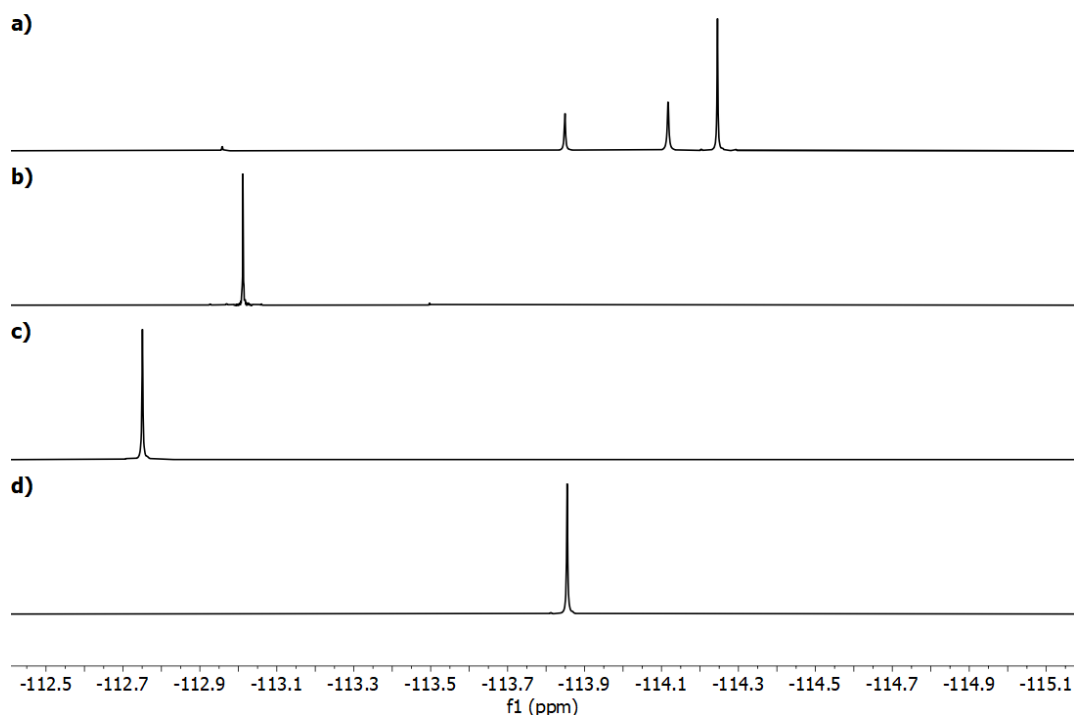


Figure 3.6: a) $^{19}\text{F}\{\text{H}\}$ NMR spectra of the product from the synthesis of $[\text{Ag}_2(\text{L13})_2](\text{PF}_6)_2$ using the MeOH route. b) $^{19}\text{F}\{\text{H}\}$ NMR spectra of $[\text{H}_2\text{L13}](\text{Br})_2$. c) $^{19}\text{F}\{\text{H}\}$ NMR spectra of $[\text{H}_2\text{L13}](\text{PF}_6)_2$ d) $^{19}\text{F}\{\text{H}\}$ NMR spectra of the product from the synthesis of $[\text{Ag}_2(\text{L13})_2](\text{PF}_6)_2$ using the MeCN route, (d_6 -DMSO, 470.6 MHz).

$[\text{Ag}_2(\text{L13})_2](\text{PF}_6)_2$ was instead successfully synthesised using **method 1**. The $^{19}\text{F}\{\text{H}\}$ NMR spectrum is shown in **Figure 3.6(d)** with a peak at -113.85 ppm. This same resonance was observed as one of the minor resonances from the MeOH route, indicating that like $[\text{Ag}_2(\text{L8})_2](\text{PF}_6)_2$ the target complex is a minor product using this route. ^1H NMR spectra for the products of both reactions (**method 1** and **2**) are shown in **Figure 3.7**. The peaks annotated with an asterisk are from $[\text{Ag}_2(\text{L13})_2](\text{PF}_6)_2$, whereas, the peaks marked with a cross are related to a second unidentified product (major product), the integrations and COSY spectrum (**Appendix 8.47**) were used to confirm this was one species. However, the major product and the other minor product have yet to be identified. Attempts were made to obtain crystals of the products from the reaction, but they were unsuccessful. Due to these results **method 1** was selected to synthesise the other complexes. The general synthesis is shown below in **Scheme 3.3**.

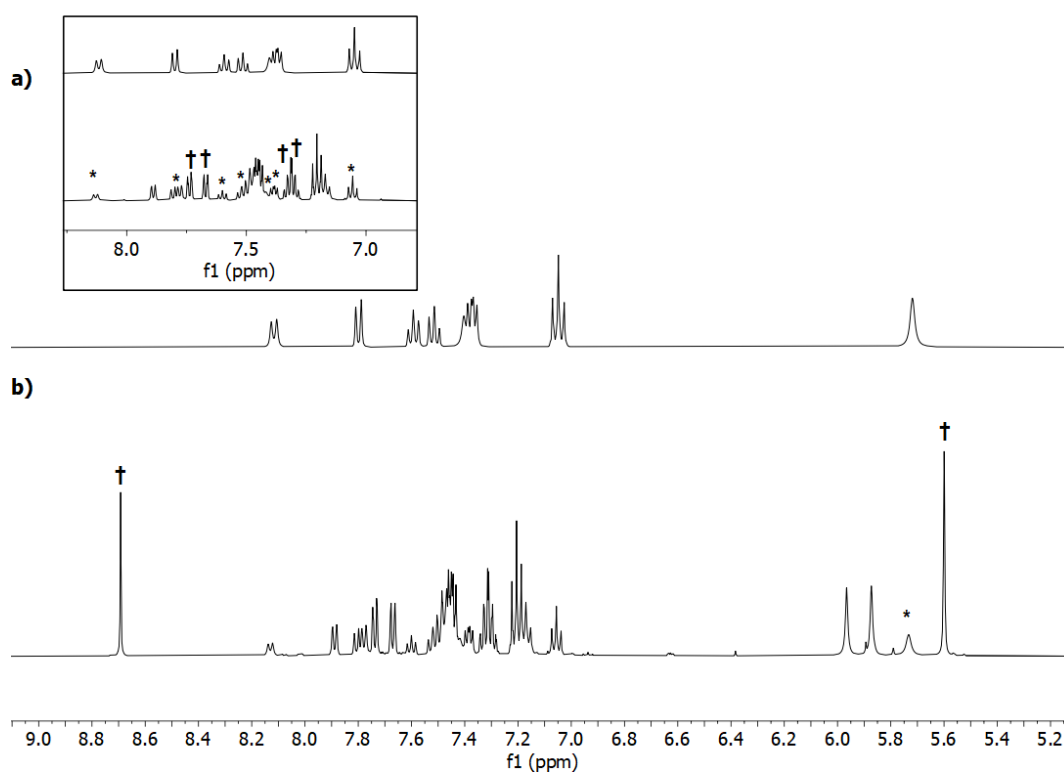
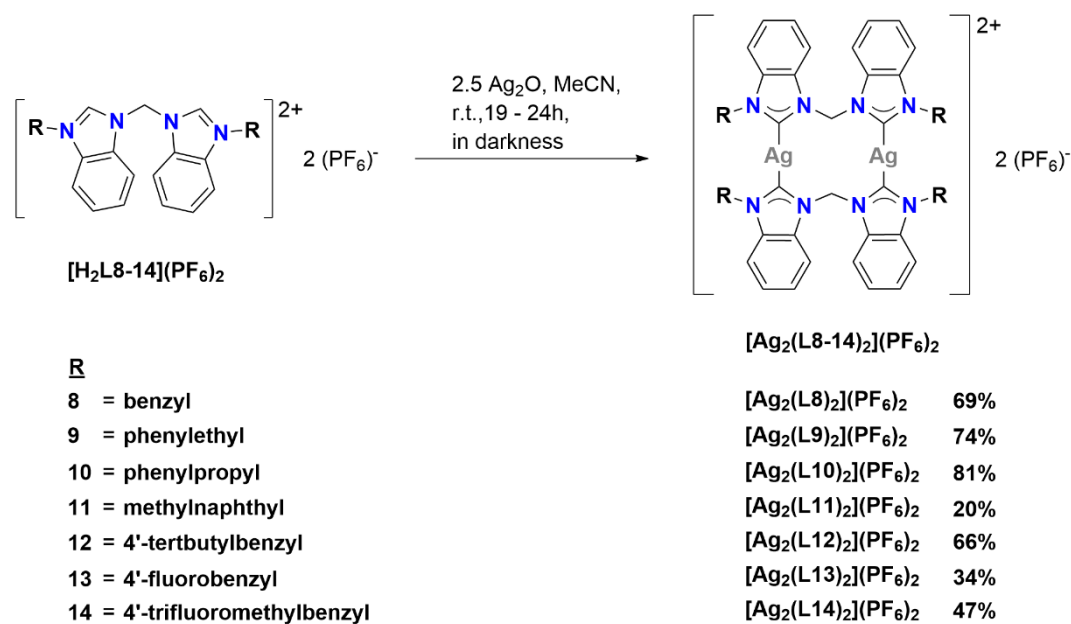


Figure 3.7: ^1H NMR spectra of $[\text{Ag}_2(\text{L13})_2](\text{PF}_6)_2$ using a) the MeCN route or b) the MeOH route (d_6 -DMSO, 400 or 500 MHz). Resonances labelled with an asterisk are $[\text{Ag}_2(\text{L13})_2](\text{PF}_6)_2$ and an unidentified major product is labelled with a cross.



Scheme 3.3: General synthesis of binuclear benzimidazole Ag(I)-NHC complexes.

As described earlier, the deprotonation and disappearance of the C2 proton in the ^1H - spectra (10.13 – 10.60 ppm) is the most indicative change upon complexation. The other major change is the broadening of the methylene bridge proton H8, which in $[\text{H}_2\text{L8-14}](\text{PF}_6)_2$ is a sharp singlet between 7.31 – 7.40 ppm and once complexed, it forms a broad singlet for $[\text{Ag}_2(\text{L8,11-14})_2](\text{PF}_6)_2$ or a broad multiplet for $[\text{Ag}_2(\text{L9-10})_2](\text{PF}_6)_2$ (Figure 3.8), with the methylene bridge resonance indicated with an asterisk). Due to the distance of the C2 proton from the protons in the backbone of the ligands, there are no changes to the multiplicity of the backbone resonances (which was seen for the imidazole derivatives).

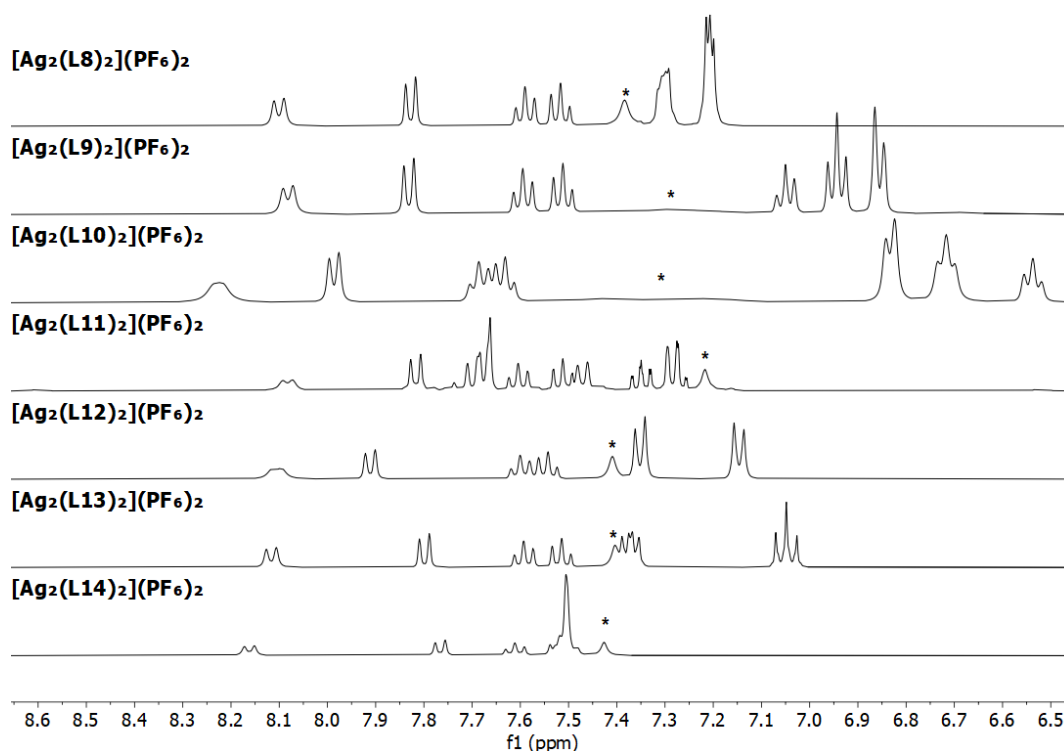


Figure 3.8: ^1H NMR spectra of $[\text{Ag}_2(\text{L8-14})_2](\text{PF}_6)_2$ showing the aromatic region, with the resonance for the methylene bridge indicated by an asterisk (d_6 -DMSO, 400 MHz, 298 K).

Further confirmation of complexation is observed in the $^{13}\text{C}\{^1\text{H}\}$ NMR spectra, namely the disappearance of the C2 resonance in the corresponding ligands which is between 143.4 – 144.6 ppm. This is similar to what was observed for the majority of the complexes described in **Chapter 2**, where the disappearance of this signal is due to an already weak quaternary resonance being split further by coupling with the two NMR active isotopes of silver. For complex $[\text{Ag}_2(\text{L13})_2](\text{PF}_6)_2$, the C2 resonance is visible and the peak shifts downfield from 144.1 to 190.7 ppm. The signal changes from a singlet into a pair of doublets with $^1J(^{13}\text{C}-^{107/109}\text{Ag})$ with coupling constants of 176.1 and 213.9 Hz for ^{107}Ag and ^{109}Ag respectively. The ATR-FTIR spectra of the complexes provides further evidence of complexation with the disappearance of a peak at *ca.* 1560 -1570 cm^{-1} which corresponds to the C2-H stretch of the ligand.

For the new complexes EA was performed, and whilst $[\text{Ag}_2(\text{L10})_2](\text{PF}_6)_2$, $[\text{Ag}_2(\text{L13})_2](\text{PF}_6)_2$ and $[\text{Ag}_2(\text{L14})_2](\text{PF}_6)_2$ were elementally pure, the other complexes had values were much lower than expected. The ^1H NMR spectra for the

impure complexes did not have any impurities to account for this low value. It is also notable that the C, H, and N are all low by approximately the same ratio, which means that the major impurity does not contain any of these elements. The two most likely impurities are silver(I) oxide or Ag(0) species. Attempts were made to further purify complexes $[\text{Ag}_2(\text{L8,9,11 and 12})_2](\text{PF}_6)_2$, however, to date these were unsuccessful.

3.1.3 Variable Temperature NMR Spectroscopy

The dynamics of the new benzimidazoles were investigated using VT-NMR spectroscopy experiments and compared to the imidazole analogues. For both series the same solvents and temperatures were used ($\text{d}_3\text{-MeCN}$ and temperatures between $-40 - 60\text{ }^\circ\text{C}$). The benzimidazole analogues of $[\text{Ag}_2(\text{L1-3})_2](\text{PF}_6)_2$ are $[\text{Ag}_2(\text{L8-10})_2](\text{PF}_6)_2$. In these complexes, the length of the chain between (benz)imidazole core and phenyl rings changes from one to three.

Figure 3.9 shows how the ^1H NMR spectrum of $[\text{Ag}_2(\text{L8})_2](\text{PF}_6)_2$ changes upon cooling, where both the methylene bridge (*ca.* 7.0 ppm) and wingtip (*ca.* 5.5 ppm) become broader. At $-40\text{ }^\circ\text{C}$ two separate peaks are observed for each of them, however, unlike the imidazole derivative these peaks are not resolved into two doublets. For the methylene bridge the T_c can be seen clearly at $-30\text{ }^\circ\text{C}$, which is *ca.* $30\text{ }^\circ\text{C}$ lower than the T_c for $[\text{Ag}_2(\text{L1})_2](\text{PF}_6)_2$, indicating that changing from imidazole to benzimidazole makes the 12-membered ring more flexible.

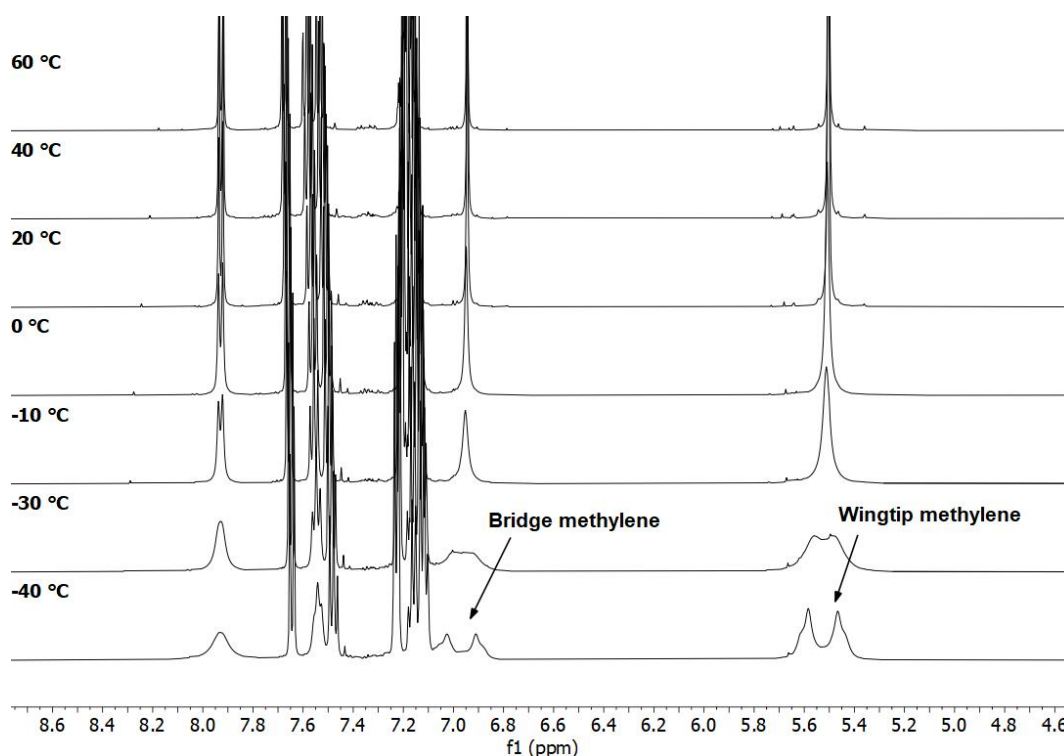


Figure 3.9: Stacked ^1H NMR spectra of $[\text{Ag}_2(\text{L8})_2](\text{PF}_6)_2$ when measured between temperatures of -40 to 60 $^\circ\text{C}$, with the resonances for the methylene bridge and wingtip shown at 5.52 and 6.95 ppm respectively ($d_3\text{-MeCN}$, 500 MHz).

^1H NMR spectra for $[\text{Ag}_2(\text{L9})_2](\text{PF}_6)_2$ at -40 and 60 $^\circ\text{C}$ (**Figure 3.10**) shows that at high temperatures the methylene bridge resonance is a sharp singlet, and it is expected that at -40 $^\circ\text{C}$ this peak will become two pairs of doublets. However, in the spectrum only one doublet (of the pair) is visible, whilst the other is masked by the phenyl protons (**Figure 3.10**, red). The T_c for the bridge could not be determined for this complex. There is a noticeable difference between the behaviour of the protons on each of the ethyl positions on the wingtip, where the resonance for H10 becomes broader at lower temperatures but maintains the same triplet splitting pattern, however, H9 forms a complicated multiplet with two major peaks which are from the two diastereotopic protons. The T_c for H9 is between $0 - 10$ $^\circ\text{C}$ (**Appendix 8.42**), whilst T_c for H10 is below -40 $^\circ\text{C}$. This difference indicates that the movement around C9 is much more restricted than for C10. The imidazole version of $[\text{Ag}_2(\text{L9})_2](\text{PF}_6)_2$ (**Chapter 2**) had two conformers at low temperatures, however, this behaviour is not observed for the benzimidazole version.

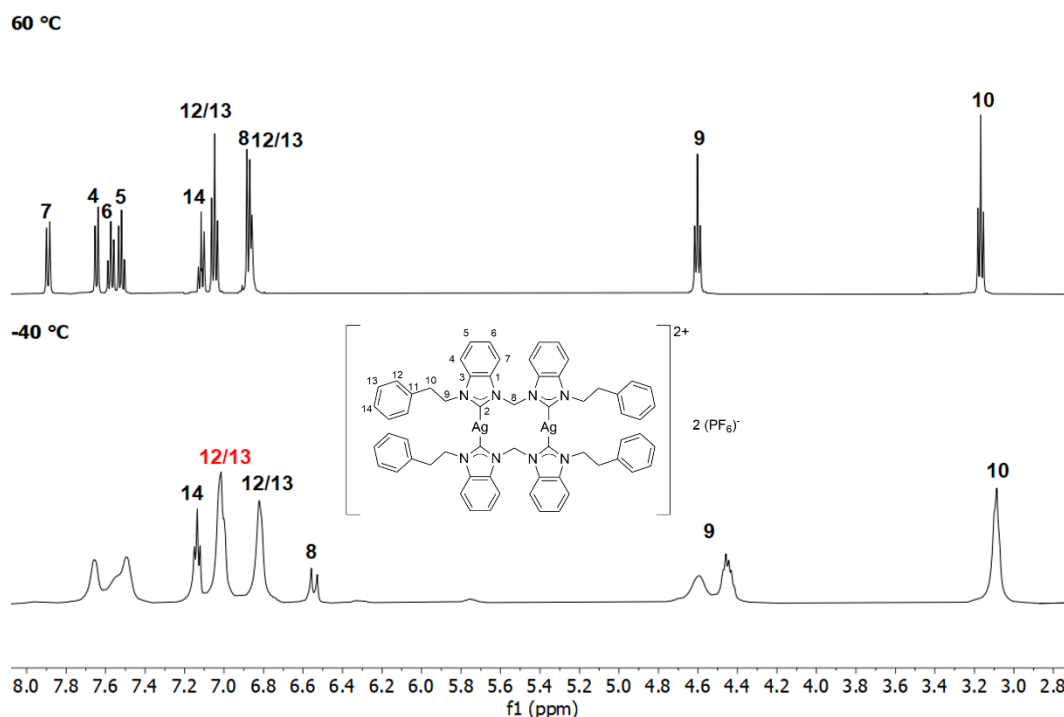


Figure 3.10: Stacked ^1H NMR spectra of $[\text{Ag}_2(\text{L9})_2](\text{PF}_6)_2$ measured -40 and 60 $^\circ\text{C}$ ($d_3\text{-MeCN}$, 500 MHz).

The last in this set of complexes is $[\text{Ag}_2(\text{L10})_2](\text{PF}_6)_2$, the spectra at -40 $^\circ\text{C}$ and 60 $^\circ\text{C}$ are shown in **Figure 3.11**. At 60 $^\circ\text{C}$ the spectrum is well resolved, with sharp resonances, however, the spectrum changes significantly when the sample is cooled to -40 $^\circ\text{C}$. The phenyl resonances H13-15 and benzimidazole resonances H4-7 become broad, for the phenyl resonances the movement is so restricted that the protons on each ring become inequivalent, the overlapping of these close resonances leads to broadening. A pair of doublets corresponding to $\text{H}_{8\text{a/b}}$ is observed with a J coupling of 14.9 Hz, which is in the range expected for $^2J(^1\text{H}\text{-}^1\text{H})$ coupling. The distance between the two doublets ($\Delta\nu$) is 160 Hz, and from these data the approximate rate constant was calculated at 370 s^{-1} . This value is higher than the imidazole equivalent $[\text{Ag}_2(\text{L3})_2](\text{PF}_6)_2$ which was calculated at 310 s^{-1} . This increase suggests that the rate of exchange is slightly faster for the benzimidazole derivative.

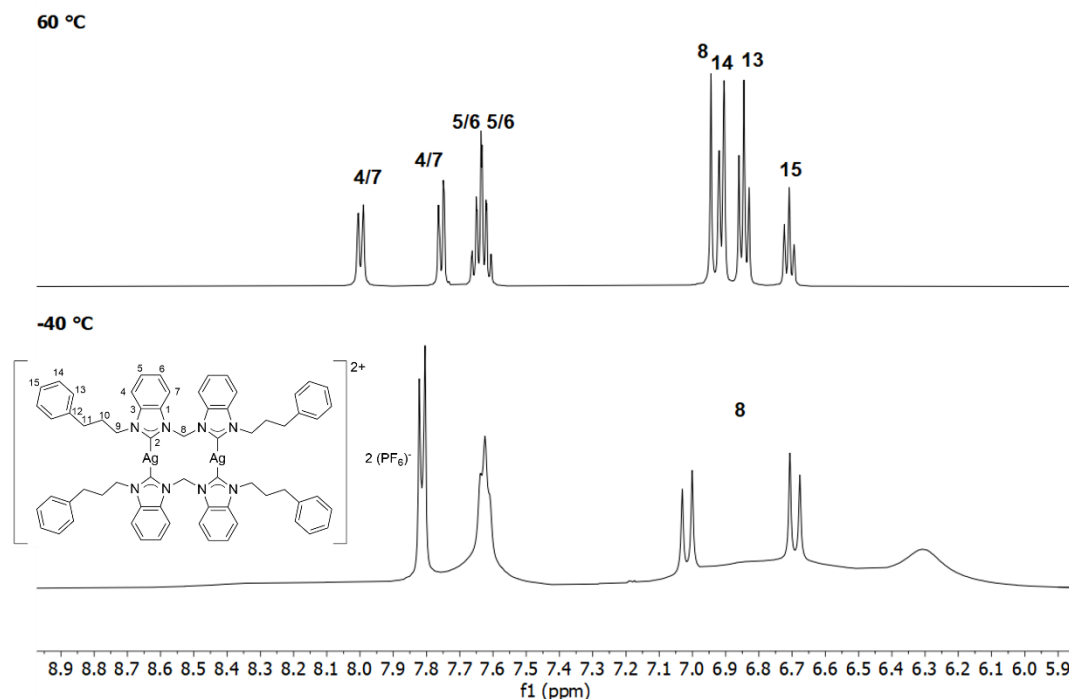


Figure 3.11: VT ^1H NMR spectra showing the aromatic region for $[\text{Ag}_2(\text{L10})_2](\text{PF}_6)_2$ at -40 and $60\text{ }^\circ\text{C}$ ($d_3\text{-MeCN}$, 500 MHz).

The aliphatic region for $[\text{Ag}_2(\text{L10})_2](\text{PF}_6)_2$ is shown in **Figure 3.12**. There are three resonances that correspond to the propyl chain on the wingtip; at $60\text{ }^\circ\text{C}$ these appear as two triplets (H9 and H11) and a quintet (H10), and these resonances become broader upon cooling. Similar to $[\text{Ag}_2(\text{L9})_2](\text{PF}_6)_2$, the protons adjacent to the nitrogen of the benzimidazole (H9) and the phenyl (H11) each split into two broad resonances, which can be seen clearer in **Appendix 8.43** (where the figure is presented with the full temperature range). The T_c for H9 and H11 are $0\text{ }^\circ\text{C}$ and $-10 - 0\text{ }^\circ\text{C}$ respectively.

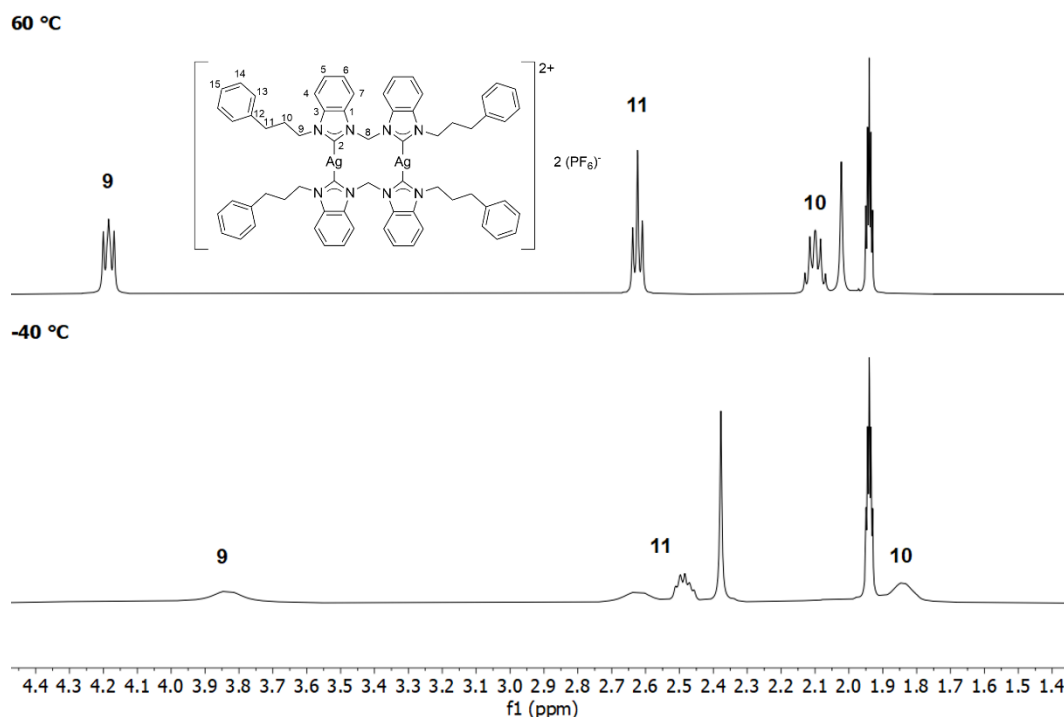


Figure 3.12: VT ^1H NMR spectra showing the aliphatic region for $[\text{Ag}_2(\text{L10})_2](\text{PF}_6)_2$ at -40 and 60 °C ($d_3\text{-MeCN}$, 500 MHz).

The complexes that showed the fastest exchange for the methylene bridge protons described in **Chapter 2** were $[\text{Ag}_2(\text{L5-7})_2](\text{PF}_6)_2$, the benzimidazole versions of these complexes are $[\text{Ag}_2(\text{L12-14})_2](\text{PF}_6)_2$ (full temperature range spectra are shown in **Appendix 8.44** - **Appendix 8.46**). The low temperature VT NMR spectra for these complexes is shown in **Figure 3.13** with the methylene resonances H8 and H9 explicitly labelled. For both $[\text{Ag}_2(\text{L13})_2](\text{PF}_6)_2$ and $[\text{Ag}_2(\text{L14})_2](\text{PF}_6)_2$ the methylene bridge resonance is a singlet which means that $T_c < -40$ °C, this is in contrast to $[\text{Ag}_2(\text{L6})_2](\text{PF}_6)_2$ and $[\text{Ag}_2(\text{L7})_2](\text{PF}_6)_2$ which had T_c of 0 °C and 0 – 20 °C respectively. For $[\text{Ag}_2(\text{L12})_2](\text{PF}_6)_2$ T_c lays between -10 – -30 °C, which is *ca.* 30 °C lower than the imidazole derivative $[\text{Ag}_2(\text{L5})_2](\text{PF}_6)_2$. This is further evidence that the methylene bridge in the benzimidazole derivatives has less restricted rotation compared to the imidazole versions.

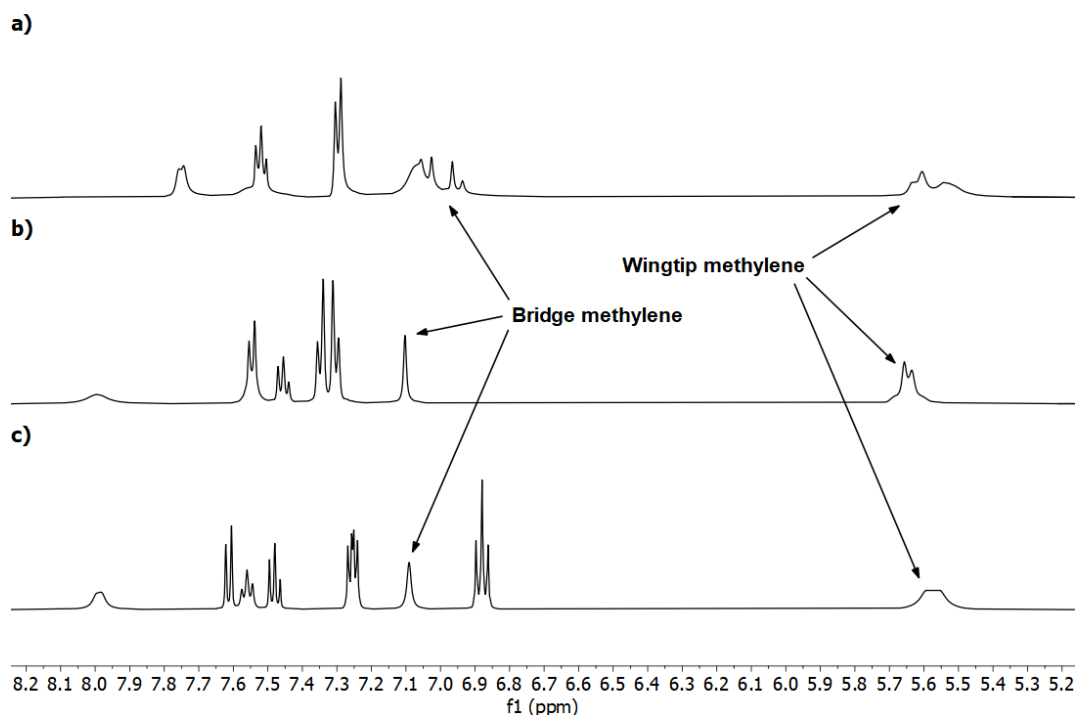


Figure 3.13: Stacked ^1H NMR spectra of a) $[\text{Ag}_2(\text{L12})_2](\text{PF}_6)_2$ at $-40\text{ }^\circ\text{C}$, b) $[\text{Ag}_2(\text{L13})_2](\text{PF}_6)_2$ at $-30\text{ }^\circ\text{C}$, c) $[\text{Ag}_2(\text{L14})_2](\text{PF}_6)_2$ at $-40\text{ }^\circ\text{C}$ ($d_3\text{-MeCN}$, 500 MHz).

3.1.4 X-ray Characterisation of $[\text{Ag}_2(\text{L9})_2](\text{PF}_6)_2$

Colourless irregular crystals of $[\text{Ag}_2(\text{L9})_2](\text{PF}_6)_2$ suitable for scXRD analysis were obtained through vapour diffusion of Et_2O into a concentrated acetone solution of complex. The data was collected by Dr Benjamin Hofmann. The crystal was solved in a monoclinic cell and the structural solution was performed in the $P2_1$ space group, with one molecule in the asymmetric unit. The molecular structure is shown in **Figure 3.14**, with the wingtip groups all on the same side of the central 12-membered ring. The C-Ag bond lengths of $2.082(4) - 2.113(4)\text{ \AA}$ fall within the reported range for Ag(I)-NHC complexes. The C-Ag-C angles of $173.46(18) - 174.05(18)^\circ$ are close to the ideal 180° linear geometry. The distance between the silvers is 3.15 \AA indicating an intramolecular argentophilic interaction.

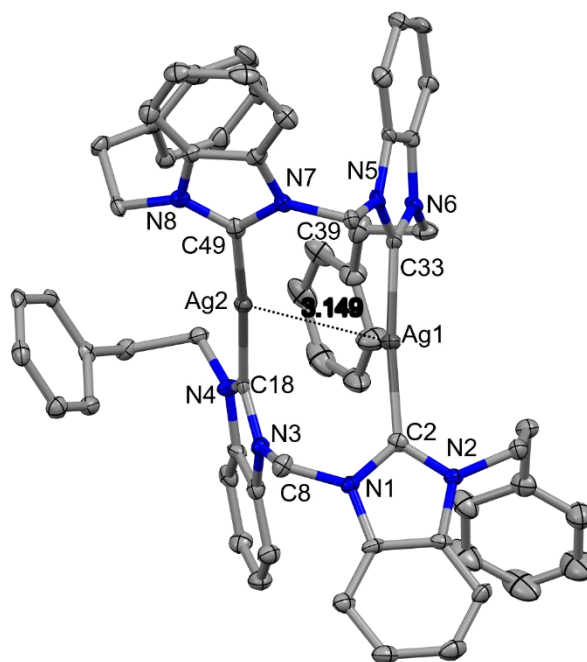


Figure 3.14: Molecular structure of $[\text{Ag}_2(\text{L9})_2](\text{PF}_6)_2$ with displacement ellipsoids shown at the 50% probability level and counter ions, solvent molecules and hydrogen atoms omitted for clarity.

Table 3.2: Selected XRD parameters for $[\text{Ag}_2(\text{L9})_2](\text{PF}_6)_2$ with s.u.s (Standard uncertainties) in parenthesis.

Atoms	Bond lengths (Å)
Ag1-C2	2.083(5)
Ag1-C33	2.083(5)
Ag2-C18	2.112(5)
Ag2-C49	2.105(6)
Ag1---Ag2	3.1491(5)
C-H---F	2.412 – 2.602
C-H---O	2.29
Atoms	Angle (°)
C2-Ag1-C33	173.6(2)
C18-Ag2-C49	174.1(2)

The crystal packing diagram (Figure 3.15) shows two molecules of $[\text{Ag}_2(\text{L9})_2](\text{PF}_6)_2$ aligned along the *b*-axis, however, the distance between the rings is too large for π - π stacking interactions. There are weak intermolecular hydrogen bonds between the complex and acetone and PF_6^- , which are shown in Figure 3.15. Both the hydrogens from the wingtip and bridge methylenes and the wingtip phenyl

groups are interacting with the fluorides of the PF_6^- , with C-H...F distances of 2.412 – 2.602 Å. The oxygen from the acetone also interacts with a hydrogen from the bridge methylene with a distance of 2.290 Å (C-H...O).

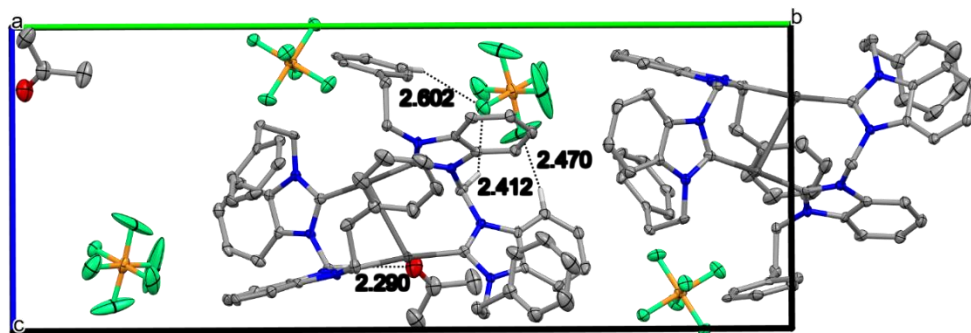


Figure 3.15: Packing diagram of $[\text{Ag}_2(\text{L9})_2](\text{PF}_6)_2$ shown along the *a*-axis, intermolecular interactions between the complex and acetone and PF_6^- counter ions are shown.

3.1.5 X-ray Characterisation of Two Conformers of $[\text{Ag}_2(\text{L13})_2](\text{PF}_6)_2$

Crystals suitable for scXRD analysis of $[\text{Ag}_2(\text{L13})_2](\text{PF}_6)_2$ were prepared using two different methods, (i) vapour diffusion of Et_2O into a concentrated MeCN solution and (ii) slow evaporation of a MeCN solution of complex, the former produced needle-like colourless crystals and the latter yielded irregular colourless crystals. The crystal data was collected by Dr Rianne Lord and Dr Benjamin Hofmann respectively. The needle-like crystals were solved in monoclinic cell and solved in a $P2_1/n$ space group and the irregular crystal was solved in a monoclinic cell and $P2_1/c$ space group, both had one molecule of $[\text{Ag}_2(\text{L13})_2](\text{PF}_6)_2$ in the unit cell. The solved structures for both crystals are shown in Error! Reference source not found.. The molecular structures revealed two different conformers, where $[\text{Ag}_2(\text{L13})_2](\text{PF}_6)_2\text{-A}$ crystallised with four molecules of MeCN (crystallisation from (i)) in the unit cell, and $[\text{Ag}_2(\text{L13})_2](\text{PF}_6)_2\text{-B}$ had no solvent molecules within the crystal structure (crystallisation from (ii)). Selected parameters for both complexes are shown in

. The Ag-C bond lengths for both complexes are between 2.087(2) – 2.110(3) Å, and both conformers have short Ag-Ag bond distances 2.996 and 2.987 Å for **A** and **B** respectively which correspond to argentophilic interactions. These values are

within the margin of error so there is no statistical difference between them. The C-Ag-C bond angle varies between the conformers, for **A** both angles are the same (within experimental accuracy) with values of 176.53(14) and 176.05(14)°, whilst for **B**, the angles deviate further from ideal 180°, with angles of 170.09(9) and 174.64(9)°. Another difference is the orientation of the wingtip, in **A** the benzyl groups are all on one side of the central 12-membered ring, whereas for **B**, one benzyl is on the other side of the ring (to the other three).

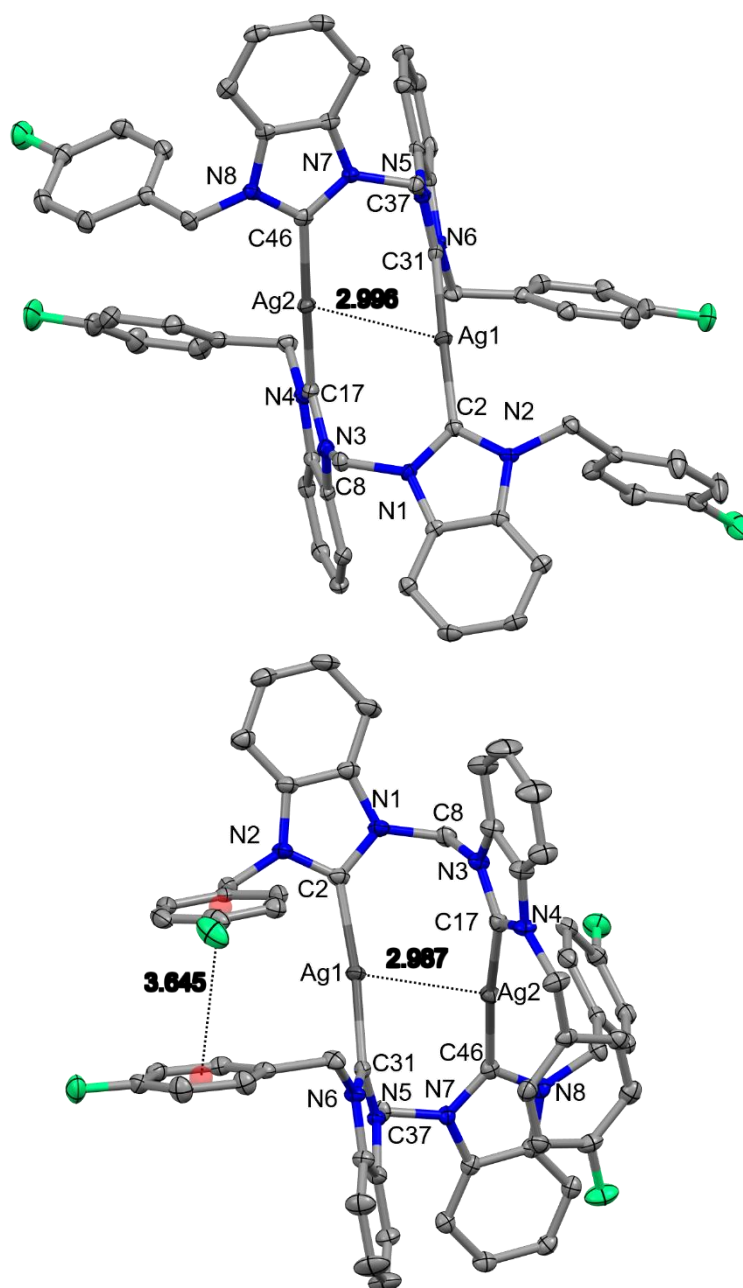


Figure 3.16: *Sc-XRD structure of [Ag₂(L13)₂](PF₆)₂-A (top) and [Ag₂(L13)₂](PF₆)₂-B (bottom) displacement ellipsoids are shown at the 50% probability level and counter ions, solvent molecules and hydrogen atoms are omitted for clarity.*

Table 3.3: Selected XRD parameters for both conformers of $[\text{Ag}_2(\text{L13})_2](\text{PF}_6)_2$ with s.u.s in parenthesis.

Atoms	Bond lengths (Å) (conformer A/B)
Ag1-C2	2.106(3)/2.087(2)
Ag1-C31	2.102(3)/2.087(2)
Ag2-C17	2.111(3)/2.106(2)
Ag2-C46	2.100(3)/2.103(2)
Ag1---Ag2	2.9959(3)/2.9874(2)
C-H---F	2.434 – 2.653/2.392 – 2.661
C-H---N	2.479 – 2.564/-
Atoms	Angle (°) (conformer A/B)
C2-Ag1-C31	176.02(13)/170.09(9)
C17-Ag2-C46	176.49(13)/174.62(9)

In both conformers, the benzimidazoles that are *trans* are twisted in relationship to each other. The degree of twisting was quantified by calculating planes for each benzimidazole and then measuring the angle of intersection between the planes. The dihedral angles for all the plane intersections are shown in **Table 3.4**. An example is shown in **Figure 3.17**, where the angle between the planes C2(benz) and C31(benz) in $[\text{Ag}_2(\text{L13})_2](\text{PF}_6)_2\text{-A}$ is 87.8° which means that the benzimidazoles are almost perpendicular to each other (this is also the case for C10(benz) and C39(benz)), and the degree of twisting is less in conformer **B** with intersection angles of 63.3 and 81.6° . Figures of the other plane intersections for both conformers are shown in **Appendix 8.48 – Appendix 8.50**.

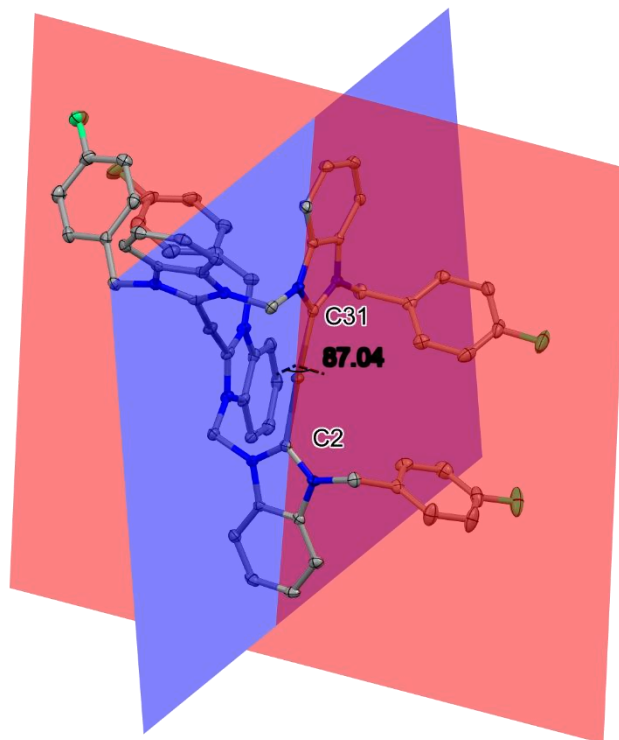


Figure 3.17: Structure showing the intersection of the planes from C2(benz) (blue) and C31(benz) (red) in $[Ag_2(L13)_2](PF_6)_2-A$.

Table 3.4: Measured plane intersection angles between opposite benzimidazoles in for the **A** and **B** conformers of $[Ag_2(L13)_2](PF_6)_2$.

Structure	Dihedral angle (°)	
	C2/C31	C10/C39
$[Ag_2(L13)_2](PF_6)_2-A$	87.0	86.6
$[Ag_2(L13)_2](PF_6)_2-B$	63.3	81.6

In conformer **B** there are intramolecular π - π stacking interactions (**Figure 3.18**) between two of the wingtip benzyl rings, with a centroid distance of 3.646 Å. This distorts the C2-Ag-C31 (170.09(9)°) angle more than the other side of the molecule, C17-Ag-C46 (174.64(9)°). For both conformers there are intermolecular π - π stacking interactions, for **A** these interactions are between benzimidazole rings on neighbouring molecules and have distances between 3.615 – 3.913 Å (**Figure 3.18, top**). In **B** these π - π stacking interactions are between both two benzimidazoles

(3.481 Å) and the phenyl of one imidazole and a neighbouring molecules benzyl wingtip (3.879 Å) (Figure 3.18, bottom).

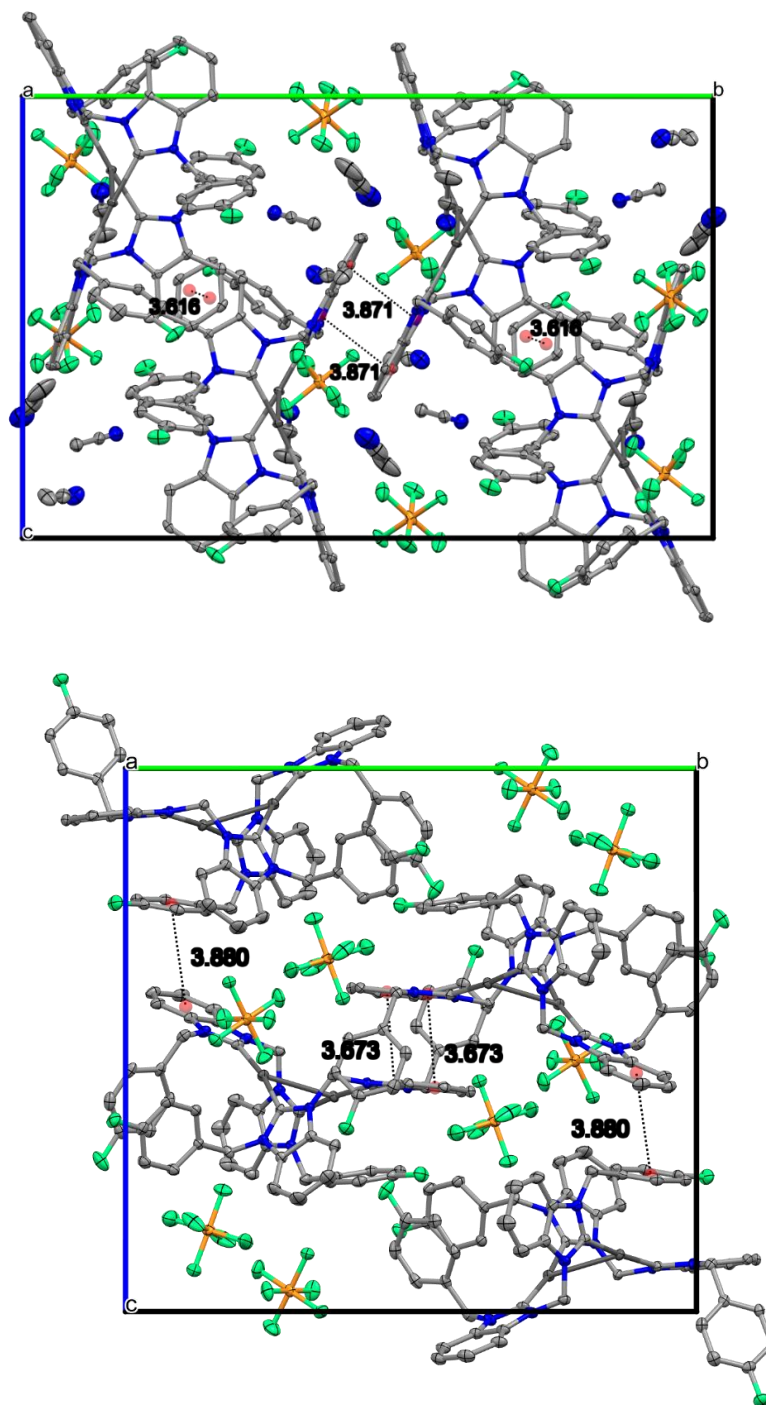


Figure 3.18: Packing diagrams both conformers of $[Ag_2(L13)_2](PF_6)_2$ α (top) and β (bottom) showing intermolecular π - π stacking interactions.

Conformer **A** has weak hydrogen bonding interactions between fluorides of the PF_6^- anion and the hydrogens on the phenyl wingtip, benzimidazole backbone and both bridge, wingtip methylene and MeCN, with C-H...F distances of 2.478 – 2.653 Å. The nitrogen of the MeCN interacts with hydrogens on the benzimidazole backbone and bridge methylene with distances of 2.564 and 2.479 Å respectively, these interactions can be seen in **Figure 3.19**. Like conformer **A**, **B** also has interactions between the fluoride on the PF_6^- and the hydrogens on the bridge and wingtip methylenes and wingtip benzyl with C-H...F distances of 2.392 – 2.661 Å.

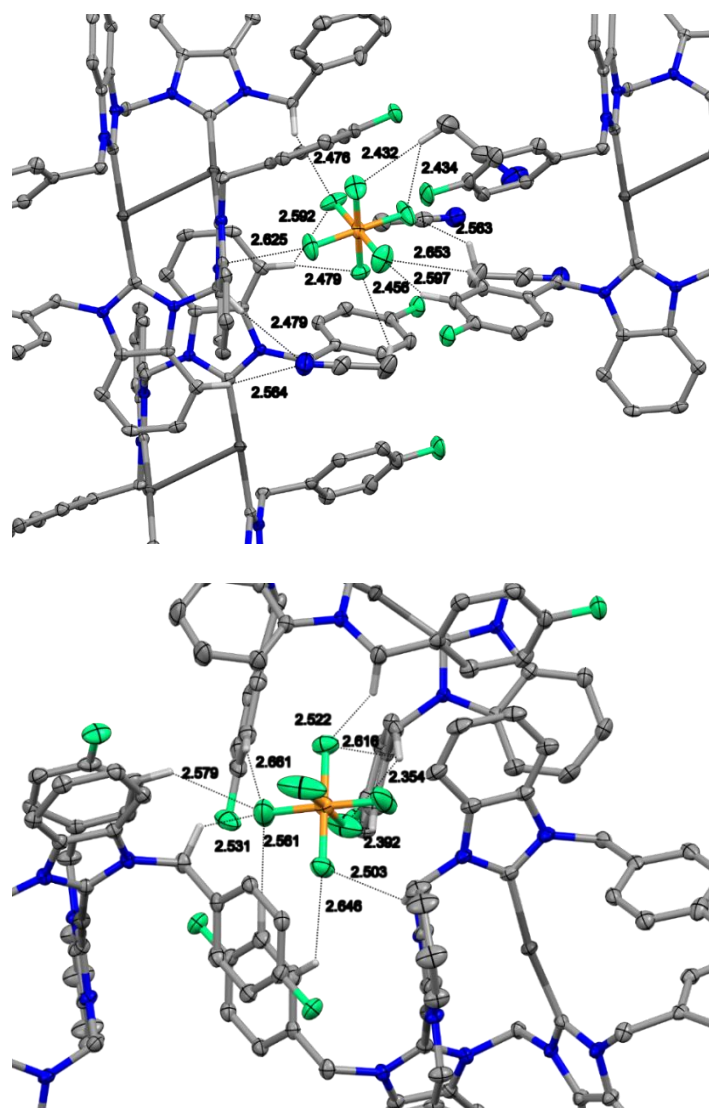


Figure 3.19: Packing diagrams both conformers of $[\text{Ag}_2(\text{L13})_2](\text{PF}_6)_2$ - **A** (top) and **B** (bottom) showing intermolecular between the complexes and the PF_6^- anion and solvent molecules.

3.2 Synthesis of Monodentate Homoleptic Silver(I) *N*-Heterocyclic Carbene Complexes

To compare the influence of the nuclearity on biological activity, two monodentate derivatives of *p*-fluorobenzyl complexes reported in **Chapter 2** and **3.1** were synthesised. Cytotoxicity data reported in **Chapter 4** indicated that the fluorine functionalised complexes were the most active, so these wingtips were chosen to be derivatised. The target complexes are shown in **Figure 3.20**.

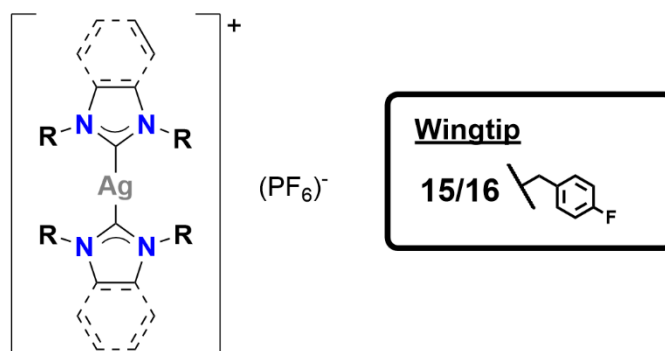
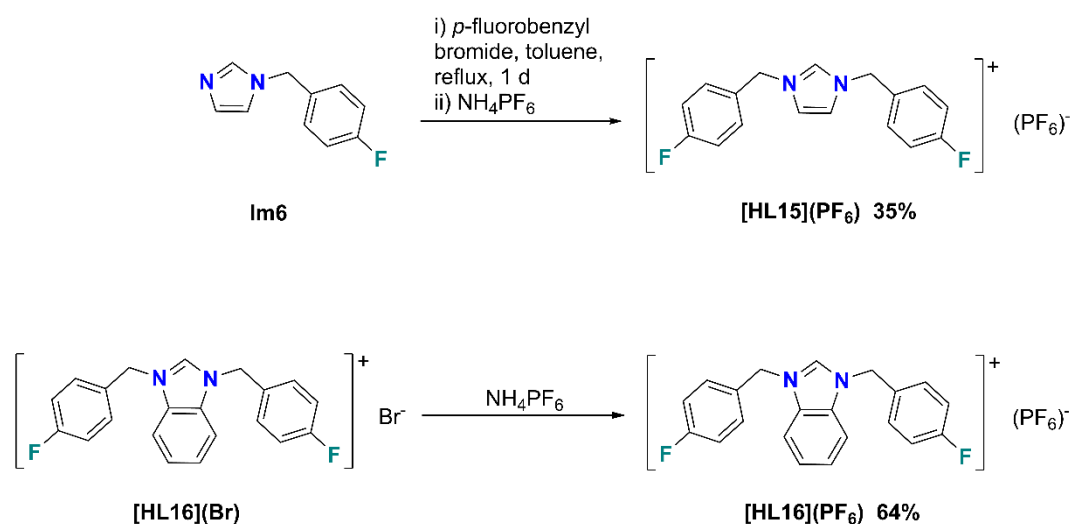


Figure 3.20: Target monodentate homoleptic Ag(I)-NHC complexes $[Ag(L15-16)_2](PF_6)$, where $[Ag(L15)_2](PF_6)$ is imidazole and $[Ag(L16)_2](PF_6)$ is benzimidazole.

3.2.1 Synthesis and Characterisation of Monodentate Imidazolium and Benzimidazolium Ligands

The ligands were prepared by the reaction of a functionalised imidazole or benzimidazole with an aryl bromide, followed by an anion exchange with ammonium hexafluorophosphate. The bromide salts $[HL15-16](Br)$, have been reported before in literature and were synthesised via literature methods, however, the hexafluorophosphate salts $[HL15-16](PF_6)$ are reported here for the first time.^{131,170–172}

Ligand $[HL15](PF_6)$ was synthesised without isolating the bromide salt before the ion exchange (**Scheme 3.4**), but prior to the ion exchange, the bromide salt was isolated in the synthesis of $[HL16](PF_6)$.



Scheme 3.4: Reaction conditions for the synthesis of $[HL15](PF_6)$ (top). Ion exchange from $[HL16](Br)$ to obtain $[HL16](PF_6)$ (bottom).

Successful substitution of the second wingtip can be seen in the 1H NMR spectra (**Figure 3.21**). Firstly, the C2 proton resonance shifts downfield from 7.74 – 8.46 ppm to 9.31 – 9.93 ppm. Upon ion exchange there is an upfield shift in the C2 proton resonances by between 0.30 – 0.73 ppm (**Table 3.5**). The substitution of the second wingtip makes the ligands C_{2v} symmetric, which simplifies the spectrum, for example in 1-(4-fluorobenzyl)-1*H*-imidazole the backbone proton resonances appear as two apparent triplets (**Figure 3.21**) and upon substitution the backbone protons become equivalent and only couple to the C2 proton, leading to one doublet at 7.80 ppm.

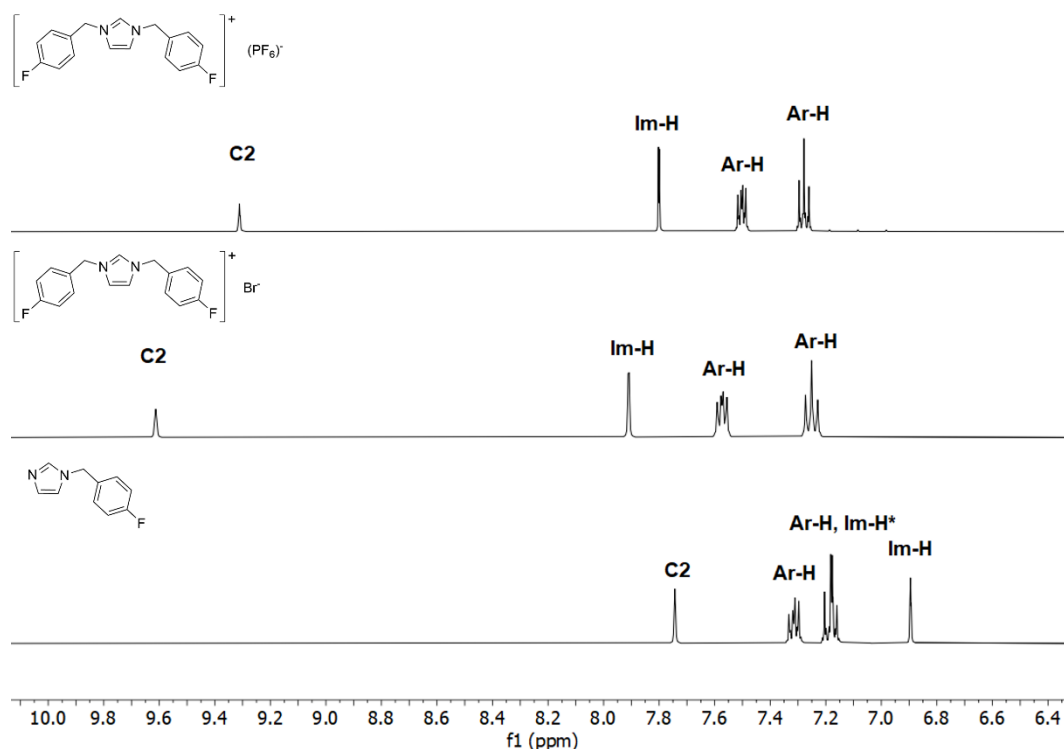


Figure 3.21: ^1H NMR spectra of 1-(4-fluorobenzyl)-1H-imidazole (bottom), $[\text{HL15}](\text{Br})$ (middle) and $[\text{HL15}](\text{PF}_6)$ (top) showing the aromatic region of the spectra (d_6 -DMSO, 400 MHz).

Table 3.5: Chemical shifts in ^1H NMR of the C2 protons.

Compound	Chemical shift (δ)		Change
	X = Br	X = PF_6	
$[\text{HL15}](\text{X})$	9.61	9.31	0.30
$[\text{HL16}](\text{X})$	10.66	9.93	0.73

Further evidence for successful ion exchange can be seen in ATR-IR, where the broad peak at 830 cm^{-1} is indicative of the PF_6 anion (spectra can be seen in **Appendix 8.16** and **Appendix 8.17**). Further confirmation is shown the $^{19}\text{F}\{^1\text{H}\}$ NMR spectra, whereby a doublet at -70.1 ppm is observed, due to the coupling of the fluoride and the phosphorus in the PF_6 anion, $^1J(^{31}\text{P}-^{19}\text{F}) = 710.6\text{ Hz}$, and the *p*-fluoro wingtip which appear as a singlet at 113.0 ppm . The integration of the singlet and doublet approximately correspond to the 1:3 ratio between the fluorines in the ligand and the fluorides in counterion (**Figure 3.22** for $[\text{HL15}](\text{PF}_6)$).

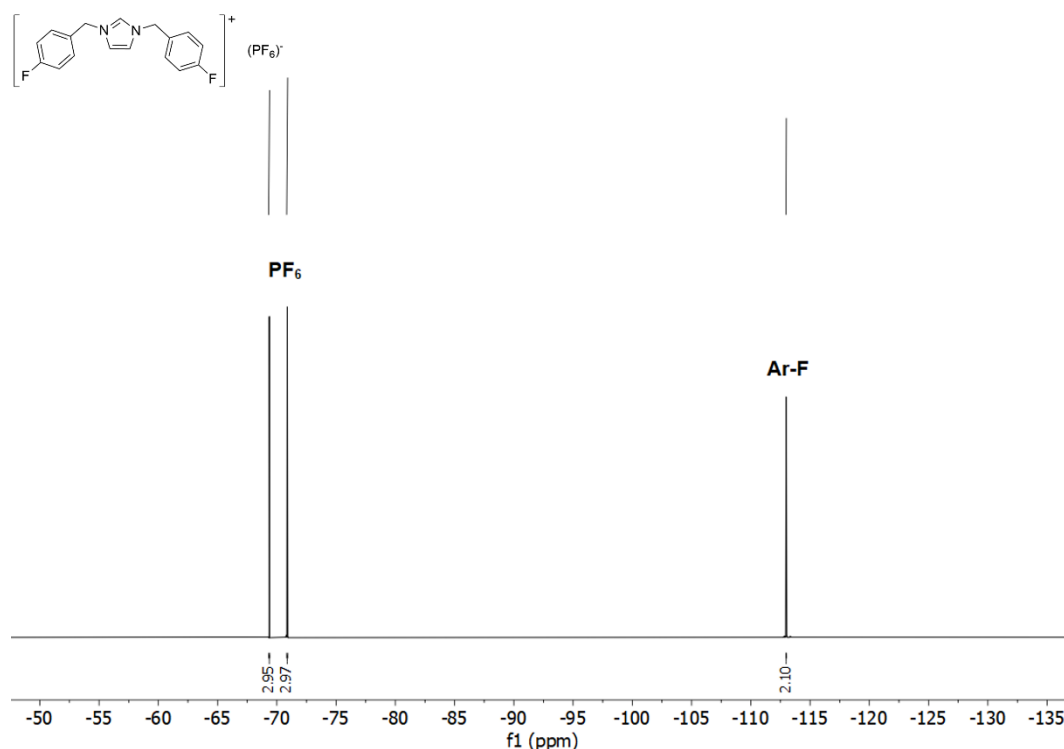
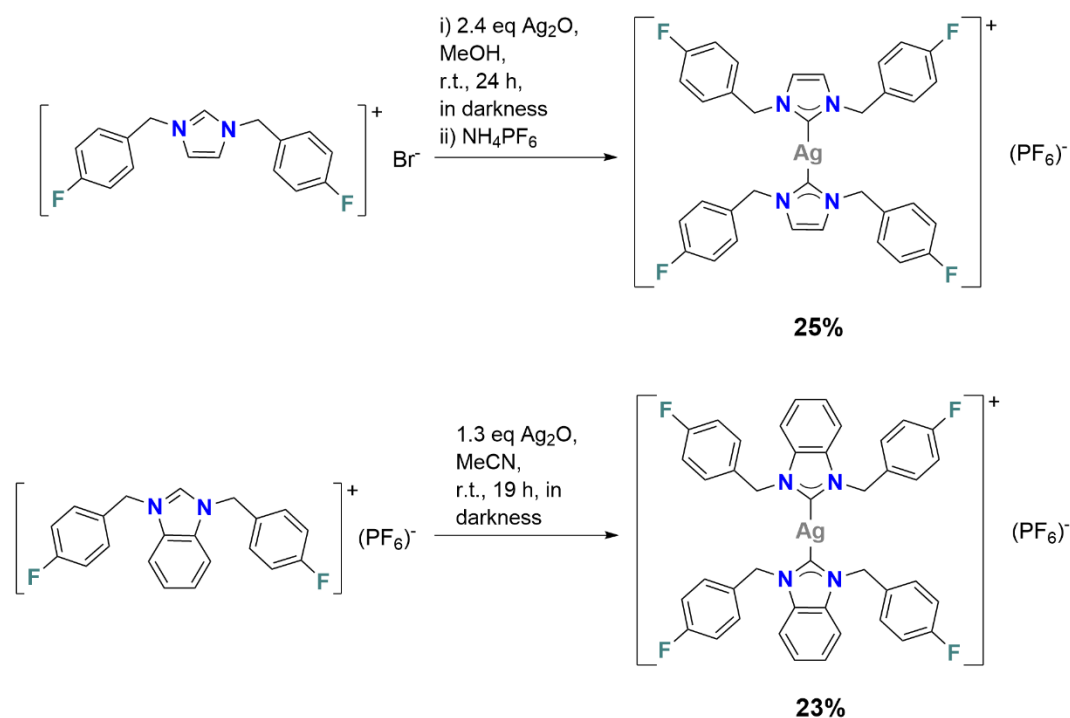


Figure 3.22: $^{19}\text{F}\{^1\text{H}\}$ NMR spectrum of $[\text{HL15}](\text{PF}_6)$ (d_6 -DMSO, 500 MHz).

3.2.2 Synthesis and Characterisation of *p*-Fluoro Monodentate Silver(I) *N*-Heterocyclic Carbene Complexes

The two routes described in **Chapter 2** were employed to synthesise the target *p*-fluoro complexes $[\text{Ag}(\text{L15})_2](\text{PF}_6)$ and $[\text{Ag}(\text{L16})_2](\text{PF}_6)$ (**Scheme 3.5**). $[\text{Ag}(\text{L16})_2](\text{PF}_6)$ was synthesised from the bromide salt through the reaction with excess silver(I) oxide followed an ion exchange. Whereas $[\text{Ag}(\text{L16})_2](\text{PF}_6)$ was synthesised directly from the hexafluorophosphate salt, and fewer equivalents were used for this reaction to lower the chances of impurities. The yields for both reactions were low at 23 – 25% in comparison to other literature examples (40¹⁷³ - 84%¹⁷⁴). The low yields could be due to the workup procedure, where during the filtering through Celite® and washing (the Celite®) with MeCN, complex $[\text{Ag}(\text{L15})_2](\text{PF}_6)$ showed signs of decomposition (ligand was present in the ^1H NMR spectrum), this decomposition is likely due to prolonged exposure to wet solvent. Carrying out this reaction in anhydrous conditions with dry solvents may lead to a higher yield.



Scheme 3.5: Synthetic routes for $[\text{Ag}(\text{L15})_2](\text{PF}_6)$ (top) and $[\text{Ag}(\text{L16})_2](\text{PF}_6)$ (bottom).

Successful complexation can be seen in the ^1H NMR spectra (**Figure 3.23**) where the C2 resonance disappears upon deprotonation. For $[\text{Ag}(\text{L15})_2](\text{PF}_6)$ the resonance for the backbone proton (H1) changes from a doublet to a singlet due to the removal of the C2 proton, but such a change in splitting is not seen for $[\text{Ag}(\text{L16})_2](\text{PF}_6)$, this is due to the benzimidazole backbone protons being too far away from the C2 proton to couple, only an upfield shift in protons was observed.

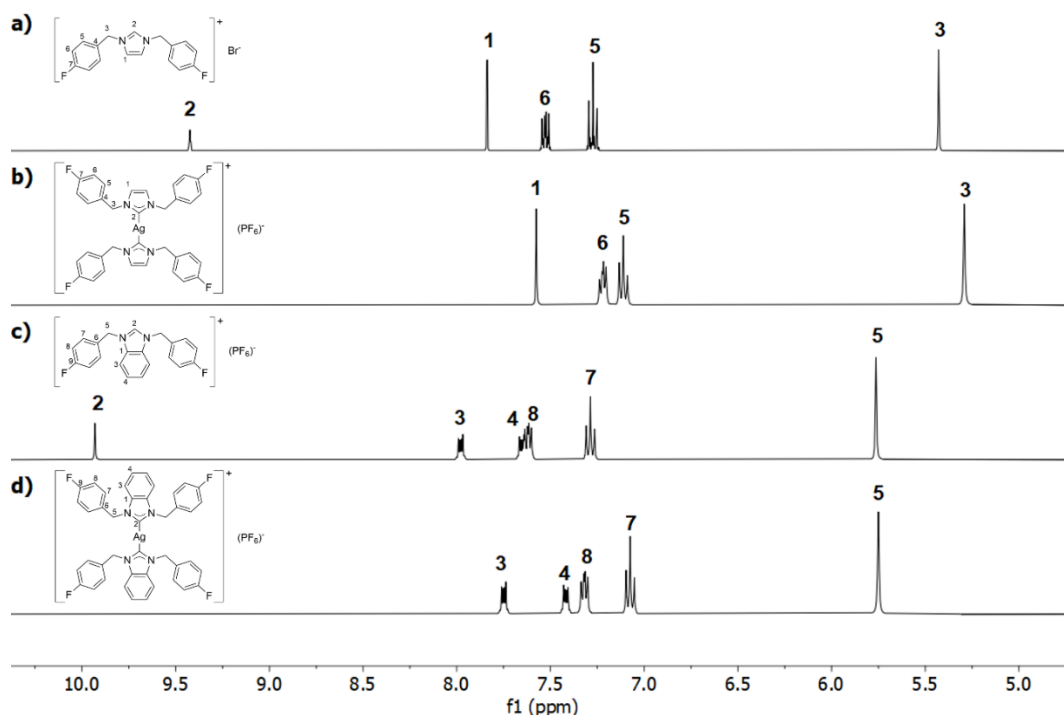


Figure 3.23: ^1H NMR spectra of a) $[\text{HL15}](\text{Br})$, b) $[\text{Ag}(\text{L15})_2](\text{PF}_6)$, $[\text{HL16}](\text{PF}_6)$ and $[\text{Ag}(\text{L16})_2](\text{PF}_6)$, (d_6 -DMSO, 400 MHz).

Figure 3.24 shows the $^{13}\text{C}\{^1\text{H}\}$ spectra for $[\text{Ag}(\text{L15})](\text{PF}_6)$, $[\text{Ag}(\text{L16})_2](\text{PF}_6)$ and their corresponding ligands. The resonances of the phenyl ring could be unambiguously assigned by using the magnitude of the couplings between the fluorine and aromatic carbon. The *para*, *meta*, *ortho* and *ipso* aromatic carbons coupling to the fluorine with J coupling constants of 244.5 – 245.5 Hz, 21.1 – 21.4 Hz, 7.5 – 9.1 Hz and 2.5 – 3.0 Hz respectively. The strongest evidence for successful complexation is either the disappearance of the C2 resonance (136.2 ppm) for $[\text{HL15}](\text{PF}_6)$ to $[\text{Ag}(\text{L15})_2](\text{PF}_6)$ or a shift of the resonance which for $[\text{HL16}](\text{PF}_6)$ to $\text{Ag}(\text{L15})_2](\text{PF}_6)$ shifts from 142.7 to 187.9 ppm and the resonance splits into two doublets due to the coupling to the two spin active isotopes of silver. The $^{19}\text{F}\{^1\text{H}\}$ NMR spectra provide further evidence of complexation, where the ratio of Ar-F and the PF_6 integration gets smaller upon complexation 1:3 in the ligand to 2:3 in the complex. An example can be seen in **Figure 3.25** comparing $[\text{HL16}](\text{PF}_6)$ and $[\text{Ag}(\text{L16})_2](\text{PF}_6)$. For both $[\text{Ag}(\text{L15})_2](\text{PF}_6)$ and $[\text{Ag}(\text{L16})_2](\text{PF}_6)$ *p*-fluoro resonance shifts from 113.0 to 114.2 upon complexation.

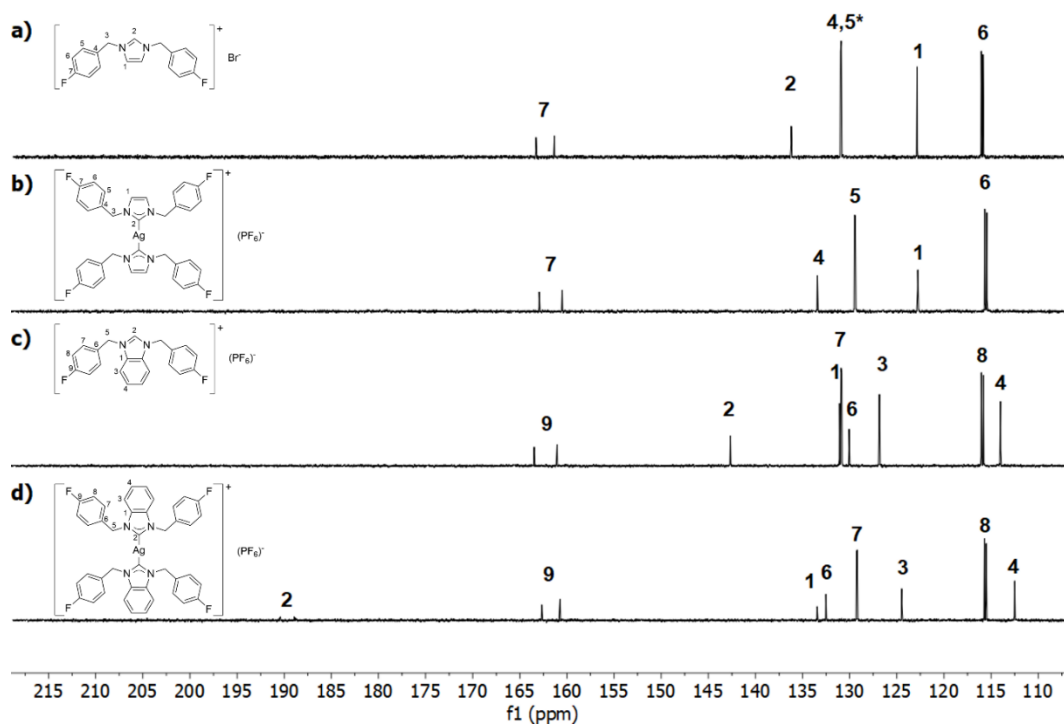


Figure 3.24: $^{13}\text{C}\{^1\text{H}\}$ NMR spectra of a) $[\text{HL15}](\text{PF}_6)$, b) $[\text{Ag}(\text{L15})_2](\text{PF}_6)$, c) $[\text{HL16}](\text{PF}_6)$ and d) $[\text{Ag}(\text{L16})_2](\text{PF}_6)$, (d_6 -DMSO, 101 or 126 MHz).

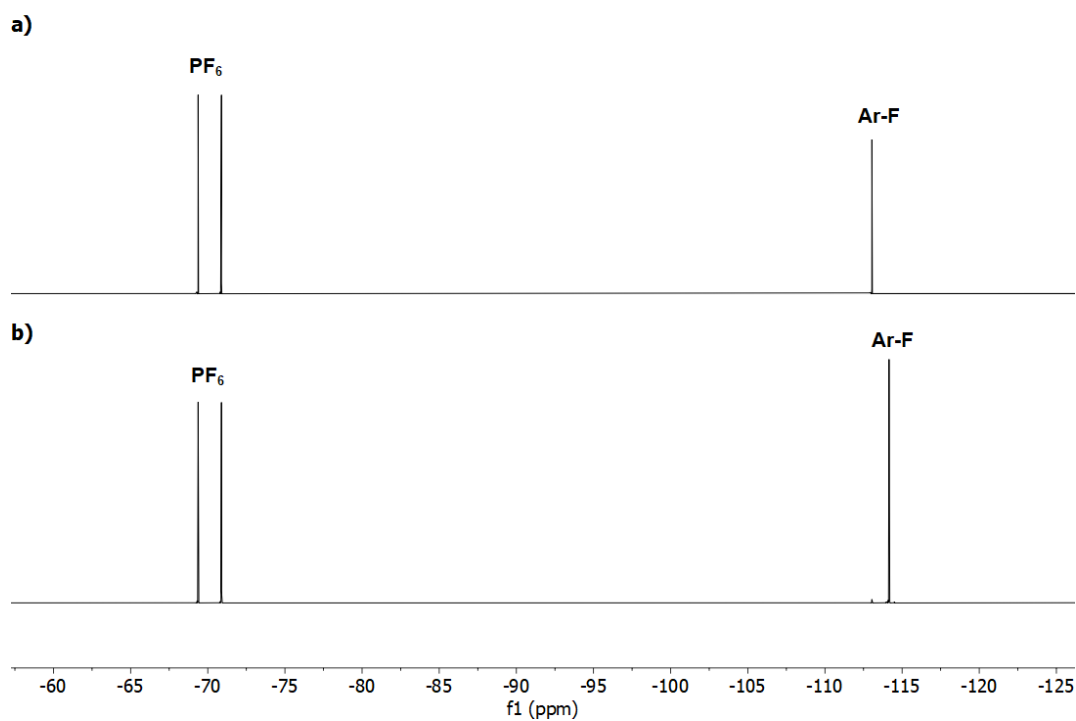


Figure 3.25: $^{19}\text{F}\{^1\text{H}\}$ NMR spectra of a) $[\text{HL16}](\text{PF}_6)$, b) $[\text{Ag}(\text{L16})_2](\text{PF}_6)$ (d_6 -DMSO, 470.6 MHz).

ATR-FTIR data of the complexes further confirmed successful complexation with the disappearance of the ligand C2-H stretch between 1553 – 1563 cm⁻¹. Complexes [Ag(L15)₂](PF₆) and [Ag(L16)₂](PF₆) and their respective ligands were analysed by EA and were found to be elementally pure, they will be tested for their biological activity (see **Chapter 4**).

3.2.2.1 X-ray Characterisation of [Ag(L16)₂](PF₆)

Colourless irregular-shaped crystals of [Ag(L16)₂](PF₆) suitable for scXRD analysis were obtained through vapour diffusion of Et₂O into a concentrated MeCN solution. The data was collected by Dr Rianne Lord. The crystal was solved in a centrosymmetric triclinic cell and the structural solution was performed in the *P*-1 space group, with half a molecule in the asymmetric unit. Compared to the structures described in **Chapter 2.2.5** and **Chapter 3.1.4-5** this complex has no strain from a constrained ring, and the wingtips are not bulky, allowing for the C-Ag-C to be colinear and adopt an ideal angle of 180.0°. The molecular structure is shown in **Figure 3.26**, and the wingtip groups fall on both sides of the benzimidazole rings. The Ag-C bond length of 2.0984(14) Å is within the reported range for Ag(I)-NHC complexes, and selected parameters are shown in **Table 3.6**.

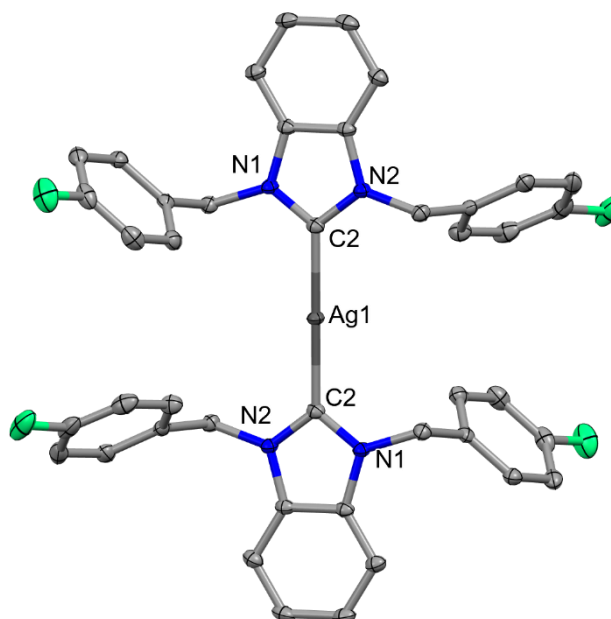


Figure 3.26: Molecular structure of $[Ag(L16)_2](PF_6)$ with displacement ellipsoids shown at the 50% probability level, and counter ion and hydrogen atoms omitted for clarity.

Table 3.6: Selected XRD parameters for $[Ag(L16)_2](PF_6)$ with s.u.s in parenthesis.

Atoms	Bond lengths (Å)
Ag1-C2	2.0984(14)
C-F---H	2.465 – 2.660
Atoms	Angle (°)
C2-Ag1-C2 ¹	180

¹1-X,-Y,1-Z

Within the crystal lattice there are strong hydrogen bonding interactions between four molecules of $[Ag(L16)_2](PF_6)$ and the PF_6^- with bond distances are between 2.465 – 2.660 Å (**Figure 3.27**). Other intermolecular interactions including π - π stacking interactions between the benzimidazoles and benzyis of three molecules of $[Ag(L16)_2](PF_6)$ (**Figure 3.28**) with a centroid distance 4.074 and 3.662 Å respectively.

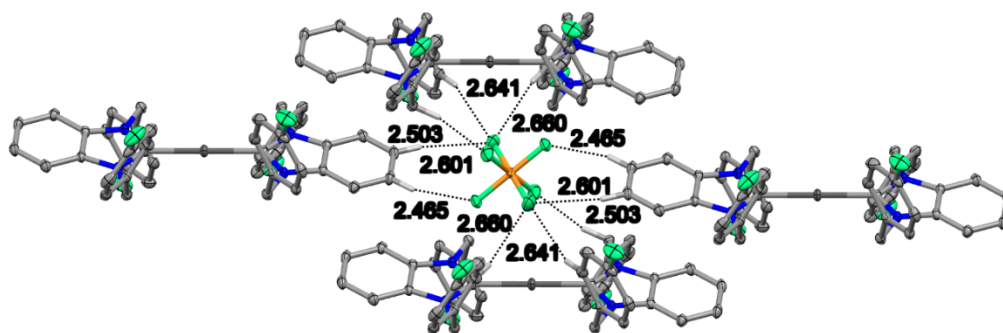


Figure 3.27: Packing diagram of $[\text{Ag}(\text{L16})_2](\text{PF}_6)$ showing the hydrogen bonding interactions between the PF_6^- and four molecules of the complex. Only the interacting hydrogens are shown for clarity.

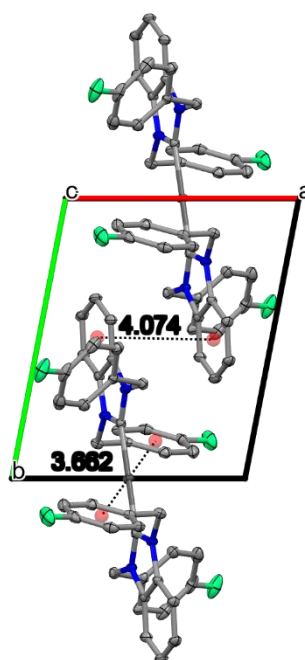


Figure 3.28: Packing diagram showing the intermolecular π - π stacking interactions between molecules of $[\text{Ag}(\text{L16})_2](\text{PF}_6)$ shown along the c -axis, hydrogens and counterions omitted for clarity.

3.3 Conclusions and Future work

A range of bridged benzimidazolium based ligands were successfully synthesised from monofunctionalised imidazole precursors, with ligands **[H₂L8-14](PF₆)₂** being reported for the first time as well as a smaller series of monodentate (benz)imidazolium **[HL15-16](PF₆)**. They were fully characterised by ¹H, ¹³C{¹H} NMR and IR spectroscopy, where successful substitution was confirmed by a shift downfield of the C2 proton, and the ion exchange to PF₆ confirmed by the presence of the characteristic 830 cm⁻¹ peak in the IR. It was identified that the MeOH route used to synthesise a majority of the imidazole complexes reported in **Chapter 2** was not suitable for the benzimidazole derivatives, hence MeCN was used to synthesise **[Ag₂(L8-14)₂](PF₆)₂**. Successful complexation was confirmed by the disappearance of the C2 proton and the broadening of the methylene bridge resonance. The conformational dynamics were also studied by VT-NMR spectroscopy, and generally the methylene bridge is more flexible in the benzimidazole derivatives compared to the imidazole. For **[Ag₂(L9)₂](PF₆)₂** and **[Ag₂(L13)₂](PF₆)₂** crystals suitable for scXRD were obtained, where **[Ag₂(L13)₂](PF₆)₂** was crystallised as two different conformations. The central 12-membered ring adopts a boat-like conformation with the methylene bridges pointing in the same direction. The C-Ag bond lengths are in a similar range to those found in the imidazole complexes reported in **Chapter 2**. All three complexes showed intramolecular argentophilic interactions with Ag-Ag bond distances < 3.44 Å, and intermolecular interactions with between the complex and the PF₆ anion and with solvent molecules (in the crystals that contained solvent). Ligands **[H₂L8-14](PF₆)₂** and complexes **[Ag₂(L10)₂](PF₆)₂**, **[Ag₂(L13)₂](PF₆)₂** and **[Ag₂(L14)₂](PF₆)₂** were found to be pure enough by EA to undergo biological testing.

Two monodentate homoleptic Ag(I)-NHC complexes **[Ag(L15-16)₂](PF₆)** containing *p*-fluoro ligands were synthesised using the MeOH route for imidazole **[Ag(L15)₂](PF₆)** and MeCN route for benzimidazole **[Ag(L16)₂](PF₆)**. Successful complexation was confirmed by the disappearance of the C2 proton in the ¹H NMR spectra and either a shift or disappearance of the C2 carbon in ¹³C{¹H} NMR spectra. Complexation was further confirmed by the disappearance of the C2-H peak in the IR spectra of the complexes. For **[Ag(L16)₂](PF₆)** a crystal suitable for

scXRD was obtained and was solved in a triclinic crystal system in the *P*-1 space group, unlike the bridged complexes $[\text{Ag}(\text{L16})_2](\text{PF}_6)$ adopts the ideal 180° geometry for the C-Ag-C angle. Intermolecular π - π stacking interactions were observed between molecules of $[\text{Ag}(\text{L16})_2](\text{PF}_6)$. The ligands $[\text{HL15-16}](\text{PF}_6)$ and complexes $[\text{Ag}(\text{L15-16})_2](\text{PF}_6)$ were found to be pure by EA and will be tested for their biological activity (see **Chapter 4**).

Further work needs to be carried out to understand why the MeOH route is not suitable for the benzimidazole derivatives and identifying the byproducts from the reactions is essential. With this knowledge this issue could be overcome potentially a different ion exchange agent is required such as KPF_6 , which has been used by other groups when synthesising benzimidazole based binuclear Ag(I)-NHC using the MeOH route.¹¹⁵ Expanding the series of monodentate complexes to include all wingtips would be useful in confirming any SARs between nuclearity of the complexes and their activity.

4 Biological Evaluation of Silver(I) *N*-Heterocyclic Carbene Complexes

4.1 Stability in Aqueous Media

It has been hypothesised that the speed at which Ag^+ is released from Ag(I)-NHC complexes can influence their bioactivity.¹⁷⁵ Prior to biological testing the stability of all compounds should be studied in aqueous media. Youngs et al. reported the stability of Ag(I)-NHC complexes using ^1H and ^{13}C NMR spectroscopy and noted a large range in stabilities between 1.5 hours to 17 weeks in D_2O .¹⁷⁶ However, these studies are not possible for most Ag(I)-NHC complexes, as they have low solubility in water. For this reason, literature reports varying ratios of DMSO:aqueous media, and most complexes were stable in these mediums for between 1 to 5 days.^{177–179}

A major drawback for measuring stabilities by NMR methods is the concentration of complex in the solution needs to be high to obtain a good spectrum, and this limits the percentage of aqueous media that can be used in the experiments. Other methods have been used to study decomposition, where Ashraf et al. used HPLC-DAD (High-performance liquid chromatography with diode-array detection) to study the stability of xylyl bridged binuclear Ag(I)-NHC complexes, sampling at different time points and monitoring the change in the peaks observed in the chromatogram. No changes were observed, and they concluded that their complexes were stable during the testing period of 64 hours.¹²⁰

Another method that has been used is UV-vis spectroscopy, as the technique is more sensitive and lower concentrations of sample can be used, which allows for a higher concentration of aqueous media. Ashraf et al also used this technique to study the stability of *p*-xylyl bridged binuclear Ag(I)-NHC complexes in DMSO:PBS media and observed good stability for 48 hours.¹⁸⁰

UV-vis spectroscopy was therefore selected as the method to test stability of the EA pure complexes $[\text{Ag}_2(\text{L1-7})](\text{PF}_6)_2$, $[\text{Ag}_2(\text{L13})_2](\text{PF}_6)_2$, $[\text{Ag}(\text{L15})_2](\text{PF}_6)$ and $[\text{Ag}(\text{L16})_2](\text{PF}_6)$ (Figure 4.1). Their stability in $\text{H}_2\text{O}:\text{DMSO}$ (95:5) was tested at room temperature for time points up to 24 hours. The high percentage of water gives a more realistic idea of the stability of these complexes in the biological testing conditions.

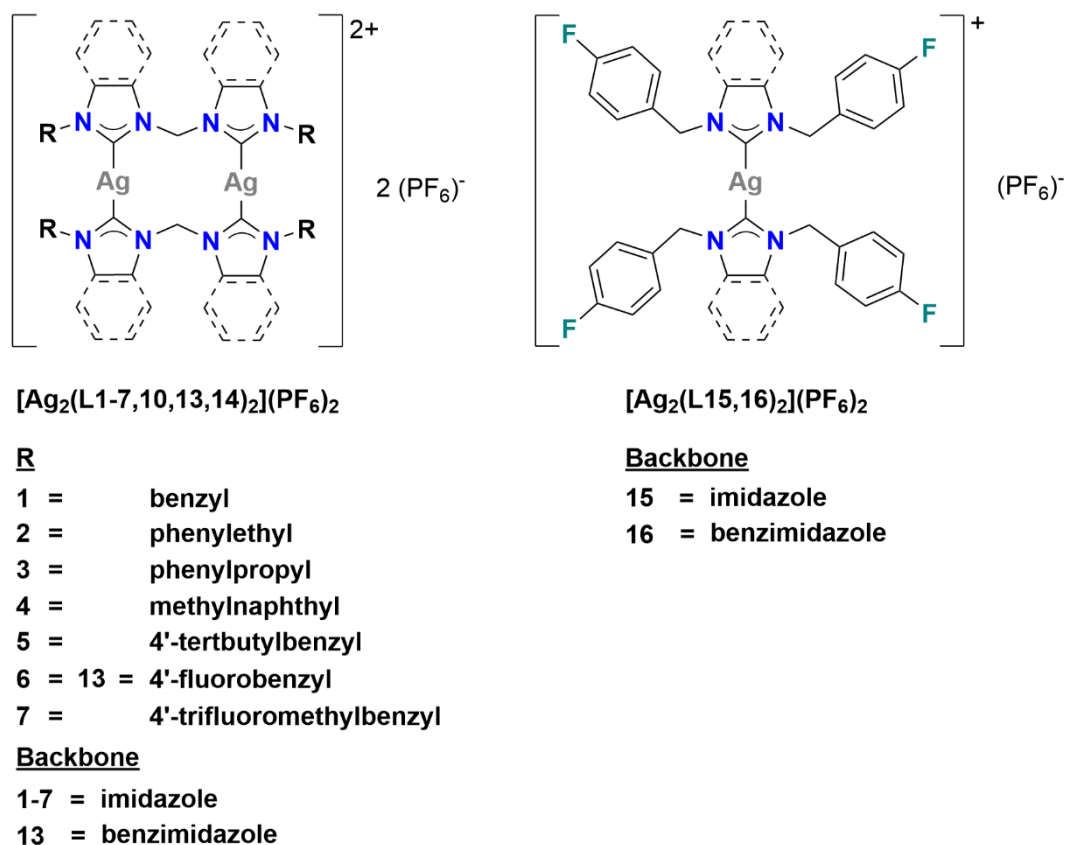


Figure 4.1: Ag(I)-NHC complexes tested for their stability in H₂O:DMSO (95:5) over a period of 24 hours.

Representative UV-Vis spectra are shown in **Figure 4.2** for [Ag₂(L1)₂](PF₆)₂, [Ag₂(L6)₂](PF₆)₂, [Ag₂(L13)₂](PF₆)₂ and [Ag(L15)₂](PF₆), and all other spectra can be found in **Appendix 8.56 - Appendix 8.60**, the decay constants extracted from the spectra (fitting the data with an exponential curve) are reported in **Table 4.1**. Regarding trends for the imidazole series [Ag₂(L1-7)₂](PF₆)₂, the stabilities of the *p*-fluorobenzyl substituted complex [Ag₂(L6)₂](PF₆)₂ and *p*-tert-butylbenzyl complex [Ag₂(L5)₂](PF₆)₂ are negligible when compared to the unsubstituted complex [Ag₂(L1)₂](PF₆)₂. When compared to [Ag₂(L1)₂](PF₆)₂, [Ag₂(L6)₂](PF₆)₂ decomposes 1.3 times faster (calculated from the rates of decay obtained from the spectra) and [Ag₂(L5)₂](PF₆)₂ decomposed 1.1 times slower. The substitution of *p*-trifluoromethylbenzyl complex [Ag₂(L7)₂](PF₆)₂ exhibits the most significant effect on stability, and this complex decomposes 2 times slower than [Ag₂(L1)₂](PF₆)₂.

The *p*-fluorobenzyl binuclear imidazole $[\text{Ag}_2(\text{L6})_2](\text{PF}_6)_2$, the benzimidazole $[\text{Ag}_2(\text{L13})_2](\text{PF}_6)_2$ complexes and the mononuclear analogue $[\text{Ag}(\text{L15})_2](\text{PF}_6)$ were also tested for their stability. The benzimidazole complex **Figure 4.2(b)** decomposes 2 times slower than the imidazole derivative **Figure 4.2(c)**. There is a striking difference between the stability of the mononuclear complex $[\text{Ag}(\text{L15})_2](\text{PF}_6)$ (**Figure 4.2(d)**) and binuclear complex $[\text{Ag}_2(\text{L6})_2](\text{PF}_6)_2$ (**Figure 4.2 (b)**), where the mononuclear analogue decomposes 38 times faster. The results from these studies show that nuclearity has the largest influence on stability while the substitution of the benzyl has a smaller influence.

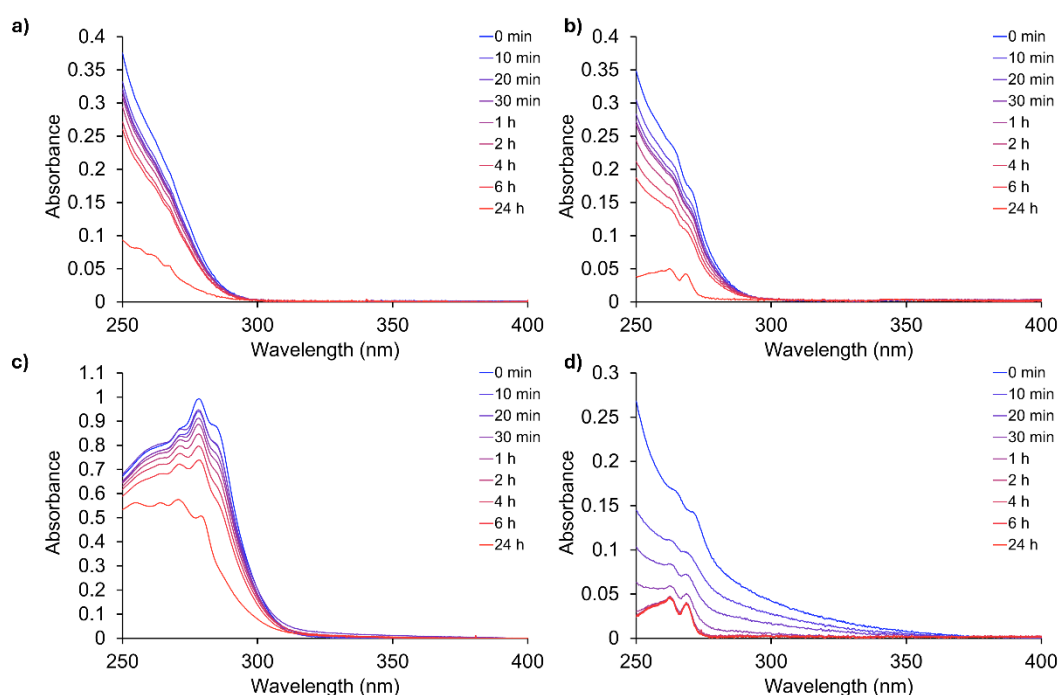


Figure 4.2: UV-vis spectra of Ag(I)-NHC complexes in $\text{H}_2\text{O}:\text{DMSO}$ (95:5) over a period of 24 hours, a) $[\text{Ag}_2(\text{L1})_2](\text{PF}_6)_2$, b) $[\text{Ag}_2(\text{L6})_2](\text{PF}_6)_2$, c) $[\text{Ag}_2(\text{L13})_2](\text{PF}_6)_2$ and d) $[\text{Ag}(\text{L15})_2](\text{PF}_6)$.

Table 4.1 Decay constants calculated from the Uv-Vis spectra between time points 0 – 6 h.

Complex	decay constant (1/min)
[Ag ₂ (L1) ₂](PF ₆) ₂	0.0008
[Ag ₂ (L2) ₂](PF ₆) ₂	0.001
[Ag ₂ (L5) ₂](PF ₆) ₂	0.0007
[Ag ₂ (L6) ₂](PF ₆) ₂	0.001
[Ag ₂ (L7) ₂](PF ₆) ₂	0.0003
[Ag ₂ (L13) ₂](PF ₆) ₂	0.0005
[Ag(L15) ₂](PF ₆)	0.038

To compare with literature experiments an ¹H NMR stability experiment was conducted [Ag₂(L13)₂](PF₆)₂ with D₂O:d₆-DMSO (30:70), low percentages due to solubility) up to 24 hours, and there was no sign of decomposition (see **Appendix 8.55**). This indicates that the concentration of water is important to how stable the complex will be in the solution.

4.2 Lipophilicity

One important parameter that influences drug compounds effectiveness is the lipophilicity, which can be used to determine how likely compounds are to be absorbed in the body. The lipophilicity is reported as a LogP value which is defined as the logarithm of the partition coefficient (P), which is the ratio of the solute in the organic and aqueous layers (**Equation 3**)

$$\text{LogP} = \log_{10} \frac{[\text{Organic}]}{[\text{Aqueous}]} \quad \text{Equation 3}$$

The larger the LogP value, the more lipophilic the complex and its ability to be absorbed through the phospholipid bilayer increases. Lipinski's "Rules of five" stipulates that for oral availability the LogP should be below 5, where LogP of 1.3 – 1.8 are most suitable for gastrointestinal absorption.¹⁸¹ A moderate lipophilicity is also required for the drugs to pass through the cell membrane.¹⁸² If the compound is actively transported adherence to this rule is less important. Due to the lack of long-term aqueous stability of the Ag(I)-NHC complexes herein, accurate

experimental LogP values would be difficult to obtain, therefore, SwissADME software has been used to predict their trends (**Table 4.2**).¹⁸³

Table 4.2: LogP values calculated for functionalised azoles, ligands and complexes calculated computationally using SwissADME software, the values are an average of four computational methods used to estimate lipophilicity (XLOGP3, WLOGP, MLOGP and SILICOS-IT).¹⁸³

Func-azole	LogP	Ligand	LogP	Silver complex	LogP
Im1	1.7	[H ₂ L1](PF ₆) ₂	7.43	[Ag ₂ (L1) ₂](PF ₆) ₂	9.27
Im2	1.97	[H ₂ L2](PF ₆) ₂	8.06	[Ag ₂ (L2) ₂](PF ₆) ₂	10.49
Im3	2.31	[H ₂ L3](PF ₆) ₂	8.72	[Ag ₂ (L3) ₂](PF ₆) ₂	11.81
Im4	2.77	[H ₂ L4](PF ₆) ₂	9.42	[Ag ₂ (L4) ₂](PF ₆) ₂	13.12
Im5	3	[H ₂ L5](PF ₆) ₂	10.08	[Ag ₂ (L5) ₂](PF ₆) ₂	14.31
Im6	2.06	[H ₂ L6](PF ₆) ₂	8.25	[Ag ₂ (L6) ₂](PF ₆) ₂	10.7
Im7	2.93	[H ₂ L7](PF ₆) ₂	9.96	[Ag ₂ (L7) ₂](PF ₆) ₂	14.09
Im8	2.95	[H ₂ L8](PF ₆) ₂	9.78	[Ag ₂ (L8) ₂](PF ₆) ₂	13.85
Im9	3.23	[H ₂ L9](PF ₆) ₂	10.41	[Ag ₂ (L9) ₂](PF ₆) ₂	15.07
Im10	3.56	[H ₂ L10](PF ₆) ₂	11.07	[Ag ₂ (L10) ₂](PF ₆) ₂	16.37
Im11	4	[H ₂ L11](PF ₆) ₂	11.74	[Ag ₂ (L11) ₂](PF ₆) ₂	- ^a
Im12	4.25	[H ₂ L12](PF ₆) ₂	12.42	[Ag ₂ (L12) ₂](PF ₆) ₂	- ^a
Im13	3.31	[H ₂ L13](PF ₆) ₂	10.59	[Ag ₂ (L13) ₂](PF ₆) ₂	15.28
Im14	4.18	[H ₂ L14](PF ₆) ₂	12.3	[Ag ₂ (L14) ₂](PF ₆) ₂	- ^a
-	-	[HL15](PF ₆)	6.21	[Ag(L15) ₂](PF ₆)	9.32
-	-	[HL16](PF ₆)	7.41	[Ag(L16) ₂](PF ₆)	11.63

^acomplexes are too large to for the LogP to be calculated using the SwissADME software.¹⁸³

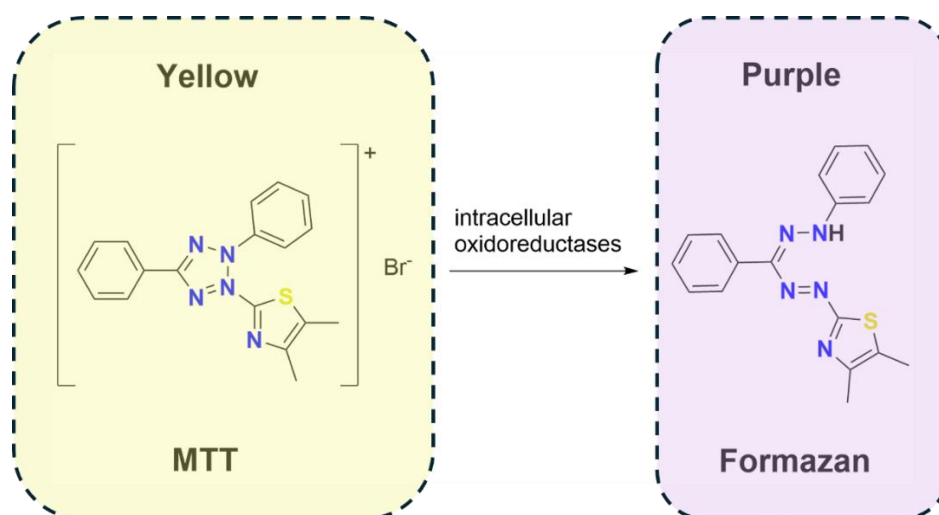
The software overestimates the values of the charged ligands and complexes but is still useful for comparison of relative lipophilicity within the series. When varying the wingtip in each of the series the order of lipophilicity trends is the same; benzyl < phenylethyl < *p*-fluorobenzyl < phenylpropyl < methylnaphthyl < *p*-trifluoromethylbenzyl < *p*-*tert*-butylbenzyl. The benzimidazole derivatives are more lipophilic than the corresponding imidazoles and the monodentate analogues

are less lipophilic than the bridging complexes. The relationship between the lipophilicity and activity of these compounds will be discussed in the next section.

4.3 Cytotoxicity Studies

4.3.1 24-hour MTT Assay

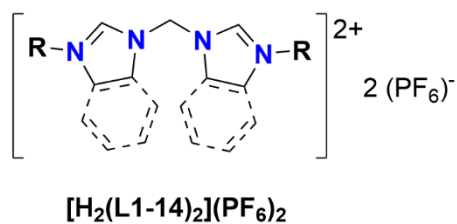
The MTT assay is an established colorimetric method to ascertain a compounds activity against a particular cell type. The assay uses yellow 3-(4,5-dimethylthiazol-2-yl)-2,5-diphenyltetrazolium bromide (MTT) which is converted into purple formazan by intercellular redox enzymes (oxidoreductases) via the cleavage of the tetrazolium 5-membered ring (**Scheme 4.1**).^{184,185} The amount of formazan present is directly proportional to the amount of metabolic activity and therefore the population of live cells present can be estimated by measuring the formazan absorbance at 540 nm and comparing into an untreated cell control. The untreated control absorbance is set as the 100% value; a range of drug concentrations are then tested and their absorbances are compared to the control to get percentage inhibition values. A sigmoidal curve is fitted and the concentration at 50% survival (IC_{50} value) is calculated, the final IC_{50} value is determined from the average of three independent experiments ($n = 9$). The data presented here was collected and processed by Dr Rianne Lord.



Scheme 4.1: A reaction scheme showing the reduction of MTT (yellow) to formazan (purple) by mitochondrial oxidoreductases, the basis for the MTT cytotoxicity assay.^{184,185}

Elementally pure compounds were tested against two breast cancer cell lines, a hormone-independent TNBC cell line (MDA-MB-231), a hormone sensitive breast cancer (MCF-7), and one non-cancerous retinal epithelial cell line (ARPE-19). Some compounds were also compared to a non-cancerous breast cell line (MCF10A). The cells were incubated with either the compounds or positive controls cisplatin (CDDP) and tamoxifen (TAM) for 24 hours.

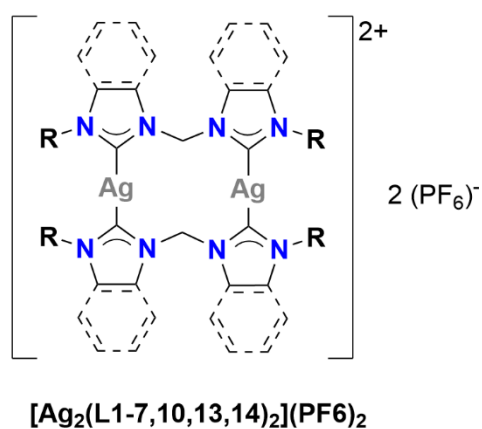
The activities of all the complexes and ligands tested (**Figure 4.3**) are shown in **Table 4.3**. Selectivity indexes (SI), which ratio of activity in cancerous and non-cancerous cell lines have also been calculated and are shown in **Table 4.4**. The higher the SI the more targeted the compound is towards the cancer cell. Where both IC_{50} values are $> 100 \mu M$, an SI cannot be calculated, and this information has been omitted from **Table 4.3**.

R

- 1 = 8 = benzyl
 2 = 9 = phenylethyl
 3 = 10 = phenylpropyl
 4 = 11 = methylnaphthyl
 5 = 12 = 4'-tertbutylbenzyl
 6 = 13 = 4'-fluorobenzyl
 7 = 14 = 4'-trifluoromethylbenzyl

Backbone

- 1-7 = imidazole
 8-14 = benzimidazole

R

- 1 = benzyl
 2 = phenylethyl
 3 = 10 = phenylpropyl
 4 = methylnaphthyl
 5 = 4'-tertbutylbenzyl
 6 = 13 = 4'-fluorobenzyl
 7 = 14 = 4'-trifluoromethylbenzyl

Backbone

- 1-7 = imidazole
 10,13,14 = benzimidazole

Figure 4.3: Structures of the ligands and Ag(I)-NHC complexes that have been tested for their activity.

Table 4.3: IC_{50} values of ligands, complexes, cisplatin (CDDP) and tamoxifen (TAM) when tested against MDA-MB-231, MCF-7, ARPE-19 and MCF10A with an incubation period of 24 hours. Values shown with the \pm SEM (standard error of the mean) in parentheses ($n = 9$). ND = not determined.

Compound	IC_{50} (\pm SEM) μ M			
	MDA-MB-321	MCF-7	ARPE-19	MCF10A
[H ₂ L1](PF ₆) ₂	>100.0	>100.0	>100.0	>100.0
[H ₂ L2](PF ₆) ₂	>100.0	>100.0	>100.0	>100.0
[H ₂ L3](PF ₆) ₂	>100.0	>100.0	>100.0	>100.0
[H ₂ L4](PF ₆) ₂	55.5 (\pm 5.4)	73.5 (\pm 0.72)	53.0 (\pm 3.4)	72.9 (\pm 1.0)
[H ₂ L5](PF ₆) ₂	>100.0	>100.0	>100.0	>100.0
[H ₂ L6](PF ₆) ₂	>100.0	>100.0	>100.0	>100.0
[H ₂ L7](PF ₆) ₂	>100.0	>100.0	>100.0	>100.0
[H ₂ L8](PF ₆) ₂	>100.0	>100.0	>100.0	>100.0
[H ₂ L9](PF ₆) ₂	>100.0	>100.0	>100.0	>100.0
[H ₂ L10](PF ₆) ₂	>100.0	>100.0	>100.0	>100.0
[H ₂ L11](PF ₆) ₂	70.2 (\pm 1.1)	73.4 (\pm 0.8)	66.1 (\pm 1.7)	66.7 (\pm 1.7)
[H ₂ L12](PF ₆) ₂	46.7 (\pm 1.9)	44 (\pm 1.2)	47.4 (\pm 0.9)	38.2 (\pm 1.1)
[H ₂ L13](PF ₆) ₂	>100.0	>100.0	>100.0	ND
[H ₂ L14](PF ₆) ₂	>100.0	98.9 (\pm 0.9)	>100.0	ND
[HL15](PF ₆)	ND	>100.0	>100.0	ND
[HL16](PF ₆)	42.6 (\pm 0.5)	>100.0	>100.0	ND
[Ag ₂ (L1) ₂](PF ₆) ₂	13.4 (\pm 1.0)	18.6 (\pm 0.4)	35.1 (\pm 1.8)	8.0 (\pm 0.2)
[Ag ₂ (L2) ₂](PF ₆) ₂	15.7 (\pm 0.3)	18.1 (\pm 0.4)	32.3 (\pm 1.8)	8.9 (\pm 0.3)
[Ag ₂ (L3) ₂](PF ₆) ₂	8.6 (\pm 0.3)	12.8 (\pm 0.3)	8.6 (\pm 0.2)	8.4 (\pm 0.2)
[Ag ₂ (L4) ₂](PF ₆) ₂	8.6 (\pm 0.1)	10.3 (\pm 0.6)	32.8 (\pm 1.7)	7.1 (\pm 0.01)
[Ag ₂ (L5) ₂](PF ₆) ₂	8.2 (\pm 0.2)	9.1 (\pm 0.2)	15.9 (\pm 0.9)	6.4 (\pm 0.2)
[Ag ₂ (L6) ₂](PF ₆) ₂	5.5 (\pm 0.2)	18.3 (\pm 0.2)	37.7 (\pm 0.8)	9.4 (\pm 0.3)
[Ag ₂ (L7) ₂](PF ₆) ₂	7.4 (\pm 0.1)	9.8 (\pm 0.4)	31.6 (\pm 1.1)	5.5 (\pm 0.2)
[Ag ₂ (L10) ₂](PF ₆) ₂	6.7 (\pm 0.4)	11.9 (\pm 0.6)	38.4 (\pm 1.2)	ND
[Ag ₂ (L13) ₂](PF ₆) ₂	4.5 (\pm 0.3)	8.5 (\pm 0.1)	31.6 (\pm 1.2)	6.4 (\pm 1.0)
[Ag ₂ (L14) ₂](PF ₆) ₂	6.6 (\pm 0.4)	10.7 (\pm 0.1)	20.5 (\pm 0.9)	ND
[Ag(L15) ₂](PF ₆)	10.8 (\pm 0.2)	20.7 (\pm 0.4)	24.7 (\pm 0.1)	ND
[Ag(L16) ₂](PF ₆)	3.7 (\pm 0.3)	5.0 (\pm 0.2)	15.8 (\pm 0.5)	ND
CDDP	>100.0	54.4 (\pm 2.9)	>100.0	41.7 (\pm 1.3)
TAM	39.6 (\pm 0.1)	35.9 (\pm 1.2)	74.8 (\pm 1.5)	38.3 (\pm 0.9)

Table 4.4: Selectivity index (SI) of ligands, complexes, cisplatin (CDDP, and tamoxifen (TAM) when comparing the activity of against cancerous and non-cancerous cell lines. ND = not determined. * = minimum value as one of the values used to calculate it was $> 100 \mu\text{M}$.

Compound	Selectivity index (SI)			
	MDA-MB-231 cf. ARPE-19	MCF-7 cf. ARPE-19	MDA-MB-231 cf. MCF10A	MCF-7 cf. MCF10A
[H ₂ L4](PF ₆) ₂	ND	0.7	1.3	1.0
[H ₂ L11](PF ₆) ₂	0.9	0.9	1.0	0.9
[H ₂ L12](PF ₆) ₂	ND	1.1	0.8	0.9
[HL16](PF ₆)	2.3*	ND	ND	ND
[Ag ₂ (L1) ₂](PF ₆) ₂	2.6	1.9	0.6	0.4
[Ag ₂ (L2) ₂](PF ₆) ₂	2.1	1.8	0.6	0.5
[Ag ₂ (L3) ₂](PF ₆) ₂	1.0	0.7	1.0	0.7
[Ag ₂ (L4) ₂](PF ₆) ₂	3.8	3.2	0.8	0.7
[Ag ₂ (L5) ₂](PF ₆) ₂	1.9	1.7	0.8	0.7
[Ag ₂ (L6) ₂](PF ₆) ₂	6.8	2.1	1.7	0.5
[Ag ₂ (L7) ₂](PF ₆) ₂	4.3	3.2	0.7	0.6
[Ag ₂ (L10) ₂](PF ₆) ₂	5.7	3.2	ND	ND
[Ag ₂ (L13) ₂](PF ₆) ₂	7.1	3.7	1.4	0.8
[Ag ₂ (L14) ₂](PF ₆) ₂	3.1	1.9	ND	ND
[Ag(L15) ₂](PF ₆)	2.3	1.2	ND	ND
[Ag(L16) ₂](PF ₆)	4.3	3.2	ND	ND
CDDP	ND	1.8	0.4	0.8
TAM	1.9	2.1	1.0	1.1

Most of the bridged imidazole ligands [H₂L1-7](PF₆)₂ are non-toxic (IC₅₀ $> 100 \mu\text{M}$) against all of the cell lines tested, with only the methylnaphthyl functionalised ligand [H₂L4](PF₆)₂ exhibiting moderate cytotoxicity against all cell lines (IC₅₀ values 53.0 – 73.5 μM). The bridged benzimidazole derivatives [H₂L8-14](PF₆)₂ were also screened against the same cell lines and generally exhibit low activity. The least lipophilic ligands [H₂L8-10](PF₆)₂ and [H₂L13-14](PF₆)₂ are non-toxic (IC₅₀ $> 100 \mu\text{M}$), whilst the most lipophilic ligand [H₂L12](PF₆)₂ has moderate activity (IC₅₀ values 38.2 – 47.4 μM). When comparing the values against MDA-MB-231 the results against MCF-7 ($P > 0.05$) and ARPE-19 ($P > 0.05$), and not statistically different. Similar to [H₂L4](PF₆)₂, which was the most active imidazole

ligand, the benzimidazole derivative $[\text{H}_2\text{L11}](\text{PF}_6)_2$ is moderately active against all four cell lines, with IC_{50} values 66.1 – 73.4 μM .

Complexes $[\text{Ag}_2(\text{L1-7})_2](\text{PF}_6)_2$ are more active than CDDP and TAM against all the cell lines tested. In general, the complexes are more active against MDA-MB-231 compared to MCF-7 and ARPE-19 (all have $P < 0.05$), and in all but one of the complexes, they are most active against MCF10A. In all cases the bridging imidazole Ag(I)-NHC complexes are more active than the corresponding ligand by between 5.5 – > 22.5 times, and this indicates that silver is important for activity. Despite the naphthylmethyl functionalised ligand $[\text{H}_2(\text{L4})_2](\text{PF}_6)_2$ being the only active one in imidazole series, the naphthylmethyl functionalised $[\text{Ag}_2(\text{L4})_2](\text{PF}_6)_2$ is only 6.4 times more active against MDA-MB-231, whereas the *p*-fluorobenzyl derivative $[\text{Ag}_2(\text{L6})_2](\text{PF}_6)_2$ is > 18.1 times more active than the corresponding ligand. When comparing the IC_{50} values against MDA-MB-231, the substituted benzyl derivatives $[\text{Ag}_2(\text{L5-7})_2](\text{PF}_6)_2$ are more active than the unsubstituted benzyl complex $[\text{Ag}_2(\text{L1})_2](\text{PF}_6)_2$ ($13.4 \pm 1.0 \mu\text{M}$), with the fluoro-substituted complexes exhibiting the highest activities ($[\text{Ag}_2(\text{L6})_2](\text{PF}_6)_2 = 5.5 \pm 0.2 \mu\text{M}$, $[\text{Ag}_2(\text{L7})_2](\text{PF}_6)_2 = 7.4 \pm 0.1 \mu\text{M}$).

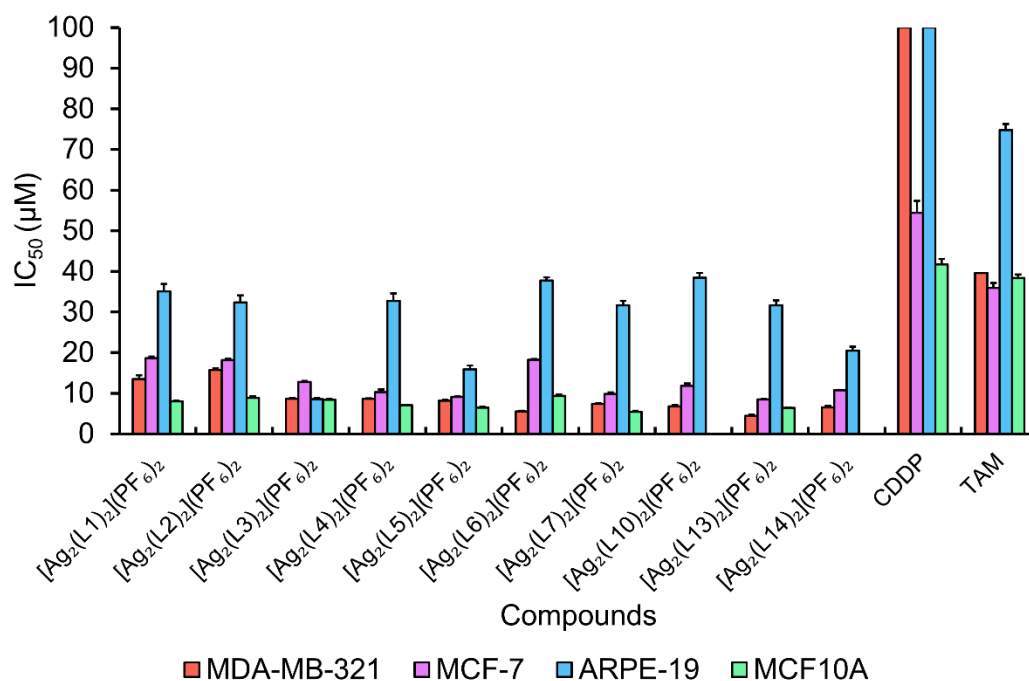


Figure 4.4: Bar chart representing the activity ($IC_{50} \pm SEM$) of binuclear Ag(I)-NHC complexes $[Ag_2(L1-7)_2](PF_6)_2$, $[Ag_2(L10)_2](PF_6)_2$, $[Ag_2(L13-14)_2](PF_6)_2$, CDDP and TAM against MDA-MB-231, MCF-7, ARPE-19 and MCF10A cell lines after 24-hour incubation.

Figure 4.5 shows the selectivity index (SI) of complexes $[Ag_2(L1-7)_2](PF_6)_2$. SI values > 1 indicate the complex is more selective towards the cancer cell line compared to non-cancerous cell line, SI values < 1 indicate a higher selectivity against non-cancerous cell line and SI = 1 means the cytotoxicity are equally toxic in both cell lines. All complexes, except $[Ag_2(L3)_2](PF_6)_2$, are more selective towards both cancer cell lines compared to the ARPE-19 cell line, with SI values of 1.9 – 6.8 (MDA-MB-231) and 1.7 – 3.2 (MCF-7). Regarding the MCF10A cell line, all compounds except $[Ag_2(L6)_2](PF_6)_2$ which has SI = 1.7, are non-selective and more active in the non-cancerous cell line. The low selectivity in these complexes is a deviation to what has been reported in literature for Ag(I)-NHC complexes, where a majority the complexes are less active against MCF10A compared to MCF-7 or MDA-MB-231, this has been reported both for neutral and homoleptic (ionic) Ag(I)-NHC complexes.^{101,186,187}

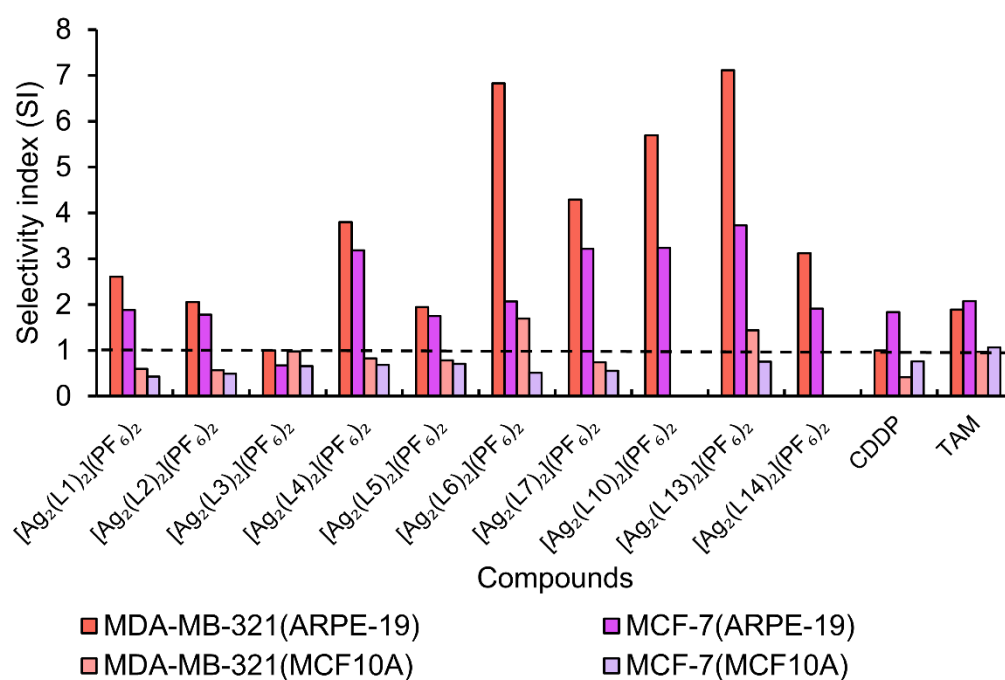


Figure 4.5: Bar chart showing the selectivity index (SI) of the Ag(I)-NHC complexes comparing their activity against non-cancerous cell lines ARPE-19 and MCF10A. SI values >1 indicate the complex is more selective towards the cancer cell line compared to non-cancerous cell line, SI values <1 indicates a higher selectivity against non-cancerous cell line and SI = 1 means the cytotoxicity are equally toxic in both cell lines.

To understand SARs between cytotoxicity and lipophilicity, the IC₅₀ values of the imidazole complexes were plotted against LogP values (**Figure 4.6**). For MCF-7 there is a correlation between lipophilicity and activity ($R^2 = 0.92$), however, for the other three cell lines no clear relationships are observed.

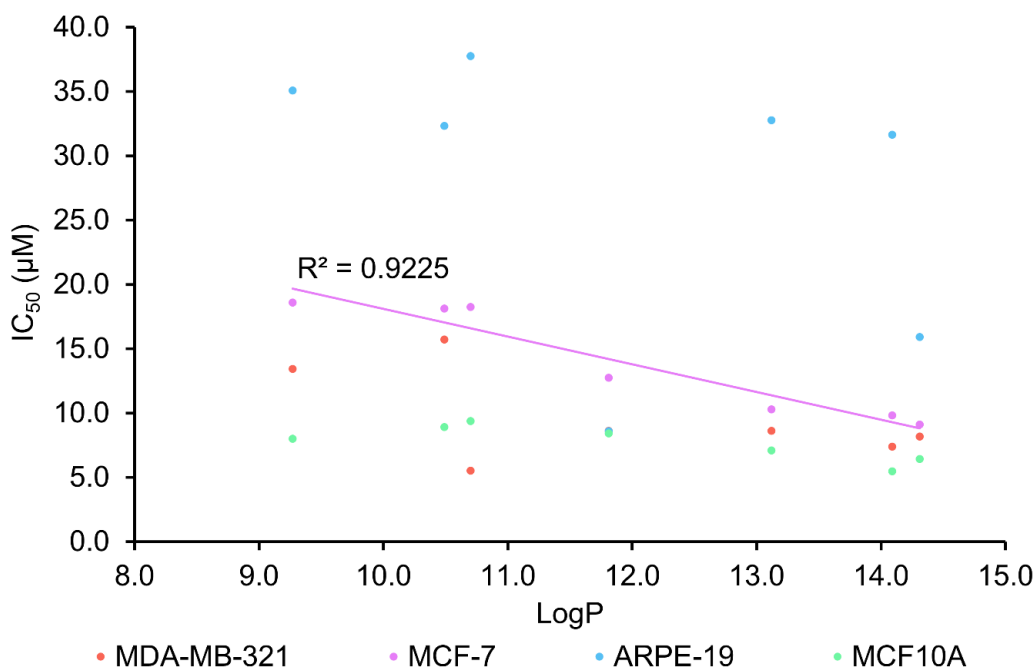


Figure 4.6: Plot of LogP against IC_{50} values for the complexes $[AgL1-7](PF_6)_2$ against MDA-MB-231, MCF-7, ARPE-19 and MCF10A cell lines, the R^2 value and line of best fit is shown for MCF-7 only.

The series of benzimidazole based Ag(I)-NHC complexes (**Figure 4.4**) were also screened against MDA-MB-231, MCF-7 and ARPE-19, however, from this series, only $[Ag_2(L10)_2](PF_6)_2$, $[Ag_2(L13)_2](PF_6)_2$ and $[Ag_2(L14)_2](PF_6)_2$ were of the required purity for biological testing. Like the imidazole derivatives, the benzimidazole Ag(I)-NHC complexes are more active than CDDP and TAM against all the cell lines tested. Against both breast cancer cell lines $[Ag_2(L13)_2](PF_6)_2$ was the most active complex, with IC_{50} values of $4.5 \pm 0.3 \mu M$ (MDA-MB-231) and $8.5 \pm 0.1 \mu M$ (MCF-7). As with the imidazole complex $[Ag_2(L6)_2](PF_6)_2$, the benzimidazole analogue $[Ag_2(L13)_2](PF_6)_2$ is selective towards both MDA-MB-231 and MCF-7 when compared to the non-cancerous ARPE-19 cell line, with a SI values of 7.1 and 3.8 respectively, and this is higher than any of the other complexes tested. When comparing the data against MDA-MB-231, there is a small improvement in activity when changing from the imidazole derivatives ($[Ag_2(L3)_2](PF_6)_2 = 8.6 \pm 0.3 \mu M$ and $[Ag_2(L6)_2](PF_6)_2 = 5.5 \pm 0.2 \mu M$) to the benzimidazole derivatives ($[Ag_2(L10)_2](PF_6)_2 = 6.7 \pm 0.4 \mu M$ and $[Ag_2(L13)_2](PF_6)_2 = 4.5 \pm 0.3 \mu M$, $0.05 < P$). For the other cell lines, there are no

clear relationships observed. Further benzimidazole derivatives would need to be tested to fully understand the structure activity relationships. The range of values measured for the complexes outlined in this work are similar to the activities reported for similar binuclear homoleptic Ag(I)-NHC complexes in literature such as the benzimidazole based complexes reported by Asif et al. who reported activities between 5.28 – 9.50 μM (MDA-MB-231).¹¹⁴ Conversely against MCF-7 the complexes reported by Asif et al. are more active (1.48 – 4.71 μM), it should be noted that for both cell lines Asif et al. incubated for a longer period (48 h vs 24 h).

4.3.2 Varying Nuclearity

As the *p*-fluorobenzyl substituted complexes were the most promising out of all the wingtips tested, mononuclear versions of the two most active complexes $[\text{Ag}_2(\text{L6})_2](\text{PF}_6)_2$ and $[\text{Ag}_2(\text{L13})_2](\text{PF}_6)_2$ were synthesised to probe the influence of nuclearity on cytotoxicity and selectivity towards cancerous cells (**Figure 4.7**). The IC_{50} values of the monodentate ligands, like their bridged versions, were inactive against the cell lines tested ($\text{IC}_{50} > 100 \mu\text{M}$).

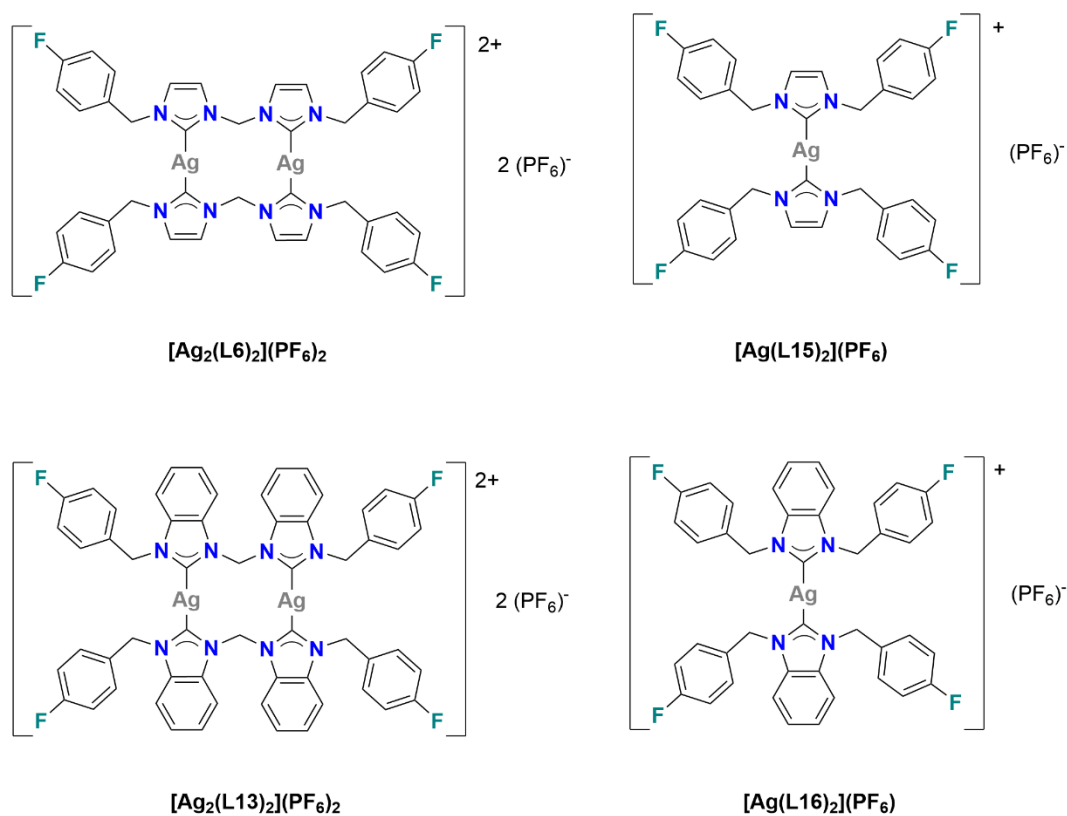


Figure 4.7: Structures of the mono and binuclear complexes functionalised with a *p*-fluorobenzyl wingtip.

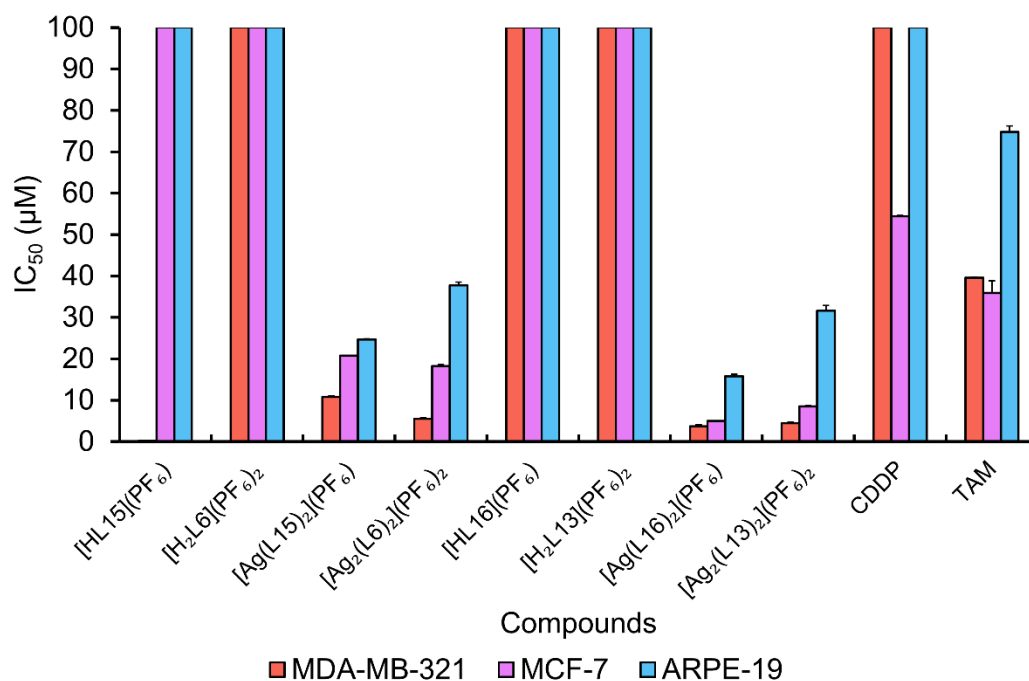


Figure 4.8: Bar chart representing the IC_{50} (\pm SEM) values of the mono and binuclear Ag(I)-NHC *p*-fluorobenzyl complexes, their respective pro-ligands, CDDP and TAM, when screened against MDA-231, MCF-7 and ARPE-19 cell lines using a 24-hour incubation period ($n = 9$).

For MDA-MB-231, the activity of the mononuclear complexes is either less (imidazole) or the same ($P > 0.05$) as the binuclear (benzimidazole), whilst for MCF-7 there are no clear relationships between the complexes tested. These observations are in contrast with the findings of Monterio et al. in which the binuclear complexes were more active than the mononuclear derivative (see 1.3.4.3).¹¹⁹ Selectivity index values were calculated and compared for the Ag(I)-NHC complexes, confirming their selectivity towards MDA-MB-231 (compared to ARPE-19) (**Figure 4.9**). When comparing nuclearity in the MDA-MB-231 cell line, the SI for the binuclear complexes ($[Ag_2(L6)_2](PF_6)_2 = 6.8$ and $[Ag_2(L13)_2](PF_6)_2 = 7.1$) are higher than their mononuclear derivatives ($[Ag(L15)_2](PF_6) = 2.3$ and $[Ag(L16)_2](PF_6) = 4.3$).

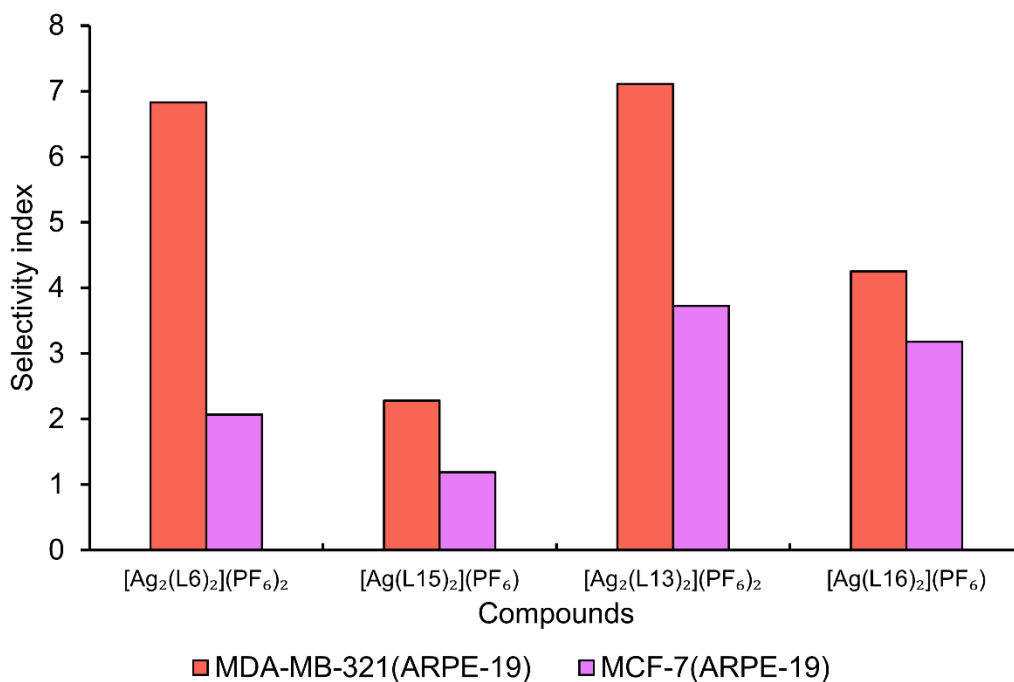


Figure 4.9: Selectivity index of the mononuclear Ag(I)-NHC *p*-fluorobenzyl complexes $[\text{Ag}(\text{L15})_2](\text{PF}_6)$ and $[\text{Ag}(\text{L16})_2](\text{PF}_6)$ and binuclear Ag(I)-NHC *p*-fluorobenzyl complexes $[\text{Ag}_2(\text{L6})_2](\text{PF}_6)_2$ and $[\text{Ag}_2(\text{L13})_2](\text{PF}_6)_2$ when activities against MDA-MB-231 and MCF-7 are compared to ARPE-19.

4.4 Mechanistic Studies

Four complexes were taken forward for further biological evaluation which were $[\text{Ag}_2(\text{L1})_2](\text{PF}_6)_2$, $[\text{Ag}_2(\text{L4})_2](\text{PF}_6)_2$, $[\text{Ag}_2(\text{L6})_2](\text{PF}_6)_2$ and $[\text{Ag}_2(\text{L13})_2](\text{PF}_6)_2$. $[\text{Ag}_2(\text{L1})_2](\text{PF}_6)_2$ was chosen as one of the least active of the complexes and also as the simplest complex from which all of the other compounds are derived. $[\text{Ag}_2(\text{L6})_2](\text{PF}_6)_2$ and $[\text{Ag}_2(\text{L13})_2](\text{PF}_6)_2$ were chosen as they are the most active complexes in their respective series (imidazole and benzimidazole), and finally $[\text{Ag}_2(\text{L4})_2](\text{PF}_6)_2$ was chosen as the naphthyl moiety could have potential interactions with biomolecules such as DNA which the other complexes may not have.

4.4.1 4-hour MTT Assay

Due to the high cytotoxicity and selectivity against the MDA-MB-231 cell line, but lack of compound stability, incubation times were reduced and MTT assays repeated after 4-hour incubation (**Figure 4.10**).

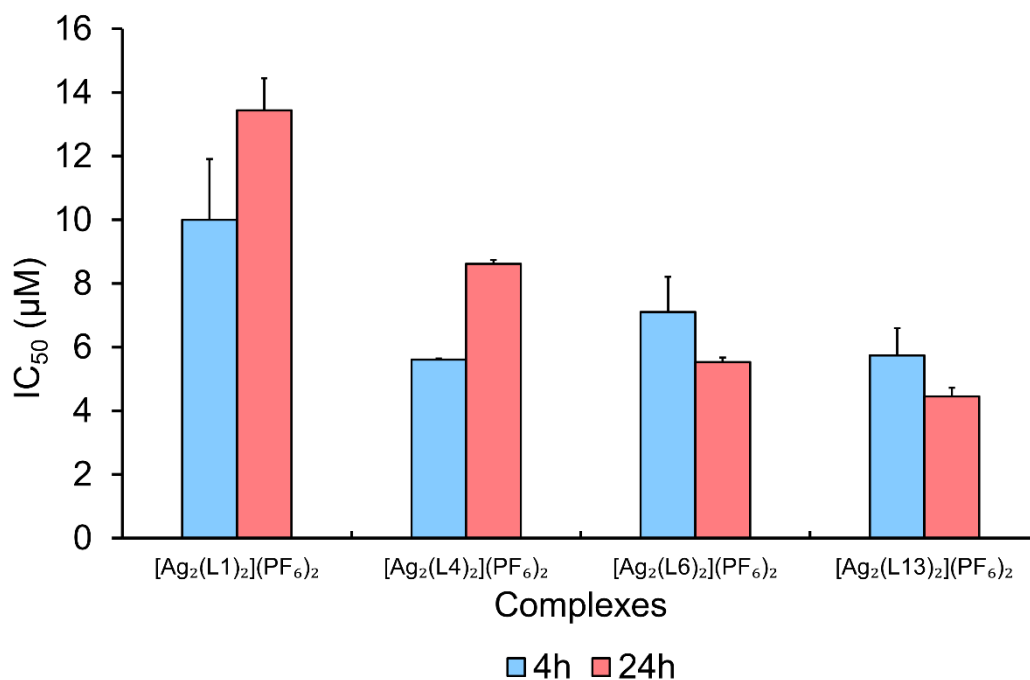


Figure 4.10: Comparison of IC_{50} (\pm SEM) values of selected Ag(I)-NHC complexes after both 4-hour and 24-hour incubation periods using the MDA-MB-231 cell line.

For most compounds, the IC_{50} values are not statistically different between the two different incubation times. All compounds are active even after 4 hours, with IC_{50} values ranging from 5.6 – 15.7 μ M. However, a statistical difference is observed for [Ag₂(L4)₂](PF₆)₂ showing that the complex is more active after 4-hours and cell viabilities recovers marginally after 24-hours.

4.4.2 Morphological Changes Upon Incubation

When cells start to go through cell death pathways, one of the major changes is cell morphology and the formation of apoptotic bodies can be observed. These changes were followed using an optical microscope (10x magnification) and by taking images at different timepoints after the drug additions. **Figure 4.12** shows the change in morphology of MDA-MB-231 cells upon addition of 10 μ M or 50 μ M of the unsubstituted benzyl complex [Ag₂(L1)₂](PF₆)₂ (**Figure 4.11**) and the naphthyl complex [Ag₂(L4)₂](PF₆)₂ (**Figure 4.12**). At the earliest time point recorded (30 min) and 10 μ M addition, and the morphology is similar to the control (DMSO

0.05%), showing the classical stellate shape (**Figure 4.11(a)** and **Figure 4.12(d)**).¹⁸⁸ After increasing the incubation times, the cells begin to detach from the plate and become more rounded in shape. This is seen earlier in the higher dosage of 50 μM , where after 30 mins, complex $[\text{Ag}_2(\text{L4})_2](\text{PF}_6)$ causes detachment of the cells **Figure 4.12(g)**.

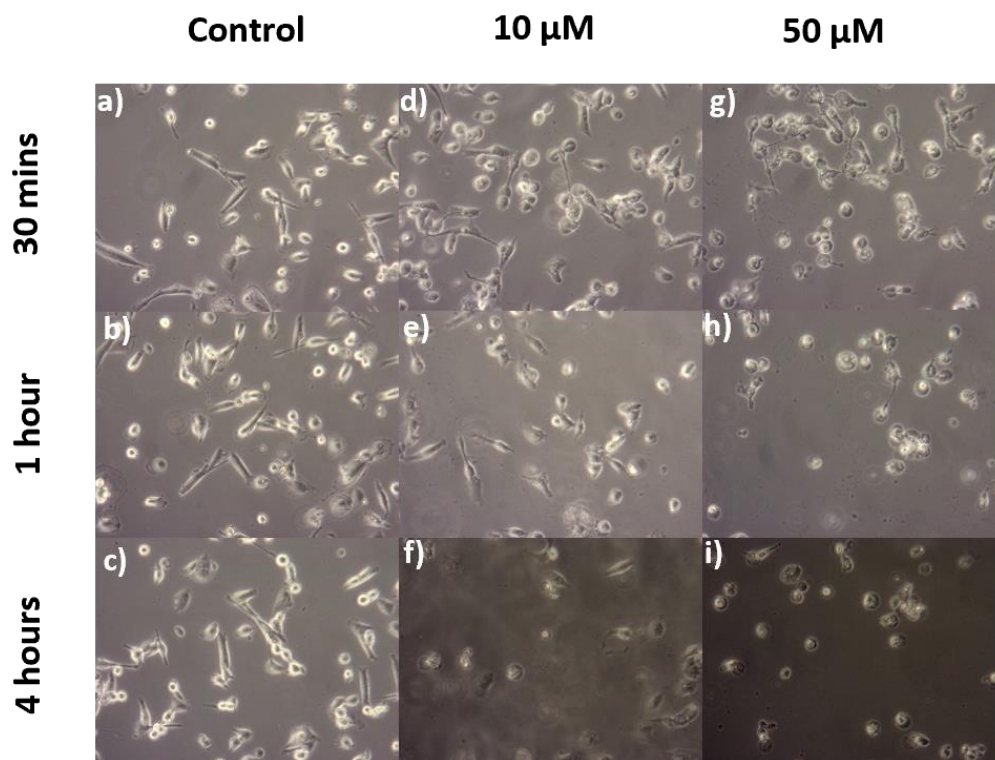


Figure 4.11: MDA-MB-231 cells after being treated with $[\text{Ag}_2(\text{L1})_2](\text{PF}_6)_2$ - a) control (DMSO 0.05%) 30 mins, b) control (DMSO 0.05%), 1 hour, c) control (DMSO 0.05%), 4 hours, d) 10 μM 30 mins, e) 10 μM 1 hour, f) 10 μM 4 hours, g) 50 μM 30 mins, h) 50 μM 1 hour, i) 50 μM 4 hours.

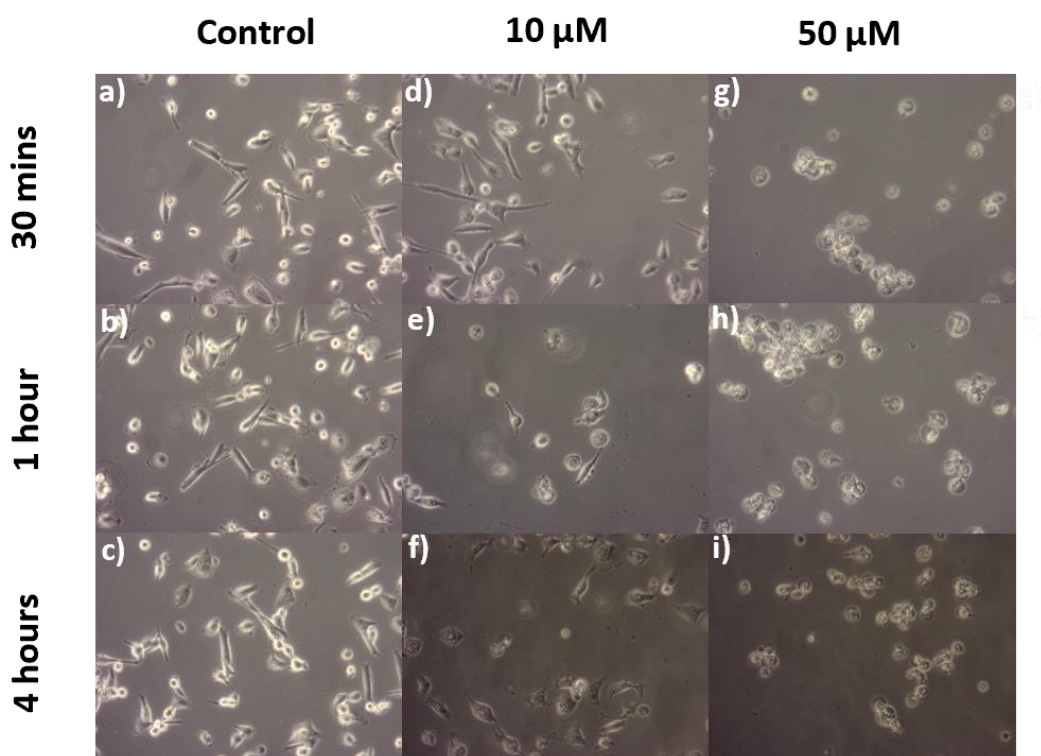


Figure 4.12: MDA-MB-231 cells after being treated with $[Ag_2(L4)_2](PF_6)_2$ - a) control (DMSO 0.05%) 30 mins, b) control (DMSO 0.05%), 1 hour, c) control (DMSO 0.05%), 4 hours, d) 10 μM 30 mins, e) 10 μM 1 hour, f) 10 μM 4 hours, g) 50 μM 30 mins, h) 50 μM 1 hour, i) 50 μM 4 hours.

The binuclear *p*-fluorobenzyl imidazole $[Ag_2(L6)_2](PF_6)_2$ and benzimidazole $[Ag_2(L13)_2](PF_6)_2$ complexes were also studied for their effect on cell morphology (shown in **Figure 4.13** and **Figure 4.14**). After 1 hour at 10 μM , the cells already start to show major morphological changes (for both complexes), for example, loss of elongation and detachment from the surface of the well plate. The cells highlighted with blue circles **Figure 4.14(i)** show signs of the formation of vesicles, which could potentially be apoptotic bodies, however more detailed and higher magnification images would be needed to confirm this.¹⁸⁹

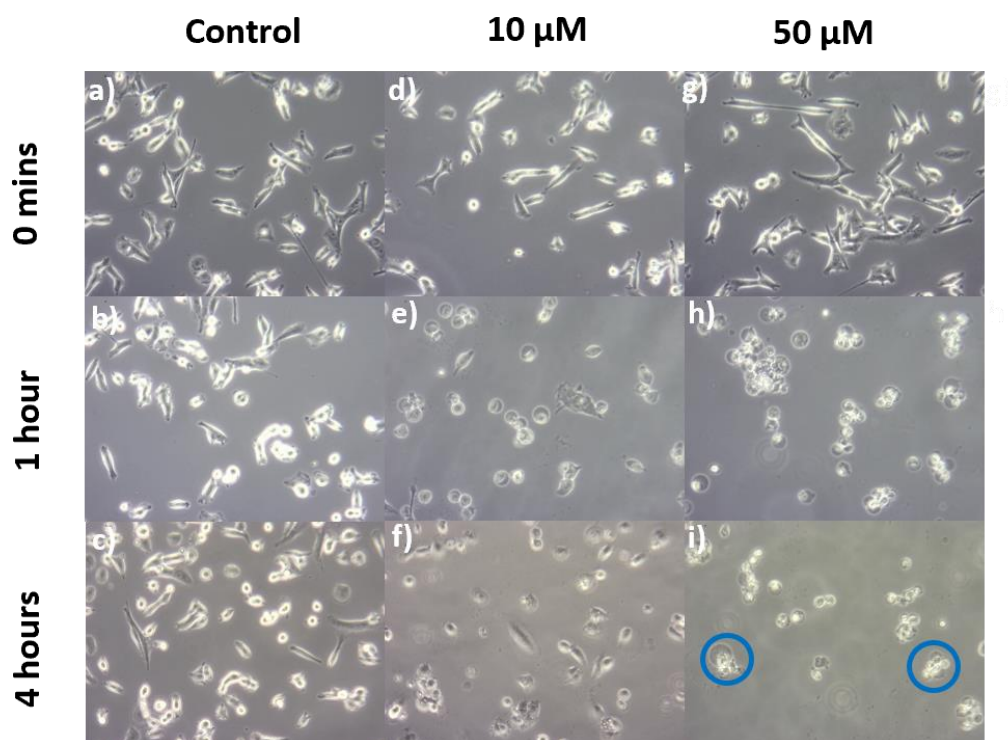


Figure 4.13: MDA-MB-231 cells after being treated with $[Ag_2(L6)_2](PF_6)_2$ - a) control (DMSO 0.05%) 0 minutes, b) control (DMSO 0.05%), 1 hour, c) control (DMSO 0.05%), 4 hours, d) 10 μM 0 minutes, e) 10 μM 1 hour, f) 10 μM 4 hours, g) 50 μM 0 minutes, h) 50 μM 1 hour, i) 50 μM 4 hours.

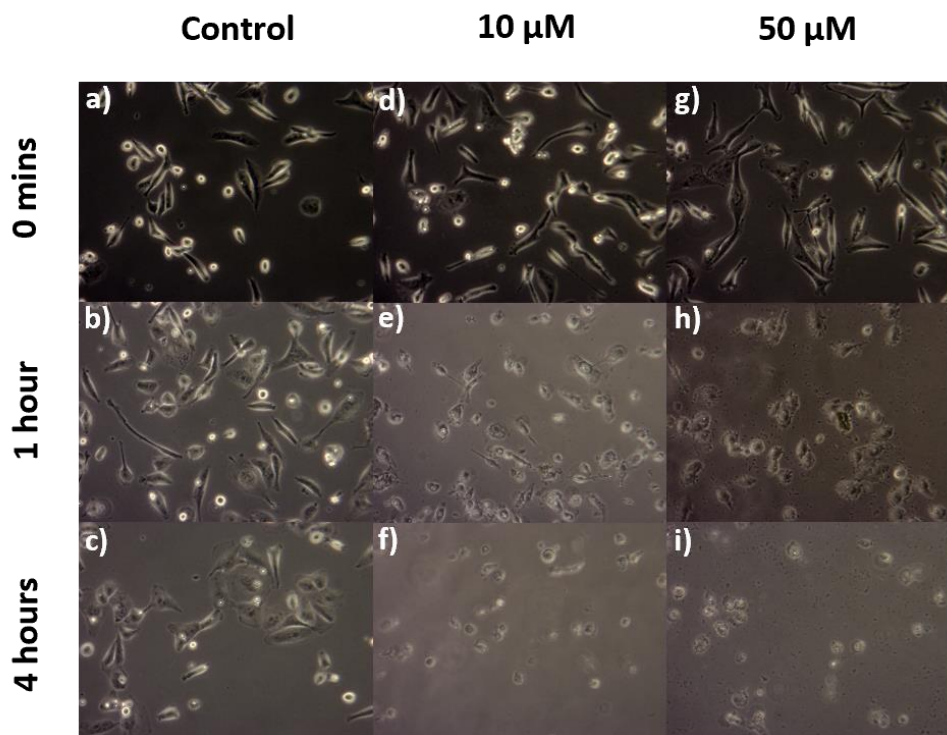


Figure 4.14: MDA-MB-231 cells after being treated with $[Ag_2(L13)_2](PF_6)_2$ - a) control (DMSO 0.05%) 0 minutes, b) control (DMSO 0.05%), 1 hour, c) control (DMSO 0.05%) 4 hours, d) 10 μM 0 minutes, e) 10 μM 1 hour, f) 10 μM 4 hours, g) 50 μM 0 minutes, h) 50 μM 1 hour, i) 50 μM 4 hours.

4.4.3 Interactions with DNA

Deoxyribonucleic acid (DNA) is an important biomolecule comprised of a polymeric chain of nucleotides (A, T, C and G). Each of the nucleotides have a complementary base pair (AT and CG), and in B-DNA, the strands form a right-handed double helix. The helix contains two types of grooves a major and a minor groove, as shown in **Figure 4.15**. The major function of DNA is to encode the genetic information needed to produce the proteins the organism needs to survive. The code is transcribed into mRNA which is then translated in the ribosomes into amino-acid chains which then fold into the final protein.

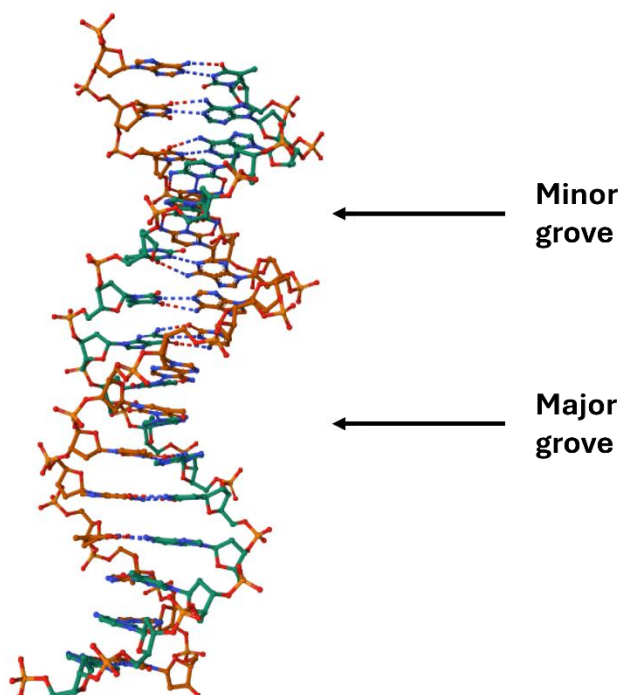


Figure 4.15: Crystal structure of B-DNA (16 base pairs) with the minor and major grooves highlighted. The hydrogen bonds between the base pairs are shown as dotted lines. The crystal structure was obtained from the Protein Data Bank (structure-3BSE).

DNA as a common target for the chemotherapeutic drugs such as cisplatin, where intra- and interstrand cross links are formed. Another important mode of interaction is intercalation of compounds with DNA base pairs, which is employed by chemotherapeutics such as doxorubicin.¹⁹⁰ Intercalation is more likely in molecules that have aromatic residues which are planar and can therefore fit between two base-pairs of DNA.¹⁹¹ An intercalated molecule can interfere with the replication mechanisms of DNA, disrupting the cell cycle, and eventually leading to cell death.¹⁹²

To quantify the degree of intercalation between new molecules and DNA, the ethidium bromide (EtBr) displacement assay is commonly used.^{193,194} Ethidium bromide is an intrinsically fluorescent molecule; however, its fluorescence intensity is quenched by molecular oxygen within the solvent.¹⁹⁴ When EtBr intercalates between the strands of DNA, this quenching is prevented, and the fluorescence

intensity increases by up to 20 times.^{195,196} Displacement of EtBr by a stronger intercalator can be used to probe the intercalative properties of a drug compound.

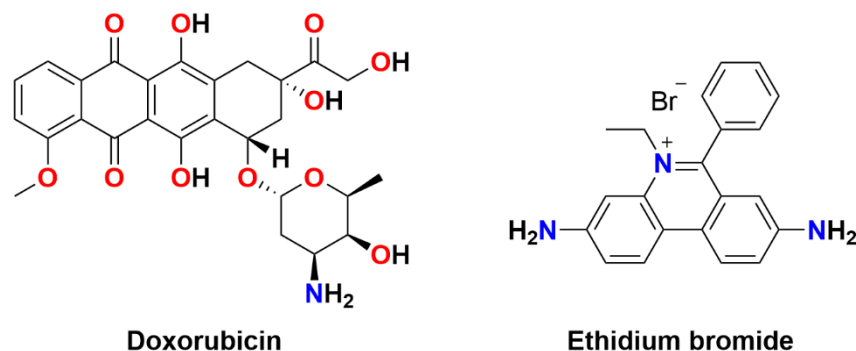


Figure 4.16: Two known intercalators ethidium bromide and (right) doxorubicin (left).

DNA, e.g., calf thymus (ct-DNA), can be incubated with EtBr to give increased fluorescence, which is measured using fluorescence spectroscopy. A drug molecule is then titrated into the solution, and if the drug molecule intercalates with DNA, it displaces the intercalated EtBr and the fluorescence is quenched. The concentration of the quencher and the reduction in fluorescence intensity are related by the Stern-Volmer equation (**Equation 4**), where the Stern-Volmer constant (K_{sv}) can then be used as a measure of a compound's intercalative ability.

$$\frac{F_0}{F} = K_{sv}[Q] + 1 \quad \text{Equation 4}$$

The four complexes $[\text{Ag}_2(\text{L1})_2](\text{PF}_6)_2$, $[\text{Ag}_2(\text{L4})_2](\text{PF}_6)_2$, $[\text{Ag}_2(\text{L6})_2](\text{PF}_6)_2$, $[\text{Ag}_2(\text{L13})_2](\text{PF}_6)_2$ and ligand $[\text{H}_2\text{L4}](\text{PF}_6)_2$ were tested using the EtBr assay using Tris.HCl as the buffer. An illustrative example of one of the titrations is shown in the **Figure 4.17 (a)** for $[\text{Ag}_2(\text{L13})_2](\text{PF}_6)_2$. From these results a Stern-Volmer graph can be plotted, e.g., **Figure 4.17(b)** by using the quencher concentration (drug compound) and the ratio between the fluorescence intensity at the maxima of EtBr at 603 nm with (F) and without quencher (F_0). The gradient of the graph is the Stern-Volmer constant, and the more efficient the drug is an intercalator, the larger the K_{sv} value. The plots of the other complexes are shown in the appendix (**Appendix 8.61 - Appendix 8.65**).

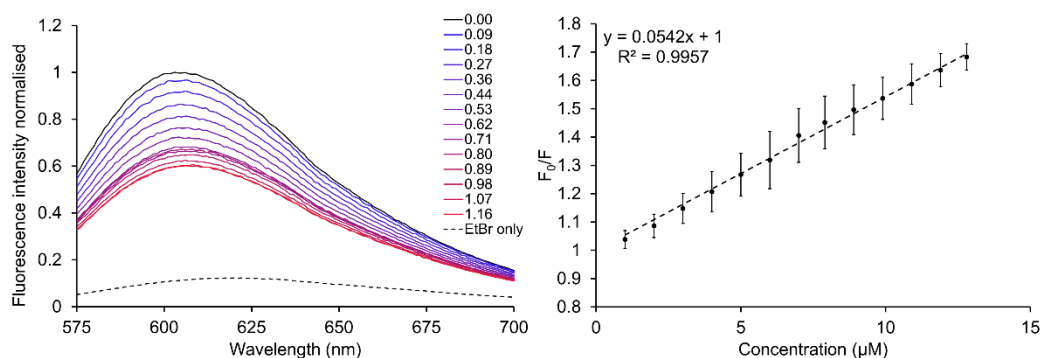


Figure 4.17: a) Fluorescence emission spectra of sequential additions of $[\text{Ag}_2(\text{L13})_2](\text{PF}_6)_2$ to a solution of ct-DNA/EtBr (2.5/1), black line = no complex, blue – red = 0.09 – 1.16 molar equivalents of $[\text{Ag}_2(\text{L13})_2](\text{PF}_6)_2$ to EtBr and dotted line = EtBr without ct-DNA. b) Stern-Volmer plot with standard errors from three independent experiments.

The data for all the complexes tested is shown in **Table 4.5**, and the K_{sv} values show that all complexes can intercalate with ct-DNA. The benzyl type complexes $[\text{Ag}_2(\text{L1})_2](\text{PF}_6)_2$, $[\text{Ag}_2(\text{L6})_2](\text{PF}_6)_2$, $[\text{Ag}_2(\text{L13})_2](\text{PF}_6)_2$ all have values of *ca.* $5 \times 10^4 \text{ M}^{-1}$, this indicates that substitution ($[\text{Ag}_2(\text{L1})_2](\text{PF}_6)_2$ vs $[\text{Ag}_2(\text{L6})_2](\text{PF}_6)_2$) or extension of the backbone ($[\text{Ag}_2(\text{L6})_2](\text{PF}_6)_2$ vs $[\text{Ag}_2(\text{L13})_2](\text{PF}_6)_2$) does not influence these complexes ability to intercalate. There is however a significant difference between the values of the benzyl complex $[\text{Ag}_2(\text{L1})_2](\text{PF}_6)_2$ and the naphthyl derivative $[\text{Ag}_2(\text{L4})_2](\text{PF}_6)_2$ with K_{sv} values of $5.3 \pm 1.5 \times 10^4$ and $21.0 \pm 0.8 \times 10^4 \text{ M}^{-1}$ respectively. This confirms the addition of an extended ring system on the wingtips increases the ability of the compounds to intercalate with ct-DNA by approximately 4 times.

Table 4.5: Stern-Volmer constants (K_{sv}) for compounds $[Ag_2(L1)_2](PF_6)_2$, $[Ag_2(L4)_2](PF_6)_2$, $[Ag_2(L6)_2](PF_6)_2$, $[Ag_2(L13)_2](PF_6)_2$ and $[H_2L4](PF_6)_2$ calculated experimental from Stern-Volmer plots

Compound	$K_{sv} \times 10^4 (\pm \text{SEM}, \text{M}^{-1})$
$[H_2L4](PF_6)_2$	3.0 (± 0.1)
$[Ag_2(L1)_2](PF_6)_2$	5.3 (± 1.5)
$[Ag_2(L4)_2](PF_6)_2$	21.0 (± 0.6)
$[Ag_2(L6)_2](PF_6)_2$	6.5 (± 0.3)
$[Ag_2(L13)_2](PF_6)_2$	5.4 (± 0.8)

The naphthyl ligand $[H_2L4](PF_6)_2$ was also tested to investigate the influence of the complexation to silver. Whilst the ligand exhibits some intercalation with ct-DNA, the binding affinity is increased by 7-fold when the ligand is complexed to silver. This indicates that the extended aromatic wingtip is not the only factor in activity, but also that the silver, and possibility due to the restricted rotation of ligands within the complex. All the compounds tested were either comparable to or better than known anticancer agents which are also DNA intercalators, for example, doxorubicin has a $K_{sv} = 3.27 \pm 0.31 \times 10^4 \text{ M}^{-1}$, whilst complex $[Ag_2(L4)_2](PF_6)_2$ has a K_{sv} which is 6.4 times higher. When comparing the activities of the Ag(I)-NHC complexes, the intercalation abilities do not correlate to cytotoxicity, with both $[Ag_2(L6)_2](PF_6)_2$ and $[Ag_2(L13)_2](PF_6)_2$ having higher cytotoxicity but lower affinity for ct-DNA intercalation. This indicates that intercalation cannot be the only mechanism for activity, and more cellular DNA studies are required to confirm trends.

4.4.4 Molecular Docking

Molecular docking can be used to investigate the interactions between compounds and biomolecules. Dr Tameryn Stringer performed the docking experiments outline in this section. The molecular docking software AutoDock 4.2.6, was employed to investigate the interactions between $[Ag_2(L13)_2](PF_6)_2$ and a double strand (ds)-DNA dodecamer.¹⁹⁷ The crystal structure of the B-DNA dodecamer was obtained from the Protein Data Bank (ILU5). The xyz coordinates from the scXRD of

$[\text{Ag}_2(\text{L13})_2](\text{PF}_6)_2$ were used and optimised by DFT (method outlined in experimental) calculations. These optimisation calculations were performed by Dr Benjamin Hofmann. The docking simulations with 100 poses were repeated three times to confirm reproducibility, and the lowest energy conformation is shown in **Figure 4.18**. The estimated free binding energy (the energy difference between the bound and unbound state) is $-7.93 \text{ kcal}\cdot\text{mol}^{-1}$. This is a relatively strong binding energy and is lower than the cut-off often employed in screening of drug-biomolecules ($-6.0 \text{ kcal mol}^{-1}$).¹⁹⁸

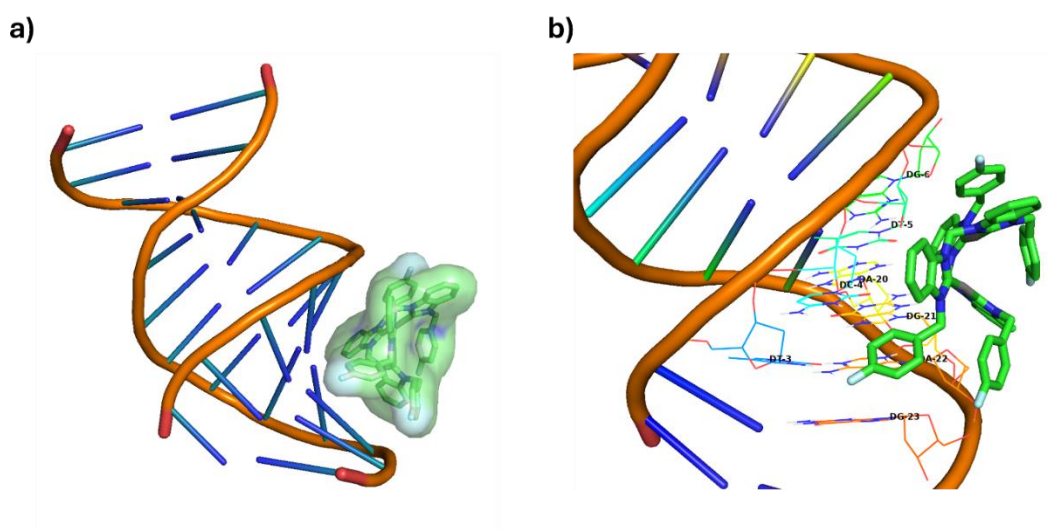


Figure 4.18: The lowest energy binding mode between $[\text{Ag}_2(\text{L13})_2](\text{PF}_6)_2$ and the B-DNA dodecamer ILU5. a) surface representation and b) specific base-pair residues shown explicitly. Images were rendered using Pymol software.¹⁶⁹

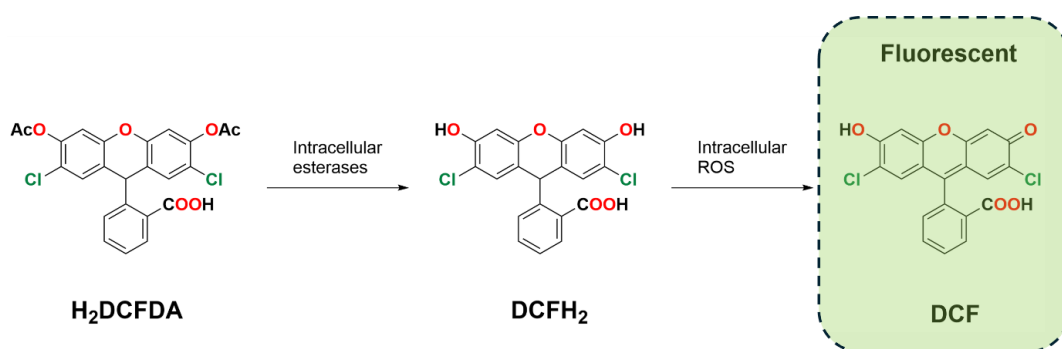
$[\text{Ag}_2(\text{L13})_2](\text{PF}_6)_2$ binds into the major groove of DNA with non-polar interactions and with eight of the residues (DA-20, DA-22, DC-4, DG-6, DG-21, DG-23, DT-3 and DT-5). The complex has close contacts ($< 3 \text{ \AA}$) between residues DG-6 and DG-20 with the benzimidazole rings and between the *p*-fluorobenzyl wingtips and residues DA-22, DG-23 and DT-3. These results indicate that complex $[\text{Ag}_2(\text{L13})_2](\text{PF}_6)_2$ interacts primarily through van der Waals interactions.¹⁶⁹

4.4.5 Reactive Oxygen Species Generation

ROS are small oxygen containing reactive molecules for example superoxide ($\text{O}_2^{\bullet-}$) and hydroxyl radicals (OH^{\bullet}) and non-radical species such as hydrogen peroxide (H_2O_2).¹⁹⁹ They are found in healthy cells and exist in a redox homeostasis and serve

biological functions such as signalling.²⁰⁰ This balance can be disrupted by the generation of excess ROS by either a molecule that can generate ROS or by something that can inhibit the antioxidant enzymes that maintain homeostasis.^{199,201} The increase in ROS leads to oxidative stress which can activate apoptotic pathways leading to cell death.^{201,202} There are reports in the literature that Ag(I) can lead to an increase in ROS within cancer cells.²⁰³

A commonly employed dye for measuring ROS levels in cells, is fluorescein (H_2DCFDA),²⁰⁴ which is readily taken up by cells after which the acetate groups are cleaved forming ($DCFH_2$), this is then oxidised by intercellular ROS to yield the fluorescent species DCF (**Scheme 4.2**). The degree of DCF present can be recorded via microscopy or flow cytometry.²⁰⁴



Scheme 4.2: The pathway in which fluorescein (H_2DCFDA) is converted intracellularly in the presence of ROS to form the fluorescent molecule DCF.²⁰⁴

MDA-MB-231 cells were treated with 1 x IC_{50} concentration (at 24 h) of $[Ag_2(L1)_2](PF_6)_2$, $[Ag_2(L4)_2](PF_6)_2$, $[Ag_2(L6)_2](PF_6)_2$ and $[Ag_2(L13)_2](PF_6)_2$ for 4 hours (**Figure 4.19(a – d)**). The control sample (**Figure 4.19(e)**) contains a small amount of fluorescence as untreated cells which is normal for cancer cells. Cells incubated with complexes at 1x IC_{50} show an increase in fluorescence compared to the control, which indicates these Ag(I)-NHC complexes induce redox stress within the cells.

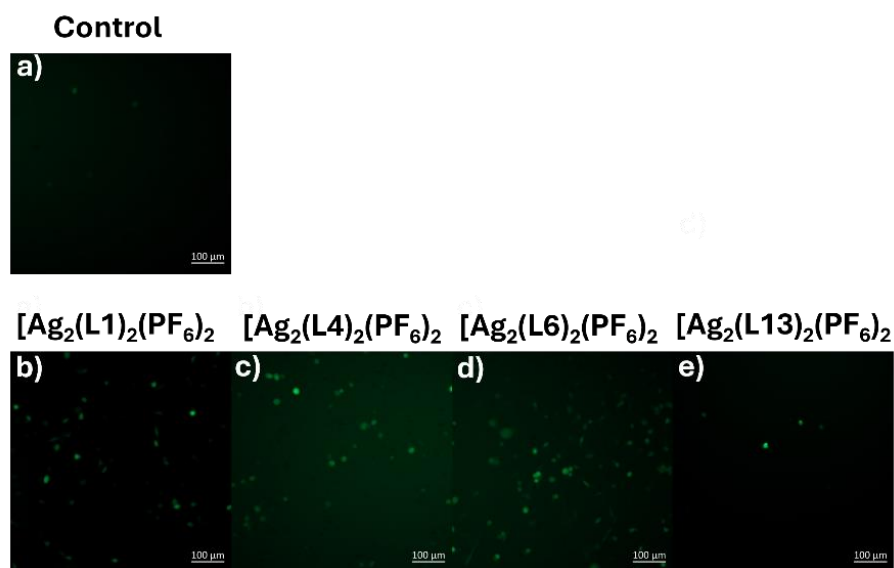


Figure 4.19: ROS observed after MDA-MB-231 cells were incubated for 3.5 hours with a)) control (DMSO 0.1%) and 1 x IC_{50} of b) $[Ag_2(L1)_2](PF_6)_2$, c) $[Ag_2(L4)_2](PF_6)_2$, d) $[Ag_2(L6)_2](PF_6)_2$, and e) $[Ag_2(L13)_2](PF_6)_2$, followed by H_2DCFDA (20 μM) for 30 min. All images were taken using an Observer-7 microscope (scale bar at 100 μm) and recorded using $ex/em = 494/512$ nm.

MDA-MB-231 cells were also incubated with complexes $[Ag_2(L1)_2](PF_6)_2$, $[Ag_2(L6)_2](PF_6)_2$ and $[Ag_2(L13)_2](PF_6)_2$ at 5 x IC_{50} concentrations (Figure 4.20). The cells that were incubated with the higher concentration of complex (Figure 4.20(d – f)) show an increase in fluorescence compared to the lower concentration (Figure 4.20(a – c)), indicating there is a concentration dependence with respect to ROS generation. These findings agree with literature in which ROS generation by Ag(I)- NHCs have been reported.²⁰⁵

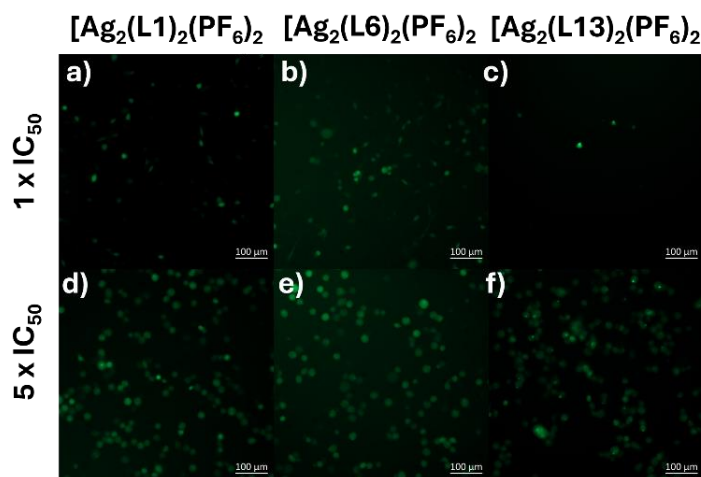


Figure 4.20: ROS observed after MDA-MB-231 cells were incubated for 3.5 hours with 1 x IC₅₀ a) [Ag₂(L1)₂](PF₆)₂, b) [Ag₂(L6)₂](PF₆)₂, c) [Ag₂(L13)₂](PF₆)₂, and 5 x IC₅₀ d) [Ag₂(L1)₂](PF₆)₂, e) [Ag₂(L6)₂](PF₆)₂, f) [Ag₂(L13)₂](PF₆)₂, followed by H₂DCFDA (20 μM) for 30 min. All images were taken using an Observer-7 microscope (scale bar at 100 μm) and recorded using ex/em = 494/512 nm.

To investigate whether ROS is the primary cause of cytotoxicity, a measurement of the toxicity in the presence of an antioxidant is required. The antioxidant will remove the excess ROS that is produced by the cell. If the cytotoxicity decreases, this confirms that generation of ROS is vital in the observed toxicity. Within literature the most reported antioxidant used in experiments with metal-NHC complexes is N-acetylcysteine (NAC).^{205–207} Before running these experiments, studies were conducted to test any potential interactions of the antioxidant with the test compound.

The stability of [Ag₂(L6)₂](PF₆)₂ towards NAC was investigated using ¹H NMR spectroscopy. A 1:1 ratio of complex:NAC was used, and spectra recorded in *d*₆-DMSO at 5 minutes and 1 hour (**Figure 4.21**). The spectrum show the complex (**Figure 4.21(a)**) and free ligand (**Figure 4.21(d)**) with no inclusion of NAC, whilst the spectra in **Figure 4.21(b)** and **Figure 4.21(c)** show the complex:NAC reaction after 5 minutes and 1 hour respectively. After addition of one equivalent of NAC and only 5 minutes, new peaks can be seen which correspond to the free ligand, and these do not change after 1 hour. The ratio between complex and ligand is 1:1 after the addition of NAC, the stoichiometry of silver to NAC is 2:1 which explains

why only half of the sample is decomposed. There is no resonance between 10 – 14 ppm which would be indicative of the carboxylic acid proton in NAC, this suggests that the acid protonates the carbene which decomposes the complex.

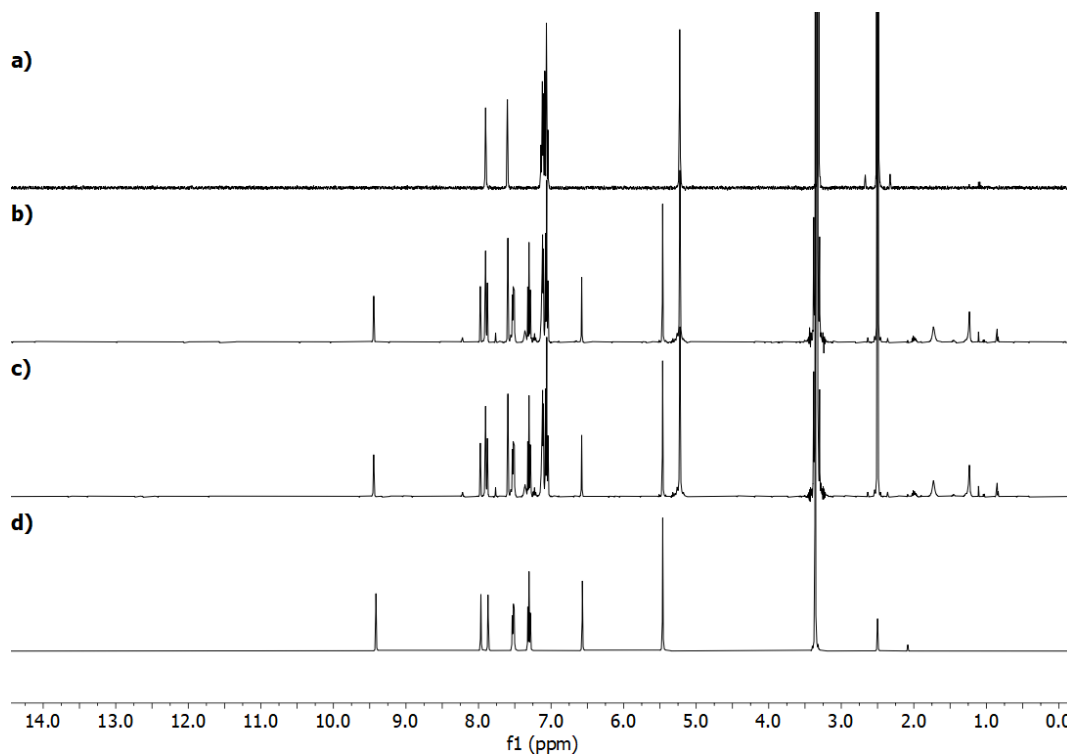


Figure 4.21: a) $[Ag_2(L6)_2](PF_6)_2$, $[Ag_2(L6)_2](PF_6)_2:NAC$ (1:1) at b) 5 minutes, c) 1 hour and, $[H_2L6](PF_6)_2$ (d_6 -DMSO, 400 or 500 MHz).

This instability towards NAC means that it is not an appropriate antioxidant to use for ROS experiments, and the results would give a false positive, as the toxicity of the decomposition products (ligand and Ag-NAC) would be lower than that of the complex. This effect would still be seen even if ROS generation was not a major factor in the toxicity. Further stability experiments need to be carried out against a panel of other antioxidants which do not contain any thiol or carboxylic acid groups, such as vitamin E.²⁰⁸

4.4.6 Cellular Uptake

Cellular uptake is an important factor to investigate when designing new drugs. One method for obtaining uptake is whole-cell inductively coupled mass spectrometry (ICP-MS). This technique allows for the quantification of metals contained within a sample to extremely low concentrations.²⁰⁹ Silver is a xenobiotic metal in humans, it does not form part of any known metabolic pathways, and for this reason, it is not

naturally present within human cells, meaning any silver found in treated cells will be from the Ag(I)-NHC complexes.²¹⁰ Dr Tameryn Stringer carried out the cell preparation and Dr Amy Managh (Loughborough University) conducted the ICP-MS measurements.

The cellular uptake of the most selective complex $[\text{Ag}_2(\text{L13})_2](\text{PF}_6)_2$ and the mononuclear derivative $[\text{Ag}(\text{L16})_2](\text{PF}_6)$ (including controls) were assessed in MDA-MB-231 and MCF-7 cells. The cells were treated with 1 μM of each complex for 1 hour, before being harvested, centrifuged, washed, counted and prepared for ICP-MS analysis. The data is presented as number of ^{107}Ag atoms/cell (**Table 4.6**), and as expected, no silver was found in either the untreated MDA-MB-231 or MCF-7 cells. For MDA-MB-231 cells treated with complexes $[\text{Ag}_2(\text{L13})_2](\text{PF}_6)_2$ and $[\text{Ag}(\text{L16})_2](\text{PF}_6)$, there is no statistical difference in silver uptake ($P > 0.05$), and this is reflected in their similar IC_{50} values. For MCF-7 cells, the monodentate complex $[\text{Ag}(\text{L16})_2](\text{PF}_6)$ has significantly higher levels of silver uptake when compared to the binuclear complex $[\text{Ag}_2(\text{L13})_2](\text{PF}_6)_2$, with values of $4.91 (\pm 3\%)$ and $2.86 (\pm 21\%)$ Ag atoms/cell, respectively. The difference in uptake is reflected in the lower IC_{50} value for $[\text{Ag}(\text{L16})_2](\text{PF}_6)$ compared to $[\text{Ag}_2(\text{L13})_2](\text{PF}_6)_2$.

Table 4.6: Amount of Ag-107 detected by ICP-MS in MDA-MB-231 and MCF-7 cells after incubation for 1 h with 1 μ M of $[\text{Ag}(\text{L16})_2](\text{PF}_6)$ and $[\text{Ag}_2(\text{L13})_2](\text{PF}_6)_2$.

Cell Line	Treatment	Ag atoms / cell (\pm %) RSD (n=3)	IC ₅₀ (μ M)
MDA-MB-231	Control	Not detected	-
	$[\text{Ag}(\text{L16})_2](\text{PF}_6)$	$8.84 \times 10^7 (\pm 35)$	3.7 ± 0.3
	$[\text{Ag}_2(\text{L13})_2](\text{PF}_6)_2$	$8.20 \times 10^7 (\pm 3)$	4.5 ± 0.3
MCF-7	Control	Not detected	-
	$[\text{Ag}(\text{L16})_2](\text{PF}_6)$	$4.91 \times 10^7 (\pm 3)$	5.0 ± 0.2
	$[\text{Ag}_2(\text{L13})_2](\text{PF}_6)_2$	$2.86 \times 10^7 (\pm 21)$	8.5 ± 0.1

This data also suggests that the monodentate complex is more easily up taken by the cells compared to the binuclear bridged version. One might assume that the cells incubated with the binuclear complex will uptake more silver, as per mole these complexes contain twice as much silver (compared to the mononuclear derivatives), however, this is not the case. One possibility is the more moderate lipophilicity of the mononuclear complexes leads to better uptake though the phospholipid bilayer. Further experiments with a range of mono and binuclear complexes would be needed to confirm this hypothesis.

4.5 Conclusions

Complexes $[\text{Ag}_2(\text{L1-7})_2](\text{PF}_6)_2$, $[\text{Ag}_2(\text{L13})_2](\text{PF}_6)_2$, and $[\text{Ag}(\text{L15-16})_2](\text{PF}_6)_2$ were tested for their stability in aqueous media (95:5 H₂O:DMSO). It was found that they decomposed over time. The substitution of the wingtip had a mild influence on the rate of decomposition, the nuclearity was found to have a greater influence (mononuclear decompose faster). Cytotoxicity evaluations show the bridged ligands are generally non-toxic towards all the cell lines tested with only the naphthylmethyl ($[\text{H}_2\text{L4}](\text{PF}_6)_2$ and $[\text{H}_2\text{L4}](\text{PF}_6)_2$) and *p-tert*-butyl-benzyl ($[\text{H}_2\text{L12}](\text{PF}_6)_2$) exhibiting moderate cytotoxicity. The monodentate *p*-fluorobenzyl ligand

[HL16](PF₆) was active against MDA-MB-231 unlike its bridged derivative [H₂L13](PF₆)₂, and the ligands showed no selectivity towards cancer cells.

All Ag(I)-NHC complexes tested were more active than their parent ligands against all cell lines, for example, [Ag₂(L13)₂](PF₆)₂ was > 22 times more active against MDA-MB-231 than [H₂L13](PF₆)₂. The Ag(I)-NHC complexes tested are more active against MDA-MB-231 *cf.* MCF-7 and for all but one complex ([Ag₂(L3)₂](PF₆)₂) they are more active against MDA-MB-231 *cf.* ARPE-19. However, when comparing MDA-MB-231 to the non-cancerous cell line MCF10A, only the *p*-fluorobenzyl imidazole complex [Ag₂(L6)₂](PF₆)₂ and its benzimidazole derivative [Ag₂(L13)₂](PF₆)₂ were selective for the cancerous line. These complexes exhibited the highest cytotoxicity against MDA-MB-231 with IC₅₀ values of 5.5 ± 0.2 and 4.5 ± 0.3 μ M respectively. Correlation between lipophilicity and activity were discussed and trends are only evident against MCF-7. Against MDA-MB-231 there is only a weak relationship between the identity of the backbone and activity with a marginal improvement when the backbone was changed to benzimidazole. There was no clear relationship between nuclearity and activity against either MDA-MB-231 or MCF-7.

Four complexes were chosen for further testing [Ag₂(L1)₂](PF₆)₂, [Ag₂(L4)₂](PF₆)₂, [Ag₂(L6)₂](PF₆)₂ and [Ag₂(L13)₂](PF₆)₂. They were tested at a shorter incubation time of 4 hours and found to be active. Optical imaging of the MDA-MB-231 cells incubated with the complexes show changes to cellular morphology, with the cells becoming round and showing the formation of small vesicles, which could be signs of apoptosis. Complexes were shown to intercalate with ct-DNA (measured using EtBr titration) and in some cases, had larger binding affinities than doxorubicin, a well-known DNA intercalating drug. The naphthyl complex [Ag₂(L4)₂](PF₆)₂ was the strongest intercalator (3 times higher than the next best complex) with a K_{sv} of $21.0 \pm 0.8 \times 10^4$ M⁻¹, whilst the naphthyl ligand [H₂L4](PF₆)₂ had a value almost 7 times lower ($3.0 \pm 0.1 \times 10^4$ M⁻¹), this indicates that both the wingtip and coordination to silver influences the interaction with DNA. Molecular docking studies indicate that [Ag₂(L13)₂](PF₆)₂ interacts with ct-DNA though van der Waals interactions in the major groove and with a binding energy of -7.93 kcal mol⁻¹.

The complexes $[\text{Ag}_2(\text{L1})_2](\text{PF}_6)_2$, $[\text{Ag}_2(\text{L4})_2](\text{PF}_6)_2$, $[\text{Ag}_2(\text{L6})_2](\text{PF}_6)_2$ and $[\text{Ag}_2(\text{L13})_2](\text{PF}_6)_2$ all induced redox stress within MDA-MB-231 after a 4 hour incubation with 1 x IC_{50} concentrations. The complexes $[\text{Ag}_2(\text{L1})_2](\text{PF}_6)_2$, $[\text{Ag}_2(\text{L6})_2](\text{PF}_6)_2$ and $[\text{Ag}_2(\text{L13})_2](\text{PF}_6)_2$ were also tested at 5 x IC_{50} concentrations and showed a dose dependant increase in ROS production. ICP-MS studies with $[\text{Ag}_2(\text{L13})_2](\text{PF}_6)_2$ and $[\text{Ag}(\text{L16})_2](\text{PF}_6)$ showed that for MCF-7 the uptake of silver into the cell is related to activity.

5 Vanadium β -Diketonate *N*-Heterocyclic Carbene Complexes

5.1 Biological Relevance of Vanadium Complexes

Vanadium has many advantages as a transition metal candidate for drug development, for example (i) it has a wide range of accessible oxidation states between -III – V, with oxidation states III, IV and V being the most biologically relevant,^{211,212} (ii) it exists within biological systems, such as the haloperoxidases found in some algae and bacteria, and (iii) is an abundant metal which means that it is inexpensive and easily available.^{212–214} These desirable properties led to interest in vanadium as a potential candidate for developing drugs that can overcome the draw backs of cisplatin.

In the 1980s it was shown that vanadate ions (VO_4^{3-}) could act as an insulin mimetic in rats, lowering the amount of serum glucose to the level of the non-diabetic controls.²¹⁵ Other medicinal uses of reported vanadium compounds have included antiviral, antituberculosis and antiparasitic.^{216–218} More recently groups have investigated anticancer properties of these types of complexes. The most promising candidate to date is Metvan (4,7-dimethyl-1,10-phenanthroline sulfatooxidovanadium(IV), **Figure 5.1**),²¹⁹ which has shown high activity against a wide range of cancers including prostate, ovarian and breast cancer.²¹⁹ Metvan has shown promise in *in-vivo* studies showing reduction in breast tumour mass.²²⁰

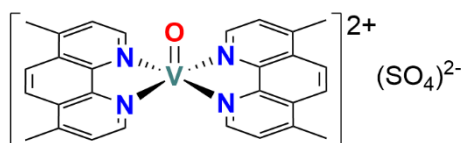


Figure 5.1: Structure of the anticancer vanadium(IV) complex Metvan.

The success of Metvan has led researchers to investigate the activity of other oxido-vanadium(IV) complexes. Ni et al. synthesised reported an active phenanthroline oxalate coordinated complex which were active against cervical cancer, and further mechanistic studies indicated that these complexes initiated cell cycle arrest which then led to apoptosis.²²¹ Riberio et al. showed that a series of amino acid-pyridyl-phenol coordinated oxido-vanadium(IV) complexes were able to cause DNA

damage through singlet oxygen generation, and were able to induce apoptosis in lung cancer cells.²²² These studies indicate that these compounds are able to target a broad range of cancer types and act through multiple mechanisms to induce apoptosis.

Vanadyl acetylacetonate (acac), **Figure 5.2** where $R_1 = R_2 = \text{Me}$, is a vanadium complex that has received great interest in the last twenty years for its insulin memetic and anticancer properties.^{223,224} Other groups have made modifications on this structure, e.g., Sgarbossa et al. tested a range of compounds where $R_1 = \text{CF}_3$ and $R_2 = \text{an aromatic group}$, and they showed activity against colon cancer cells, however there were also active against healthy cells.²²⁵ Mohamadi et al. studied the activity of the symmetrical complex $\text{VO}(\text{bzbz})_2$ where $R_1 = R_2 = \text{Ph}$, and this compound was more effective than cisplatin against breast and colon cancer cells.²²⁶ Chinthala et al. have also synthesised a series of asymmetric V(IV) complexes where $R_1 = \text{Me}$ and $R_2 = \text{CF}_3$ or ^tBu , and they reported their high active against cervical cancer cells.²²⁷

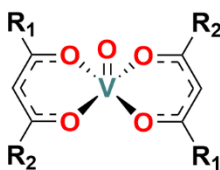


Figure 5.2: General structure of vanadyl β -diketonate complexes.

The success of vanadium β -diketonate complexes previously reported has driven our group to explore this class of compound, with a focus on complexes of phenyl substituted vanadium β -diketonate complexes and their derivatives (**Figure 5.3**).²²⁸ These are active against a wide variety of cell types including lung, colon and breast cancer, and importantly they are less toxic to non-cancerous retinal epithelial cells.²²⁸ Follow up work investigated the potential mechanisms of these complexes, where the complexes exhibit DNA nicking, and this effect was halted when a singlet oxygen scavenger (NaN_3) was added, which is evidence that singlet oxygen is involved in this DNA interaction.²²⁹ The oxidative damage was further studied using a COMET assay which can be used to probe double strand breaks (DSB), and all complexes showed dose-dependent DNA damage. An FID assay confirmed that these complexes can intercalate with ds-DNA, with a preference for binding AT

over CG, and they also exhibited dose-dependent cell death when assessed using Annexin-V and Caspase-3/7 assays.²²⁹

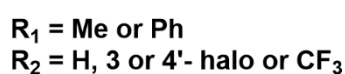
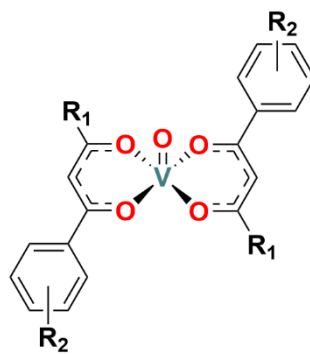


Figure 5.3: Symmetric and asymmetric $VO(\text{bzac})_2$ and $VO(\text{bzbz})_2$ complexes reported by Zegke et al.²²⁸

A common feature of these $VO(\text{bzac})_2$ and $VO(\text{bzbz})_2$ complexes is the vacant 6th coordinate axial position, where another ligand can be coordinated. This ligand could potentially have biological properties that are orthogonal to the vanadium complex increasing the complexes activity. However, there are few studies that have probed this binding site and no examples with the addition of NHC ligands.

5.2 Vanadium N-Heterocyclic Carbene Complexes

The first vanadium NHC complexes were synthesised in the late 1990s and early 2000s.^{230–232} This was an octahedral V(II) complex reported by Herrman et al. (**Figure 5.4(a)**) in which the vanadium is coordinated to two chlorides and four methyl functionalised NHCs.²³⁰ The group of Wacker et al. synthesised an anionic homoleptic tetracarbene V(III) complex (**Figure 5.4(b)**), where the distorted tetrahedral structure was confirmed by scXRD.²³¹ In 2003, Abernethy et al. described the first high valence vanadium NHC complex (**Figure 5.4(c)**).²³² The complex was synthesised through the coordination of a the free carbene IMes (1,3-bis(2,4,6-trimethylphenyl)-1,3-dihydro-2H-imidazol-2-ylidene) to VOCl_3 .²³² An scXRD study highlighted an interaction between a lone pair on one of the chlorides and the empty p -orbital on the carbene carbon.²³² It was noted that this complex was stable in air and in dichloromethane solution over months.²³²

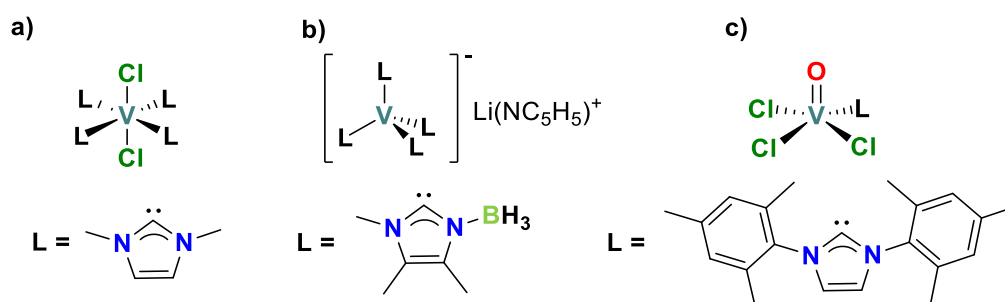


Figure 5.4: First reported vanadium NHC complexes synthesised by (a) Herrmann et al., (b) Wacker et al. and (c) Abernethy et al..^{230–232}

The current applications of vanadium NHC complexes are summarised in **Figure 5.5**, where the most common application is polymerisation, in particular in ethylene and propylene polymerisation.^{233–236} Complexes that can perform ring-opening metathesis polymerisation (ROMP) have also been described.²³⁷ Vanadium-NHC complexes have also been shown to perform ring closing metathesis and degenerate olefin metathesis,^{238,239} or reported as chemical weapon destruction agents.²⁴⁰ As of writing there are no examples of vanadium NHC complexes that have been tested for their biological activity in literature.

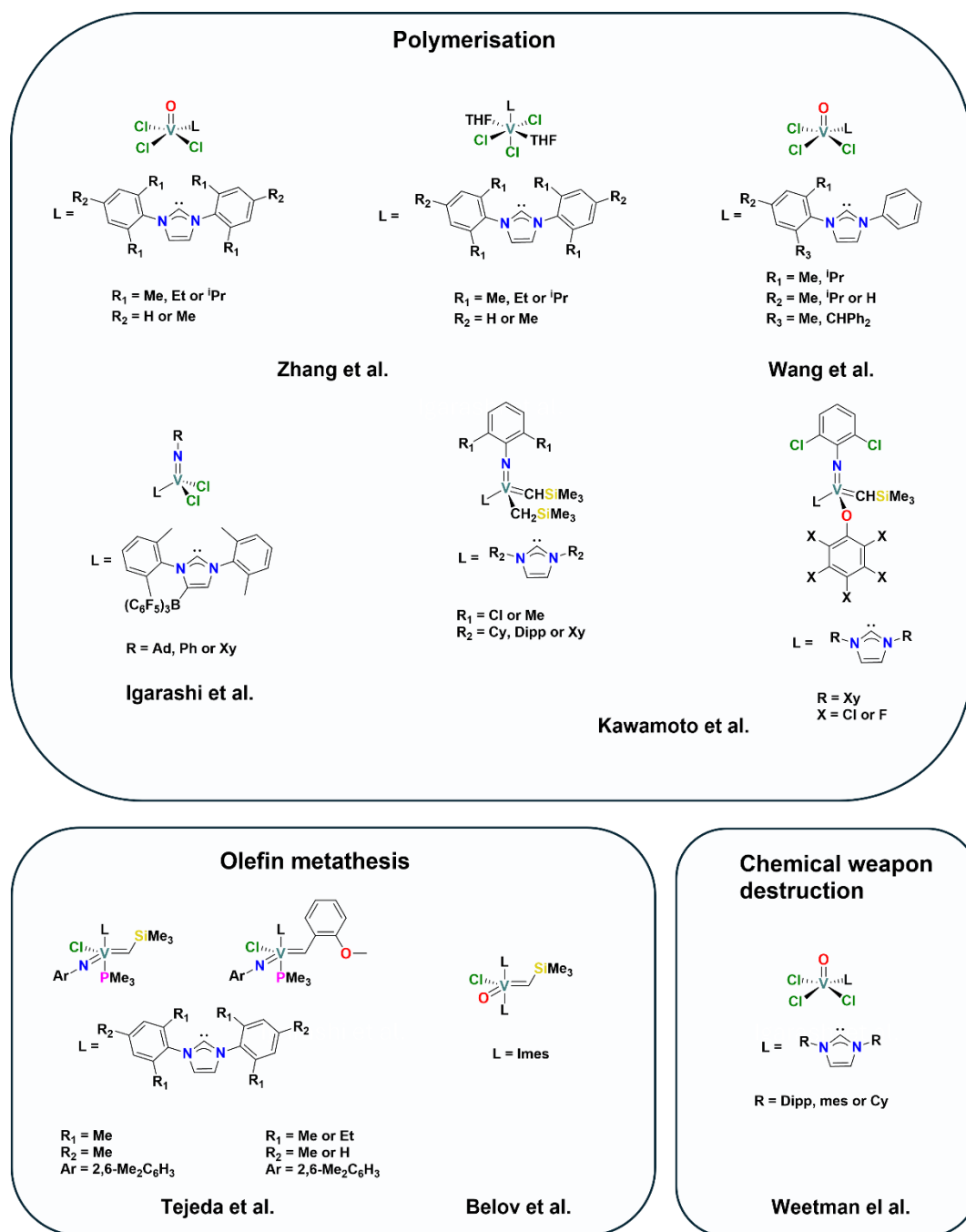


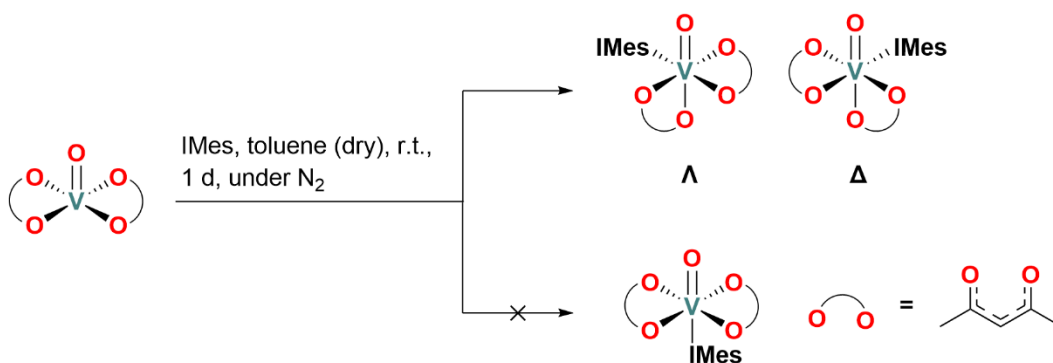
Figure 5.5: Summary of the applications of vanadium-NHC complexes.

5.3 Synthesis and Characterisation of Vanadium (IV and V) β -diketonate *N*-Heterocyclic Carbene Complexes

5.3.1 Synthesis and Characterisation of VO(acac)₂(IMes) (V1)

Literature examples exist of β -diketonate NHC complexes with metals including Cu, Ni, Pt, Rh, Fe, Ir and Pd.^{241–247} However, there are no examples of such complexes with vanadium, thus making their synthesis and exploration an exciting opportunity.

To explore the viability of this chemistry, the first target complex chosen (**V1**, **Scheme 5.1**) was the simplest system, and conducted using commercially available starting materials. In brief, equimolar equivalents of VO(acac)₂ and IMes were stirred together in dry toluene and under a nitrogen atmosphere, the colour changes from teal to a deep green. A deep-green powder was obtained through layered diffusion of a concentrated solution of complex in toluene with n-hexane at room temperature.



Scheme 5.1: Synthesis of **V1** through the reaction of VO(acac)₂ with IMes in dry toluene at room temperature, showing the possible isomers formed.

There are two ways that the IMes could potentially bind, either equatorial where the diketonates are *cis* or axial where the diketonates are *trans*, in the former case the complex is chiral and two optical isomers will be possible (**Scheme 5.1**). FT-IR analysis gave the first indication that the coordination of the IMes was successful, as a shift in the VO(acac)₂ V=O stretch from 993 cm⁻¹ to 960 cm⁻¹ was observed. This is due to the σ -donation of electrons from the NHC into the vanadium centre and weakening of the V=O bond. Further evidence for coordination comes from the appearance of peaks that are associated with the IMes ligand, e.g., the aromatic

stretching C-H at 3131 and 3160 cm^{-1} . The carbonyl (C=O) stretching frequencies in $\text{VO}(\text{acac})_2$ are found *ca.* 1519 cm^{-1} , and a change in this region can be observed, indicating a different arrangement of the diketonate ligands. This is also suggestive that IMes could be bound equatorially and not axially. In the case of axial binding there would be no major changes in the appearance of the C=O band.

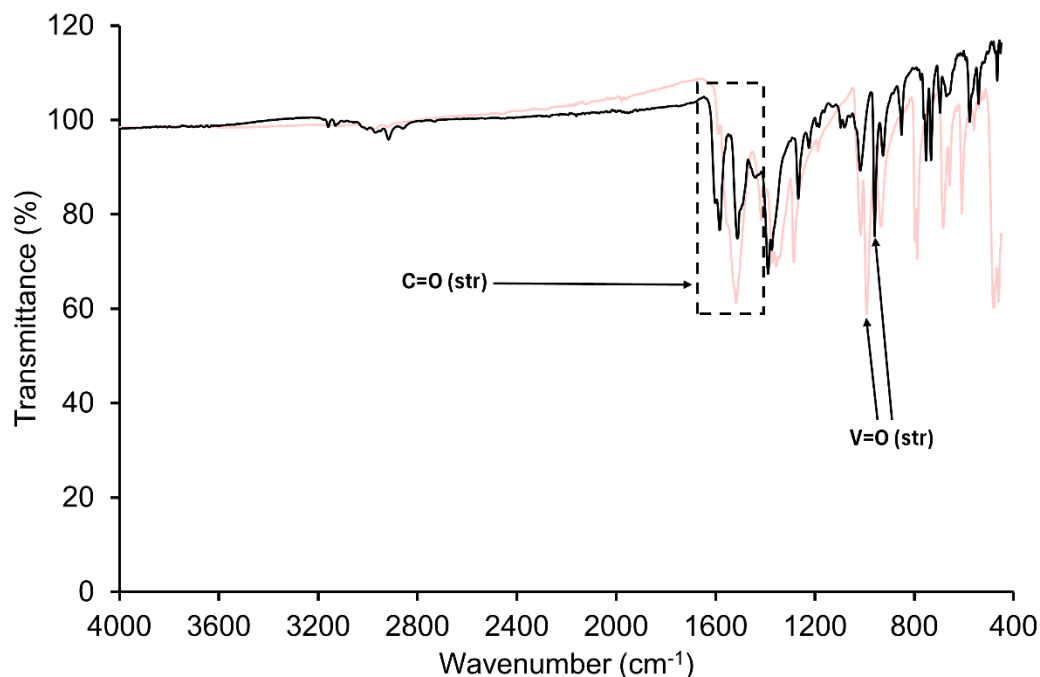


Figure 5.6: ATR-IR spectra of **V1**(black) and $\text{VO}(\text{acac})_2$ (light red) taken between 450 and 4000 cm^{-1} .

Single green plates of **V1**, which were suitable for scXRD analysis were grown from slow evaporation of a concentrated solution of toluene. The data collected by Dr Rianne Lord. The crystal was solved in a triclinic cell and the structural solution was performed in the P-1 space group. The molecular structure is shown in **Figure 5.7** with selected parameters reported in **Table 5.1**. The data shows that the NHC ligand has coordinated to the vanadium centre forming a distorted octahedral complex with IMes in the equatorial position, which agrees with the observations from the IR data. The crystal structure shows the Λ isomer, however as the space group contains an inversion centre it means that the enantiomer (Δ) must be present in equal amounts within the crystal.

The bond angles between $\text{V}=\text{O}_{\text{oxo}}$ and the equatorial ligands (L_{eq}) are 95.13(8) – 98.72 9(8) $^\circ$, and as expected, this is smaller than the equivalent angles in $\text{VO}(\text{acac})_2$

(105.01(7) – 107.23°).²⁴⁸ In both cases they are bent away from the V=O_{oxo} due to repulsion, however, due to the occupation of the axial position in **V1**, the angles are pushed closer to an octahedral geometry.

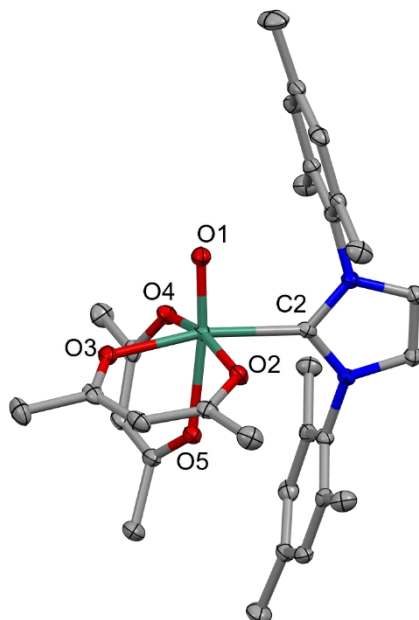


Figure 5.7: Molecular structure of **A-V1** with displacement ellipsoids are shown at the 50% probability level, and solvent and hydrogen atoms omitted for clarity.

Table 5.1: Selected *scXRD* parameters for **V1** and VO(acac)₂ with s.u.s. shown in parentheses.²⁴⁸

Atoms	V1	VO(acac) ₂ ^a
	Bond length (Å)	
V1 – O1	1.6051(16)	1.5859(15)
V1 – O2	2.0056(17)	1.9644(13) – 1.9727(13)
V1 – O3	2.0678(16)	
V1 – O4	2.0046(16)	
V1 – O5	2.1452(16)	
V1 – C2	2.194(2)	-
C-H...O	2.579 – 2.689	
Atoms	Angle (°)	
O1-V1-O2	98.72(8)	105.01(7) – 107.23(8)
O1-V1-O3	95.13(8)	
O1-V1-O4	96.27(8)	
O1-V1-O5	173.14(8)	
O1-V1-C2	95.13(8)	-

^aValues reported from literature²⁴⁸

The V1 – O1 (V=O_{oxo}) bond length of 1.6051(16) Å is significantly longer than the same bond in VO(acac)₂ (1.5859(15) Å), and this is due (i) the “*trans* effect” and the presence of a ligand opposite to V=O and (ii) the presence of the strong σ donor NHC ligand which weakens the π bonding in V=O_{oxo}. The V–O_{acac} bond lengths in **V1** are all longer than the equivalent bonds in VO(acac)₂. The vanadium carbene (V1–C2) bond length is 2.194 (2) Å, is between V–C bond lengths that have been reported in literature for V–NHC complexes.^{238,249}

The crystal packing diagram in **Figure 5.8** shows two molecules of **V1** along the *b*-axis, where intermolecular interactions (C–H...O) are observed between hydrogen atoms on the NHC backbone the O_{oxo} and O_{acac}, forming weak hydrogen bonds (2.579 – 2.593 Å), a hydrogen on the toluene (in the crystal lattice) also forms a weak hydrogen bonding interaction with the O_{oxo} (2.689 Å).

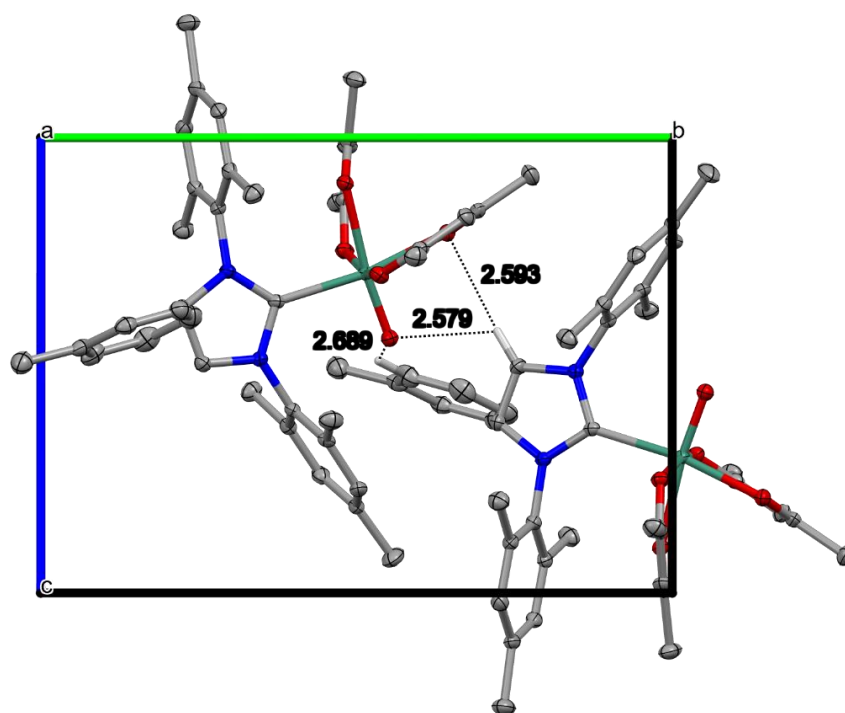
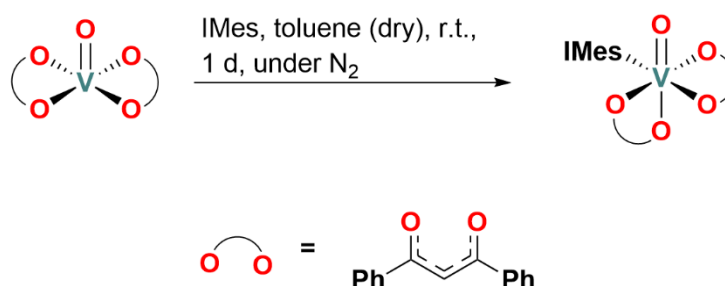


Figure 5.8: Packing diagram of **A-V1** along the *a*-axis with intermolecular hydrogen bonding between two molecules of **A-V1** and one molecule of toluene. Only hydrogens involved in the interactions are explicitly shown.

5.3.2 Synthesis and Characterisation of VO(bz bz)₂(IMes) (V2)

Following from the successful synthesis of **V1** the chemistry was explored further using VO(bz bz)₂. These precursors were synthesised using literature methods and their successful synthesis was confirmed by ¹H NMR and ATR-FTIR spectroscopy. The reaction conditions for the synthesis of **V2** is shown in **Scheme 5.2**. In brief, IMes was added to a suspension of VO(bz bz)₂ in dry toluene, and the colour changed from a bright green to a deep brown colour. After stirring for one day the product was obtained through precipitation via layered diffusion of concentrated toluene solution with n-hexane. The resultant powder was analysed by ATR-FTIR spectroscopy, and the indicative V=O stretch for VO(bz bz)₂ (991 cm⁻¹) shifts to 959 cm⁻¹ upon coordination of IMes (see **Appendix 8.34**).



Scheme 5.2: Synthetic conditions for synthesis of **V2** (VO(bz bz)₂(IMes)).

Single irregular yellowish crystals, suitable for scXRD analysis, were grown by layered diffusion of n-heptane into a concentrated solution of toluene at room temperature. The molecular structure is shown in **Figure 5.9** and selected parameters are reported in **Table 5.2**. **V2** crystallised in a tri clinic crystal system, and the structure was solved in the *P*-1 space group, with two molecules in the asymmetric unit. Like **V1**, the complex is obtained and the β -diketonate ligands are forced into a *cis* conformation.

The V1-C2 bond is shorter in **V2** when compared to **V1**, with lengths of 2.1796(13) and 2.194(2) Å respectively. This can be rationalised by the electron withdrawing effects of the phenyls on the β -diketonate ligands in **V2**, leading to weaker donation to the vanadium and therefore a weaker *trans* effect on the vanadium carbene bond, giving rise to a shorter and stronger bond.

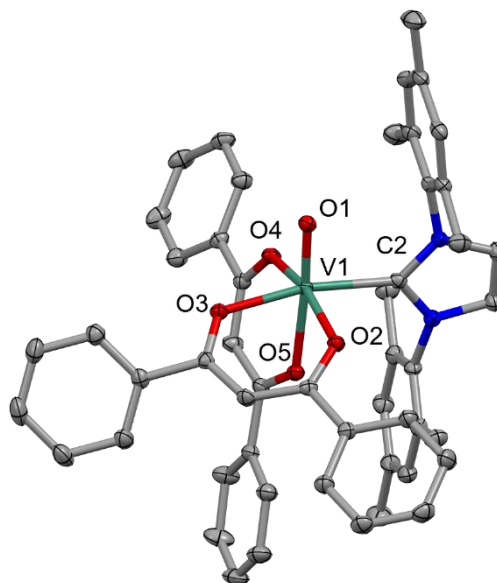


Figure 5.9: Molecular structure of **1-V2**, displacement ellipsoids are shown at the 50% probability level. Solvent and hydrogen atoms are omitted for clarity.

Table 5.2: Selected *sc*XRD parameters for **V2** and $\text{VO}(\text{bzbz})_2$ ²²⁶ with *s.u.s.* shown in parentheses.

Atoms	V1	$\text{VO}(\text{bzbz})_2^a$
	Bond length (Å)	
V1 – O1	1.6052(10)	1.579(4)
V1 – O2	2.0299(10)	1.956(4) – 1.969(4)
V1 – O3	2.1333(10)	
V1 – O4	2.0649(10)	
V1 – O5	2.0027(10)	
V1 – C2	2.1796(13)	-
C-H...O	2.461 – 2.715	
Atoms	Angle (°)	
O1-V1-O2	100.37(5)	105.9(2) – 107.8(2)
O1-V1-O3	96.72(5)	
O1-V1-O4	96.47(5)	
O1-V1-O5	175.92(5)	
O1-V1-C2	93.78(5)	
		-

^aData taken from literature.²²⁶

The crystal packing diagram in **Figure 5.10** shows two molecules of **V2**, where intermolecular interactions (C-H...O_{oxo}) are observed between hydrogen atoms on the on the NHC backbone with O_{oxo} and O_{bz}, forming hydrogen bonds (2.461 – 2.715 Å).²⁴⁶

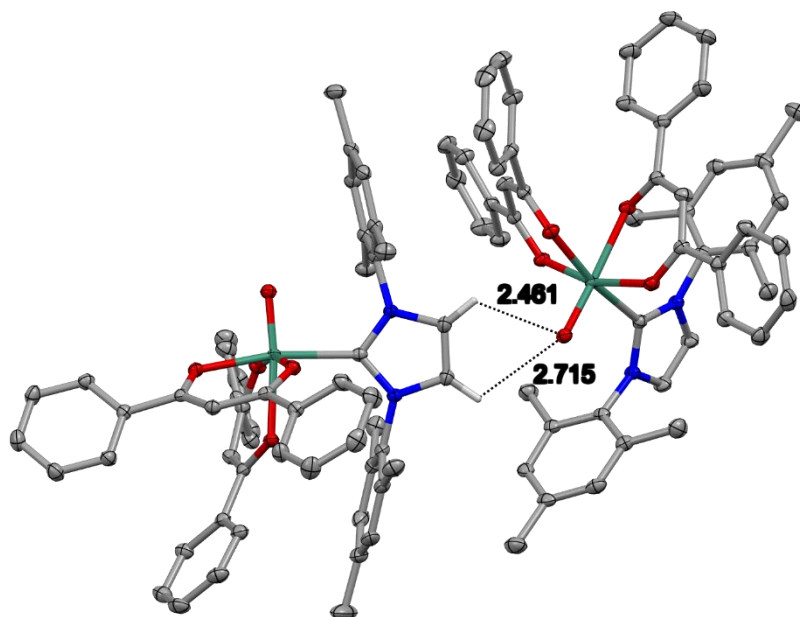
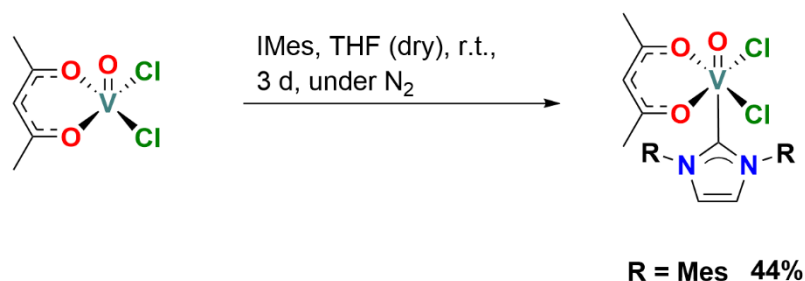


Figure 5.10: Two molecules of **A-V2** with the interactions between the backbone of the imidazole and the VI-O1 shown. Only the hydrogens involved in the interactions are shown.

5.3.3 Synthesis and Characterisation of VO(acac)Cl₂(IMes) (**V3**)

Unlike the previous two examples, a V(V) β -diketonate precursor (VO(acac)Cl₂) with two chlorides ligands was trialled. The precursor was synthesised through a known literature procedure, and is diamagnetic, allowing for additional spectroscopic measurements.²⁵⁰ In brief, **V3** was synthesised by through the reaction of VO(acac)Cl₂ and IMes in dry THF (**Scheme 5.3**).



Scheme 5.3: Synthetic conditions for synthesis of **V3**.

V3 was analysed by ⁵¹V NMR spectroscopy and the spectrum compared to the starting material VO(acac)Cl₂ (**Figure 5.11**). The resonance for VO(acac)Cl₂ in

CDCl_3 is found at -199.10 ppm, and after addition of IMes, this shifted to -357.9 ppm. This shift is due to the further shielding of the vanadium by the electron density donated by the NHC. A similar upfield shift was reported in which the ^{51}V NMR shift of $\text{VOCl}_3(\text{Imes})$ was -77 ppm the precursor VOCl_3 by definition is 0 ppm (as the reference standard).²³² The weak signal in CDCl_3 is an indication that the complex may be decomposed by the solvent, it was for this reason that the ^{51}V and ^1H NMR spectra were also taken in d_8 -THF (for the ^{51}V NMR spectrum see **Appendix 8.70**). The ^1H NMR spectrum (**Figure 5.12**) shows broad resonances which could be a combination of two factors (i) the experiment was carried out in a Young's NMR tube and therefore is a non-spin experiment and (ii) there may be a small amount of paramagnetic impurity present. However, even if accurate integrals cannot be obtained there is evidence that successful coordination of the IMes has occurred, such as the presence of multiple resonances in the aromatic region that are from the imidazole backbone and phenyl ring of the IMes, as well as new peaks in the aliphatic region from the methyl groups of IMes.

$\text{VO}(\text{acac})\text{Cl}_2$

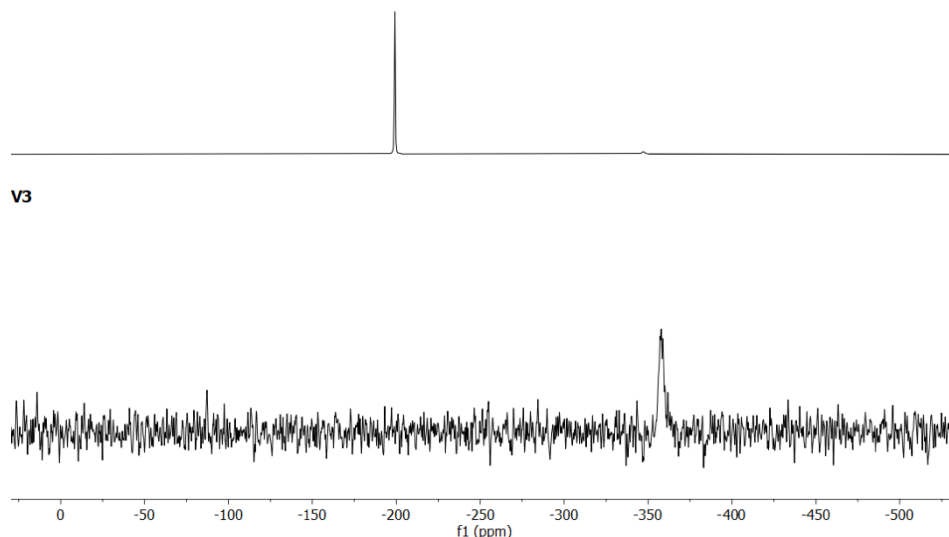


Figure 5.11: ^{51}V NMR spectra of $\text{VO}(\text{acac})\text{Cl}_2$ and **V3** in CDCl_3 (131.62 MHz).

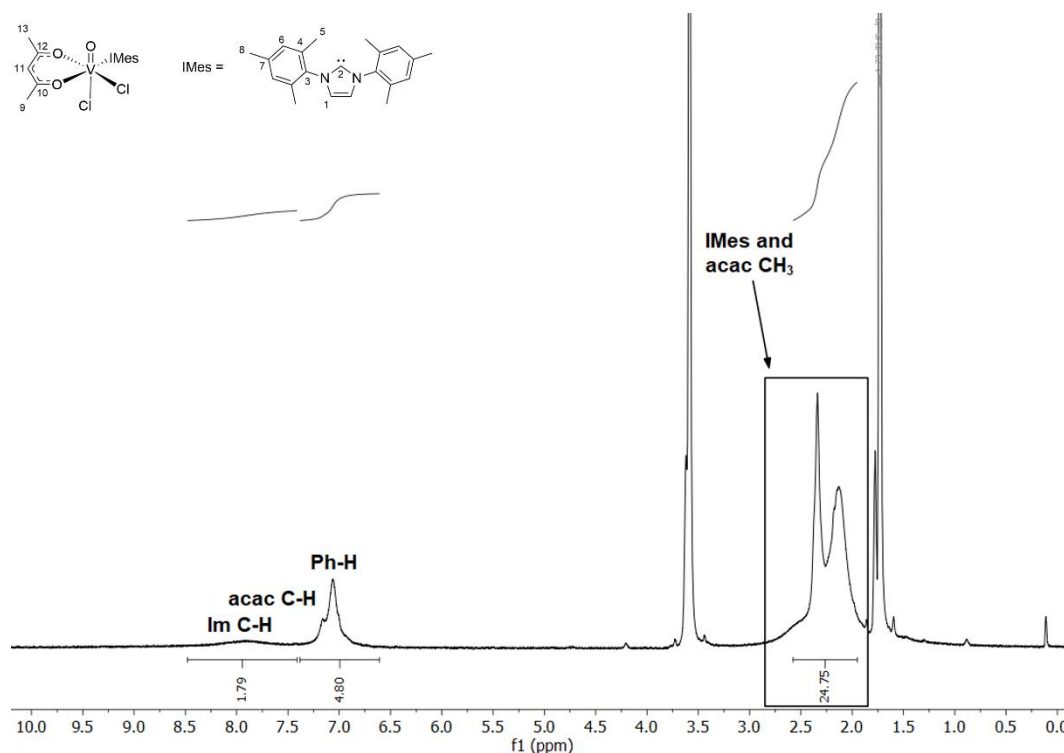
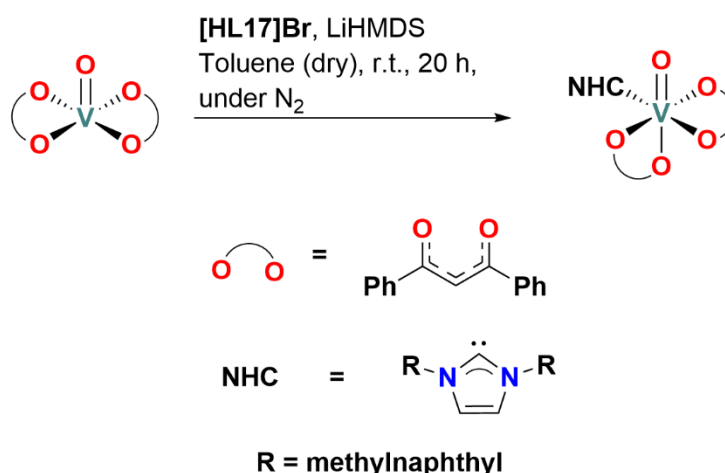


Figure 5.12: ^1H NMR spectrum of **V3**, (d_8 -THF, 500 MHz).

5.3.4 Synthesis and Characterisation of $\text{VO}(\text{bzbz})_2(\text{L17})$ (**V4**)

The scope of this chemistry was further explored by trialling a synthesis of a $\text{VO}(\text{bzbz})_2$ adduct with the ligands reported in previous chapters. **[HL17](Br)** (a mono imidazolium salt with methylnaphthyl wingtips) was chosen as the naphthyl wingtip is good for crystallisation, and scXRD would be useful to probe the structure of the complex.²⁵¹ The synthesis of **V4** is shown in **Scheme 5.4**.



Scheme 5.4: Synthetic conditions for synthesis of **V4**.

Unlike for the examples described earlier, **[HL17](Br)** needs to be deprotonated *in situ*, and this was done using lithium bis(trimethylsilyl)amide (LiHMDS). The byproducts from the deprotonation can be easily removed by filtration (LiBr) and *in vacuo* (HMDS). The product was isolated as a deep blue solid with a yield of 8%. FT-IR analysis (**Figure 5.13**) of **V4** is similar to **V1** and **V2**, where there are more the C=O peaks, indicating that the complex has a similar binding mode (equatorial and not axial). The V=O stretch peak, which is found at 991 cm^{-1} for $\text{VO}(\text{bzbz})_2$, disappears after the reaction, however, unlike **V1** and **V2** the shifted stretch cannot be easily identified and could be under the broad peak found between $881 - 964\text{ cm}^{-1}$. The peaks at 2850 and 2925 cm^{-1} are from the CH_2 stretching vibrations of the NHC methylene and are not found in the $\text{VO}(\text{bzbz})_2$ precursor.

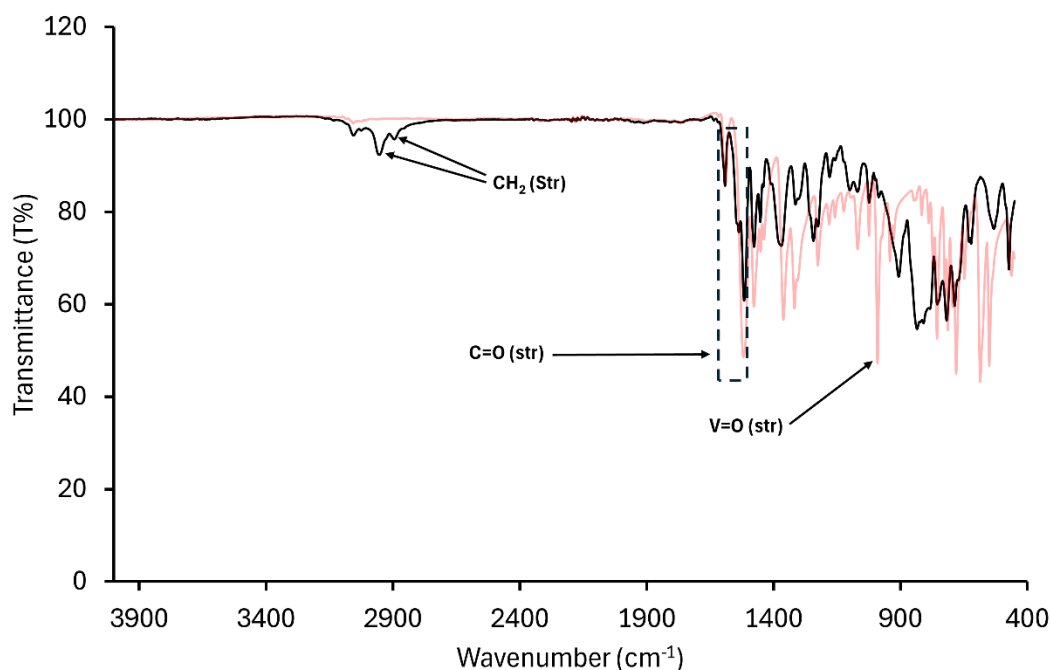


Figure 5.13: ATR-FTIR spectrum of **V4** (black) and **VO(bz bz)₂** (light red) between 450 – 4000 cm^{-1} .

An attempt to obtain single crystals was made by layered diffusion of n-heptane into a concentrated solution of **V4** in toluene. While crystals did form, none were suitable for scXRD analysis. The vial was removed from the glovebox, and the solvent was allowed to evaporate in aerobic conditions, this led to the formation of blue prismatic crystals that were suitable for scXRD, and the data was collected by Dr Benjamin Hofmann. The crystal was solved in a monoclinic crystal system with a $C2/c$ space group, and the asymmetric unit contains half a molecule. The molecular structure obtained is shown in **Figure 5.14**, with selected bond lengths and angles shown in **Table 5.3**. There are two vanadium centres that are bridged by an oxo μ -**O-(V4)₂**, and there is a 2-fold screw axis through the bridge. Like the other two structures reported in this chapter the geometry around the vanadium centres is distorted octahedral. The connectivity of this molecule indicates that the vanadium centres are V(III) and not V(IV), however, the mechanism of this reduction has not been elucidated, disproportionation is a possible route to V(III). Examples do exist in literature where moisture from the air has led to the formation of μ -oxo bridges, however in those literature examples the $\text{V}=\text{O}$ group remained intact, and the oxidation state of the complex did not change.²⁵²

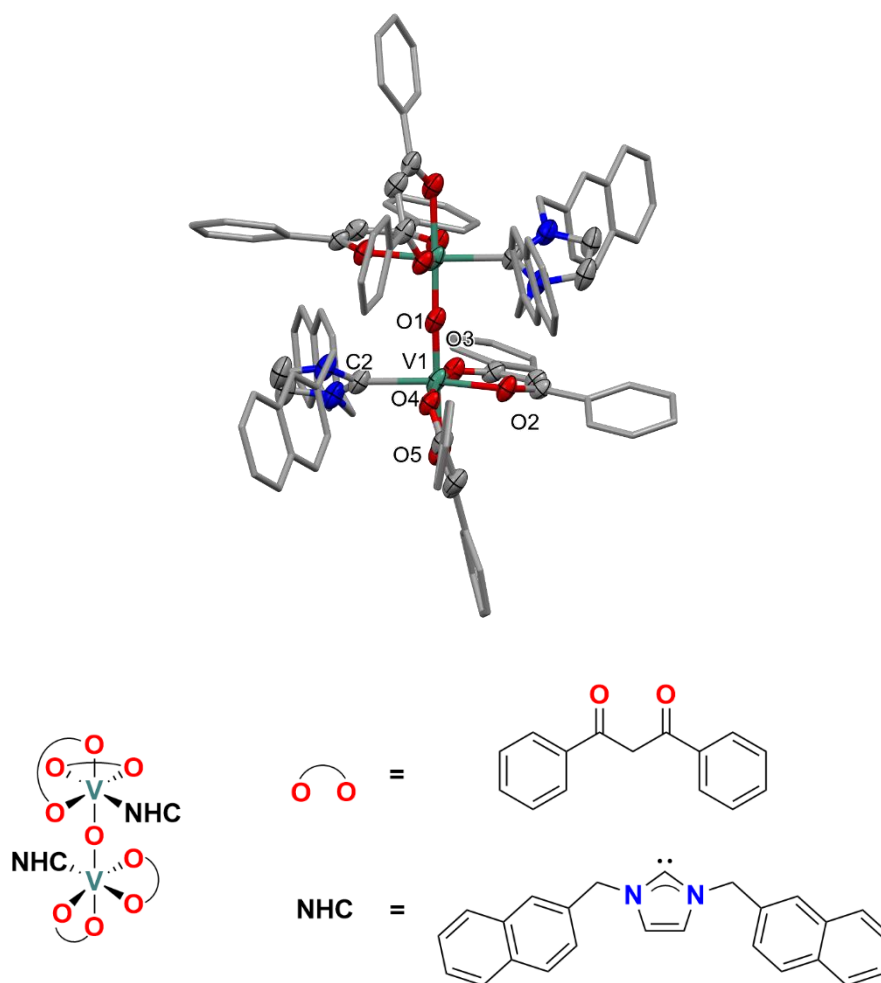


Figure 5.14: Molecular structure of a decomposition product $\Lambda\Lambda$ - μ -O-(V4)₂ with displacement ellipsoids shown at the 50% probability level and hydrogen atoms and solvent omitted for clarity (top). Chemdraw of crystallisation product (bottom).

Table 5.3: Selected *scXRD* parameters for μ -O-(V4)₂ with s.u.s. shown in parentheses.

Atoms	Bond length (Å)
V1 – O1	1.7829(4)
V1 – O2	2.0310(13)
V1 – O3	2.0377(13)
V1 – O4	2.0298(13)
V1 – O5	2.0761(16)
V1 – C2	2.231(2)
Atoms	Angle (°)
O1-V1-O2	94.85(7)
O1-V1-O3	94.63(4)
O1-V1-O4	94.63(7)
O1-V1-O5	178.55(4)
O1-V1-C2	91.33(6)
O1-V1-O1 ¹	174.65(10)

$$^1 I-X, +Y, 3/2-Z$$

The vanadium carbene (V1-C2) bond length is significantly longer in μ -O-(V4)₂ (2.231(2) Å) when compared to **VI** and **V2**. The V-O_{oxo} bond length of 1.7829(4) Å is comparable to μ -oxo bonds found in similar complexes in literature.²⁵² The μ -oxo bridge angle is bent from linear with an angle of 174.65(10)°, and this is most likely due to the steric strain of the bulky ligands. The disappearance of the oxo peak in the IR of the product does indicate that it is possible that the oxo-product formed from the reaction.

The EA of the product isolated from the reaction showed a large deviation from the expected value (C -11.2, N +1.34, +0.98), which indicates there are impurities in the sample. The impurity coupled with the low yield means that this synthesis must be optimised. The crystal structure confirms that it is possible to coordinate symmetric imidazolium salts with benzyl type wingtips. To confirm whether the bridged oxo product is directly synthesised from the reaction, a technique such as EPR spectroscopy would be able to help confirm the oxidation state and geometry. Another more efficient approach would be to isolate and purify the free NHC first and then coordinate it to the vanadium precursor.

5.4 Stability of Vanadium (IV) β -diketonate *N*-Heterocyclic Carbene Complexes

The stability of complexes **V1** and **V2** in toluene were studied using UV-vis spectroscopy (**Figure 5.15(a and b)**), the vanadium precursors are not soluble in toluene and were therefore not measured. The samples were prepared in a glovebox and placed into a cuvette with a seal and septum. As a control, measurements were taken over the course of 4 hours in dry toluene. Over the course of the experiment there are few changes in the spectra, which shows that they are stable over this period of time. For **V1**, strong LMCT bands with maxima 301 nm and 353 nm, and a weak *d-d* transition band between 496 – 662 nm was observed. For **V2**, the very strong band at 361 nm is assigned to the π - π^* transitions of the bz bz ligand, whilst the bands at *ca.* 433 and 532 nm are from LMCT and *d-d* transitions respectively.

The measurements were repeated using fresh sample and after injection of water (10 μ L), isosbestic points at 294 and 370 nm for **V1** and 293 nm for **V2** (**Figure 5.15 (c and d)**) are observed. The presence of isosbestic points indicates that the complexes are reacting with the water and decomposing into well-defined species (but not necessarily one species). The identity of the hydrolysis product(s) has not been identified, but possibilities include the loss of the NHC, coordination of a water or the formation of an oxo bridge.

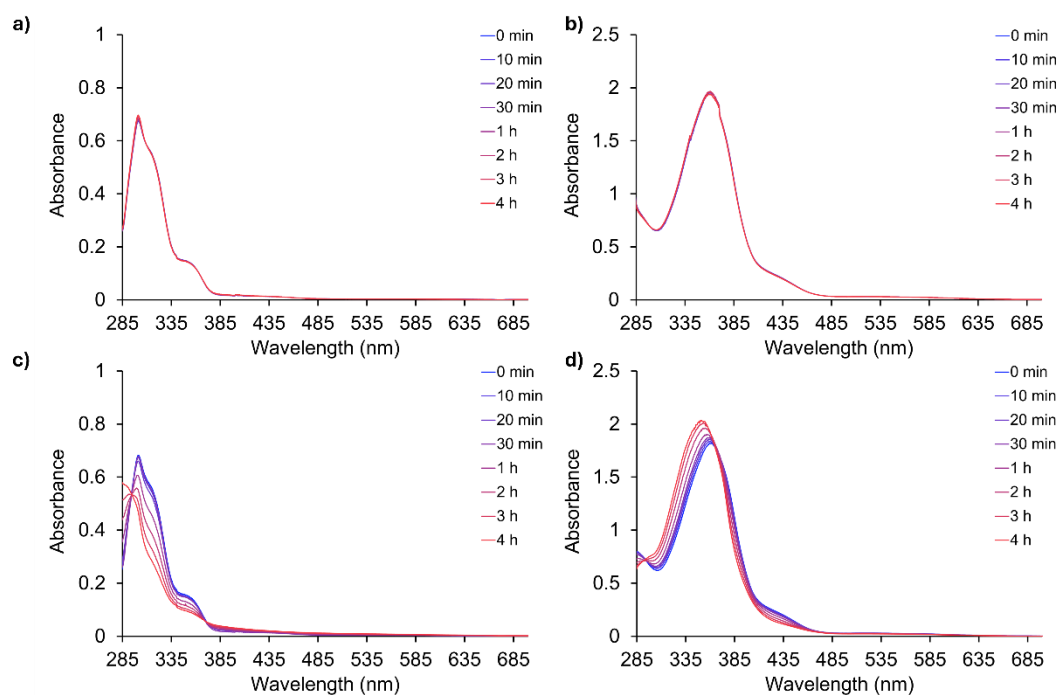


Figure 5.15: UV-Vis spectra of vanadium complexes taken in toluene between 0 – 4 hours; a) **V1** (63.75 μ M), b) **V2** (63.75 μ M), c) **V1** (63.75 μ M) + water 10 μ L and d) **V2** (63.75 μ M) + water 10 μ L.

5.5 Conclusions and Outlook

Three new vanadium-NHC complexes (**V1**, **V2** and **V3**) have been synthesised. For complexes **V1** and **V2** monomeric crystal structures were obtained both complexes and adopted a distorted octahedral geometry with the IMes ligand in an equatorial position and both β -diketonate ligands in a *cis* arrangement. The V-carbene bond measured (2.1796(13) – 2.194(2) Å) falls within literature reported values. For **V1** and **V2**, the V=O stretch weakens on coordination of a strong σ -donor NHC ligand, and this was observed in the FT-IR spectra. For the diamagnetic complex **V3**, the shift upfield in the ^{51}V NMR spectrum compared to VO(acac)Cl₂ provided evidence of complexation, which was also confirmed by ^1H NMR spectroscopy, where resonances relating to the IMes ligand were observed. An attempt was made to synthesis of **V4**. The reaction was low yielding, and whilst FT-IR showed signs of successful coordination (such as the splitting of the C=O carbonyl peak and the presence of peaks associated with the methylene bridge of the NHC ligand), no further analysis was obtained to fully confirm its successful synthesis. Crystals suitable for scXRD were only obtained once the crystallisation system

(toluene/heptane) was removed from the glovebox and the solvent was allowed to evaporate in aerobic conditions. This resulted in a dimeric vanadium(III) species, where two vanadium centres were connected by an μ -oxo bridge and the with the NHC equatorial in relation to the bridge. As this complex contains an NHC, it highlights the possibility that other complexes can be synthesised using the monodentate ligands described in **Chapter 3**. The EA results indicated the sample was impure, so more work needs to be done to optimise this synthesis. Isolating the free NHC before complexation may be a more effective route to access **V4** as this route was successful for the other complexes.

The stability of complexes **V1** and **V2** in toluene or toluene/water mixtures were studied using UV-Vis spectroscopy. In dry toluene and between 0 – 4 hours, the complexes were stable with few changes observed, however, on addition of water there were spectral changes for both compounds. Isosbestic points were present, indicating one or more new species were forming, however, the identity of the formed species is yet to be determined.

The exploration of the chemistry of these complexes is still in the early stages and there are a lot of aspects of the chemistry which requires investigation. Several possible avenues for future work stated below:

- i. The study of the paramagnetic species by EPR to aid in full characterisation of these compounds, as this could confirm the geometry in solution and allow comparison with the solid state scXRD. This technique would be able to identify the *in-situ* oxidation state of **V4** and confirm if V(III) or V(IV) is present. It would also give indication of ligand environment and help to determine if the μ -O-(**V4**)₂ species forms during the reaction or only on exposure to air. The Evan's method NMR experiment could also be used probe the number of unpaired electrons in the sample and therefore the oxidation state of the complex.
- ii. Cyclic voltammetry (CV) experiments will be able to elucidate the oxidation and reduction potentials of the complexes described. These will have to be carried out in anaerobic conditions.

- iii. Using the data obtained from the CV experiments, V(III) and V(V) complexes of **V1** and **V2** could be accessed by reactions with suitable 1 e^- oxidation and reduction agents such as FcPF_6 and KC_8 .
- iv. Further ligands could be synthesised to improve stability such as incorporating the NHC as a tether in one of the acac ligands (e.g., **Figure 5.16**).
- v. If it is found that these complexes are too unstable to be useful in biological applications, then their ability to be used as catalysts for polymerisation or C-H activation should be explored.

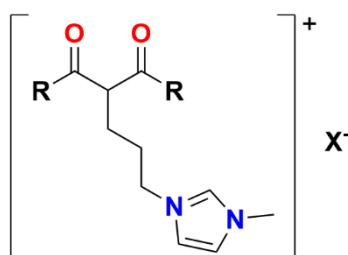


Figure 5.16: Proposed hybrid β -diketonate NHC ligand, where $R = \text{Me}$ or Ph , $X = \text{Br}$ or Cl .

6 Conclusions and Future work

This section will summarise the findings from the Ag(I)-NHC work. After identifying a lack of literature on cytotoxicity studies of binuclear benzyl functionalised Ag(I)-NHC complexes for treatments against breast cancers, this work focused on addressing this gap by designing a series of imidazole based binuclear Ag(I)-NHC complexes of the type $[\text{Ag}_2(\text{L1-7})_2](\text{PF}_6)_2$ (where **L1-7** = a functionalised bridging imidazole ligand). These complexes were synthesised via the corresponding bromide salt $[\text{H}_2\text{LX}](\text{Br})_2$ and silver(I) oxide in MeOH, followed by ion exchange or from the respective hexafluorophosphate salt $[\text{H}_2\text{LX}](\text{PF}_6)_2$ and silver(I) oxide in MeCN and characterised by suitable spectroscopic methods (^1H , $^{13}\text{C}\{^1\text{H}\}$ NMR, ATR-FTIR spectroscopy, scXRD, and EA to confirm suitable purity for biological testing).

An attempt to synthesise the benzimidazole complexes $[\text{Ag}_2(\text{L8-14})_2](\text{PF}_6)_2$ (where **L8-14** = a functionalised bridging benzimidazole ligand) using the MeOH route was trialled, however, the same methodology yielded a mixture of compounds with only small amounts of the target product, and side products which have not been identified. An alternative route using silver(I) oxide and the hexafluorophosphate salt of the ligands ($[\text{H}_2\text{LX}](\text{PF}_6)_2$) was carried out in MeCN. Three elementally pure complexes $[\text{Ag}_2(\text{L10})_2](\text{PF}_6)_2$, $[\text{Ag}_2(\text{L13})_2](\text{PF}_6)_2$ and $[\text{Ag}_2(\text{L14})_2](\text{PF}_6)_2$ were obtained. The other complexes had good NMR and IR spectra, however, EA values were lower than expected which indicates a non-hydrogen or carbon containing impurity such as Ag(0) species or silver(I) oxide. Monodentate derivatives of the binuclear *p*-fluorobenzyl complexes were also synthesised $[\text{Ag}(\text{L15})_2](\text{PF}_6)$, and $[\text{Ag}(\text{L16})_2](\text{PF}_6)$ and obtained with elemental purity.

The ligands and complexes that were analytically pure were screened against MDA-MB-231, MCF-7, ARPE-19 and some were screened against MCF10A. The binuclear imidazole complexes $[\text{Ag}_2(\text{L1-7})_2](\text{PF}_6)_2$, their respective ligands $[\text{H}_2\text{L1-7}](\text{PF}_6)_2$, cisplatin and tamoxifen were screened against breast cancer cell lines MDA-MB-231, and MCF-7, and non-cancerous cell lines ARPE-19 and MCF10A. In general, the ligands were moderate to non-toxic ($\text{IC}_{50} = 53.0$ to >100 μM). All Ag(I)-NHC complexes were active against all the cell lines with the highest activity in MDA-MB-231. Only $[\text{Ag}_2(\text{L6})_2](\text{PF}_6)_2$ is selective for MDA-MB-231 when

compared to MCF10A (non-cancerous breast). This is contrary to the few examples that are reported in literature where the Ag(I)-NHC complexes tested were non/less toxic against MCF10A compared to breast cancer cells.^{100,187} The activity of the complexes was compared to their LogP (computationally calculated), and correlations between lipophilicity and activity were observed only for MCF-7. This correlation was not found by other groups when they varied alkyl chain lengths in similar binuclear complexes.^{115,117} For MDA-MB-231 the most active complex $[\text{Ag}_2(\text{L6})_2](\text{PF}_6)_2$ was one of the least lipophilic of the series, exemplifying that increasing lipophilicity in these complexes is not a good strategy for obtaining higher activity. For binuclear benzimidazole complexes there is only a small improvement in activity against MDA-MB-231 compared to their imidazole analogues, with no clear trend for the other cell lines. No clear relationships for the *p*-fluorobenzyl complexes were found between nuclearity and activity.

Mechanisms of action were investigated for four complexes $[\text{Ag}_2(\text{L1})_2](\text{PF}_6)_2$, $[\text{Ag}_2(\text{L4})_2](\text{PF}_6)_2$, $[\text{Ag}_2(\text{L6})_2](\text{PF}_6)_2$ and $[\text{Ag}_2(\text{L13})_2](\text{PF}_6)_2$. An optical microscope was used to determine cell morphology changes in MDA-MB-231 cells after 4 hours of incubation. The cells became smaller and rounder in shape as well as detaching from the plate, showing signs of cell death. Intercalation experiments confirmed that these complexes can intercalate with ct-DNA, with the methylnaphthyl functionalised complex $[\text{Ag}_2(\text{L4})_2](\text{PF}_6)_2$ showing the greatest ability to intercalate, highlighting the importance of the extended aromatic ring. The K_{sv} of $[\text{Ag}_2(\text{L4})_2](\text{PF}_6)_2$ is 7-fold higher than the corresponding ligand $[\text{H}_2(\text{L4})_2](\text{PF}_6)_2$, highlighting that the inclusion of silver is important for the DNA interactions. DNA interactions with the most active complex $[\text{Ag}_2(\text{L13})_2](\text{PF}_6)_2$ was studied using molecular docking, where it was found to interact with the major groove of DNA with a free binding energy of $-7.93 \text{ kcal mol}^{-1}$. The ability of the complexes to induce ROS in MDA-MB-321 cells was measured using a fluorescein dye assay, and a dose-dependent increase in ROS (compared to the control) was observed.

The most active and selective complex $[\text{Ag}_2(\text{L13})_2](\text{PF}_6)_2$ was chosen to investigate the relationship between nuclearity and cell uptake. The results were compared to the monodentate silver analogue $[\text{Ag}(\text{L16})_2](\text{PF}_6)$. The uptake was measured by ICP-MS analysis in both MDA-MB-231 and MCF-7 cells and reported as

^{107}Ag atoms/cell. For MDA-MB-231 both complexes had similar uptake values and IC_{50} values. There was a statistically significance between the uptake in MCF-7, with the mononuclear complex $[\text{Ag}(\text{L16})_2](\text{PF}_6)$ having a higher uptake and IC_{50} value when compared to $[\text{Ag}_2(\text{L13})_2](\text{PF}_6)_2$. These results show that uptake of silver is important for activity.

6.1 Future Work and Outlook

To also help determine possible biomolecular interactions, fractionated ICP-MS would be crucial in determining metal location, for example, uptake from the cytoplasm, mitochondria or nucleus, which will help to focus the future modes of action work.²⁵³ Then further mechanistic studies are required to understand mode of cell death, such as apoptosis studies (with propidium iodide and Annexin V) or necrosis to confirm death pathways, or cell cycle arrest to confirm any interactions with the cell cycle. As the complexes described were shown to generate redox stress it would be useful to see if they inhibit the redox enzyme TrxR as other $\text{Ag}(\text{I})\text{-NHC}$ have been shown to be potent inhibitors.

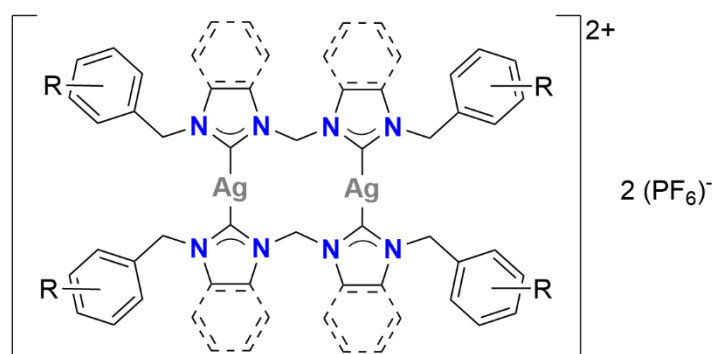
To better understand how the complexes interact with DNA, additional assays with more specific binders such as Hoechst which binds preferentially to A-T rich regions are required. These results would also feed into the cell cycle arrest studies and help to confirm whether inhibition of DNA synthesis is a major component of activity.¹⁸⁹ Other DNA structures such as G-quadruplex or i-motif (both targets for anticancer therapies) could also be possible targets for the compounds described in this thesis, and the complexes varied three dimensional structures may be able to achieve interactions that may not be possible for simple organic molecules.^{254,255} Literature has indicated that $\text{Ag}(\text{I})\text{-NHC}$ can reach the mitochondria, therefore studies to investigate the complexes interactions with mitochondrial DNA (mtDNA) would be crucial in helping to confirming possible modes of action.^{102,256} As mentioned in the introduction, there have already been reports on the ability of $\text{Ag}(\text{I})\text{-NHC}$ complexes promoting depolarisation, therefore, mitochondrial experiments to study the effects of the complexes on mitochondrial membrane potential ($\Delta\Psi\text{m}$) could help to confirm if mitochondria is a useful target.

The data showed that the complexes generate ROS within MDA-MB-231, but to confirm whether this is the main cause of cell death antioxidant studies with an

antioxidant that does not decompose the Ag(I)-NHC complexes should be carried out, such as vitamin E.²⁵⁷ Quantification of ROS generated using flow cytometry experiments would be useful to probe the relationship between ROS and activity.

The results for the *p*-fluorobenzyl complexes **[Ag₂(L6)₂](PF₆)₂** and **[Ag₂(L13)₂](PF₆)₂** were the most promising, as they were the only ones that were selective for MDA-MB-231 compared to non-cancerous breast MCF10A, and they were also generally the most active. Using this information coupled with the observation that the binuclear complexes are more stable a proposed design for future complexes is shown below **Figure 6.1**. Other complexes with *o/m*/multi-fluoro derivatives or the use of different halogens, e.g., Cl, Br and I, should be explored. Halogens are found in one-third of drugs currently clinical trials, and they can interact with aromatic functional groups on protein residues through halogen- π bonds, which can help with selectivity.²⁵⁸ Halogens such as fluorine can also increase metabolic stability of drug compounds.²⁵⁹ Another route to increase activity would be to include moiety in the complex that can generate ROS inside cells such as ferrocene (from the Fenton reaction), and such hetero-bimetallic complexes have already been reported in the literature.^{260,261}

Another modification could be the incorporation of a fluorescent wingtip such as anthracenyl, which would be useful in monitoring the cellular localisation of the complexes, and helpful in identifying possible cellular targets and provide additional and extended ring system for intercalative properties.²⁶² This approach has already been used by Citta et al. using neutral Ag(I)-NHC complexes.²⁶³ ²⁵⁸Another possible approach is to include a wingtip that can be further functionalised either in synthesis or in the cell, such as alkynes, which can undergo click reactions with biomolecules (e.g. sugars or proteins) or dyes.²⁶⁴ This would be an efficient way to generate a large library of azolium salts that could be screened for activity.



R = F, Cl, Br, I, anthracenyl, ferrocenyl or alkyne

Figure 6.1: Proposed design of future binuclear Ag(I)-NHC complexes, with varied substitution patterns of halogens on the benzyl wingtips.

7 Experimental and Procedures

7.1 General Information

Chemicals were purchased from Sigma-Aldrich (Merck KGaA), Fisher Scientific and Fluorochem and used without further purification. ^1H , $^{13}\text{C}\{^1\text{H}\}$ and $^{19}\text{F}\{^1\text{H}\}$ NMR spectra were recorded either on a Bruker Avance III 400 (Ultrashield 400 Plus) or a Bruker Avance III 500 (Ascent 500) and referenced to TMS using the respective residual solvent signal as secondary standard. ^{51}V spectra were referenced to a VOCl_3 standard. The spectra were processed in MNova 14.0.1, and the multiplicities are abbreviated as s = singlet, d = doublet, t = triplet, q = quartet, p = pentet, br = broad, m = multiplet. IR spectra were collected on a Perkin Elmer Spectrum Two FT-IR spectrometer (UATR Two probe), the intensities are abbreviated vs = very strong, s = strong, m = medium, w = weak and br = broad. UV-vis spectra were collected on a JASCO 730 UV-Visible Spectrophotometer equipped with a PAC-743R temperature control unit. Fluorescence spectra were collected on an Edinburgh FS5 Spectrofluorometer. Optical cell images were taken on a ZEISS Primo Vert microscope at 10X magnification with a GXCAM digital camera mounted and processed in the GT Vision GXCapture-T software. Fluorescence images were taken on Zeiss Observer 7 microscope, images were processed using Zeiss Zen 3.8 imaging software.

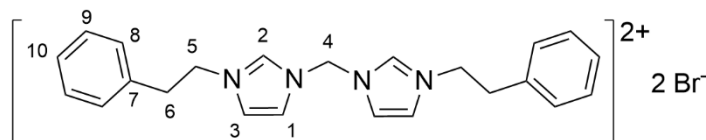
7.2 Experimental

Monofunctionalised azoles **Im1-14**, 1-(benzyl)-1*H*-imidazole,²⁶⁵ 1-(2-phenylethyl)-1*H*-imidazole,²⁶⁶ 1-(3-phenylpropyl)-1*H*-imidazole,²⁶⁷ 1-(naphthalen-2-ylmethyl)-1*H*-imidazole,²⁶⁸ 1-(4-*tert*-butylbenzyl)-1*H*-imidazole,²⁶⁹ 1-(4-fluorobenzyl)-1*H*-imidazole,²⁷⁰ 1-(4-trifluoromethylbenzyl)-1*H*-imidazole,²⁷⁰ 1-(benzyl)-1*H*-benzimidazole,²⁷¹ 1-(2-phenylethyl)-1*H*-benzimidazole,²⁷² 1-(3-phenylpropyl)-1*H*-benzimidazole,²⁷³ 1-(2-naphthalenylmethyl)-1*H*-benzimidazole,²⁷⁴ 1-(4-*tert*-butylbenzyl)-1*H*-benzimidazole,²⁷⁵ 1-(4-fluorobenzyl)-1*H*-benzimidazole,²⁷¹ 1-(4-(trifluoromethylbenzyl)-1*H*-benzimidazole,²⁷⁶ azolium salts, $[\text{H}_2\text{L1}](\text{Br})_2$,¹³⁶ $[\text{H}_2\text{L1}](\text{PF}_6)_2$,²⁷⁷ $[\text{H}_2\text{L5}](\text{Br})_2$,¹³⁶ $[\text{H}_2\text{L6}](\text{Br})_2$,²⁷⁸ $[\text{HL17}](\text{Br})$,²⁵¹ and $[\text{HL15}](\text{Br})$,¹⁶⁹ and Ag(I)-NHC complex $[\text{Ag}_2(\text{L1})_2](\text{PF}_6)_2$, are all previously reported in literature and were synthesised using standard procedures

and the purity was confirmed by ^1H NMR spectroscopy.²⁷⁹ Unless otherwise specified, the reactions were carried out at room temperature and in aerobic conditions.

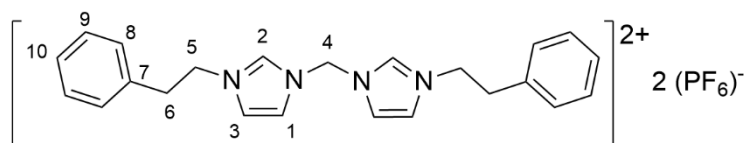
7.2.1 Bridged ligands

7.2.1.1 Synthesis of 1,1'-Bis(ethylphenyl)-3,3'-methylenediimidazolium dibromide - $[\text{H}_2\text{L2}](\text{Br})_2$



1-(2-Phenylethyl)-1*H*-imidazole (0.34g, 2.00 mmol) was dissolved in dibromomethane (10 mL) forming a yellow solution which was heated to reflux for 4 d, and after which a white precipitate formed. The reaction mixture was allowed to cool to room temperature and the precipitate was collected by vacuum filtration, washed with acetone (3 x 40 mL) and Et_2O (3 x 40 mL) and dried *in vacuo* yielding a white powder (0.37 g, 0.71 mmol, 71%). ^1H NMR (400 MHz, $\text{DMSO}-d_6$, 298K) δ : 9.57 (s, 2H, H_2), 8.01, (appt.t, 4H, $^3/4J(^1\text{H}-^1\text{H}) = 1.8$ Hz, H_1), 7.91 (appt.t, 4H, $^3/4J(^1\text{H}-^1\text{H}) = 1.8$ Hz, H_3), 7.71 – 7.31 (m, 10H, H_{8-10}), 6.70 (s, 2H, H_4), 4.53 (t, 4H, $^3J(^1\text{H}-^1\text{H}) = 7.4$ Hz, H_5), 3.17 (t, 4H $^3J(^1\text{H}-^1\text{H}) = 7.4$ Hz, H_6); $^{13}\text{C}\{^1\text{H}\}$ NMR (101 MHz, $\text{DMSO}-d_6$, 298K) δ : 137.4 ($\underline{\text{C}}\text{H}$, C_2), 136.6 (Q $\underline{\text{C}}$, C_7), 128.7 ($\underline{\text{C}}\text{H}$, C_8), 128.6 ($\underline{\text{C}}\text{H}$, C_9), 126.9 ($\underline{\text{C}}\text{H}$, C_{10}), 123.3 ($\underline{\text{C}}\text{H}$, C_3), 122.0 ($\underline{\text{C}}\text{H}$, C_1), 57.9 ($\underline{\text{C}}\text{H}_2$, C_4), 50.3 ($\underline{\text{C}}\text{H}_2$, C_5), 35.1 ($\underline{\text{C}}\text{H}_2$, C_6); ATR-IR $\nu_{\text{max}}/\text{cm}^{-1}$: 3429 (m(br), H_2O), 3127 (w, $\text{C}_{\text{Ar}}-\text{H}$), 3060 (w, $\text{C}_{\text{Ar}}-\text{H}$), 2050, 1604 (m, aromatic C-C), 1564 (m, C_2-H), 1549, 1497, 1455, 1441, 1364, 1332, 1267, 1159 (s, imidazole bending), 1082, 1029, 857, 832, 758, 735, 718, 699, 636, 626, 614, 558, 501.

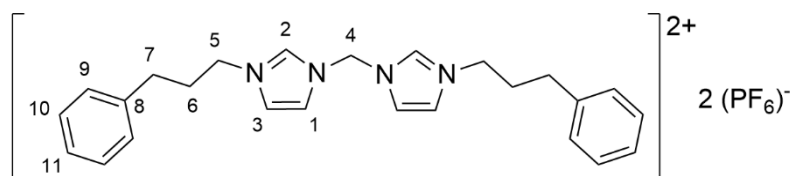
7.2.1.2 Synthesis of 1,1'-Bis(ethylphenyl)-3,3'-methylenediimidazolium hexafluorophosphate - $[\text{H}_2\text{L2}](\text{PF}_6)_2$



1-(2-Phenylethyl)-1*H*-imidazole (0.40 g, 2.32 mmol) and diiodomethane (0.31 g, 1.16 mmol) were dissolved in EtOAc (6 mL) and sealed in a microwave tube. The

mixture was heated at 170°C for 1 h in a microwave reactor, after which a brown oil had formed. The supernatant was discarded, and the oil was dissolved in a small amount of MeOH. The methanolic solution was then added to a stirring solution of ammonium hexafluorophosphate (0.5 g, 3.06 mmol) in deionised water (40 mL). Upon addition, a pale brown precipitate formed. The mixture was allowed to stir for 1 h after which the precipitate was collected by vacuum filtration, washed with Et₂O (40 mL) and dried *in vacuo*. The sample was washed further with MeOH (40 mL) and dried *in vacuo*, yielding an off-white powder (0.23 g, 0.352 mmol, **30%**). **¹H NMR (400 MHz, DMSO-*d*₆, 298K) δ:** 9.23 (t, 2H, ³*J*(¹H-¹H) = 1.6 Hz, H₂), 7.86 (appt.t, 2H, ^{3/4}*J*(¹H-¹H) = 1.8 Hz, H₁), 7.82 (appt.t, 2H, ^{3/4}*J*(¹H-¹H) = 1.8 Hz, H₃), 7.35 – 7.21 (m, 6H, H_{9,10}), 7.21 – 7.15 (m, 4H, H₈), 6.53 (s, 2H, H₄), 4.52 (t, 4H, ³*J*(¹H-¹H) = 7.3 Hz, H₅), 3.14 (t, 4H, ³*J*(¹H-¹H) = 7.3 Hz, H₆); **¹³C{¹H} NMR (101 MHz, DMSO-*d*₆, 298K) δ:** 137.3 (C_H, C₂), 136.6 (Q C, C₇), 128.7 (C_H, C₈), 128.6 (C_H, C₉), 127.0 (C_H, C₁₀), 123.4 (C_H, C₃), 122.1 (C_H, C₁), 58.3 (C_H₂, C₄), 50.3 (C_H₂, C₅), 35.2 (C_H₂, C₆); **ATR-IR ν_{max}/cm⁻¹:** 3164, 3140, 3116, 1608 (m, aromatic C-C), 1579 (m, C2-H), 1553, 1499, 1459, 1455, 1429, 1412, 1402, 1363, 1339, 1324, 1294, 1265, 1171, 1164 (s, imidazole bending), 1111, 1083, 1050, 1033, 819, 766, 762, 739, 717, 705, 696, 689, 640, 630, 619, 555, 499, 470; **Elemental Analysis Calculated for (C₂₃H₂₆F₁₂N₄P₂):** C, 42.60; H, 4.04; N 8.64%; **Analysis Found:** C, 42.28; H, 3.56; N 8.54%.

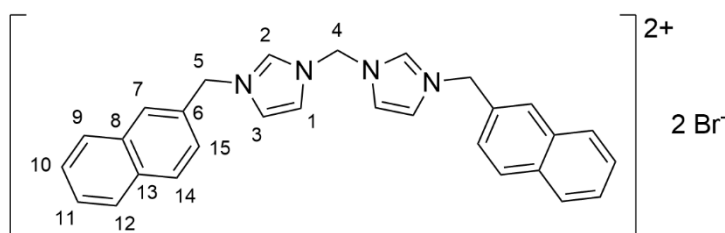
7.2.1.3 Synthesis of 1'-Bis(phenylpropyl)-3,3'-methylenediimidazolium dihexafluorophosphate - [H₂L3](PF₆)₂



1-(3-Phenylpropyl)-1*H*-imidazole (1.00 g, 5.36 mmol) and diiodomethane (0.72 g, 2.68 mmol) was dissolved in toluene (10 mL) forming a yellow solution. The solution was heated at reflux for 3 d. A white precipitate formed, was collected via vacuum filtration and dissolved in a small amount of DMSO. This was added dropwise to a stirring solution of ammonium hexafluorophosphate (2.25 g, 13.8 mmol) in deionised water (100 mL), and a viscous brown oil formed. The deionised water was decanted, and Et₂O (40 mL) was added, this solidified the oil. The solid

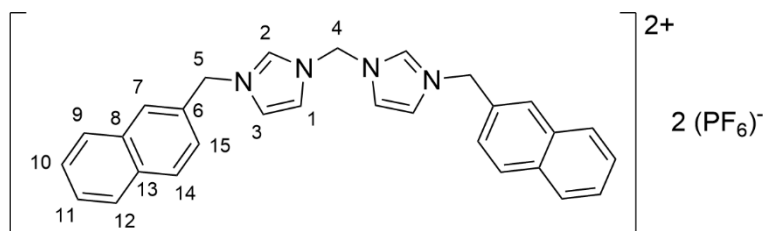
was collected by vacuum filtration, washed with deionised water (4 x 20 mL), Et₂O (4 x 20 mL) and MeOH (40 mL), and dried *in vacuo* yielding a pale-yellow powder (0.60 g, 0.88 mmol, **33%**). **¹H NMR (400 MHz, DMSO-*d*₆, 298K) δ:** 9.39 (t, 2H, ³*J*(¹H-¹H) = 1.6 Hz, H₂), 7.95 (appt.t, 2H, ^{3/4}*J*(¹H-¹H) = 1.9 Hz, H₁), 7.92 (appt.t, 2H, ^{3/4}*J*(¹H-¹H) = 1.8 Hz, H₃), 7.30 (t, 4H, ³*J*(¹H-¹H) = 7.5 Hz, H₁₀), 7.24 – 7.17 (m, 6H, H₉ and ₁₁), 6.58 (s, 2H, H₄), 4.25 (t, 4H, ³*J*(¹H-¹H) = 7.3 Hz, H₅), 3.17 (MeOH), 2.63 (t, 4H, ³*J*(¹H-¹H) = 7.3, H₇), 2.14 (p, 4H, ³*J*(¹H-¹H) = 7.5 Hz, H₆); **¹³C{¹H} NMR (101 MHz, DMSO-*d*₆, 298K) δ:** 140.38 (Q C, C₈), 137.5 (CH, C₂), 128.5 (CH, C₉), 123.2 (CH, C₁₀) 126.2 (CH, C₁₁), 123.2 (CH, C₃), 122.3 (CH, C₁), 58.4 (CH₂, C₄), 49.0 (CH₂, C₅), 31.6 (CH₂, C₇), 30.6 (CH₂, C₆). **ATR-IR ν_{max}/cm⁻¹:** 3161 (w, C_{Ar}-H), 2361, 1578 (m, C₂-H), 1549, 1498, 1454, 1381, 1330, 1160 (s, imidazole bending), 1108, 1033, 874, 817 (vs, br, PF₆), 770, 756, 742, 700, 674, 618; **Elemental Analysis Calculated for (C₂₅H₃₀F₁₂N₄P₂):** C, 44.39; H, 4.47; N 8.28%; **Analysis Found:** C, 44.36; H, 3.58; N 8.18%

7.2.1.4 Synthesis of 1,1'-Bis(methylnaphthyl)-3,3'-methylenediimidazolium dibromide - [H₂L4](Br)₂



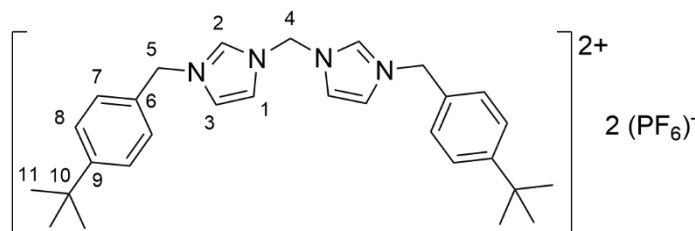
1-(Naphthalen-2-ylmethyl)-1H-imidazole (0.99 g, 4.75 mmol) was dissolved in dibromomethane (10 mL) forming a brown solution which was heated to reflux for 16 h, after which a white precipitate had formed. The mixture was allowed to cool to room temperature, the precipitate was collected by vacuum filtration, washed with acetone (3 x 40 mL) and Et₂O (3 x 40 mL), and dried *in vacuo* yielding a white powder (0.73 g, 1.23 mmol, **52%**). **¹H NMR (400 MHz, DMSO-*d*₆, 298K) δ:** 9.68 (t, 2H, ⁴*J*(¹H-¹H) = 1.6 Hz, H₂), 8.12 (dd, 2H, ³*J*(¹H-¹H) = 2.2, Hz, ⁴*J*(¹H-¹H) = 1.8 Hz, H₃), 7.91 – 8.04 (m, 10H, H_{Ar}), 7.53 – 7.63 (m, 6H, H_{nap}), 6.71 (s, 2H, H₄), 5.68 (s, 4H, H₅). (known but synthesised via a different route)

7.2.1.5 Synthesis of 1,1'-Bis(methylnaphthyl)-3,3'-methylenediimidazolium dihexafluorophosphate - $[H_2L4](PF_6)_2$



1-(Naphthalen-2-ylmethyl)-1H-imidazole (1.01 g, 4.84 mmol) was dissolved in dibromomethane (10 mL) and heated to reflux for 1 d. After which the mixture was allowed to cool down to room temperature, and the solvent removed under reduced pressure. The resulting solid was washed with acetone (40 mL), collected by vacuum filtration, washed with acetone (2 x 40 mL) and Et₂O (3 x 40 mL), resulting in a white powder. The powder was then suspended in acetone (50 mL) after which ammonium hexafluorophosphate (0.98 g, 6.00 mmol) was then added and stirred for 2 h. The resulting suspension was gravity filtered, and the solvent was removed under reduced pressure. The resulting white powder was then stirred in deionised water (50 mL) for 30 min. The solid was then collected by vacuum filtration, washed with deionised water (2 x 40 mL) and Et₂O (3 x 40 mL), and dried *in vacuo* yielding a white powder (0.88 g, 1.21, **50%**) **¹H NMR (400 MHz, DMSO-*d*₆, 298K)** δ : 9.48 (t, 2H, $^4J(^1H-^1H) = 1.6$, H₂), 8.04 – 7.89 (m, 12H, H_{Ar}), 7.62 – 7.56 (m, 4H, H_{10,11}), 7.53 (dd, 2H $^3J(^1H-^1H) = 8.38$, Hz, $^4J(^1H-^1H) = 1.85$ Hz, H₉ or H₁₂), 6.60 (s, 2H, H₄), 5.65 (s, 4H, H₅); **¹³C{¹H} NMR (101 MHz, DMSO-*d*₆, 298K)** δ : 137.8 (CH, C₂), 132.8 (Q C, C₆ or C₈ or C₁₃), 132.7 (Q C, C₆ or C₈ or C₁₃), 131.5 (Q C, C₆ or C₈ or C₁₃), 128.9 (CH, C_{nap}), 128.0 (CH, C_{nap}), 127.9 (CH, C_{nap}), 127.7 (CH, C_{nap}), 127.0 (CH, C₁₀ or C₁₁), 126.9 (CH, C₁₀ or C₁₁), 125.9 (CH, C₉ or C₁₂), 123.5 (CH, C₃), 122.6 (CH, C₁), 58.6 (CH₂, C₄), 52.6 (CH₂, C₅); **ATR-IR ν_{max}/cm^{-1}** : 3165 (w, C_{Ar}-H), 2358, 1586, 1547, 1511, 1421, 1369, 1334, 1296, 1254, 1178, 1150 (s, imidazole bending), 1112, 1049, 954, 920, 847, 822 (vs, br, PF₆), 779, 762, 746, 618; **Elemental Analysis Calculated for (C₂₉H₂₆F₁₂N₄P₂)**: C, 48.35; H, 3.64; N 7.78%; **Analysis Found**: C, 48.83; H, 2.60; N 7.49%

7.2.1.6 Synthesis of 1,1'-Bis(4-*tert*-butylbenzyl)-3,3'-methylenediimidazolium dihexafluorophosphate - [H₂L5](PF₆)₂



1-(4-*tert*-Butylbenzyl)-1*H*-imidazole (2.00g, 9.31 mmol) was dissolved in dibromomethane (10 mL) and heated to reflux for 1 d. After which the mixture was allowed to cool to room temperature, and the solvent was removed under reduced pressure. The resulting solid was washed with acetone (40 mL), collected by vacuum filtration and washed with acetone (2 x 40 mL) and Et₂O (3 x 40 mL), resulting in a white powder. The powder was then suspended in acetone (50 mL) after which ammonium hexafluorophosphate (1.90 g, 11.68 mmol) was then added. The mixture was then stirred for 1 day, and the solvent was removed under reduced pressure. The resulting solid was then stirred in deionised water (50 mL) for 1 h, collected by vacuum filtration, washed with deionised water (2 x 40 mL) and Et₂O (3 x 40 mL), and dried *in vacuo* yielding a white powder (2.43 g, 3.32 mmol, **71%**).

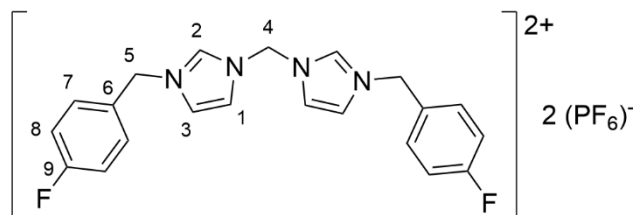
¹H NMR (400 MHz, DMSO-*d*₆, 298K) δ: 9.44 (t, 2H, ⁴*J*(¹H-¹H) = 1.6 Hz, H₂), 7.98 (dd, 2H, ³*J*(¹H-¹H) = 2.0, Hz, ⁴*J*(¹H-¹H) = 1.6, H₁), 7.89 (dd, 2H, ³*J*(¹H-¹H) = 2.0, Hz, ⁴*J*(¹H-¹H) = 1.6, H₃), 7.47 (d, 4H, ³*J*(¹H-¹H) = 8.4 Hz, H₇), 7.38 (d, 4H, ³*J*(¹H-¹H) = 8.4 Hz, H₈), 6.58 (s, 2H, H₄), 5.43 (s, 4H, H₅), 1.28 (s, 18H, H₁₁);

¹³C{¹H} NMR (101 MHz, DMSO-*d*₆, 298K) δ: 151.6 (Q C, C₆ or C₉), 137.6 (CH, C₂), 131.2 (Q C, C₆ or C₉), 128.5 (CH, C₇ or C₈), 125.8 (CH, C₇ or C₈), 123.3 (CH, C₃), 122.6 (CH, C₁), 58.5 (CH₂, C₄), 52.1 (CH₂, C₅), 34.4 (Q C, C₁₀), 31.0 (CH₃, C₁₁);

ATR-IR ν_{max}/cm⁻¹: 3166 (w, C_{Ar}-H), 3122 (w, C_{Ar}-H), 2961 (w, CH₃ asym), 2870, 1618, 1588, 1548, 1513, 1475, 1457, 1421, 1363 (w, CH₃ umbrella mode), 1337, 1294, 1269, 1255, 1220, 1203, 1150 (s, imidazole bending), 1110, 1047, 1025, 841, 819, 770, 747, 729, 681, 656, 618, 556, 529;

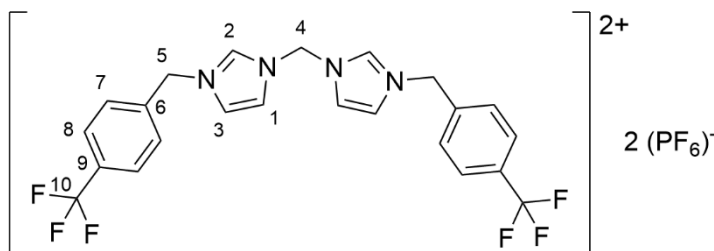
Elemental Analysis
Calculated for (C₂₉H₃₆F₁₂N₄P₂): C, 47.55; H, 5.32; N 7.65%; **Analysis Found:** C, 47.83; H, 4.50; N 7.56%

7.2.1.7 Synthesis of 1,1'-Bis(4-fluorobenzyl)-3,3'-methylenediimidazolium dihexafluorophosphate - $[H_2L6](PF_6)_2$ ¹⁶⁹



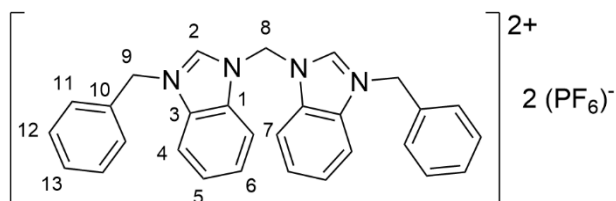
1-(4-Fluorobenzyl)-1*H*-imidazole (1.00g, 5.70 mmol) was dissolved in dibromomethane (2 mL) and heated to 80°C for 1 d, after which a precipitate formed. The mixture was allowed to cool to room temperature, the precipitate collected by vacuum filtration, and washed with Et₂O (3 x 40 mL), resulting in a white powder. The powder was then suspended in acetone (50 mL) after which ammonium hexafluorophosphate (1.15 g, 7.07 mmol) was then added. The mixture was then stirred for 1 d, and the solvent was removed under reduced pressure. The resulting solid was then stirred in deionised water (50 mL) for 1.5 h. The solid was then collected by vacuum filtration, washed with deionised water (2 x 40 mL) and Et₂O (3 x 40 mL), and dried *in vacuo* yielding a white powder (1.30 g, 1.98 mmol, 69%). **¹H NMR (400 MHz, DMSO-*d*₆, 298K) δ:** 9.41 (t, 2H, ⁴*J*(¹H-¹H) = 1.8 Hz, H₂), 7.97 (dd, 2H, ³*J*(¹H-¹H) = 2.1 Hz, ⁴*J*(¹H-¹H) = 1.8 Hz, H₁), 7.87 (dd, 2H, ³*J*(¹H-¹H) = 2.1 Hz, ⁴*J*(¹H-¹H) = 1.8 Hz, H₃), 7.55-7.49 (m, 4H, H₇), 7.33-7.29 (m, 4H, H₈), 6.57 (s, 2H, H₄), 5.46 (s, 4H, H₅); **¹³C{¹H} NMR (101 MHz, DMSO-*d*₆, 298K) δ:** 162.4 (Q C, d, ¹*J*(¹³C-¹⁹F) = 246 Hz, C₉), 137.7 (CH, C₂), 131.2 (CH, d, ³*J*(¹³C-¹⁹F) = 8.5 Hz, C₇), 130.4 (Q C, d, ⁴*J*(¹³C-¹⁹F) = 3.2 Hz, C₆), 123.1 (CH, C₃), 122.9 (CH, C₁), 116.0 (CH, d, ²*J*(¹³C-¹⁹F) = 20.2 Hz, C₈), 58.6 (CH₂, C₅), 51.60 (CH₂, C₄); **¹⁹F{¹H} NMR (471 MHz, DMSO-*d*₆, 298 K) δ:** -70.9 (PF₆, d, ¹*J*(¹⁹F-³¹P) = 710.6 Hz), -112.8 (CF); **ATR-IR ν_{max}/cm⁻¹:** 3188 (w, Ar-H), 3168 (w, C₂-H), 3319, 1613 (s), 1605 (m, aromatic C-C), 1586, 1561 (m, C₂-H), 1551, 1515 (s, aromatic C-C), 1457, 1428, 1361, 1339, 1297, 1261, 1224, 1153, 1114, 1049, 1018, 849, 825 (vs, br, PF₆), 776, 747, 712, 656, 618, 556, 538, 520; **Elemental Analysis Calculated for (C₂₁H₂₀F₁₄N₄P₂):** C, 38.43; H, 3.07; N 8.54%; **Analysis Found:** C, 38.33; H, 2.05; N 8.36%

7.2.1.8 Synthesis of 1,1'-Bis(4-trifluoromethylbenzyl)-3,3'-methylenediimidazolium dihexafluorophosphate - [H₂L7](PF₆)₂



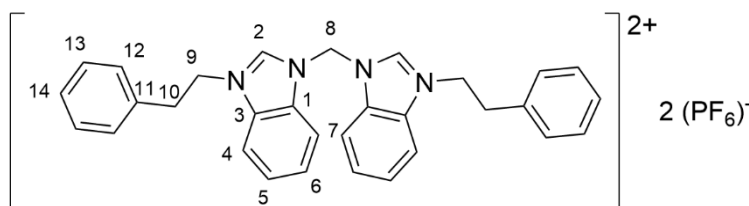
1-(4-Trifluoromethylbenzyl)-1*H*-imidazole (1.34 g, 5.92 mmol) was dissolved in dibromomethane (10 mL) and heated to reflux for 1 d, after which a precipitate formed. The mixture was allowed to cool to room temperature, the precipitate collected by vacuum filtration, washed with acetone (3 x 20 mL) and Et₂O (3 x 20 mL), and dried *in vacuo* resulting in a white powder. This powder was suspended in acetone (40 mL) after which ammonium hexafluorophosphate (1.25 g, 7.66 mmol) was added. The mixture was stirred for 24 h, the solvent evaporated, and the resulting white powder stirred in deionised water (40 mL) for 1 h. The precipitate was collected by vacuum filtration, washed with Et₂O (4 x 10 mL) and dried *in vacuo* yielding a white powder (1.57 g, 2.07 mmol, **92%**). **¹H NMR (500 MHz, DMSO-*d*₆, 298K) δ:** 9.47 (t, 2H, ⁴*J*(¹H-¹H) = 1.5 Hz, H₂), 8.00 (dd, 2H, ³*J*(¹H-¹H) = 2.0, ⁴*J*(¹H-¹H) = 1.5, H₁), 7.91 (dd, 2H, ³*J*(¹H-¹H) = 2.0, ⁴*J*(¹H-¹H) = 1.5, H₃), 7.84 (d, 4H, ³*J*(¹H-¹H) = 8.2 Hz, H₈), 7.64 (d, 4H, ³*J*(¹H-¹H) = 8.2 Hz, H₇), 6.60 (s, 2H, H₅), 5.50 (s, 4H, H₄); **¹³C{¹H} NMR (125 MHz, DMSO-*d*₆, 298K) δ:** 138.8 (Q, C₆), 138.1 (CH, C₂), 129.5 (Q, ²*J*(¹³C-¹⁹F) = 31.9 Hz, C₉), 129.4 (CH, C₇), 125.9 (CH, d, ³*J*(¹³C-¹⁹F) = 3.8 Hz, C₈), 124.1 (Q, ¹*J*(¹³C-¹⁹F) = 244.7 Hz, C₁₀), 123.4 (CH, C₃), 122.8 (CH, C₁), 58.6 (CH₂, C₄), 51.7 (CH₂, C₅); **¹⁹F{¹H} NMR (471 MHz, DMSO-*d*₆) δ:** -61.23 (CF₃), -70.1 (PF₆, ¹*J*(¹⁹F-³¹P) = 710.6 Hz); **ATR-IR ν_{max}/cm⁻¹:** 3171 (w, C_{Ar}-H), 3124 (w, C_{Ar}-H), 1622, 1589, 1552 (m, C₂-H), 1474, 1458, 1427, 1359, 1321, 1296, 1258, 1213, 1195, 1161 (s, imidazole bending), 1129, 1116, 1067, 1050, 1023, 967, 849, 819 (vs, br, PF₆), 775, 747, 729, 665, 635, 617, 594, 556, 506, 475, 463 **Elemental Analysis Calculated for (C₂₃H₂₀F₁₈N₄P₂):** C, 36.52; H, 2.67; N 7.41%; **Analysis Found:** C, 36.78; H, 1.79; N 7.35%

7.2.1.9 Synthesis of 1,1'-Bis(benzyl)-3,3'-methylenedibenzimidazolium dihexafluorophosphate - [H₂L8](PF₆)₂



1-(Benzyl)-1*H*-benzimidazole (1.00 g, 4.83 mmol) was dissolved in dibromomethane (10 mL) and heated at reflux for 1 d. The reaction mixture was allowed to cool to room temperature, during which a white precipitate formed. The precipitate was collected by vacuum filtration, washed with acetone (3 x 40 mL) and Et₂O (3 x 40 mL), and dried *in vacuo* resulting in a white powder. The precipitate was suspended in acetone (50 mL) and ammonium hexafluorophosphate (0.98 g, 6.00 mmol) was added. The mixture was stirred for 1.5 h, then filtered by gravity. The solvent was removed yielding a white solid, which was stirred in deionised water (50 mL) for 1 h. The precipitate was collected by vacuum filtration, washed with deionised water (2 x 40 mL) and Et₂O (3 x 40 mL) and dried *in vacuo* yielding a white powder (0.71 g, 0.98 mmol, 40 %) **¹H NMR (400 MHz, DMSO-*d*₆, 298K) δ**: 10.39 (s, 2H, H₂), 8.36 (d, 2H, ³*J*(¹H-¹H) = 8.4 Hz, H₇), 8.04 (d, 2H, ³*J*(¹H-¹H) = 8.3 Hz, H₄), 7.80 (t, 2H, ³*J*(¹H-¹H) = 7.7 Hz, H₆), 7.73 (t, 2H, ³*J*(¹H-¹H) = 7.8 Hz, H₅), 7.50-7.55 (m, 4H, H₁₁), 7.40 - 7.47 (m, 6H, H_{12,13}), 7.39 (s, 2H, H₈), 5.85 (s, 4H, H₉); **¹³C{¹H} NMR (101 MHz, DMSO-*d*₆, 298K) δ**: 144.1 (CH, C₂), 133.8 (Q C, C₁₀), 130.9 (Q C, C₁ or C₃), 130.8 (Q C, C₁ or C₃), 129.0 (CH, C₁₁), 129.0 (CH, C₁₂), 128.4 (CH, C₁₃), 127.6 (CH, C₅), 127.3 (CH, C₆), 114.4 (CH₂, C₄), 113.8 (CH, C₇), 55.3 (CH₂, C₈), 50.3 (CH₂, C₉); **ATR-IR ν_{max}/cm⁻¹**: 3159 (w, C_{Ar}-H), 3105 (w, C_{Ar}-H), 1617 (w, aromatic, C-C), 1569 (w, C2-H), 1489, 1476, 1457, 1427, 1400, 1344, 1315, 1273, 1261, 1217, 1186, 1139, 1084, 1016, 930, 826 (vs, br, PF₆), 773, 750, 740, 707, 696, 639, 615, 603, 583, 568, 555, 514, 469; **Elemental Analysis Calculated for (C₂₉H₂₆F₁₂N₄P₂)**: C, 48.35; H, 3.64; N 7.78%; **Analysis Found**: C, 48.27; H, 3.31; N 7.47%

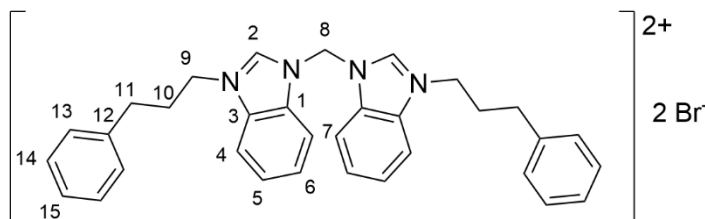
7.2.1.10 Synthesis of 1,1'-Bis(phenylethyl)-3,3'-methylenedibenzimidazolium dihexafluorophosphate – [H₂L9](PF₆)₂



1-(2-Phenylethyl)-1*H*-benzimidazole (0.40 g, 1.79 mmol) was dissolved in dibromomethane (10 mL) and heated to reflux for 1 d, after which a white precipitate formed. This was collected by vacuum filtration and washed with acetone (3 x 40 mL) and Et₂O (3 x 40 mL), resulting in a white powder. The powder was then suspended in acetone (50 mL) after which ammonium hexafluorophosphate (0.36 g, 2.24 mmol) was added. The mixture was stirred for 1 h, gravity filtered, and the solvent was removed under reduced pressure. The resulting solid was then stirred deionised water (50 mL) for 1 h. The solid was then collected by vacuum filtration, washed with deionised water (2 x 40 mL) and Et₂O (3 x 40 mL), and dried *in vacuo* yielding a white solid (0.28 g, 0.43 mmol, **48%**)

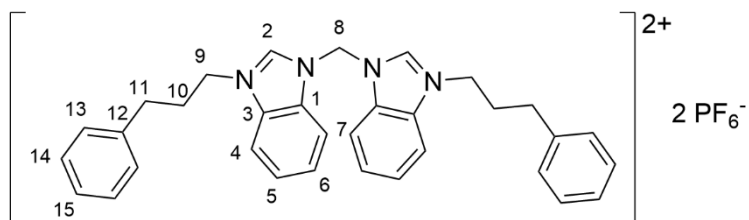
¹H NMR (400 MHz, DMSO-*d*₆, 298K) δ: 10.13 (s, 2H, H₂), 8.19 (d, ³*J*(¹H-¹H) = 8.2, 2H, H₇), 8.16 (d, ³*J*(¹H-¹H) = 8.0, 2H, H₄), 7.80 (t, 2H, ³*J*(¹H-¹H) = 8.0 Hz, H₆), 7.73 (t, 2H, ³*J*(¹H-¹H) = 8.0 Hz, H₅), 7.31 (s, 2H, H₈), 7.14-7.24 (m, 10H, H_{12,13,14}), 4.86 (t, 4H, ³*J*(¹H-¹H) = 7.3 Hz, H₉), 3.26 (t, 4H, ³*J*(¹H-¹H) = 7.3 Hz, H₁₀); **¹³C{¹H} NMR (101 MHz, DMSO-*d*₆, 298K) δ:** 143.6 (CH, C₂), 136.5 (Q C, C₁₁), 130.6 (Q C, C₁ or C₃), 130.2 (Q C, C₁ or C₃), 128.7 (CH, C₁₂), 128.6 (CH, C₁₃), 127.7 (CH, C₅ or C₆ or C₁₄), 127.3 (CH, C₅ or C₆ or C₁₄), 126.6 (CH, C₅ or C₆ or C₁₄), 114.4 (CH, C₄ or C₇), 113.5 (CH, C₄ or C₇), 55.0 (CH₂, C₈), 48.2 (CH₂, C₉), 34.3 (CH₂, C₁₀); **ATR-IR ν_{max}/cm⁻¹:** 3158 (w, C_{Ar}-H), 3099 (w, C_{Ar}-H), 1614 (w, aromatic, C-C), 1564 (m, C₂-H), 1492, 1476, 1456, 1426, 1408, 1391, 1366, 1331, 1275, 1214, 1192, 1166, 1142, 1083, 1038, 879, 825 (vs, br, PF₆), 750, 701, 629, 610, 589, 555, 488; **Elemental Analysis Calculated for (C₃₁H₃₀F₁₂N₄P₂):** C, 49.74; H, 4.04; N 7.48%; **Analysis Found:** C, 49.69; H, 4.21; N 7.31%

7.2.1.11 Synthesis of 1,1'-Bis(phenylpropyl)-3,3'-methylenedibenzimidazolium dibromide – $[H_2L10](Br)_2$



1-(3-Phenylpropyl)-1*H*-benzimidazole (1.50 g, 6.35 mmol) was dissolved in dibromomethane (10 mL) and heated to reflux for 1 d. The mixture was allowed to cool to room temperature, and the solvent was removed under reduced pressure. The resulting solid was washed with acetone (40 mL), collected by vacuum filtration, washed with acetone (4 x 20 mL) and Et₂O (4 x 20 mL), and dried *in vacuo* resulting in a white powder (1.64 g, 2.53 mmol, **80 %**). **¹H NMR (400 MHz, DMSO-*d*₆, 298K) δ**: 10.38 (s, 2H, H₂), 8.39 (d, 2H, ³*J*(¹H-¹H) = 8.0 Hz, H₇), 8.16 (d, 2H, ³*J*(¹H-¹H) = 8.0 Hz, H₄), 7.73 – 7.81 (m, 4H, H_{5,6}), 7.39 (s, 2H, H₈), 7.24 – 7.29 (m, 4H, H₁₄), 7.16 – 7.22 (m, 6H, H_{13,15}), 4.60 (t, 4H, ³*J*(¹H-¹H) = 7.0 Hz, H₉), 2.70 – 2.76 (m, 4H, H₁₁), 2.22 – 2.31 (m, 4H, H₁₀); **ATR-IR ν_{max}/cm⁻¹**: 3399 (m, H₂O), 3055 (w, C_{Ar}-H), 3022 (w, C_{Ar}-H), 2992 (w, CH₂), 2925 (w, CH₂), 2324, 2077, 1830, 1611 (w, aromatic, C-C), 1562 (w, C2-H), 1496, 1484, 1454, 1419, 1404, 1333, 1264, 1208, 1179, 1155, 1133, 1086, 1063, 1026, 1014, 951, 915, 787, 768, 755, 699, 607, 587, 530, 488

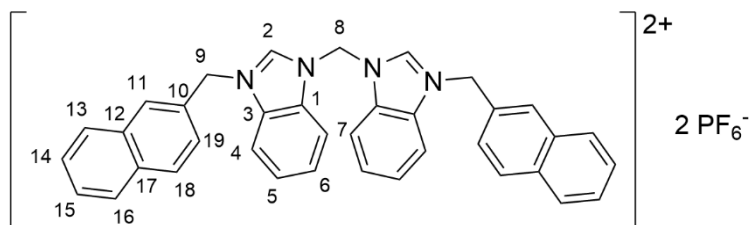
7.2.1.12 Synthesis of 1,1'-Bis(phenylpropyl)-3,3'-methylenedibenzimidazolium dihexafluorophosphate – $[H_2L10](PF_6)_2$



$[H_2L10](Br)_2$ (1.50 g, 2.32) was suspended in acetone (40 mL) after which ammonium hexafluorophosphate (1.51 g, 9.26 mmol) was added. The mixture was then stirred for 4 h, and the solvent removed under reduced pressure. The resulting off-white solid was stirred in deionised water (50 mL) for 1 h, collected by vacuum

filtration, washed with Et₂O (4 x 10 mL), and dried *in vacuo* yielding an off-white solid (1.57 g, 2.02 mmol, **87%**) ¹H NMR (400 MHz, DMSO-*d*₆, 298K) δ : 10.60 (s, 2H, H₂), 8.46 (d, 2H, ³*J*(¹H-¹H) = 8.2 Hz, H₇), 8.17 (d, 2H, ³*J*(¹H-¹H) = 8.2 Hz, H₄), 7.81-7.70 (m, 4H, H_{5,6}), 7.50 (s, 2H, H₄), 7.29-7.14 (m, 10H, H_{13,14,15}), 4.26 (t, 4H, ³*J*(¹H-¹H) = 7 Hz, H₉), 2.73 (t, 4H, ³*J*(¹H-¹H) = 7.2 Hz, H₁₁), 2.28 (p, 4H, ³*J*(¹H-¹H) = 7.2 Hz, H₁₀); ¹³C{¹H} NMR (101 MHz, DMSO-*d*₆, 298K) δ : 144.0 (CH, C₂), 140.5 (Q C, C₁₂), 131.1 (Q C, C₁ or C₃), 130.5 (Q C, C₁ or C₃), 128.4 (CH, C₁₃), 128.2 (CH, C₁₄), 127.4 (CH, C₅ or C₆), 127.1 (CH, C₅ or C₆), 126.1 (CH, C₁₅), 114.2 (CH, C₄), 113.8 (CH, C₇), 55.1 (CH₂, C₈), 47.0 (CH₂, C₉), 31.7 (CH₂, C₁₁), 29.9 (CH₂, C₁₀); ATR-IR $\nu_{\max}/\text{cm}^{-1}$: 3160 (w, C_{Ar}-H), 3096 (w, C_{Ar}-H), 2951 (w, CH₂), 1614 (w, aromatic, C-C), 1566 (m, C2-H), 1491, 1474, 1456, 1428, 1396, 1378, 1351, 1334, 1280, 1261, 1208, 1178, 1157, 1139, 1089, 1032, 826 (vs, br, PF₆), 791, 750, 705, 680, 664, 649, 587, 556, 502, 475; **Elemental Analysis Calculated for (C₃₃H₃₄F₁₂N₄P₂):** C, 51.04; H, 4.41; N 7.21%; **Analysis Found:** C, 50.95; H, 4.22; N 7.07%

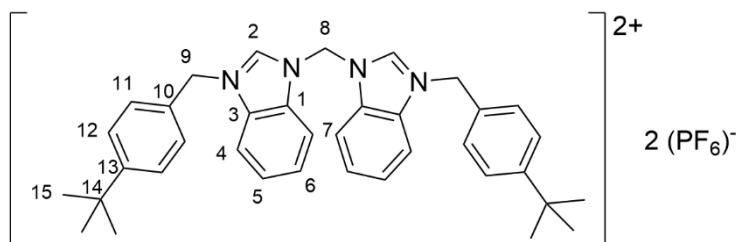
7.2.1.13 Synthesis of 1,1'-Bis(methylnaphthyl)-3,3'-methylenedibenzimidazolium dihexafluorophosphate – [H₂L11](PF₆)₂



1-(2-Naphthalenylmethyl)-1*H*-benzimidazole (0.72 g, 2.78 mmol) was dissolved in dibromomethane (10 ml) and heated to reflux 17 h. The resulting brownish solution was allowed to cool to room temperature, after which a white precipitate started to form. The solvent volume was reduced to 2 mL under reduced pressure, the precipitate collected by vacuum filtration, washed with acetone (3 x 40 mL) and Et₂O (3 x 40 mL), and dried *in vacuo*, giving a white powder. This powder was then stirred in acetone (50 mL) with ammonium hexafluorophosphate (0.57 g, 3.47 mmol) for 1 h. The suspension was gravity filtered, and the solvent was removed from the filtrate giving a white powder, which was then stirred in deionised water (50 mL) for 1 h. The solid was collected by vacuum filtration, washed with

deionised water (3 x 40 mL), Et₂O (3 x 40 mL) and MeOH (3 x 40 mL), and dried *in vacuo* yielding a white solid (0.20 g, 0.24 mmol, **17%**) **¹H NMR (400 MHz, DMSO-*d*₆, 298K) δ**: 10.38 (s, 2H, H₂), 8.37 (d, ³*J*(¹H-¹H) = 8.4 Hz, 2H, H₄), 8.08 – 8.13 (m, 4H, H_{Ar}), 7.99 (d, ³*J*(¹H-¹H) = 8.4 Hz, 2H, H₁₈ or H₁₉), 7.92 – 7.97 (m, 2H, H₁₃ or H₁₆), 7.87 – 7.92 (m, 2H, H₁₃ or H₁₆), 7.80 (td, 2H, ³*J*(¹H-¹H) = 8.0 Hz, ⁴*J*(¹H-¹H) = 1.0 Hz, H₆), 7.73 (dt, 2H, ³*J*(¹H-¹H) = 7.9 Hz, ⁴*J*(¹H-¹H) = 1.0 Hz, H₅), 7.56 – 7.61 (m, 6H, H_{nap}), 7.40 (s, 2H, H₈), 6.01 (s, 4H, H₉) **¹³C{¹H} NMR (101 MHz, DMSO-*d*₆, 298K) δ**: 143.4 (CH, C₂), 132.8 (Q C, C₁ or C₃), 132.7 (Q C, C₁ or C₃), 131.0 (Q C, C₁₂ or C₁₇), 130.8 (Q C, C₁₂ or C₁₇), 128.9 (CH, C₁₄ or C₁₅), 127.9 (CH, C_{Ar}, two resonances), 127.8 (CH, C_{Ar}), 127.6 (CH, C₅ or C₆), 127.4 (CH, C₅ or C₆), 127.0 (CH, C_{nap}), 126.9 (CH, C_{nap}), 125.7 (CH, C_{nap}), 114.4 (CH, C₄ or C₇), 113.8 (CH, C₄ or C₇), 55.4 (CH₂, C₈), 50.6 (CH₂, C₉), Q C₁₀ not found; **ATR-IR ν_{max}/cm⁻¹**: 3152 (w, C_{Ar}-H), 3133 (w, C_{Ar}-H), 3095 (w, C_{Ar}-H), 3050 (w, C_{Ar}-H), 1621, 1572 (m, C₂-H), 1463, 1449, 1421, 1404, 1384, 1323, 1246, 1230, 1168, 1119, 1066, 1017, 947, 844, 833 (vs, br, PF₆), 820, 792, 776, 749, 724, 713, 691, 670, 654, 636, 608, 591, 557, 502, 464; **Elemental Analysis Calculated for (C₃₇H₃₀F₁₂N₄P₂)**: C, 54.16; H, 3.69; N 6.83%; **Analysis Found**: C, 53.88; H, 3.72; N 6.52%

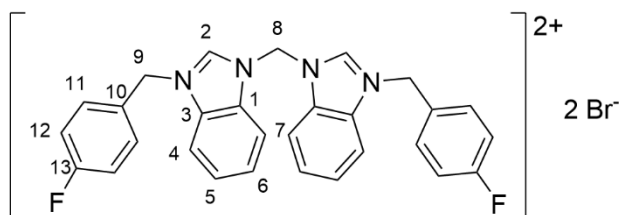
7.2.1.14 Synthesis of 1,1'-Bis(*p*-*tert*-butylbenzyl)-3,3'-methylenedibenzimidazolium dihexafluorophosphate – [H₂L12](PF₆)₂



1-(4-*tert*-Butylbenzyl)-1*H*-benzimidazole (2.01 g, 7.59 mmol) was dissolved in dibromoethane (10 mL) and heated to reflux for 1 d. The mixture was allowed to cool to room temperature, and the solvent removed under reduced pressure. The resulting yellow solid was washed with acetone (40 mL), collected by vacuum filtration, washed with acetone (2 x 40 mL) and Et₂O (3 x 40 mL), resulting in a white powder. The powder was then suspended in acetone (50 mL) after which ammonium hexafluorophosphate (1.54 g, 9.47 mmol) was then added. The mixture

was then stirred for 1 d, and the solvent was removed *in vacuo*. The resulting solid was stirred in deionised water (50 mL) for 1 h, collected by vacuum filtration, washed with deionised water (2 x 40 mL) and Et₂O (3 x 40 mL), and dried *in vacuo* yielding a white solid (2.28 g, 2.74 mmol, **72%**) **¹H NMR (400 MHz, DMSO-*d*₆, 298K) δ**: 10.38 (s, 2H, H₂), 8.36 (d, 2H, ³*J*(¹H-¹H) = 8.4 Hz, H₇), 8.10 (d, 2H, ³*J*(¹H-¹H) = 8.4 Hz, H₄), 7.80 (t, 2H, ³*J*(¹H-¹H) = 8.0 Hz, H₆), 7.73 (t, 2H ³*J*(¹H-¹H) = 8.0 Hz, H₅), 7.42 – 7.51 (m, 8H, H_{11,12}), 7.38 (s, 2H, H₈), 5.80 (s, 4H, H₉), 1.26 (s, 18H, H₁₅); **¹³C{¹H} NMR (101 MHz, DMSO-*d*₆, 298K) δ**: 151.5 (Q C, C₁₃), 144.0 (CH, C₂), 130.9 (Q C, C₁ or C₃ or C₁₀), 130.8 (Q C, C₁ or C₃ or C₁₀), 130.6 (Q C, C₁ or C₃ or C₁₀), 128.3 (CH, C₁₁ or C₁₂), 127.6 (CH, C₅ or C₆), 127.3 (CH, C₅ or C₆), 125.8 (CH, C₁₁ or C₁₂), 114.4 (CH, C₄), 113.8 (CH, C₇), 55.3 (CH₂, C₈), 50.0 (CH₂, C₉), 34.4 (Q, C₁₄), 30.7 (CH₃, C₁₅); **ATR-IR ν_{max}/cm⁻¹**: 3157 (w, C_{Ar}-H), 3096 (w, C_{Ar}-H), 2965 (CH₃, asym), 1710, 1614 (w, aromatic, C-C), 1561 (m, C₂-H), 1516 (w, aromatic, C-C), 1491, 1474, 1447, 1408, 1361 (m, CH₃, umbrella mode), 1336, 1291, 1273, 1218, 1193, 1137, 1109, 1029, 829 (vs, PF₆), 785, 750, 707, 680, 636, 615, 584, 556, 532, 471, 458; **Elemental Analysis Calculated for (C₃₇H₄₂F₁₂N₄P₂)**: C, 53.37; H, 5.08; N 6.73%; **Analysis Found**: C, 53.55; H, 5.51; N 6.33%

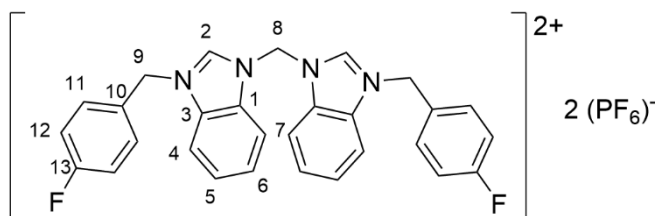
7.2.1.15 Synthesis of 1,1'-Bis(*p*-fluorobenzyl)-3,3'-methylenedibenzimidazolium dibromide – [H₂L13](Br)₂¹⁶⁹



1-(4-Fluorobenzyl)-1*H*-benzimidazole (1.50 g, 6.63 mmol) was dissolved in dibromomethane (10 mL) and heated to reflux for 1 d. The mixture was allowed to cool to room temperature, and the solvent was removed under reduced pressure. The resulting yellow solid was washed with acetone (40 mL), collected by vacuum filtration, washed further with acetone (4 x 10 mL) and Et₂O (4 x 10 mL), and dried *in vacuo* resulting in a white powder (1.58 g, 2.52 mmol, **76%**). **¹H NMR (400 MHz, DMSO-*d*₆, 298K) δ**: 10.48 (s, 2H, H₂), 8.39 (d, 2H, ³*J*(¹H-¹H) = 8.4 Hz, H₇), 8.04 (d, 2H, ³*J*(¹H-¹H) = 8.4 Hz, H₄), 7.79 (td, 2H, ³*J*(¹H-¹H) = 8.4, Hz, ⁴*J*(¹H-¹H) =

0.8 Hz, H₆), 7.72 (td, 2H, $^3J(^1\text{H}-^1\text{H}) = 7.8$, Hz, $^4J(^1\text{H}-^1\text{H}) = 0.8$ Hz, H₅), 7.61 – 7.68 (m, 4H, H₁₁), 7.43 (s, 2H, H₈), 7.26 – 7.33 (m, 4H, H₁₂), 5.85 (s, 4H, H₉); $^{13}\text{C}\{^1\text{H}\}$ NMR (125.8 MHz, DMSO-*d*₆, 298K) δ : 162.3 (Q $\underline{\text{C}}$, d, $^1J(^{13}\text{C}-^{19}\text{F}) = 245.3$ Hz, C₁₃), 144.2 ($\underline{\text{CH}}$, C₂), 131.1 ($\underline{\text{CH}}$, d, $^3J(^{13}\text{C}-^{19}\text{F}) = 8.8$ Hz, C₁₁), 130.74 (Q $\underline{\text{C}}$, C₁ or C₃), 130.72 (Q, C₁ or C₃), 129.7 (Q, d, $^4J(^{13}\text{C}-^{19}\text{F}) = 3.8$ Hz, C₁₀), 127.6 ($\underline{\text{CH}}$, C₅ or C₆), 127.3 ($\underline{\text{CH}}$, C₅ or C₆), 115.9 ($\underline{\text{CH}}$, d, $^2J(^{13}\text{C}-^{19}\text{F}) = 21.4$ Hz, C₁₂), 114.3 ($\underline{\text{CH}}$, C₄), 114.0 ($\underline{\text{CH}}$, C₇), 55.4 ($\underline{\text{CH}_2}$, C₈), 49.5 ($\underline{\text{CH}_2}$, C₉); $^{19}\text{F}\{^1\text{H}\}$ NMR (471 MHz, DMSO-*d*₆) δ : -112.8 (ArF); ATR-IR $\nu_{\text{max}}/\text{cm}^{-1}$: 3459 (s, asym (H₂O)), 3401 (m, s(H₂O)), 3125 (w, C_{Ar}-H), 3109 (s, C_{Ar}-H), 2991 (m, br, C₂-H), 2065, 1784, 1606 (w, aromatic C-C), 1556 (s, C₂-H), 1511 (s, aromatic C-C), 1488, 1475, 1439, 1429, 1416, 1377, 1357, 1345, 1305, 1274, 1213, 1193, 1158, 1129, 1100, 1040, 1013, 979, 957, 940, 930, 899, 844, 833, 822, 813, 797, 789, 767, 745, 713, 685, 652, 631, 615, 587, 572, 540, 530, 510, 488, 463; Elemental Analysis Calculated for (C₂₉H₂₄Br₂F₂N₄·H₂O): C, 54.06; H, 4.07; N 8.70%; Analysis Found: C, 54.33; H, 3.51; N 8.12%.

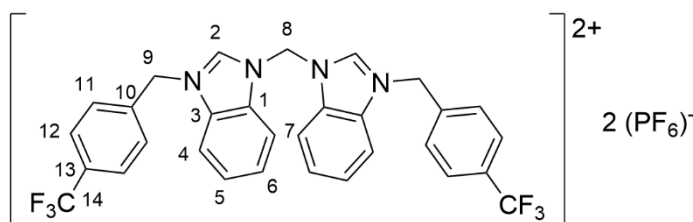
7.2.1.16 Synthesis of 1,1'-Bis(*p*-fluorobenzyl)-3,3'-methylenedibenzimidazolium dihexafluorophosphate - [H₂L13](PF₆)₂¹⁶⁹



[H₂L13](Br) (1.50 g, 2.39 mmol) was suspended in acetone (50 mL) after which ammonium hexafluorophosphate (0.98 g, 6.01 mmol) was then added. The mixture was then stirred for 1 d. The resulting suspension was then gravity filtered, and the solvent was removed under reduced pressure. The resulting white solid was then stirred in deionised water (50 mL) for 1 h. The solid was then collected by vacuum filtration and washed with deionised water (2 x 40 mL) and Et₂O (3 x 40 mL) and dried *in vacuo* yielding a white powder (1.65 g, 2.18 mmol, 91%) ^1H NMR (400 MHz, DMSO-*d*₆, 298K) δ : 10.30 (s, 2H, H₂), 8.34 (d, 2H, $^3J(^1\text{H}-^1\text{H}) = 8.4$ Hz, H₇), 8.04 (d, 2H, $^3J(^1\text{H}-^1\text{H}) = 8.4$ Hz, H₄), 7.80 (td, 2H, $^3J(^1\text{H}-^1\text{H}) = 7.3$ Hz, $^4J(^1\text{H}-^1\text{H}) = 0.9$ Hz, H₆), 7.73 (td, 2H, $^3J(^1\text{H}-^1\text{H}) = 7.3$ Hz, $^4J(^1\text{H}-^1\text{H}) = 0.9$ Hz, H₅), 7.63-7.56 (m, 4H, H₁₂), 7.35 (s, 2H, H₈), 7.33-7.27 (m, 4H, H₁₁), 5.81 (s, 4H, H₉); $^{13}\text{C}\{^1\text{H}\}$

NMR (101 MHz, DMSO-*d*₆, 298 K) δ : 162.3 (Q $\underline{\text{C}}$, d, $^1J(^{13}\text{C}-^{19}\text{F}) = 245.5$ Hz, C₁₃), 144.1 ($\underline{\text{CH}}$, C₂), 130.9 ($\underline{\text{CH}}$, d, $^3J(^{13}\text{C}-^{19}\text{F}) = 8.0$ Hz, C₁₁), 130.80 (Q $\underline{\text{C}}$, C₁ or C₃), 130.79 (Q $\underline{\text{C}}$, C₁ or C₃), 129.6 (Q $\underline{\text{C}}$, d, $^4J(^{13}\text{C}-^{19}\text{F}) = 3.0$ Hz, C₁₀), 127.6 ($\underline{\text{CH}}$, C₅ or C₆), 127.4 ($\underline{\text{CH}}$, C₅ or C₆), 116.0 ($\underline{\text{CH}}$, d, $^2J(^{13}\text{C}-^{19}\text{F}) = 22.1$ Hz, C₁₂), 114.3 ($\underline{\text{CH}}$, C₄), 113.8 ($\underline{\text{CH}}$, C₇), 55.3 ($\underline{\text{CH}_2}$, C₈), 49.6 ($\underline{\text{CH}_2}$, C₉); **$^{19}\text{F}\{^1\text{H}\}$ NMR (471 MHz, DMSO-*d*₆, 298 K) δ :** -70.1 (PF_6 , d, $^1J(^{19}\text{F}-^{31}\text{P}) = 710.6$ Hz,) -112.7 (CF); **ATR-IR $\nu_{\text{max}}/\text{cm}^{-1}$:** 3164 (w, C_{Ar}-H), 3147 (w, C₂-H) 3109 (m, C_{Ar}-H), 2323, 2193, 2169, 2052, 1980, 1785, 1616 (w, aromatic C-C), 1571 (m, C₂-H), 1516 (s, aromatic C-C), 1493, 1476, 1455, 1428, 1400, 1384, 1364, 1343, 1321, 1272, 1260, 1237, 1216, 1187, 1164, 1141, 1100, 1017, 988, 943, 873, 829 (vs, br, PF₆), 811, 782, 764, 749, 739, 695, 628, 600, 576, 554, 537, 519, 475; **Elemental Analysis Calculated for (C₂₉H₂₄F₁₄N₄P₂):** C, 46.05; H, 3.20; N 7.41%; **Analysis Found:** C, 45.79; H, 2.41; N 7.34%

7.2.1.17 Synthesis of 1,1'-Bis(*p*-trifluoromethylbenzyl)-3,3'-methylenedibenzimidazolium dihexafluorophosphate – [H₂L14](PF₆)₂

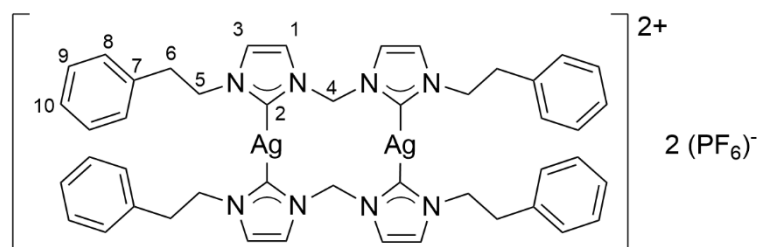


1-(4-(Trifluoromethylbenzyl)-1*H*-benzimidazole (1.00 g, 3.62 mmol) was dissolved in dibromoethane (10 mL) and heated to reflux for 1 d. After which the mixture was allowed to cool down, and the precipitate that formed was collected by vacuum filtration and washed with a further acetone (3 x 40 mL) and Et₂O (3 x 40 mL) resulting in a white powder. The powder was then suspended in acetone (50 mL) after which ammonium hexafluorophosphate (0.74 g, 4.53 mmol) was then added. The mixture was then stirred for 1 h. The resulting suspension was then gravity filtered, and the solvent was removed under reduced pressure. The resulting solid was then stirred in deionised water (50 mL) for 1 h. The solid was then collected by vacuum filtration and washed with deionised water (2 x 40 mL) and Et₂O (3 x 40 mL) and dried *in vacuo* yielding a white powder (0.81 g, 0.95 mmol, 52%) **^1H NMR (400 MHz, DMSO-*d*₆, 298K) δ :** 10.37 (s, 2H, H₂), 8.39 (d, 2H, $^3J(^1\text{H}-^1\text{H}) = 8.4$ Hz, H₇), 8.03 (d, 2H, $^3J(^1\text{H}-^1\text{H}) = 8.3$ Hz, H₄), 7.85-7.79 (m, 6H, H_{6,12}), 7.76-7.70 (m,

6H, H_{5,11}), 7.41 (s, 2H, H₈), 5.97 (s, 4H, H₉), 2.08 (acetone); $^{13}\text{C}\{^1\text{H}\}$ NMR (101 MHz, DMSO-*d*₆) δ : 144.6 ($\underline{\text{CH}}$, C₂), 138.2 (Q $\underline{\text{C}}$, C₁₀), 130.85 (Q $\underline{\text{C}}$, C₁ or C₃), 130.83 (Q $\underline{\text{C}}$, C₁ or C₃) 129.4 (Q $\underline{\text{C}}$, q, $^2J(^{13}\text{C}-^{19}\text{F}) = 32.0$ Hz, C₁₃) 129.2 ($\underline{\text{CH}}$, C₁₁), 127.7 ($\underline{\text{CH}}$, C₅ or C₆), 127.4 ($\underline{\text{CH}}$, C₅ or C₆), 125.9 ($\underline{\text{CH}}$, q, $^3J(^{13}\text{C}-^{19}\text{F}) = 3.7$ Hz, C₁₂), 124.0 (Q, q, $^1J(^{13}\text{C}-^{19}\text{F}) = 272.7$ Hz, C₁₄), 114.2 ($\underline{\text{CH}}$, C₄), 114.0 ($\underline{\text{CH}}$, C₇), 55.4 ($\underline{\text{CH}_2}$, C₈), 49.7 ($\underline{\text{CH}_2}$, C₉), 30.7 (acetone); ATR-IR $\nu_{\text{max}}/\text{cm}^{-1}$: 3156 (w, C_{Ar}-H), 3095, 1616 (w, aromatic C-C), 1563, 1476, 1455, 1412, 1362, 1322, 1278, 1219, 1194, 1165, 1131, 1115, 1067, 1032, 1019, 831 (vs, br, PF₆), 787, 755, 740, 677, 640, 594, 579, 556; **Elemental Analysis Calculated for (C₃₂H₂₈F₁₈N₄P₂):** C, 44.05; H, 3.23; N 6.42%; **Analysis Found:** C, 44.14; H, 2.37; N 6.30%

7.2.2 Binuclear Silver(I) *N*-Heterocyclic Carbene Complexes

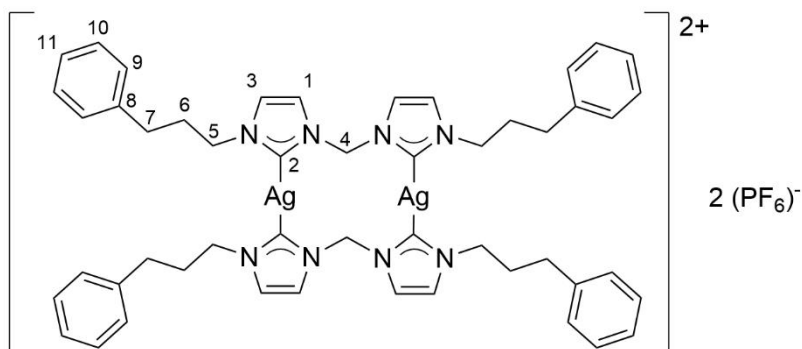
7.2.2.1 Synthesis of Di(1,1'-bis(phenylethyl)-3,3'-methylenedibenzimidazolium-2-ylidene))disilver(I) dihexafluorophosphate - [Ag₂(L2)₂](PF₆)₂



In the absence of light [H₂L2](Br)₂ (0.30 g, 0.58 mmol) and silver(I) oxide (0.33 g, 1.44 mmol) were stirred in MeOH (10 mL) for 19 h after which the brown suspension was passed through Celite® and the volume was made up to 10 mL. This colourless solution was stirred and to the solution ammonium hexafluorophosphate (0.20 g, 1.22 mmol) dissolved in deionised water (10 mL) was added forming a white suspension, the mixture was stirred for 2 h after which the precipitate was collected by vacuum filtration and washed with deionised water (3 x 25 mL) and Et₂O (3 x 25 mL) and dried *in vacuo* yielding a white powder (0.11 g, 0.09 mmol, 31%) ^1H NMR (400 MHz, DMSO-*d*₆, 298K) δ : 7.80 (br, 4H, H₁), 7.55 (br, 4H, H₃), 7.17-7.09 (m, 12H, H₁₀ and H₉ or H₈), 6.97-6.92 (m, 8H, H₉ or H₈), 6.85-6.13 (br, 4H, H₄), 4.33 (t, 8H, $^3J(^1\text{H}-^1\text{H}) = 7.0$ Hz, H₅), 3.03 (t, 8H, $^3J(^1\text{H}-^1\text{H}) = 7.0$ Hz, H₆); $^{13}\text{C}\{^1\text{H}\}$ NMR (101 MHz, DMSO-*d*₆, 298K) δ : 137.8 (Q $\underline{\text{C}}$, C₇), 129.0 ($\underline{\text{CH}}$, C₈), 128.9 ($\underline{\text{CH}}$, C₉), 127.1 ($\underline{\text{CH}}$, C₁₀), 123.5 ($\underline{\text{CH}}$, C₃), 122.3 ($\underline{\text{CH}}$, C₁), 64.0 ($\underline{\text{CH}_2}$, C₄), 53.1 ($\underline{\text{CH}_2}$, C₅), 37.4 ($\underline{\text{CH}_2}$, C₆), C₂ not found; ATR-IR $\nu_{\text{max}}/\text{cm}^{-1}$

3141 (w, C_{Ar}-H), 1573 (w, imidazole ring stretching), 1496, 1455, 1426, 1334, 1236, 1197, 1118, 1082, 1056, 1030, 830 (vs, PF₆), 787, 743, 702, 670, 556, 496;
Elemental Analysis Calculated for (C₄₆H₅₂Ag₂F₁₂N₈P₂): C, 45.34; H, 9.20; N 3.97%; **Analysis Found**: C, 45.54; H, 8.91; N 3.44%.

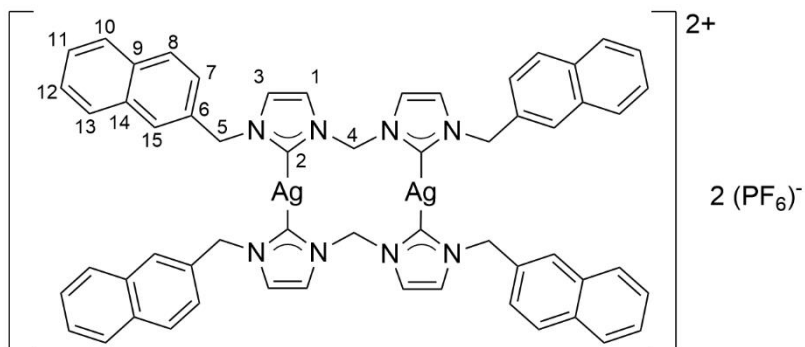
7.2.2.2 Synthesis of Di(1,1'-bis(phenylpropyl)-3,3'-methylenediimidazolium-2-ylidene))disilver(I) dihexafluorophosphate - [Ag₂(L3)](PF₆)₂



In the absence of light [H₂L3](PF₆)₂ (0.5 g, 0.74 mmol) and silver(I) oxide (0.43 g, 1.84 mmol) were stirred in MeCN (6 ml) for 19 h in darkness. The mixture was passed through Celite® and the solvent was removed under reduced giving a brown waxy solid. The solid was washed with Et₂O (20 mL) followed heating in hot MeOH (*ca.* 20 mL), this gave a white powder which was then collected via vacuum filtration and washed with Et₂O (3 x 40 mL) and dried *in vacuo* giving a white powder which was dissolved in MeCN (3 mL) and crystallised through vapour diffusion of Et₂O, the crystals that formed were collected by vacuum filtration and washed with MeOH (3 x 40 mL) and Et₂O (3 x 40 mL) and dried *in vacuo* yielding off-white crystals (0.12 g, 0.095 mmol, **26%**). **¹H NMR (400 MHz, DMSO-*d*₆, **298K**) δ**: 7.89 (d, 4H, ³*J*(¹H-¹H) = 1.9 Hz, H₁), 7.65 (d, 4H, ³*J*(¹H-¹H) = 1.8 Hz, H₃), 7.11 – 7.03 (m, 12H, H₁₁ and H₁₀ or H₉), 7.00 – 6.93 (m, 8H, H₁₀ or H₉), 6.92 – 6.16 (br, 4H, H₄), 3.91 (t, 8H, ³*J*(¹H-¹H) = 7.6 Hz, H₅), 2.41 (t, 8H, ³*J*(¹H-¹H) = 7.5 Hz, H₇), 1.94 (quint, ³*J*(¹H-¹H) = 7.5 Hz, 8H, H₆); **¹³C{¹H} NMR (101 MHz, DMSO-*d*₆, **298K**) δ**: 140.2 (Q ⊂, C₈), 128.2 (⊂CH, C₉), 128.1 (⊂CH, C₁₀), 125.9 (⊂CH, C₁₁), 122.9 (⊂CH, C₃), 122.0 (⊂CH, C₁), 63.3 (⊂CH₂, C₄), 50.8 (⊂CH₂, C₅), 32.1 (⊂CH₂, C₆), 31.5 (⊂CH₂, C₇), C₂ not found; **ATR-IR ν_{max}/cm⁻¹**: 3178 (w, C_{Ar}-H), 1744, 1573 (w, imidazole ring stretch), 1496, 1455, 1422, 1371, 1334, 1232, 1154, 1115, 1057, 828 (vs, PF₆), 784, 743, 701, 655; **Elemental Analysis Calculated for**

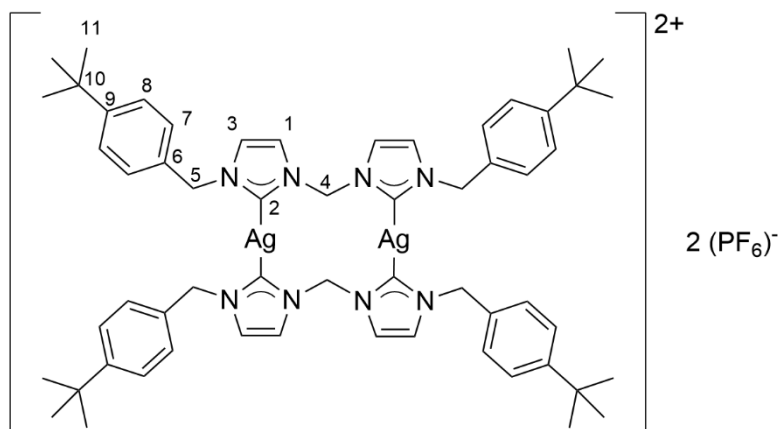
(C₅₀H₅₆Ag₂F₁₂N₈P₂): C, 47.11; H, 4.43; N 8.79%; **Analysis Found:** C, 46.67; H, 4.15; N 8.70%

7.2.2.3 Synthesis of Di(1,1'-bis(phenylpropyl)-3,3'-methylenediimidazolium-2-ylidene))disilver(I) dihexafluorophosphate - [Ag₂(L4)₂](PF₆)₂



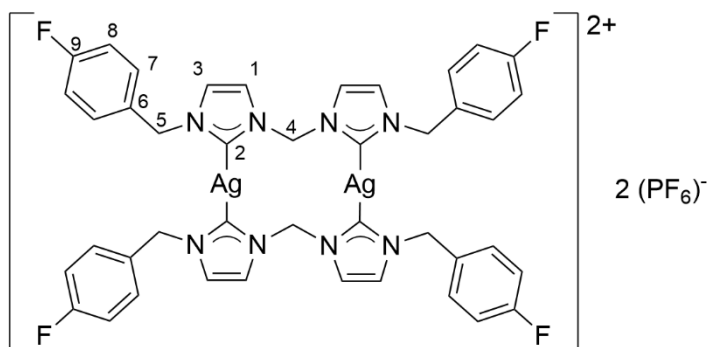
In the absence of light [H₂L4](Br)₂ (0.50g, 0.84 mmol) and silver(I) oxide (0.69 g, 2.96 mmol) were stirred in MeOH (10 mL) 19 h and filtered through Celite® twice, the level of the solvent was made up to 20 mL, this yellow solution was then stirred and ammonium hexafluorophosphate (0.29 g, 1.77 mmol) in deionised water (20 mL), this mixture was stirred for 3 h after which the white precipitate was collected by vacuum filtration and washed with deionised water (3 x 40 mL) and Et₂O (3 x 40 mL) and dried *in vacuo* yielding a white powder (0.13 g, 0.09 mmol, **21%**) ¹H NMR (400 MHz, DMSO-*d*₆, 298K) δ: 7.86 (d, 4H, ³J(¹H-¹H) = 1.9 Hz, H₁), 7.77 (d, ³J(¹H-¹H) = 8.5 Hz, H₇ or H₈), 7.66 (d, 4H, ³J(¹H-¹H) = 8.5 Hz, H₇ or H₈), 7.58 – 7.63 (m, 8H, H_{Ar}), 7.39 – 7.49 (m, 12H, H_{nap}), 7.07 (dd, 4H, ³J(¹H-¹H) = 8.5, ⁴J(¹H-¹H) = 1.8 Hz, H₁₀ or H₁₃), 6.20 – 6.88 (br, 4H, H₄), 5.20 (s, 8H, H₅); ¹³C{¹H} NMR (101 MHz, DMSO-*d*₆, 298K) δ: 134.0 (Q C, C₆), 132.5 (Q C, C₉ or C₁₄), 132.3 (Q C, C₉ or C₁₄), 128.4 (CH, C₇ or C₈), 127.5 (CH, C_{nap}), 127.5 (CH, C_{nap}), 126.6 (CH, C_{nap}), 126.4 (CH, C_{nap}), 126.0 (CH, C_{nap}), 124.7 (CH, C_{nap}), 123.7 (CH, C₁), 122.2 (CH, C₃), 65.4 (CH₂, C₄), 54.7 (CH₂, C₅), 15.6 (Et₂O), C₂ not found; ATR-IR ν_{max}/cm⁻¹: 3171 (w, C_{Ar}-H), 2195, 1573 (w, imidazole ring stretching), 1510, 1462, 1403, 1372, 1332, 1238, 1165, 1117, 1056, 968, 836 (vs, PF₆), 790, 764, 738, 620, 557, 477; **Elemental Analysis Calculated for (C₅₈H₄₈Ag₂F₁₂N₈P₂):** C, 51.12; H, 3.55; N 8.22%; **Analysis Found:** C, 50.84; H, 3.26; N 7.87%

7.2.2.4 Synthesis of Di(1,1'-bis(4-tertbutylbenzyl)-3,3'-methylenediimidazolium-2-ylidene))disilver(I) dihexafluorophosphate - [Ag₂(L5)₂](PF₆)₂



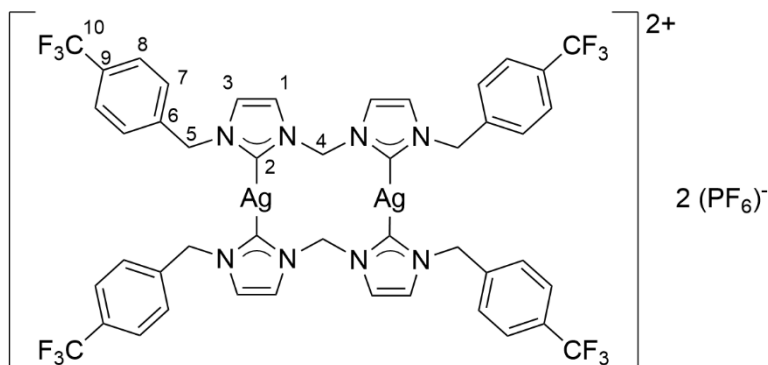
In the absence of light [H₂L5](Br)₂ (0.15 g, 0.25 mmol) was stirred with silver(I) oxide (0.14 g, 0.62 mmol) in MeOH (10 mL) for 19 h, the brown suspension was then passed through Celite®, the light yellow filtrate was made up to 20 mL with MeOH after which ammonium hexafluorophosphate (0.09 g, 0.56 mmol) dissolved in deionised water (20 mL) was added forming a white suspension, the mixture was stirred for 3 h, and the white precipitate was collected by vacuum filtration and washed with deionised water (3 x 40 mL) and Et₂O (3 x 40 mL) and dried *in vacuo* yielding a white powder (0.05 g, 0.03 mmol, **28%**) ¹H NMR (400 MHz, DMSO-*d*₆, **298K**) δ: 7.88 (d, 4H, ³J(¹H-¹H) = 1.9 Hz, H₁), 7.62 (d, 4H, ³J(¹H-¹H) = 1.8 Hz, H₃), 7.23 (m, 8H, H₇), 7.07 (m, 8H, H₈), 7.02 – 6.26 (m, 4H, H₄), 5.20 (s, 8H, H₅), 1.14 (s, 36H, H₁₁); ¹³C{¹H} NMR (101 MHz, DMSO-*d*₆, **298K**) δ: 150.5 (Q C, C₆ or C₉), 133.5 (Q C, C₆ or C₉), 127.1 (CH, C₇ or C₈), 125.5 (CH, C₇ or C₈), 123.5 (CH, C₁), 122.4, (CH, C₃), 63.5 (CH₂, C₄), 54.2 (CH₂, C₅), 34.2 (Q C, C₁₀), 30.9 (CH₃, C₁₁), C₂ not found; ATR-IR ν_{max}/cm⁻¹: 3142 (w, C_{Ar}-H), 2959 (m, CH₃, asym), 2868, 1571 (w, imidazole ring stretch), 1516, 1462, 1402, 1364 (m, CH₃, umbrella mode), 1343, 1270, 1239, 1163, 1109, 1054, 1018, 829 (vs, PF₆), 788, 775, 736, 684, 649, 612, 556; **Elemental Analysis Calculated for (C₅₈H₇₂Ag₂F₁₂N₄P₂):** C, 50.23; H, 5.32; N 8.08%; **Analysis Found:** C, 50.20; H, 4.40; N 7.89%

7.2.2.5 Synthesis of Di(1,1'-bis(4-fluorobenzyl)-3,3'-methylenediimidazolium-2-ylidene))disilver(I) dihexafluorophosphate - $[Ag_2(L6)_2](PF_6)_2$ ¹⁶⁹



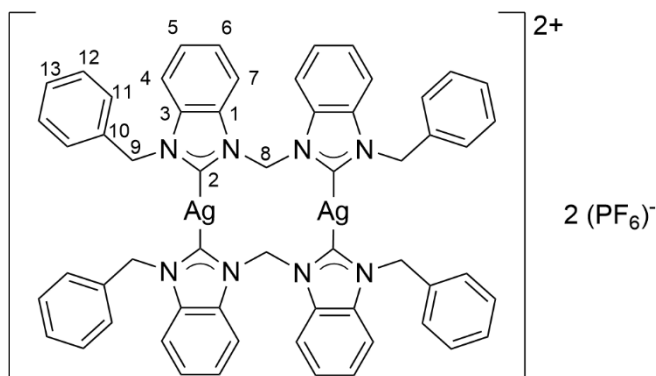
In the absence of light $[H_2L6](Br)_2$ (0.20 g, 0.38 mmol) and silver(I) oxide (0.22 g, 0.95 mmol) were stirred in MeOH (10 mL) for 19 h, the resulting brown suspension was passed through Celite® giving a light-yellow solution and the volume was made up to 20 mL. To the MeOH solution ammonium hexafluorophosphate (0.13 g, 0.80 mmol) in deionised water (60 mL) was added this formed a white suspension, the mixture was stirred for 1 h, the white precipitate was collected by vacuum filtration and washed with deionised water (3 x 40 mL) and Et₂O (3 x 40 mL) and dried *in vacuo* yielding a white powder (0.13 g, 0.11 mmol, **56%**) ¹H NMR (**500 MHz, DMSO-*d*₆, 298K**) δ : 7.91 (d, 4H, $^3J(^1H-^1H) = 1.58$ Hz, H₃), 7.60 (d, 4H, $^3J(^1H-^1H) = 1.76$ Hz, H₁), 7.11-7.15 (m, 8H, H₈), 7.04-7.09 (m, 8H, H₇), 6.22 – 7.02 (br, 4H, H₄), 5.23 (s, 8H, H₅) ¹³C{¹H} NMR (**101 MHz, DMSO-*d*₆, 298K**) δ : 181.5 (Q C, d, $J(^{13}C-^{109}Ag) = 213.9$) and d, $J(^{13}C-^{107}Ag) = 176.1$, C₂), 161.7 (\underline{CH} , d, $^1J(^{13}C-^{19}F) = 244.7$ Hz, C₉), 132.8 (Q \underline{C} , d, $^4J(^{13}C-^{19}F) = 2.5$ Hz, C₆) 129.2 (\underline{CH} , d, $J(^{13}C-^{19}F) = 8.3$ Hz, C₇), 123.5 (\underline{CH} , C₁), 122.5 (\underline{CH} , C₃), 115.6 (\underline{CH} , d, $J(^{13}C-^{19}F) = 21.7$ Hz, C₈), 63.6 (\underline{CH}_2 , C₄), 53.6 (\underline{CH}_2 , C₅); ¹⁹F{¹H} NMR (**470.6 MHz, DMSO-*d*₆**) δ : -70.1 (\underline{PF}_6 , $^1J(^{19}F-^{31}P) = 710.6$ Hz) -114.1 (\underline{CF}); ATR-IR ν_{max}/cm^{-1} : 3176 (w, C_{Ar}-H), 1606 (m, aromatic C-C), 1573 (w, imidazole ring stretch), 1511 (s, aromatic C-C), 833 (vs, br, PF₆); **Elemental Analysis Calculated for (C₄₂H₃₆Ag₂F₁₆N₈P₂):** C, 40.86; H, 2.94; N 9.08%; **Analysis Found:** C, 40.96; H, 2.41; N 8.69%.

7.2.2.6 Synthesis of Di(1,1'-bis(4-trifluoromethylbenzyl)-3,3'-methylenediimidazolium-2-ylidene))disilver(I) dihexafluorophosphate - [Ag₂(L7)₂](PF₆)₂



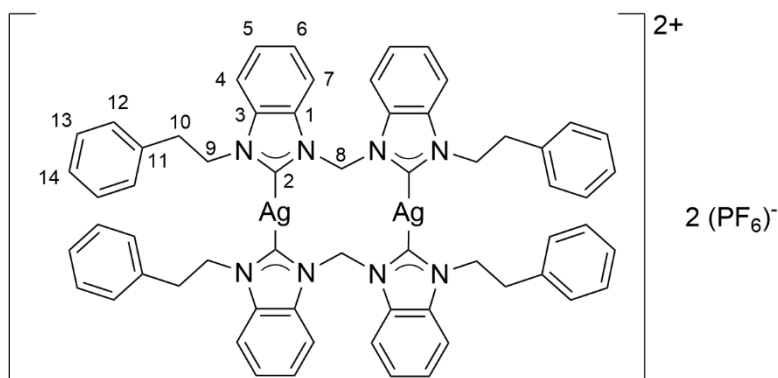
In the absence of light **[H₂L7](PF₆)₂** (0.20 g, 0.26 mmol) and silver(I) oxide (0.14 g, 0.58 mmol) were stirred in MeCN (15 ml) for 19 h. The mixture was passed through Celite® and the solvent was removed under reduced pressure, the white oil was dissolved in MeOH (5 mL) and precipitated by the addition of deionised water (40 mL) forming a white precipitate which was collected by vacuum filtration, and washed with Et₂O (40 mL) after which the sample became oily, the oil was redissolved in MeOH (10 mL) and the solvent was removed under *in vacuo* yielding a greyish powder (0.04 g, 0.027 mmol, 23%). **¹H NMR (400 MHz, DMSO-*d*₆, 298K) δ:** 7.95 (d, 4H, ³*J*(¹H-¹H) = 1.7 Hz, H₁), 7.61 (d, 4H, ³*J*(¹H-¹H) = 1.7 Hz, H₃), 7.54 (d, 8H, ³*J*(¹H-¹H) = 8.2, H₈), 7.23 (d, 8H, ³*J*(¹H-¹H) = 8.2, H₇), 7.11 - 6.29 (br, 4H, H₄), 5.35, (s, 8H, H₅), **¹³C{¹H} NMR (101 MHz, DMSO-*d*₆) δ:** 141.1 (Q C, C₆), 127.6 (CH, C₇), 125.5 (CH, q, ³*J*(¹³C-¹⁹F) = 3.4 Hz, C₈), 123.9 (Q C, q, ¹*J*(¹³C-¹⁹F) = 273.0 Hz, C₁₀) 123.6 (CH, C₃), 122.7 (CH, C₁), 53.8 (CH₂, C₅), Q - C₄, C₉ and C₂ not found; **¹⁹F{¹H} NMR (470.6 MHz, DMSO-*d*₆) δ:** -61.3 (CF₃), -70.1 (PF₆, d, ¹*J*(¹⁹F-³¹P) = 710.6 Hz.); **ATR-IR ν_{max}/cm⁻¹:** 3158 (w, C_{Ar}-H), 1621, 1572 (w, imidazole ring stretch), 1463, 1449, 1421, 1404, 1384, 1323, 1246, 1230, 1168 (s, imidazole bending), 1119, 1066, 1017, 947, 844, 833 (vs, PF₆), 820, 792, 776, 749, 724, 713, 691, 670, 654, 636, 608, 591, 557, 502, 464; 463; **Elemental Analysis Calculated for (C₄₆H₃₆Ag₂F₂₄N₄P₂):** C, 38.52; H, 2.53; N 7.81%; **Analysis Found:** C, 38.23; H, 1.68; N 7.49%

7.2.2.7 Synthesis of Di(1,1'-bis(benzyl)-3,3'-methylenedibenzimidazolium-2-ylidene))disilver(I) dihexafluorophosphate – [Ag₂(L8)₂](PF₆)₂



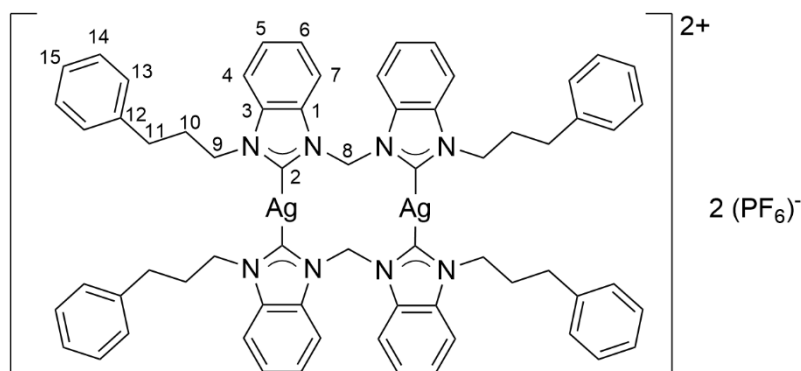
In the absence of light [H₂L8](PF₆)₂ (0.20 g, 0.28 mmol) and silver(I) oxide (0.16 g, 0.69 mmol) were stirred in MeCN (10 ml) for 20 h. The resulting brown suspension was passed through Celite®, the colourless filtrate was collected, and the solvent was removed, the resulting white solid was stirred in a MeOH/deionised water (5:95) mixture (100 mL) and then collected by vacuum filtration and washed with Et₂O (3 x 40 mL) and dried *in vacuo*, yielding white powder (0.15 g, 0.107 mmol, 76%) ¹H NMR (400 MHz, DMSO-*d*₆, 298K) δ: 8.09 (d, 4H, ³J(¹H-¹H) = 8.1 Hz, H₇), 7.82 (d, 4H, ³J(¹H-¹H) = 8.1 Hz, H₄), 7.58 (t, 4H, ³J(¹H-¹H) = 7.7 Hz, H₆), 7.51 (t, 4H, ³J(¹H-¹H) = 7.5 Hz, H₅), 7.38 (br, 4H, H₈), 7.26 – 7.32 (m, 8H, H₁₁ or H₁₂), 7.18 – 7.22 (m, 12H, H₁₃ and H₁₁ or H₁₂), 5.69 (s, 8H, H₉), 1.77; ¹³C{¹H} NMR (101 MHz, DMSO-*d*₆) δ: 135.7 (Q C, C₁₀), 133.5 (Q C, C₁ or C₃), 133.0 (Q C, C₁ or C₃), 128.8 (CH, C₁₁), 128.2 (CH, C₁₂), 127.5 (CH, C₁₃), 125.3 (CH, C₅ or C₆), 125.1 (CH, C₅ or C₆), 113.2 (CH, C₄), 111.8 (CH, C₇), 59.7 (CH₂, C₈), 52.7 (CH₂, C₉), C₂ not found; ATR-IR ν_{max}/cm⁻¹: 3064 (w, C_{Ar}-H), 2323, 2162, 2038, 1981, 1605 (w, C-C aromatic), 1497, 1480, 1454, 1392, 1334, 1320, 1278, 1188, 1132, 1080, 1029, 831 (vs, PF₆), 781, 742, 722, 705, 637, 599, 578, 556, 456; Elemental Analysis Calculated for (C₅₈H₄₈Ag₂F₁₂N₈P₂): C, 51.12; H, 3.55; N 8.22%; Analysis Found: C, 47.27; H, 2.75; N 7.31%

7.2.2.8 Synthesis of Di(1,1'-bis(phenylethyl)-3,3'-methylenedibenzimidazolium-2-ylidene))disilver(I) dihexafluorophosphate – [Ag₂(L9)₂](PF₆)₂



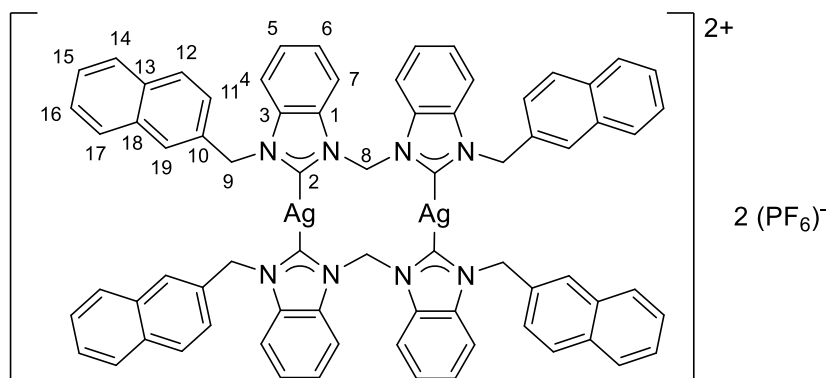
In the absence of light [H₂L9](PF₆)₂ (0.20 g) and silver(I) oxide (0.16 g) were stirred in MeCN (15 ml) for 19h in. The resulting brown suspension was passed through Celite® and the solvent was removed under reduced giving a white oil, upon addition of MeOH (5 mL) the oil solidified, deionised water (95 mL) was then added, and the flask was mixed. The white powder was then collected by vacuum filtration and washed with Et₂O (3 x 40 mL) and dried *in vacuo* yielding a greyish powder (0.17 g, 0.116 mmol, 86%) **¹H NMR (400 MHz, DMSO-*d*₆, 298K) δ**: 8.07 (d, 4H, ³*J*(¹H-¹H) = 8.1 Hz, H₇), 7.82 (d, 4H, ³*J*(¹H-¹H) = 8.2 Hz, H₄), 7.59 (t, 4H, ³*J*(¹H-¹H) = 8.0 Hz, H₆), 7.51 (t, 4H, ³*J*(¹H-¹H) = 7.8 Hz, H₅), 7.14 – 7.44 (br, 4H, H₈) 7.04 (tt, 4H, ³*J*(¹H-¹H) = 7.4 Hz, ⁴*J*(¹H-¹H) = 1.2 Hz, H₁₄), 6.91 – 6.96 (m, 8H, H₁₃), 6.82 – 6.87 (m, 8H, H₁₂), 4.69 (t, 8H, ³*J*(¹H-¹H) = 7.0 Hz, H₉), 3.10 (t, 8H, ³*J*(¹H-¹H) = 7.0 Hz, H₁₀); **¹³C{¹H} NMR (101 MHz, DMSO-*d*₆, 298K) δ**: 171.5 (unknown), 137.2 (Q C, C₁₁), 133.2 (Q, C₁ or C₃), 132.8 (Q C, C₁ or C₃), 128.6 (CH, C₁₂), 128.3 (CH, C₁₃), 126.6 (CH, C₁₄), 125.1 (CH, C₅ or C₆), 125.0 (CH, C₅ or C₆), 113.0 (CH, C₄), 111.8 (CH, C₇), 59.3 (CH₂, C₈), 50.6 (CH₂, C₉), 36.1 (CH₂, C₁₀), 22.5 (unknown impurity), C₂ not found; **ATR-IR ν_{max}/cm⁻¹**: 3029 (w, C_{Ar}-H), 2323, 2163, 2051, 1651, 1603 (w, C-C aromatic), 1480, 1454, 1394, 1356, 1321, 1279, 1181, 1082, 1040, 832 (vs, PF₆), 744, 703, 556, 495; **Elemental Analysis Calculated for (C₆₂H₅₆Ag₂F₁₂N₈P₂):** C, 52.48; H, 3.98; N 7.90%; **Analysis Found:** C, 45.67; H, 2.97; N 6.93%

7.2.2.9 Synthesis of Di(1,1'-bis(phenylpropyl)-3,3'-methylenedibenzimidazolium-2-ylidene))disilver(I) dihexafluorophosphate – [Ag₂(L10)₂](PF₆)₂



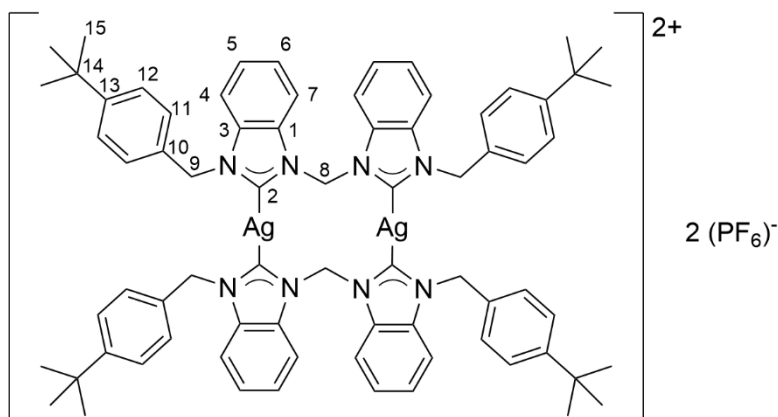
In the absence of light [H₂L10](PF₆)₂ (0.30 g) and silver(I) oxide (0.23 g) were stirred in MeCN (10 ml) 19 h. The resulting brown suspension was passed through Celite® and a further portion of MeCN (50 mL) was passed through the plug, and the solvent was removed under reduced pressure yielding a white powder. The white powder was stirred in a MeOH/deionised water (5:95) (100 mL) and collected by vacuum filtration and washed with Et₂O (3 x 40 mL) and dried *in vacuo* yielding a white powder (0.23 g, 0.157 mmol, 81%) **¹H NMR (400 MHz, DMSO-*d*₆, 298K)** δ: 8.28-8.14 (br, 4H, H₇), 7.98 (d, 4H, ³*J*(¹H-¹H) = 8 Hz, H₄), 7.67 (t, 4H, ³*J*(¹H-¹H) = 7.8 Hz, H₆), 7.62 (t, 4H, ³*J*(¹H-¹H) = 7.7 Hz, H₅), 7.42-7.15 (br, 4H, H₈), 6.84 (d, 8H, ³*J*(¹H-¹H) = 7.6 Hz, H₁₃), 6.72 (t, 8H, ³*J*(¹H-¹H) = 8.0 Hz, H₁₄), 6.54 (t, 4H, ³*J*(¹H-¹H) = 7.8 Hz, H₁₅), 4.32-4.03 (br, H₈, H₉), 2.60 (br, 8H, H₁₁), 2.03-1.86 (br, 8H, H₁₀); **¹³C{¹H} NMR (101 MHz, DMSO-*d*₆, 298K)** δ: 189.30 (Q C, d, *J*(¹³C-¹⁰⁷Ag) = 182.1 Hz and *J*(¹³C-¹⁰⁹Ag) = 211.3 Hz, C₂), 140.2 (Q C, C₁₂), 133.1 (Q C, C₁ or C₃), 132.9 (Q C, C₁ or C₃), 128.0 (CH, C₁₃), 127.9 (CH, C₁₄), 125.4 (CH, C₁₅), 125.20 (CH, C₅ or C₆), 125.19 (CH, C₅ or C₆) 112.7 (CH, C₇), 112.0 (CH, C₄), 58.4 (CH₂, C₈), 48.5 (CH₂, C₉), 31.7 (CH₂, C_{10,11}); **ATR-IR ν_{max}/cm⁻¹**: 2936 (w, CH₂), 1602 (w, C-C aromatic), 1481, 1455, 1396, 1334, 1272, 1251, 1180, 1131, 1030, 833 (vs, PF₆), 795, 781, 748, 701, 556, 492, 469; **Elemental Analysis Calculated for (C₆₆H₆₄Ag₂F₁₂N₈P₂)**: C, 53.75; H, 4.73; N 7.60%; **Analysis Found**: C, 53.12; H, 3.64; N 7.24%

7.2.2.10 Synthesis of Di(1,1'-bis(naphthylmethyl)-3,3'-methylenedibenzimidazolium-2-ylidene))disilver(I) dihexafluorophosphate – $[Ag_2(L11)_2](PF_6)_2$



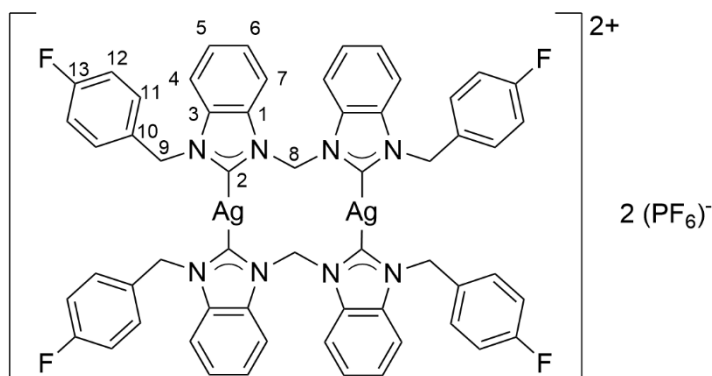
In the absence of light $[H_2L11](PF_6)_2$ (0.30 g, 0.37 mmol) and silver(I) oxide (0.22 g, 0.93 mmol) were stirred in MeCN (6 ml) for 19 h. The resulting brown suspension was passed through Celite® and the solvent was removed *in vacuo* and the resulting solid was dissolved in a minimum amount of acetone *ca.* 1 mL and crystallised through vapour diffusion of resulting in a mixture of white crystals and brown powder, the supernatant was discarded, the sample was redissolved in acetone (10 mL) and precipitated by the addition of Et₂O (60 mL) the white precipitate was collected by vacuum filtration and washed with Et₂O (3 x 40 mL) yielding a white powder (0.10 g, 0.074 mmol, 20 %); **¹H NMR (400 MHz, DMSO-*d*₆, 298K)** δ: 8.08 (d, 4H, ³*J*(¹H-¹H) = 8 Hz, H₄), 7.81 (d, 4H ³*J*(¹H-¹H) = 8 Hz, H₇), 7.71 – 7.65 (m, 12H, H_{Ar}), 6.60 (t, 4H, ³*J*(¹H-¹H) = 7.5 Hz, H₅ or H₆), 7.45 – 7.52 (m, 8H, H_{Ar}), 7.32 – 7.36 (m, 4H, H_{nap}), 7.25 – 7.30 (m, 8H, H_{nap}), 7.21 (s, 4H, H₈), 5.66 (s, 8H, H₉); **ATR-IR ν_{max}/cm⁻¹**: 1601 (w, C-C aromatic), 1510, 1480, 1453, 1393, 1320, 1277, 1189, 1034, 834 (vs, PF₆), 783, 743, 556, 472; **Elemental Analysis Calculated for (C₇₄H₅₆Ag₂F₁₂N₈P₂)**: C, 56.87; H, 3.61; N 7.17%; **Analysis Found**: C, 53.16; H, 2.28; N 6.47%

7.2.2.11 Synthesis of Di(1,1'-bis(4-tertbutylbenzyl)-3,3'-methylenedibenzimidazolium-2-ylidene))disilver(I) dihexafluorophosphate – [Ag₂(L12)₂](PF₆)₂



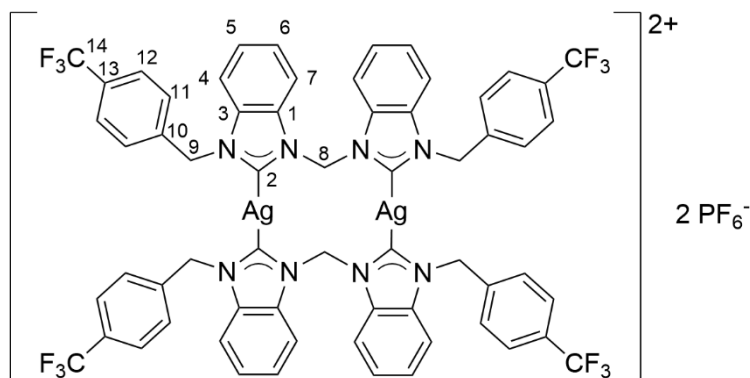
In the absence of light [H₂L12](PF₆)₂ (1.00 g, 1.20 mmol) and silver(I) oxide (0.70 g, 3.00 mmol) were stirred in MeCN (6 ml) for 19 h. The resulting brown suspension was passed through Celite® and the solvent was removed from the filtrate yielding an off-white solid. The solid was dissolved in a (50:50) mixture of MeOH/acetone (70 mL) and passed through a Celite® plug and the solvent from the colourless filtrate was removed *in vacuo* yielding an off-white powder (0.71 g, 0.44 mmol, 73%) ¹H NMR (400 MHz, DMSO-*d*₆, 298K) δ: 8.10 (d, 4H, ³J(¹H-¹H) = 7.2 Hz, H₇), 7.91 (d, 4H, ³J(¹H-¹H) = 8.2 Hz, H₄), 7.60 (t, 4H, ³J(¹H-¹H) = 7.8 Hz, H₆), 7.55 (t, 4H, ³J(¹H-¹H) = 7.5 Hz, H₅), 7.41 (s, 4H, H₈), 7.35 (d, 8H, ³J(¹H-¹H) = 8.3 Hz, H₁₁), 7.15 (d, 8H, ³J(¹H-¹H) = 8.3 Hz, H₁₂), 5.70 (s, 8H, H₉), 1.03, (s, 36H, H₁₅); ¹³C{¹H} NMR (101 MHz, DMSO-*d*₆, 298K) δ: 151.3 (Q C, C₁₄), 133.9 (Q C, C₁ or C₃), 133.6 (Q C, C₁ or C₃), 132.7 (Q C, C₁₀), 128.2 (CH, C₁₁ or C₁₂), 126.0 (CH, C₁₁ or C₁₂), 125.8 (CH, C₅ or C₆), 125.6 (CH, C₅ or C₆), 113.7 (CH, C₄), 112.3 (CH, C₇), 59.9 (CH₂, C₈), 54.7, (CH₂, C₉), 34.9 (Q C, C₁₃), 31.2 (CH₃, C₁₅), 23.0 (impurity), C₂ not found; ATR-IR ν_{max}/cm⁻¹: 2961 (m, CH₃, asym), 2869, 2323, 2193, 2172, 2051, 1982, 1666, 1610 (m, C-C aromatic), 1515, 1478, 1454, 1392, 1321, 1274, 1184, 1129, 1109, 1032, 1018, 936, 832 (vs, PF₆), 797, 785, 761, 740, 716, 700, 682, 629, 610, 592, 556; **Elemental Analysis Calculated for (C₇₄H₈₀Ag₂F₁₂N₈P₂):** C, 56.00; H, 5.08; N 7.06%; **Analysis Found:** C, 50.92; H, 4.12; N 6.34%

7.2.2.12 Synthesis of Di(1,1'-bis(4-fluorobenzyl)-3,3'-methylenedibenzimidazolium-2-ylidene))disilver(I) dihexafluorophosphate – [Ag₂(L13)₂](PF₆)₂¹⁶⁹



In the absence of light [H₂L13](PF₆)₂ (1.50 g, 1.98 mmol) and silver(I) oxide (1.15 g, 4.96 mmol) were stirred in MeCN (6 ml) for 19 h. The resulting brown suspension was passed through Celite® and the solvent was removed from the filtrate giving a brown powder. The powder was dissolved in acetone (20 mL) and passed through Celite®, the solvent was removed from the filtrate giving a yellow oil, which was redissolved in acetone (5 mL) and made up to 20 mL with MeOH, deionised water (60 mL) was then added and an off-white precipitate formed, which was collected by vacuum filtration and washed with MeOH (5 mL) and petroleum ether (5 mL) and dried *in vacuo* yielding an off-white solid (0.49 g, 0.34 mmol, 34%); ¹H NMR (400 MHz, DMSO-*d*₆, 298K) δ: 8.12 (d, 4H, ³J(¹H-¹H) = 8.2 Hz, H₇), 7.80, (d, 4H, ³J(¹H-¹H) = 8.2 Hz, H₄), 7.60 (t, 4H, ³J(¹H-¹H) = 7.9 Hz, H₆), 7.52 (t, 4H, ³J(¹H-¹H) = 7.9 Hz, H₅), 7.43-7.34 (m, 12H, H_{8,11}), 7.01-7.07 (m, 8H, H₁₂), 5.72 (s, 8H, H₉), 2.09 (acetone); ¹³C{¹H} NMR (101 MHz, DMSO-*d*₆, 298K) δ: 190.71 (Q C, d, ¹J(¹³C-¹⁰⁷Ag) = 176.1 Hz and ¹J(¹³C-¹⁰⁹Ag) = 213.9 Hz, C₂), 161.8 (Q, d, ¹J(¹³C-¹⁹F) = 246 Hz, C₁₃), 133.2(Q C, C₁ or C₃), 133.1(Q C, C₁ or C₃), 131.8 (Q C, d, ⁴J(¹³C-¹⁹F) = 3.1 Hz, C₁₀), 129.6 (CH, d, ³J(¹³C-¹⁹F) = 8.4 Hz, C₁₁), 124.5 (CH, C₅ or C₆), 125.2 (CH, C₅ or C₆), 115.6 (CH, d, ²J(¹³C-¹⁹F) = 21.8 Hz, C₁₂), 113.2 (CH, C₄), 111.9 (CH, C₇), 59.4 (CH₂, C₈), 51.6 (CH₂, C₉); ¹⁹F{¹H} NMR (471 MHz, (CD₃)₂SO, 298 K) δ: -70.1 (PF₆, d, ¹J(¹⁹F-³¹P) = 715.3 Hz), -113.8 (CF); ATR-IR ν_{max}/cm⁻¹: 3117 (w, C_{Ar}-H), 1605 (m, aromatic C-C), 1510 (s, aromatic C-C), 832 (vs, br, PF₆); Elemental Analysis Calculated for (C₅₈H₄₄Ag₂F₁₆N₄P₂): C, 48.56; H, 3.09; N 7.81%; Analysis Found: C, 48.37; H, 2.93; N 7.49%

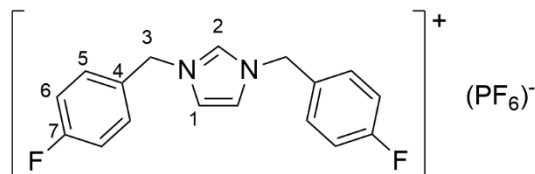
7.2.2.13 Synthesis of Di(1,1'-bis(4-trifluoromethylbenzyl)-3,3'-methylenedibenzimidazolium-2-ylidene))disilver(I) dihexafluorophosphate – [Ag₂(L14)₂](PF₆)₂



In the absence of light [H₂L14](PF₆)₂ (0.20 g, 0.23 mmol) and silver(I) oxide (0.13 g, 0.57 mmol) were stirred in MeCN (10 mL) for 19 h. The resulting brown suspension was passed through Celite®, giving a colourless filtrate. The solvent was removed giving a white powder. The powder was dissolved in MeOH (5 mL) followed by addition of deionised water (90 mL) forming a white precipitate which was collected by vacuum filtration and washed with deionised water (40 mL) and hexanes (40 mL) and dried *in vacuo* yielding a white powder (0.091 g, 0.056 mmol, 47%); ¹H NMR (400 MHz, DMSO-*d*₆, 298K) δ: 8.16 (d, 4H, ³*J*(¹H-¹H) = 8.3, H₇), 7.76 (d, 4H, ³*J*(¹H-¹H) = 8.3, H₄), 7.60 (t, 4H, ³*J*(¹H-¹H) = 7.8, H₆), 7.53-7.47 (m, 20H, H_{5,11,12}), 7.42 (s, 4H, H₈), 5.84 (s, 8H, H₉); ¹³C{¹H} NMR (101 MHz, DMSO-*d*₆, 298K) δ: 140.1 (Q ⊔, C₁₀), 133.3 (Q ⊔, C₁ or C₃), 133.15 (Q ⊔, C₁ or C₃), 128.8 (Q ⊔, q, ²*J*(¹³C-¹⁹F) = 31.4 Hz, C₁₃), 128.1 (⊔CH, C₁₁), 125.6 (⊔CH, C₅ or C₆), 125.5 (⊔CH, q, ³*J*(¹³C-¹⁹F) = 3.4 Hz, C₁₂), 125.3 (⊔CH, C₅ or C₆), 123.9 (Q ⊔, q, ¹*J*(¹³C-¹⁹F) = 217.7 Hz, C₁₄), 113.1 (⊔CH, C₄), 112.0 (⊔CH, C₇), 59.50 (⊔CH₂, C₈), 51.85 (⊔CH₂, C₉), C₂ not found; ATR-IR ν_{max}/cm⁻¹: 1621, 1480, 1453, 1394, 1322, 1279, 1166, 1113, 1067, 1037, 1018, 952, 829 (vs, br, PF₆), 782, 741, 716, 648, 624, 593, 556, 493; Elemental Analysis Calculated for (C₆₂H₄₄Ag₂F₂₄N₄P₂): C, 45.55; H, 2.71; N 6.85%; Anal. Found: C, 45.44; H, 2.21; N 6.55%

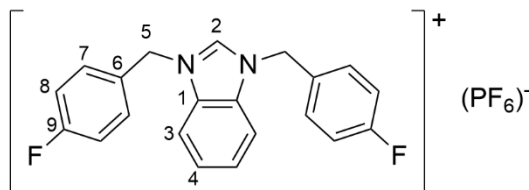
7.2.3 Monodentate ligands

7.2.3.1 Synthesis of 1,3-Bis-(4-fluorobenzyl)imidazolium hexafluorophosphate – [HL15](PF₆)¹⁶⁹



1-(4-Fluorobenzyl)-1*H*-imidazole (1.00 g, 5.68 mmol) and 4-fluorobenzyl bromide (1.19 g, 6.27 mmol) were stirred in MeCN (10 mL) and heated to reflux for 24 h, the solvent was removed in vacuo to yield a brown oil. To the oil acetone (25 mL) was added followed by ammonium hexafluorophosphate (1.16 g, 7.10 mmol) and they were stirred for 1 d, the solvent was removed, and the resulting white powder was suspended in deionised water (40 mL) and stirred for 1 h, the white powder was collected by vacuum filtration and washed with deionised water (2 x 40 mL) and Et₂O (3 x 40 mL) and dried *in vacuo* yielding a white powder (0.86 g, 2.00 mmol, 35%); ¹H NMR (500 MHz, DMSO-*d*₆, 298K) δ: 9.31 (t, 1H, ⁴*J*(¹H-¹H) = 1.6 Hz, H₂), 7.80 (d, 2H, ⁴*J*(¹H-¹H) = 1.6 Hz, H₁), 7.48 – 7.53 (m, 4H, H₅), 7.25 – 7.30 (m, 4H, H₆), 5.40 (s, 4H, H₃); ¹³C{¹H} NMR (125.8 MHz, DMSO-*d*₆, 298K) δ: 162.3 (Q C, d, ¹*J*(¹³C-¹⁹F) = 245.3 Hz, C₇), 136.2 (CH, C₂), 130.94 (CH, d, ³*J*(¹³C-¹⁹F) = 8.8 Hz, C₅), 130.93 (Q C, C₄), 122.9 (CH, C₁), 115.9 (CH, d, ⁴*J*(¹³C-¹⁹F) = 21.4 Hz, C₆), 51.3 (CH₂, C₃); ¹⁹F{¹H} NMR (470.6 MHz, DMSO-*d*₆, 298K) δ: 70.1 (PF₆, d, ¹*J*(¹⁹F-³¹P) = 710.6 Hz), 113.0 (CF); ATR-IR ν_{max}/cm⁻¹: 3177 (w, C_{Ar}-H), 3161 (w, C₂-H), 3111, 1607 (m, aromatic C-C), 1569 (sh, C₂-H), 1510 (s, aromatic C-C), 1452, 1421, 1355, 1305, 1223, 1206, 1171, 1158, 1101, 1033, 1016, 929, 824 (vs, br, PF₆), 765, 741, 687, 641, 627, 555, 526, 512, 491; **Elemental Analysis Calculated for (C₁₇H₁₅F₈N₂P)**: C, 47.45; H, 3.51; N 6.51%; **Analysis Found**: C, 47.28; H, 3.27; N 5.89%.

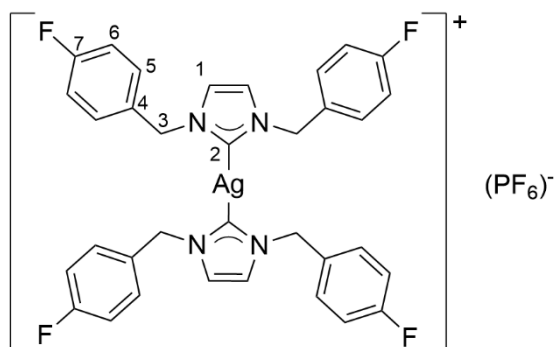
7.2.3.2 Synthesis of 1,3-Bis-(4-fluorobenzyl)benzimidazolium hexafluorophosphate – [HL16](PF₆)¹⁶⁹



[HL16](Br) (0.62 g, 1.49 mmol) was stirred in acetone (50 mL) with ammonium hexafluorophosphate (0.31 g, 1.87 mmol) for 1 h. The suspension was filtered by gravity and the solvent was removed yielding a white powder (0.46 g, 0.95 mmol, 64%); ¹H NMR (400 MHz, DMSO-*d*₆, 298K) δ: 9.93 (s, 1H, H₂), 7.98 (dd, ³*J*(¹H-¹H) = 8.0 Hz, ⁴*J*(¹H-¹H) = 2.8 Hz, 2H, H₃), 7.59 – 7.68 (m, 6H, H₄ and H₈), 7.25 – 7.32 (m, 4H, H₇), 5.76 (s, 4H, H₅), 2.08 (acetone); ¹³C{¹H} NMR (101 MHz, DMSO-*d*₆) δ: 162.3 (Q C, d, ¹*J*(¹³C-¹⁹F) = 245.5 Hz, C₉), 142.7 (CH, C₂), 131.0 (Q, C₁), 130.9 (CH, d, ³*J*(¹³C-¹⁹F) = 9.1 Hz, C₇), 130.0 (CH, d, ⁴*J*(¹³C-¹⁹F) = 3.0 Hz, C₆), 127.3 (C₃), 115.9 (CH, d, ²*J*(¹³C-¹⁹F) = 21.1 Hz, C₈), 114.0 (CH, C₄), 49.3 (CH, C₅); ¹⁹F{¹H} NMR (470.6 MHz, DMSO-*d*₆) δ: -70.1 (d, ¹*J*(¹⁹F-³¹P) = 715.3 Hz, PF₆), -113.0 (ArF); ATR-IR ν_{max}/cm⁻¹: 3152 (w, C2-H), 3093, 1606 (m, aromatic C-C), 1563 (m, C2-H), 1510 (s, aromatic C-C), 1478, 1451, 1421, 1380, 1225, 1215, 1194, 1165, 1133, 1104, 1018, 965, 946, 843, 817 (vs, br, PF₆), 779, 771, 751, 735, 702, 683, 636, 620, 600, 559, 541, 513, 489, 478 ; Elemental Analysis Calculated for (C₂₁H₁₇F₈N₂P): C, 52.51; H, 3.57; N 5.83%; Analysis Found: C, 52.93; H, 3.60; N 5.85%.

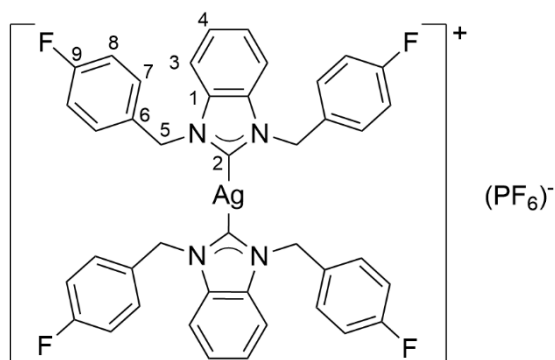
7.2.4 Mononuclear Silver(I) *N*-Heterocyclic Carbene Complexes

7.2.4.1 Synthesis of Di(1,3-bis(4-fluorobenzyl)imidazol-2-ylidene)silver hexafluorophosphate – [Ag(L15)₂](PF₆)¹⁶⁹



In the absence of light **[HL15](Br)** (0.20 g, 0.55 mmol) and silver(I) oxide (0.16 g, 1.30 mmol) were stirred in MeOH (10 mL) 24 h. The brownish suspension was passed through Celite®, and the plug was washed with a further 20 mL of MeOH, giving a light-yellowish solution. The solution was added to a stirring solution of deionised water (70 mL) which had ammonium hexafluorophosphate (0.095 g, 0.58 mmol) dissolved in it. An oily yellowish solid settled, the supernatant was decanted. Et₂O (20 mL) was added to the oil and the mixture was titrated giving a loose powder, the powder was collected by vacuum filtration and dried *in vacuo* yielding an off-white powder (0.057 g, 0.069 mmol, 25%); **¹H NMR (400 MHz, DMSO-*d*₆, 298K) δ**: 7.58 (s, 4H, H₁), 7.19 – 7.25 (m, 8H, H₅), 7.07 – 7.14 (m, 8H, H₆), 5.29 (s, 8H, H₃); **¹³C{¹H} NMR (101 MHz, DMSO-*d*₆) δ**: 161.7 (Q C, d, ¹J(¹³C-¹⁹F) = 244.5 Hz, C₇), 133.4 (Q C, d, ⁴J(¹³C-¹⁹F) = 3.0 Hz, C₄), 129.4 (CH, d, ²J(¹³C-¹⁹F) = 8.0 Hz, C₅), 122.8 (CH, C₁), 115.6 (CH, d, ²J(¹³C-¹⁹F) = 21.1 Hz, C₆), 53.4 (CH₂, C₃), C₂ not found; **¹⁹F{¹H} NMR (470.6 MHz, DMSO-*d*₆) δ**: -70.1 (d, ¹J(¹⁹F-³¹P) = 715.3 Hz, PF₆), -114.2 (ArF); **ATR-IR ν_{max}/cm⁻¹**: 3177(w, C-H), 2164, 1604 (m, aromatic C-C), 1566, 1509 (s, aromatic C-C), 1459, 1417, 1357, 1302, 1281, 1222, 1158, 1112, 1095, 1045, 1017, 959, 932, 880, 830 (vs, br, PF₆), 784, 772, 753, 746, 694, 683, 671, 666, 635, 616, 557, 542, 513, 499, 488; **Elemental Analysis Calculated for (C₃₄H₂₈AgF₁₀N₄P)**: C, 49.71; H, 3.44; N 6.82%; **Analysis Found**: C, 49.24; H, 3.68; N 6.33%.

7.2.4.2 Synthesis of Di(1,3-bis(4-fluorobenzyl)benzimidazol-2-ylidene)silver hexafluorophosphate - [Ag(L16)₂](PF₆)¹⁶⁹



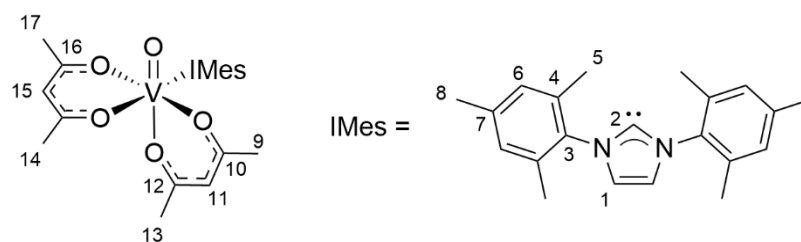
In the absence of light **[HL16](PF₆)** (0.20 g, 0.42 mmol) was stirred with silver(I) oxide (0.12 g, 0.53 mmol) in MeCN (10 mL) under the exclusion of light for 19 h. The brown suspension was passed through Celite® and washed with MeCN

(50 mL). The solvent was removed under reduced pressure to give a waxy colorless solid. The solid was titrated with MeOH (10 mL) forming a loose powder, which was collected by vacuum filtration and washed with MeOH (10 mL) and n-heptane (20 mL) and then dried *in vacuo* yielding a white powder (0.05 g, 0.047 mmol, 23%); **^1H NMR (400 MHz, DMSO- d_6 , 298K) δ :** 7.75 (dd, 4H, $^3J(^1\text{H}-^1\text{H}) = 6.0$ Hz, $^4J(^1\text{H}-^1\text{H}) = 3.2$ Hz, H₃), 7.42 (dd, 4H, $^3J(^1\text{H}-^1\text{H}) = 6.4$ Hz, $^4J(^1\text{H}-^1\text{H}) = 2.8$ Hz, H₄), 7.35 – 7.29 (m, 4H, H₇), 7.11 – 7.04 (m, 4H, H₈), 5.75 (s, 8H, H₅); **$^{13}\text{C}\{^1\text{H}\}$ NMR (125.9 MHz, DMSO- d_6) δ :** 162.7 (Q C, d, $^1J(^{13}\text{C}-^{19}\text{F}) = 245.3$ Hz, C₉), 133.4 (Q C, C₁), 132.5 (Q C, d, $^4J(^{13}\text{C}-^{19}\text{F}) = 2.5$ Hz, C₆), 129.2 (CH, d, $^3J(^{13}\text{C}-^{19}\text{F}) = 7.5$ Hz, C₇), 124.5 (CH, C₃), 115.6 (CH, d, $^2J(^{13}\text{C}-^{19}\text{F}) = 21.4$ Hz, C₈), 112.5 (CH, C₄), 51.0 (CH₂, C₅), C₂ not found; **$^{19}\text{F}\{^1\text{H}\}$ NMR (470.6 MHz, DMSO- d_6) δ :** -70.1 (d, $^1J(^{19}\text{F}-^{31}\text{P}) = 715.3$ Hz, PF₆), -114.2 (ArF); **ATR-IR $\nu_{\text{max}}/\text{cm}^{-1}$:** 3090, 2942, 1605 (m, aromatic C-C), 1566, 1510 (s, aromatic C-C), 1478, 1447, 1421, 1400, 1350, 1340, 1300, 1270, 1225, 1182, 1160, 1133, 1098, 1034, 1015, 964, 940, 824 (vs, br, PF₆), 798, 786, 768, 744, 702, 680, 658, 633, 618, 596, 570, 556, 528, 516, 485; **Elemental Analysis Calculated for (C₄₂H₃₂AgF₁₀N₄P):** C, 54.74; H, 3.50; N 6.08%; **Analysis Found:** C, 54.81; H, 2.98; N 6.03%.

7.2.5 Vanadium N-Heterocyclic Carbene Complexes

Unless otherwise specified all additions and manipulations were either carried out in a glovebox or using standard Schlenk techniques. All solvents were dried using appropriate methods and stored on molecular sieves either 3 or 4 Å. Starting materials VO(bz bz)₂ and VO(acac)Cl₂ were synthesised using reported literature procedures with the purity confirmed by ATR-FTIR and ^1H NMR respectively.^{226,250}

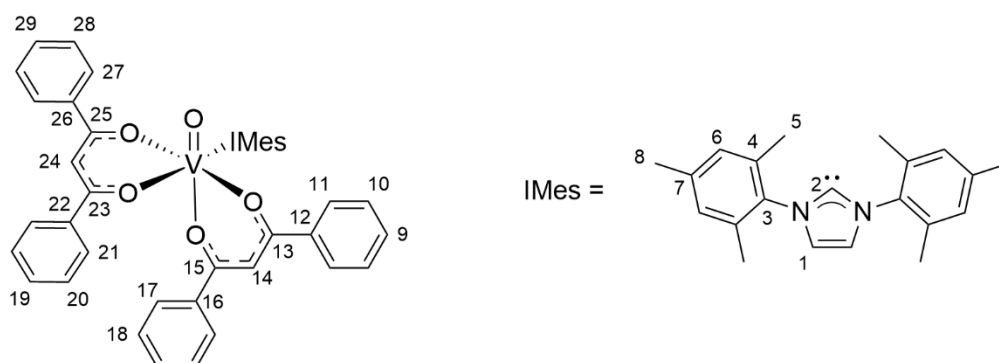
7.2.5.1 Synthesis of VO(acac)₂(Imes) - VI



VO(acac)₂ (0.17 g, 0.65 mmol) was partially dissolved in toluene (1.5 mL), separately 1,3-bis-(2,4,6-trimethylphenyl)imidazol-2-ylidene (Imes) (0.20 g,

0.66 mmol) was dissolved in toluene (1.5 mL), then the IMes solution was added to the stirring suspension of $\text{VO}(\text{acac})_2$. The colour changed from a blueish green to a brownish green immediately, and the reaction was left to stir for 19 h, after which the mixture had become a deep green solution. To the solution, hexane (10 mL) was layered on top and after 1 d a green precipitate formed. The supernatant was removed, and the green solid was washed with a further portion of n-hexane (10 mL) and then dried *in vacuo* yielding a dark-green powder (0.29 g, 0.50 mmol, 77%); **ATR-IR** $\nu_{\text{max}}/\text{cm}^{-1}$: 3160 (w, $\text{C}_{\text{Ar}}\text{-H}$), 3131 (w, $\text{C}_{\text{Ar}}\text{-H}$), 2970 (w, CH_3), 2917, 1601, 1584 (w, imidazole ring stretch), 1512, 1439, 1389, 1374 (s, CH_3 , umbrella mode), 1267, 1224, 1193, 1184 (w, imidazole bending), 1097, 1081, 1018, 960 (s, V=O), 926, 852, 774, 762, 753, 732, 696, 671, 605, 593, 577, 542, 485, 466, 453
Elemental Analysis Calculated for $(\text{C}_{31}\text{H}_{38}\text{N}_2\text{O}_5\text{V})$: C, 65.37; H, 6.72; N 4.92%;
Analysis Found: C, 65.23; H, 6.67; N 4.53%

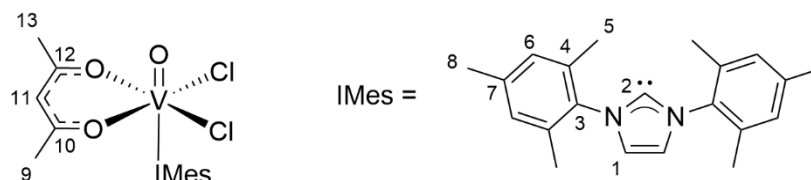
7.2.5.2 Synthesis of $\text{VO}(\text{bzbz})_2(\text{IMes}) - \text{V2}$



$\text{VO}(\text{bzbz})_2$ (0.11 g, 0.21 mmol) was suspended in toluene (2 mL) and separately 1,3-bis-(2,4,6-trimethylphenyl)imidazol-2-ylidene (IMes) (0.063 g, 0.21 mmol) was dissolved in toluene (2 mL). The IMes solution was then added to the stirring suspension of $\text{VO}(\text{bzbz})_2$, and the colour changed from green to brown. The reaction was allowed to stir for 19 h, after which the mixture was passed through a Celite® filter, and n-hexane (10 mL) was layered on top, and after 4 d a brownish green precipitate had formed. The supernatant was removed and the solid was washed with a portion of n-hexane (5 mL) and then dried *in vacuo* yielding a brownish green powder (0.067 g, 0.081 mmol, 39%); **ATR-IR** $\nu_{\text{max}}/\text{cm}^{-1}$: 3172 (w, $\text{C}_{\text{Ar}}\text{-H}$), 3059 (w, $\text{C}_{\text{Ar}}\text{-H}$), 3024 (w, $\text{C}_{\text{Ar}}\text{-H}$), 2917, 1595, 1547, 1516, 1477, 1453, 1374 (m, CH_3 , umbrella mode), 1311, 1268, 1224, 1180 (w, imidazole bending), 1158, 1127, 1099,

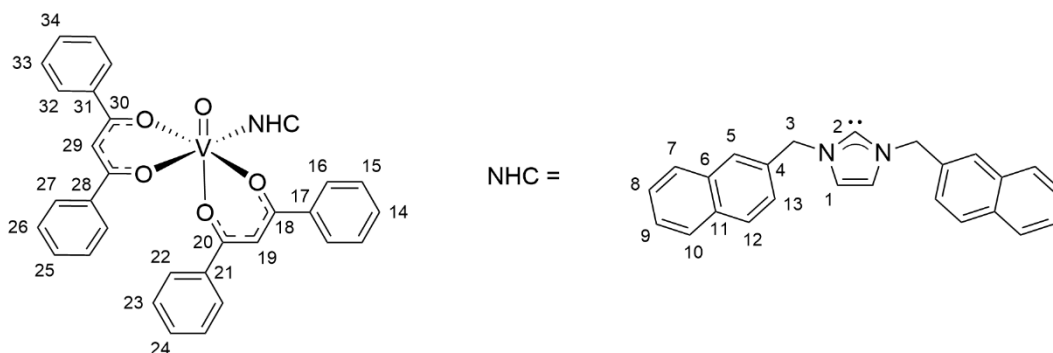
1066, 1024, 1000, 960 (V=O), 942, 927, 849, 810, 785, 750, 732, 719, 688, 629, 621, 569, 548, 528, 510, 467, 456; **Elemental analysis Calculated for (C₅₁H₄₆N₂O₅V):** C, 74.90; H, 5.67; N 3.43%; **Analysis Found:** C, 75.03; H, 5.28; N 2.30%

7.2.5.3 Synthesis of VOCl₂(acac)(IMes) – V3



Separately VO(acac)Cl₂ (0.078 g, 0.33 mmol) and 1,3-bis-(2,4,6-trimethylphenyl)imidazol-2-ylidene (IMes) (0.10 g, 0.33 mol) were both dissolved in THF (2 mL) forming a yellow and green solution respectively. The IMes solution was added to the stirring solution of VO(acac)Cl₂, and no colour change upon addition. The reaction was allowed to stir for 23 h, after which the whole mixture was placed in the freezer at -30°C. After 3 d a light brown precipitate had formed, the supernatant was collected and filtered, the solvent was then removed *in vacuo* yielding a brown crystalline solid (0.08 g, 0.15 mmol, 44%); ⁵¹V NMR (131.6 MHz, THF-*d*₈, 298K) δ: -361.8; ⁵¹V NMR (131.6 MHz, CDCl₃, 298K) δ: -358.2 **Elemental analysis Calculated for (C₂₆H₃₁Cl₂N₂O₃V):** C, 57.68; H, 5.77; N 5.17%; **Analysis Found:** C, 55.90; H, 5.57; N 4.40%

7.2.5.4 Synthesis of VO(bz bz)₂(L17) – V4



VO(bz bz)₂ (0.10 g, 0.48 mmol) and [HL17](PF₆) (0.25 g, 0.48 mmol) were stirred in toluene (10 mL), followed by the addition of LiHMDS (0.80 g, 0.48 mmol), the suspension turned a darker green. The mixture was allowed to stir for 20 h after which the suspension was passed through Celite®, yielding a deep green solution.

The solvent was removed giving a green oil, which was redissolved in toluene (3 mL) and layered with n-hexane (10 mL). After 1 d a brown precipitate formed, and the supernatant was filtered and collected and the solvent was removed *in vacuo* yielding an intense blue oil which was placed in a freezer at -30°C for 2 d after which a yielded a dark blue powder (0.034 g, 0.039 mmol, 8%); **ATR-IR** $\nu_{\text{max}}/\text{cm}^{-1}$ 3055 (w, C_{Ar}-H) , 2954 (w, CH₂), 2895 (w, CH₂) ,1912 ,1592 (w, imidazole ring stretch) ,1537 ,1516 ,1477 ,1452 ,1370 ,1314 ,1243 ,1225 ,1180 (w, imidazole bending) ,1100 ,1069 ,1024 ,986 ,907 ,835 ,809 ,755 ,718 ,687 ,630 ,622 ,532 ,473; **Elemental analysis Calculated for (C₂₆H₃₁Cl₂N₂O₃V):** C, 76.59; H, 5.06; N 3.20%; **Analysis Found:** C, 65.16; H, 6.25; N 4.23%

7.3 Single Crystal X-ray Diffraction

A suitable single crystal was selected and submerged in fomblin oil. The crystal was then mounted on a goniometer head on an XtaLAB Synergy Dualflex, HyPix diffractometer fitted with a Hybrid Pixel Array Detector, using mirror monochromated Mo-K α radiation ($\lambda = 0.71073 \text{ \AA}$) or Cu-K α radiation ($\lambda = 1.54184 \text{ \AA}$) sources. The crystal was cooled to 100 K by an Oxford Cryostream low temperature device. The full data set was recorded, and the images processed using CrysAlis Pro software.²⁸⁰ Structure solution by direct methods was achieved through the use of SHELXT and SHELXL programs,^{281,282} and the structural model was refined by full matrix least squares on F² using the program Olex2 V2-1.5.²⁸³ Hydrogen atoms were placed using idealised geometric positions (with free rotation for methyl groups), allowed to move in a “riding model” along with the atoms to which they were attached, and refined isotopically. Editing of the CIFs and construction of tables of bond lengths and angles was achieved using Olex2 1.5.²⁸³ All molecular images were generated using Mercury 4.0.²⁸⁴

7.4 Variable Temperature NMRs

Complexes (8 – 12 mg) were dissolved in *d*₃-MeCN (0.5 mL), and using a 500 MHz NMR spectrometer, the ¹H NMR spectrum were recorded starting -40 °C. The temperature was then ramped up to the next setpoint (at least 3 min) after which another spectrum was taken at -30°C. The step was repeated for -10, 0, 20, 40 and 60 °C.

7.5 NMR Stability Studies

[Ag₂(L13)₂](PF₆)₂ (5.0 mg) was dissolved in *d*₆-DMSO (150 μL) and D₂O (350 μL), and the sample was mixed well. The ¹H NMR spectra were collected on a 500 MHz NMR spectrometer at 0, 1 and 24 h timepoints.¹⁶⁹

7.6 UV-vis stability studies

7.6.1 Stability of Silver(I) *N*-Heterocyclic Carbene Complexes

Stock samples of Ag(I)-NHC complexes (100 μL) were prepared in DMSO, added to a quartz cuvette and followed by deionised water (1900 μL), giving a final concentration of complex of 25 μM. Spectra were obtained at 25 °C between 250 and 400 nm at 0, 10, 20, 30 mins and 1, 2, 4, 6 and 24 h after addition.¹⁶⁹

7.6.2 Stability of Vanadium(IV) *N*-Heterocyclic Carbene Complexes

In the glovebox a solution of V(IV)-NHC complex was prepared in dry toluene (2 mL) in an airtight cuvette to give a final concentration of 63.75 μM. For the control measurement the sample was then taken out of the glovebox and the spectra was obtained at 25 °C between 285 – 700 nm, throughout the duration of the experiment there was a nitrogen purge in the measurement chamber. Spectra were taken at 0, 10, 20, 30 min, 1, 2, 3 and 4 hours. For the water stability measurements, the same procedure as above was carried out except for the addition of 10 μL of deionised water before the measurements were collected.

7.7 Cell Viability Assay

7.7.1 Cell Culturing

All cytotoxicity assays were conducted using human cell lines: breast adenocarcinomas (MDA-MB-231 and MCF-7) and a non-cancerous epithelial retinal ARPE-19 cell line, some were tested on the non-cancerous breast cell line MCF10A. All cell lines were routinely maintained as monolayer cultures in appropriate complete medium: MCF-7 and ARPE-19 in high glucose DMEM complete medium (+ 10% FBS + 1 mM sodium pyruvate + 2 mM L-glutamine + 1% pen-strep) and MDA-MB-231 in RPMI-1640 complete medium (+ 10% FBS + 1 mM sodium pyruvate + 2 mM L-glutamine + 1% pen-strep), MCF10A in DMEM/F12 complete medium (1% pen-strep + 0.5 ng/mL hydrocortisone + cholera

toxin 100 ng/mL + insulin 10 ug/mL + 5% horse serum + EGF 20 ng/mL) and grown in either T-25 or T-75 flasks at 37 °C and 5% CO₂.

7.7.2 MTT Assay

Prior to chemosensitivity studies, cell monolayers were passaged using Trypsin-EDTA (0.05%) and diluted to a concentration of 4×10^4 cells/mL. All assays were conducted using 96-well plates, in which 100 μ L of the cell suspension was added for 24 h at 37 °C and 5% CO₂. Compound stocks were made using DMSO at 100 mM prior to dilution and a maximum of 0.1% DMSO used in each assay. 100 μ L compound/medium dilutions were added to the plates for a further 24 h. MTT (3-(4,5-dimethylthiazol-2-yl)-2,5-diphenyltetrazolium bromide (20 μ L at 5 mg/mL in PBS) was added to each well and incubated for 3 h at 37 °C and 5% CO₂. All solutions were then aspirated, DMSO (150 μ L) added to each well and the absorbance of each well was measured at 540 nm using a ClarioStar spectrophotometer microplate reader. Results were plotted on a logarithmic scale, and the half maximal inhibitory concentration (IC₅₀) determined from triplicate of triplicate repeats (n = 9) and reported as an IC₅₀ \pm standard error (SEM). For the 4 hour experiments the same procedure as outlined above was followed apart from changing the compound incubation time to 4 hours.¹⁶⁹

7.8 Optical Imaging Cell Studies

MDA-MB-231 cells were seeded at a concentration of 4×10^5 cells/well in 1 mL of complete media in a 6-well plate and then incubated at 37 °C and 5% CO₂ for 24 h. The media was removed, and the cells washed with PBS (1 mL). Complete media (1 mL) spiked with the Ag(I)-NHC complexes (10 μ M, 50 μ M or 0.05% DMSO control) for 0 - 4 h. The images were taken on a GXCAM digital camera mounted on a ZEISS Primo Vert microscope at a magnification of 10X.¹⁶⁹

7.9 EtBr Intercalation Assay

Collection conditions: excitation wavelength 545 nm, collection range 575 – 700 nm (emission bandwidth \pm 4 nm)

In a fluorescence cuvette ct-DNA (27.7 μ M) and EtBr (11.25 μ M) were combined with a ratio of 1:2.5 (EtBr:DNA) in 10 mM Tris buffer (pH 7.4) to a volume of 1900 μ L, DMSO 100 μ L was then added. The components were then thoroughly

mixed through inversion of the cuvette multiple times. The samples were allowed to stand for 30 mins after which the first fluorescence spectrum was taken. The test compounds (1 mM) in DMSO (2 μ L) were added to the cuvette, mixed, and allowed to equilibrate for 5 mins after which a fluorescence spectrum was taken, this step was repeated for all further additions.¹⁶⁹

7.10 Molecular Docking of DNA with [Ag₂(L13)₂](PF₆)₂

The crystal structure of a DNA dodecamer was accessed from the protein data bank (<http://www.rcsb.org> PDB ID:1LU5). The molecular structure optimization of the most selective complex [Ag₂(L13)₂](PF₆)₂ was performed using DFT calculations, using ORCA 5.0.4.²⁸⁵ The complex was optimised without any constraint using the PBE0 functional²⁸⁶ and the def2-TZVP basis set combined with a 28-electron effective core potential (def2-ECP)²⁸⁷ for Ag and the def2-SVP basis set for all other atoms.²⁸⁸ The Chain of Spheres Exchange variant of the Resolution of Identity approximation (RIJCOSX) was used to speed up the calculations using the def2/J auxiliary basis set.²⁸⁹ The optimised structure was identified as the true ground state by the absence of negative Eigenvalues in the frequency calculation. The CIF (scXRD) and XYZ (DFT) files were converted to the PDB format using UCSF Chimera,²⁹⁰ where counterions were omitted for simplicity (<http://www.cgl.ucsf.edu/chimera/>) (carried out by Dr Benjamin Hofmann). The molecular docking study was performed using AutoDock 4.2.6 software¹⁹⁷ using the Lamarckian Genetic Algorithm. The DNA structure was kept rigid, while the metal complex was allowed to have rotatable bonds. The grid map was set to 76 x 62 x 104 Å³ along the x, y, and z axes with 0.375 Å grid spacing. The analysis was performed at least three times to confirm reproducibility with the lowest free binding energy conformation reported. PyMOL (The PyMOL Molecular Graphics System, Version 2.5.2 Schrödinger, LLC.) was used to produce images (molecular docking was performed by Dr Tameryn Stringer).¹⁶⁹

7.11 Reactive Oxygen Species Studies

MDA-MB-231 cells (maintained as described above) were seeded in a Nunc® MicroWell 96 well optical bottom plate at a concentration of 8 x 10³ cells/well in indicator-free complete RPMI (100 μ L) and incubated at 37°C and 5% CO₂ for 2 days, after which complete RPMI (100 μ L) spiked with Ag(I)-NHC complex (1, 2

and 5x IC₅₀ (at 24 hours) or DMSO 0.1% control) was added for 3.5 hours. H₂DCFDA (20 µL) in PBS:DMSO (91:3) was added to give a final dye concentration of 20 µM, and incubated for 30 min. The media was removed, and the wells were washed with PBS (3 x 200 µL) and complete RMPI (100 µL) was added. The cells were imaged on an Observer-7 microscope, ex: 494 nm and em: 512 nm.¹⁶⁹

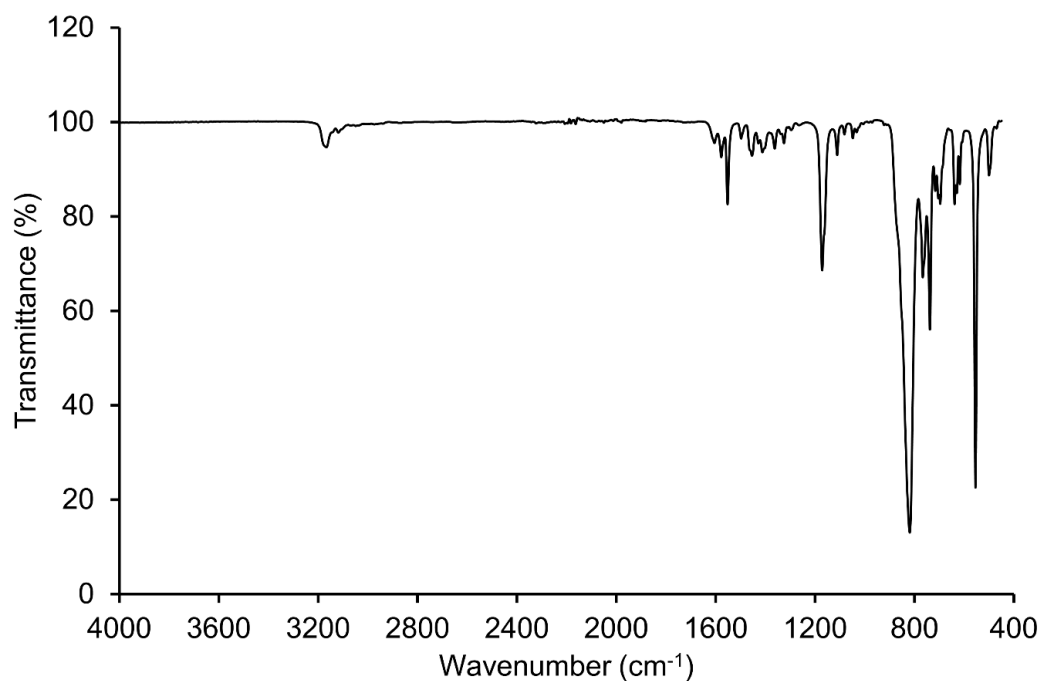
7.12 Cell Uptake

MDA-MB-231 and MCF-7 cells were maintained as described in the cell culture protocol above. All assays were conducted in 6-well plates and cells were diluted to a concentration of 1 x 10⁶ cells/well in 1 mL of complete media. After 24 h, complex [Ag(L16)₂](PF₆) or [Ag₂(L13)₂](PF₆)₂ (1 µM) were added to the plates for 1 h. The media was removed, and the cells were washed with PBS (2 x 1 mL) and trypsin-EDTA (0.05%) was added for 2-3 minutes. Complete media was added to dilute the trypsin, and the cell suspension was collected in Falcon tubes. The samples were centrifuged at 1500 rpm for 5 mins, then resuspended and washed with PBS and gently vortexed in between. The washing step was repeated three times to remove residual silver complex. Cell pellets were digested by addition of 100 µL of ultra-pure grade 67% nitric acid (Rohm) with heating at 70 °C for 1 h, followed by addition of 100 µL of ultra-trace grade 30% hydrogen peroxide (Merck) and heating at 70 °C for a further 4 h. The digested samples were diluted to 2% nitric acid prior to analysis. A range of calibration standards were prepared by dilution of multi elemental standard solution IV (Merck). Analysis of the ¹⁰⁷Ag isotope was performed on a sector-field ICP-MS (Element 2XR, Thermo Scientific). The instrument was fitted with a cyclonic spray chamber (Glass Expansion), conical glass concentric nebuliser (Glass Expansion) and 0.25 I.D. probe (Elemental Scientific). The results are reported as Ag atoms/cell from a triplicate of repeats.¹⁶⁹

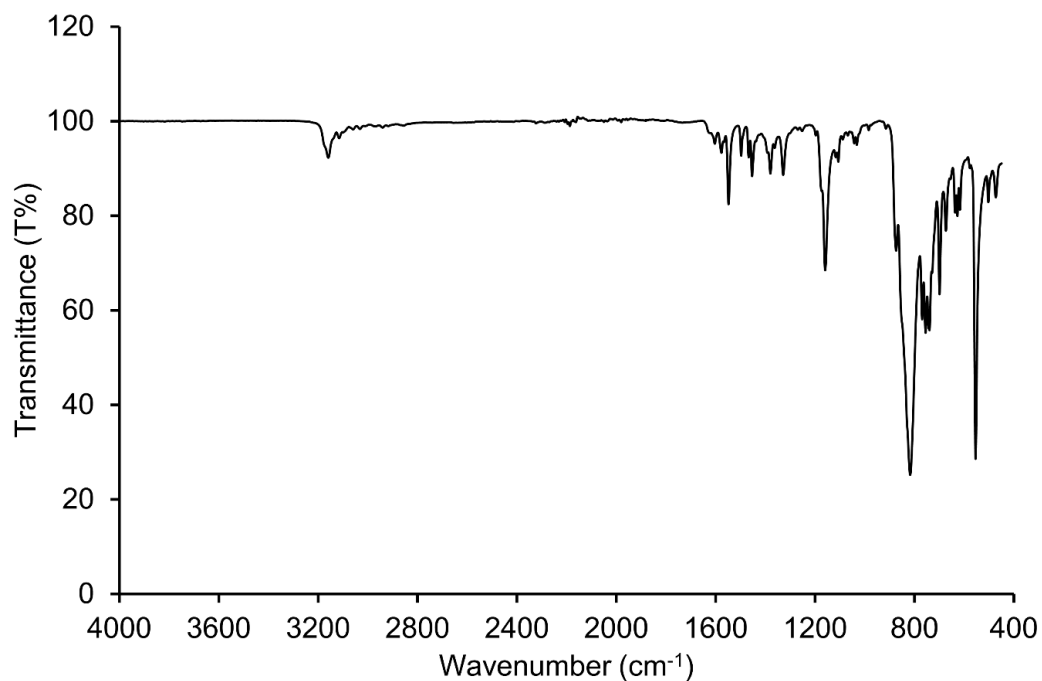
8 Appendix

8.1 ATR-FTIR spectra

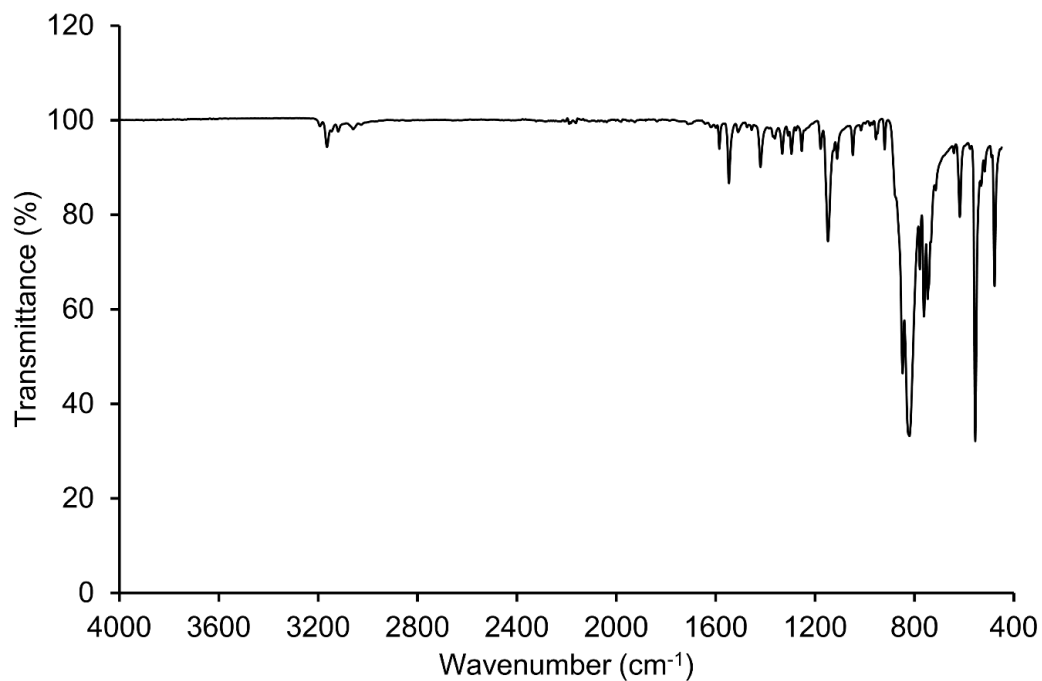
8.1.1 Ligands



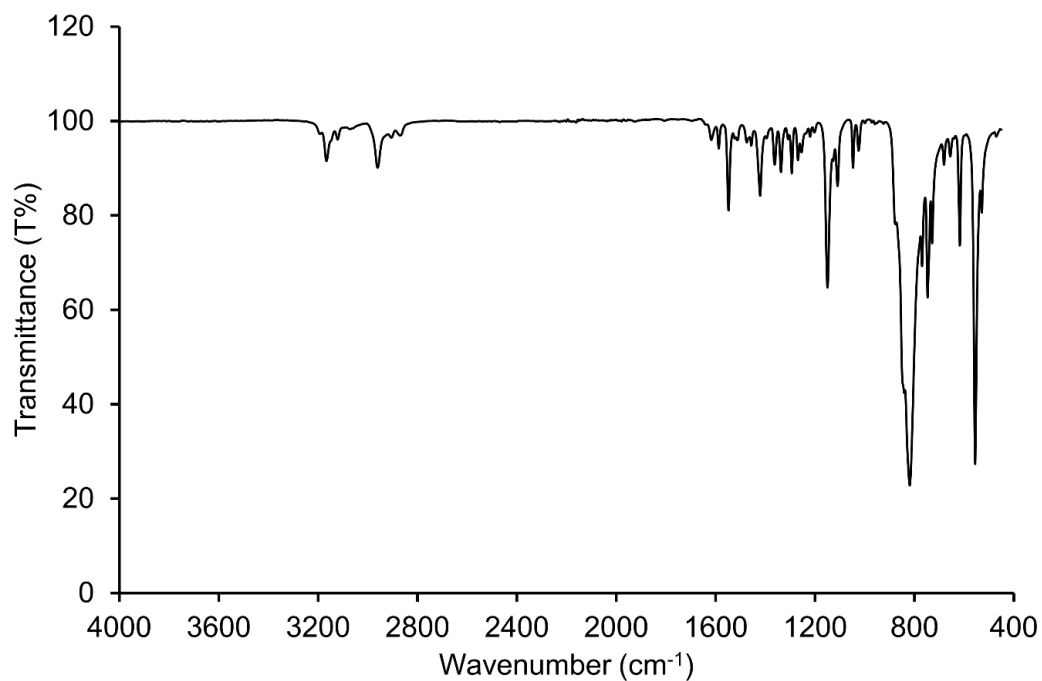
Appendix 8.1: ATR-FTIR spectrum of [H₂L2](PF₆)₂ between 450 – 4000 cm⁻¹.



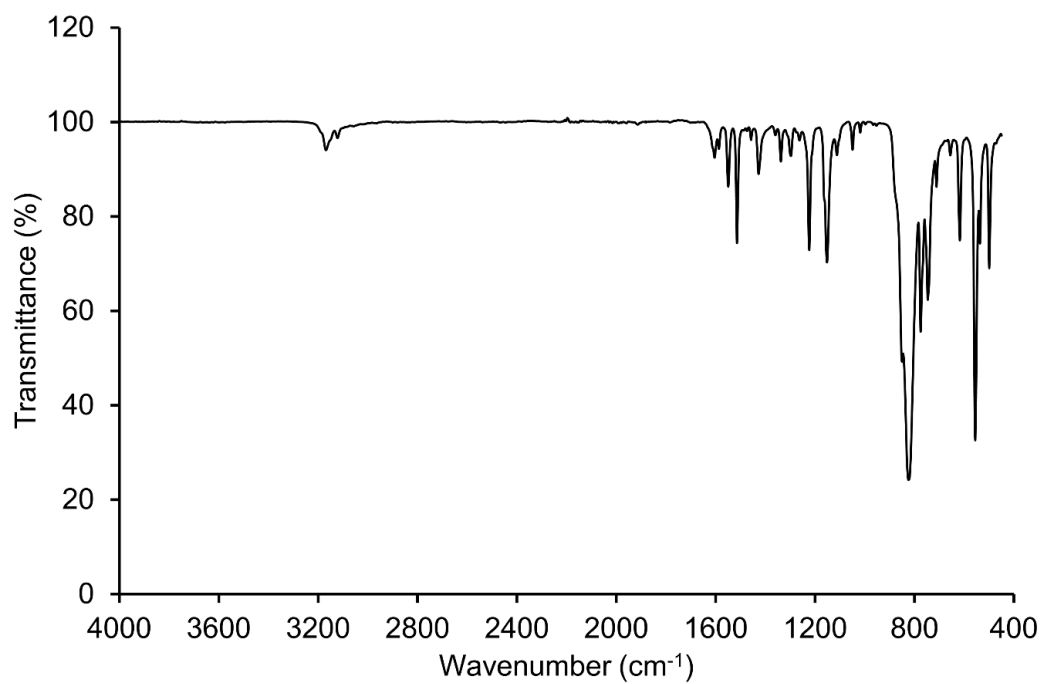
Appendix 8.2: ATR-FTIR spectrum of [H₂L3](PF₆)₂ between 450 – 4000 cm⁻¹.



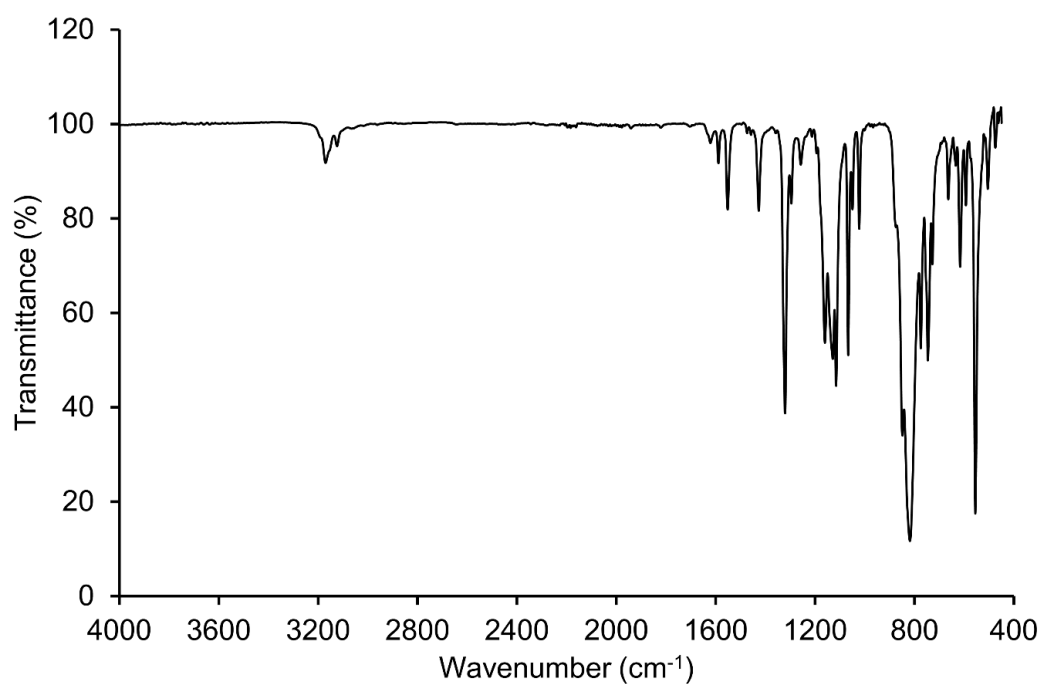
Appendix 8.3: ATR-FTIR spectrum of $[H_2L4](PF_6)_2$ between 450 – 4000 cm^{-1}



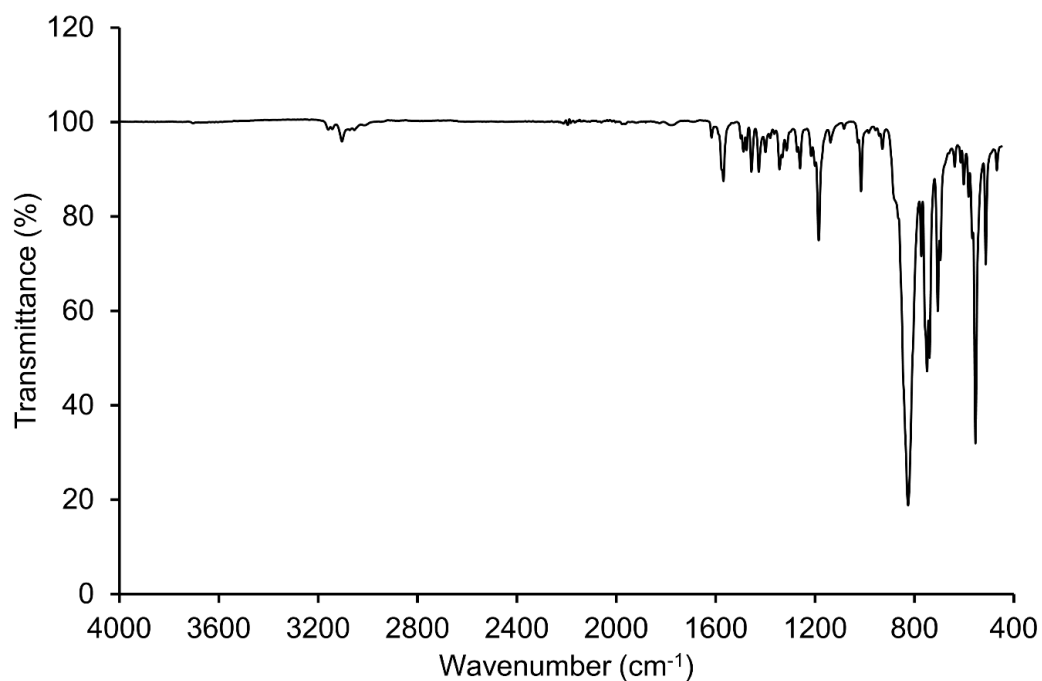
Appendix 8.4: ATR-FTIR spectrum of $[H_2L5](PF_6)_2$ between 450 – 4000 cm^{-1}



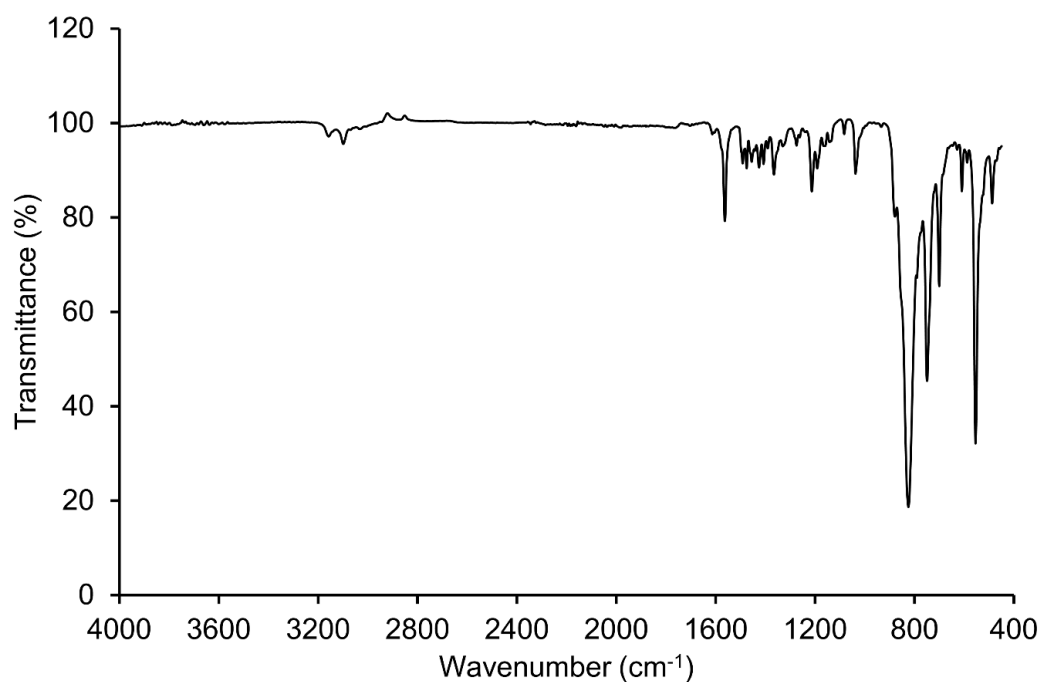
Appendix 8.5: ATR-FTIR spectrum of $[H_2L6](PF_6)_2$ between 450 – 4000 cm^{-1} .¹



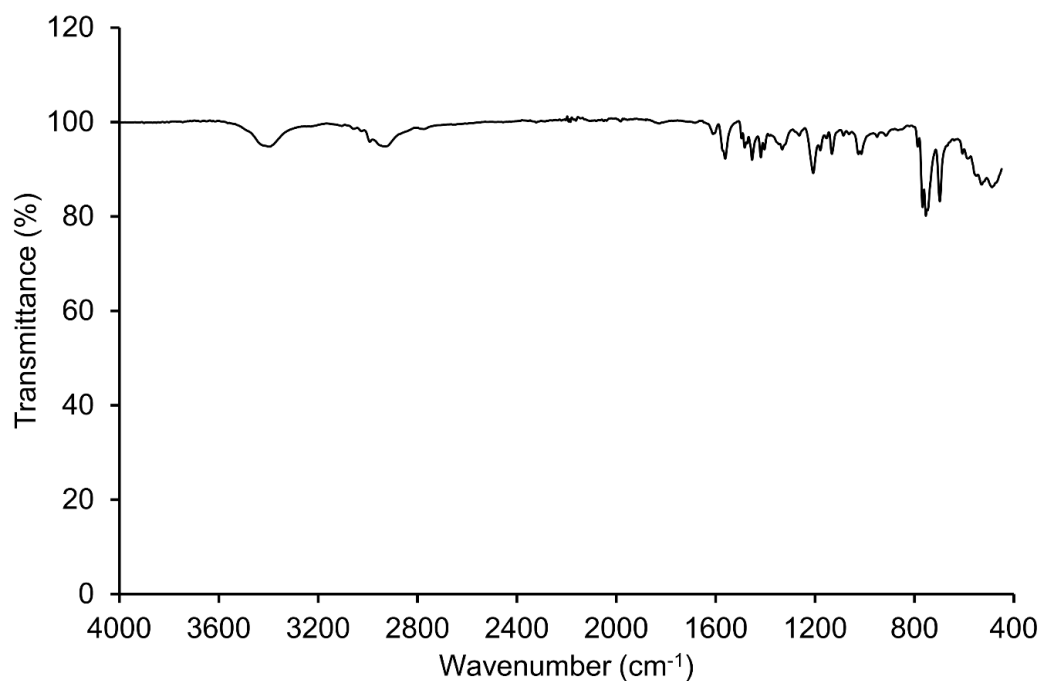
Appendix 8.6: ATR-FTIR spectrum of $[H_2L7](PF_6)_2$ between 450 – 4000 cm^{-1} .¹



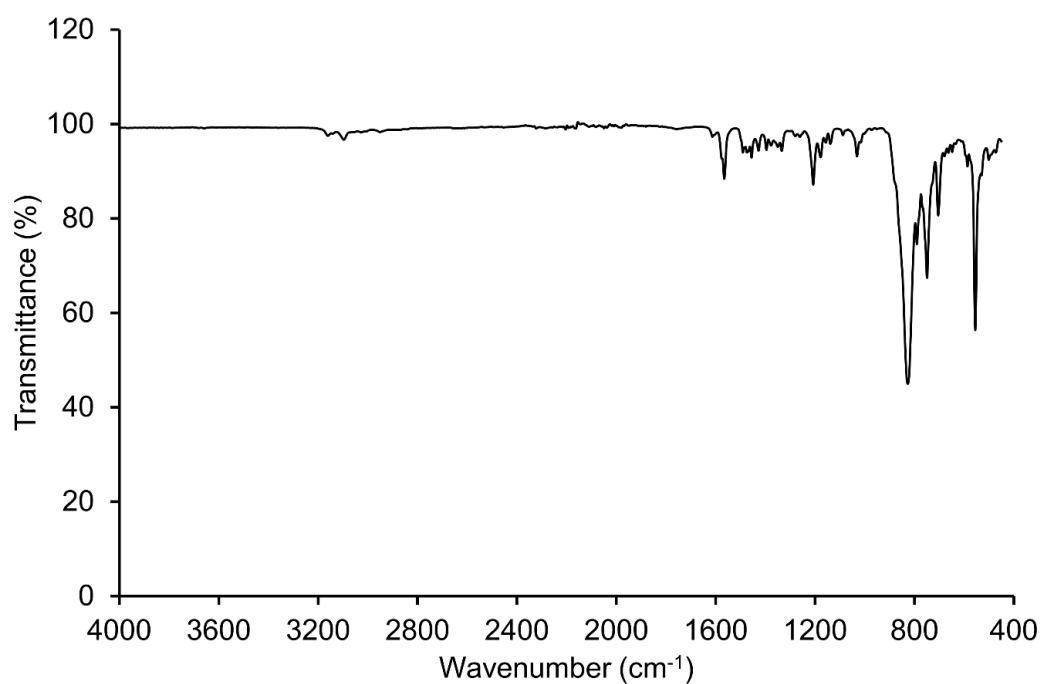
Appendix 8.7: ATR-FTIR spectrum of $[H_2L8](PF_6)_2$ between 450 – 4000 cm^{-1} .



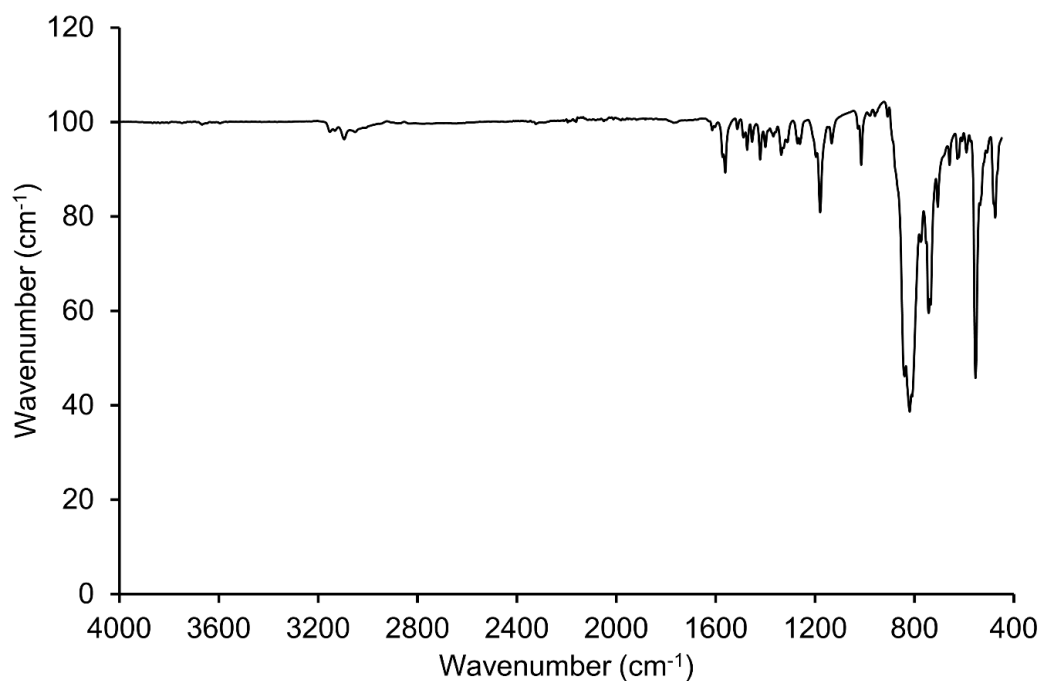
Appendix 8.8: ATR-FTIR spectrum of $[H_2L9](PF_6)_2$ between 450 – 4000 cm^{-1} .



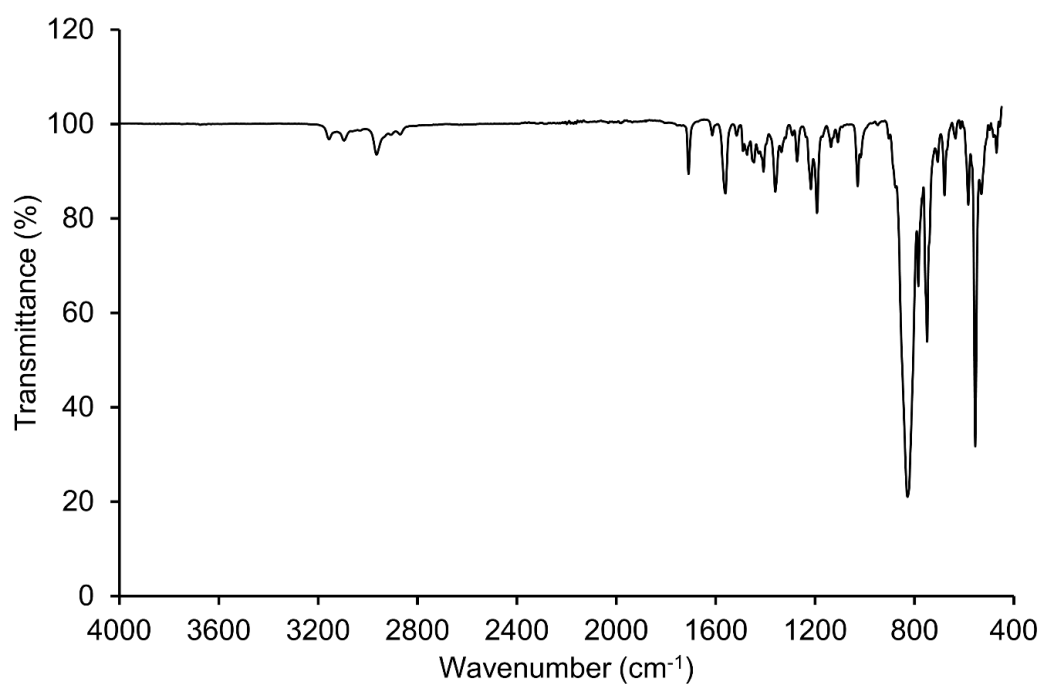
Appendix 8.9: ATR-FTIR spectrum of $[H_2L10](Br)_2$ between 450 – 4000 cm^{-1} .



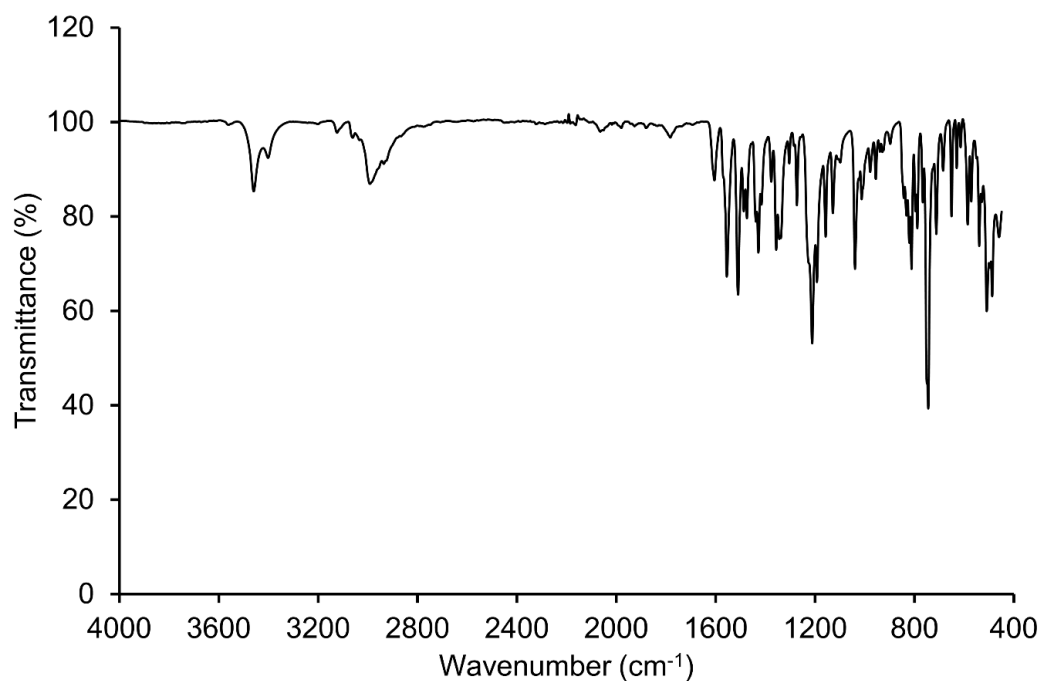
Appendix 8.10: ATR-FTIR spectrum of $[H_2L10](PF_6)_2$ between 450 – 4000 cm^{-1} .



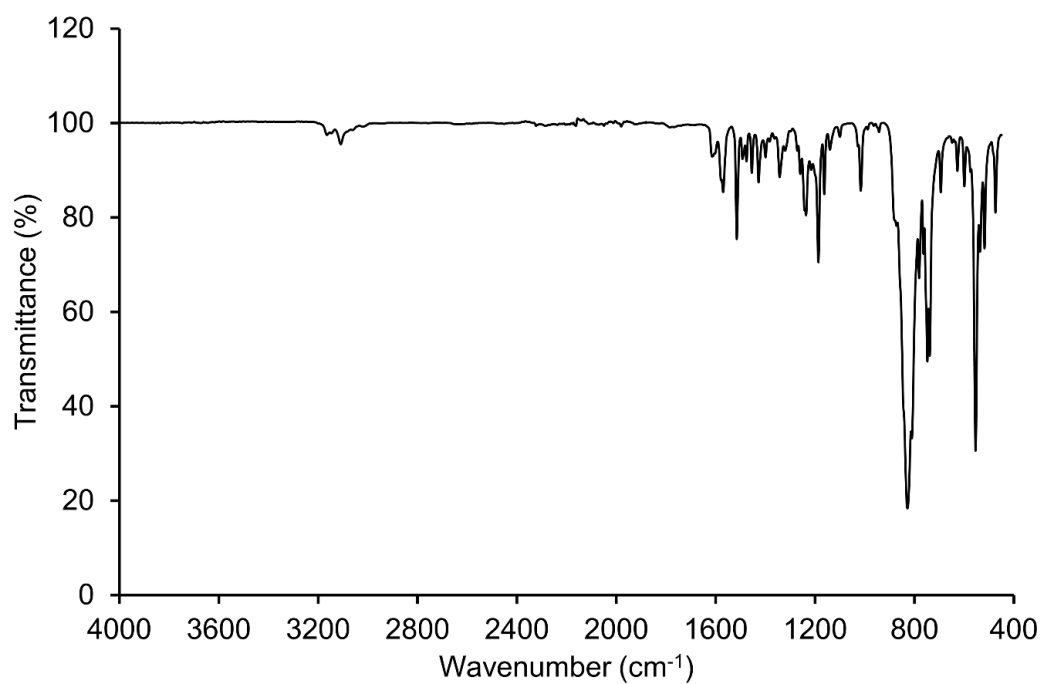
Appendix 8.11: ATR-FTIR spectrum of $[H_2L11](PF_6)_2$ between $450 - 4000\text{ cm}^{-1}$.



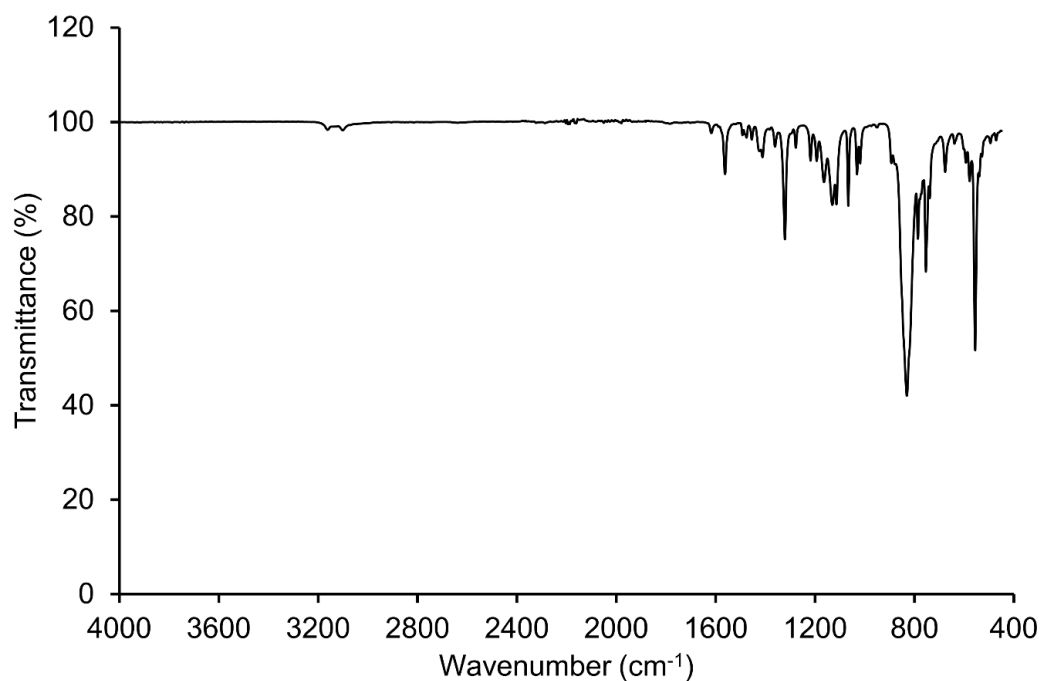
Appendix 8.12: ATR-FTIR spectrum of $[H_2L12](PF_6)_2$ between $450 - 4000\text{ cm}^{-1}$.



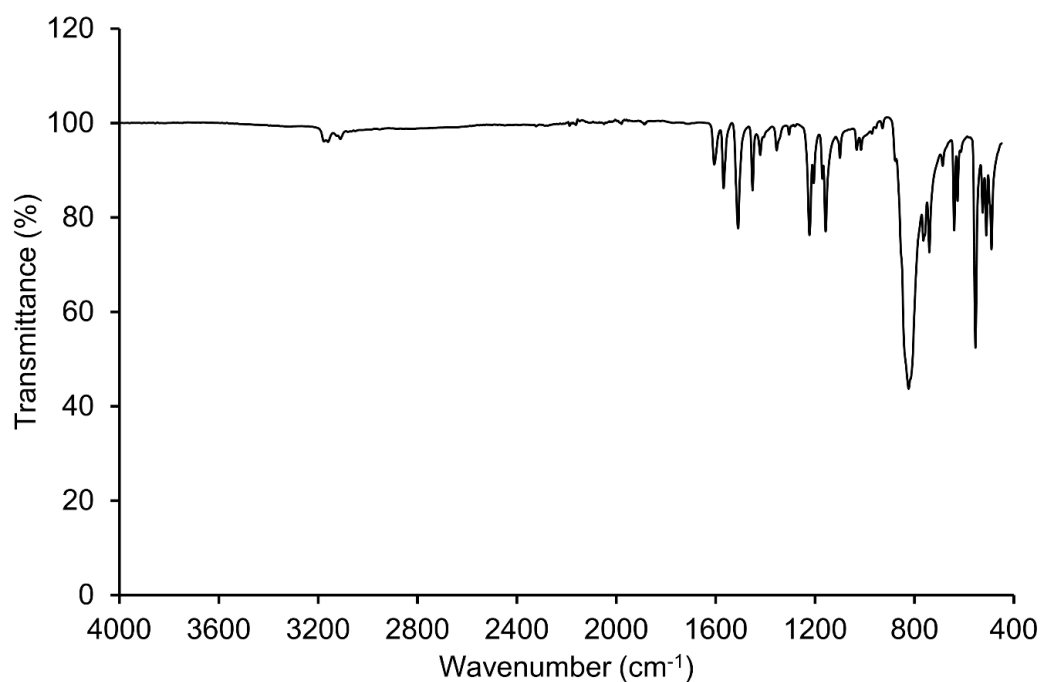
Appendix 8.13: ATR-FTIR spectrum of $[H_2L13](Br)_2$ between 450 – 4000 cm^{-1} .



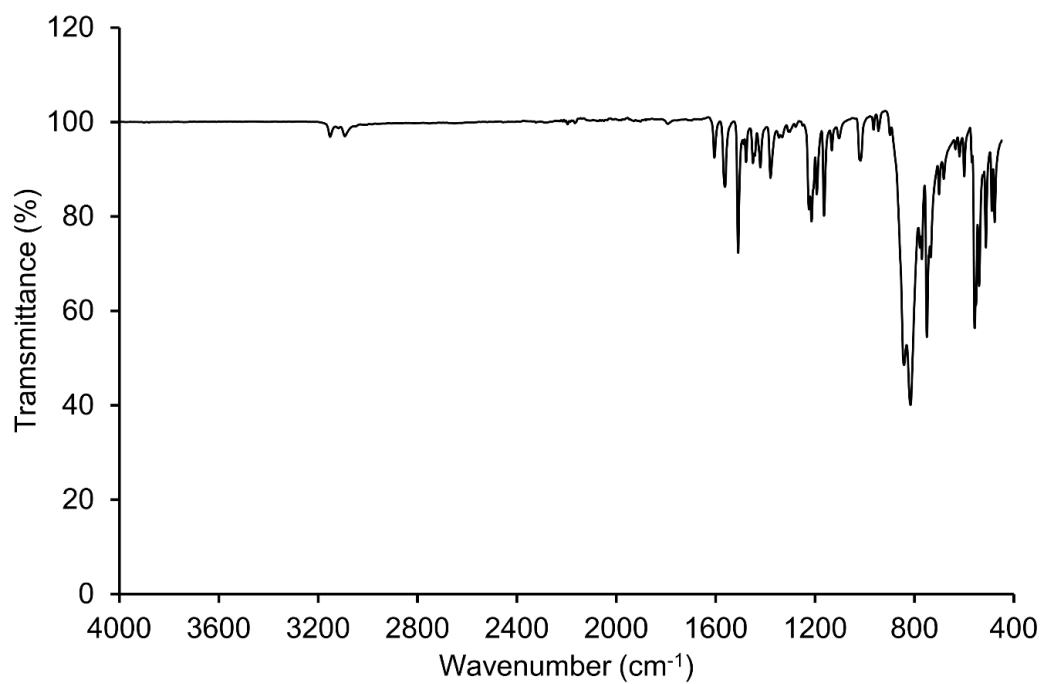
Appendix 8.14: ATR-FTIR spectrum of $[H_2L13](PF_6)_2$ between 450 – 4000 cm^{-1} .



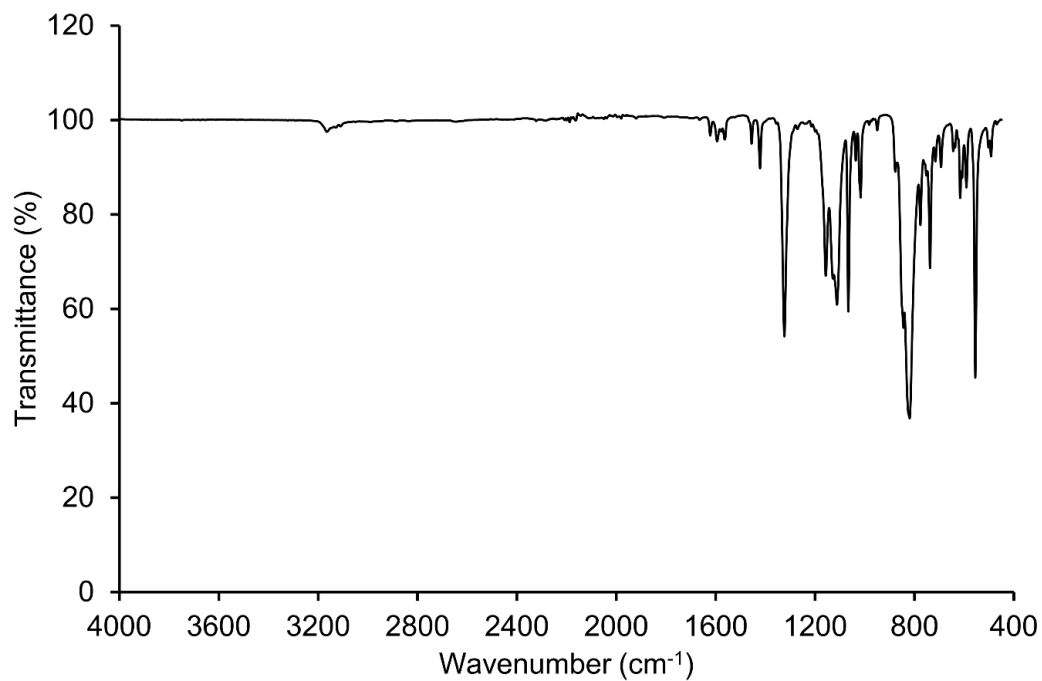
Appendix 8.15: ATR-FTIR spectrum of $[H_2L14](PF_6)_2$ between 450 – 4000 cm^{-1} .



Appendix 8.16: ATR-FTIR spectrum of $[HL15](PF_6)_2$ between 450 – 4000 cm^{-1} .

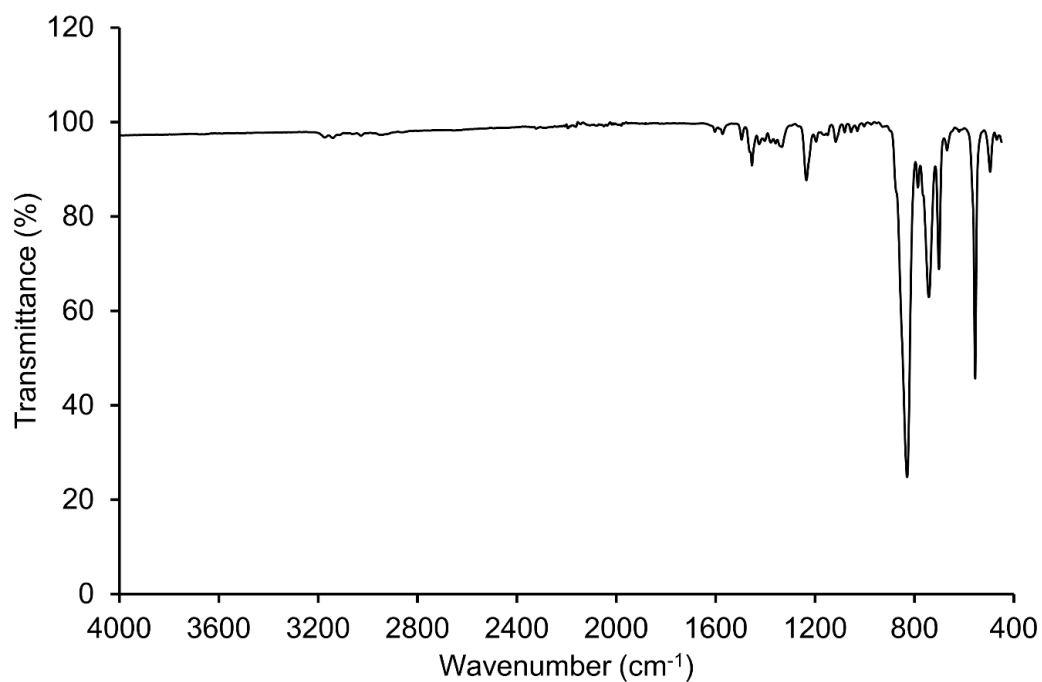


Appendix 8.17: ATR-FTIR spectrum of [HL16](PF₆)₂ between 450 – 4000 cm⁻¹.

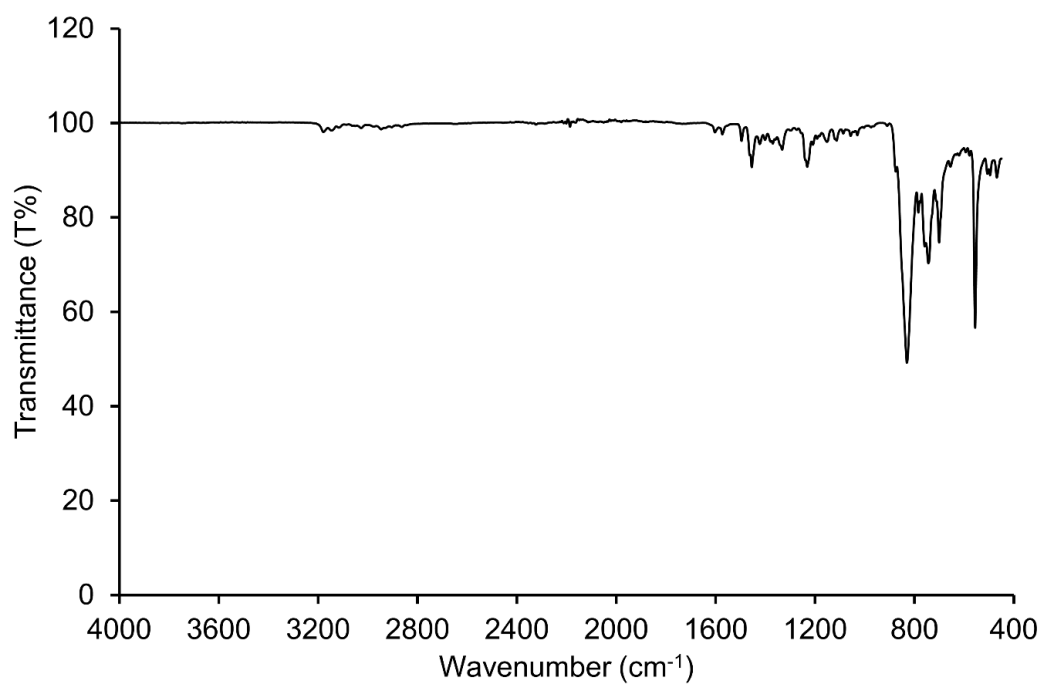


Appendix 8.18: ATR-FTIR spectrum of [HL17](PF₆)₂ between 450 – 4000 cm⁻¹.

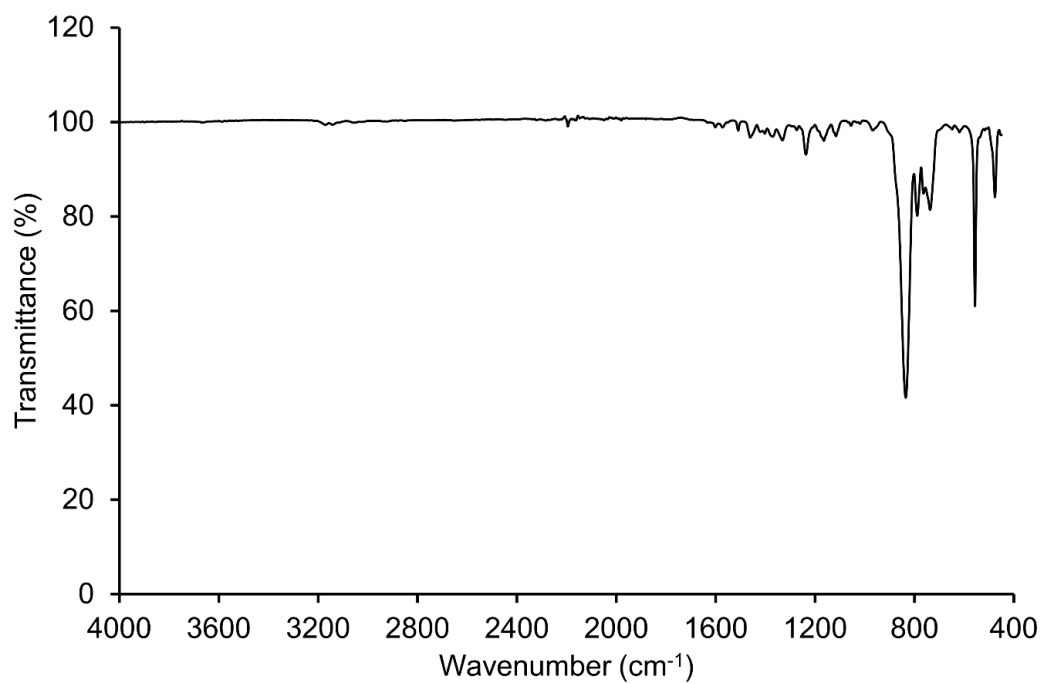
8.1.2 Silver Complexes



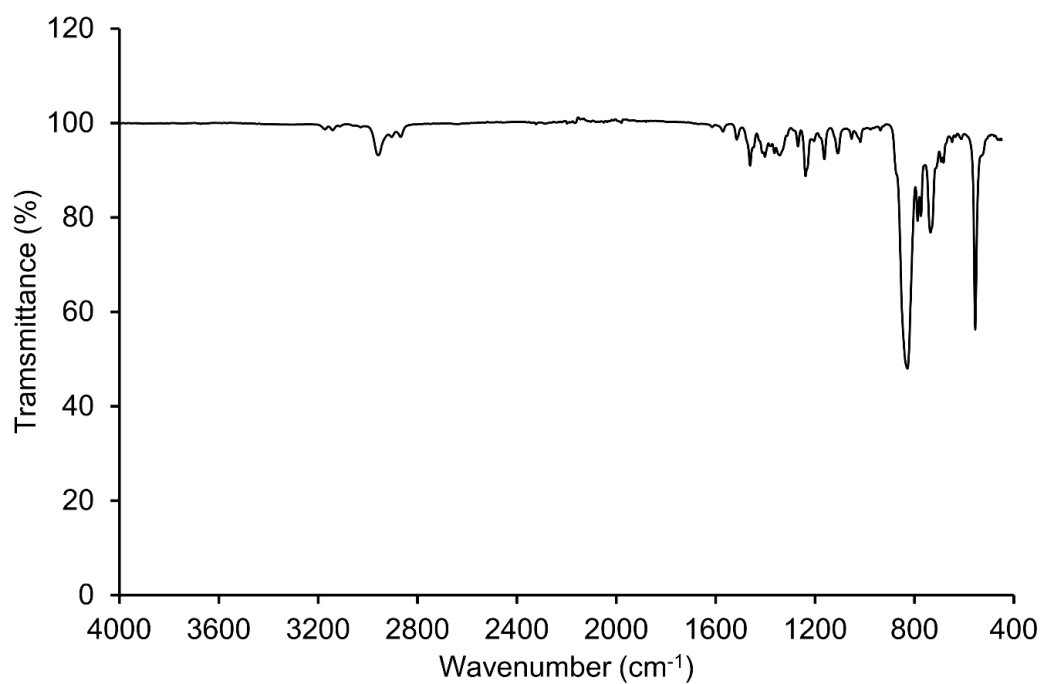
Appendix 8.19: ATR-FTIR spectrum of $[Ag_2(L2)_2](PF_6)_2$ between 450 – 4000 cm^{-1} .



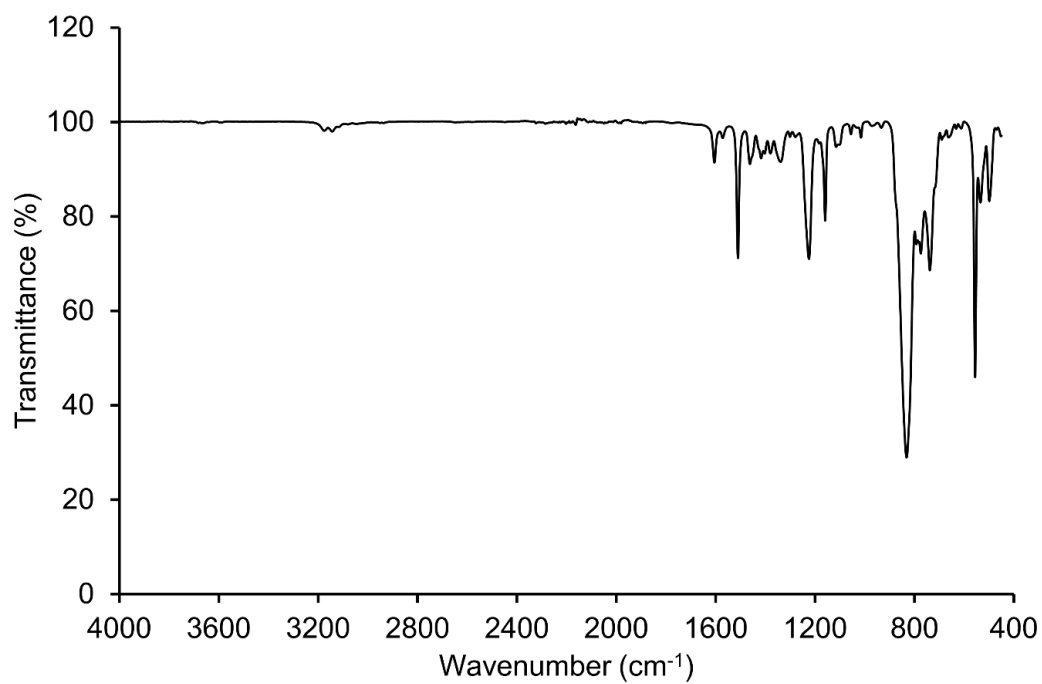
Appendix 8.20: ATR-FTIR spectrum of $[Ag_2(L3)_2](PF_6)_2$ between 450 – 4000 cm^{-1} .



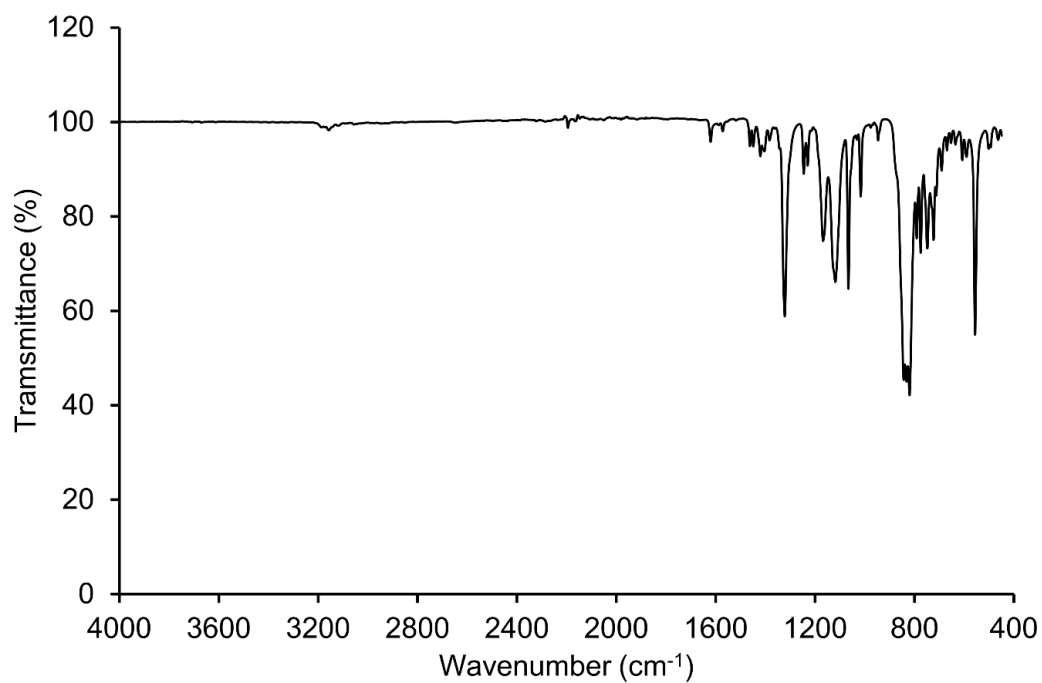
Appendix 8.21: ATR-FTIR spectrum of $[Ag_2(L4)_2](PF_6)_2$ between 450 – 4000 cm^{-1} .



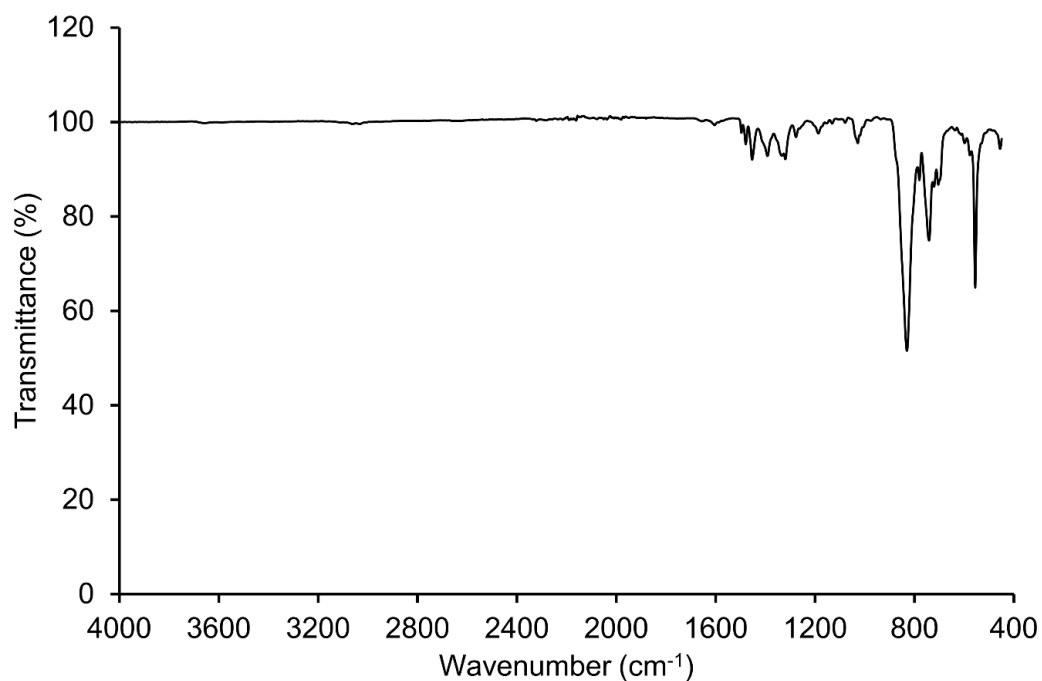
Appendix 8.22: ATR-FTIR spectrum of $[Ag_2(L5)_2](PF_6)_2$ between 450 – 4000 cm^{-1} .



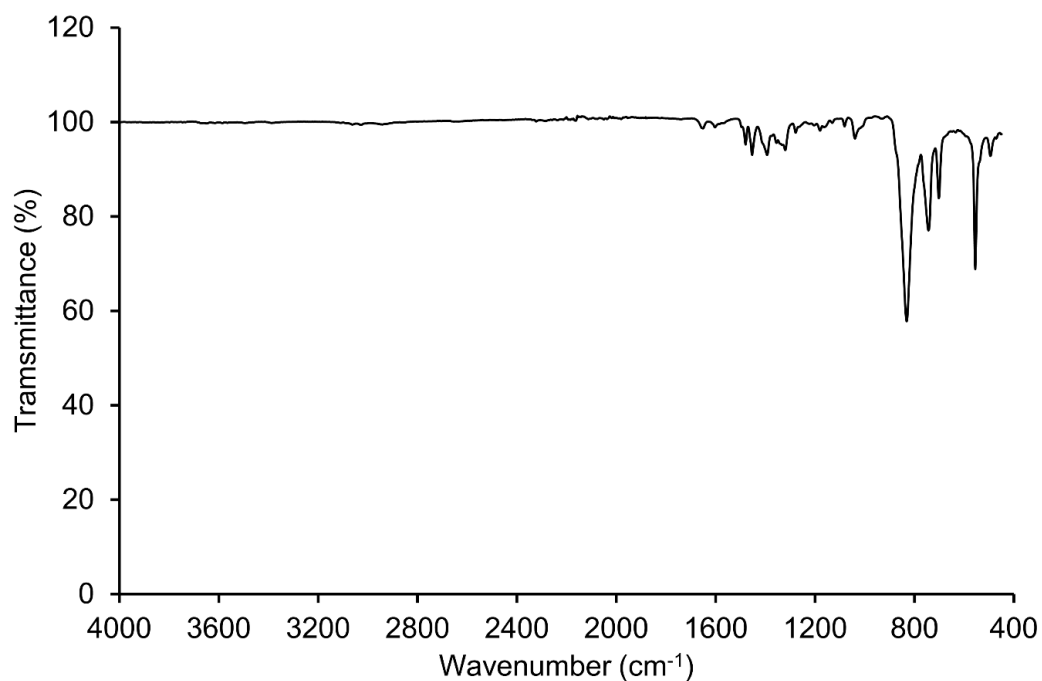
Appendix 8.23: ATR-FTIR spectrum of $[Ag_2(L6)_2](PF_6)_2$ between $450 - 4000\text{ cm}^{-1}$.



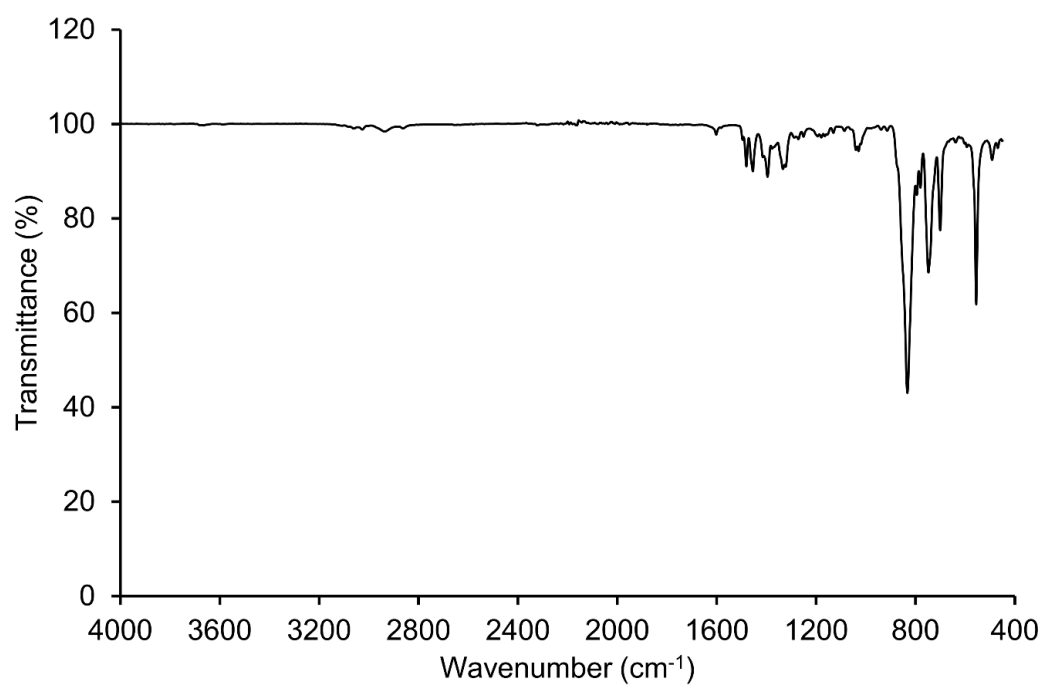
Appendix 8.24: ATR-FTIR spectrum of $[Ag_2(L7)_2](PF_6)_2$ between $450 - 4000\text{ cm}^{-1}$.



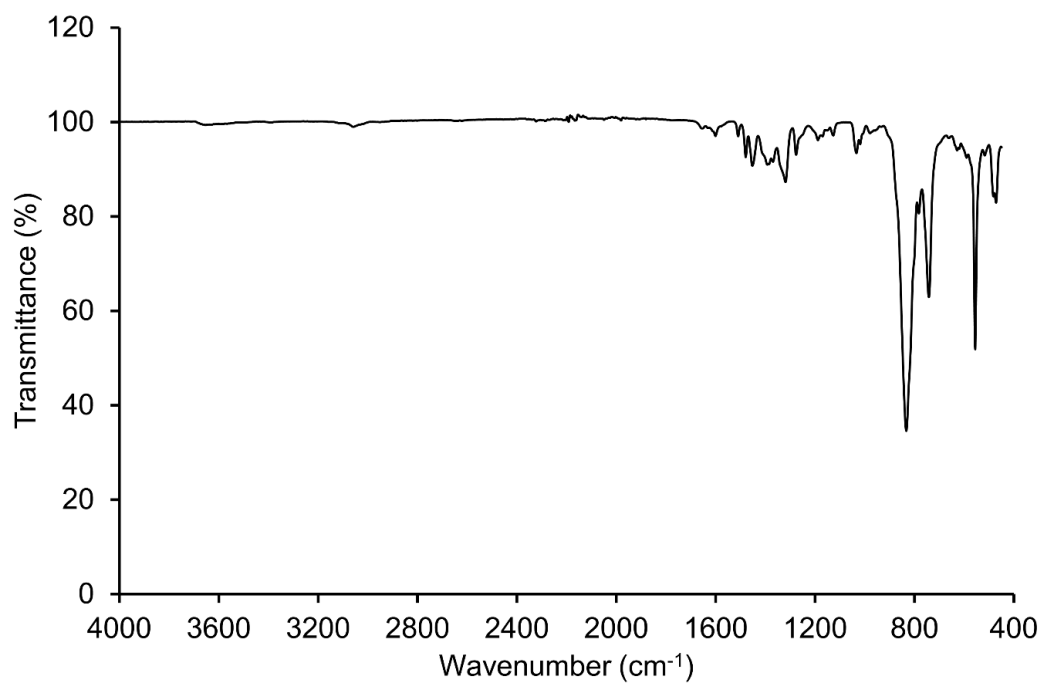
Appendix 8.25: ATR-FTIR spectrum of $[Ag_2(L8)_2](PF_6)_2$ between $450 - 4000\text{ cm}^{-1}$.



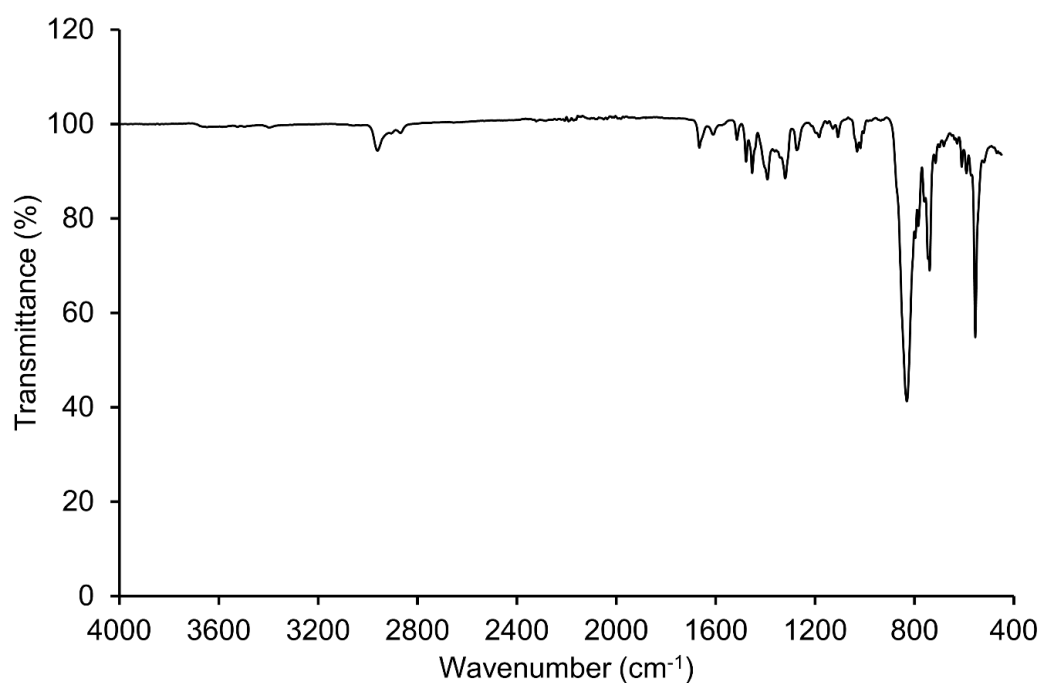
Appendix 8.26: ATR-FTIR spectrum of $[Ag_2(L9)_2](PF_6)_2$ between $450 - 4000\text{ cm}^{-1}$.



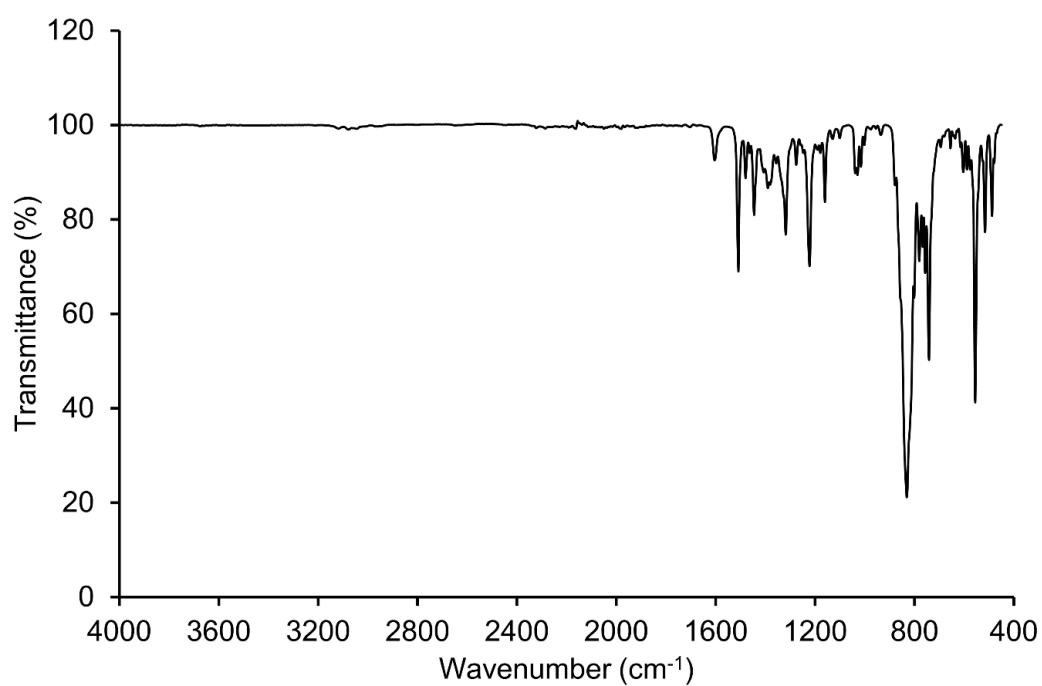
*Appendix 8.27: ATR-FTIR spectrum of $[Ag_2(L10)_2](PF_6)_2$ between
450 – 4000 cm^{-1} .*



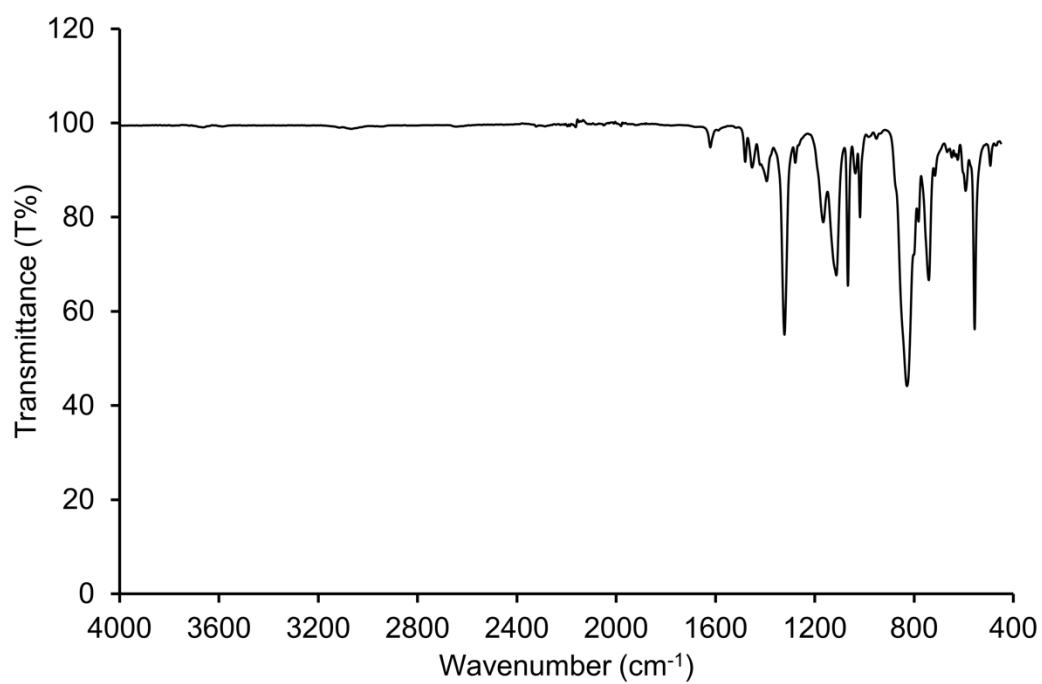
Appendix 8.28: ATR-FTIR spectrum of $[Ag_2(L11)_2](PF_6)_2$ between $450 - 4000\text{ cm}^{-1}$.



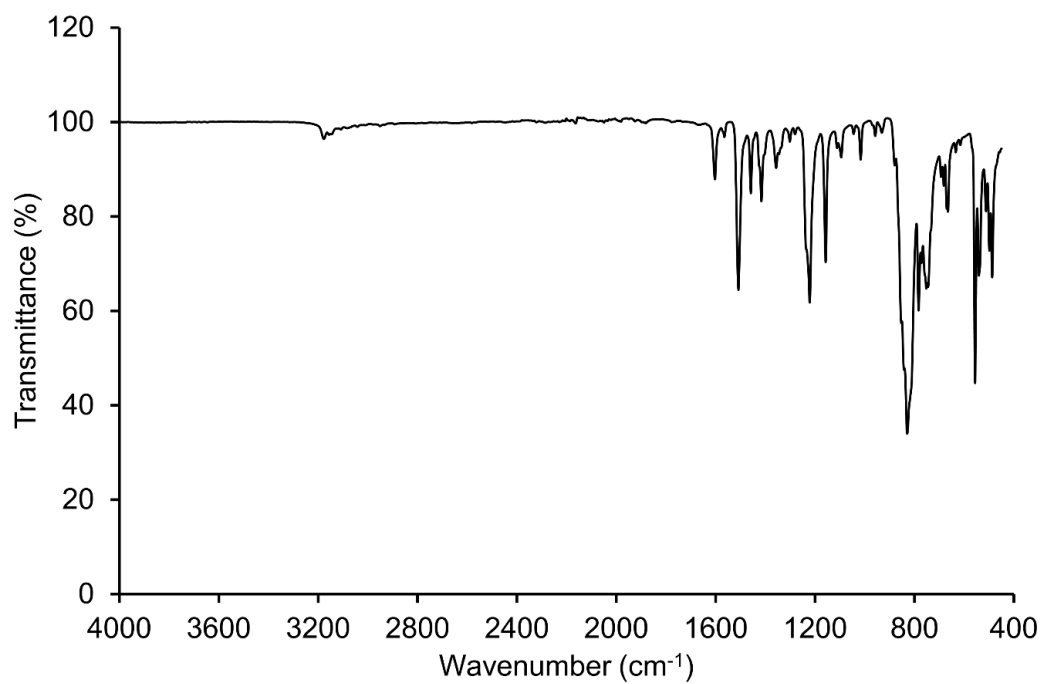
Appendix 8.29: ATR-FTIR spectrum of $[Ag_2(L12)_2](PF_6)_2$ between $450 - 4000\text{ cm}^{-1}$.



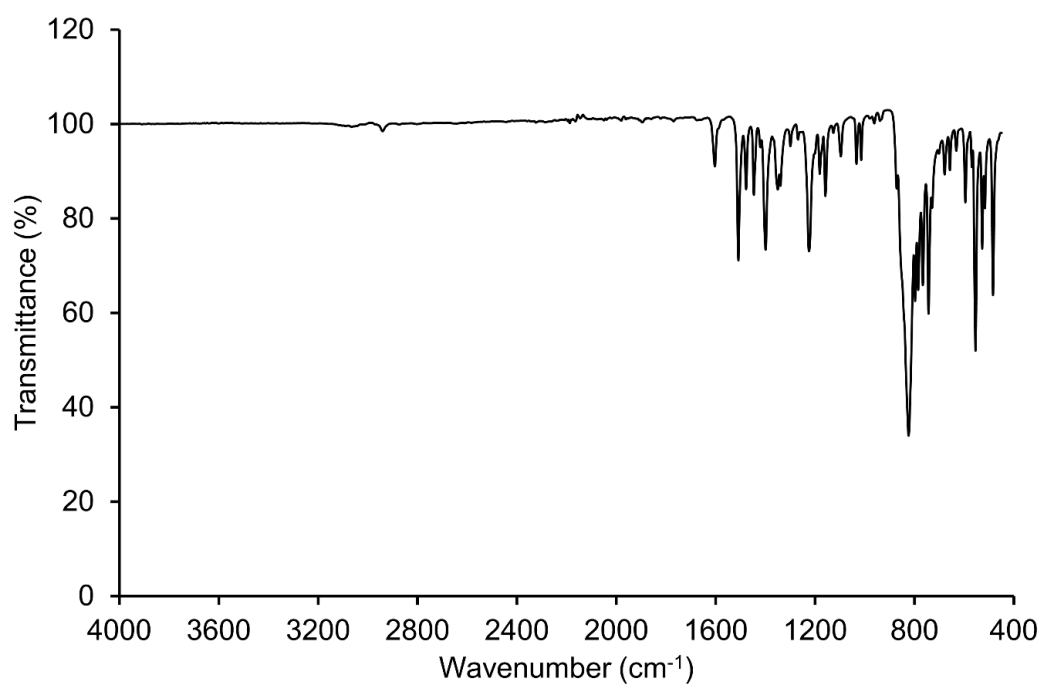
Appendix 8.30: ATR-FTIR spectrum of $[Ag_2(L13)_2](PF_6)_2$ between 450 – 4000 cm^{-1} .



Appendix 8.31: ATR-FTIR spectrum of $[Ag_2(L14)_2](PF_6)_2$ between 450 – 4000 cm^{-1} .

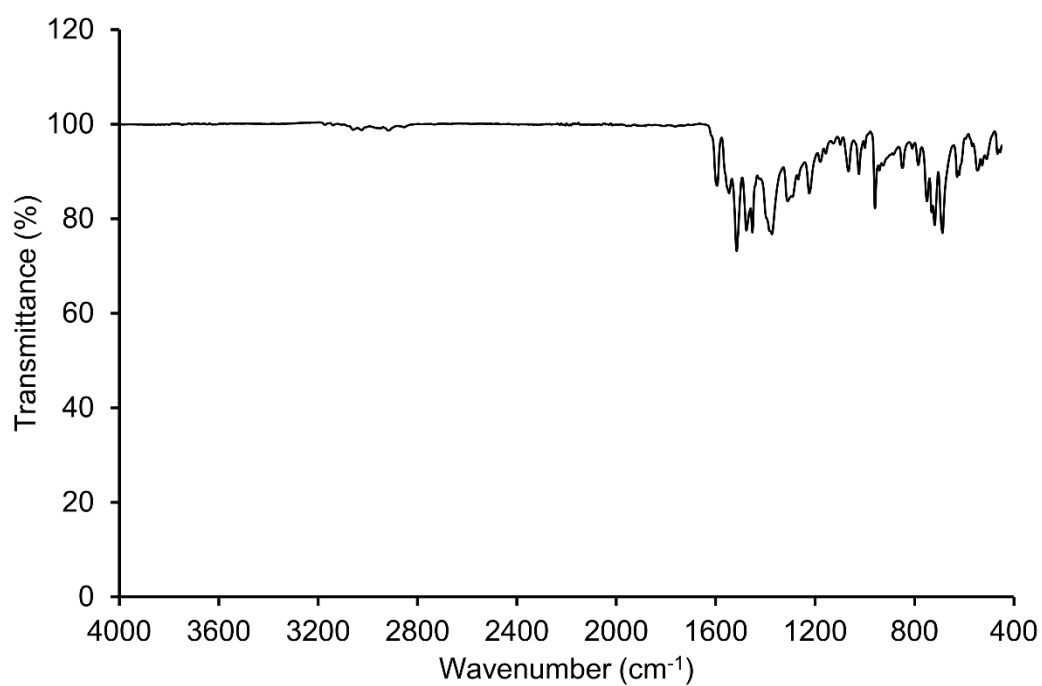


Appendix 8.32: ATR-FTIR spectrum of [Ag(L15)₂](PF₆) between 450 – 4000 cm⁻¹.



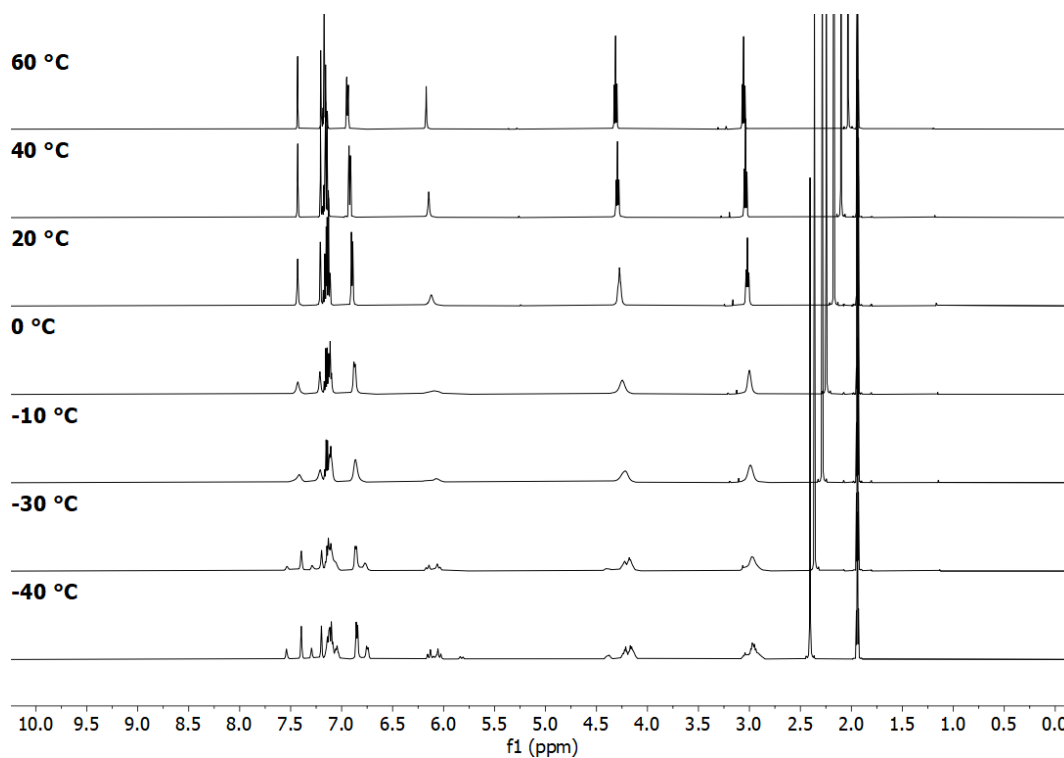
Appendix 8.33: ATR-FTIR spectrum of [Ag(L16)₂](PF₆) between 450 – 4000 cm⁻¹.

8.1.3 Vanadium Complexes

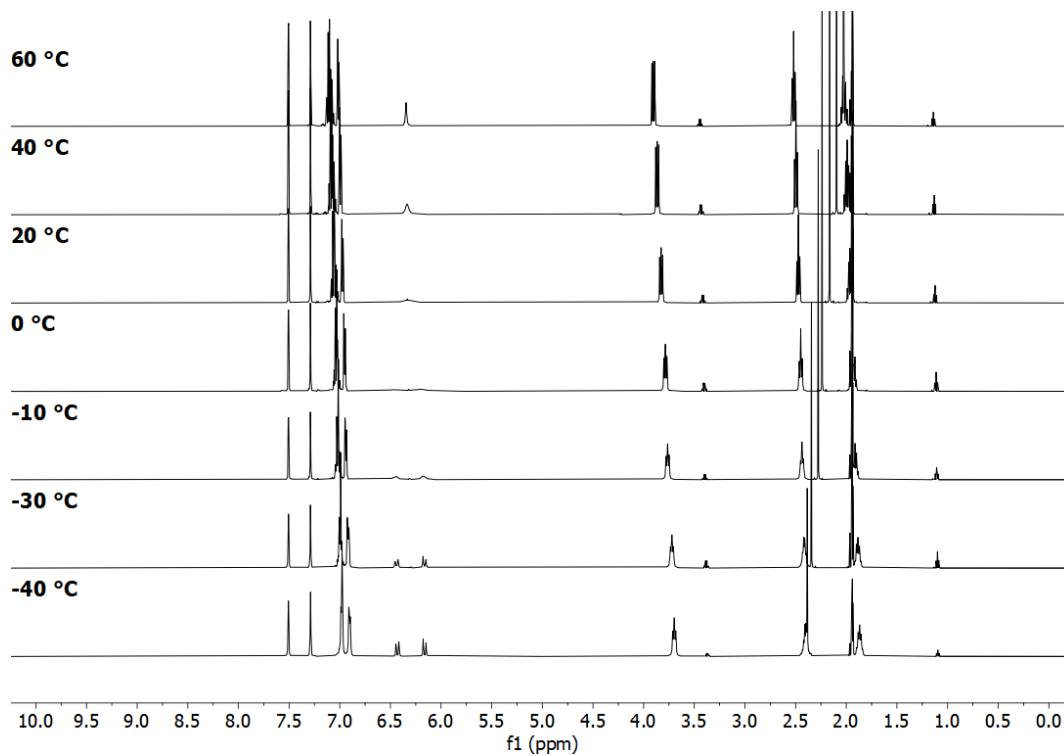


Appendix 8.34: ATR-FTIR spectrum of V2 between 450 – 4000 cm⁻¹.

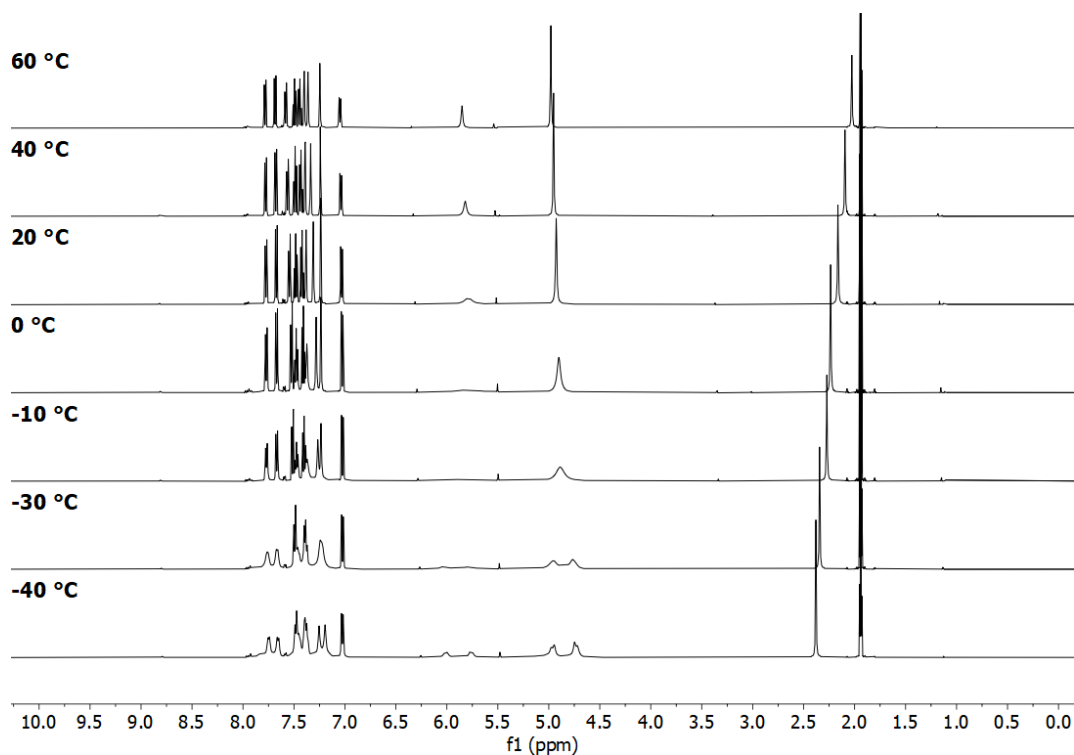
8.2 Variable Temperature ^1H NMR Spectra



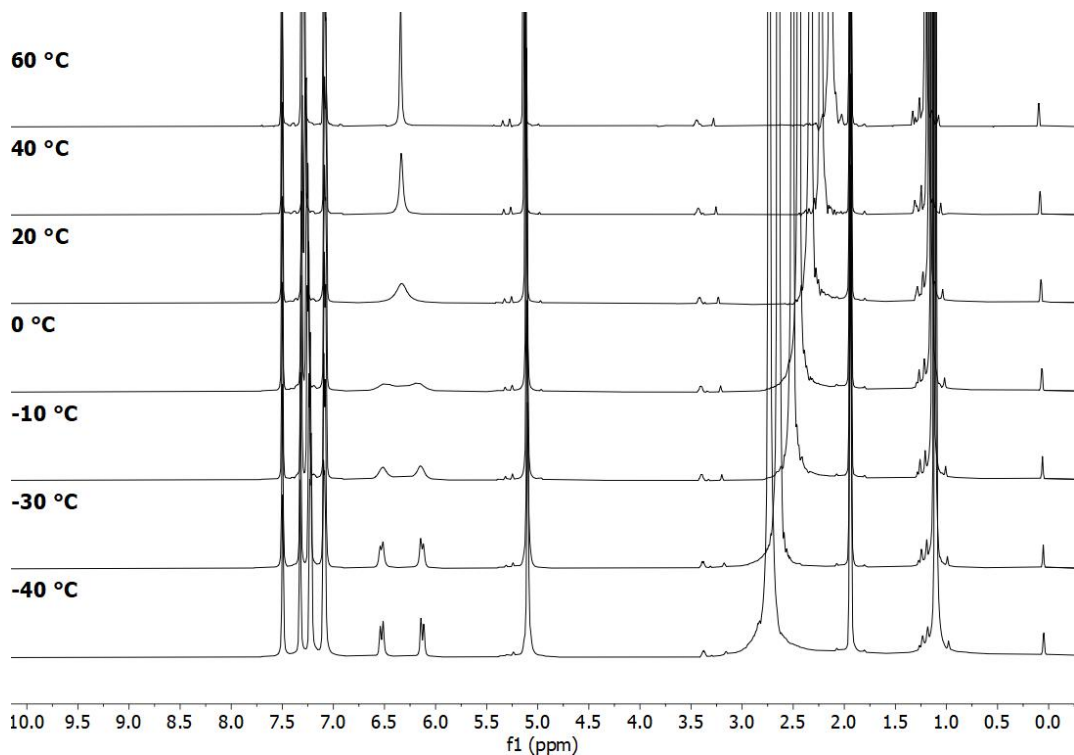
Appendix 8.35: Variable temperature ^1H NMR spectra of $[\text{Ag}_2(\text{L2})_2](\text{PF}_6)_2$ between -40 and 60 °C ($d_3\text{-MeCN}$, 500 MHz).



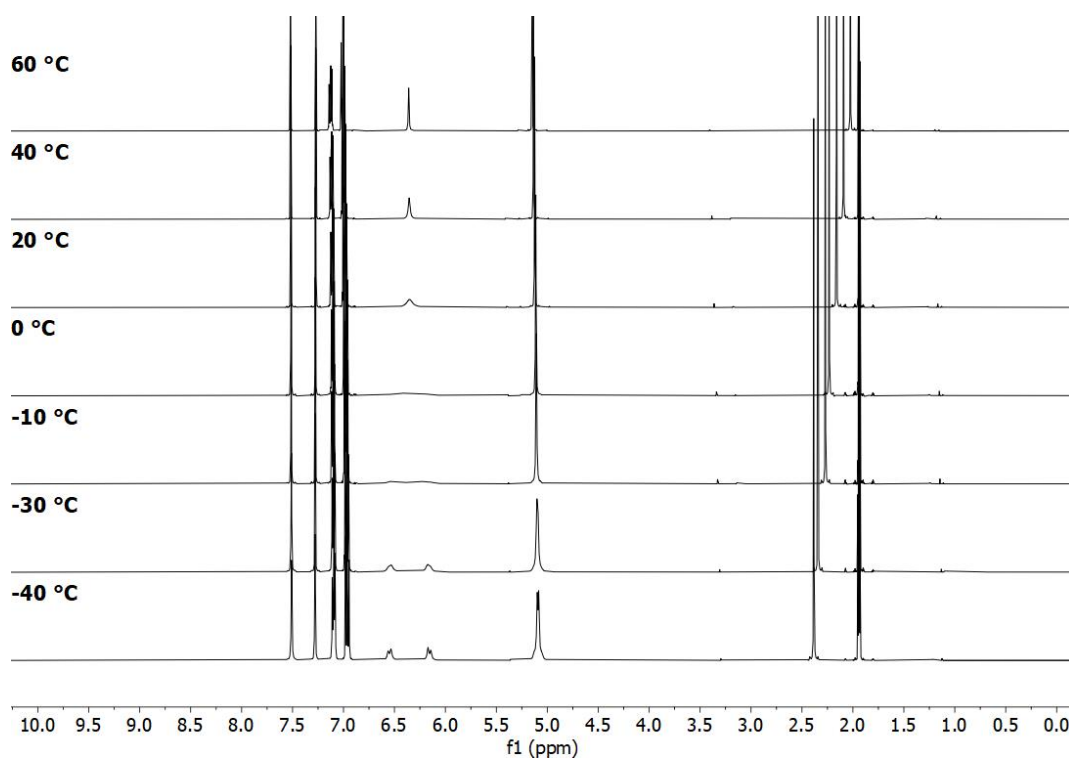
Appendix 8.36: Variable temperature ^1H NMR spectra of $[\text{Ag}_2(\text{L3})_2](\text{PF}_6)_2$ between -40 and 60 °C ($d_3\text{-MeCN}$, 500 MHz).



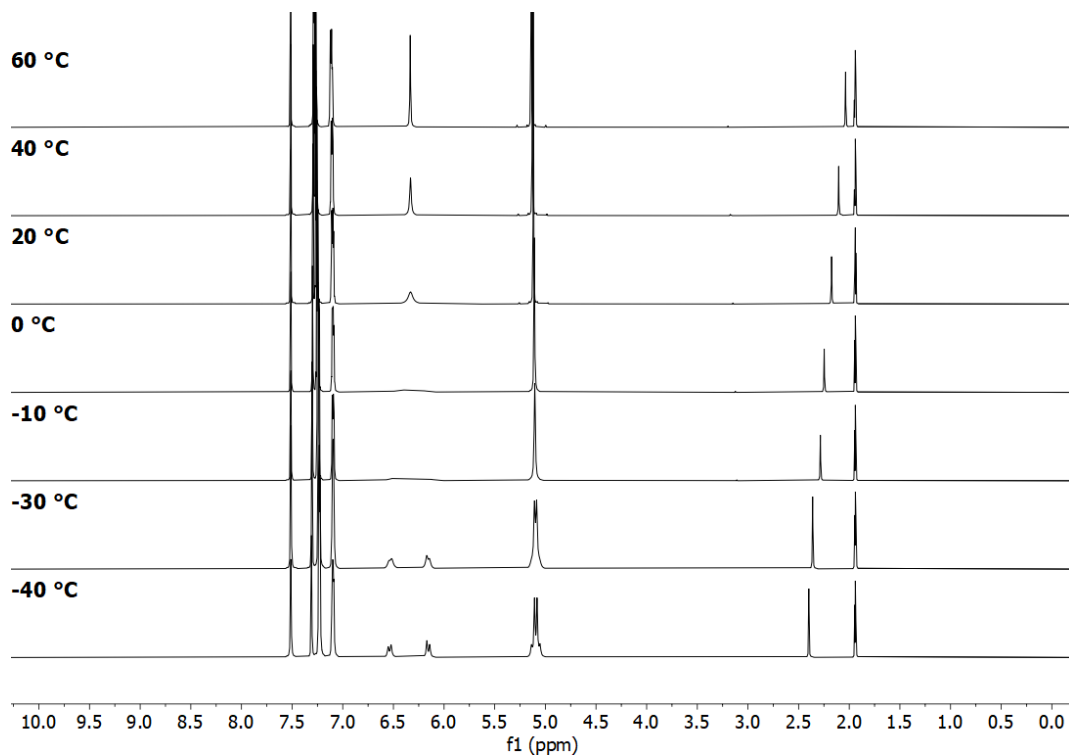
Appendix 8.37: Variable temperature ^1H NMR spectra of $[\text{Ag}_2(\text{L4})_2](\text{PF}_6)_2$ between -40 and 60°C ($d_3\text{-MeCN}$, 500 MHz).



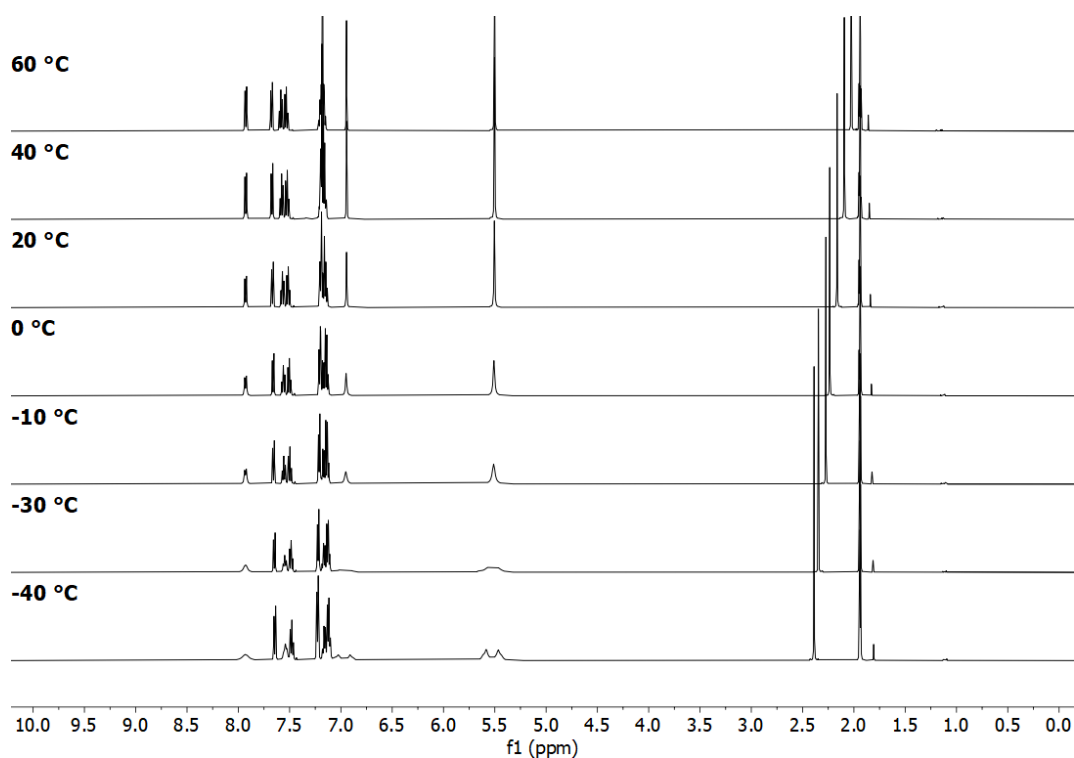
Appendix 8.38: Variable temperature ^1H NMR spectra of $[\text{Ag}_2(\text{L5})_2](\text{PF}_6)_2$ between -40 and 60°C ($d_3\text{-MeCN}$, 500 MHz).



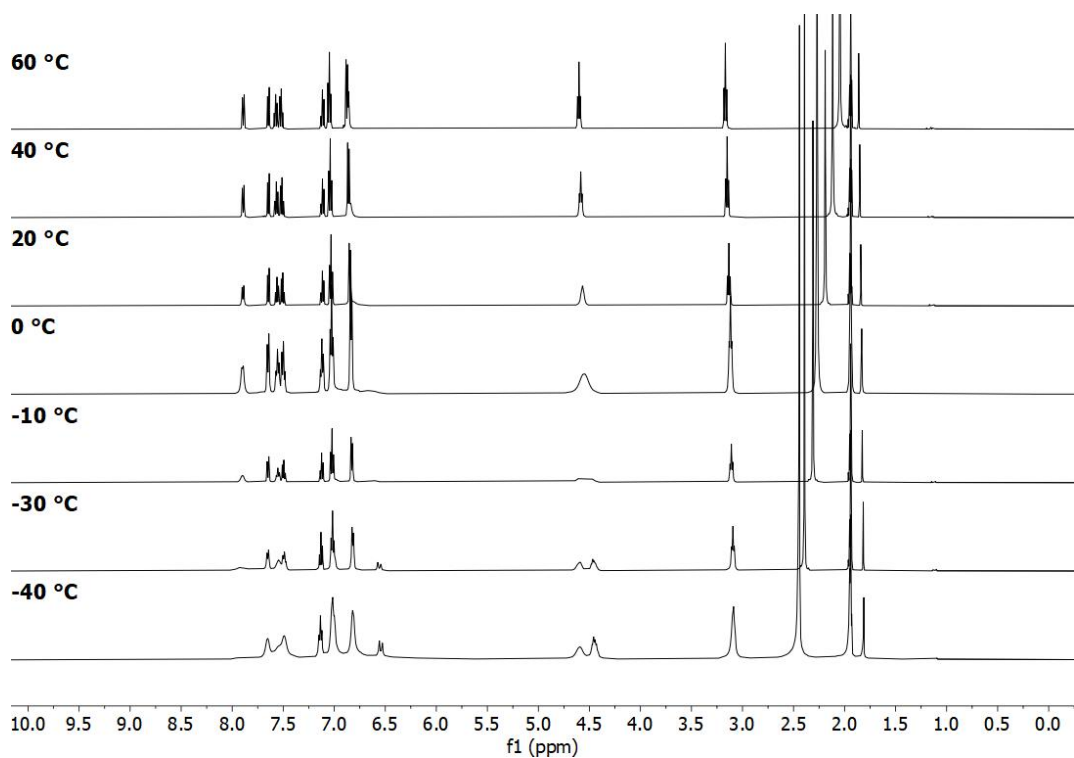
Appendix 8.39: Variable temperature ^1H NMR spectra of $[\text{Ag}_2(\text{L6})_2](\text{PF}_6)_2$ between -40 and 60 °C ($d_3\text{-MeCN}$, 500 MHz).



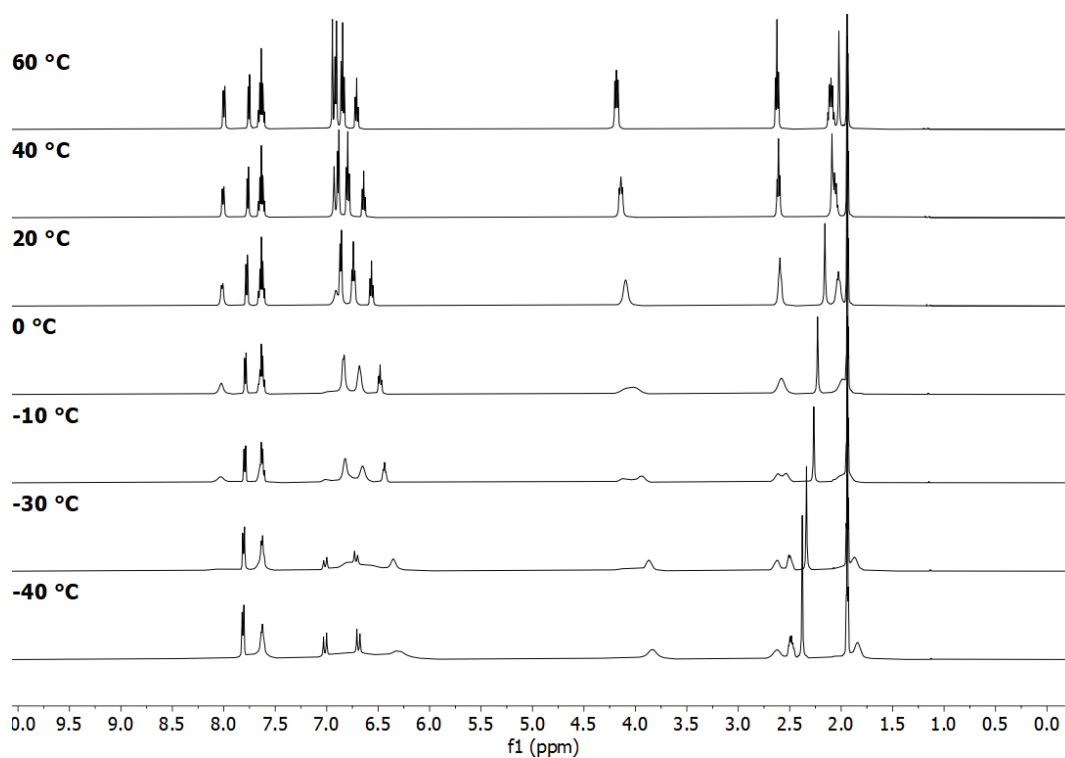
Appendix 8.40: Variable temperature ^1H NMR spectra of $[\text{Ag}_2(\text{L7})_2](\text{PF}_6)_2$ between -40 and 60 °C ($d_3\text{-MeCN}$, 500 MHz).



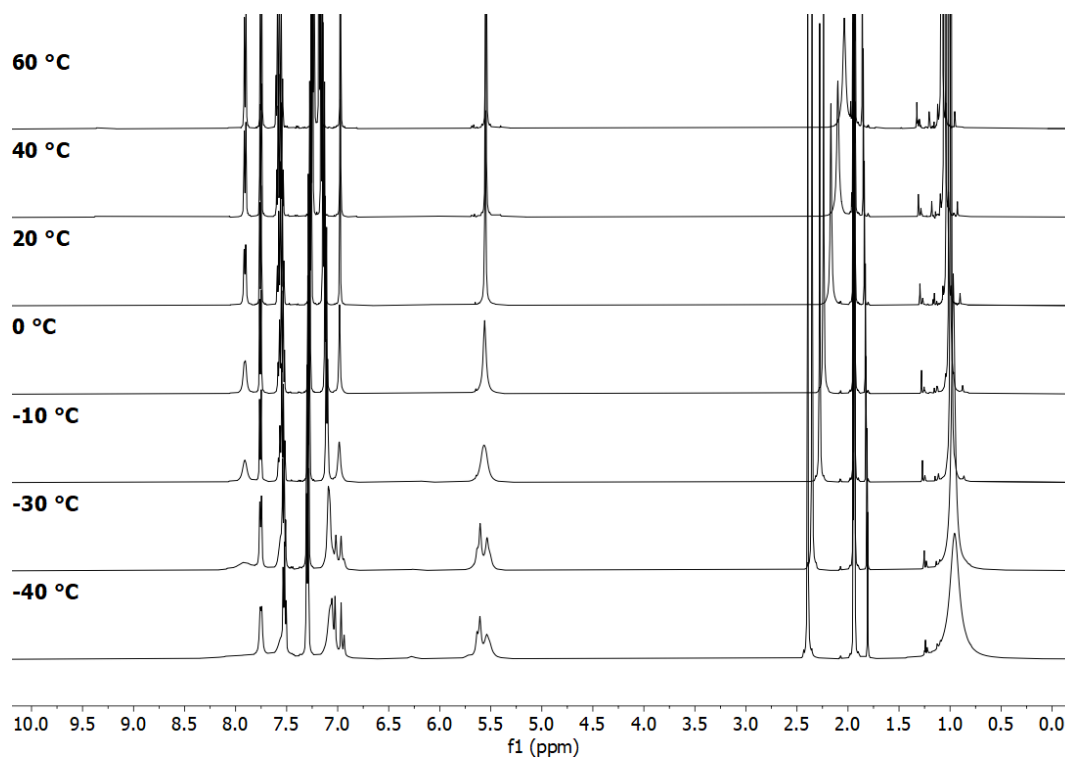
Appendix 8.41: Variable temperature ^1H NMR spectra of $[\text{Ag}_2(\text{L8})_2](\text{PF}_6)_2$ between -40 and 60°C ($d_3\text{-MeCN}$, 500 MHz).



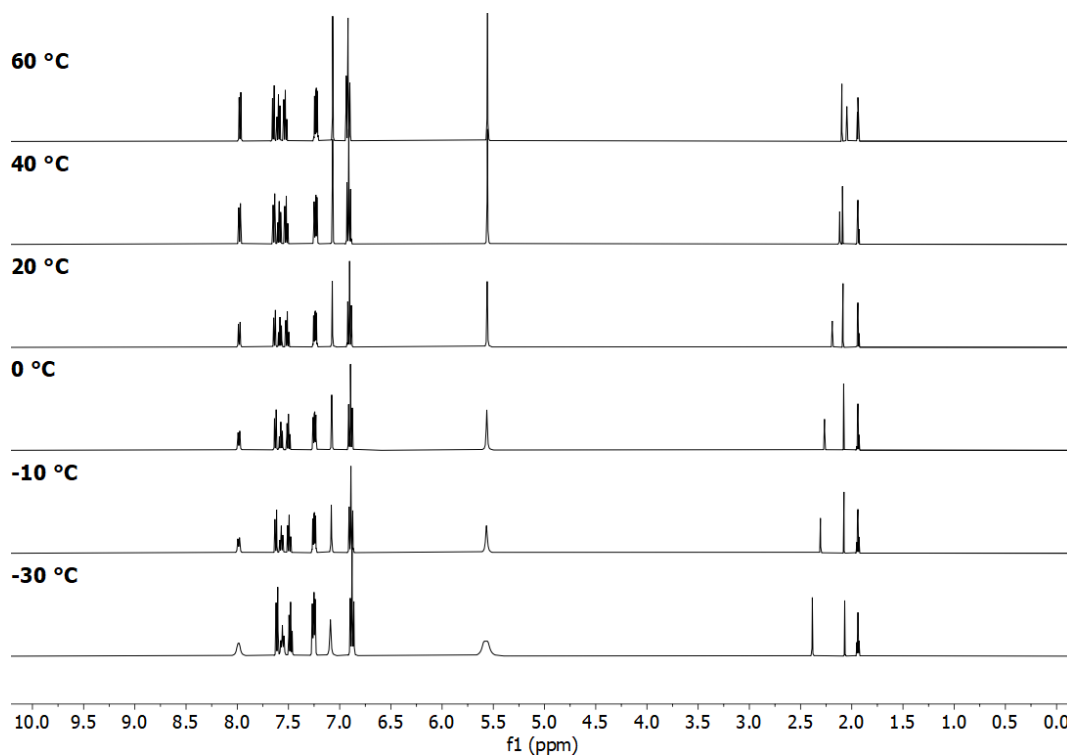
Appendix 8.42: Variable temperature ^1H NMR spectra of $[\text{Ag}_2(\text{L9})_2](\text{PF}_6)_2$ between -40 and 60°C ($d_3\text{-MeCN}$, 500 MHz).



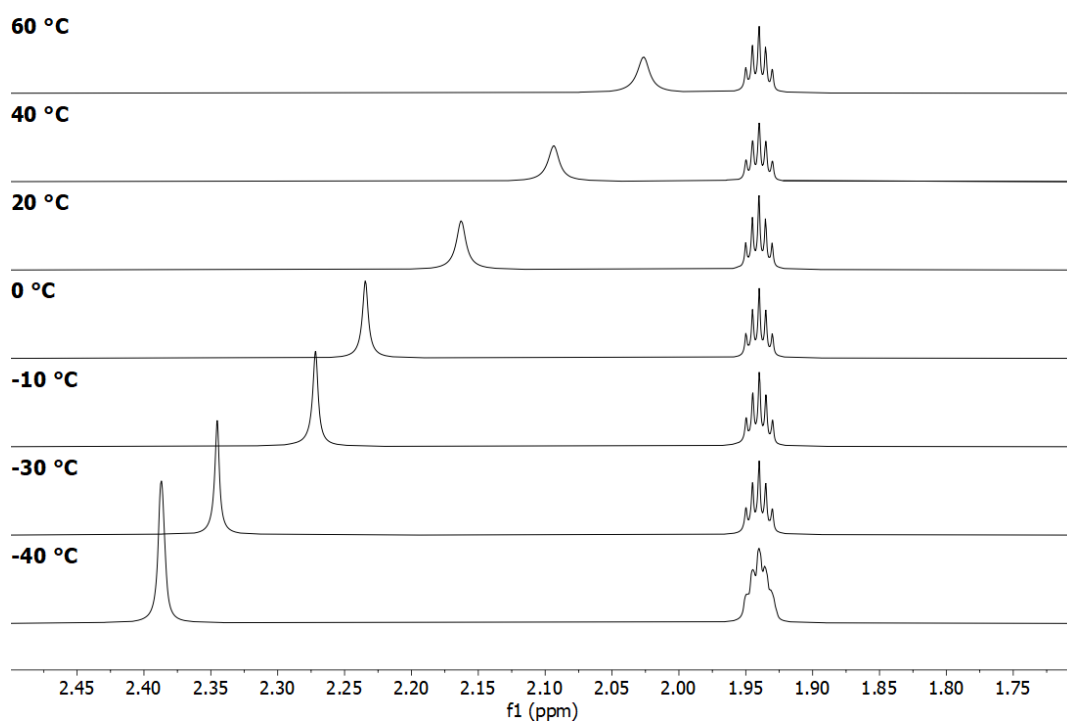
Appendix 8.43: Variable temperature ^1H NMR spectra of $[\text{Ag}_2(\text{L10})_2](\text{PF}_6)_2$ between -40 and 60 °C ($d_3\text{-MeCN}$, 500 MHz).



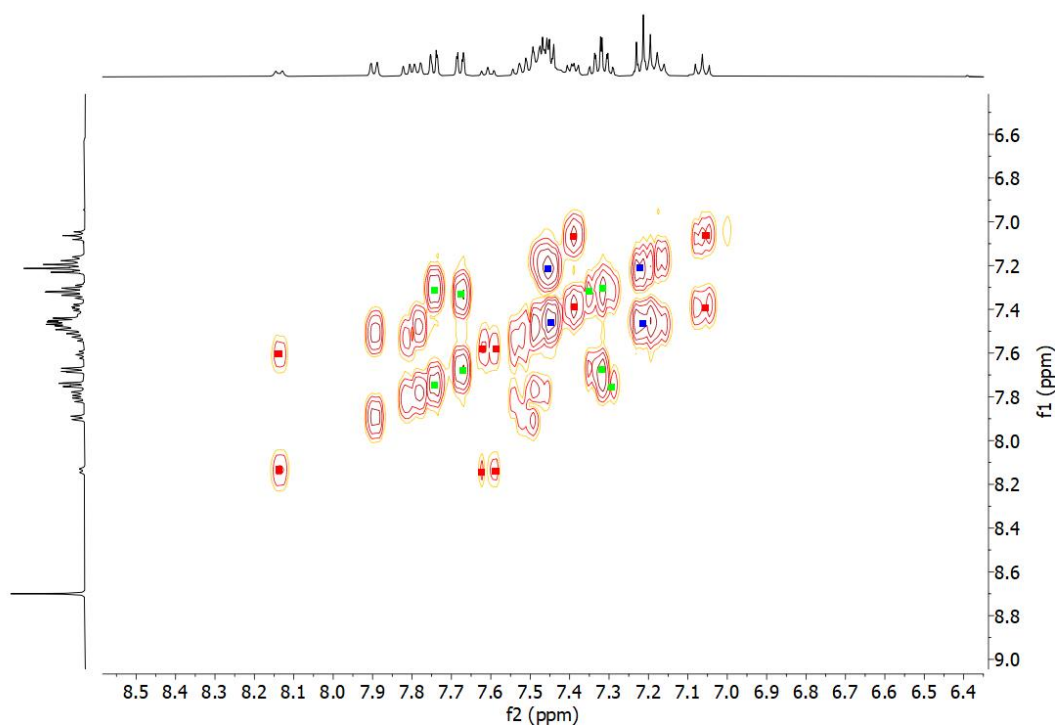
Appendix 8.44: Variable temperature ^1H NMR spectra of $[\text{Ag}_2(\text{L12})_2](\text{PF}_6)_2$ between -40 and 60 °C ($d_3\text{-MeCN}$, 500 MHz).



Appendix 8.45: Variable temperature ^1H NMR spectra of $[\text{Ag}_2(\text{L13})_2](\text{PF}_6)_2$ between -30 and 60 °C ($d_3\text{-MeCN}$, 500 MHz).

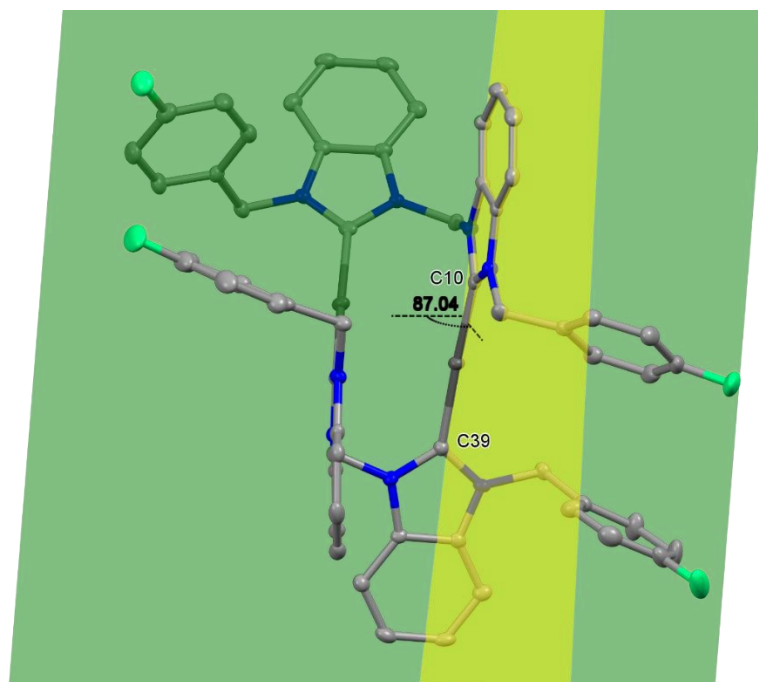


Appendix 8.46: Variable temperature ^1H NMR spectra of $[\text{Ag}_2(\text{L14})_2](\text{PF}_6)_2$ between -40 and 60 °C ($d_3\text{-MeCN}$, 500 MHz).

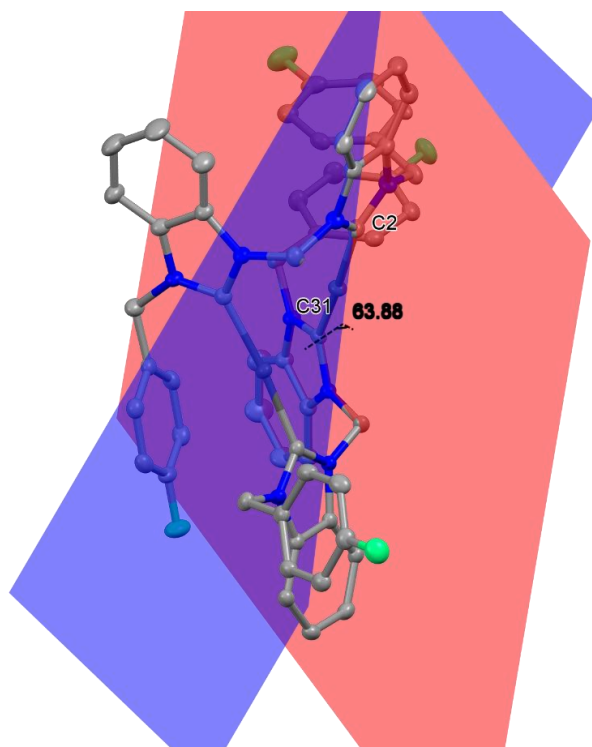


Appendix 8.47: ^1H -COSY spectrum of the products from the attempted synthesis of $[\text{Ag}_2(\text{L13})_2](\text{PF}_6)_2$ using the MeOH route. The different species are indicated by the red, green and blue squares.

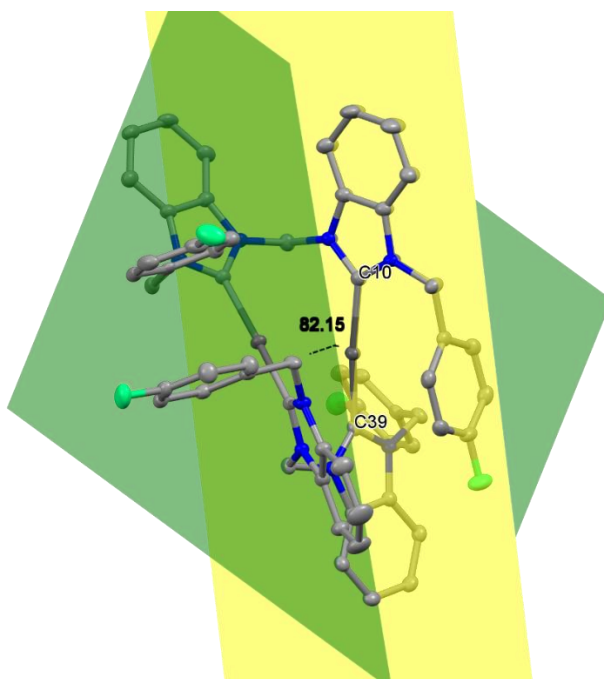
8.3 Sc-XRD



Appendix 8.48: Structure showing the intersection of the planes from benz_{C39} (green) and benz_{C10} (yellow) in [Ag₂(L13)₂](PF₆)₂·A



Appendix 8.49: Structure showing the intersection of the planes from benzC₃₁ (blue) and benzC₂ (red) in [Ag₂(L13)₂](PF₆)₂·B



Appendix 8.50: Structure showing the intersection of the planes from C39(benz) (green) and C10(benz) (yellow) in $[Ag_2(L13)_2](PF_6)_2 \cdot B$

Identification code	[Ag ₂ (L3) ₂](PF ₆) ₂	[Ag ₂ (L4) ₂](PF ₆) ₂	[Ag ₂ (L6) ₂](PF ₆) ₂
Empirical formula	C ₅₀ H ₅₄ Ag ₂ F ₁₂ N ₈ P ₂	C ₆₆ H ₆₈ Ag ₂ F ₁₂ N ₈ O ₂ P ₂	C ₅₀ H ₅₆ Ag ₂ F ₁₆ N ₈ O ₂ P ₂
Formula weight	1272.69	1510.96	1382.70
Temperature/K	99.9(2)	100.00(10)	100.00(18)
Crystal system	monoclinic	monoclinic	triclinic
Space group	I2/m	P2 ₁ /c	P-1
a/Å	16.7837(9)	11.7666(3)	13.4465(3)
b/Å	13.8118(6)	19.6071(4)	14.1618(3)
c/Å	22.8059(11)	14.0110(4)	17.0902(4)
α/°	90	90	83.345(2)
β/°	95.960(5)	100.781(2)	82.594(2)
γ/°	90	90	61.905(2)
Volume/Å ³	5258.1(4)	3175.41(14)	2841.33(12)
Z	4	2	2
ρ _{calc} /g/cm ³	1.608	1.580	1.616
μ/mm ⁻¹	0.892	0.755	0.844
F(000)	2568.0	1536.0	1392.0
Crystal size/mm ³	0.189 × 0.155 × 0.102	0.292 × 0.213 × 0.130	0.279 × 0.144 × 0.054
Radiation	MoKα (λ = 0.71073)	Mo Kα (λ = 0.71073)	Mo Kα (λ = 0.71073)
2Θ range for data collection/°	3.828 to 64.022	4.09 to 61.668	3.934 to 61.906
Index ranges	-23 ≤ h ≤ 23, -17 ≤ k ≤ 18, -32 ≤ l ≤ 28	-16 ≤ h ≤ 14, -28 ≤ k ≤ 23, -17 ≤ l ≤ 17	-17 ≤ h ≤ 18, -20 ≤ k ≤ 19, -24 ≤ l ≤ 24
Reflections collected	31726	34251	44077
Independent reflections	7079 [R _{int} = 0.2254, R _{sigma} = 0.1105]	8122 [R _{int} = 0.0332, R _{sigma} = 0.0303]	14456 [R _{int} = 0.0599, R _{sigma} = 0.0663]
Data/restraints/parameters	7079/0/460	8122/0/417	14456/0/725
Goodness-of-fit on F ²	1.058	0.965	1.027
Final R indexes [I ≥ 2σ(I)]	R ₁ = 0.0862, wR ₂ = 0.2380	R ₁ = 0.0357, wR ₂ = 0.1174	R ₁ = 0.0500, wR ₂ = 0.1046
Final R indexes [all data]	R ₁ = 0.1036, wR ₂ = 0.2694	R ₁ = 0.0424, wR ₂ = 0.1228	R ₁ = 0.0794, wR ₂ = 0.1138
Largest diff. peak/hole / e Å ⁻³	2.21/-2.15	1.60/-0.82	1.84/-0.70

Appendix 8.51: Crystal data and structure refinement for [Ag₂(L3)₂](PF₆)₂, [Ag₂(L4)₂](PF₆)₂ and [Ag₂(L6)₂](PF₆)₂.

Identification code	[Ag ₂ (L7) ₂](PF ₆) ₂	[Ag ₂ (L9) ₂](PF ₆) ₂	[Ag ₂ (L13) ₂](PF ₆) ₂ -A
Empirical formula	C ₂₃ H ₁₈ AgF ₁₂ N ₄ P	C ₆₅ H ₆₂ Ag ₂ F ₁₂ N ₈ O P ₂	C ₆₆ H ₅₆ Ag ₂ F ₁₆ N ₁₂ P ₂
Formula weight	717.25	1476.90	1598.90
Temperature/K	99.99(10)	100.00(11)	100.00(10)
Crystal system	triclinic	monoclinic	monoclinic
Space group	P-1	P2 ₁	P2 ₁ /n
a/Å	9.6582(2)	10.1144(3)	14.9660(4)
b/Å	11.5304(2)	27.8888(6)	26.2548(7)
c/Å	12.8967(3)	10.9354(3)	16.7971(4)
α/°	105.399(2)	90	90
β/°	111.405(2)	95.025(2)	93.534(2)
γ/°	94.317(2)	90	90
Volume/Å ³	1265.20(5)	3072.78(14)	6587.5(3)
Z	2	2	4
ρ _{calc} /cm ³	1.883	1.596	1.612
μ/mm ⁻¹	0.971	0.777	0.740
F(000)	708.0	1496.0	3216.0
Crystal size/mm ³	0.331 × 0.175 × 0.175	0.237 × 0.117 × 0.095	0.337 × 0.159 × 0.131
Radiation	Mo Kα (λ = 0.71073)	Mo Kα (λ = 0.71073)	Mo Kα (λ = 0.71073)
2θ range for data collection/°	4.278 to 61.89	4.014 to 61.824	3.864 to 61.856
Index ranges	-13 ≤ h ≤ 13, -16 ≤ k ≤ 16, -18 ≤ l ≤ 17	-12 ≤ h ≤ 12, -36 ≤ k ≤ 38, -13 ≤ l ≤ 14	-20 ≤ h ≤ 18, -36 ≤ k ≤ 31, -20 ≤ l ≤ 22
Reflections collected	20896	32756	39395
Independent reflections	6404 [R _{int} = 0.0405, R _{sigma} = 0.0395]	14343 [R _{int} = 0.0516, R _{sigma} = 0.0670]	16132 [R _{int} = 0.0435, R _{sigma} = 0.0595]
Data/restraints/parameters	6404/0/370	14343/1/813	16132/0/887
Goodness-of-fit on F ²	1.060	1.093	1.039
Final R indexes [I ≥ 2σ(I)]	R ₁ = 0.0329, wR ₂ = 0.0665	R ₁ = 0.0389, wR ₂ = 0.0935	R ₁ = 0.0438, wR ₂ = 0.1151
Final R indexes [all data]	R ₁ = 0.0361, wR ₂ = 0.0681	R ₁ = 0.0452, wR ₂ = 0.1082	R ₁ = 0.0694, wR ₂ = 0.1278
Largest diff. peak/hole / e Å ⁻³	0.75/-0.47	1.10/-0.83	0.79/-0.91

Appendix 8.52: Crystal data and structure refinement for [Ag₂(L7)₂](PF₆)₂, [Ag₂(L9)₂](PF₆)₂ and [Ag₂(L13)₂](PF₆)₂-A.

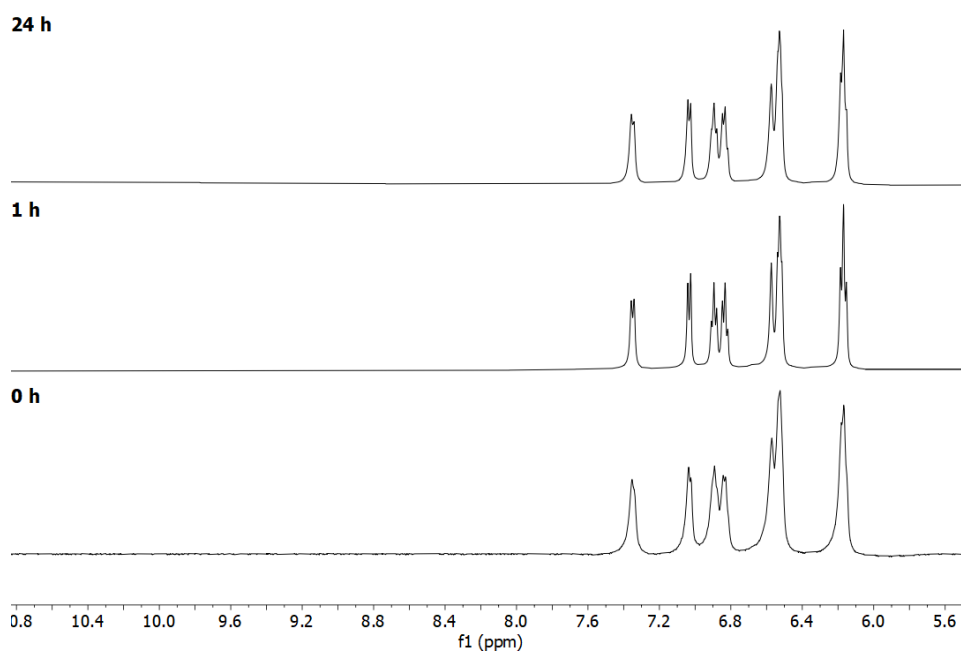
Identification code	[Ag ₂ (L13) ₂](PF ₆) ₂ -B	[Ag(L16) ₂](PF ₆)	V1
Empirical formula	C ₅₈ H ₄₃ Ag ₂ F ₁₆ N ₈ P ₂	C ₄₂ H ₃₂ AgF ₁₀ N ₄ P	C ₃₈ H ₄₆ N ₂ O ₅ V
Formula weight	1433.68	921.55	661.71
Temperature/K	100.00(10)	100.00(10)	120(30)
Crystal system	monoclinic	triclinic	monoclinic
Space group	P2 ₁ /c	P-1	P2 ₁
a/Å	12.79460(10)	8.1718(2)	11.7087(6)
b/Å	21.39110(10)	10.6325(3)	14.3608(4)
c/Å	20.9969(2)	11.9432(2)	11.8542(5)
α/°	90	110.163(2)	90
β/°	104.3720(10)	94.565(2)	119.265(6)
γ/°	90	98.557(2)	90
Volume/Å ³	5566.81(8)	953.64(4)	1738.84(15)
Z	4	1	2
ρ _{calc} /cm ³	1.711	1.605	1.264
μ/mm ⁻¹	7.096	0.657	0.330
F(000)	2860.0	464.0	702.0
Crystal size/mm ³	0.326 × 0.118 × 0.085	0.517 × 0.286 × 0.126	0.914 × 0.382 × 0.125
Radiation	Cu Kα (λ = 1.54184)	Mo Kα (λ = 0.71073)	Mo Kα (λ = 0.71073)
2θ range for data collection/°	5.996 to 154.406	3.67 to 61.692	3.988 to 62.12
Index ranges	-14 ≤ h ≤ 16, -26 ≤ k ≤ 23, -26 ≤ l ≤ 23	-10 ≤ h ≤ 11, -13 ≤ k ≤ 13, -15 ≤ l ≤ 16	-16 ≤ h ≤ 16, -18 ≤ k ≤ 20, -16 ≤ l ≤ 16
Reflections collected	44897	14571	28195
Independent reflections	10847 [R _{int} = 0.0323, R _{sigma} = 0.0263]	4778 [R _{int} = 0.0335, R _{sigma} = 0.0297]	8551 [R _{int} = 0.0366, R _{sigma} = 0.0377]
Data/restraints/parameters	10847/0/775	4778/0/265	8551/1/427
Goodness-of-fit on F ²	1.053	1.055	1.098
Final R indexes [I ≥ 2σ(I)]	R ₁ = 0.0289, wR ₂ = 0.0727	R ₁ = 0.0247, wR ₂ = 0.0582	R ₁ = 0.0360, wR ₂ = 0.0917
Final R indexes [all data]	R ₁ = 0.0307, wR ₂ = 0.0737	R ₁ = 0.0270, wR ₂ = 0.0589	R ₁ = 0.0390, wR ₂ = 0.0986
Largest diff. peak/hole / e Å ⁻³	1.00/-0.85	0.51/-0.46	0.54/-0.41

Appendix 8.53: Crystal data and structure refinement for [Ag₂(L13)₂](PF₆)₂-B, [Ag(L16)₂](PF₆) and V1.

Identification code	V2	V4
Empirical formula	C ₅₈ H ₅₄ N ₂ O ₅ V	C ₁₁₀ H ₈₄ N ₄ O ₉ V ₂
Formula weight	909.97	1707.69
Temperature/K	99.97(13)	100.01(13)
Crystal system	triclinic	monoclinic
Space group	P-1	C2/c
a/Å	13.2688(2)	19.3734(3)
b/Å	19.8202(5)	20.9003(3)
c/Å	20.7425(6)	25.5349(4)
α /°	65.686(3)	90
β /°	74.009(2)	111.840(2)
γ /°	74.750(2)	90
Volume/Å ³	4708.7(2)	9597.2(3)
Z	4	4
$\rho_{\text{calc}}/\text{cm}^3$	1.284	1.182
μ/mm^{-1}	0.264	2.099
F(000)	1916.0	3560.0
Crystal size/mm ³	0.266 × 0.076 × 0.024	0.125 × 0.122 × 0.075
Radiation	Mo K α (λ = 0.71073)	Cu K α (λ = 1.54184)
2 θ range for data collection/°	4.142 to 61.868	6.484 to 155.002
Index ranges	-17 ≤ h ≤ 17, -27 ≤ k ≤ 26, -29 ≤ l ≤ 30	-23 ≤ h ≤ 24, -25 ≤ k ≤ 26, -31 ≤ l ≤ 19
Reflections collected	72300	59762
Independent reflections	23878 [R _{int} = 0.0362, R _{sigma} = 0.0392]	9822 [R _{int} = 0.0430, R _{sigma} = 0.0208]
Data/restraints/parameters	23878/0/1203	9822/0/564
Goodness-of-fit on F ²	1.048	1.046
Final R indexes [I ≥ 2 σ (I)]	R ₁ = 0.0427, wR ₂ = 0.1108	R ₁ = 0.0457, wR ₂ = 0.1183
Final R indexes [all data]	R ₁ = 0.0562, wR ₂ = 0.1181	R ₁ = 0.0585, wR ₂ = 0.1262
Largest diff. peak/hole / e Å ⁻³	0.77/-0.41	0.30/-0.3

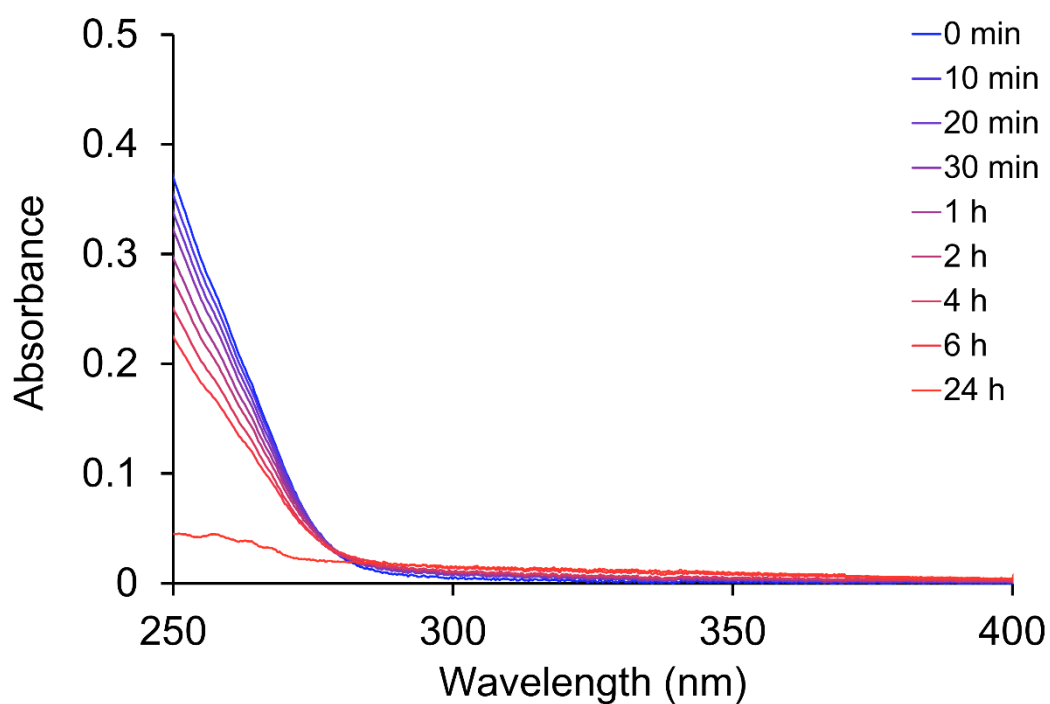
Appendix 8.54: Crystal data and structure refinement for V2 and V4.

8.4 NMR Stability

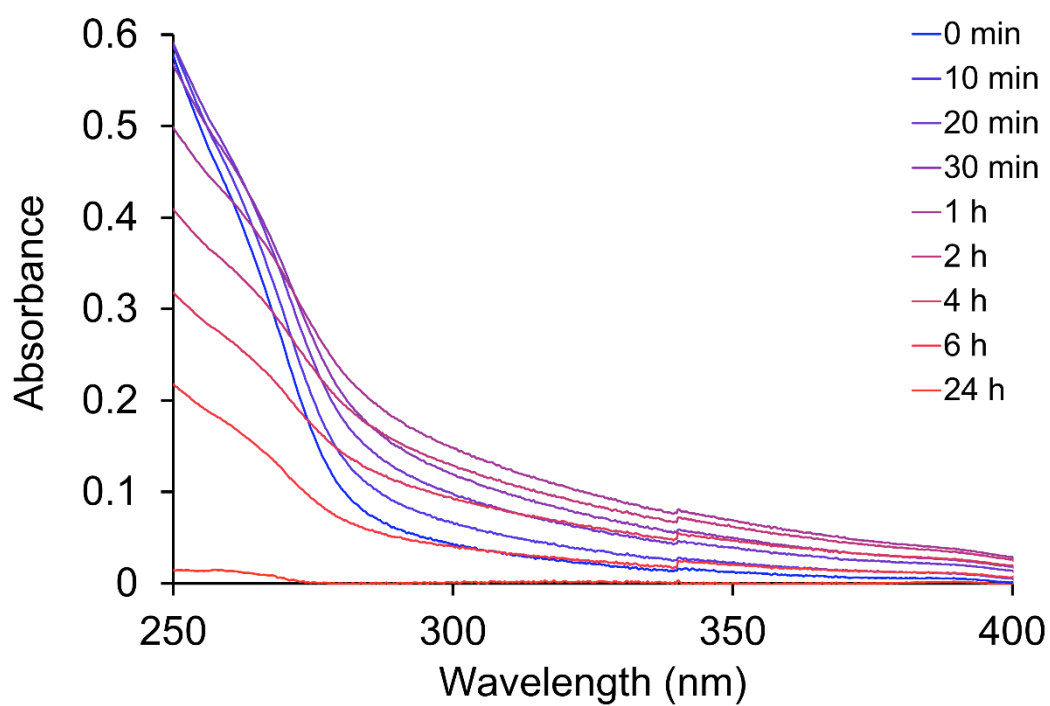


Appendix 8.55: ^1H NMR spectra of $[\text{Ag}_2(\text{L13})_2](\text{PF}_6)_2$ in $\text{D}_2\text{O}:\text{d}_6\text{-DMSO}$ (30:70) taken at 0, 1 and 24 hour time points, only the aromatic region is shown (500 MHz).

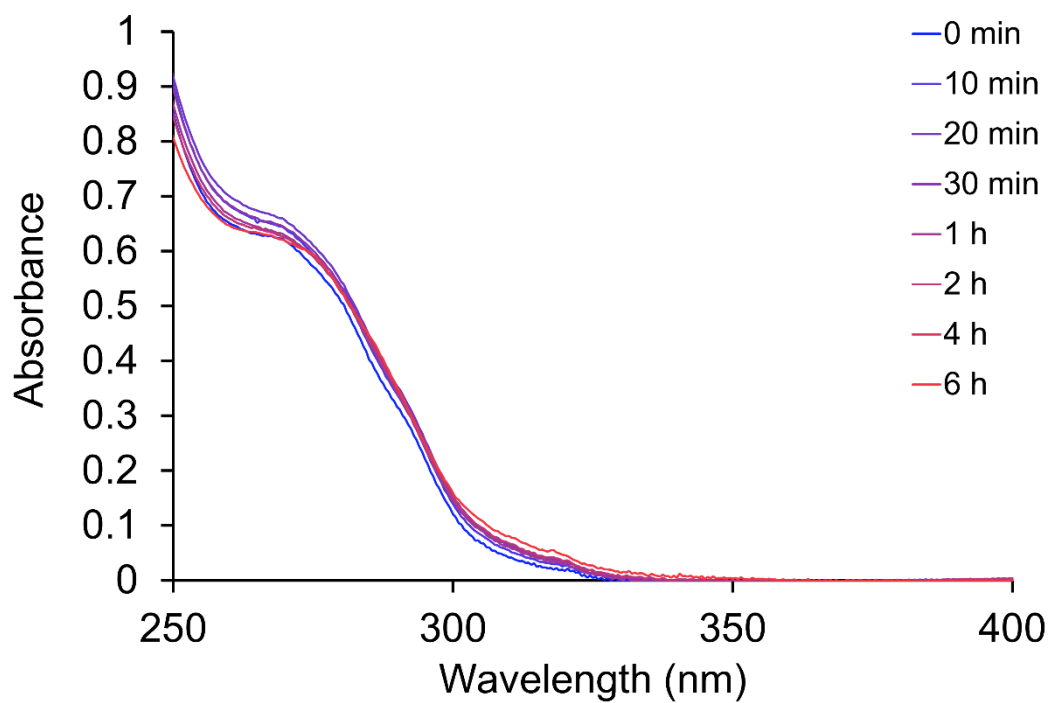
8.5 UV-Vis Stability



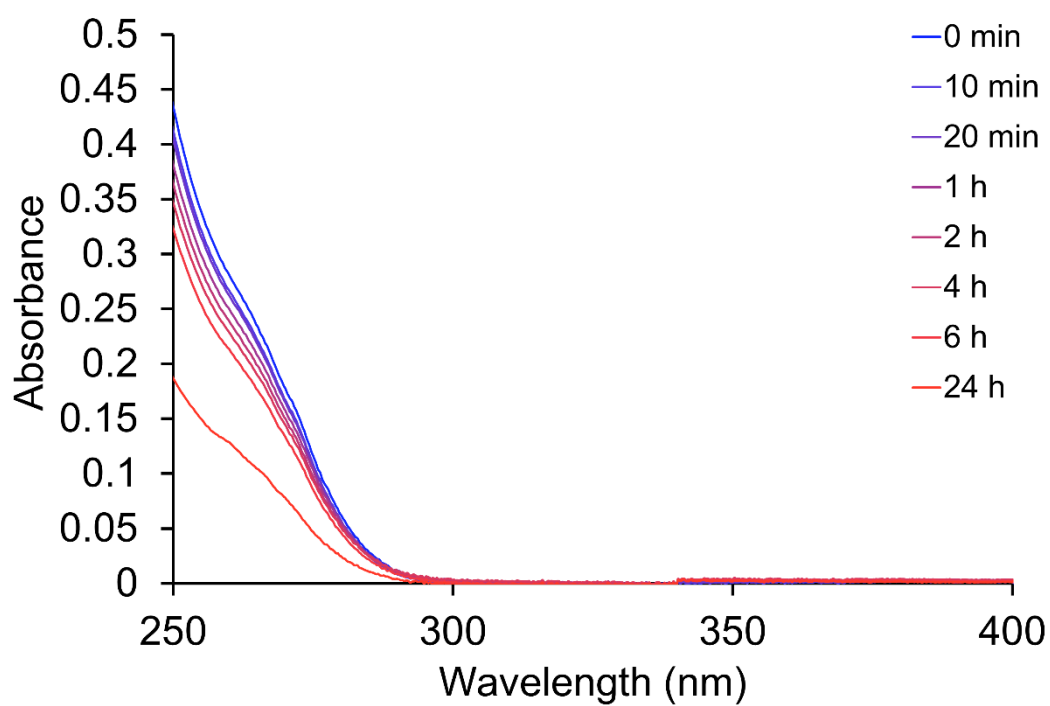
Appendix 8.56: UV-vis spectra of $[Ag_2(L2)_2](PF_6)_2$ in $H_2O:DMSO$ (95:5) over a period of 24 hours.



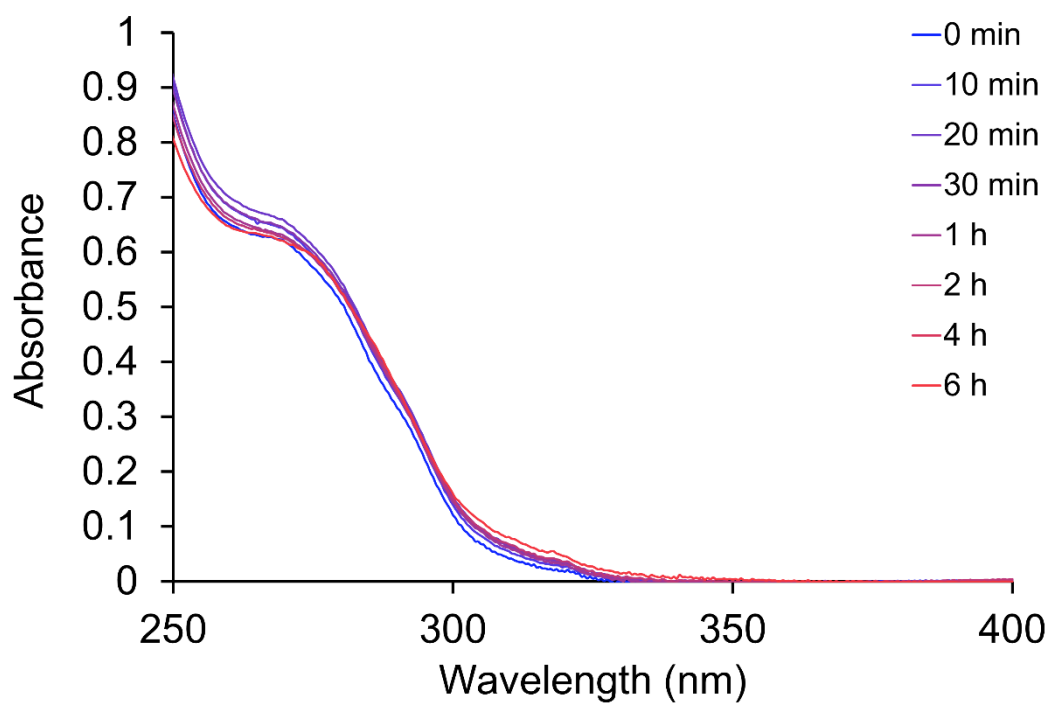
Appendix 8.57: UV-vis spectra of $[\text{Ag}_2(\text{L3})_2](\text{PF}_6)_2$ in $\text{H}_2\text{O}:\text{DMSO}$ (95:5) over a period of 24 hours.



Appendix 8.58: UV-vis spectra of $[\text{Ag}_2(\text{L4})_2](\text{PF}_6)_2$ in $\text{H}_2\text{O}:\text{DMSO}$ (95:5) over a period of 24 hours.

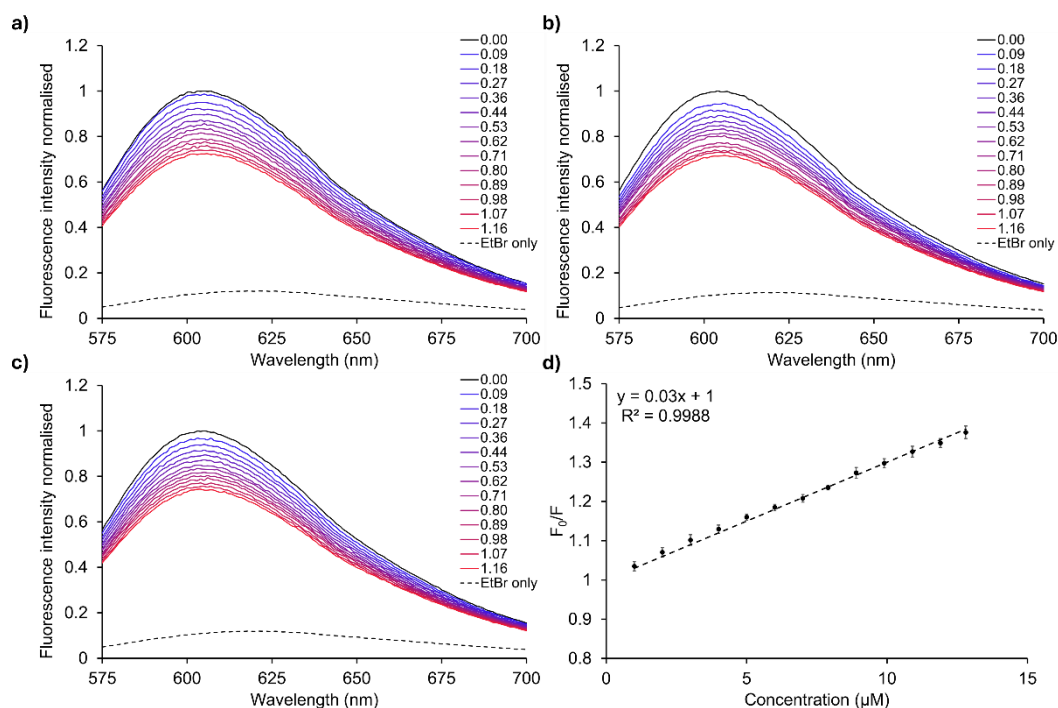


Appendix 8.59: UV-vis spectra of $[Ag_2(L5)_2](PF_6)_2$ in $H_2O:DMSO$ (95:5) over a period of 24 hours.

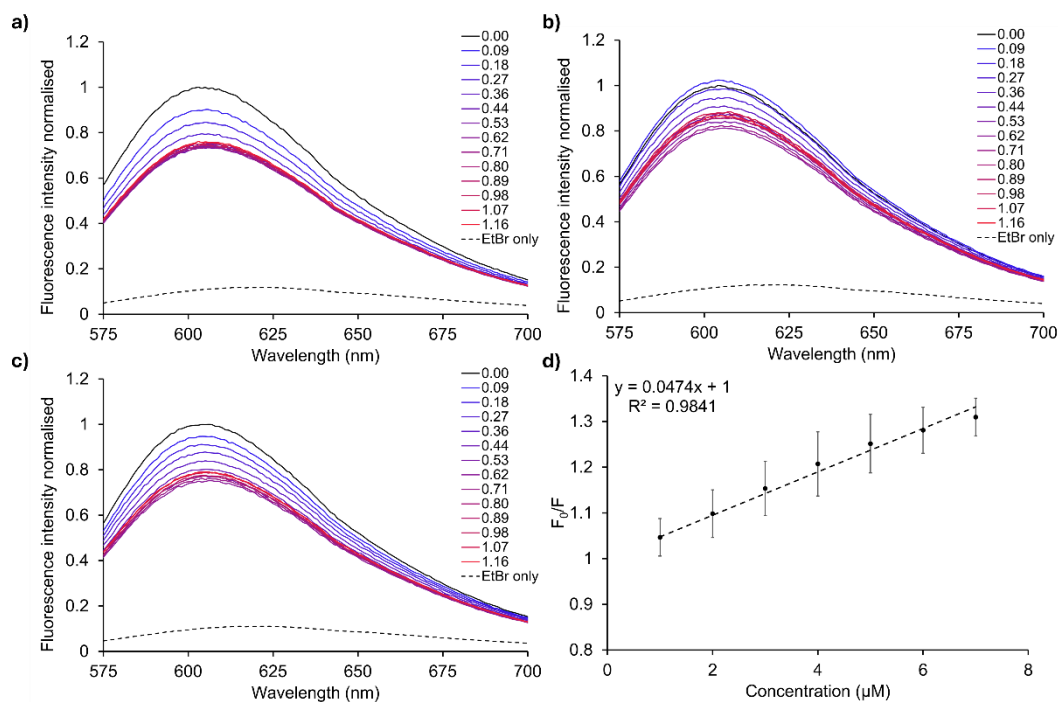


Appendix 8.60: UV-vis spectra of $[Ag_2(L7)_2](PF_6)_2$ in $H_2O:DMSO$ (95:5) over a period of 6 hours.

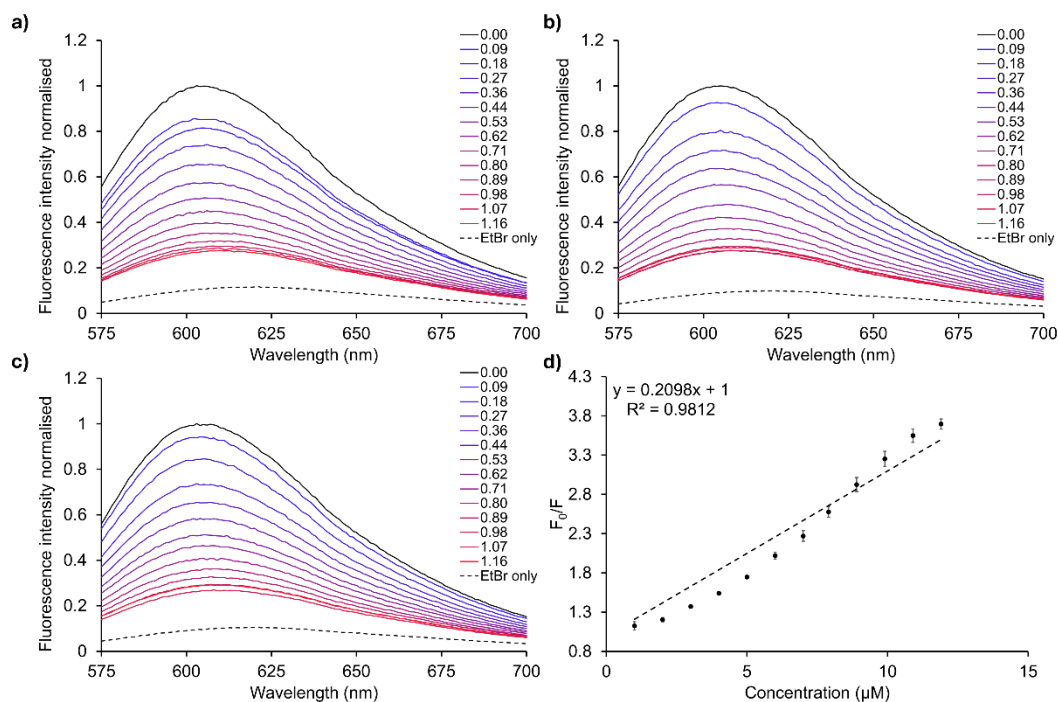
8.6 EtBr Data



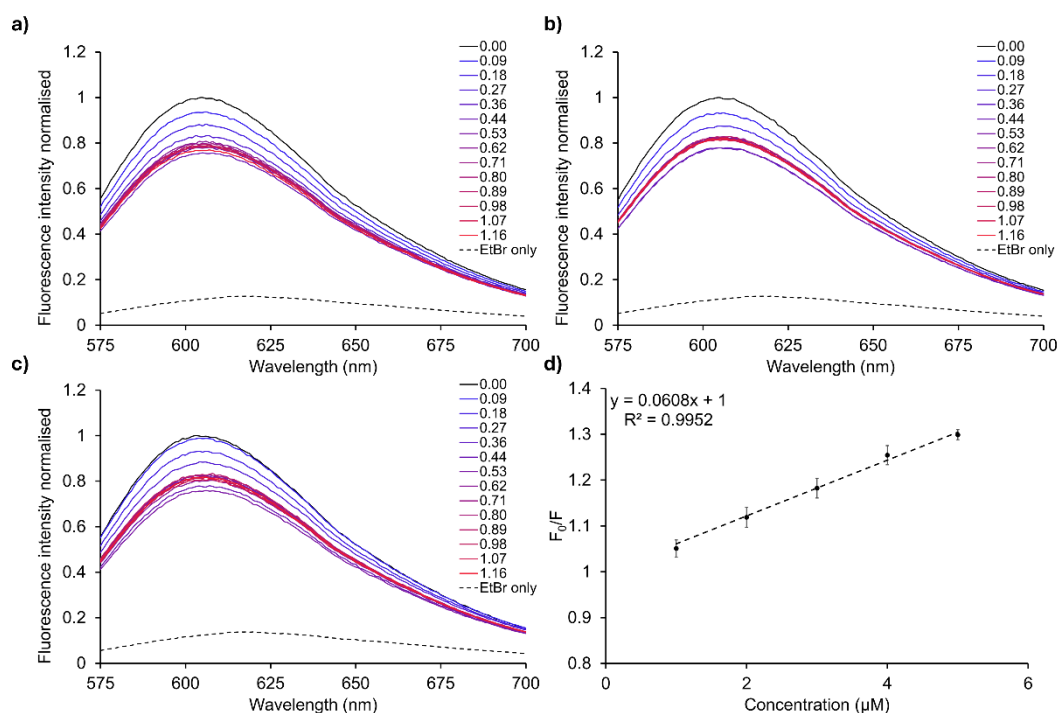
Appendix 8.61: a - c) Fluorescence emission spectra of sequential additions of $[\text{H}_2(\text{L4})_2](\text{PF}_6)_2$ to a solution of ct-DNA/EtBr (2.5/1), black line = no complex), blue – red = 0.09 – 1.16 molar equivalents of complex to EtBr and dotted line = EtBr without ct-DNA. d) Stern-Volmer plot with standard errors from three independent experiments.



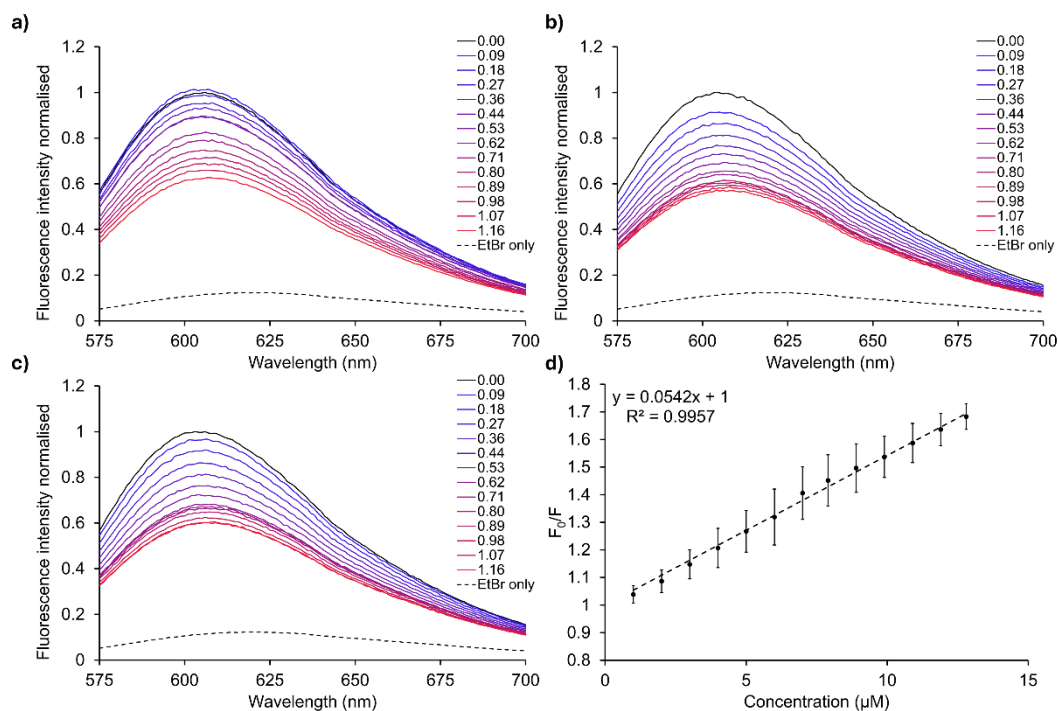
Appendix 8.62: a) Fluorescence emission spectra of sequential additions of $[\text{Ag}_2(\text{L1})_2](\text{PF}_6)_2$ to a solution of ct-DNA/EtBr (2.5/1), black line = no complex), blue – red = 0.09 – 1.16 molar equivalents of complex to EtBr and dotted line = EtBr without ct-DNA. b) Stern-Volmer plot with standard errors from three independent experiments.



Appendix 8.63: a) Fluorescence emission spectra of sequential additions of $[Ag_2(L4)_2](PF_6)_2$ to a solution of ct-DNA/EtBr (2.5/1), black line = no complex), blue – red = 0.09 – 1.16 molar equivalents of complex to EtBr and dotted line = EtBr without ct-DNA. b) Stern-Volmer plot with standard errors from three independent experiments.

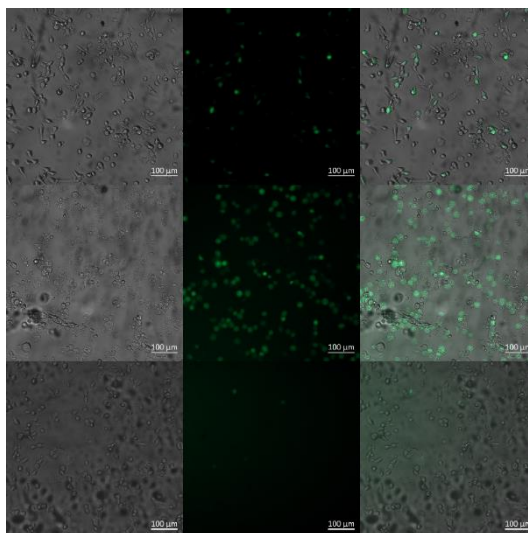


Appendix 8.64: a) Fluorescence emission spectra of sequential additions of $[Ag_2(L6)](PF_6)_2$ to a solution of ct-DNA/EtBr (2.5/1), black line = no complex), blue – red = 0.09 – 1.16 molar equivalents of complex to EtBr and dotted line = EtBr without ct-DNA. b) Stern-Volmer plot with standard errors from three independent experiments.

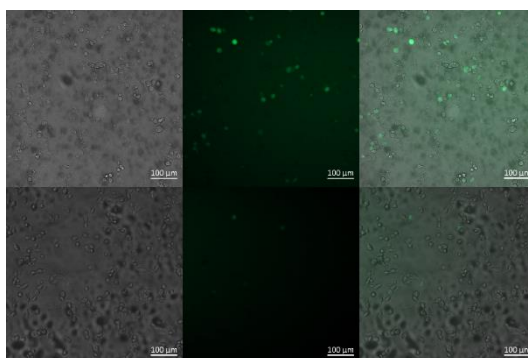


Appendix 8.65: a) Fluorescence emission spectra of sequential additions of $[Ag_2(L13)_2](PF_6)_2$ to a solution of ct-DNA/EtBr (2.5/1), black line = no complex), blue – red = 0.09 – 1.16 molar equivalents of complex to EtBr and dotted line = EtBr without ct-DNA. b) Stern-Volmer plot with standard errors from three independent experiments.

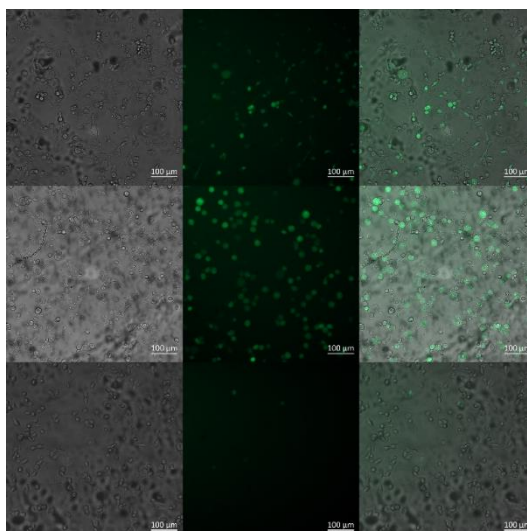
8.7 ROS Images



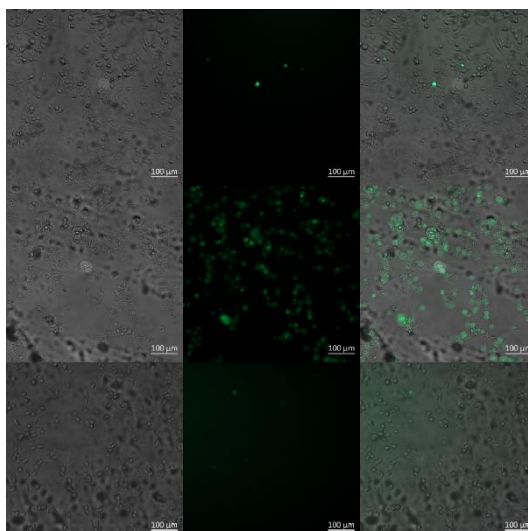
Appendix 8.66: ROS observed after MDA-MB-231 cells were incubated for 3.5 hours with $[\text{Ag}_2(\text{L1})_2](\text{PF}_6)_2$ $1 \times \text{IC}_{50}$ (top) and $5 \times \text{IC}_{50}$ (bottom), followed by H_2DCFDA ($20 \mu\text{M}$) for 30 min. All images were taken using an Observer-7 microscope (scale bar at $100 \mu\text{m}$) and recorded using $\text{ex/em} = 494/512 \text{ nm}$. The brightfield, fluorescence and combined images are shown.



Appendix 8.67: ROS observed after MDA-MB-231 cells were incubated for 3.5 hours with $[\text{Ag}_2(\text{L4})_2](\text{PF}_6)_2$ $1 \times \text{IC}_{50}$ (top) and control (DMSO 0.1%) (bottom), followed by H_2DCFDA ($20 \mu\text{M}$) for 30 min. All images were taken using an Observer-7 microscope (scale bar at $100 \mu\text{m}$) and recorded using $\text{ex/em} = 494/512 \text{ nm}$. The brightfield, fluorescence and combined images are shown.

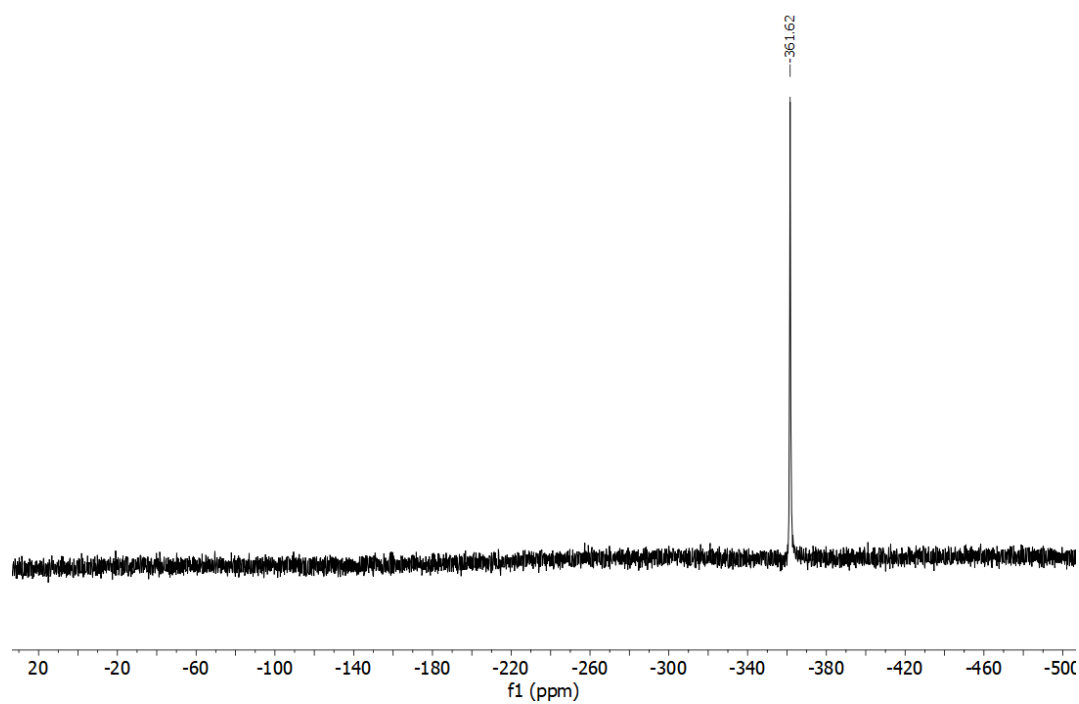


Appendix 8.68: ROS observed after MDA-MB-231 cells were incubated for 3.5 hours with $[\text{Ag}_2(\text{L6})_2](\text{PF}_6)_2$ 1 x IC_{50} (top), 5 x IC_{50} (middle) and control (DMSO 0.1%) (bottom), followed by H_2DCFDA (20 μM) for 30 min. All images were taken using an Observer-7 microscope (scale bar at 100 μm) and recorded using ex/em = 494/512 nm. The brightfield, fluorescence and combined images are shown.



Appendix 8.69: ROS observed after MDA-MB-231 cells were incubated for 3.5 hours with $[\text{Ag}_2(\text{L13})_2](\text{PF}_6)_2$ $1 \times \text{IC}_{50}$ (top), $5 \times \text{IC}_{50}$ (middle) and control (DMSO 0.1%) (bottom), followed by H_2DCFDA ($20 \mu\text{M}$) for 30 min. All images were taken using an Observer-7 microscope (scale bar at $100 \mu\text{m}$) and recorded using $\text{ex/em} = 494/512 \text{ nm}$. The brightfield, fluorescence and combined images are shown.

8.8 ^{51}V NMR Spectroscopy



Appendix 8.70: ^{51}V NMR spectrum of complex V3 (d_8 -THF, 131.62 MHz).

9 References

- 1 M. Shurin, *ImmunoTargets Ther.*, 2012, **1**, 1–6.
- 2 J. Boutry, S. Tissot, B. Ujvari, J.-P. Capp, M. Giraudeau, A. M. Nedelcu and F. Thomas, *Biochim. Biophys. Acta Rev. Cancer*, 2022, **1877**, 188643.
- 3 J. S. Brown, S. R. Amend, R. H. Austin, R. A. Gatenby, E. U. Hammarlund and K. J. Pienta, *Mol. Cancer Res.*, 2023, **21**, 1142–1147.
- 4 P. Bisoyi, in *Understanding Cancer: From Basics to Therapeutics*, Elsevier, 2022, pp. 1–20.
- 5 F. Bray, M. Laversanne, H. Sung, J. Ferlay, R. L. Siegel, I. Soerjomataram and A. Jemal, *CA: Cancer J. Clin.*, 2024, **74**, 229–263.
- 6 <http://www.CancerDisparitiesProgressReport.org/>, (accessed 20 November 2024).
- 7 <https://www.wcrf.org/preventing-cancer/cancer-statistics/worldwide-cancer-data/>, (accessed 20 November 2024).
- 8 E. Orrantia-Borunda, P. Anchondo-Nuñez, L. E. Acuña-Aguilar, F. O. Gómez-Valles and C. A. Ramírez-Valdespino, in *Breast Cancer*, ed. H. N. Mayrovitz, Exon Publications, 2022, pp. 31–42.
- 9 M. C. Casey, K. J. Sweeney, J. A. L. Brown and M. J. Kerin, *Int. J. Cancer Res.*, 2016, **139**, 12–22.
- 10 O. Yersal, *World J. Clin. Oncol.*, 2014, **5**, 412.
- 11 E. Hsu, S. M. Arezo and S. L. Graff, *Curr. Treat. Options Oncol.*, 2024, **25**, 1323–1334.
- 12 O. Obidiro, G. Battogtokh and E. O. Akala, *Pharmaceutics*, 2023, **15**, 1796.
- 13 A. Burguin, C. Diorio and F. Durocher, *J. Pers. Med.*, 2021, **11**, 808.
- 14 J. C. Dean, S. E. Salmon and K. S. Griffith, *N. Engl. J. Med.*, 1979, **301**, 1427–1429.
- 15 J. Kirshner, M. Hatch, D. D. Hennessy, M. Fridman and R. E. Tannous, *Oncologist*, 2004, **9**, 25–32.

- 16 L. P. Arendsen, R. Thakar and A. H. Sultan, *Clin. Microbiol. Rev.*, 2019, **32**, e00125-18.
- 17 G. Liu, Y. Song, C. Li, R. Liu, Y. Chen, L. Yu, Q. Huang, D. Zhu, C. Lu, X. Yu, C. Xiao and Y. Liu, *Eur. J. Med. Chem.*, 2021, **221**, 113519.
- 18 J. Parascandola, in *Encyclopedia of Life Sciences*, Wiley, 2001.
- 19 D. Keogan and D. Griffith, *Molecules*, 2014, **19**, 15258–15297.
- 20 S. Shen, J. Shen, Z. Luo, F. Wang and J. Min, *Coord. Chem. Rev.*, 2023, **493**, 215323.
- 21 B. Rosenberg, L. Vancamp and T. Krigas, *Nature*, 1965, **205**, 698–699.
- 22 B. Rosenberg, L. Vancamp, J. E. Trosko and V. H. Mansour, *Nature*, 1969, **222**, 385–386.
- 23 R. V. de Brito, M. W. Mancini, M. das N. Palumbo, L. H. O. de Moraes, G. J. Rodrigues, O. Cervantes, J. A. Sercarz and M. B. Paiva, *Int. J. Mol. Sci.*, 2022, **23**, 5934.
- 24 S. Ghosh, *Bioorg. Chem.*, 2019, **88**, 102925.
- 25 N. D. Eljack, H. Y. M. Ma, J. Drucker, C. Shen, T. W. Hambley, E. J. New, T. Friedrich and R. J. Clarke, *Metallomics*, 2014, **6**, 2126–2133.
- 26 Z. H. Siddik, *Oncogene*, 2003, **22**, 7265–7279.
- 27 Y.-M. Choi, H.-K. Kim, W. Shim, M. A. Anwar, J.-W. Kwon, H.-K. Kwon, H. J. Kim, H. Jeong, H. M. Kim, D. Hwang, H. S. Kim and S. Choi, *PLoS One*, 2015, **10**, e0135083.
- 28 <https://www.nursinghero.com/study-guides/wmopen-nmbiology1/storing-genetic-information/>, (accessed 11 March 2025).
- 29 S. Rottenberg, C. Disler and P. Perego, *Nat. Rev. Cancer*, 2021, **21**, 37–50.
- 30 R. Oun, Y. E. Moussa and N. J. Wheate, *Dalton Trans.*, 2018, **47**, 6645–6653.
- 31 M. Kartalou and J. M. Essigmann, *Mutat. Res. Fundam. Mol. Mech. Mutagenesis*, 2001, **478**, 23–43.

- 32 A. M. P. Romani, *Biochem. Pharmacol.*, 2022, **206**, 115323.
- 33 C. R. R. Rocha, M. M. Silva, A. Quinet, J. B. Cabral-Neto and C. F. M. Menck, *Clinics*, 2018, **73**, e478s.
- 34 D. Huang, S. R. Savage, A. P. Calinawan, C. Lin, B. Zhang, P. Wang, T. K. Starr, M. J. Birrer and A. G. Paulovich, *Oncogene*, 2021, **40**, 6395–6405.
- 35 S. Dilruba and G. V. Kalayda, *Cancer Chemother. Pharmacol.*, 2016, **77**, 1103–1124.
- 36 E. Wong and C. M. Giandomenico, *Chem. Rev.*, 1999, **99**, 2451–2466.
- 37 S. Zhang, K. S. Lovejoy, J. E. Shima, L. L. Lagpacan, Y. Shu, A. Lapuk, Y. Chen, T. Komori, J. W. Gray, X. Chen, S. J. Lippard and K. M. Giacomini, *Cancer Res.*, 2006, **66**, 8847–8857.
- 38 G. Sava, S. Pacor, G. Mestroni and E. Alessio, *Clin. Exp. Metastasis*, 1992, **10**, 273–280.
- 39 E. Alessio, *Eur. J. Inorg. Chem.*, 2017, **2017**, 1549–1560.
- 40 S. Leijen, S. A. Burgers, P. Baas, D. Pluim, M. Tibben, E. van Werkhoven, E. Alessio, G. Sava, J. H. Beijnen and J. H. M. Schellens, *Investig. New Drugs*, 2015, **33**, 201–214.
- 41 C. G. Hartinger, M. A. Jakupec, S. Zorbas-Seifried, M. Groessl, A. Egger, W. Berger, H. Zorbas, P. J. Dyson and B. K. Keppler, *Chem. Biodivers.*, 2008, **5**, 2140–2155.
- 42 R. Trondl, P. Heffeter, C. R. Kowol, M. A. Jakupec, W. Berger and B. K. Keppler, *Chem. Sci.*, 2014, **5**, 2925–2932.
- 43 H. A. Burris, S. Bakewell, J. C. Bendell, J. Infante, S. F. Jones, D. R. Spiegel, G. J. Weiss, R. K. Ramanathan, A. Ogden and D. Von Hoff, *ESMO Open*, 2016, **1**, e000154.
- 44 J. Spratlin, G. O’Kane, D.-Y. Oh, S. Y. Rha, E. McWhirter, E. Elimova, P. Kavan, M. K. Choi, D. W. Kim, R. Goodwin, J. R. Hecht, S. T. Kim, D.-H. Koo, K. Halani, E. R. McAllister, M. Jones, M. Snow, Y. Lemmerick, G. Spera and J. Pankovich, *Cancer Res.*, 2023, **83**, CT149–CT149.

- 45 M. V. Babak, K. R. Chong, P. Raptá, M. Zannikou, H. M. Tang, L. Reichert, M. R. Chang, V. Kushnarev, P. Heffeter, S. M. Meier-Menches, Z. C. Lim, J. Y. Yap, A. Casini, I. V. Balyasnikova and W. H. Ang, *Angew. Chem. - Int. Ed.*, 2021, **60**, 13405–13413.
- 46 C. Lu, A. Eskandari, P. B. Cressey and K. Suntharalingam, *Chem. Eur. J.*, 2017, **23**, 11366–11374.
- 47 C. Lu, J. M. Heldt, M. Guille-Collignon, F. Lemaître, G. Jaouen, A. Vessièrès and C. Amatore, *ChemMedChem*, 2014, **9**, 1286–1293.
- 48 L. Cai, Y. Wang, Y. Chen, H. Chen, T. Yang, S. Zhang, Z. Guo and X. Wang, *Chem. Sci.*, 2023, **14**, 4375–4389.
- 49 M. A. Zoroddu, J. Aaseth, G. Crisponi, S. Medici, M. Peana and V. M. Nurchi, *J. Inorg. Biochem.*, 2019, **195**, 120–129.
- 50 K. Mijndonckx, N. Leys, J. Mahillon, S. Silver and R. Van Houdt, *BioMetals*, 2013, **26**, 609–621.
- 51 S. Top, J. Tang, A. Vessièrès, D. Carrez, C. Provot and G. Jaouen, *Chem. Commun.*, 1996, 955–956.
- 52 P. Chellan and P. J. Sadler, *Chem. Eur. J.*, 2020, **26**, 8676–8688.
- 53 M. N. Hopkinson, C. Richter, M. Schedler and F. Glorius, *Nature*, 2014, **510**, 485–496.
- 54 M. C. Jahnke and F. E. Hahn, in *N-Heterocyclic Carbenes*, Royal Society of Chemistry, Cambridge, 2016, pp. 1–45.
- 55 H. W. Wanzlick, *Angew. Chem., Int. Ed.*, 1962, **1**, 75–80.
- 56 H. Wanzlick and E. Schikora, *Chem. Ber.*, 1961, **94**, 2389–2393.
- 57 H. -W. Wanzlick and H. -J. Schönherr, *Angew. Chem. - Int. Ed.*, 1968, **7**, 141–142.
- 58 K. Öfele, *J. Organomet. Chem.*, 1968, **12**, P42–P43.
- 59 A. J. Arduengo, R. L. Harlow and M. Kline, *J. Am. Chem. Soc.*, 1991, **113**, 361–363.

- 60 A. J. Arduengo, H. V. R. Dias, R. L. Harlow and M. Kline, *J. Am. Chem. Soc.*, 1992, **114**, 5530–5534.
- 61 F. E. Hahn and M. C. Jahnke, *Angew. Chem. - Int. Ed.*, 2008, **47**, 3122–3172.
- 62 K. M. Hindi, M. J. Panzner, C. A. Tessier, C. L. Cannon and W. J. Youngs, *Chem. Rev.*, 2009, **109**, 3859–3884.
- 63 Q. Zhao, G. Meng, S. P. Nolan and M. Szostak, *Chem. Rev.*, 2020, **120**, 1981–2048.
- 64 H. V. Huynh, *Chem. Rev.*, 2018, **118**, 9457–9492.
- 65 G. Meng, L. Kakalis, S. P. Nolan and M. Szostak, *Tetrahedron Lett.*, 2019, **60**, 378–381.
- 66 S. Medici, M. Peana, V. M. Nurchi and M. A. Zoroddu, *J. Med. Chem.*, 2019, **62**, 5923–5943.
- 67 A. B. G. Lansdown, *Adv. Pharmacol. Sci.*, 2010, **2010**, 1–16.
- 68 A. Melaiye and W. J. Youngs, *Expert Opin. Ther. Pat.*, 2005, **15**, 125–130.
- 69 J. S. Holler, B. A. Fowler and G. F. Nordberg, in *Handbook on the Toxicology of Metals*, Elsevier, 2015, pp. 1209–1216.
- 70 M. Alotaibi, B. Eldeeb, M. Al-Otaibi, B. El-Deeb and N. Mostafa, *ASRJETS*, 2018, **46**, 160–177.
- 71 H. J. Klasen, *Burns*, 2000, **26**, 117–130.
- 72 D. J. Barillo and D. E. Marx, *Burns*, 2014, **40**, S3–S8.
- 73 A. Heyneman, H. Hoeksema, D. Vandekerckhove, A. Pirayesh and S. Monstrey, *Burns*, 2016, **42**, 1377–1386.
- 74 N. J. Levin, Y. Erben, Y. Li, T. J. Brigham and A. J. Bruce, *Cureus*, 2022, **14**, e30815.
- 75 A. Melaiye, R. S. Simons, A. Milsted, F. Pingitore, C. Wesdemiotis, C. A. Tessier and W. J. Youngs, *J. Med. Chem.*, 2004, **47**, 973–977.
- 76 A. Melaiye, Z. Sun, K. Hindi, A. Milsted, D. Ely, D. H. Reneker, C. A. Tessier and W. J. Youngs, *J. Am. Chem. Soc.*, 2005, **127**, 2285–2291.

- 77 A. J. Arduengo, H. V. R. Dias, J. C. Calabrese and F. Davidson, *Organometallics*, 1993, **12**, 3405–3409.
- 78 O. Guerret, S. Solé, H. Gornitzka, G. Trinquier and G. Bertrand, *Adv. Organomet. Chem.*, 2000, **600**, 112–117.
- 79 H. M. J. Wang and I. J. B. Lin, *Organometallics*, 1998, **17**, 972–975.
- 80 I. J. B. Lin and C. S. Vasam, *Coord. Chem. Rev.*, 2007, **251**, 642–670.
- 81 J. M. Hayes, M. Viciano, E. Peris, G. Ujaque and A. Lledós, *Organometallics*, 2007, **26**, 6170–6183.
- 82 P. De Frémont, N. M. Scott, E. D. Stevens, T. Ramnial, O. C. Lightbody, C. L. B. Macdonald, J. A. C. Clyburne, C. D. Abernethy and S. P. Nolan, *Organometallics*, 2005, **24**, 6301–6309.
- 83 C. K. Lee, K. M. Lee and I. J. B. Lin, *Organometallics*, 2002, **21**, 10–12.
- 84 Q. X. Liu, F. B. Xu, Q. S. Li, X. S. Zeng, X. Bin Leng, Y. L. Chou and Z. Z. Zhang, *Organometallics*, 2003, **22**, 309–314.
- 85 I. S. Edworthy, M. Rodden, S. A. Mungur, K. M. Davis, A. J. Blake, C. Wilson, M. Schröder and P. L. Arnold, *J. Organomet. Chem.*, 2005, **690**, 5710–5719.
- 86 T. Ramnial, C. D. Abernethy, M. D. Spicer, I. D. McKenzie, I. D. Gay and J. A. C. Clyburne, *Inorg. Chem.*, 2003, **42**, 1391–1393.
- 87 D. R. Joshi and N. Adhikari, *Int. j. pharm. pharm. res.*, 2019, **28**, 1–18.
- 88 A. A. D. Tulloch, A. A. Danopoulos, S. Winston, S. Kleinhenz and G. Eastham, *J. Chem. Soc., Dalton Trans.*, 2000, **2000**, 4499–4506.
- 89 X. Hu, Y. Tang, P. Gantzel and K. Meyer, *Organometallics*, 2003, **22**, 612–614.
- 90 K. M. Lee, H. M. J. Wang and I. J. B. Lin, *J. Chem. Soc., Dalton Trans.*, 2002, **2002**, 2852–2856.
- 91 P. J. Altmann and A. Pöthig, *J. Am. Chem. Soc.*, 2016, **138**, 13171–13174.
- 92 J. S. Craig, L. Melidis, H. D. Williams, S. J. Dettmer, A. A. Heidecker, P. J. Altmann, S. Guan, C. Campbell, D. F. Browning, R. K. O. Sigel, S. Johannsen, R.

- T. Egan, B. Aikman, A. Casini, A. Pöthig and M. J. Hannon, *J. Am. Chem. Soc.*, 2023, **145**, 13570–13580.
- 93 B. N. Ahamed, R. Dutta and P. Ghosh, *Inorg. Chem.*, 2013, **52**, 4269–4276.
- 94 D. A. Medvetz, K. M. Hindi, M. J. Panzner, A. J. Ditto, Y. H. Yun and W. J. Youngs, *Met.-based drug.*, 2008, **2008**, 1–7.
- 95 Z. J. Lin, J. Bies, S. S. Johnson, J. D. Gorden, J. F. Strickland, M. Frazier, J. M. Meyers and K. L. Shelton, *J. Heterocycl. Chem.*, 2019, **56**, 533–538.
- 96 R. A. Haque, S. Budagumpi, H. Zetty Zulikha, N. Hasanudin, M. B. Khadeer Ahamed and A. M. S. Abdul Majid, *Inorg. Chem. Commun.*, 2014, **44**, 128–133.
- 97 R. A. Haque, N. Hasanudin, M. A. Hussein, S. A. Ahamed and M. A. Iqbal, *Inorg. Nano-Met. Chem.*, 2017, **47**, 131–137.
- 98 A. Habib, M. A. Iqbal and H. N. Bhatti, *J. Coord. Chem.*, 2019, **72**, 2065–2079.
- 99 M. O. Karataş, Ü. Keleştemur, A. Mumcu, N. Özdemir, A. Erdoğan and H. Küçükbay, *Transit. Met. Chem.*, 2024, **49**, 365–372.
- 100 A. Mariconda, D. Iacopetta, M. Sirignano, J. Ceramella, C. Costabile, M. Pellegrino, C. Rosano, A. Catalano, C. Saturnino, H. El-Kashef, S. Aquaro, M. S. Sinicropi and P. Longo, *ChemMedChem*, 2022, **17**, e202200345.
- 101 D. Iacopetta, C. Costabile, M. La Chimia, A. Mariconda, J. Ceramella, D. Scumaci, A. Catalano, C. Rosano, G. Cuda, M. S. Sinicropi and P. Longo, *ACS Medicinal Chem. Lett.*, 2023, **14**, 1567–1575.
- 102 L. Eloy, A. S. Jarrousse, M. L. Teyssot, A. Gautier, L. Morel, C. Jolival, T. Cresteil and S. Roland, *ChemMedChem*, 2012, **7**, 805–814.
- 103 F. Hackenberg, G. Lally, H. Müller-Bunz, F. Paradisi, D. Quaglia, W. Streciwilk and M. Tacke, *J. Organomet. Chem.*, 2012, **717**, 123–134.
- 104 F. Hackenberg, G. Lally, H. Müller-Bunz, F. Paradisi, D. Quaglia, W. Streciwilk and M. Tacke, *Inorg. Chim. Acta*, 2013, **395**, 135–144.
- 105 W. Streciwilk, J. Cassidy, F. Hackenberg, H. Müller-Bunz, F. Paradisi and M. Tacke, *J. Organomet. Chem.*, 2014, **749**, 88–99.

- 106 M. N. Hopkinson, C. Richter, M. Schedler and F. Glorius, *Nature*, 2014, **510**, 485–496.
- 107 A. Sarfraz, R. Ashraf, S. Ali, T. Taskin-Tok, Z. Khalid, S. Ullah, T. Kahlid, M. Mushtaq, S. M. El-Bahy and Z. M. El-Bahy, *J. Mol. Struct.*, 2022, **1251**, 131946.
- 108 M. Marinelli, M. Pelli, C. Cimarrelli, H. V. R. Dias, C. Marzano, F. Tisato, M. Porchia, V. Gandin and C. Santini, *J. Organomet. Chem.*, 2016, **806**, 45–53.
- 109 V. Gandin, M. Pelli, M. Marinelli, C. Marzano, A. Dolmella, M. Giorgetti and C. Santini, *J. Inorg. Biochem.*, 2013, **129**, 135–144.
- 110 S. Y. Hussaini, R. A. Haque, T. Fatima, T. M. Agha, A. M. S. Abdul Majid, H. H. Abdallah and M. R. Razali, *Transit. Met. Chem.*, 2018, **43**, 301–312.
- 111 S. Y. Hussaini, R. A. Haque, T. Fatima, M. T. Agha, A. M. S. Abdul Majid and M. R. Razali, *J. Coord. Chem.*, 2018, **71**, 2787–2799.
- 112 S. Y. Hussaini, R. A. Haque, M. T. Agha, A. M. S. Abdul Majid and M. R. Razali, *Inorg. Nano-Met. Chem.*, 2018, **48**, 247–256.
- 113 C. H. Wong, B.-K. Khor, G. T. J. K. Anak Inggang, N. A. Mohd. Nor Affandi, V. Murugaiyah, N. J.-Y. Chear and W. Yam, *Inorg. Chim. Acta*, 2024, **567**, 122040.
- 114 M. Asif, M. A. Iqbal, M. A. Hussein, C. E. Oon, R. A. Haque, M. B. Khadeer Ahamed, A. S. Abdul Majid and A. M. S. Abdul Majid, *Eur. J. Med. Chem.*, 2016, **108**, 177–187.
- 115 S. Y. Hussaini, R. A. Haque, P. O. Asekunowo, A. M. S. Abdul Majid, M. Taleb Agha and M. R. Razali, *J. Organomet. Chem.*, 2017, **840**, 56–62.
- 116 A. Habib, M. A. Iqbal, H. N. Bhatti and M. Shahid, *Transit. Met. Chem.*, 2019, **44**, 431–443.
- 117 N. Abdurrahman, F. S. Braim, N. Yoshinari, N. N. A. Nik Abd Razak and Mohd. R. Razali, *J. Coord. Chem.*, 2024, **77**, 1067–1084.
- 118 R. A. Haque, N. Hasanudin, M. A. Hussein, S. A. Ahamed and M. A. Iqbal, *Inorg. Nano-Met. Chem.*, 2016, **47**, 131–137.

- 119 D. C. F. Monteiro, R. M. Phillips, B. D. Crossley, J. Fielden and C. E. Willans, *Dalton Trans.*, 2012, **41**, 3720–3725.
- 120 R. Ashraf, H. N. Bhatti, M. A. Iqbal and Y. Jamil, *Inorg. Chem. Commun.*, 2020, **119**, 108077.
- 121 E. S. J. Arnér and A. Holmgren, *Eur. J. Biochem.*, 2000, **267**, 6102–6109.
- 122 L. Zhong, E. S. J. Arnér and A. Holmgren, *Proc. Natl. Acad. Sci. U.S.A.*, 2000, **97**, 5854–5859.
- 123 M. A. Iqbal, R. A. Haque, M. B. K. Ahamed, A. M. S. A. Majid and S. S. Al-Rawi, *Med. Chem. Res.*, 2013, **22**, 2455–2466.
- 124 M. R. Southerland, M. A. DeBord, N. A. Johnson, S. R. Crabtree, N. E. Alexander, M. L. Stromyer, P. O. Wagers, M. J. Panzner, C. Wesdemiotis, L. P. Shriver, C. A. Tessier and W. J. Youngs, *Bioorg. Med. Chem.*, 2021, **30**, 115893.
- 125 X. García-LLinás, A. Bauzá, S. K. Seth and A. Frontera, *J. Phys. Chem. A*, 2017, **121**, 5371–5376.
- 126 G. Anusha, M. Indira, I. S. Kumar, L. S. Sarma, K. R. Reddy, P. V. Govardhana Reddy and T. M. Aminabhavi, *Chemosphere*, 2022, **301**, 134751.
- 127 A. Titi, S. M. Almutairi, A. F. Alrefaei, S. Manoharadas, B. A. Alqurashy, P. K. Sahu, B. Hammouti, R. Touzani, M. Messali and I. Ali, *J. Mol. Liq.*, 2020, **315**, 113778.
- 128 I. Shahid, C. H. Patel, S. Dhanani, C. P. Owen and S. Ahmed, *J. Steroid Biochem. Mol. Biol.*, 2008, **110**, 18–29.
- 129 B. Thomas, R. E. Duval, S. Fontanay, M. Varbanov and M. Boisbrun, *ChemMedChem*, 2019, **14**, 1232–1237.
- 130 L. Roumen, J. W. Peeters, J. M. A. Emmen, I. P. E. Beugels, E. M. G. Custers, M. de Gooyer, R. Plate, K. Pieterse, P. A. J. Hilbers, J. F. M. Smits, J. A. J. Vekemans, D. Leysen, H. C. J. Ottenheijm, H. M. Janssen and J. J. R. Hermans, *J. Med. Chem.*, 2010, **53**, 1712–1725.
- 131 S. Gülcemal, D. Gülcemal, G. F. S. Whitehead and J. Xiao, *Chem. Eur. J.*, 2016, **22**, 10513–10522.

- 132 J. Tessier and A. R. Schmitzer, *RSC Adv.*, 2020, **10**, 9420–9430.
- 133 H. Küçükbay, R. Durmaz, E. Orhan and S. Günal, *Il Farmaco*, 2003, **58**, 431–437.
- 134 J. O’Connell, E. Moriarty and F. Aldabbagh, *Synth.*, 2012, **44**, 3371–3377.
- 135 M. O. Karatas, B. Alici, E. Çetinkaya, Ç. Bilen, N. Gençer and O. Arslan, *Russ. J. Bioorganic Chem.*, 2014, **40**, 461–466.
- 136 T. A. P. Paulose, S.-C. Wu, J. A. Olson, T. Chau, N. Theaker, M. Hassler, J. W. Quail and S. R. Foley, *Dalton Trans.*, 2012, **41**, 251–260.
- 137 M. Albrecht, J. R. Miecznikowski, A. Samuel, J. W. Faller and R. H. Crabtree, *Organometallics*, 2002, **21**, 3596–3604.
- 138 H. M. Lee, C. Y. Lu, C. Y. Chen, W. L. Chen, H. C. Lin, P. L. Chiu and P. Y. Cheng, *Tetrahedron*, 2004, **60**, 5807–5825.
- 139 H. V. Huynh, T. T. Lam and H. T. T. Luong, *RSC Adv.*, 2018, **8**, 34960–34966.
- 140 N. M. Logacheva, V. E. Baulin, A. Yu. Tsivadze, E. N. Pyatova, I. S. Ivanova, Y. A. Velikodny and V. V. Chernyshev, *Dalton Trans.*, 2009, 2482.
- 141 T. Wagner, B. M. Zeglis, S. Groveman, C. Hille, A. Pöthig, L. C. Francesconi, W. A. Herrmann, F. E. Kühn and T. Reiner, *J. Label. Compd. Radiopharm.*, 2014, **57**, 441–447.
- 142 A. Sarfraz, R. Ashraf, S. Ali, T. Taskin-Tok, Z. Khalid, S. Ullah, T. Kahlid, M. Mushtaq, S. M. El-Bahy and Z. M. El-Bahy, *J. Mol. Struct.*, 2022, **1251**, 131946.
- 143 C. Schulte to Brinke, T. Pape and F. E. Hahn, *Dalton Trans.*, 2013, **42**, 7330.
- 144 R. A. Haque, N. Hasanudin, M. A. Iqbal, A. Ahmad, S. Hashim, A. Abdul Majid and M. B. K. Ahamed, *J. Coord. Chem.*, 2013, **66**, 3211–3228.
- 145 K. M. Blatchford, C. J. Mize, S. Roy and D. M. Jenkins, *Dalton Trans.*, 2022, **51**, 6153–6156.
- 146 Y. L. Loh, U. F. M. Haziz, R. A. Haque, A. A. Amirul, O. N. Aidda and M. R. Razali, *J. Coord. Chem.*, 2019, **72**, 894–907.
- 147 D. Demir Atlı and S. Güllü, *J. Mol. Struct.*, 2019, **1179**, 576–580.

- 148 D. Kost and A. Zeichner, *Tetrahedron*, 1974, 4533–4536.
- 149 O. Reany, I. Goldberg, S. Abramson, L. Golender, B. Ganguly and B. Fuchs, *J. Org. Chem.*, 1998, **63**, 8850–8859.
- 150 Z. Zhou, Y. He, X. Qiu, D. Redwine, J. Potter, R. Cong and M. Miller, *Macromol. Symp.*, 2013, **330**, 115–122.
- 151 H. Schmidbaur and A. Schier, *Angew. Chem. - Int. Ed.*, 2015, **54**, 746–784.
- 152 J. M. MacLeod and F. Rosei, in *Comprehensive Nanoscience and Technology*, Elsevier, Amsterdam, 2011, vol. 3, pp. 13–68.
- 153 Y. Bansal and O. Silakari, *Bioorg. Med. Chem.*, 2012, **20**, 6208–6236.
- 154 Y. T. Lee, Y. J. Tan and C. E. Oon, *Acta Pharm. Sin. B*, 2023, **13**, 478–497.
- 155 P. Cabildo, R. Claramunt, J. L. Lavandera, D. Sanz, J. Elguero, C. Enjalbal and J. L. Aubagnac, *J. Heterocycl. Chem.*, 1997, **34**, 367–374.
- 156 C. Gradert, J. Krahmer, F. D. Sönnichsen, C. Näther and F. Tuczek, *J. Organomet. Chem.*, 2014, **770**, 61–68.
- 157 J. De Tovar, F. Rataboul and L. Djakovitch, *ChemCatChem*, 2020, **12**, 5797–5808.
- 158 K. B. Avery, W. G. Devine, C. M. Kormos and N. E. Leadbeater, *Tetrahedron Lett.*, 2009, **50**, 2851–2853.
- 159 Y. Zhang, J. Clavadetscher, M. Bachmann, O. Blacque and K. Venkatesan, *Inorg. Chem.*, 2014, **53**, 756–771.
- 160 J. Černochová, P. Branná, M. Rouchal, P. Kulhánek, I. Kuřitka and R. Vicha, *Chem. Eur. J.*, 2012, **18**, 13633–13637.
- 161 J. Cao, G. Xiong, Z. Luo, Q. Huang, W. Zhou, I. Dragutan, V. Dragutan, Y. Sun and F. Ding, *Inorg. Chim. Acta*, 2024, **568**, 122076.
- 162 J. De Tovar, F. Rataboul and L. Djakovitch, *J. Catal.*, 2021, **398**, 133–147.
- 163 S. Demir, I. Özdemir and B. Çetinkaya, *Appl. Organomet. Chem.*, 2006, **20**, 254–259.

- 164 J. D. Cope, P. E. Sheridan, C. J. Galloway, R. F. Awoyemi, S. L. Stokes and J. P. Emerson, *Organometallics*, 2020, **39**, 4457–4464.
- 165 A. Volpe, A. Sartorel, C. Graiff, M. Bonchio, A. Biffis, M. Baron and C. Tubaro, *J. Organomet. Chem.*, 2020, **917**, 121260.
- 166 Z. Xi, X. Zhang, W. Chen, S. Fu and D. Wang, *Organometallics*, 2007, **26**, 6636–6642.
- 167 N. Touj, I. S. A. Nasr, W. S. Koko, T. A. Khan, I. Özdemir, S. Yasar, L. Mansour, F. Alresheedi and N. Hamdi, *J. Coord. Chem.*, 2020, **73**, 2889–2905.
- 168 A. A. Penney, V. V. Sizov, E. V. Grachova, D. V. Krupenya, V. V. Gurzhiy, G. L. Starova and S. P. Tunik, *Inorg. Chem.*, 2016, **55**, 4720–4732.
- 169 O. S. King, B. J. Hofmann, A. E. Boakye-Smith, A. J. Managh, T. Stringer and R. M. Lord, *Organometallics*, 2024, **43**, 2662–2673.
- 170 J. Z. Vlahakis, C. Lazar, I. E. Crandall and W. A. Szarek, *Bioorg. Med. Chem.*, 2010, **18**, 6184–6196.
- 171 China, CN2020-10650021, 2020.
- 172 K. Hayat, M. Shkeel, M. A. Iqbal, C. K. Quah, Q. A. Wong, M. Nazari V, Mohd. B. K. Ahamed and S. Hameed, *J. Organomet. Chem.*, 2023, **985**, 122593.
- 173 S. Garmendia, S. B. Lawrenson, M. C. Arno, R. K. O'Reilly, D. Taton and A. P. Dove, *Macromol. Rapid Commun.*, 2019, **40**, 1970033.
- 174 R. A. Haque, H. Z. Zulikha, M. Z. Ghdhayeb, S. Budagumpi and A. W. Salman, *Heteroat. Chem.*, 2012, **23**, 486–497.
- 175 H. Zetty Zulikha, R. A. Haque, S. Budagumpi and A. M. S. Abdul Majid, *Inorg. Chim. Acta*, 2014, **411**, 40–47.
- 176 K. M. Hindi, T. J. Siciliano, S. Durmus, M. J. Panzner, D. A. Medvetz, D. V. Reddy, L. A. Hogue, C. E. Hovis, J. K. Hilliard, R. J. Mallet, C. A. Tessier, C. L. Cannon and W. J. Youngs, *J. Med. Chem.*, 2008, **51**, 1577–1583.
- 177 G. Achar, C. R. Shahini, S. A. Patil and S. Budagumpi, *J. Organomet. Chem.*, 2017, **833**, 28–42.

- 178 P. O. Asekunowo and R. A. Haque, *J. Coord. Chem.*, 2014, **67**, 3649–3663.
- 179 M. Napoli, C. Saturnino, E. I. Cianciulli, M. Varcamonti, A. Zanfardino, G. Tommonaro and P. Longo, *J. Organomet. Chem.*, 2013, **725**, 46–53.
- 180 R. Ashraf, S. Akram, M. El-Naggar, A. Kanwal, T. T. Tok, M. A. Iqbal, H. N. Bhatti, M. A. Amin, S. M. El-Bahy and Z. M. El-Bahy, *Inorg. Chim. Acta*, 2024, **571**, 122181.
- 181 C. A. Lipinski, B. W. Dominy and P. J. Feeney, *Adv. Drug Deliv. Rev.*, 1997, **23**, 3–25.
- 182 K. Soliman, F. Grimm, C. A. Wurm and A. Egner, *Sci. Rep.*, 2021, **11**, 6991.
- 183 A. Daina, O. Michielin and V. Zoete, *Sci. Rep.*, 2017, **7**, 42717.
- 184 M. V. Berridge, P. M. Herst and A. S. Tan, *Biotechnol. Annu. Rev.*, 2005, **11**, 127–152.
- 185 Y. J. Oh and J. Hong, *LWT*, 2022, **153**, 112565.
- 186 D. Iacopetta, A. Mariconda, C. Saturnino, A. Caruso, G. Palma, J. Ceramella, N. Muià, M. Perri, M. S. Sinicropi, M. C. Caroleo and P. Longo, *ChemMedChem*, 2017, **12**, 2054–2065.
- 187 A. Mondal, R. K. Tripathy, P. Dutta, M. K. Santra, A. A. Isab, C. W. Bielawski, H. K. Kisan, S. K. Chandra and J. Dinda, *Appl. Organomet. Chem.*, 2019, **33**, e4692.
- 188 P. A. Kenny, G. Y. Lee, C. A. Myers, R. M. Neve, J. R. Semeiks, P. T. Spellman, K. Lorenz, E. H. Lee, M. H. Barcellos-Hoff, O. W. Petersen, J. W. Gray and M. J. Bissell, *Mol. Oncol.*, 2007, **1**, 84–96.
- 189 N. A. Rahman, L. S. Yazan, A. Wibowo, N. Ahmat, J. B. Foo, Y. S. Tor, S. K. Yeap, Z. A. Razali, Y. S. Ong and S. Fakurazi, *BMC Complement. Altern. Med.*, 2016, **16**, 354.
- 190 M. Kciuk, A. Gielecińska, S. Mujwar, D. Kołat, Ż. Kałuzińska-Kołat, I. Celik and R. Kontek, *Cells*, 2023, **12**, 659.
- 191 A. Mukherjee and W. D. Sasikala, in *Advances in Protein Chemistry and Structural Biology*, Academic Press Inc., 2013, vol. 92, pp. 1–62.

- 192 J. M. Yuan, N. Y. Chen, H. R. Liao, G. H. Zhang, X. J. Li, Z. Y. Gu, C. X. Pan, D. L. Mo and G. F. Su, *New J. Chem.*, 2020, **44**, 11203–11214.
- 193 O. Sanchez, S. González, M. Fernández, A. R. Higuera-Padilla, Y. Leon, D. Coll, A. Vidal, P. Taylor, I. Urdanibia, M. C. Goite and W. Castro, *Inorg. Chim. Acta*, 2015, **437**, 143–151.
- 194 P. R. Inamdar and A. Sheela, *J. Photochem. Photobiol.*, 2016, **159**, 133–141.
- 195 J. R. Lakowicz and G. Weber, *Biochemistry*, 1973, **12**, 4162–4170.
- 196 D. Satapathi, M. Das, K. Rajak, S. Laha, Md. M. Islam, I. Choudhuri, N. Bhattacharyya, S. Das, B. C. Samanta and T. Maity, *Appl. Organomet. Chem.*, 2022, **36**, e6473.
- 197 G. M. Morris, R. Huey, W. Lindstrom, M. F. Sanner, R. K. Belew, D. S. Goodsell and A. J. Olson, *J. Comput. Chem.*, 2009, **30**, 2785–2791.
- 198 S. Shityakov and C. Förster, *Adv. Appl. Bioinform. Chem.*, 2014, **7**, 23–36.
- 199 M. Redza-Dutordoir and D. A. Averill-Bates, *Biochim. Biophys. Acta - Mol. Cell Res.*, 2016, **1863**, 2977–2992.
- 200 H. Sies, V. V. Belousov, N. S. Chandel, M. J. Davies, D. P. Jones, G. E. Mann, M. P. Murphy, M. Yamamoto and C. Winterbourn, *Nat. Rev. Mol. Cell Biol.*, 2022, **23**, 499–515.
- 201 M. Bian, R. Fan, S. Zhao and W. Liu, *J. Med. Chem.*, 2019, **62**, 7309–7321.
- 202 M. Redza-Dutordoir and D. A. Averill-Bates, *Biochim. Biophys. Acta - Mol. Cell Res.*, 2016, **1863**, 2977–2992.
- 203 D. Guo, L. Zhu, Z. Huang, H. Zhou, Y. Ge, W. Ma, J. Wu, X. Zhang, X. Zhou, Y. Zhang, Y. Zhao and N. Gu, *Biomaterials*, 2013, **34**, 7884–7894.
- 204 A. Gomes, E. Fernandes and J. L. F. C. Lima, *J. Biochem. Biophys. Methods*, 2005, **65**, 45–80.
- 205 S. J. Allison, M. Sadiq, E. Baronou, P. A. Cooper, C. Dunnill, N. T. Georgopoulos, A. Latif, S. Shepherd, S. D. Shnyder, I. J. Stratford, R. T. Wheelhouse, C. E. Willans and R. M. Phillips, *Cancer Lett.*, 2017, **403**, 98–107.

- 206 L. Tang, X. Chang, J. Shi, Z. Wen, C. Bi and W. Liu, *Eur. J. Med. Chem.*, 2024, **282**, 117014.
- 207 J. Zhang, H. Zou, J. Lei, B. He, X. He, H. H. Y. Sung, R. T. K. Kwok, J. W. Y. Lam, L. Zheng and B. Z. Tang, *Angew. Chem. - Int. Ed.*, 2020, **132**, 7163–7171.
- 208 A. J. Didier, J. Stiene, L. Fang, D. Watkins, L. D. Dworkin and J. F. Creeden, *Antioxidants*, 2023, **12**, 632.
- 209 J. Kruszewska, A. Kur, D. Kulpińska, I. Grabowska-Jadach, M. Matczuk, B. K. Keppler, A. R. Timerbaev and M. Jarosz, *J. Pharm. Biomed. Anal.*, 2019, **174**, 300–304.
- 210 A. B. G. Lansdown, *Adv. Pharmacol. Sci.*, 2010, **2010**, 1–16.
- 211 O. Monfort and P. Petrisková, *Processes*, 2021, **9**, 1–57.
- 212 J. Costa Pessoa, E. Garribba, M. F. A. Santos and T. Santos-Silva, *Coord. Chem. Rev.*, 2015, **301–302**, 49–86.
- 213 A. Sigel, H. Sigel and R. K. O. Sigel, *Met. Ions Life Sci.*, 2013, **13**, 139–169.
- 214 P. Chirik and R. Morris, *Acc. Chem. Res.*, 2015, **48**, 2495–2495.
- 215 C. E. Heyliger, A. G. Tahiliani and J. H. McNeill, *Science (1979)*, 1985, **227**, 1474–1477.
- 216 J. Benítez, L. Guggeri, I. Tomaz, J. C. Pessoa, V. Moreno, J. Lorenzo, F. X. Avilés, B. Garat and D. Gambino, *J. Inorg. Biochem.*, 2009, **103**, 1386–1394.
- 217 A. Ross, D. C. Soares, D. Covelli, C. Pannecouque, L. Budd, A. Collins, N. Robertson, S. Parsons, E. De Clercq, P. Kennepohl and P. J. Sadler, *Inorg. Chem.*, 2010, **49**, 1122–1132.
- 218 I. Correia, P. Adão, S. Roy, M. Wahba, C. Matos, M. R. Maurya, F. Marques, F. R. Pavan, C. Q. F. Leite, F. Avecilla and J. Costa Pessoa, *J. Inorg. Biochem.*, 2014, **141**, 83–93.
- 219 M. L. Cacicedo, M. C. Ruiz, S. Scioli-Montoto, M. E. Ruiz, M. A. Fernández, R. M. Torres-Sanchez, E. J. Baran, G. R. Castro and I. E. León, *New J. Chem.*, 2019, **43**, 17726–17734.

- 220 R. K. Narla, C. L. Chen, Y. Dong and F. M. Uckun, *J. Exp. Clin. Cancer Res.*, 2001, **7**, 2124–33.
- 221 L. Ni, H. Zhao, L. Tao, X. Li, Z. Zhou, Y. Sun, C. Chen, D. Wei, Y. Liu and G. Diao, *Dalton Trans.*, 2018, **47**, 10035–10045.
- 222 N. Ribeiro, I. Bulut, B. Cevatemre, C. Teixeira, Y. Yildizhan, V. André, P. Adão, J. C. Pessoa, C. Acilan and I. Correia, *Dalton Trans.*, 2021, **50**, 157–169.
- 223 M. W. Makinen and M. J. Brady, *J. Biol. Chem.*, 2002, **277**, 12215–12220.
- 224 Y. Fu, Q. Wang, X.-G. Yang, X.-D. Yang and K. Wang, *J. Biol. Inorg. Chem.*, 2008, **13**, 1001–1009.
- 225 S. Sgarbossa, E. Diana, D. Marabello, A. Deagostino, S. Cadamuro, A. Barge, E. Laurenti, M. Gallicchio, V. Boscaro and E. Ghibaudi, *J. Inorg. Biochem.*, 2013, **128**, 26–37.
- 226 M. Mohamadi, S. Yousef Ebrahimipour, M. Torkzadeh-Mahani, S. Foro and A. Akbari, *RSC Adv.*, 2015, **5**, 101063–101075.
- 227 C. P. Chinthala and S. Angappan, *Appl. Organomet. Chem.*, 2017, **31**, e3700.
- 228 M. Zegke, H. L. M. Spencer and R. M. Lord, *Chem. Eur. J.*, 2019, **25**, 12275–12280.
- 229 B. Sergi, I. Bulut, Y. Xia, Z. A. E. Waller, Y. Yildizhan, C. Acilan and R. M. Lord, *ChemMedChem*, 2021, **16**, 2402–2410.
- 230 W. A. Herrmann, K. Qfele, M. Elison, F. E. Kuhn and P. W. Roesky, *J. Organomet. Chem.*, 1994, **480**, 7–9.
- 231 A. Wacker, C. Guo Yan, G. Kaltenpoth, A. Ginsberg, A. M. Arif, R. D. Ernst, H. Pritzkow and W. Siebert, *J. Organomet. Chem.*, 2002, **641**, 195–202.
- 232 C. D. Abernethy, G. M. Codd, M. D. Spicer and M. K. Taylor, *J. Am. Chem. Soc.*, 2003, **125**, 1128–1129.
- 233 S. Zhang, W.-C. Zhang, D.-D. Shang, Z.-Q. Zhang and Y.-X. Wu, *Dalton Trans.*, 2015, **44**, 15264–15270.
- 234 S. Zhang, W. Zhang, D. Shang and Y. Wu, *J. Polym. Sci. A: Polym. Chem.*, 2019, **57**, 553–561.

- 235 Y.-C. Wang, H. Zha, P.-Y. Cheng, S. Zhang, X.-W. Liu and Y.-X. Wu, *Chin. J. Polym. Sci.*, 2024, **42**, 32–41.
- 236 A. Igarashi, E. L. Kolychev, M. Tamm and K. Nomura, *Organometallics*, 2016, **35**, 1778–1784.
- 237 Y. Kawamoto, I. Elser, M. R. Buchmeiser and K. Nomura, *Organometallics*, 2021, **40**, 2017–2022.
- 238 G. Tejeda, D. S. Belov, D. A. Fenoll, K. L. Rue, C. Tsay, X. Solans-Monfort and K. V. Bukhryakov, *Organometallics*, 2022, **41**, 361–365.
- 239 D. S. Belov, C. M. Acosta, M. Garcia-Molina, K. L. Rue, X. Solans-Monfort and K. V. Bukhryakov, *Organometallics*, 2022, **41**, 2897–2902.
- 240 C. Weetman, S. Notman and P. L. Arnold, *Dalton Trans.*, 2018, **47**, 2568–2574.
- 241 L. Kuehn, A. F. Eichhorn, T. B. Marder and U. Radius, *J. Organomet. Chem.*, 2019, **881**, 25–33.
- 242 M. Henrion, A. M. Oertel, V. Ritleng and M. J. Chetcuti, *ChemComm*, 2013, **49**, 6424–6426.
- 243 S. Stipurin and T. Strassner, *J. Organomet. Chem.*, 2023, **1000**, 122785.
- 244 S. G. Guillet, I. Ibni Hashim, M. Beliš, K. Van Hecke, C. S. J. Cazin and Steven. P. Nolan, *Eur. J. Inorg. Chem.*, 2023, **26**, e202300327.
- 245 Y. Zhang, B. Liu, H. Wu and W. Chen, *Bull. Chin. Acad. Sci.*, 2012, **57**, 2368–2376.
- 246 V. Adamovich, S. Bajo, P. L. T. Boudreault, M. A. Esteruelas, A. M. López, J. Martín, M. Oliván, E. Onate, A. U. Palacios, A. San-Torcuato, J. Y. Tsai and C. Xia, *Inorg. Chem.*, 2018, **57**, 10744–10760.
- 247 E. S. Degtyareva, J. V. Burykina, A. N. Fakhrutdinov, E. G. Gordeev, V. N. Khrustalev and V. P. Ananikov, *ACS Catal.*, 2015, **5**, 7208–7213.
- 248 E. V. Fedorova, V. B. Rybakov, V. M. Senyavin, A. V. Anisimov and L. A. Aslanov, *Crystallogr. Rep.*, 2005, **50**, 224–229.
- 249 F. R. Neururer, D. Leitner, S. Liu, K. Wurst, H. Kopacka, M. Seidl and S. Hohloch, *Eur. J. Inorg. Chem.*, 2023, **26**, e202300180.

- 250 B. J. Blackburn, J. H. Crane, C. E. Knapp, M. J. Powell, P. Marchand, D. Pugh, J. C. Bear, I. P. Parkin and C. J. Carmalt, *Mater. Des.*, 2016, **108**, 780–790.
- 251 B. D. Wright, M. C. Deblock, P. O. Wagers, E. Duah, N. K. Robishaw, K. L. Shelton, M. R. Southerland, M. A. DeBord, K. M. Kersten, L. J. McDonald, J. A. Stiel, M. J. Panzner, C. A. Tessier, S. Paruchuri and W. J. Youngs, *Med. Chem. Res.*, 2015, **24**, 2838–2861.
- 252 L. Suresh, J. Finnstad, K. W. Törnroos and E. Le Roux, *Inorg. Chim. Acta*, 2021, **521**, 120301.
- 253 K. Qiu, Y. Chen, T. W. Rees, L. Ji and H. Chao, *Coord Chem Rev*, 2019, **378**, 66–86.
- 254 S. Neidle, *J. Med. Chem.*, 2016, **59**, 5987–6011.
- 255 V. Sanchez-Martin, C. Lopez-Pujante, M. Soriano-Rodriguez and J. A. Garcia-Salcedo, *Int. J. Mol. Sci.*, 2020, **21**, 8900.
- 256 Y. Lin, B. Yang, Y. Huang, Y. Zhang, Y. Jiang, L. Ma and Y.-Q. Shen, *Cell Insight*, 2023, **2**, 100113.
- 257 S. Vibet, C. Goupille, P. Bougnoux, J. P. Steghens, J. Goré and K. Mahéo, *Free Radic. Biol. Med.*, 2008, **44**, 1483–1491.
- 258 M. B. Shah, J. Liu, Q. Zhang, C. D. Stout and J. R. Halpert, *ACS Chem. Biol.*, 2017, **12**, 1204–1210.
- 259 B. M. Johnson, Y.-Z. Shu, X. Zhuo and N. A. Meanwell, *J. Med. Chem.*, 2020, **63**, 6315–6386.
- 260 Q. Li, X. Li, J. Yang, H. Bin Song and L. F. Tang, *Polyhedron*, 2013, **59**, 29–37.
- 261 J. Věžník, M. Konhefr, Z. Fohlerová and K. Lacina, *J. Inorg. Biochem.*, 2021, **224**, 111561.
- 262 F. Binacchi, F. Guarra, D. Cirri, T. Marzo, A. Pratesi, L. Messori, C. Gabbiani and T. Biver, *Molecules*, 2020, **25**, 5446.
- 263 A. Citta, E. Schuh, F. Mohr, A. Folda, M. L. Massimino, A. Bindoli, A. Casini and M. P. Rigobello, *Metallomics*, 2013, **5**, 1006.

- 264 H. Pfeiffer, A. Rojas, J. Niesel and U. Schatzschneider, *Dalton Trans.*, 2009, 4292.
- 265 J. E. Bara, *Ind. Eng. Chem. Res.*, 2011, **50**, 13614–13619.
- 266 J. Z. Vlahakis, C. Lazar, G. Roman, D. Vukomanovic, K. Nakatsu and W. A. Szarek, *ChemMedChem*, 2012, **7**, 897–902.
- 267 I. Shahid, C. H. Patel, S. Dhanani, C. P. Owen and S. Ahmed, *J. Steroid Biochem. Mol. Biol.*, 2008, **110**, 18–29.
- 268 P. Dowari, S. Das, B. Pramanik and D. Das, *Chem. Commun.*, 2019, **55**, 14119–14122.
- 269 T. A. P. Paulose, J. A. Olson, J. Wilson Quail and S. R. Foley, *J. Organomet. Chem.*, 2008, **693**, 3405–3410.
- 270 J. L. Harper, R. A. J. Smith, J. J. Bedford and J. P. Leader, *Synthesis, Acidity and ¹⁵N NMR Characteristics of Imidazoles bearing l-Fluorinated Substituents with Potential Application as Probes for Intracellular pH Determination*, 1997, vol. 53.
- 271 T. Chatterjee, N. T. Kumar and S. K. Das, *Polyhedron*, 2017, **127**, 68–83.
- 272 A. Sharifian, K. Parang, H. Zorrieh-Amirian, M. Nazarinia and A. Shafiee, *J. Heterocycl. Chem.*, 1994, **31**, 1421–1423.
- 273 V. O. Iaroshenko, D. Ostrovskyi, M. Miliutina, A. Maalik, A. Villinger, A. Tolmachev, D. M. Volochnyuk and P. Langer, *Adv. Synth. Catal.*, 2012, **354**, 2495–2503.
- 274 M. O. Karatas, B. Alici, E. Çetinkaya, Ç. Bilen, N. Gençer and O. Arslan, *Russ. J. Bioorganic Chem.*, 2014, **40**, 461–466.
- 275 N. Touj, I. S. Al Nasr, W. S. Koko, T. A. Khan, I. Özdemir, S. Yasar, L. Mansour, F. Alresheedi and N. Hamdi, *J. Coord. Chem.*, 2020, **73**, 2889–2905.
- 276 J. Tessier and A. R. Schmitzer, *RSC Adv.*, 2020, **10**, 9420–9430.
- 277 N. Noujeim, L. Leclercq and A. R. Schmitzer, *J. Org. Chem.*, 2008, **73**, 3784–3790.
- 278 H. M. Lee, C. Y. Lu, C. Y. Chen, W. L. Chen, H. C. Lin, P. L. Chiu and P. Y. Cheng, *Tetrahedron*, 2004, **60**, 5807–5825.

- 279 R. Lum, H. Zhang, W. Zhang, S. Q. Bai, J. Zhao and T. S. A. Hor, *Dalton Trans.*, 2013, **42**, 871–873.
- 280 <https://rigaku.com/products/crystallography/x-ray-diffraction/crystalispro> .
- 281 G. M. Sheldrick, *Acta Crystallogr. C*, 2015, **71**, 3–8.
- 282 G. M. Sheldrick, *Acta Crystallogr. A*, 2015, **71**, 3–8.
- 283 O. V. Dolomanov, L. J. Bourhis, R. J. Gildea, J. A. K. Howard and H. Puschmann, *J. Appl. Crystallogr.*, 2009, **42**, 339–341.
- 284 C. F. Macrae, I. Sovago, S. J. Cottrell, P. T. A. Galek, P. McCabe, E. Pidcock, M. Platings, G. P. Shields, J. S. Stevens, M. Towler and P. A. Wood, *J. Appl. Crystallogr.*, 2020, **53**, 226–235.
- 285 F. Neese, *Wiley Interdiscip. Rev. Comput. Mol. Sci.*, 2022, **12**, e1606.
- 286 C. Adamo and V. Barone, *J. Chem. Phys.*, 1999, **110**, 6158–6170.
- 287 D. Andrae, U. H. Iubermann, M. Dolg, H. Stoll and H. Preub, *Theor. Chim. Acta*, 1990, **77**, 123–141.
- 288 F. Weigend and R. Ahlrichs, *Phys. Chem. Chem. Phys.*, 2005, **7**, 3297–3305.
- 289 F. Weigend, *Phys. Chem. Chem. Phys.*, 2006, **8**, 1057.
- 290 E. F. Pettersen, T. D. Goddard, C. C. Huang, G. S. Couch, D. M. Greenblatt, E. C. Meng and T. E. Ferrin, *J. Comput. Chem.*, 2004, **25**, 1605–1612.